ΕΘΝΙΚΟ ΜΕΤΣΟΒΙΟ ΠΟΛΥΤΕΧΝΕΙΟ

ΣΧΟΛΗ ΠΟΛΙΤΙΚΩΝ ΜΗΧΑΝΙΚΩΝ
ΤΟΜΕΑΣ ΓΕΩΤΕΧΝΙΚΗΣ

NATIONAL TECHNICAL UNIVERSITY OF ATHENS

SCHOOL OF CIVIL ENGINEERING
GEOTECHNICAL DEPARTMENT

Διδακτορική Διατριβή

Αντισεισμικός σχεδιασμός με κριτήρια επιτελεστικότητας και μέθοδοι ενίσχυσης θεμελιώσεων σε ρευστοποιήσιμα εδάφη

PhD Thesis

Performance based design and soil improvement methods of shallow foundations on liquefiable soils

Βασιλική Ε. Δημητριάδη
Πολιτικός Μηχανικός

Vasiliki E. Dimitriadi
Civil Engineer

Επιβλέπων Καθηγητής
Γιώργος Μπουκοβάλας

Supervisor
George Bouckovalas

Αθήνα, 2014

Athens, 2014

ΕΘΝΙΚΟ ΜΕΤΣΟΒΙΟ ΠΟΛΥΤΕΧΝΕΙΟ
ΣΧΟΛΗ ΠΟΛΙΤΙΚΩΝ ΜΗΧΑΝΙΚΩΝ
ΤΟΜΕΑΣ ΓΕΩΤΕΧΝΙΚΗΣ

ΑΝΤΙΣΕΙΣΜΙΚΟΣ ΣΧΕΔΙΑΣΜΟΣ ΜΕ ΚΡΙΤΗΡΙΑ ΕΠΙΤΕΛΕΣΤΙΚΟΤΗΤΑΣ ΚΑΙ ΜΕΘΟΔΟΙ ΕΝΙΣΧΥΣΗΣ ΘΕΜΕΛΙΩΣΕΩΝ ΣΕ ΡΕΥΣΤΟΠΟΙΗΣΙΜΑ ΕΔΑΦΗ

ΔΙΔΑΚΤΟΡΙΚΗ ΔΙΑΤΡΙΒΗ

Βασιλικής Ε. Δημητριάδη

Διπλωματούχου Πολιτικού Μηχανικού Ε.Μ.Π., M.Sc.

Η διατριβή υποβλήθηκε στη Σχολή Πολιτικών Μηχανικών του Εθνικού Μετσόβιου Πολυτεχνείου προς εκπλήρωση των προϋποθέσεων του τίτλου του Διδάκτορος Μηχανικού.

ΤΡΙΜΕΛΗΣ ΣΥΜΒΟΥΛΕΥΤΙΚΗ ΕΠΙΤΡΟΠΗ:

1. Γ. ΜΠΟΥΚΟΒΑΛΑΣ, Καθηγητής Ε.Μ.Π. (Επιβλέπων)
2. Μ. ΚΑΒΒΑΔΑΣ, Αν. Καθηγητής Ε.Μ.Π.
3. ΑΧ. ΠΑΠΑΔΗΜΗΤΡΙΟΥ, Επ. Καθηγητής Παν. Θεσσαλίας

ΕΠΤΑΜΕΛΗΣ ΕΞΕΤΑΣΤΙΚΗ ΕΠΙΤΡΟΠΗ:

1. Γ. ΜΠΟΥΚΟΒΑΛΑΣ, Καθηγητής Ε.Μ.Π. (Επιβλέπων)
2. Μ. ΚΑΒΒΑΔΑΣ, Αν. Καθηγητής Ε.Μ.Π.
3. ΑΧ. ΠΑΠΑΔΗΜΗΤΡΙΟΥ, Επ. Καθηγητής Παν. Θεσσαλίας
4. Χ. ΓΑΝΤΕΣ, Καθηγητής Ε.Μ.Π.
5. Ι. ΨΥΧΑΡΗΣ, Αν. Καθηγητής Ε.Μ.Π.
6. Β. ΓΕΩΡΓΙΑΝΝΟΥ, Αν. Καθηγήτρια Ε.Μ.Π.
7. Γ. ΜΥΛΩΝΑΚΗΣ, Καθηγητής Παν. Πατρών

Ευρωπαϊκή Ένωση
Ευρωπαϊκό Κοινωνικό Ταμείο
ΕΠΙΧΕΙΡΗΣΙΑΚΟ ΠΡΟΓΡΑΜΜΑ ΕΚΠΑΙΔΕΥΣΗ ΚΑΙ ΔΙΑ ΒΙΟΥ ΜΑΘΗΣΗ
επένδυση στην κοινωνία της γνώσης
ΥΠΟΥΡΓΕΙΟ ΠΑΙΔΕΙΑΣ ΚΑΙ ΘΡΗΣΚΕΥΜΑΤΩΝ
ΕΙΔΙΚΗ ΥΠΗΡΕΣΙΑ ΔΙΑΧΕΙΡΙΣΗΣ
Με τη συγχρηματοδότηση της Ελλάδας και της Ευρωπαϊκής Ένωσης
ΕΣΠΑ 2007-2013
ΕΥΡΩΠΑΪΚΟ ΚΟΙΝΩΝΙΚΟ ΤΑΜΕΙΟ

Η παρούσα έρευνα έχει συγχρηματοδοτηθεί από την Ευρωπαϊκή Ένωση (Ευρωπαϊκό Κοινωνικό Ταμείο - ΕΚΤ) και από εθνικούς πόρους μέσω του Επιχειρησιακού Προγράμματος «Εκπαίδευση και Δια Βίου Μάθηση» του Εθνικού Στρατηγικού Πλαισίου Αναφοράς (ΕΣΠΑ) – Ερευνητικό Χρηματοδοτούμενο Έργο: Ηράκλειτος ΙΙ. Επένδυση στην κοινωνία της γνώσης μέσω του Ευρωπαϊκού Κοινωνικού Ταμείου.

NATIONAL TECHNICAL UNIVERSITY OF ATHENS

SCHOOL OF CIVIL ENGINEERING

GEOTECHNICAL DEPARTMENT

PERFORMANCE BASED DESIGN AND SOIL IMPROVEMENT METHODS OF SHALLOW FOUNDATIONS ON LIQUEFIABLE SOILS

PhD THESIS by

Vasiliki E. Dimitriadi

Civil Engineer N.T.U.A., M.Sc.

The thesis is submitted to the School of Civil Engineering of the National Technical University of Athens in fulfilment of the requirements for the Degree of Doctor of Philosophy

ADVISORY COMMITTEE:

1. G. BOUCKOVALAS, Professor N.T.U.A. (Supervisor)
2. M. KAVVADAS, Associate Professor N.T.U.A.
3. Ach. PAPADIMITRIOU, Assistant Professor, Univ. of Thessaly

EXAMINATION COMMITTEE:

1. G. BOUCKOVALAS, Professor N.T.U.A. (Supervisor)
2. M. KAVVADAS, Associate Professor N.T.U.A.
3. Ach. PAPADIMITRIOU, Assistant Professor, Univ. of Thessaly
4. Ch. GANTES, Professor, N.T.U.A.
5. I. PSYCHARIS, Assist. Professor, N.T.U.A.
6. V. GEORGIANNOU, Assist. Professor N.T.U.A.
7. G. MYLONAKIS, Professor, Univ. of Patras

European Union
European Social Fund

OPERATIONAL PROGRAMME EDUCATION AND LIFELONG LEARNING
investing in knowledge society
MINISTRY OF EDUCATION & RELIGIOUS AFFAIRS
MANAGING AUTHORITY
Co- financed by Greece and the European Union

NSRF 2007-2013
EUROPEAN SOCIAL FUND

This research has been co-financed by the European Union (European Social Fund – ESF) and Greek national funds through the Operational Program "Education and Lifelong Learning" of the National Strategic Reference Framework (NSRF) - Research Funding Program: Heracleitus II. Investing in knowledge society through the European Social Fund.

Ευχαριστίες

«*Άδειο ποτήρι η ζωή,*
ή το γεμίζεις ή σε κόβει» [1]

Έχω ακούσει το αντίστοιχο τραγούδι πολλές φορές, αλλά η σημερινή ήταν που ο συγκεκριμένος στίχος ήχησε στο μυαλό μου περίεργα και με έκανε να σκεφτώ τη δική μου ζωή.

Διαπίστωσα λοιπόν, ότι ένα σημαντικό κομμάτι αυτής είναι αφιερωμένο στην εκπόνηση της παρούσας διδακτορικής διατριβής. Οι αρχικοί λόγοι που με οδήγησαν να ξεκινήσω διδακτορικό δεν έχουν πολλή σημασία πια, καθώς έχουν αλλάξει μέσα στο πέρασμα του χρόνου. Σίγουρα όμως, η στάση απέναντι στην έρευνα του κ. Γιώργου Μπουκοβάλα υπήρξε ένα ισχυρό ερέθισμα για να ξεκινήσω. Με βοήθησε να αναπτύξω περαιτέρω τις δεξιότητές μου, αλλά και να εξερευνήσω νέες. Οι πρωτοπόρες και φρέσκιες ιδέες του στην αντιμετώπιση και ερμηνεία πολύπλοκων φαινομένων, η συστηματικότητα της δουλειάς, η επιμονή, η διεισδυτικότητα της σκέψης του, είναι ένα μικρό μόνο δείγμα των χαρακτηριστικών που διαθέτει. Οι συμβουλές του ήταν πάντα μικρές φωτιές στο σκοτάδι, πολύτιμες και καθοδηγητικές κάθε φορά που συναντούσα αδιέξοδα. Η παρουσία του ήταν συνεχής καθόλη τη διάρκεια εκπόνησης της διατριβής, όχι μόνο σε ερευνητικό επίπεδο, αλλά όταν η ανελέητη γραφειοκρατία έβαζε φρένο στην ερευνητική διαδικασία και δηλητηρίαζε την όρεξη για έρευνα. Εκείνος ήταν εκεί, σε ανθρώπινο προπαντώς επίπεδο, για να μου υπενθυμίσει ότι χρειάζεται συνεχή αγώνα και προσήλωση στο στόχο. Ότι τελικά, σημασία έχει η ποιότητα της δουλειάς, το ήθος του χαρακτήρα, και η αξιοπρεπής στάση.

Θα ήθελα στη συνέχεια, να εκφράσω και τις ειλικρινείς μου ευχαριστίες προς τα υπόλοιπα μέλη της Τριμελούς Συμβουλευτικής Επιτροπής, τον κ. Μιχάλη Καββαδά, αναπληρωτή καθηγητή Ε.Μ.Π. και τον κ. Αχιλλέα Παπαδημητρίου, Επίκουρο καθηγητή στο Πανεπιστήμιο Θεσσαλίας, για το ενδιαφέρον τους και την αμέριστη βοήθεια και καθοδήγηση, οποτεδήποτε και αν τη χρειάστηκα. Επίσης, θα ήθελα να ευχαριστήσω και τα υπόλοιπα μέλη της Επταμελούς Εξεταστικής Επιτροπής, τους κ. Ι. Ψυχάρη και Χ. Γαντέ, Καθηγητές Ε.Μ.Π., τον Γ. Μυλωνάκη, Καθηγητή στο Πανεπιστήμιο Πατρών και στο Πανεπιστήμιο του Bristol, καθώς και τον Ν. Γερόλυμο, Επίκουρο Καθηγητή Ε.Μ.Π. για τη συμβολή τους στην τελική διαμόρφωση της παρούσας εργασίας.

Οφείλω επίσης να αναφερθώ στα υπόλοιπα μέλη της ερευνητικής ομάδας, Αχιλλέα Παπαδημητρίου, Κώστα Ανδριανόπουλο, Γιώργο Κουρετζή, Δημήτρη Καραμήτρο, Ιουλία Σοφιανού, Αλέξανδρο Βαλσαμή, Γιάννη Χαλούλο, και Γιάννη Τσιάπα. Ο καθένας με τον τρόπο του, συνέβαλε στην εξέλιξη της διατριβής. Όλοι μου δίδαξαν και από κάτι

[1] Τίτλος τραγουδιού: Απ'τα κρυμμένα να σωθείς
Στίχοι – μουσική: Κώστας Καλδάρας
1η εκτέλεση: Μελίνα Κανά.

διαφορετικό, και με έκαναν να αισθανθώ αναπόσπαστο κομμάτι μιας ζωντανής και δημιουργικής ομάδας. Ευχαριστώ επίσης και τους φοιτητές με τους οποίους συνεργαστήκαμε στα πλαίσια των διπλωματικών εργασιών, τις οποίες συνεπέβλεψα με τον κ. Γιώργο Μπουκοβάλα. Ο Γιάννης, η Αλεξάνδρα και ο Αργύρης υπήρξαν πολύτιμοι συνεργάτες, οι οποίοι διευκόλυναν και επιτάχυναν τη ροή της έρευνας.

Και επειδή στην έρευνα υπάρχουν πάντα ανατροπές η έγκαιρη επανάληψη των παραμετρικών αριθμητικών αναλύσεων δεν θα ήταν εφικτή χωρίς την πολύτιμη βοήθεια των Καθηγητών του Ε.Μ.Π. κ. κ. Χάρη Γαντέ και Γιάννη Ψυχάρη, των Υποψήφιων Διδακτόρων Βασίλη Μελισσιανό και Γιάννη Καλυβιώτη, καθώς και του Δρ. Δημήτριου Σαργιώτη, Υπεύθυνου του εργαστηρίου Ηλεκτρονικών Υπολογιστών της Σχολής Πολιτικών Μηχανικών. Η άμεση ανταπόκρισή τους στις συνθήκες έκτακτης ανάγκης που βρέθηκα και η αμέριστη βοήθειά τους διευκόλυναν σημαντικά αυτή την επίπονη και αγχωτική διαδικασία.

Τα χρόνια που πέρασα στον Τομέα Γεωτεχνικής, έχω ήδη αρχίσει να τα αναπολώ. Ζώντας μακριά απο την οικογένειά μου, αισθάνομαι κομμάτι μιας δεύτερης ιδιότυπης οικογένειας. Σε κάθε ευκαιρία, μοιραζόμασταν στο ίδιο τραπέζι, φαγητό, κρασί, προβληματισμούς, αστεία, τις ζωές μας. Ακόμα κι αν οι υποχρεώσεις μας δεν επέτρεπαν την καθημερινή επικοινωνία, πάντα υπήρχαν οι θρυλικές ραδιοφωνικές βραδιές του Rock Pourri, οι βραδιές barbeque, και τόσες άλλες στιγμές, που μας έχουν αφήσει ανεξίτηλες αναμνήσεις.

Η εκπόνηση διδακτορικού είναι μια πορεία αρκετά μοναχική, σε απομακρύνει από οικογένεια, φίλους, και αγαπημένα πρόσωπα. Απέναντι σε αρκετούς από αυτούς τους ανθρώπους δεν υπήρξα τόσο συνεπής όσο θα έπρεπε. Τους ευχαριστώ για την υπομονή και τη σιωπηλή τους συμπαράσταση.

Κατά την περίοδο του διδακτορικού, υπήρξαν ευχάριστες και στενάχωρες στιγμές. Επιτυχίες, αλλά και πολλές περισσότερες αποτυχίες. Αξιόλογοι συνεργάτες, οι οποίοι εξελιχθήκαν και σε καλούς φίλους. Άνθρωποι που στάθηκαν και άλλοι που προχώρησαν. Και όλα αυτά νομίζω γεμίζουν το ποτήρι...

Κική Δημητριάδη, Φεβρουάριος 2014.

Διδακτορική Διατριβή

Αντισεισμικός σχεδιασμός με κριτήρια επιτελεστικότητας και μέθοδοι ενίσχυσης επιφανειακών θεμελιώσεων σε ρευστοποιήσιμα εδάφη.

Performance based design and soil improvement methods of shallow foundations on liquefiable soils.

Βασιλικής Δημητριάδη

ΕΚΤΕΝΗΣ ΠΕΡΙΛΗΨΗ

I Περιγραφή του προβλήματος

Σύμφωνα με τους ισχύοντες αντισεισμικούς κανονισμούς, η κατασκευή τεχνικών έργων με επιφανειακή θεμελίωση σε περιοχές με κίνδυνο εκδήλωσης ρευστοποίησης λόγω σεισμού, είναι εκ προοιμίου μη αποδεκτή χωρίς την προηγούμενη βελτίωση του εδάφους. Αυτό γιατί, η εκδήλωση ρευστοποίησης προκαλεί σημαντική απομείωση της διατμητικής αντοχής του εδάφους, η οποία οδηγεί στη συσσώρευση δυναμικών καθιζήσεων, καθώς και την απομείωση της μετασεισμικής φέρουσας ικανότητας της θεμελίωσης έως και την αστοχία. Αντιπροσωπευτικά παραδείγματα των καταστρεπτικών αυτών επιπτώσεων σε περιπτώσεις κατασκευών με επιφανειακή θεμελίωση, παρουσιάζονται στην **Εικόνα 1**.

Η ισχύουσα φιλοσοφία σχεδιασμού στις συγκεκριμένες εδαφικές συνθήκες, περιλαμβάνει τη θεμελίωση των τεχνικών έργων με τη χρήση πασσάλων, οι οποίοι παρακάμπτουν το ρευστοποιήσιμο στρώμα και μεταφέρουν τα φορτία της κατασκευής σε βαθύτερες, μη-ρευστοποιήσιμες εδαφικές στρώσεις. Παράλληλα, για την απομείωση των προκαλούμενων ροπών στους πασσάλους, το περιβάλλον έδαφος συχνά βελτιώνεται με τη χρήση δυναμικής συμπύκνωσης, καθώς και χρήση χαλικοπασσάλων/στραγγιστηρίων. Τα μέτρα αυτά αποτρέπουν την ανάπτυξη υψηλών επιπέδων υδατικών υπερπιέσεων πόρων και συνεπώς την εκδήλωση ρευστοποίησης.

Εικόνα 1: Περιπτώσεις αστοχιών επιφανειακών θεμελιώσεων λόγω ρευστοποίησης, σε 4 μεγάλους σεισμούς (a) Dagupan, Philippines, 1990, M=7.8, (b) Kobe, Japan, 1995, M=7.2 (c) Adapazari, Turkey (1999) M=7.4, (d) Sendai, Japan, 2011 M=8.9.

Η ανωτέρω πρακτική σχεδιασμού εφαρμόζεται ακόμα και σε περιπτώσεις, όπου η παρουσία μιας μη-ρευστοποιήσιμης κρούστας ικανών διαστάσεων και αντοχής θα μετρίαζε τις ανωτέρω επιπτώσεις της ρευστοποίησης, εξασφαλίζοντας την ικανοποιητική σεισμική συμπεριφορά της θεμελίωσης. Μάλιστα, σημαντικές σε πρωτοτυπία πειραματικές έρευνες, αλλά και παρατηρήσεις από ιστορικά περιστατικά [Liu & Dobry, (1997), Hausler & Sitar (2001), Hausler et al.(2002), Adalier et al. (2003), Dashti et al. (2010), Sitar & Hausler, (2012)] υποδεικνύουν την ευεργετική παρουσία μιας επιφανειακής μη-ρευστοποιήσιμης εδαφικής κρούστας στην απομείωση των σεισμικών καθιζήσεων και τη συνολικά αποδεκτή συμπεριφορά της θεμελίωσης.

Πρωτοπόροι στην πειραματική διερεύνηση του προβλήματος υπήρξαν οι Liu & Dobry (1997), οι οποίοι διεξήγαγαν μια σειρά πειραμάτων σε φυγοκεντριστή, με σκοπό να διερευνήσουν την επίδραση μιας επιφανειακής ζώνης συμπυκνωμένης άμμου, επί μη-βελτιωμένου ρευστοποιήσιμου εδάφους, στη σεισμική απόκριση επιφανειακών

θεμελιώσεων. Σκοπός ήταν η διερεύνηση του μηχανισμού ανάπτυξης των δυναμικών καθιζήσεων, αλλά και η αξιολόγηση της σεισμικής απόκρισης της θεμελίωσης σε όρους επιβαλλόμενων επιταχύνσεων. Συγκεκριμένα, στα πέντε πειράματα, που πραγματοποιήθηκαν, εξετάστηκε η επίδραση του βάθους της ζώνης του συμπυκνωμένου εδάφους από μηδενικό πάχος (δηλαδή απευθείας έδραση της θεμελίωσης στο ρευστοποιήσιμο έδαφος) έως και το συνολικό πάχος της ρευστοποιήσιμης στρώσης, όπως παρουσιάζεται στο **Σχήμα 1**. Αναφέρεται ότι η εν λόγω σειρά πειραμάτων διεξήχθη σε φυγοκεντρική επιτάχυνση ίση με 80g. Συνεπώς, με βάση του νόμους κλίμακας, οι οποίοι διέπουν τα πειράματα σε φυγοκεντριστή, οι πρωτότυπες διαστάσεις του θεμελίου είναι 4.56m, ενώ το πάχος της ρευστοποιήσιμης άμμου 12.5m.

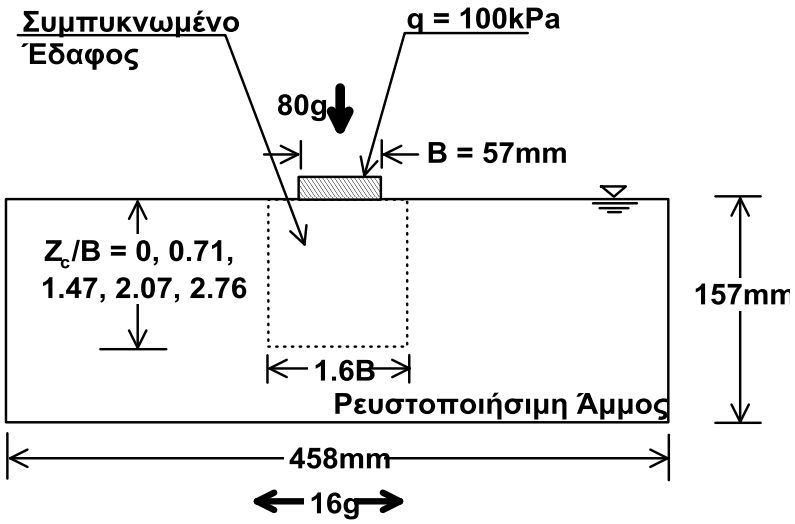

Σχήμα 1: Πειραματική διάταξη πειραμάτων Liu & Dobry (1997) με τις αντίστοιχες διαστάσεις υπό κλίμακα.

Τα αποτελέσματα των πειραμάτων των Liu & Dobry (1997), συνοψίζονται στο **Σχήμα 2**, απ' όπου διαπιστώνεται η ευεργετική επίδραση της βελτιωμένης κρούστας εδάφους στη μείωση των σεισμικών καθιζήσεων. Αντίθετα, η επέκταση της βελτιωμένης ζώνης έως το συνολικό βάθος της ρευστοποιήσιμης στρώσης έχει ως αποτέλεσμα την ενίσχυση της σεισμικής κίνησης και τη μετάδοση σημαντικών επιταχύνσεων στην εδαφική επιφάνεια και συνεπώς την επιπρόσθετη καταπόνηση της θεμελίωσης.

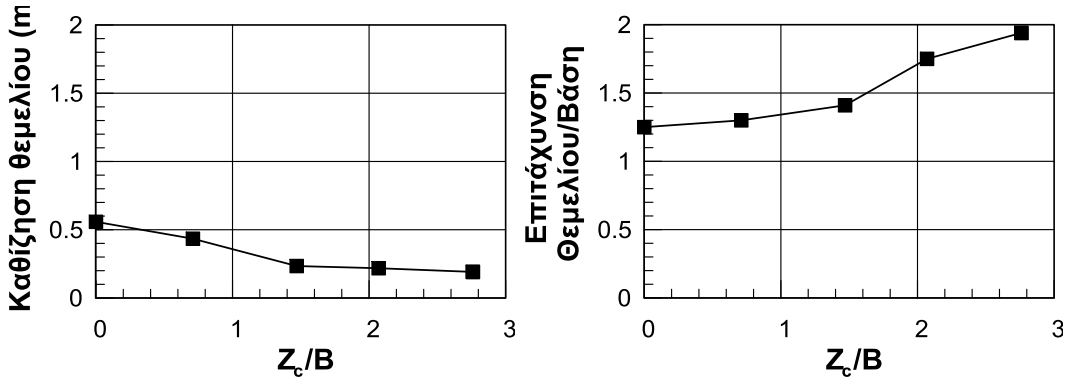

Σχήμα 2: Αποτελέσματα δυναμικών καθιζήσεων (αριστερά) και επιταχύνσεων (δεξιά) από τα πειράματα σε φυγοκεντριστή των Liu & Dobry (1997).

Σε αντίστοιχα συμπεράσματα κατάληξαν και οι Adalier et al. (2003), οι οποίοι εξέτασαν την επίδραση των χαλικοπασσάλων στη σεισμική απόκριση μιας κορεσμένης ιλυώδους εδαφικής στρώσης, αρχικά υπό συνθήκες ελεύθερου πεδίου, και στη συνέχεια υπό την παρουσία μια επιφανειακή θεμελίωσης. Οι τέσσερεις συνολικά πειραματικές διατάξεις υποβλήθηκαν σε μια σειρά τριών αλλεπάλληλων σεισμικών διεγέρσεων. Η δεύτερη ομάδα πειραμάτων, η οποία εξετάζει την σεισμική συμπεριφορά της επιφανειακής θεμελίωσης, περιγράφεται στο **Σχήμα 3** και παρουσιάζει και το μεγαλύτερο ενδιαφέρον.

Από τα αποτελέσματα των δοκιμών, αποδεικνύεται ότι η παρουσία των χαλικοπασσάλων καθυστερεί την ανάπτυξη των υδατικών υπερπιέσεων εντός του βελτιωμένου εδάφους, και συνεπώς αυξάνει τη διατμητική αντοχή του εδάφους θεμελίωσης, μειώνοντας έτσι τις δυναμικές καθιζήσεις. Προς επιβεβαίωση της εν λόγω παρατήρησης, οι δυναμικές καθιζήσεις της θεμελίωσης κατά τη διάρκεια των τριών σεισμικών διεγέρσεων, πριν και μετά την εγκατάσταση των χαλικοπασσάλων, παρουσιάζονται στο **Σχήμα 4**. Επιπρόσθετα, σύμφωνα με τους Adalier et al. (2003), ενδιαφέρον παρουσιάζει και η κατανομή των υδατικών υπερπιέσεων, οι οποίες είναι χαμηλότερες κάτω από τη θεμελίωση και αυξάνονται με το βάθος και την απόσταση από αυτή.

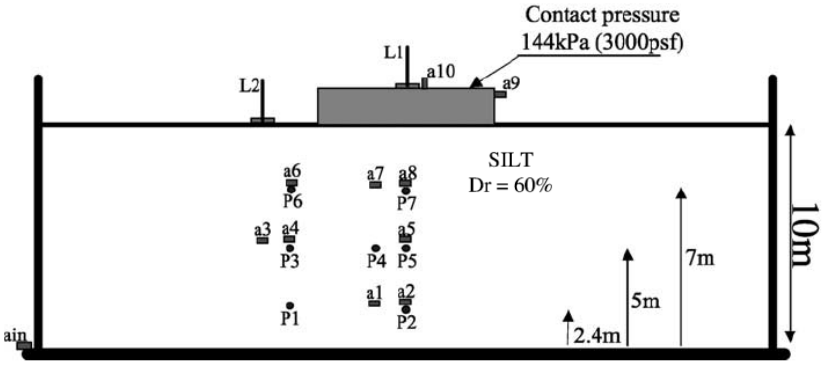

(α)

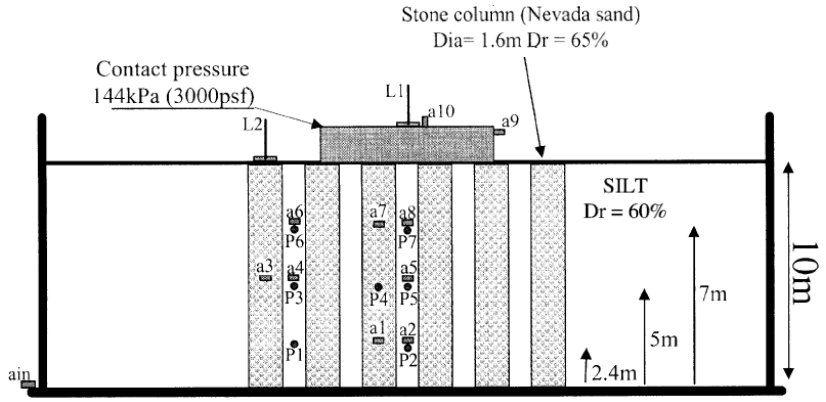

(β)

Σχήμα 3: Πειραματικές διατάξεις των Adalier et al. (2003), για την εξέταση της επίδρασης των χαλικοπασσάλων στη σεισμική απόκριση μιας επιφανειακής θεμελίωσης – **(α)** απευθείας έδραση του θεμελίου στην ιλυώδη στρώση **(β)** βελτίωση του εδάφους με χαλικοπασσάλους.

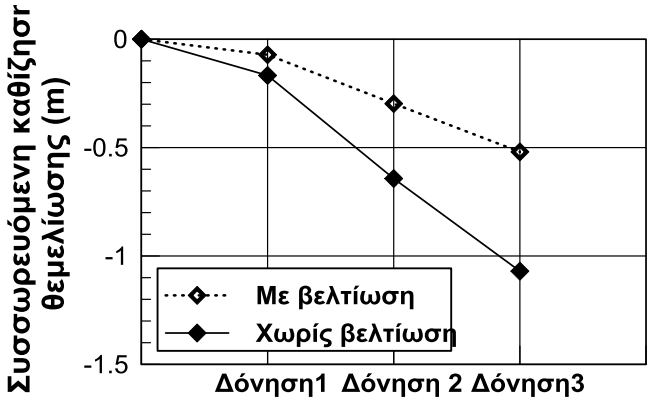

Σχήμα 4: Επίδραση των χαλικοπασσάλων στις συσσωρευόμενες καθιζήσεις λόγω σεισμού, Adalier et al. (2003).

Ακόμα πιο πρόσφατα, οι Dashti et al. (2010) αναγνώρισαν την αδυναμία εφαρμογής των υπαρχουσών εμπειρικών μεθόδων υπολογισμού των καθιζήσεων λόγω ρευστοποίησης, στην περίπτωση κτιρίων με άκαμπτη επιφανειακή θεμελίωση, με δεδομένο ότι αυτές αναφέρονται κατά κύριο λόγο σε συνθήκες ελεύθερου πεδίου. Τόνισαν επίσης, την ανάγκη δημιουργίας ενός νέου κανονιστικού πλαισίου για τον υπολογισμό των δυναμικών καθιζήσεων επιφανειακών θεμελιώσεων σε ρευστοποιήσιμα εδάφη, το οποίο να ενσωματώνει του κυρίαρχους μηχανισμούς που διέπουν το φαινόμενο.

Στα πειράματα σε φυγοκεντριστή, τα οποία πραγματοποίησαν, εξετάζεται η σεισμική απόκριση κτιρίων, εδραζόμενων μέσω άκαμπτων επιφανειακών θεμελιώσεων, σε σχετικά λεπτές στρώσεις ρευστοποιήσιμης άμμου. Η πειραματική διάταξη παρουσιάζεται στο **Σχήμα 5**. Η αξιολόγηση των αποτελεσμάτων πραγματοποιείται σε όρους καθιζήσεων, επιβαλλόμενων επιταχύνσεων και ανάπτυξης υπερπιέσεων πόρων. Από τα βασικότερα συμπεράσματα είναι ότι η έναρξη συσσώρευσης, καθώς και ο ρυθμός και το μέγεθος των σεισμικών καθιζήσεων είναι άμεση συνάρτηση της έντασης της σεισμικής διέγερσης. Παράλληλα, η σχετική πυκνότητα της ρευστοποιήσιμης άμμου διαδραματίζει σημαντικό ρόλο, καθώς ελέγχει την ανάπτυξη των υπερπιέσεων πόρων καθώς και το μέγεθος των καθιζήσεων και των επιταχύνσεων, οι οποίες μεταδίδονται στην εδαφική επιφάνεια και στην ίδια την κατασκευή.

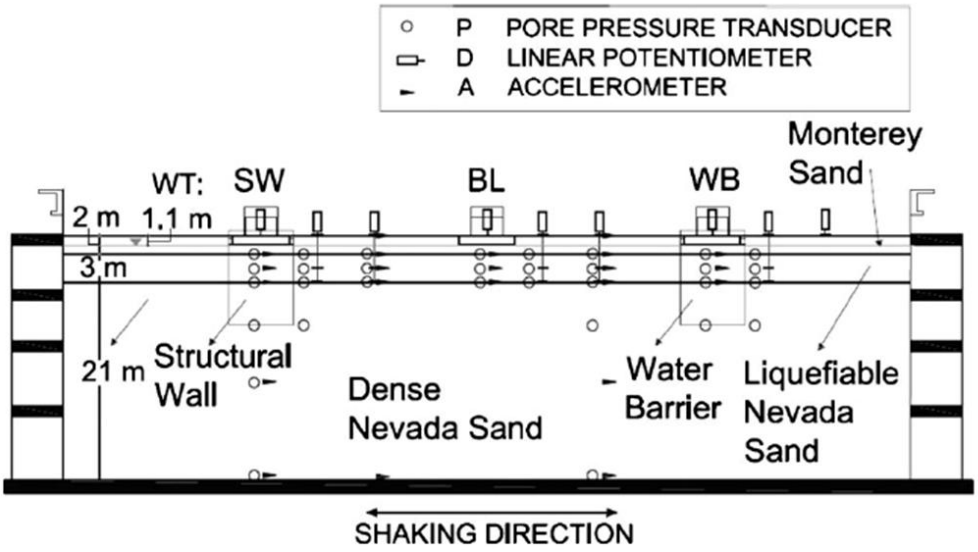

Σχήμα 5: Πειραματική διάταξη των δοκιμών σε φυγοκεντριστή των Dashti et al. (2010).

Παρ' όλες τις ανωτέρω εξαιρετικά σημαντικές και διαφωτιστικές πειραματικές εργασίες, δεν υφίσταται σήμερα μια ολοκληρωμένη μεθοδολογία σχεδιασμού επιφανειακών θεμελιώσεων σε ρευστοποιήσιμα εδάφη με περιορισμένη (όχι καθολική) βελτίωση του ρευστοποιήσιμου εδάφους. Η διαπιστωμένη αυτή έλλειψη συχνά οδηγεί το μηχανικό σε υπερ-συντηρητικές λύσεις με σημαντική επιβάρυνση του συνολικού κόστους κατασκευής του έργου. Προς αυτή την κατεύθυνση, οι Karamitros et al. (2013α&β), ανέπτυξαν την πρώτη απλοποιημένη αναλυτική μεθοδολογία για τον υπολογισμό των σεισμικών καθιζήσεων (ρ_{dyn}) καθώς και της απομειωμένης φέρουσας ικανότητας επιφανειακών θεμελιώσεων (q_{ult}^{deg}), εδραζόμενων σε μια μη-ρευστοποιήσιμη κρούστα εδάφους. Η εν λόγω μεθοδολογία όμως, αναφέρεται σε μια φυσική αργιλική κρούστα εδάφους επί ρευστοποιήσιμης άμμου. Δεν καλύπτει δηλαδή την περίπτωση στην οποία η ρευστοποιήσιμη άμμος εκτείνεται έως την επιφάνεια του εδάφους και επομένως η μη ρευστοποίησιμη κρούστα θα πρέπει να δημιουργηθεί τεχνητά. (π.χ. με δυναμική συμπύκνωση και στραγγιστήρια).

II Σκοπός της διατριβής

Με σκοπό την κάλυψη του εν λόγω κενού, η παρούσα διατριβή πραγματεύεται **την ανάπτυξη μιας ολοκληρωμένης μεθοδολογίας σχεδιασμού επιφανειακών θεμελιώσεων μεγάλου μήκους (πεδιλοδοκών) σε ρευστοποιήσιμα εδάφη, με περιορισμένο βάθος και πλάτος βελτίωσης, λαμβάνοντας υπόψη κριτήρια επιτελεστικότητας (καθιζήσεων και φέρουσας ικανότητας).**

Σύμφωνα με τη νέα μεθοδολογία, τα βασικά στάδια σχεδιασμού περιλαμβάνουν:

- Τον υπολογισμό της πυκνότητας του καννάβου των χαλικοπασσάλων και των διαστάσεων (βάθος και πλάτος), στις οποίες θα πρέπει να επεκταθεί η βελτίωση του εδάφους, καθώς και των απαιτούμενων τεχνικών προδιαγραφών.
- Τον υπολογισμό της απομειωμένης (αμέσως μετά το πέρας της σεισμικής δόνησης) στατικής φέρουσας ικανότητας της θεμελίωσης.
- Τον υπολογισμό των καθιζήσεων οι οποίες συσσωρεύονται κατά τη διάρκεια της δόνησης.

Οι βασικές διαφορές της εν λόγω μεθοδολογίας με αυτή των Karamitros et al. (2013) για αργιλική κρούστα εδάφους, οι οποίες κατέστησαν αναγκαία την εκπόνηση της παρούσας διδακτορικής διατριβής, συνοψίζονται στα εξής:

- Στην παρούσα διατριβή, η επιφανειακή κρούστα μη ρευστοποιήσιμου εδάφους έχει προέλθει από τη βελτίωση της ρευστοποιήσιμης άμμου με βαθιά δονητική συμπύκνωση και χαλικοπασσάλους και συνεπώς είναι διαπερατή.
- Λόγω της ανωτέρω ιδιότητας, κατά τη διάρκεια της σεισμικής δόνησης αναπτύσσονται εντός της κρούστας ελεγχόμενες, και προκαθορισμένες από το σχεδιασμό, υδατικές υπερπιέσεις, οι οποίες οδηγούν αναπόφευκτα σε μερική απώλεια διατμητικής αντοχής.
- Κατ' επέκταση του ανωτέρου, μεταξύ της βελτιωμένης κρούστας και του φυσικού εδάφους δημιουργείται μια μεταβατική ζώνη με μερικώς ρευστοποιημένο έδαφος, η οποία θα πρέπει επίσης να ληφθεί υπόψη στη διαστασιολόγηση του θεμελίου.
- Εκτός από το βάθος, η τεχνητή κρούστα βελτιωμένου εδάφους έχει πεπερασμένο πλάτος, το οποίο θα πρέπει να ληφθεί υπόψη ως ξεχωριστή παράμετρος στο σχεδιασμό.
- Τέλος, επειδή η μη ρευστοποιημένη κρούστα είναι τεχνητά διαμορφωμένη, υπεισέρχονται στη διαδικασία σχεδιασμού της και οικονομικο-τεχνικές παράμετροι.

III Επιμέρους Ερευνητικές Εργασίες

Ε.Ε.1. Βιβλιογραφική Αναδρομή

Όπως έχει προαναφερθεί, η τεχνητά διαμορφωμένη επιφανειακή κρούστα θα πρέπει να πληροί συγκεκριμένες προδιαγραφές κατασκευής, και να είναι σχεδιασμένη σύμφωνα με καλά τεκμηριωμένες μεθοδολογίες. Στα πλαίσια αυτά, στο *κεφάλαιο 2* της διδακτορικής διατριβής, παρουσιάζονται τα αποτελέσματα μιας εκτενούς αναδρομής στη διεθνή βιβλιογραφία, σχετικά με:

- **Προδιαγραφές κατασκευής χαλικοπασσάλων σε μη συνεκτικά εδάφη.-** Αναλυτικότερα, περιγράφονται και ταξινομούνται οι κυριότερες μέθοδοι κατασκευής, όπως φαίνεται στο **Σχήμα 6**, ενώ περιγράφεται και ο απαιτούμενος μηχανικός εξοπλισμός σε κάθε κατηγορία.

- **Προδιαγραφές υλικού, και μεθοδολογίες υπολογισμού των μηχανικών χαρακτηριστικών του βελτιωμένου εδάφους.-** Περιγράφονται οι ισχύουσες προδιαγραφές των χρησιμοποιούμενων υλικών για την κατασκευή των χαλικοπασσάλων (διαπερατότητα και κοκκομετρική διαβάθμιση). Παράλληλα, παρουσιάζονται εμπειρικά διαγράμματα προσδιορισμού των βελτιωμένων εδαφικών ιδιοτήτων λόγω της επιβαλλόμενης δόνησης κατά τη φάση κατασκευής των χαλικοπασσάλων (αριθμός SPT, σχετική πυκνότητα).

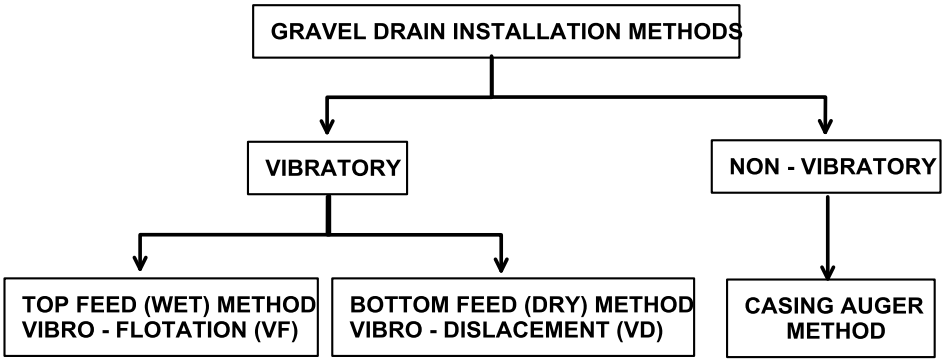

Σχήμα 6: Κατηγοριοποίηση διαθέσιμων μεθόδων κατασκευής χαλικοπασσάλων.

- **Μεθοδολογίες για τον υπολογισμό των υδατικών υπερπιέσεων λόγω σεισμού.-** Αναφέρονται οι απαραίτητες παράμετροι σχεδιασμού και στη συνέχεια περιγράφονται οι βασικότερες αναλυτικές μεθοδολογίες σχεδιασμού, οι οποίες λαμβάνουν υπόψη την αποστραγγιστική δράση των χαλικοπασσάλων. Εξ' αυτών ιδιαίτερη μνεία γίνεται εδώ στην πρόσφατα προταθείσα μεθοδολογία των Bouckovalas et al. (2009), η οποία και υιοθετήθηκε στην παρούσα διατριβή.

Συγκεκριμένα, οι Bouckovalas et al. (2009) επανεξέτασαν την μαθηματική έκφραση της ανάπτυξης υδατικών υπερπιέσεων r_U-N/N_L από τη θεωρία των Seed & Booker (1977). Σκοπός ήταν να ενσωματώσουν φαινόμενα συμπύκνωσης του εδαφικού σκελετού (shake-down effects), τα οποία αναπτύσσονται στο φυσικό έδαφος υπό ανακυκλιζόμενη φόρτιση και να αναθεωρήσουν τα υπάρχοντα διαγράμματα σχεδιασμού.

Οι γεωμετρικές διαστάσεις a και b, οι οποίες απαιτούνται για την χρήση των εν λόγω διαγραμμάτων εμφανίζονται στο **Σχήμα 7**, ενώ επιπλέον:

$$T_{ad} = \frac{k_s t_d}{m_{v,3} \gamma_w a^2} \qquad [1]$$

όπου k_s (m/sec) = η διαπερατότητα του εδάφους κατά την οριζόντια διεύθυνση

t_d (sec) = χρόνος δυναμικής φόρτισης

$m_{v,3}$ (1/kPa) = συντελεστής ογκομετρικής συμπιεστότητας

γ_w (kN/m^3) = ειδικό βάρος του νερού

a (m) = η ακτίνα του στραγγιστηρίου

Τα νέα προτεινόμενα διαγράμματα σχεδιασμού των Bouckovalas et al. (2009) παρουσιάζονται στο **Σχήμα 8**.

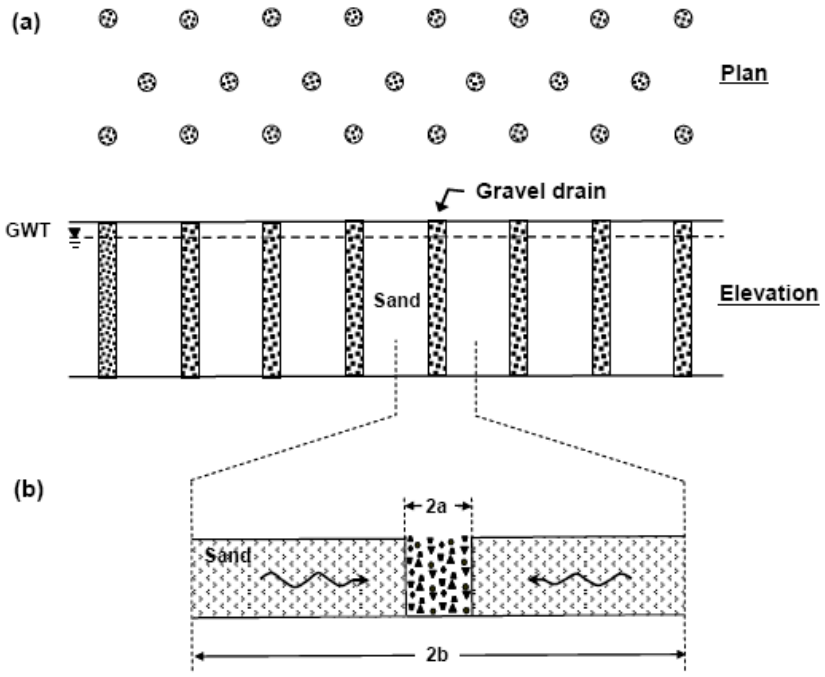

Σχήμα 7: **(a)** Κάτοψη και **(b)** τομή της διάταξης των χαλικοπασσάλων εντός ρευστοποιήσιμου εδάφους (Seed & Booker, 1977).

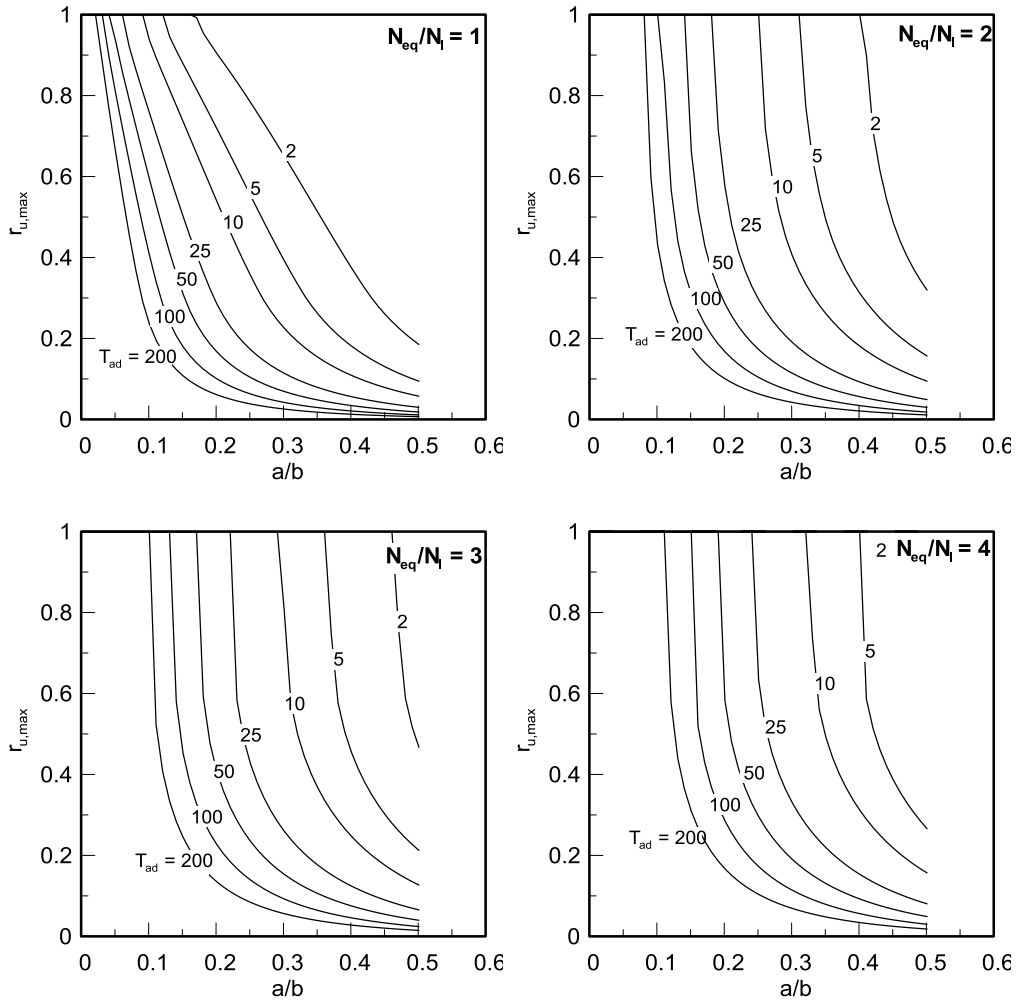

Σχήμα 8: Νέα διαγράμματα σχεδιασμού στραγγιστηρίων από τους Bouckovalas et al., 2009.

Εναλλακτικοί τύποι στραγγιστηρίων.- Η εγκατάσταση των χαλικοπασσάλων συνοδεύεται από σημαντική όχληση, ενώ ανάλογα με την μέθοδο εγκατάστασης παράγονται σημαντικές ποσότητες δυνητικά επικίνδυνων υλικών. Επιπρόσθετα, σύνηθες φαινόμενο κατά την εγκατάσταση, αλλά και την περίοδο λειτουργίας των χαλικοπασσάλων, αποτελεί η απόφραξή τους (γνωστή και ως clogging), η οποία αποδυναμώνει την αποστραγγιστική τους ικανότητα. Για την αντιμετώπιση αυτών των μειονεκτημάτων έχουν αναπτυχθεί εναλλακτικοί τύποι στραγγιστηρίων, όπως τα EQ-Drains και τα επονομαζόμενα Screen pipes. Στο *κεφάλαιο 3*, της διδακτορικής διατριβής αναφέρονται οι βασικές προδιαγραφές εξοπλισμού, εγκατάστασης και σχεδιασμού των νέων αυτών τεχνολογιών, ενώ παρουσιάζονται και τυπικά αποτελέσματα από την πειραματική αξιολόγηση και των δύο

ομάδων στραγγιστηρίων. Παράλληλα, πραγματοποιείται συγκριτική αξιολόγηση μεταξύ των νέων εναλλακτικών τύπων στραγγιστηρίων και των κλασσικών χαλικοπασσάλων.

Κριτήρια Επιτελεστικότητας.- Στο *κεφάλαιο 4* της διδακτορικής διατριβής, συνοψίζονται τα αποτελέσματα της βιβλιογραφικής αναδρομής σχετικά με την επικρατούσα φιλοσοφία σχεδιασμού με βάση κριτήρια επιτελεστικότητας (performance based design). Συγκεκριμένα, αναλύονται τα τρία βασικά στάδια στο σχεδιασμό γεφυρών και κτιρίων, τα οποία συνοψίζονται στα εξής:

- ***Σεισμικές δράσεις σχεδιασμού.-*** οι οποίες διαφέρουν ανάλογα με την κατηγορία της κατασκευής. Οι εν λόγω σεισμικές δράσεις χαρακτηρίζονται από μια πιθανότητα εκδήλωσης κατά της διάρκεια ζωής του έργου (ή την περίοδο επαναφοράς) και ποικίλουν ανάλογα με τη σεισμικότητα της περιοχής.
- ***Επίπεδα λειτουργικότητας.-*** τα οποία προσδιορίζουν την έκταση των βλαβών και την ποιότητα υπηρεσίας του τεχνικού έργου, μετά την εκδήλωση της σεισμικής δράσης σχεδιασμού.
- ***Επιτρεπόμενα όρια παραμορφώσεων.-*** τα οποία ποσοτικοποιούν σε όρους επιτρεπόμενων παραμορφώσεων τα ανωτέρω επίπεδα λειτουργικότητας, ανάλογα με τον τύπο και το υλικό κατασκευής του φέροντα οργανισμού. Από τη βιβλιογραφική έρευνα, διαπιστώθηκε ότι οι ισχύοντες Σεισμικοί Κώδικες δεν παρέχουν επαρκείς πληροφορίες σχετικά με επιτρεπόμενα όρια σεισμικών παραμορφώσεων, συνεπώς, τα όρια που παρουσιάζονται αφορούν τις επιτρεπόμενες τιμές υπό στατικές συνθήκες.

Τονίζεται ότι τα όρια των επιτρεπόμενων καθιζήσεων υπό στατικές συνθήκες που παρουσιάζονται, θα πρέπει να χρησιμοποιούνται με προσοχή, καθώς έχουν προκύψει υπό την παραδοχή ότι οι αντίστοιχες κατασκευές εδράζονται σε ομοιόμορφα αμμώδη ή αργιλικά εδάφη. Αυτό συνεπάγεται, ότι πολλές περιπτώσεις ανομοιογενών εδαφικών συνθηκών δεν περιγράφονται ικανοποιητικά, δυσχεραίνοντας έτσι τον καθορισμό επιτρεπόμενων τιμών καθιζήσεων. Σε αυτές τις περιπτώσεις, ο βαθμός ανομοιογένειας και η επίδρασή του στην κατασκευή θα πρέπει να καθορίζεται μέσω επί τόπου γεωτρήσεων και εργαστηριακών δοκιμών. Παράλληλα, οι επιτρεπόμενες παραμορφώσεις στους ισχύοντες κανονισμούς, αναφέρονται σε τυπικές κατασκευές, και επομένως η εφαρμογή τους σε κατασκευές με μη-ομοιόμορφα κατανεμημένο φορτίο έχει μικρότερη αξιοπιστία.

Ε.Ε.2. Μεθοδολογία Σχεδιασμού Χαλικοπασσάλων

Η βελτίωση του εδάφους έναντι ρευστοποίησης, επιτυγχάνεται με τη βοήθεια χαλικοπασσάλων και οφείλεται σε δύο βασικούς παράγοντες:

- τη συμπύκνωση των ρευστοποιήσιμων εδαφικών στρώσεων, κατά την δονητική κατασκευή των χαλικοπασσάλων, η οποία αποτιμάται με την βοήθεια εμπειρικών διαγραμμάτων τα οποία και αναζητήθηκαν στην διεθνή βιβλιογραφία.
- την ενεργοποίηση οριζόντιας ακτινικής στράγγισης εντός του ρευστοποιήσιμου εδάφους, η οποία οδηγεί σε μερική αποτόνωση των υδατικών υπερπιέσεων που προκαλεί η σεισμική δόνηση. Η συγκεκριμένη δράση έχει αποτελέσει αντικείμενο αναλυτικής διερεύνησης στο παρελθόν, από την οποία έχουν προκύψει μάλιστα και αντίστοιχα διαγράμματα σχεδιασμού [*π.χ. Seed & Booker (1977)*]. Ωστόσο, πειραματικές μετρήσεις έχουν δείξει ότι υπάρχει ανάγκη επανεξέτασης των παραδοχών των εν λόγω αναλυτικών λύσεων, με έμφαση στη βασική σχέση που περιγράφει την ανάπτυξη υδατικών υπερπιέσεων r_U-N/N_L.

Στο *κεφάλαιο 5* της διδακτορικής διατριβής, παρουσιάζονται αποτελέσματα δοκιμών ρευστοποίησης υπό ελεγχόμενη διατμητική παραμόρφωση, οι οποίες αποδίδουν με μεγαλύτερη ακρίβεια τις συνθήκες σεισμικής φόρτισης στη φύση. Οι εν λόγω εργαστηριακές δοκιμές εκτελέστηκαν στα πλαίσια του ερευνητικού προγράμματος *X-SOILS*[1], από την Αν. Καθηγήτρια του Ε.Μ.Π. κα Β. Γεωργιάννου. Με βάση αυτά, αποδεικνύεται ότι ο συντελεστής Α, στην παρακάτω σχέση υπολογισμού της υπερπίεσης πόρων (De Alba et al., 1975) μπορεί να λάβει μεγαλύτερες τιμές από το 0.7 που προτείνουν οι συγγραφείς.

$$\frac{u_g}{\sigma'_o} = \frac{2}{\pi}\sin^{-1}\left(\frac{N}{N_l}\right)^{\frac{1}{2A}} \qquad [2]$$

Μάλιστα, όπως παρουσιάζεται στο **Σχήμα 9**, οι προτεινόμενες τιμές του Α κυμαίνονται από Α = 1.40 – 2.00. Επίσης, αποδεικνύεται ότι η τιμή του Α εξαρτάται από τον τύπο της δοκιμής (ανακυκλική τριαξονική ή απευθείας διάτμηση), την τάση στερεοποίησης, σ'_{vo}, καθώς και από τις εκάστοτε εδαφικές ιδιότητες, όπως το ποσοστό λεπτόκοκκων και η σχετική πυκνότητα. Συνεπώς, για τη μεθοδολογία των Bouckovalas et al. (2009), επαναλήφθηκε η αναλυτική επίλυση των διαφορικών εξισώσεων 1-D υδατικής ροής γύρω από τον

[1] Το πρόγραμμα "X-SOILS: Θεμελίωση τεχνικών έργων σε σεισμικώς "προβληματικά" εδάφη υπό ισχυρή σεισμική δόνηση" (2003 – 2006), χρηματοδοτήθηκε από την Ευρωπαϊκή Ένωση και τη Γενική Γραμματεία Έρευνας και Τεχνολογίας.

χαλικοπάσσαλο, με την μέθοδο των πεπερασμένων διαφορών, για διάφορες τιμές του Α και διατυπώθηκαν νέα διαγράμματα σχεδιασμού. Στα εν λόγω διαγράμματα, έχει εξαλειφθεί η επίδραση της διάρκειας της σεισμικής δόνησης, αντικαθιστώντας τον αδιάστατο χρονικό παράγοντα T_{ad} με τον όρο $T_{al,}$ ο οποίος ορίζεται από την ακόλουθη σχέση:

$$T_{al} = \frac{k_h t_l}{m_{v,3} \gamma_w a^2} \qquad [3]$$

Επίσης, αποδεικνύεται ότι σεισμικές διεγέρσεις με ισοδύναμο αριθμό κύκλων φόρτισης μεγαλύτερο από τον απαιτούμενο αριθμό κύκλων για ρευστοποίηση ($N_{eq}/N_L > 1$) δεν έχουν σημαντική επίδραση στο σχεδιασμό, ιδιαίτερα εντός του συνήθους εύρους τιμών σχεδιασμού του επιτρεπόμενου λόγου υπερπίεσης πόρων $r_{u,max} = 0.20 \div 0.50$. Συνεπώς, τα τελικά διαγράμματα σχεδιασμού θεωρούν μια μοναδική τιμή σεισμικής έντασης N_{eq}/N_L, όπως παρουσιάζεται στο **Σχήμα 10**.

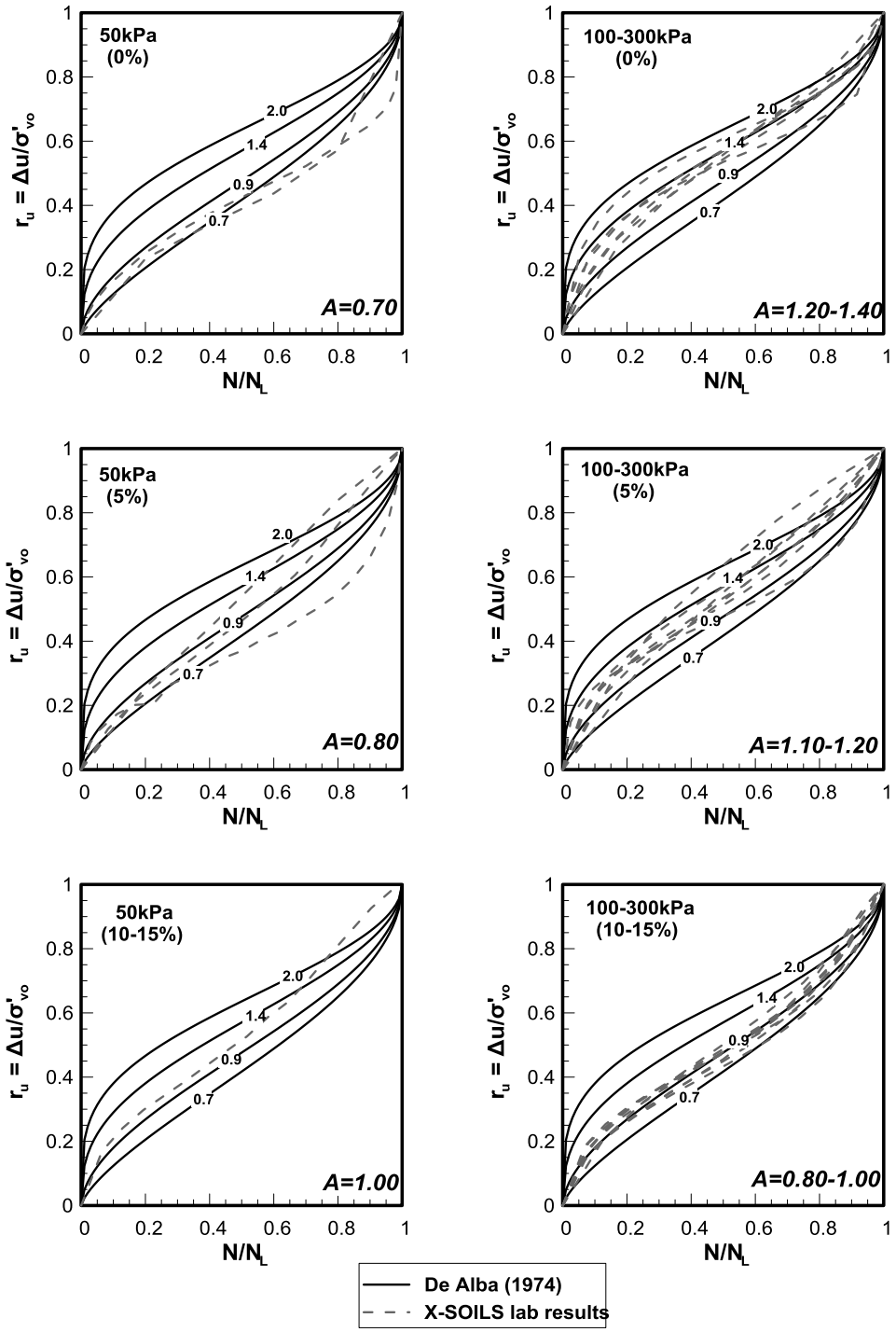

Σχήμα 9: Σύγκριση μεταξύ σύγχρονων εργαστηριακών καμπυλών ρευστοποίησης (X-SOILS) και αναλυτικής σχέσης De Alba (1974) για διάφορες τιμές του A.

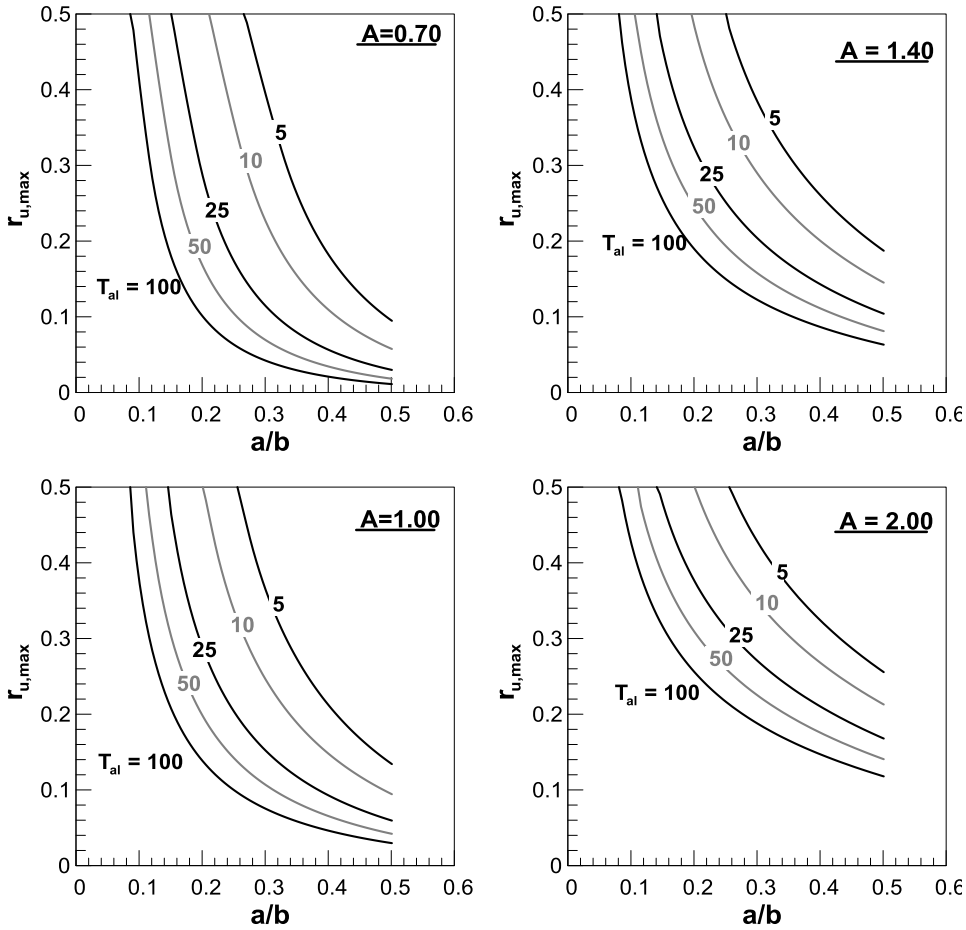

Σχήμα 10: Διαγράμματα σχεδιασμού για την αναθεωρημένη μεθοδολογία σχεδιασμού των Bouckovalas et al. (2009) για A=0.70, 1.00, 1.40, 2.00 και N_{eq}/N_L=1.00, 1.50, 2.00.

Προς επιβεβαίωση της αξιοπιστίας των νέων διαγραμμάτων σχεδιασμού της αναθεωρημένης μεθοδολογίας των Bouckovalas et al. (2009), στο *κεφάλαιο 6* πραγματοποιείται η αριθμητική προσομοίωση της αποστραγγιστικής δράσης των χαλικοπασάλων μέσω σοφιστευμένων 3-Δ δυναμικών μη-γραμμικών αναλύσεων.

Η εν λόγω αριθμητική προσομοίωση πραγματοποιήθηκε ως ακολούθως:

- Χρησιμοποιήθηκε ο κώδικας πεπερασμένων διαφορών FLAC3D. Στον εν λόγω κώδικα εφαρμόζεται ένας μη πεπλεγμένος αλγόριθμος αριθμητικής ολοκλήρωσης, γεγονός που τον καθιστά υπολογιστικά πιο αποτελεσματικό σε έντονα μη-γραμμικά προβλήματα μεγάλων μετατοπίσεων με χρονική εξέλιξη (π.χ. ροή υγρού των πόρων, δυναμική φόρτιση). Επίσης, επιτρέπει την ενσωμάτωση από τον χρήστη εξειδικευμένων καταστατικών προσομοιωμάτων (User-Defined-Models) για την ακριβέστερη προσομοίωση της συμπεριφοράς του εδαφικού στοιχείου.

- Η απόκριση της ρευστοποιήσιμης άμμου Nevada προσομοιώθηκε με το καταστατικό προσομοίωμα NTUA_SAND (Papadimitriou & Bouckovalas, 2002, και Andrianopoulos et al., 2010), όπως ενσωματώθηκε στον κώδικα FLAC3D στα πλαίσια της διδακτορικής διατριβής του Δ. Καραμήτρου (2010). Το εν λόγω προσομοίωμα βαθμονομήθηκε έναντι πειραματικών αποτελεσμάτων από μονοτονικές και ανακυκλικές δοκιμές σε άμμο Nevada

- Η απόκριση των χαλικοπασσάλων και των αργιλικών στρώσεων θεωρήθηκε ελαστική.

Ξεκινώντας από την απόκριση του εδάφους υπό συνθήκες ελεύθερου πεδίου, εν συνεχεία εξετάζεται η παρουσία των χαλικοπασσάλων εντός του ρευστοποιήσιμου εδάφους, θεωρώντας την επίδραση του αριθμού τους, της διάταξης σε μία ή δύο σειρές, καθώς και της ακαμψίας και της διαπερατότητάς τους σε σχέση με τη στρώση της άμμου. Παράλληλα, εξετάζεται η επίδραση παραμέτρων μη-σχετιζόμενων με τους χαλικοπασσάλους, όπως η διακριτοποίηση του καννάβου και οι συνοριακές συνθήκες. Τα αριθμητικά αποτελέσματα αξιολογούνται σε όρους υπερπιέσεων πόρων (Δu) και λόγου υπερπιέσεων πόρων (r_u) και δευτερευόντως σε όρους οριζόντιων επιταχύνσεων. Σε όλη των ανωτέρω διερεύνηση, η ρευστοποιήσιμη στρώση της άμμου είναι εγκιβωτισμένη μεταξύ δύο αργιλικών στρώσεων, έτσι ώστε να εξεταστεί μεμονωμένα η αποστραγγιστική δράση των χαλικοπασσάλων. Η τελικώς επιλεγείσα διάταξη παρουσιάζεται στο **Σχήμα 11**.

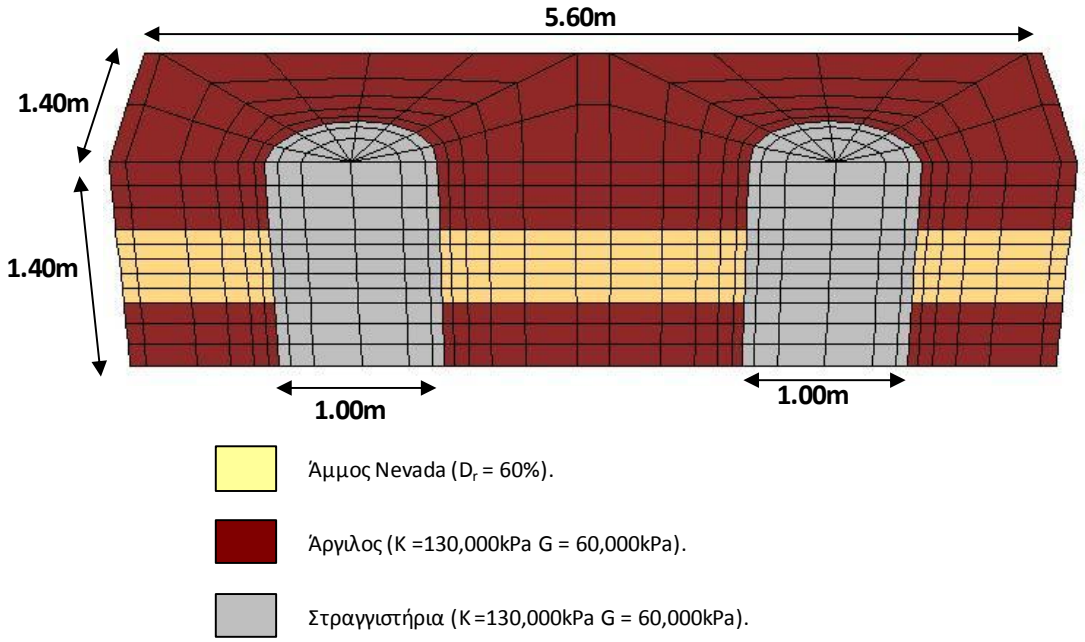

Σχήμα 11: Διάταξη εδάφους – χαλικοπασσάλων κι εδαφικές ιδιότητες.

Στη συνέχεια, πραγματοποιήθηκαν αριθμητικές αναλύσεις, στις οποίες η διαπερατότητα της άμμου μεταβαλλόταν από k_{sand} = 0 (αστράγγιστες συνθήκες) έως $1*10^{-4}$m/s, όπως παρουσιάζεται στον **Πίνακας 1**. Σε όλες τις αναλύσεις η διαπερατότητα του υλικού του χαλικοπασσάλου ήταν 100 φορές μεγαλύτερη από αυτή της άμμου.

Πίνακας 1: Τιμές συντελεστή διαπερατότητας k(m/sec).

Ανάλυση	Διαπερατότητα άμμου (m/sec)	Διαπερατότητα χαλικοπασσάλου (m/sec)
a.	10^{-4}	10^{-2}
b.	$5*10^{-5}$	$5*10^{-3}$
c.	$2*10^{-5}$	$2*10^{-3}$
d.	10^{-5}	10^{-3}
e.	$5*10^{-6}$	$5*10^{-4}$
f.	$2*10^{-6}$	$2*10^{-4}$

Οι χρονοϊστορίες του λόγου υπερπιέσεων πόρων στην κεντρική ζώνη της θεωρούμενης διάταξης παρουσιάζονται στο **Σχήμα 12**. Παρατηρείται ότι οι αριθμητικά υπολογιζόμενες καμπύλες παρουσιάζουν τη χαρακτηριστική μορφή των αναλυτικών προβλέψεων, όπου μετά την εκδήλωση μιας μέγιστης τιμής r_u, σε ενδιάμεσα στάδια της δόνησης, εν συνεχεία οι τιμές του λόγου υπερπιέσεων πόρων μειώνονται έως το τέλος αυτής.

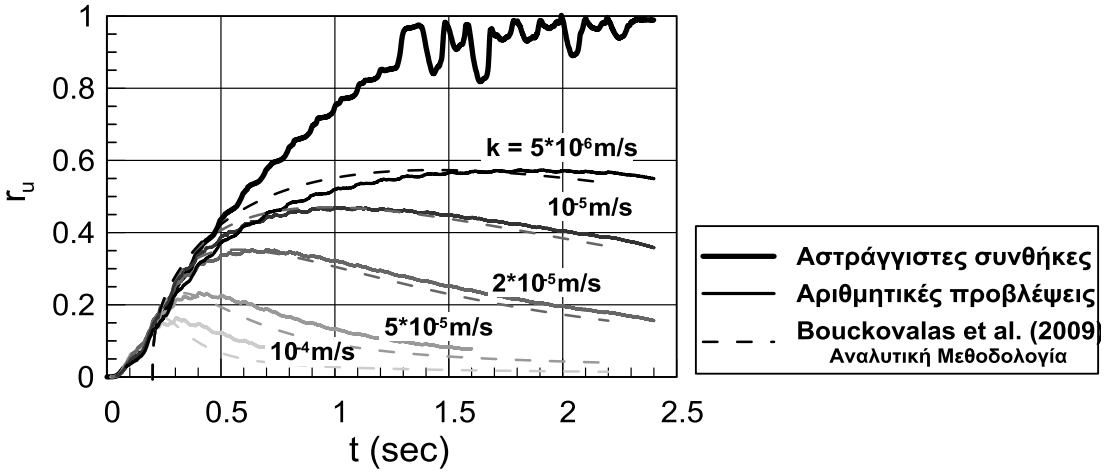

Σχήμα 12: Αριθμητικά αποτελέσματα και αναλυτικές προβλέψεις χρονοϊστοριών λόγου υπερπιέσεων πόρων (r_u) για διαφορετικές τιμές διαπερατότητας.

Το επόμενο βήμα, στη διαδικασία της αριθμητικής επαλήθευσης, αφορά τη δυνατότητα αναπαραγωγής των αριθμητικών προβλέψεων με ένα μοναδικό σετ εδαφικών παραμέτρων,

εξαιρουμένης βέβαια της διαπερατότητας, η οποία μεταβάλλεται. Προς αυτή την κατεύθυνση, αρχικά επιχειρείται η προσαρμογή της αναλυτικής σχέσης ανάπτυξης υδατικών υπερπιέσεων r_U-N/N_L των De Alba et al. (1975) υπό αστράγγιστες συνθήκες στα αριθμητικά αποτελέσματα, μέσω επαναληπτικών υπολογισμών. Όπως παρουσιάζεται και στο **Σχήμα 13**, αυτό επιτυγχάνεται για την τιμή του συντελεστή A = 1.40 και απαιτούμενο χρόνο για την εκδήλωση ρευστοποίησης ίσο προς t_l= 1.3sec.

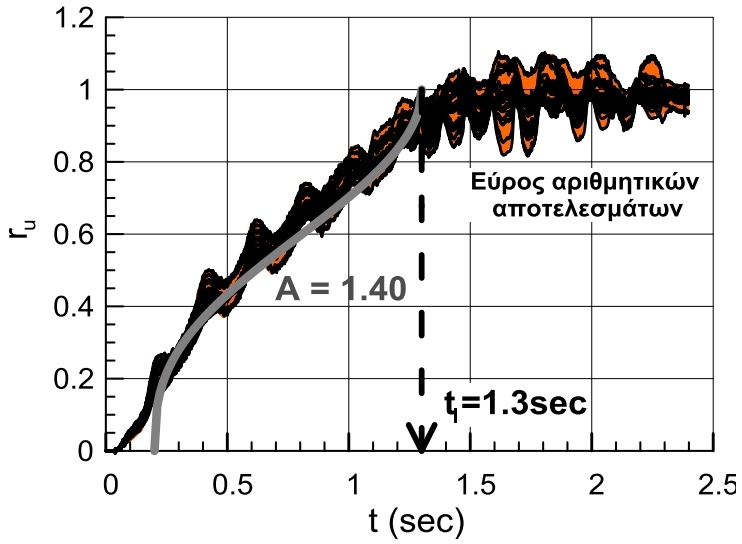

Σχήμα 13: Αριθμητικώς υπολογιζόμενη χρονοϊστορία λόγου υπερπιέσεων πόρων και αναλυτικά αποτελέσματα για A = 1.40 και t_l = 1.3sec.

Έχοντας προσδιορίσει τις παραμέτρους t_o, A, και t_l, στο επόμενο βήμα, επιδιώκεται η προσαρμογή των αριθμητικά υπολογιζόμενων χρονοϊστοριών r_u, στις αναλυτικά υπολογιζόμενες υπό στραγγιζόμενες συνθήκες. Η εν λόγω διαδικασία πραγματοποιήθηκε μέσω του επαναληπτικού υπολογισμού του συντελεστή ογκομετρικής συμπιεστότητας $m_{v,3}$, μιας και η συγκεκριμένη παράμετρος δεν απαιτείται για τη διεξαγωγή των αριθμητικών αναλύσεων.

Ο συντελεστής ογκομετρικής συμπιεστότητας αποδεικνύεται σημαντική παράμετρος στο σχεδιασμό των στραγγιστηρίων, την ίδια στιγμή που δεν υπάρχει δυνατότητα απευθείας μέτρησής του μέσω των συμβατικών δοκιμών της εδαφομηχανικής. Συνεπώς, η τιμή του $m_{v,3}$ προσδιορίζεται κατά κύριο λόγο με βάση δημοσιευμένα πειραματικά δεδομένα από αστράγγιστες δοκιμές ανακυκλικής τριαξονικής φόρτισης (PHRI, 1997). Με σκοπό την περαιτέρω διερεύνηση των κατάλληλων τιμών του συντελεστή συμπιεστότητας στο

σχεδιασμό των στραγγιστηρίων, οι προηγούμενες επαναληπτικά υπολογιζόμενες τιμές συγκρίνονται έναντι τριών ανεξάρτητων ομάδων τιμών:

- **Αριθμητικά υπολογιζόμενες τιμές $m_{v,3}$** βάσει της προσομοίωσης της μετα-σεισμικής στερεοποίησης του ρευστοποιημένου εδάφους. Συγκεκριμένα, βασιζόμενοι στον ορισμό του συντελεστή συμπιεστότητας (*Εξίσωση [4]*), κατά τη χρονική στιγμή εκδήλωσης της μέγιστης τιμής των υδατικών υπερπιέσεων, Δu_{max}, η σεισμική δόνηση διακόπτεται, και ακολουθεί μια ανάλυση στερεοποίησης, έως την πλήρη αποτόνωση των υδατικών υπερπιέσεων.

$$m_{v,3} = \frac{\Delta \varepsilon_{vol}}{\Delta u_{\max}} \qquad [4]$$

όπου Δu_{max} = η μέγιστη τιμή υπερπίεσης πόρων

$\Delta \varepsilon_{vol}$ = η ογκομετρική παραμόρφωση που αναπτύσσεται κατά τη διάρκεια της στερεοποίησης.

- **Αριθμητικά υπολογιζόμενες τιμές $m_{v,3}$ σε επίπεδο εδαφικού στοιχείου.-** Για την εκτίμηση των εν λόγω τιμών, προσομοιώθηκαν αριθμητικά, με τον κώδικα FLAC3D, εργαστηριακές δοκιμές ανακυκλικής τριαξονικής (CTX) και απλής διάτμησης (DSS), όπως προσδιορίζονται στα **Σχήμα 14** και **15**. Η αρχική τάση στερεοποίησης ορίστηκε στα 100kPa, ενώ ο υπολογισμός του $m_{v,3}$ πραγματοποιήθηκε σύμφωνα με τον ορισμό που παρουσιάστηκε ανωτέρω.

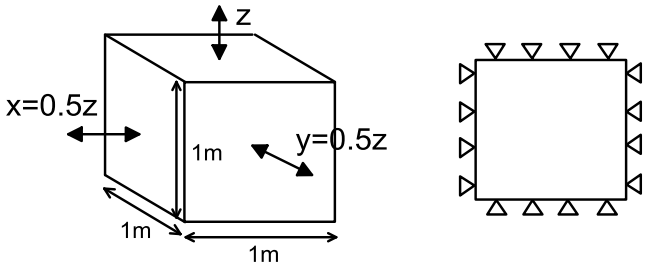

Σχήμα 14: Διάταξη και συνοριακές συνθήκες για την αριθμητική προσομοίωση ανακυκλικής τριαξονικής δοκιμής ρευστοποίησης.

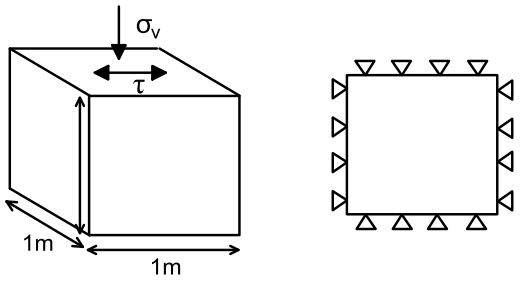

Σχήμα 15: Διάταξη και συνοριακές συνθήκες για την αριθμητική προσομοίωση ανακυκλικής δοκιμής ρευστοποίησης απλής διάτμησης.

- **Πειραματικές τιμές από τη διεθνή βιβλιογραφία (PHRI,1997).-** για άμμους διαφορετικής κοκκομετρικής διαβάθμισης. Οι εν λόγω τιμές, αναφέρονται τόσο από την Japanese Geotechnical Society (JGS, 1998) όσο και από το Port & Harbor Research Institute (PHRI, 1997) και έχουν προκύψει από ανακυκλικές τριαξονικές δοκιμές ρευστοποίησης. Επίσης, αναφέρεται ότι οι εν λόγω τιμές αντιστοιχούν σε αρχική τάση στερεοποίησης 100kPa και επίπεδα λόγου υπερπίεσης πόρων $r_u < 0.5$.

Τα κύρια συμπεράσματα που προέκυψαν από την αριθμητική προσομοίωση της αποστραγγιστικής δράσης των χαλικοπασσάλων συνοψίζονται ακολούθως:

- Η παραδοχή των Seed & Booker (1977) και των Bouckovalas et al. (2009) περί ενός σταθερού συντελεστή συμπιεστότητας $m_{v,3}$ σε όλη την έκταση της ρευστοποιήσιμης στρώσης επαληθεύεται αριθμητικά. Μάλιστα, για το σύνηθες εύρος σχεδιασμού του λόγου υπερπιέσεων πόρων $r_{u,max}$ η τιμή του $1/m_{v,3}$ μπορεί να θεωρηθεί περίπου ίση με $3*10^5$kPa.
- Παρατηρείται ικανοποιητική συμφωνία ανάμεσα στις αριθμητικά και αναλυτικά υπολογιζόμενες τιμές $1/m_{v,3}$, για το ίδιο σετ παραμέτρων του καταστατικού προσομοιώματος, ανεξάρτητα από την ιστορία της φόρτισης.
- Η χρήση ανακυκλικών τριαξονικών δοκιμών για την εκτίμηση του $1/m_{v,3}$ οδηγεί σε τιμές μικρότερες από τις αναλυτικά και αριθμητικά υπολογιζόμενες. Συνεπώς, για δεδομένο επιτρεπόμενο λόγο υπερπιέσεων πόρων $r_{u,max}$, μικρές τιμές του $1/m_{v,3}$ οδηγούν σε μεγαλύτερο αδιάστατο χρονικό παράγοντα T_{ad}, και την επιλογή μεγαλύτερου λόγου a/b, δηλαδή σε πυκνότερη διάταξη χαλικοπασσάλων και συντηρητικό σχεδιασμό. Αντίθετα, η χρήση πειραματικών αποτελεσμάτων απλής ανακυκλικής διάτμησης οδηγεί σε περισσότερο ρεαλιστικές τιμές του $1/m_{v,3}$, ιδιαίτερα εντός του εύρους σχεδιασμού του λόγου υπερπιέσεων πόρων $r_{u,max}$. Ως εκ

τούτου, οι συγκεκριμένες εργαστηριακές δοκιμές πλεονεκτούν έναντι των τριαξονικών.

Ε.Ε.3-Α. Αναλυτική Μεθοδολογία Σχεδιασμού Επιφανειακών Θεμελιώσεων (*περιγραφή αναλύσεων και παραδοχών*)

Το πρώτο βήμα για την ανάπτυξη της αναλυτικής μεθοδολογίας σχεδιασμού επιφανειακών θεμελιώσεων σε ρευστοποιήσιμα εδάφη προϋποθέτει το σχεδιασμό μιας επιφανειακής κρούστας και τον προσδιορισμό των βελτιωμένων ιδιοτήτων αυτής. Έτσι, στο *κεφάλαιο 7*, παρουσιάζεται η θεώρηση του «*Ισοδύναμου Ομοιόμορφου Βελτιωμένου Εδάφους*», που χρησιμοποιείται για την αριθμητική προσομοίωση της επιφανειακής κρούστας βελτιωμένου εδάφους. Η εν λόγω κρούστα, θεωρείται ομοιόμορφη, με κατάλληλα βελτιωμένες εδαφικές ιδιότητες (σχετική πυκνότητα και διαπερατότητα), οι οποίες προσδιορίζονται όπως περιγράφεται στις επόμενες παραγράφους.

Σχετική πυκνότητα $D_{r,imp}$(%).- Προσδιορίζεται με βάση τη σχετική πυκνότητα του φυσικού εδάφους, τον συντελεστή αντικατάστασης α_s, και τα εμπειρικά διαγράμματα του **Σχήμα 16**. Συγκεκριμένα, σύμφωνα με τις οδηγίες της Japanese Geotechnical Society (JGS, 1998), ο αριθμός N_{SPT} στο βελτιωμένο έδαφος (N_{imp}) υπολογίζεται ως εξής:

$$N_{imp} = \alpha_s N_{pile} + (1 - \alpha_s) N_{ground} \qquad [5]$$

όπου N_{pile} είναι ο διορθωμένος αριθμός χτύπων N_{SPT} στην περιοχή του πασσάλου (**Σχήμα 16**).

N_{ground} είναι ο διορθωμένος αριθμός χτύπων N_{SPT} στο μεσο-διάστημα δύο διαδοχικών χαλικοπασσάλων (**Σχήμα 16**).

Ακολούθως, η σχετική πυκνότητα σχετίζεται με τον διορθωμένο αριθμό $N_{imp.}$, μέσω της εμπειρικής σχέσης, που προτείνεται από τους Tokimatsu & Seed (1987):

$$N_{imp} = 44 Dr^2 \qquad [6]$$

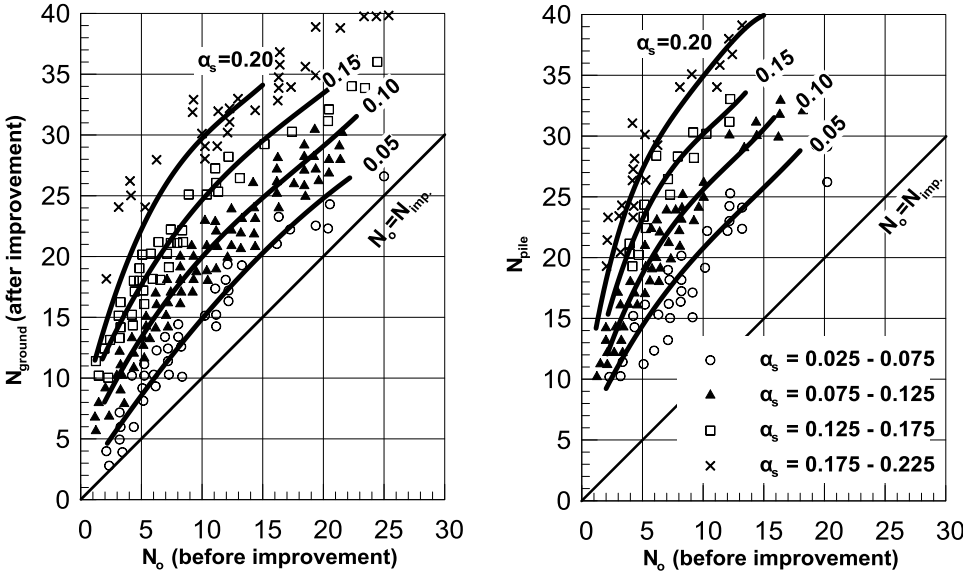

Σχήμα 16: Διαγράμματα εκτίμησης του αριθμού N_{SPT} για αμμώδη εδάφη με ποσοστό λεπτόκοκκων μικρότερο του 20% (JGS, 1998).

Συντελεστής διαπερατότητας βελτιωμένης κρούστας ($k_{eq.}$).- Σαν πρώτη προσέγγιση, η υδατική ροή διαμέσου της βελτιωμένης κρούστας, θεωρείται κατακόρυφη, έτσι ώστε η ισοδύναμη διαπερατότητα της κρούστας να μπορεί να ληφθεί ως ένας σταθμισμένος μέσος όρος των συντελεστών διαπερατότητας του φυσικού εδάφους (k_{sand}) και του χαλικοπασσάλου (k_{drain}), όπως περιγράφεται από την ακόλουθη εξίσωση:

$$k_{eq.} = \alpha_s k_{drain} + (1 - \alpha_s) k_{sand} \qquad [7]$$

Λαμβάνοντας υπόψη ότι ο λόγος k_{drain}/k_{sand} πρέπει να είναι μεγαλύτερος από 200 και επίσης ότι ο συντελεστής αντικατάστασης a_s κυμαίνεται από 0.05 έως 0.20 προκύπτει ότι $k_{eq.} > (11 \div 41)k_{sand}$.

Στη συνέχεια, η μελέτη της σεισμικής απόκρισης μιας επιφανειακής θεμελίωσης λωρίδας σε ρευστοποιήσιμο έδαφος, με προηγούμενη ελεγχόμενη βελτίωση, πραγματοποιήθηκε μέσω αριθμητικής ανάλυσης και βασίστηκε στις ακόλουθες παραδοχές:

- Χρησιμοποιήθηκε ο κώδικας πεπερασμένων διαφορών σε δύο διαστάσεις FLAC, ο οποίος παρουσιάζει τα ίδια πλεονεκτήματα με τον αντίστοιχο κώδικα σε τρεις διαστάσεις, όπως έχει προαναφερθεί.
- Η προσομοίωση των εδαφικών στρώσεων υπό στατικές και δυναμικές συνθήκες πραγματοποιήθηκε με το καταστατικό προσομοίωμα NTUA-SAND, όπως έχει επίσης

προαναφερθεί. Τονίζεται ότι για τους σκοπούς της παρούσας επιμέρους Ερευνητικής Εργασίας, το καταστατικό προσομοίωμα βαθμονομήθηκε εκ νέου, προκειμένου να περιγράφει με ακρίβεια τη διατμητική αντοχή της άμμου σε υψηλές τιμές σχετικών πυκνοτήτων. Η διαδικασία αξιολόγησης της υπάρχουσας βαθμονόμησης και οι λόγοι που οδήγησαν σε επαναπροσδιορισμό δύο εκ των παραμέτρων του καταστατικού προσομοιώματος περιγράφονται στο *Παράρτημα Β*.

- Διαφορετικές συνοριακές συνθήκες θεωρήθηκαν κατά το στάδιο της στατικής και δυναμικής φόρτισης. Συγκεκριμένα, κατά την επιβολή των γεωστατικών τάσεων και του φορτίου του θεμελίου περιορίστηκαν οι οριζόντιες μετατοπίσεις των άκρων, ενώ κατά την κατακόρυφη διεύθυνση περιορίστηκαν μόνο τα κάτω όρια του καννάβου, ώστε να επιτρέπεται η ελεύθερη καθίζηση του συστήματος. Για τη διεξαγωγή της δυναμικής φόρτισης, στα άκρα του θεωρούμενου συστήματος, επιβλήθηκαν πλευρικά σύνορα «συζευγμένων κόμβων» (tied-nodes), τα οποία χρησιμοποιούνται στην περίπτωση σεισμικής φόρτισης εδαφών με οριζόντια στρωματογραφία και οριζόντια ελεύθερη επιφάνεια.
- Το επιφανειακό θεμέλιο προσομοιώνεται περιορίζοντας τις οριζόντιες και κατακόρυφες μετατοπίσεις των αντίστοιχων κόμβων, συνδέοντάς τους μέσω ενός άκαμπτου στοιχείου δοκού και επιβάλλοντας μια ομοιόμορφη τάση έδρασης ίση με q. Θεωρείται επίσης ότι έχει μηδενική μάζα, ώστε να αποφεύγονται αδρανειακά φαινόμενα.
- Οι υπόλοιπες επιμέρους παραδοχές της αριθμητικής μεθοδολογίας (μέγεθος καννάβου, διακριτοποίηση, είδος απόσβεσης) οριστικοποιήθηκαν μετά από μια σειρά παραμετρικών αναλύσεων ευαισθησίας.

Τελικώς, ο χρησιμοποιούμενος κανναβος παρουσιάζεται στο **Σχήμα 17**.

Η αλληλουχία της φόρτισης περιλαμβάνει τρία ξεχωριστά στάδια, τα οποία παρουσιάζονται σχηματικά στο **Σχήμα 18**:

Φάση 1: Επιβάλλονται αρχικές γεωστατικές τάσεις και το φορτίο του θεμελίου επιβάλλεται σταδιακά σε βήματα των 5kPa, έως την επιθυμητή τάση έδρασης q (κλάδος a-b).

Φάση 2: Πραγματοποιείται μια πλήρως συζεγμένη δυναμική ανάλυση ενεργών τάσεων, η οποία υποβάλλει το σύστημα εδάφους – θεμελίωσης σε αρμονική διέγερση, με παράλληλη υδατική ροή. Κατά τη διάρκεια της φάσης αυτής, αναπτύσσονται

υπερπιέσεις πόρων και οι δυναμικές καθιζήσεις συσσωρεύωνται υπό σταθερή τιμή του στατικού φορτίου Q (κλάδος b-c).

Φάση 3: Μετά το τέλος της δέγερσης, και ενώ το έδαφος τελεί ακόμη υπό καθεστώς ρευστοποίησης, το στατικό φορτίο Q αυξάνεται έως την αστοχία (κλάδος c-d), προσδιορίζοντας έτσι την απομειωμένη φέρουσα ικανότητα της θεμελίωσης. Τονίζεται ότι το μετα-σεισμικό στάδιο πραγματοποιείται υπό στραγγιζόμενες συνθήκες, ωστόσο για να ληφθούν υπόψη οι συνέπειες της ρευστοποίησης, οι υπερπιέσεις πόρων διατηρούνται σταθερές. Αυτό επιτυγχάνεται, αναστέλλωντας την υδατική ροή και θέτωντας μια μικρή τιμή στο μέτρο συμπίεσης του νερού (μείωση από $2*10^6$ σε 1kPa) ώστε να μην μεταβληθούν οι υπερπιέσεις πόρων από την επιβολή επιπλέον εξωτερικού φορτίου.

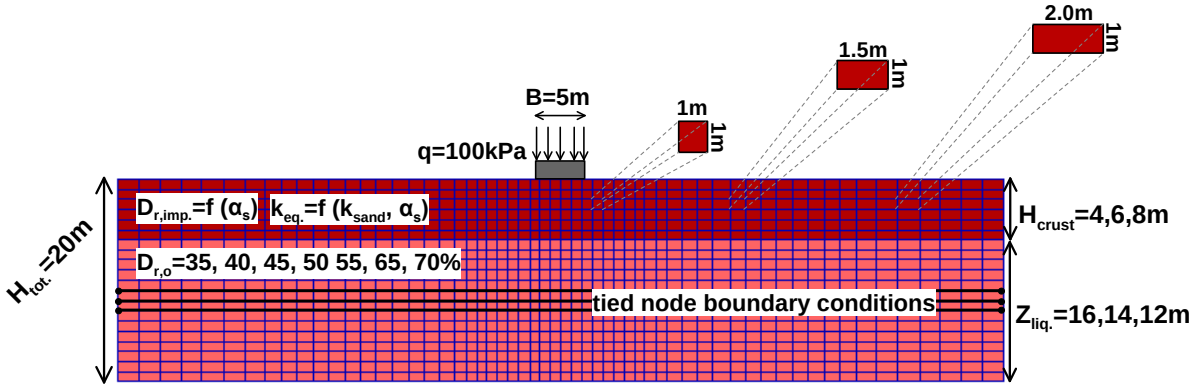

Σχήμα 17: Χρησιμοποιούμενος κάνναβος στις 2-Δ αριθμητικές αναλύσεις.

Η συστηματική εξέταση των αριθμητικών αποτελεσμάτων, σε συνδυασμό με παρατηρήσεις από σχετικά πειράματα σε φυγοκεντριστή από τη διεθνή βιβλιογραφία, υποδεικνύουν ότι η συσσώρευση των δυναμικών καθιζήσεων δεν είναι το αποτέλεσμα της δυναμικής συνίζησης της άμμου. Είναι περισσότερο το αποτέλεσμα ενεργοποίησης ενός μηχανισμού ολισθαίνοντος στερεού κατά Newmark, ο οποίος αναλύεται λεπτομερώς στα πλαίσια του *κεφαλαίου 7*. Συνοπτικά, αναφέρεται ότι η συσσώρευση των καθιζήσεων συνδέεται με την ενεργοποίηση ενός σφηνοειδούς μηχανισμού αστοχίας, ο οποίος εκδηλώνεται δύο φορές κατά τη διάρκεια ενός πλήρους κύκλου φόρτισης, μία από κάθε πλευρά του θεμελίου.

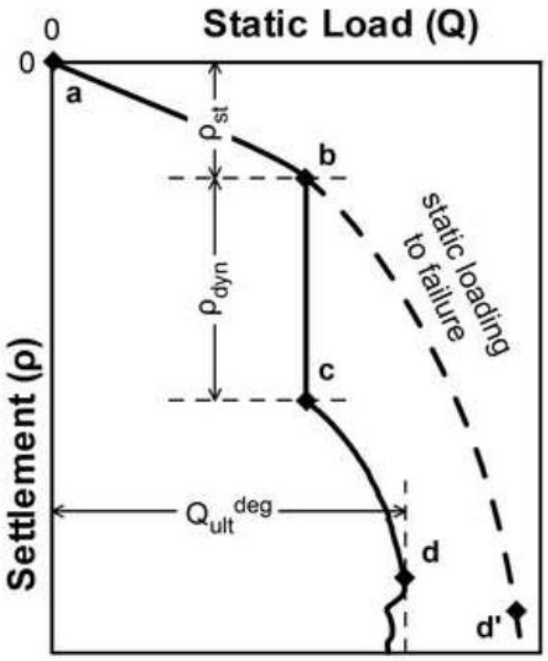

Σχήμα 18: Τυπική καμπύλη φορτίου – μετατόπισης.

Η εκδήλωση ρευστοποίησης στην άμμο, εκτός από τη συσσώρευση καθιζήσεων, επιφέρει σχεδόν ολοκληρωτική απώλεια της διατμητικής της αντοχής, καθώς και μερική απώλεια διατμητικής αντοχής στη βελτιωμένη κρούστα, ως αποτέλεσμα της αναπόφευκτης, αλλά ελεγχόμενης ανάπτυξης υπερπιέσεων πόρων. Το εν λόγω φαινόμενο προκαλεί την παροδική απομείωση της φέρουσας ικανότητας της θεμελίωσης, εντός του χρονικού διαστήματος, το οποίο απαιτείται για την πλήρη αποτόνωση των υδατικών υπερπιέσεων. Ο αναπτυσσόμενος μηχανισμός αστοχίας της επιφανειακής θεμελίωσης περιγράφεται διεξοδικά στο *κεφάλαιο 7*. Ενδεικτικά αναφέρεται, ότι η αναπτυσσόμενη επιφάνεια αστοχίας είναι αντίστοιχη του μηχανισμού που προτείνεται από τους Meyerhoff & Hanna (1978) για επιφανειακές θεμελιώσεις σε 2-στρωτα εδαφικά προφίλ, όπως παρουσιάζεται στο **Σχήμα 19**. Στην εν λόγω μεθοδολογία διευκρινίζεται ότι το πάχος της βελτίωσης (H_{imp}) καθορίζει και τη μορφή του μηχανισμού αστοχίας. Ειδικότερα, για μικρές τιμές του βάθους βελτίωσης αναπτύσσεται ένας μηχανισμός διάτρησης της θεμελίωσης εντός του υποκείμενου ρευστοποιημένου εδάφους - punching shear failure - (**Σχήμα 19α**), ενώ σε περιπτώσεις αυξημένου πάχους, ο μηχανισμός αστοχίας αναπτύσσεται εξ'ολοκλήρου εντός της κρούστας (**Σχήμα 19β**).

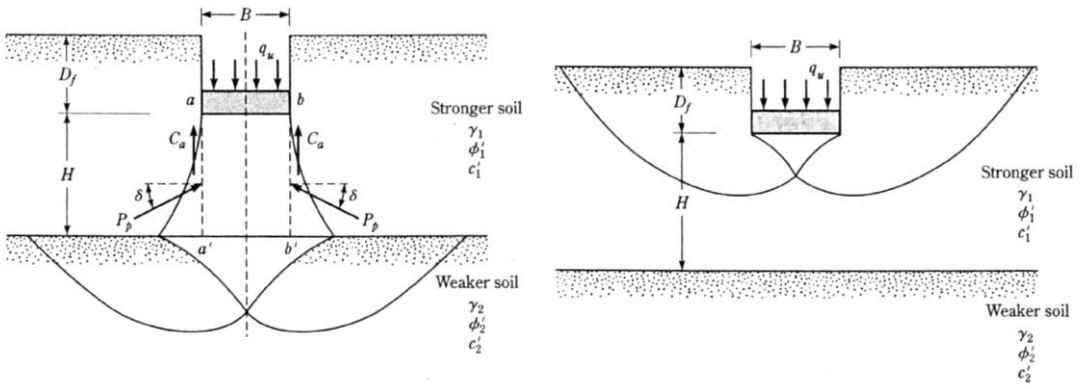

(α) **(β)**

Σχήμα 19: Φέρουσα ικανότητα επιφανειακής λωριδωτής θεμελίωσης σε δίστρωτο εδαφικό προφίλ (Meyerhof & Hanna, 1978).

Προς επιβεβαίωση της θεώρησης του *Ισοδύναμου Ομοιόμορφου Βελτιωμένου Εδάφους* και επαλήθευση της αριθμητικής μεθοδολογίας που περιγράφηκε ανωτέρω, έγινε σύγκριση με τα δημοσιευμένα και καλά τεκμηριωμένα πειραματικά αποτελέσματα σε φυγοκεντριστή των Liu & Dobry (1997), τα οποία περιγράφονται στην πρώτη ενότητα της Εκτενούς Περίληψης. Στα πλαίσια αυτά, εξετάστηκαν δύο σενάρια αναφορικά με την τιμή της διαπερατότητας του ρευστοποιήσιμου εδάφους:

- Διαπερατότητα υπό στατικές συνθήκες (Arulmoli et al.,1992)
- Διαπερατότητα υπό δυναμικές συνθήκες, όπως προτείνεται από τους ίδιους τους Liu & Dobry (1997).

Τα αριθμητικά και πειραματικά αποτελέσματα συγκρίνονται στο **Σχήμα 20**, σε όρους δυναμικών καθιζήσεων και λόγου επιταχύνσεων Θεμελίου/Βάσης. Η παρατηρούμενη ικανοποιητική συμφωνία είναι ενδεικτική της ορθότητας της αριθμητικής προσομοίωσης που υιοθετείται τελικά για τη μελέτη της σεισμικής απόκρισης του θεμελίου. Επισημαίνεται ότι η επίδραση της διαπερατότητας είναι σημαντική κυρίως στην πρόβλεψη των σεισμικών επιταχύνσεων και λιγότερο στη συσσώρευση των καθιζήσεων. Η τιμή της διαπερατότητας υπό στατικές συνθήκες προσφέρει την καλύτερη συνολικά σύγκριση με τα πειραματικά αποτελέσματα και συνεπώς υιοθετείται στις παραμετρικές αριθμητικές αναλύσεις που θα ακολουθήσουν.

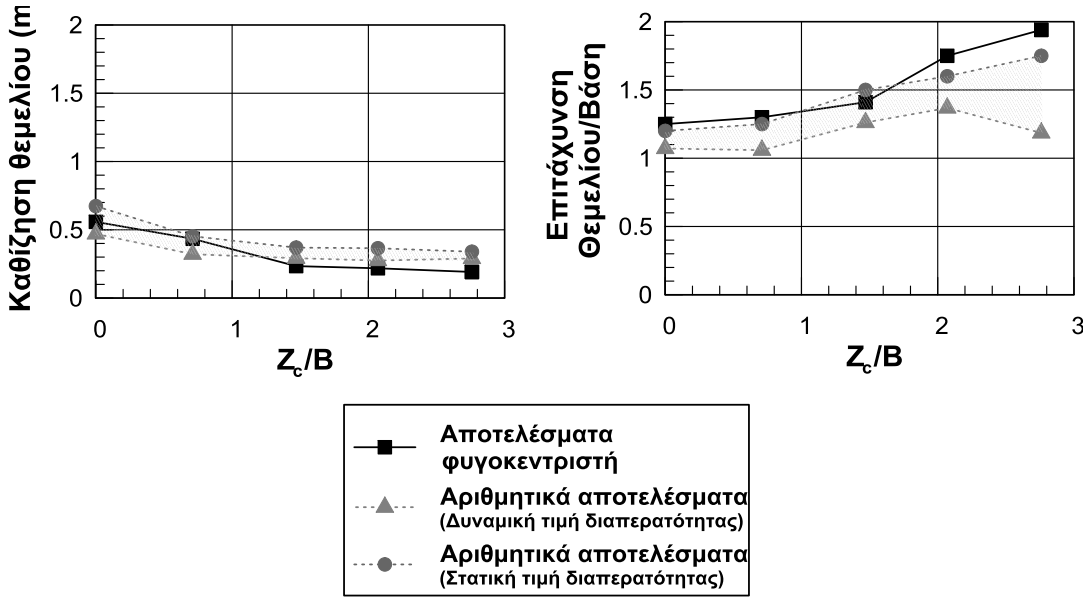

Σχήμα 20: Σύγκριση πειραματικών και αριθμητικών αποτελεσμάτων Liu & Dobry (1997).

Ε.Ε.3-Β. Αναλυτική Μεθοδολογία Σχεδιασμού Επιφανειακών Θεμελιώσεων

(*παραμετρικές αριθμητικές αναλύσεις*)

Με αποδεδειγμένη την αξιοπιστία της αριθμητικής μεθοδολογίας, στο *κεφάλαιο 8* υλοποιείται το ***πρώτο βήμα*** για τη διατύπωση της μεθοδολογίας σχεδιασμού, δηλαδή ο ***καθορισμός του απαιτούμενου συντελεστή αντικατάστασης*** α_s, ανάλογα με τον επιτρεπόμενο μέγιστο λόγο υπερπιέσεων $r_{u,max}$ εντός της βελτιωμένης εδαφικής κρούστας, το επιθυμητό πάχος αυτής (παράμετρος η οποία δεν υπεισέρχεται στα διαγράμματα σχεδιασμού των Bouckovalas et al.,2009) και την αρχική σχετική πυκνότητα του φυσικού εδάφους. Για το σκοπό αυτό πραγματοποιήθηκε μια σειρά 72 παραμετρικών αναλύσεων σεισμικής απόκρισης ελεύθερου πεδίου για τρία διαφορετικά βάθη βελτίωσης (H_{imp}=4, 6 & 8m), για συντελεστές αντικατάστασης α_s = 0, 0.05, 0.10, 0.15 & 0.20 και για αρχική σχετική πυκνότητα του φυσικού εδάφους $D_{r,o}$ = 35%, 40%, 45%, 55%, 65% & 70%. Τα αριθμητικά αποτελέσματα παρουσιάζονται υπό τη μορφή διαγραμμάτων σχεδιασμού, στο **Σχήμα 21**.

Το ***δεύτερο βήμα*** για τη διατύπωση της προτεινόμενης μεθοδολογίας, περιλαμβάνει τον ***καθορισμό των ισοδύναμων εδαφικών ιδιοτήτων της βελτιωμένης ζώνης,*** δηλαδή της σχετικής πυκνότητας και της διαπερατότητας. Οι εν λόγω ιδιότητες δύναται να προσδιοριστούν από τα διαγράμματα του **Σχήμα 22** συναρτήσει του συντελεστή αντικατάστασης α_s, ο οποίος προσδιορίστηκε στο προηγούμενο βήμα.

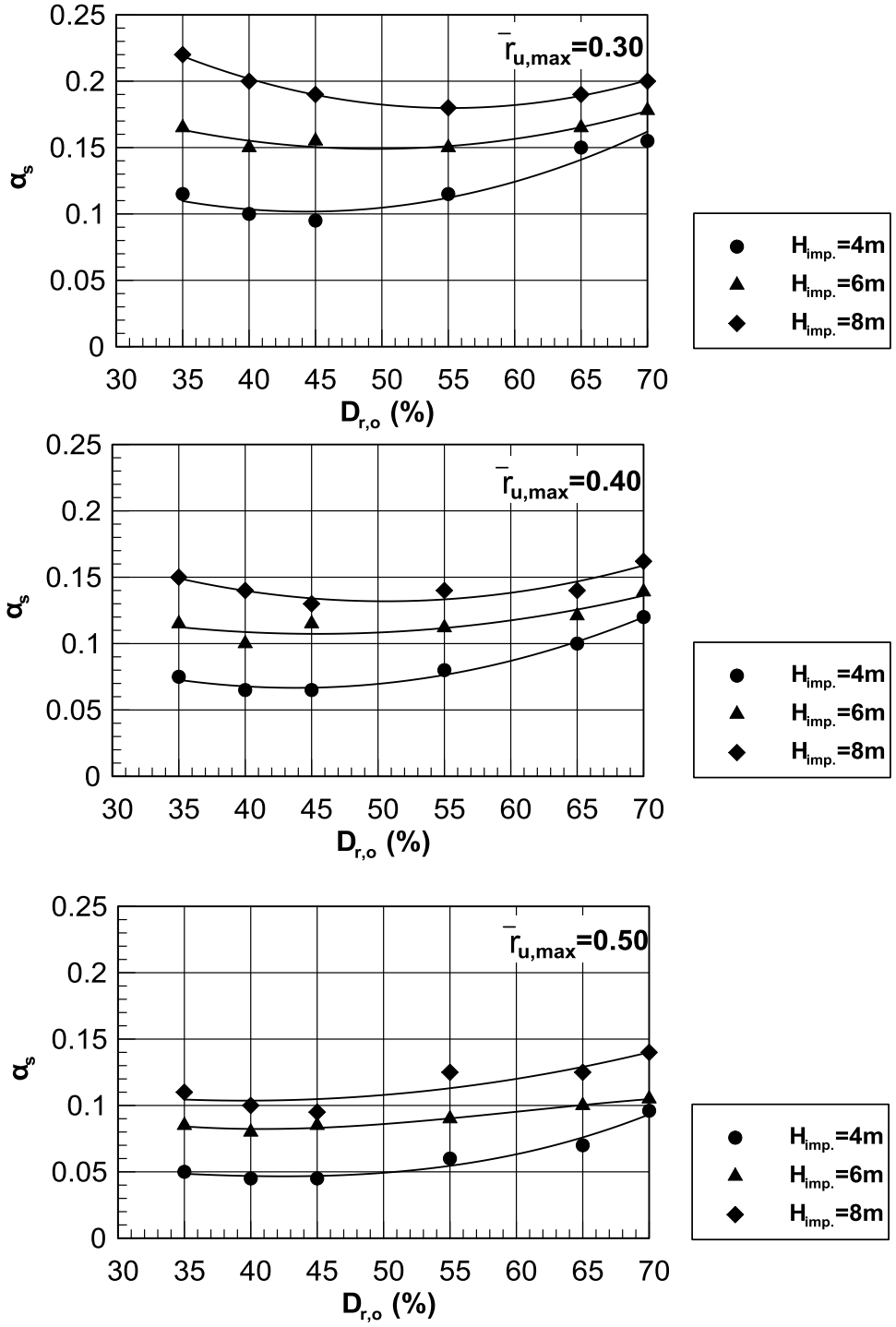

Σχήμα 21: Απαιτούμενος συντελεστής αντικατάστασης α_s σε σχέση με την αρχική σχετική πυκνότητα $Dr_{,o}$(%), τρεις τιμές πάχους βελτίωσης H_{imp} και τρεις τιμές επιτρεπόμενων $r_{u,max}$.

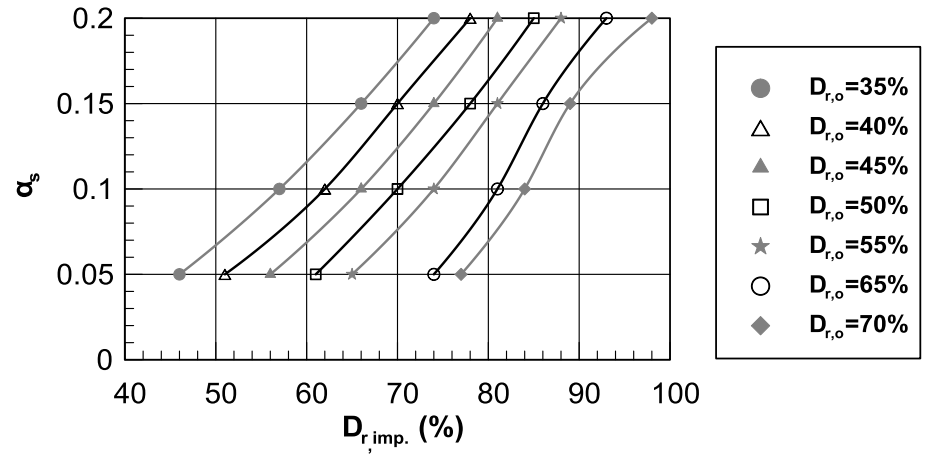

(α)

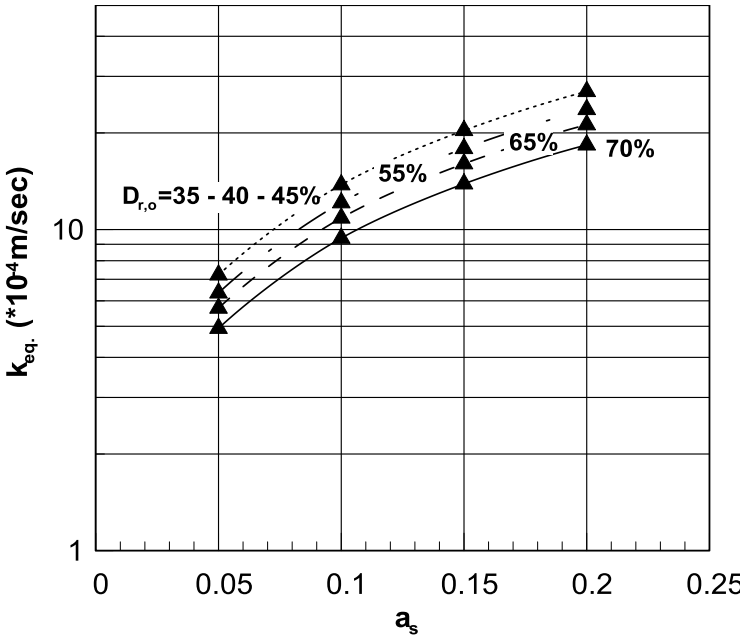

(β)

Σχήμα 22: Εκτίμηση βελτιωμένων εδαφικών ιδιοτήτων: **(α)** σχετική πυκνότητα $Dr_{,imp}$(%) και **(β)** διαπερατότητα $k_{eq.}$(m/sec), συναρτήσει του συντελεστή αντικατάστασης $\alpha_{s.}$

Στο ***τρίτο βήμα*** για τη διατύπωση της αναλυτικής μεθοδολογίας, η σεισμική συμπεριφορά της επιφανειακής θεμελίωσης αποτιμάται αρχικά για το 2-στρωτο εδαφικό προφίλ του **Σχήμα 17**, το οποίο αντιστοιχεί σε **εκτενή πλευρικής έκτασης βελτίωση του εδάφους**. Για την υλοποίηση του παρόντος βήματος, καταστρώθηκε και παρουσιάζεται στο *κεφάλαιο 8* μια εκτενής παραμετρική διερεύνηση αποτελούμενης από 84 αριθμητικές αναλύσεις οι οποίες εξετάζουν την επίδραση:

I. εδαφικών ιδιοτήτων (σχετική πυκνότητα, διαπερατότητα φυσικού εδάφους)
II. σεισμολογικών παραμέτρων (μέγιστη επιτάχυνση, περίοδος διέγερσης και αριθμός κύκλων φόρτισης) καθώς και
III. των παραμέτρων του θεμελίου (πλάτος και επιβαλλόμενη τάση)

Όπως έχει ήδη τονιστεί, οι διαστάσεις της τεχνητά διαμορφωμένης κρούστας είναι πεπερασμένες. Με δεδομένο ότι το βάθος της βελτίωσης (H_{imp}) έχει ήδη ενσωματωθεί στην προηγούμενη παραμετρική διερεύνηση, **η επίδραση του πλάτους της βελτίωσης (L_{imp})** στην απόκριση της επιφανειακής θεμελίωσης μελετάται ανεξάτητα, μέσω 96 επιπλεόν παραμετρικών αναλύσεων. Ειδικότερα, επιλέχθησαν οι πλέον αντιπροσωπευτικές περιπτώσεις από την προηγούμενη ομάδα αναλύσεων, και στη συνέχεια, σε κάθε περίπτωση το πλάτος της βελτίωσης μειωνόταν σταδιακά έως περίπου το πλάτος του ίδιου του θεμελίου.

Ε.Ε.3-Γ. Αναλυτική Μεθοδολογία Σχεδιασμού Επιφανειακών Θεμελιώσεων
(*στατιστική επεξεργασία αποτελεσμάτων αριθμητικών αναλύσεων*)

Ακολούθως, στο *κεφάλαιο 9* πραγματοποιείται η στατιστική επεξεργασία της πρώτης ομάδας των αριθμητικών αποτελεσμάτων, για εκτενή πλευρικά βελτίωση, και αναπτύσσονται κατάλληλες αναλυτικές σχέσεις υπολογισμού. Έτσι με δεδομένα τα χαρακτηριστικά

- της θεμελίωσης, δηλαδή τη μέση τάση έδρασης ***q(kPa)*** και το πλάτος του ***B(m)***
- της διέγερσης, δηλαδή της μέγιστης επιτάχυνσης στη βάση του εδαφικού στρώματος α_{max} ***(g),*** του αριθμού των σημαντικών κύκλων της φόρτισης N_o και της δεσπόζουσας περιόδου της διέγερσης T_{exc} ***(sec)***.
- Την ελαστική περίοδο της εδαφικής στήλης T_{soil} ***(sec)***.

οι ***δυναμικές καθιζήσεις*** υπολογίζονται με βάση την ακόλουθη αναλυτική σχέση:

$$\rho_{dyn} = c_1 \alpha_{\max} \left(T_{exc} + aT_{soil}\right)^2 \left(N_o + 2\right) \left(\frac{1}{F.S._{deg}^{inf}}\right)^{c_2} \left[1 + c_3 \left(\frac{1}{F.S._{deg}^{inf}}\right)^{c_4}\right] \qquad [8]$$

όπου c_1**=0.019**, c_2**=0.45**, c_3**=0.25** c_4**=4.5** and **a=0.633**

Με βάση το μηχανισμό ολισθαίνοντος στερεού κατά Newmark αποδεικνύεται ότι

$$a_{\max} T^2 N = \pi^2 \int_{t=0}^{t=N*T} abs(v(t))\,dt \qquad [9]$$

όπου v(t) είναι η χρονοϊστορία της επιβαλλόμενης ταχύτητας.

Συνεπώς, η αντίστοιχη αναλυτική έκφραση για αρμονικές διεγέρσεις μπορεί να επεκταθεί σε οποιοδήποτε τύπο σεισμικής διέγερσης.

Η ακρίβεια της προτεινόμενης αναλυτικής *Εξίσωσης [8]* για τον υπολογισμό των σεισμικών καθιζήσεων αποτιμάται στο **Σχήμα 23** με το 91.6% των προβλέψεων να αποκλίνει μεταξύ ±20% από τις αριθμητικές τιμές. Το σχετικό σφάλμα των αναλυτικών προβλέψεων παρουσιάζεται στο **Σχήμα 24**, απ' όπου υπολογίζεται ότι η τυπική απόκλιση του σχετικού σφάλματος ανέρχεται στο 14%.

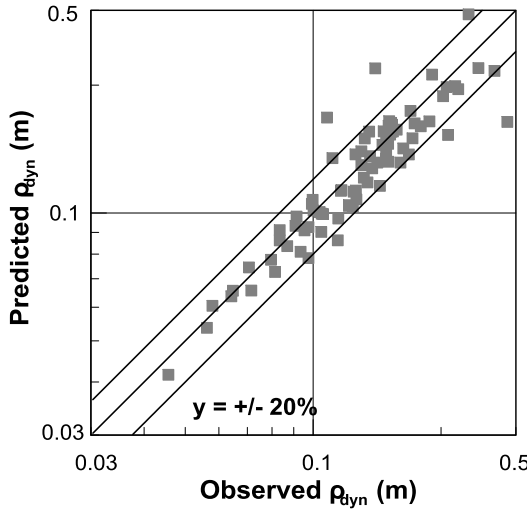

Σχήμα 23: Αριθμητικές και αναλυτικά υπολογιζόμενες τιμές σεισμικών καθιζήσεων.

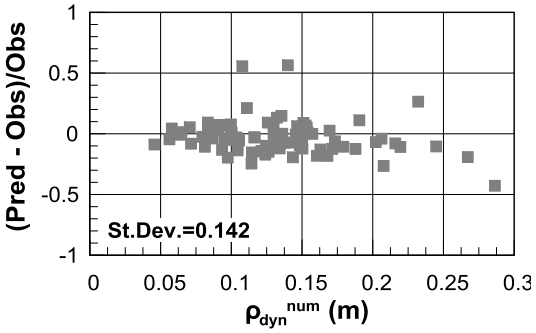

Σχήμα 24: Σχετικό σφάλμα συναρτήσει των αριθμητικά υπολογιζόμενων τιμών των σεισμικών καθιζήσεων ρ_{dyn}^{num} (m).

Πέραν της ανωτέρω σχέσης, η οποία είναι συμβατή με τη θεώρηση δυναμικής αστοχίας τύπου "ολισθαίνοντος στερεού" (Newmark), πραγματοποιήθηκε και ανεξάρτητη πολυπαραμετρική στατιστική επεξεργασία των αριθμητικών αποτελεσμάτων. Η νέα αυτή αναλυτική σχέση προβλέπει τις σεισμικές καθιζήσεις με λίγο μεγαλύτερη ακρίβεια, ωστόσο εξαρτάται από τις μονάδες κάθε παραμέτρου και δεν είναι εύκολα εφαρμόσιμη στην περίπτωση πραγματικών διεγέρσεων.

Η εκτίμηση της **απομειωμένης φέρουσας ικανότητας της θεμελίωσης q_{ultdeg}^{inf}** μετά το πέρας της δόνησης, βασίζεται στην αναλυτική σχέση των Meyerhoff & Hanna (1978), η οποία τροποποιείται κατάλληλα ώστε να περιγράφει τις ιδιαίτερες συνθήκες του προβλήματος. Συγκεκριμένα, ως αποτέλεσμα της ταχείας αποτόνωσης των υδατικών υπερπιέσεων από τη ρευστοποιήσιμη άμμο προς την περισσότερο διαπερατή βελτιωμένη κρούστα, παρατηρείται ο σχηματισμός μιας μεταβατικής ζώνης μερικώς ρευστοποιημένου εδάφους ανάμεσα στη βελτιωμένη κρούστα και το πλήρως ρευστοποιημένο έδαφος, όπως φαίνεται στο **Σχήμα 25**.

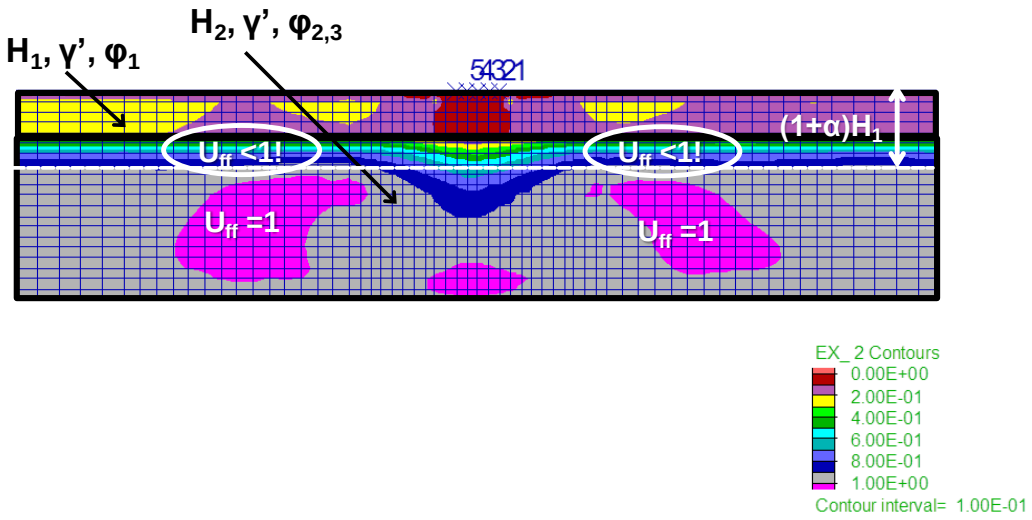

Σχήμα 25: Καμπύλες λόγου υδατικών υπερπιέσεων στο τέλος της σεισμικής διέγερσης, υποδεικνύοντας το σχηματισμό μιας μη ρευστοποιημένης ζώνης φυσικού εδάφους.

Η μεταβατική αυτή ζώνη λειτουργεί ως μια δευτερεύουσα κρούστα και ουσιαστικά αναγκάζει την επιφάνεια αστοχίας τύπου Prandl να αναπτυχθεί στο υποκείμενο πλήρως ρευστοποιημένο έδαφος. Υποθέτοντας ότι το πάχος της μεταβατικής ζώνης εκφράζεται ως

ποσοστό ***α*** της βελτιωμένης κρούστας και θεωρώντας ένα ενιαίο ειδικό βάρος για το έδαφος ($\gamma_1=\gamma_2=\gamma$), η αναλυτική σχέση των Meyerhof & Hanna (1978) μετασχηματίζεται ως εξής:

$$q_{ult,deg}=\min\left\{\begin{array}{r}\frac{1}{2}\gamma' B N\gamma_1 \\ \gamma' H_1^{\,2} K_s \frac{\tan\phi_{1,deg}}{B}+\gamma'\cdot[(1+\alpha)^2-1]\cdot H_1^{\,2}K_s\frac{\tan\phi_{2,deg}}{B}-\gamma'(1+\alpha)H_1+ \\ +\frac{1}{2}\gamma' B N_{\gamma 3}+\gamma'(1+\alpha)H_1 N_{q3}\end{array}\right\} \qquad [10]$$

Οι συντελεστές N_q & N_γ εκφράζονται από τις ακόλουθες σχέσεις:

$$N_{q,i}=\tan^2(45+\varphi_{i,\deg}/2)e^{\pi\tan\varphi_{i,\deg}} \qquad [11a]$$

$$N_{\gamma,i}=2(N_{q,i}+1)\tan\varphi_{i,\deg} \qquad [11b]$$

Η εφαρμογή της ανωτέρω σχέσης απαιτεί τον προηγούμενο προσδιορισμό των ακόλουθων παραμέτρων, οι οποίες προσδιορίστηκαν μετά από κατάλληλη στατιστική επεξεργασία των αριθμητικών αποτελεσμάτων.

Συντελεστής *α._* αφορά το πάχος της μερικώς ρευστοποιημένης μεταβατικής ζώνης, η οποία σχηματίζεται κάτω από τη βελτιωμένη ζώνη, και προσδιορίζεται με βάση την ακόλουθη αναλυτική σχέση:

$$\alpha=3.76\left[\frac{k_{eq}TN}{H_{\text{imp}}}\right]^{0.256} \qquad [11]$$

Αρχική γωνία τριβής $\varphi_{i,ini}$.- Οι συνθήκες φόρτισης δεν παραμένουν ομοιόμορφες κατά μήκος της ενεργοποιούμενης επιφάνειας αστοχίας. Συνεπώς η αρχική τιμή της γωνίας τριβής και για τις δύο εδαφικές στρώσεις εκτιμώνται με βάση την *Εξίσωση [12]*, θεωρώντας το μέσο όρο ανάμεσα σε φόρτιση τριαξονικής θλίψης, τριαξονικού εφελκυσμού και απλής διάτμησης, υπό αστράγγιστες και στραγγιζόμενες συνθήκες. Οι συγκεκριμένες τιμές προκύπτουν από την νέα βαθμονόμηση του καταστατικού προσομοιώματος στο Παράστημα Β.

$$\phi_{i,ini}=\frac{\phi_{i,TX-C}+\phi_{i,TX-E}+\phi_{i,DSS}}{3} \qquad [12]$$

Απομειωμένη γωνία τριβής $\phi_{i,deg}$.- Η απομείωση της διατμητικής αντοχής των εδαφικών στρώσεων, λόγω μερικής ή ολικής εκδήλωσης ρευστοποίησης, λαμβάνεται υπόψη μέσω της κατάλληλης απομείωσης των αντίστοιχων τιμών γωνιών τριβής. Η εν λόγω απομείωση είναι συνάρτηση του αναπτυσσόμενου λόγου υδατικών υπερπιέσεων, όπως περιγράφεται ως ακολούθως:

$$\phi_{i,deg} = \tan^{-1}[(1-U_i)\tan\phi_{i,ini}] \qquad [13]$$

όπου ο δείκτης i λαμβάνει τις τιμές, i= 1 για τη βελτιωμένη κρούστα, 2 για τη μεταβατική ζώνη και 3 για τη ρευστοποιημένη άμμο. Οι αντίστοιχοι λόγοι υπερπιέσεων πόρων U_i, προσδιορίζονται στις ακόλουθες υπο-ενότητες.

Λόγος υπερπιέσεων πόρων U_1 στη βελτιωμένη στρώση.- αντιστοιχεί στο τέλος της σεισμικής διέγερσης και υπό συνθήκες ελεύθερου πεδίου, εκφράζεται ΔΕ ως ποσοστό του μέγιστου επιτρεπόμενου λόγου υπερπιέσεων σχεδιασμού U_{design}:

$$U_1 = 0.54U_{design} \qquad [14]$$

Λόγος υπερπιέσεων πόρων στη μεταβατική ζώνη U_2.- ο οποίος αναπτύσσεται εντός της μεταβατικής ζώνης. Λαμβάνεται ίσος με τη μέση τιμή μεταξύ του λόγου U_1 και της αντίστοιχης τιμής για πλήρως ρευστοποιημένο έδαφος, η οποία ισούται με τη μονάδα:

$$U_2 = \frac{(1+U_1)}{2} = \frac{(1+0.54U_{design})}{2} \qquad [15]$$

Λόγος υπερπιέσεων πόρων στο ρευστοποιημένο έδαφος U_3.- αφορά το ρευστοποιημένο έδαφος, εντός μιας αντιπροσωπευτικής περιοχής κάτω από το θεμέλιο. Προσδιορίζεται με βάση την ακόλουθη έκφραση, συναρτήσει της απομειωμένης φέρουσας ικανότητας q_{ultdeg}^{inf}:

$$U_3 = 0.86\left(\frac{q_{ultdeg}^{inf}}{p_\alpha}\right)^{-0.18} \le 1.00 \qquad [16]$$

Συντελεστής K_s.- Αντιπροσωπεύει την ενεργοποιούμενη διατμητική αντοχή στην πλευρική επιφάνεια της μερικώς ρευστοποιημένης επιφανειακής κρούστας και της υποκείμενης μεταβατικής ζώνης, κάτω από τα άκρα του θεμελίου.

Για την καλύτερη κατανόηση της φυσικής σημασίας του συντελεστή K_s, παρουσιάζεται το ακόλουθο **Σχήμα 26** στο οποίο ο συντελεστής K_s εισάγεται στις δυνάμεις πλευρικής τριβής T_1 & T_2, ως ακολούθως:

$$T_1 = K_s P_1 = \frac{1}{2}\gamma' H_{imp}^2 K_s \tan\phi_{1,deg} \qquad [17]$$

$$T_2 = K_s P_2 = \frac{1}{2}\gamma' H_{imp}^2 K_s [(1+\alpha)^2 - 1]\tan\phi_{2,deg} \qquad [18]$$

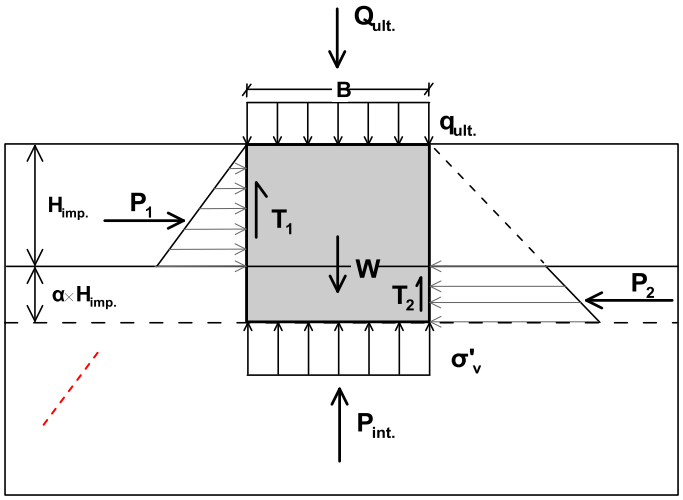

Σχήμα 26: Μηχανισμός αστοχίας του θεμελίου και αναπτυσσόμενες δυνάμεις που θεωρήθηκαν για τον προσδιορισμό του συντελεστή K_s.

Θεωρώντας ισορροπία δυνάμεων κατά την κατακόρυφη διεύθυνση, προκύπτει η αναλυτική έκφραση υπολογισμού του συντελεστή K_s (*Εξίσωση [19]*).

$$K_s = \frac{W + Q_{ult.} - P_{int.}}{\gamma' H_{imp}^2 \left\{\tan\phi_{1,deg} + \left[(1+\alpha)^2 - 1\right]\tan\phi_{2,deg}\right\}} \qquad [19]$$

Η εφαρμογή της εν λόγω αναλυτικής σχέσης σε μια ομάδα 27 επιλεγμένων αριθμητικών αναλύσεων, και η ακόλουθη στατιστική επεξεργασία των αποτελεσμάτων, οδήγησε στη διαμόρφωση της τελικώς προτεινόμενης σχέσης υπολογισμού του συντελεστή K_s:

$$K_s = 1.00\left(\frac{q}{p_\alpha}\right)^{-0.30}\left(\frac{H_{imp}}{B}\right)^{-0.50} \qquad [20]$$

όπου

p_α	η ατμοσφαιρική πίεση (= 98.1kPa)
q(kPa)	η επιβαλλόμενη τάση έδρασης του θεμελίου
H_{imp}(m)	το πάχος της βελτιωμένης ζώνης
B (m)	το πλάτος του θεμελίου

Η εξάρτητη της παραμέτρου $\boldsymbol{U_3}$ από την απομειωμένη φέρουσα ικανότητα q_{ultdeg}^{inf}, επιβάλλει την ταυτόχρονη και επαναληπτική επίλυση των *Εξισώσεων [10]* και *[16]*, έως ότου αυτές να συγκλίνουν και έτσι να προσδιοριστεί ο απομειωμένος συντελεστής ασφαλείας $F.S._{deg}^{inf*}$. Για τη βελτίωση των προβλέψεων της αναλυτικής μεθοδολογίας, στην ανωτέρω τιμή εφαρμόζεται ο ακόλουθος διορθωτικός συντελεστής και τελικώς προσδιορίζεται ο απομειωμένος συντελεστής ασφαλείας για συνθήκες εκτενούς πλευρικά (θεωρητικά "άπειρης") βελτίωσης $F.S._{deg}^{inf}$:

$$F.S._{deg}^{inf} = \frac{F.S._{deg}^{inf*}}{0.05 + 0.60\left(F.S._{deg}^{inf*}\right)^{0.85}} > 0.60 F.S._{deg}^{inf*} \qquad [21]$$

Συνεπώς, με δεδομένο τον μετα-σεισμικό συντελεστή ασφαλείας $F.S._{deg}^{inf}$, υπολογίζονται οι αντίστοιχες σεισμικές καθιζήσεις. Στο **Σχήμα 27** παρουσιάζεται η αξιολόγηση των αναλυτικών προβλέψεων της μεθοδολογίας συναρτήσει των αντίστοιχων αριθμητικών τιμών, όπως επίσης και το υπολογιζόμενο σχετικό σφάλμα με την τυπική απόκλιση αυτού.

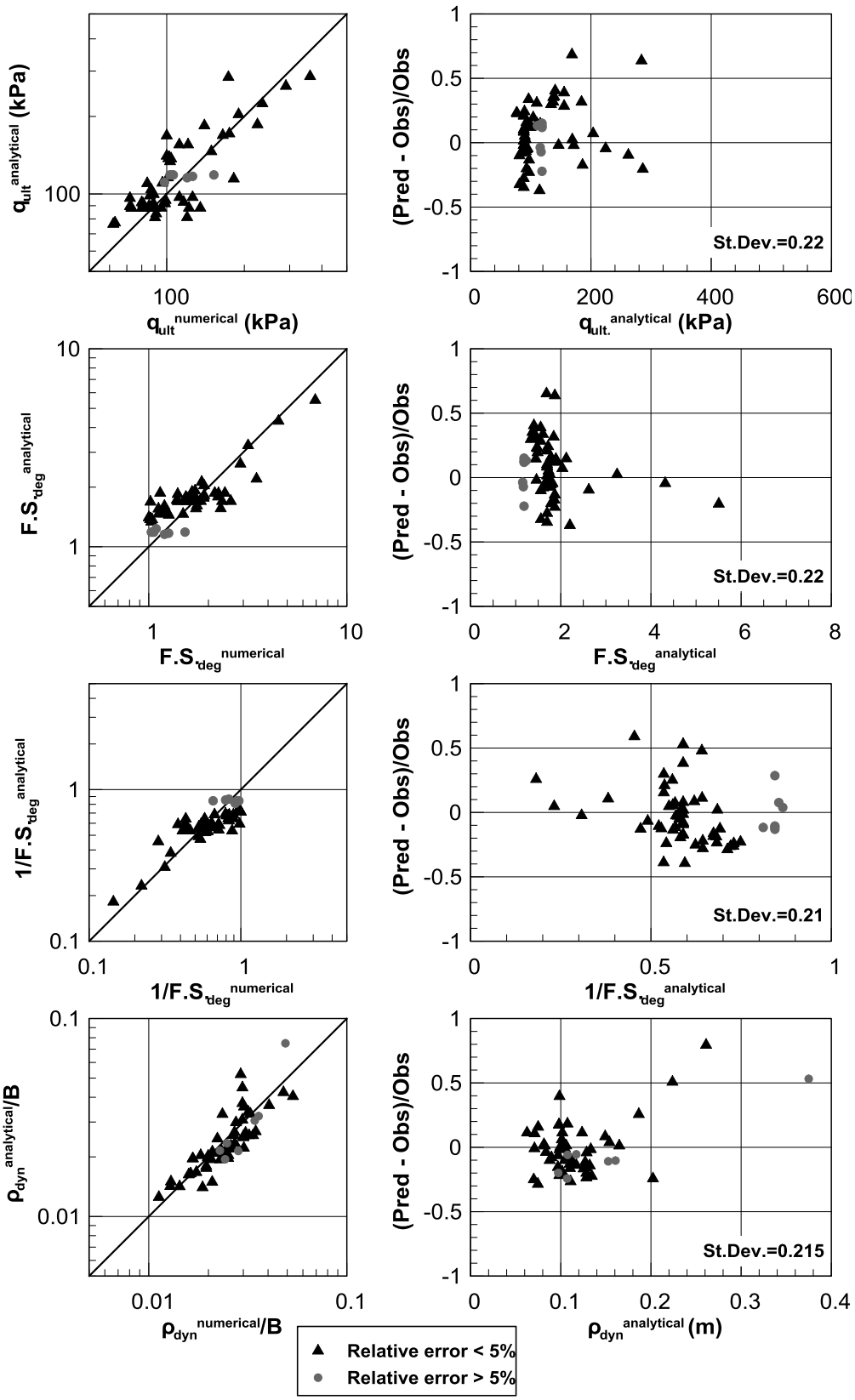

Σχήμα 27: Αξιολόγηση αναλυτικών προβλέψεων απομειωμένης φέρουσας ικανότητας, συντελεστή ασφαλείας και σεισμικών καθιζήσεων.

Σε πραγματικές εφαρμογές, η τεχνητά διαμορφωμένη κρούστα έχει πεπερασμένες διαστάσεις, η μία εκ των οποίων (το πλάτος L_{imp}) έχει έως τώρα θεωρηθεί πολύ μεγάλο (θεωρητικά άπειρο). Συνεπώς, το ***τέταρτο βήμα*** της αναλυτικής μεθοδολογίας, αφορά στον υπολογισμό των καθιζήσεων και της απομειωμένης φέρουσας ικανότητας του θεμελίου υπό συνθήκες πεπερασμένης πλευρικής έκτασης της βελτίωσης και υλοποιήθηκε με στατιστική επεξεργασία των αντιστοιχων αριθμητικών προβλέψεων.

Δυναμικές καθιζήσεις ρ_{dyn}(m).- Εκφράζονται ως συνάρτηση των διαστάσεων της βελτιωμένης κρούστας (H_{imp} και L_{imp}) κανονικοποιημένων προς το πλάτος του θεμελίου B:

$$\rho_{dyn} = \rho_{\inf} \Big/ \left[1 - \exp\left(-1.05 \left(\frac{H_{imp}}{B} \right)^{-1} \left(\frac{L_{imp}}{B} \right)^{0.30} \right) \right] \qquad [22]$$

Απομειωμένη Φέρουσα Ικανότητα q_{ult}^{deg} και Συντελεστής Ασφαλείας $F.S._{deg}$.- Λόγω της ευαισθησίας των αριθμητικών αποτελεσμάτων για τα εν λόγω μεγέθη ο προσδιορισμός του μετα-σεισμικού συντελεστή ασφαλείας για πεπερασμένη πλευρικά βελτίωση έγινε έμμεσα, από συνδυασμό των σχέσεων [8] και [22]. Κατ' αυτό τον τρόπο προέκυψε η ακόλουθη σχέση, η οποία επιλύεται επαναληπτικά:

$$\left(\frac{F.S._{deg}}{F.S._{deg}^{inf}} \right)^{0.45} = \left\{ 1 - \exp\left[-1.05 \left(\frac{H_{imp}}{B} \right)^{-1} \left(\frac{L_{imp}}{B} \right)^{0.30} \right] \right\} \frac{\left(F.S._{deg}^{inf} \right)^{4.5} + 0.25 \left(\frac{F.S._{deg}}{F.S._{deg}^{inf}} \right)^{-4.5}}{\left(F.S._{deg}^{inf} \right)^{4.5} + 0.25} \qquad [23]$$

<u>Ε.Ε.4 Διαγράμματα Σχεδιασμού</u>.

Προς διευκόλυνση στη χρήση της προτεινόμενης αναλυτικής μεθοδολογίας, τα **Σχήμα 28** έως **30** επιτρέπουν την εκτίμηση του λόγου των σεισμικών καθιζήσεων για πεπερασμένη προς άπειρη βελτίωση $\rho_{dyn}/\rho_{dyn}^{inf}$, ως συνάρτηση τριών διαφορετικών παραμέτρων σχεδιασμού, δηλαδή τους λόγους L_{imp}/B, L_{imp}/H_{imp} και V_{imp}/B^2,

όπου L_{imp} είναι το πλάτος της βελτιωμένης ζώνης,

B είναι το πλάτος του θεμελίου,

H_{imp} είναι το βάθος της βελτίωσης,

V_{imp} είναι ο όγκος της βελτιωμένης ζώνης, οριζόμενος ώς το γινόμενο του πλάτους (L_{imp}) επί το βάθος (H_{imp}) για τις 2-διάστατες συνθήκες του προβλήματος.

Ο λόγος των σεισμικών καθιζήσεων παρουσιάζεται για επτά (7) διαφορετικές τιμές του λόγου H_{imp}/B (= 0.50, 0.75, 1.00, 1.25, 1.50, 1.75, 2.00).

Σχετικά με τον κανονικοποιημένο λόγο του **απομειωμένου συντελεστή ασφαλείας** $F.S._{deg}/F.S._{deg}^{inf}$ τα αντίστοιχα διαγράμματα σχεδιασμού συνοψίζονται στα **Σχήμα 31** έως **33.** Στα εν λόγω διαγράμματα, ο λόγος των απομειωμένων συντελεστών ασφαλείας για πεπερασμένη προς άπειρη βελτίωση $F.S._{deg}/F.S._{deg}^{inf}$ παρουσιάζεται συναρτήσει των ίδιων παραμέτρων σχεδιασμού που προαναφέρθησαν.

Στα ανωτέρω σχήματα, οι παχύτερες γκρι γραμμές οριοθετούν την περιοχή πέραν της οποίας ο ρυθμός μεταβολής των καμπυλών είναι μικρότερος του 5%. Το εν λόγω όριο σημαίνει πρακτικά ότι αύξηση των διαστάσεων της κρούστας περαιτέρω αυτών των ορίων δεν είναι οικονομικά συμφέρουσα, οδηγεί δηλαδή σε μικρή βελτίωση της συμπεριφοράς του θεμελίου για μεγάλο σχετικά πρόσθετο κόστος. Είναι αξιοσημείωτο ότι τα εν λόγω όρια "βέλτιστης οικονομο-τεχνικά βελτίωσης", τα οποία προέκυψαν ουσιαστικά από τις αριθμητικές αναλύσεις, συμφωνούν ικανοποιητικά με τα όρια που προτείνονται από την Ιαπωνική Υπηρεσία Πυροπροστασίας (JFDA, 1974) και τους Tchuchida et al. (1976) για τη βελτίωση ρευστοποιήσιμων εδαφών πριν την κατασκευή επιφανειακών θεμελιώσεων. Τα εν λόγω όρια έχουν προκύψει από ανεξάρτητες πειραματικές παρατηρήσεις και παρουσιάζονται με παχιές γραμμές στα **Σχήμα 31** έως **33**. Επισημαίνεται ωστόσο, ότι στις συγκεκριμένες συστάσεις προτείνεται η βελτίωση ολόκληρου του πάχους της ρευστοποιήσιμης στρώσης και επομένως ο συνολικός όγκος του βελτιωμένου εδάφους είναι σημαντικά μεγαλύτερος από τον όγκο που προκύπτει εφαρμόζοντας την προτεινόμενη μεθοδολογία.

Με βάση την προτεινόμενη μεθοδολογία για την εκτίμηση του λόγου των *σεισμικών καθιζήσεων* διαπιστώνεται ότι υπάρχει ουσιαστική επίδραση των διαστάσεων της κρούστας (δηλαδή ο ρυθμός μεταβολής υπερβαίνει το 5%) για τιμές του λόγου L_{imp}/H_{imp} μεγαλύτερες από περίπου 5 και τιμές του κανονικοποιημένου όγκου V_{imp}/B^2 μεγαλύτερες από περίπου 7, για το μέγιστο πάχος βελτίωσης. Για μικρές τιμές των λόγων H_{imp}/B και V_{imp}/B^2 και μικρά πλάτη βελτίωσης, παρατηρείται αρκετά μικρότερη αύξηση των σεισμικών καθιζήσεων.

Ως προς το λόγο του απομειωμένου συντελεστή ασφαλείας, παρατηρείται μια αρκετά απότομη αλλαγή στις υπολογιζόμενες τιμές για αυξανόμενες τιμές του λόγου L_{imp}/H_{imp}. Η εν λόγω παρατήρηση ήταν εμφανής, ήδη από την εκτέλεση των αριθμητικών αναλύσεων, όπου ακόμα και μια μικρή μείωση του πλάτους βελτίωσης οδηγούσε σε σημαντική απομείωση στις υπολογιζόμενες τιμές του συντελεστή ασφαλείας $F.S._{deg}$, ειδικά στις περιπτώσεις μεγάλου πάχους βελτίωσης. Συνεπώς, συμπεραίνεται ότι η επιλογή ενός περιορισμένου πλάτους αλλά μεγάλου πάχους σχήματος βελτίωσης δεν εγγυάται απαραιτήτως την ικανοποιητική σεισμική συμπεριφορά του θεμελίου, σε αντίθεση με μια ευρύτερης σε πλάτος και λεπτότερης κρούστας. Ποσοτικά, η επίδραση του πλάτους της κρούστας για τιμές του λόγου L_{imp}/H_{imp} μεγαλύτερες από περίπου 2 και του λόγου V_{imp}/B^2 μεγαλύτερες από 3.

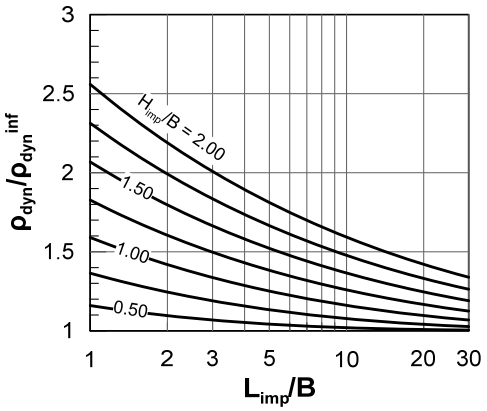

Σχήμα 28: Δυναμικές καθιζήσεις (ρ_{dyn}) κανονικοποιημένες προς την τιμή καθίζησης για άπειρη βελτίωση (ρ_{dyn}^{inf}) συναρτήσει του λόγου L_{imp}/B για διαφορετικές τιμές του λόγου H_{imp}/B.

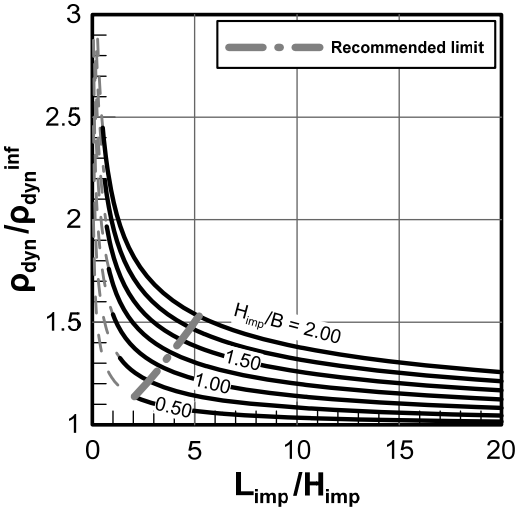

Σχήμα 29: Δυναμικές καθιζήσεις (ρ_{dyn}) κανονικοποιημένες προς την τιμή καθίζησης για άπειρη βελτίωση (ρ_{dyn}^{inf}) συναρτήσει του λόγου L_{imp}/H_{imp} για διαφορετικές τιμές του λόγου H_{imp}/B.

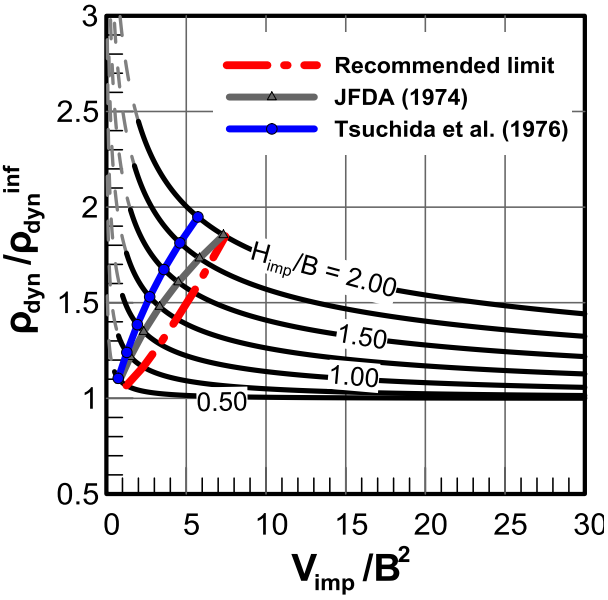

Σχήμα 30: Δυναμικές καθιζήσεις (ρ_{dyn}) κανονικοποιημένες προς την τιμή καθίζησης για άπειρη βελτίωση (ρ_{dyn}^{inf}) συναρτήσει του λόγου V_{imp}/B^2 για διαφορετικές τιμές του λόγου H_{imp}/B.

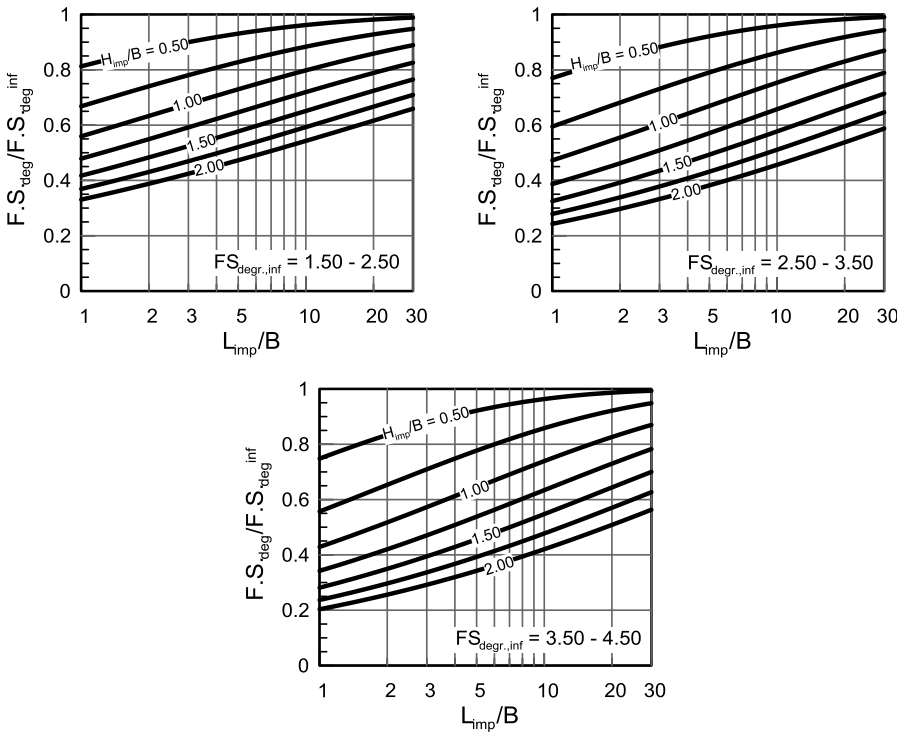

Σχήμα 31: Απομειωμένος συντελεστή ασφαλείας ($F.S._{deg}$) κανονικοποιημένος προς την αντίστοιχη τιμή για άπειρη βελτίωση ($F.S._{deg}^{inf}$) συναρτήσει του λόγου L_{imp}/B με βάση τις απλοποιημένες αναλυτικές σχέσεις και τρεις αρχικές τιμές απομειωμένου συντελεστή ασφαλείας $F.S._{deg}^{inf}$.

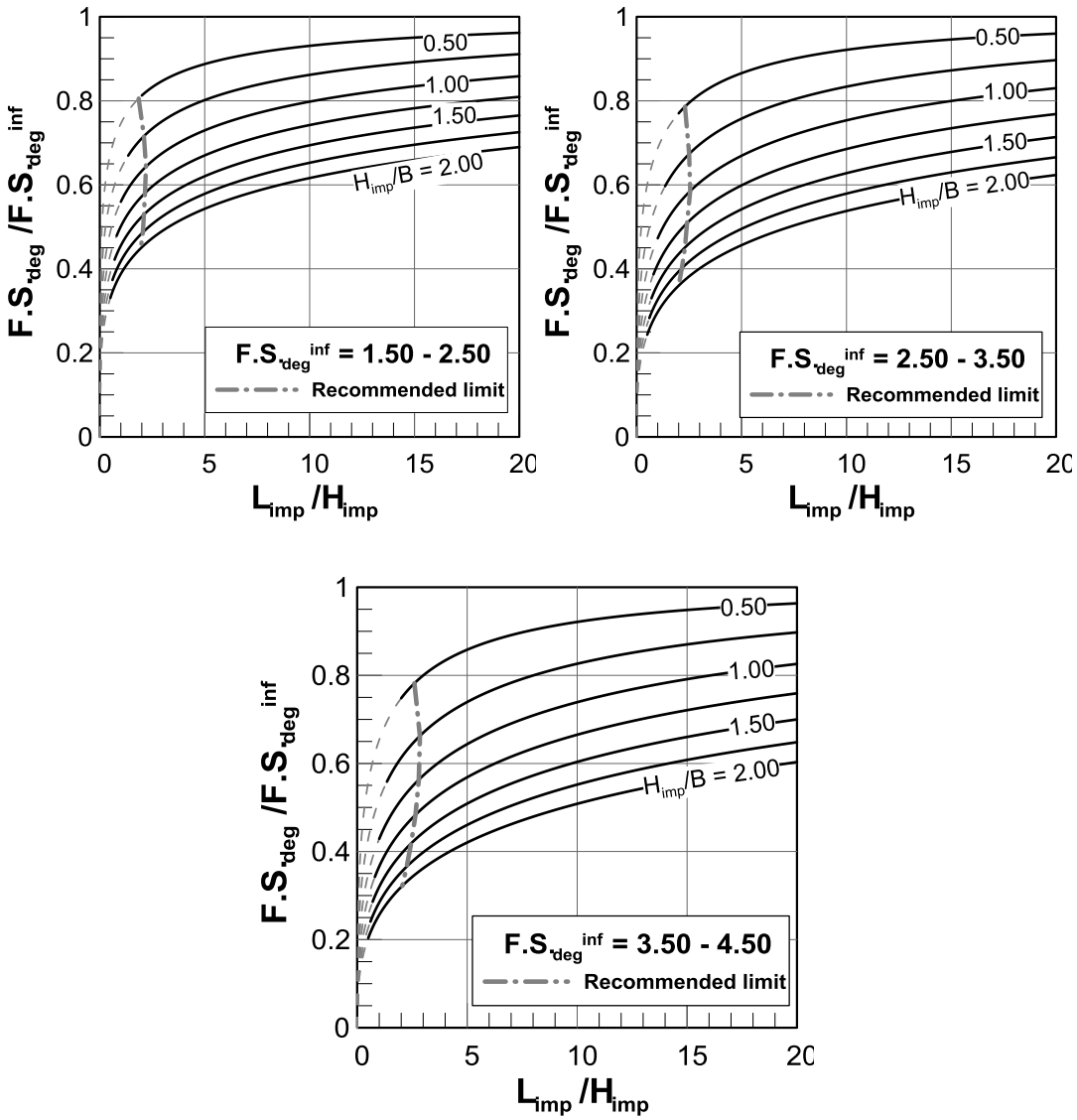

Σχήμα 32: Απομειωμένος συντελεστή ασφαλείας ($F.S._{deg}$) κανονικοποιημένος προς την αντίστοιχη τιμή για άπειρη βελτίωση ($F.S._{deg}^{inf}$) συναρτήσει του λόγου L_{imp}/H_{imp} για τρεις αρχικές τιμές απομειωμένου συντελεστή ασφαλείας $F.S._{deg}^{inf}$.

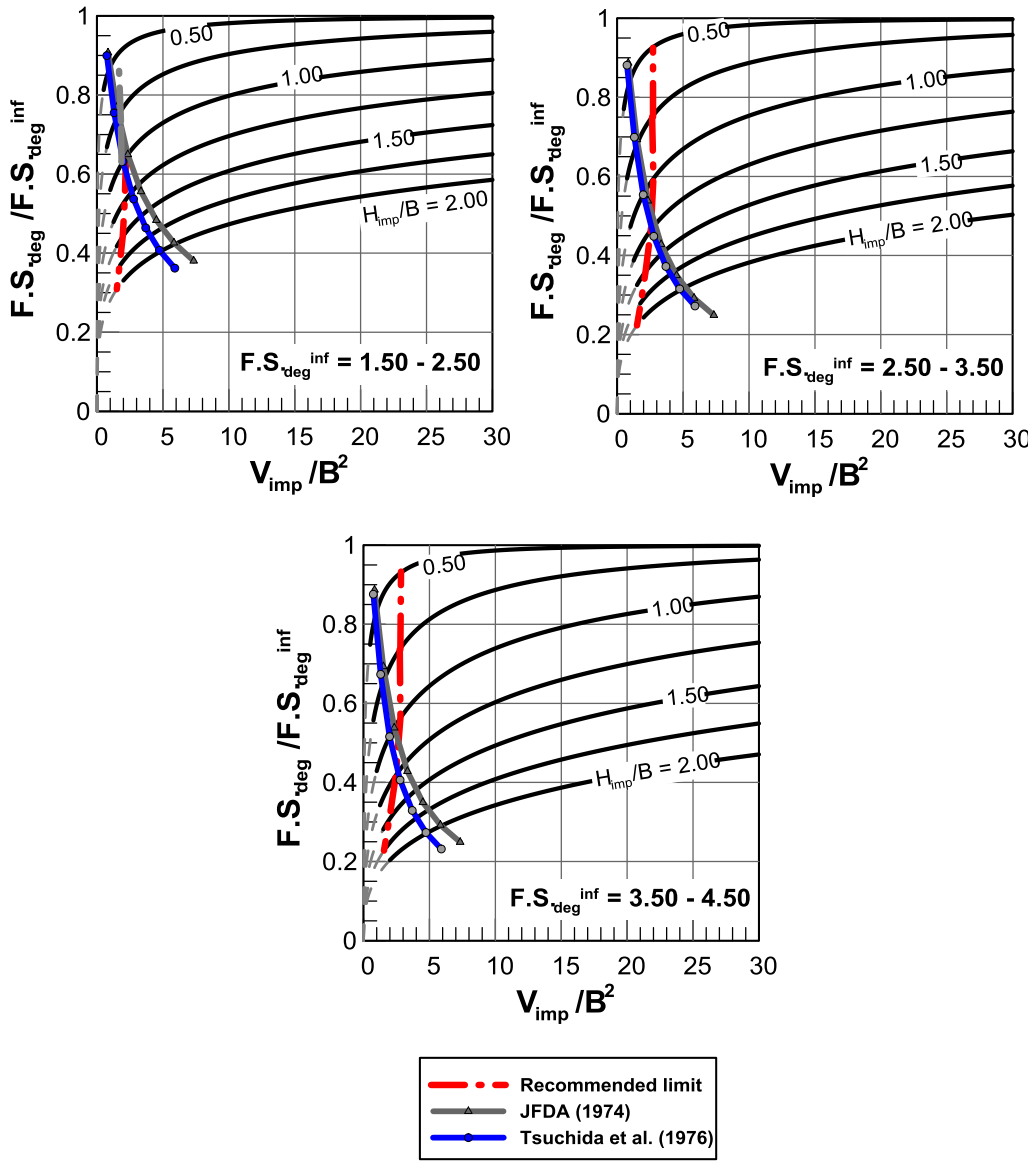

Σχήμα 33: Απομειωμένος συντελεστή ασφαλείας ($F.S._{deg}$) κανονικοποιημένος προς την αντίστοιχη τιμή για άπειρη βελτίωση ($F.S._{deg}^{inf}$) συναρτήσει του λόγου V_{imp}/B^2 για τρεις αρχικές τιμές απομειωμένου συντελεστή ασφαλείας $F.S._{deg}^{inf}$.

IV Συμπεράσματα

Τα κυριότερα συμπεράσματα της παρούσας διατριβής συνοψίζονται στα ακόλουθα:

1. Στα πλαίσια επανεξέτασης της βασικής σχέσης που περιγράφει την ανάπτυξη υδατικών υπερπιέσεων r_U-N/N_L, στην αναλυτική μεθοδολογία των Bouckovalas et al. (2009), διαπιστώνεται ότι ο συντελεστής A εξαρτάται από τον τύπο της δοκιμής (ανακυκλική τριαξονική ή απευθείας διάτμηση), την τάση στερεοποίησης, σ'_{vo}, καθώς και από τις εκάστοτε εδαφικές ιδιότητες, όπως το ποσοστό λεπτόκοκκων και η σχετική πυκνότητα. Με βάση αποτελέσματα εργαστηριακών δοκιμών, δύναται να λάβει τιμές από 0.7 έως 2.00.
2. Με δεδομένο το νέο εύρος τιμών του συντελεστή A, διατυπώνονται νέα διαγράμματα σχεδιασμού, στα οποία:
    - θεωρούνται διαφορετικές τιμές του συντελεστή A = 0.70, 1.00, 1.40 και 2.00.
    - έχει εξαλειφθεί η επίδραση της διάρκειας σεισμικής δόνησης, αντικαθιστώντας τον αδιάστατο χρονικό παράγοντα T_{ad} με τον όρο $T_{al.}$
    - αποδεικνύεται ότι και η ένταση της σεισμικής κίνησης (N_{eq}/N_L) δεν έχει σημαντική επίδραση, εντός του συνήθους εύρους τιμών σχεδιασμού του επιτρεπόμενου λόγου υπερπίεσης πόρων $r_{u,max}$ = 0.20 ÷ 0.50.
3. Η αξιοπιστία των νέων διαγραμμάτων σχεδιασμού ελέγχεται μέσω της αριθμητικής προσομοίωσης της αποστραγγιστικής δράσης των χαλικοπασσάλων, με τη βοήθεια σοφιστευμένων 3-Δ δυναμικών μη-γραμμικών αναλύσεων. Στα πλαίσια αυτά, επαληθεύεται και αριθμητικά η παραδοχή των Seed & Booker (1977) και των Bouckovalas et al. (2009) περί ενός σταθερού συντελεστή συμπιεστότητας $m_{v,3}$ σε όλη την έκταση της ρευστοποιήσιμης στρώσης. Επίσης, ο προσδιορισμός του συντελεστή συμπιεστότητας $m_{v,3}$ συνίσταται να πραγματοποιείται μέσω πειραματικών αποτελεσμάτων ανακυκλικής απλής διάτμησης.
4. Η χρησιμοποιούμενη αριθμητική μεθοδολογία για την παραμετρική διερεύνηση της σεισμικής απόκρισης της επιφανειακής θεμελίωσης επαληθεύθηκε επιτυχώς, έναντι των δημοσιευμένων και καλά τεκμηριωμένων πειραματικών αποτελεσμάτων σε φυγοκεντριστή των Liu & Dobry (1997), ως προς την ανάπτυξη των δυναμικών καθιζήσεων.

5. Η συσσώρευση των δυναμικών καθιζήσεων της επιφανειακής θεμελίωσης είναι το αποτέλεσμα της ενεργοποίησης ενός μηχανισμού ολισθαίνοντος στερεού κατά Newmark, και συνδέεται με την ενεργοποίηση ενός σφηνοειδούς μηχανισμού αστοχίας, ο οποίος εκδηλώνεται δύο φορές κατά τη διάρκεια ενός πλήρους κύκλου φόρτισης, μία από κάθε πλευρά του θεμελίου.
6. Η ανωτέρω παρατήρηση οδήγησε και στη συσχέτιση των δυναμικών καθιζήσεων, ρ_{dyn}, με τον όρο $a_{max}T^2N$, ο οποίος απορρέει από τη θεώρηση του μηχανισμού ολισθαίνοντος στερεού για την απλή περίπτωση αρμονικής διέγερσης.
7. Η αναπτυσσόμενη επιφάνεια αστοχίας κατά τη σταδιακή αύξηση του φορτίου της επιφανειακής θεμελίωσης είναι αντίστοιχη του μηχανισμού που προτείνεται από τους Meyerhoff & Hanna (1978) για επιφανειακές θεμελιώσεις σε 2-στρωτα εδαφικά προφίλ. Στην εν λόγω αναλυτική μεθοδολογία, το πάχος της βελτίωσης (H_{imp}) καθορίζει και τη μορφή του μηχανισμού αστοχίας, όπου για μικρές τιμές του βάθους βελτίωσης αναπτύσσεται ένας μηχανισμός διάτρησης της θεμελίωσης εντός του υποκείμενου ρευστοποιημένου εδάφους (punching shear failure), ενώ σε περιπτώσεις αυξημένου πάχους, ο μηχανισμός αστοχίας αναπτύσσεται εξ'ολοκλήρου εντός της κρούστας.
8. Η βελτιωμένη επιφανειακή κρούστα διαθέτει σημαντικά μεγαλύτερη διαπερατότητα σε σχέση με την υποκείμενη ρευστοποιήσιμη άμμο. Το αποτέλεσμα αυτής της διαφοράς είναι η ταχεία αποτόνωση των υδατικών υπερπιέσεων από τη ρευστοποιήσιμη άμμο προς την επιφανειακή κρούστα και ο σχηματισμός μιας μεταβατικής ζώνης μερικώς ρευστοποιημένου εδάφους μεταξύ τους. Η ύπαρξη της μεταβατικής ζώνης λαμβάνεται υπόψη στον υπολογισμό της μετασεισμικής φέρουσας ικανότητας της θεμελίωσης μέσω του κατάλληλου μετασχηματισμού της αναλυτικής σχέσης των Meyerhoff & Hanna (1978).
9. Ο προσδιορισμός της μετα-σεισμικής φέρουσας ικανότητας του θεμελίου είναι συζευγμένος με την ανάπτυξη των υδατικών υπερπιέσεων πόρων στη ρευστοποίησιμη άμμο, με αποτέλεσμα την επαναληπτική επίλυση των αντίστοιχων αναλυτικών εκφράσεων της προτεινόμενης μεθοδολογίας.
10. Τα προτεινόμενα όρια "βέλτιστης οικονομο-τεχνικά βελτίωσης", τα οποία προέκυψαν ουσιαστικά από τις αριθμητικές αναλύσεις, συμφωνούν ικανοποιητικά με τα όρια που προτείνονται από την Ιαπωνική Υπηρεσία Πυροπροστασίας (JFDA,

1974) και τους Tchuchida et al. (1976) για τη βελτίωση ρευστοποιήσιμων εδαφών πριν την κατασκευή επιφανειακών θεμελιώσεων.

11. Η μεγιστοποίηση των ωφελειών από την παρουσία της επιφανειακής βελτιωμένης κρούστας (δηλαδή η πρόβλεψη των ελάχιστων δυνατών καθιζήσεων και της μέγιστης μετασεισμικής φέρουσας ικανότητας) επιτυγχάνονται για σχετικά εκτενές εύρος βελτίωσης, το οποίο φτάνει έως και 20 φορές το πλάτος του θεμελίου. Η υιοθέτηση τόσο μεγάλων τιμών πλάτους βελτίωσης συνεπάγεται και την εκτόξευση του αντίστοιχου κόστους κατασκευής. Συνεπώς, η προτεινόμενη μεθοδολογία σχεδιασμού είναι τεχνικά και οικονομικά βιώσιμη για τιμές πλάτους βελτίωσης 2 – 5 φορές το βάθος της βελτιωμένης κρούστας, ήτοι $L_{imp} = (2 \div 5)\, H_{imp}$.

V Προτάσεις για μελλοντική έρευνα

Με βάση τα ανωτέρω συμπεράσματα, εντοπίζονται τα ακόλουθα σημεία, τα οποία αποτελούν προτάσεις για μελλοντική έρευνα:

- Η επέκταση της παρούσας αναλυτικής μεθοδολογίας σχεδιασμού, η οποία ισχύει για θεμελιώσεις μεγάλου μήκους (θεμελιολωρίδες), στην περίπτωση ορθογωνικών και τετραγωνικών θεμελίων.
- Η εξέταση της επίδρασης του βάθους εγκιβωτισμού και η κατάλληλη προσαρμογή των αντίστοιχων αναλυτικών σχέσεων υπολογισμού.
- Η εξέταση φαινομένων αλληλεπίδρασης εδάφους – κατασκευής δεδομένου ότι στην παρούσα διατριβή τέτοια φαινόμενα έχουν αγνοηθεί, εφόσον η σεισμική κίνηση στην εδαφική επιφάνεια φτάνει εξασθενημένη, εξαιτίας της εκδήλωσης ρευστοποίησης στην υποκείμενη άμμο.

Table of Contents

CHAPTER 1

Introduction

1.1 Problem description

According to contemporary seismic codes, soils susceptible to liquefaction are classified as extreme soil conditions, in which the installation of shallow foundations is, by all means, prohibited without prior soil remediation. More specifically, liquefaction occurrence causes severe shear strength degradation of the foundation soil, which may lead to the accumulation of excessive seismic settlements as well as to post-shaking bearing capacity failure. The detrimental consequences of earthquake-induced liquefaction upon shallow foundations are also evident in **Figure 1.1**. The design philosophy characterizing current practice, involves the installation of pile foundations, which essentially bypass the liquefiable layer and transfer the structure loads to deeper and non-liquefiable strata. In parallel, the liquefiable layer is often improved against excess pore pressure built up using gravel drains, while some degree of densification is obtained during their installation.

Recent experimental and theoretical studies on the seismic response of shallow foundations on liquefiable soils [Cascone & Bouckovalas (1998), Liu & Dobry, (1997), Dashti et al. (2008), Sitar & Hausler, (2012)] provide well-established evidence that the aforementioned conventional design approach may be drastically changed with beneficial effects on the overall foundation cost, while maintaining acceptable performance and safety levels. Namely, it is indicated that the presence of a naturally occuring or artificially manufactured surface crust of non-liquefiable soil may moderate the detrimental consequences of liquefaction to such an extent that the use of shallow foundations becomes acceptable. The

above objective is achieved, provided the particular crust has adequate dimensions (thickness and width below and around the footing) and shear strength to sustain the foundation loads after the onset of liquefaction in the subsoil.

Recently, Karamitros (2010) has conducted an in-depth investigation to analyze the mechanisms governing the liquefaction performance of shallow foundations resting upon a two-layer soil profile consisting of liquefiable sand overlain by a surface clay crust. The outcome of the numerical simulation of the problem is a complete analytical methodology for the performance-based design of strip and rectangular shallow foundations. The particular methodology enables the computation of seismic settlements as well as post-shaking bearing capacity degradation [Karamitros et al (2013a), Karamitros et al. (2013b)].

Figure 1.1: Liquefaction-induced failure of shallow foundations from various earthquakes (a) Dagupan, Philippines, 1990, M=7.8, (b) Kobe, Japan, 1995, M=7.2 (c) Adapazari, Turkey (1999) M=7.4, (d) Sendai, Japan, 2011 M=8.9.

1.2 Scope of work

The scope of the present thesis is to develop an analytical methodology for the performance-based design of strip shallow foundations resting directly on liquefiable soil, namely when the non-liquefiable crust is not encountered naturally but needs to be artificially created. Following the traditional requirements for the static design of shallow foundations, the specific methodology will enable the computation of the seismically induced settlements, as well as the post-shaking bearing capacity degradation.

The manufactured soil crust has the same initial consistency as the liquefiable soil, but opposite to the latter, in the occurrence of earthquake-induced liquefaction, the generated excess pore pressures are restrained to levels well below unity (e.g. r_u=0.3-0.4). The above objective is obtained through vibrocompaction or vibro-replacement methods. In both methods, along with the creation of gravel drains, which accelerate excess pore pressure dissipation and thus mitigate liquefaction, the natural soil is considerably densified. This combined intervention creates a quite complex pattern regarding the density distribution, the shear strength and the excess pore pressure dissipation mechanism in the improved ground.

The accomplishment of the aforementioned effort is based on the following resources:

- An extensive literature survey with regard to **(i)** the use of gravel drains in liquefaction mitigation, in order to define the basic design requirements and analytical methodologies used in current practice, as well as **(ii)** the available performance-based criteria, with paticular emphasis on performance levels and the associated allowable deformation limits specified in different international codes.
- The re-evaluation of the available analytical methodologies in gravel drain design, in view of new laboratory data, which aimed at improving the efficiency of the proposed design charts for drain design, hence leading to a refined and cost-effective design.
- The subsequent execution of 3-dimensional numerical analyses, aiming in the verification of the revisited analytical methodologies and the overall evaluation of the gravel drain performance.
- A well-established set of centrifuge experiments is utilized in the verification of the numerical methodology, before it is used in the parametric investigation of the problem under examination.

- A broad parametric investigation is performed with the aid of 2-dimensional numerical analyses, aiming at investigating the mechanisms governing the foundation performance,as well as providing quantitative means for evaluating the seismic settlements, and the post-shaking bearing capacity degradation. The specific investigation is targeted in two fronts, namely response of the footing under conditions of "infinite" and "finite" improvement, through two distinct sets of parametric analyses. The difference lies in the lateral width of the improved area.
- The numerical methodology applied for this purpose is based on an advanced elasto-plastic constitutive model, which is calibrated against a large number of laboratory experiments, including resonant column, monotonic and cyclic triaxial and simple shear tests.

1.3 Preview of thesis contents

Soil improvement is performed with the use of gravel drains, which should follow specific standards regarding their installation procedure, the used equipment, as well as the inserted material, which modifies the post-improvement soil properties. Their drainage capacity depends largely on the used material as well as the spacing ratio and gravel pile dimensions and allows the control over the dissipation rate of the earthquake induced excess water pressures. Drain spacing and dimensions are determined following analytical design methods, available in the literature and widely used in current practice. The above aspects of gravel drain design for liquefaction mitigation are covered through an extensive literature survey in *Chapter 2*.

Gravel drains are traditionally used as the main liquefaction countermeasure; nevertheless, they present several drawbacks. The main shortcoming appears either during installation or during the serviceable period of the drains and refers to clogging, namely the reduction of their drainage capacity, due to the migration of the finer sand particles towards the coarser fill material. Hence, in *Chapter 3*, a detailed literature survey is conducted emphasizing on alternative types of drains, which do not present many of the shortcomings of the traditional gravel piles. The particular research is performed in terms of materials, design and installation methodologies as well as equipment requirements.

The installation of shallow foundations on the previously mitigated ground against liquefaction, without the use of pile foundations, entails the accumulation of seismic settlements, which affect its structural and operational level. In the context of performance-

based engineering the significance of the induced damage, is evaluated with regard to the predefined seismic performance objective under established levels of seismic risk. Hence, *Chapter 4* summarizes the available performance-based criteria appearing in seismic design guidelines and provisions.

In view of new experimental data, *Chapter 5* revisits the two main design methodologies in drain design to account for the effect of soil properties on the empirical correlation between the excess pore pressure ratio and the number of cycles required for liquefaction. The main conclusions include the formulation of updated design charts, which improve the predicting capacity of the revised methodology, while alongside highlighting the over-conservatism of the traditional design methodology.

The validity of the previous analytical methodology is checked through a number of numerical analyses for different coefficients of the sand permeability, namely ranging from "undrained" conditions to a considerably permeable sand material (in the order of 10^{-4}m/s). The particular numerical simulation of the gravel drain performance is achieved using advanced numerical tools such as FLAC3D. The specific verification procedure is thoroughly explained in *Chapter 6*.

Before executing a parametric investigation on the liquefaction performance of shallow foundations, the simulation of the footing response is thoroughly assessed. More specifically, the theory of the *Equivalent Uniform Improved Ground* (E.U.I.G.) is introduced and established. According to this, the improved ground layer is considered uniform with appropriately computed unique soil parameters, which take into account the properties of the natural ground, the properties of the gravel, as well as the extent of ground improvement. In the sequel, the numerical methodology is validated against well-established centrifuge experiments in terms of the accumulation of seismic settlements. The above activities are included in *Chapter 7*.

In the sequel, in *Chapter 8*, an extensive parametric investigation is performed through a number of 1-D numerical analyses, simulating the free-field response of the improved ground. The intention is to identify the required replacement ratio α_s to restrain excess pore pressure generation, in the improved ground, within the target range of $\overline{r}_{u,\,max} = 0.30 – 0.50$. Additionally, the behavior of strip (2-dimensional) footings resting on a 2-layer soil profile, consisting of liquefiable sand overlain by improved ground is parametrically investigated through the execution of a considerable number of numerical analyses. The particular set of

parametric analyses incorporated the effect of only one dimension of the improved crust, namely that of the thickness of it.

The processing of the previously obtained numerical results, combined with a physical interpretation of the governing mechanisms, allows the formulation of simplified analytical relations for the evaluation of the degraded bearing capacity and the corresponding seismic settlements. The results of the numerical investigation and the resulting analytical expressions are presented in *Chapter 9*.

The lateral extent of soil remediation around a footing is a significant problem parameter, which has not been thoroughly investigated by the existing design guidelines not the previously established analytical methodology. Namely, the numerical investigation and the resulting analytical expressions of Chapter 9 are applicable to conditions of "infinite" improvement. Hence, the processing of the second set of numerical results leads to the formulation of simplified analytical relations for the evaluation of the degraded bearing capacity and the corresponding seismic settlements. The updated analytical expressions are summarized in *Chapter 10*.

Chapter 11 summarizes the main steps of the proposed analytical methodology for designing shallow foundations on liquefiable ground after proper soil improvement. Namely, the user is guided through the different stages of the performance – based design of shallow strip foundations, starting from the selection of the appropriate spacing of gravel drains, to the evaluation of the seismic settlements and the degraded post-shaking bearing capacity of the foundation, given the dimensions (thickness and width) of the improvement area.

CHAPTER 2

Gravel Drains for Liquefaction Mitigation

2.1 Introduction

Earthquake induced liquefaction is a problem commonly encountered in highly seismic areas where loose saturated sandy layers are encountered. Soil improvement is often required in such cases, either prior to any construction activity or when seismically retrofitting existing structures. The available soil remediation techniques include either densification of the natural soil through compaction and/or insertion of new material, or control and dissipation of the earthquake induced excess pore water pressures through the installation of gravel drains.

The gravel drain method is often applied in liquefaction remediation projects, aiming at improving the natural soil mainly by enhancing the overall drainage capacity of the liquefiable stratum. In the current chapter, the key aspects (design parameters, installation methods, required equipment etc) of the method are analyzed and the available design methodologies are outlined.

2.2 Installation and equipment

Gravel drains should be composed of coarse grained material, which is highly permeable compared to the surrounding liquefiable natural soil, thus allowing the fast dissipation of the earthquake – induced excess pore water pressures. Hence, the material used in current

practice is gravel or crushed stone, that follows specific standards in terms of permeability, as explained in the present paragraph.

Gravel drains are commonly installed in the form of single columns in a grid configuration, as presented in **Figure 2.1a**. Less often, drains may appear in the form of walls or mats, surrounding existing foundations (**Figure 2.1b).** Installation may be achieved with or without vibration. In the first case, some degree of densification of the surrounding soil is achieved, which can be taken into consideration during the design of the drain system. Depending on the selected installation method, different equipment requirements apply.

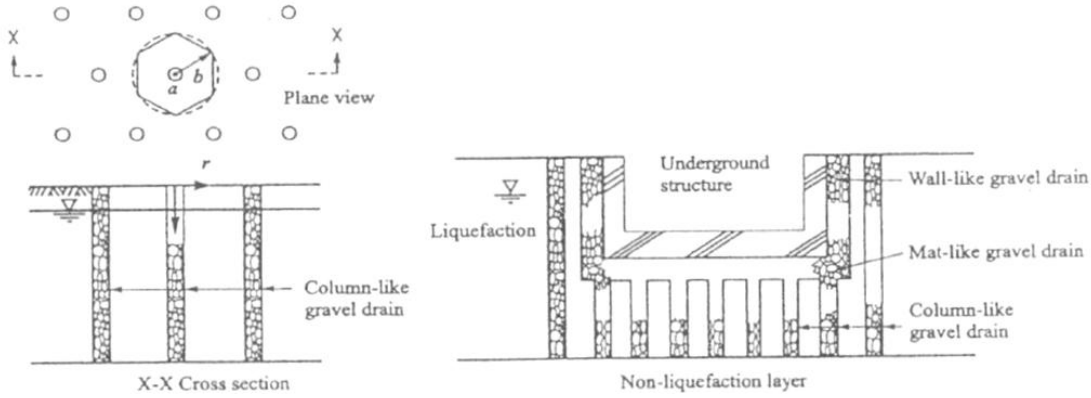

(a) **(b)**

Figure 2.1: Example of installation of gravel drains **(a)** in single columns and **(b)** wall – shaped drain surrounding an underground structure (JGS, 1998).

2.1.1 Vibratory methods

Vibratory methods for gravel drain installation involve the use of electrical vibrators to help advance the hole and densify the surrounding soil. The two primary vibratory techniques described below, concern the use of either pressurized water or air to aid the installation process.

The top feed method (Vibro-flotation).- Gravel drain installation is achieved with horizontal vibration of the vibro-flot, while jetting water from the tip of the vibrator, then gradually retracting it and inserting the gravel material from the ground surface into the hole, as it is schematically presented in **Figure 2.2**. The vibro – flot is attached to the rod of the crane and the two members are connected to the crane through a shock absorber so that vibration

does not affect the rest of the equipment. Usually, vibro-flots are 30 – 45cm in diameter, 2 to 4m in length and 4 to 8t in weight. A typical vibro-flot is presented in **Figure 2.3**.

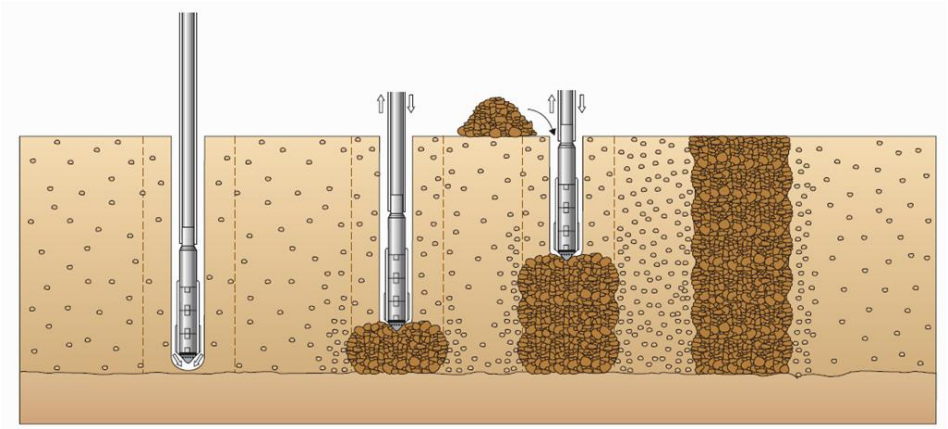

Figure 2.2: Installation stages in the vibro-flotation method (Hayward – Baker Inc.).

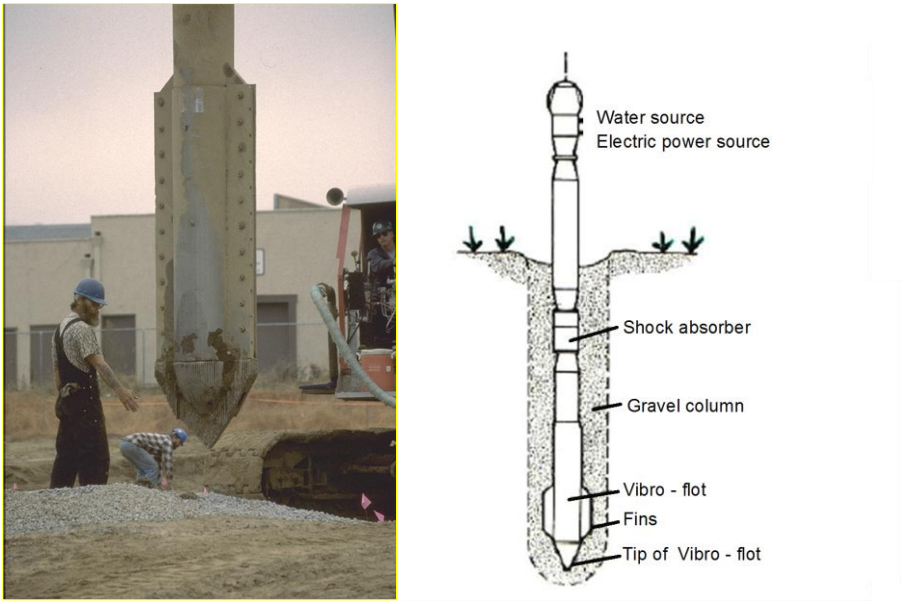

Figure 2.3: Photograph (provided by Nilex Inc.) and schematic representation of a Vibro – flot (Bell, 1993).

The vibro – flot technique is further explained **Figure 2.4.** The equipment is initially installed at the desired location and in the sequel the penetration begins, using jetted water from the tip and applying horizontal vibration, down to the design depth (phases **a** & **b**). The penetration rate is fast enough and may reach 0.5m/min in non-cohesive soils. Next, the vibro-flot is retracted at increments of 30 – 60cm/min and gravel material is fed from the ground surface, and compacted due to the continuing vibration (phase **c**). Water continues

to be flushed from the sides of the vibro-flot, in order to ensure a downward flow for the gravel transport. The resulting gravel column has a diameter of 50 to 80cm.

As a result of the applied vibration, the saturated soil adjacent to the gravel column locally liquefies and consequently a greater degree of densification is achieved. The range of vibration is 5 – 25mm with a frequency of 30 – 50Hz. A snap-shot of the top feed method is also given in **Figure 2.5**.

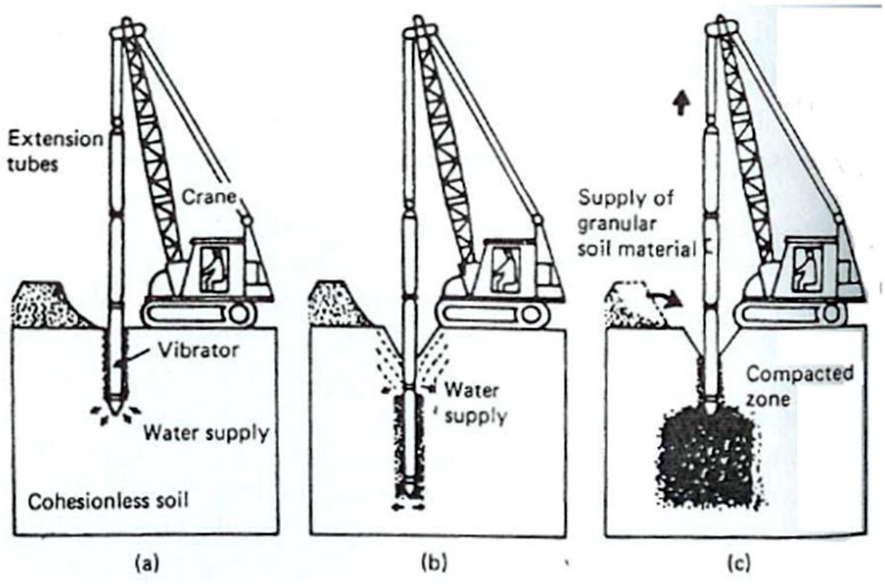

Figure 2.4: Installation stages of vibro – flotation technique (Bell, 1993).

Figure 2.5: Snap-shot of the wet top feed method (Nilex Inc.).

The bottom feed method (Vibro-displacement).- is applied in mixed grained and fine grained soils with fines content greater than 10 – 15 %. The main difference compared to the top feed method concerns the mode of insertion of the gravel material, which is now fed from the tip of the vibrator, instead of the ground surface, thus resulting in a continuous column.

The main steps of the method are outlined in **Figure 2.6a**. The vibrator is placed at the desired location and the skip is filled with aggregate. The skip is lifted and empties the aggregate into the air chamber of the vibrator. Subsequently, the vibrator penetrates into the ground and is lowered to the design depth, aided by compressed air and pull-down force stemming from the vibro-cat. Occasionally, water may be used for lubrication, in order to overcome high friction from the surrounding soils. After reaching the design depth, the vibrator is retracted in increments, releasing gravel material at the same time. The gravel material is then compacted by re-penetration of the vibrator. A closer view of the rod and the vibrator used in the present method is provided in **Figure 2.6b**.

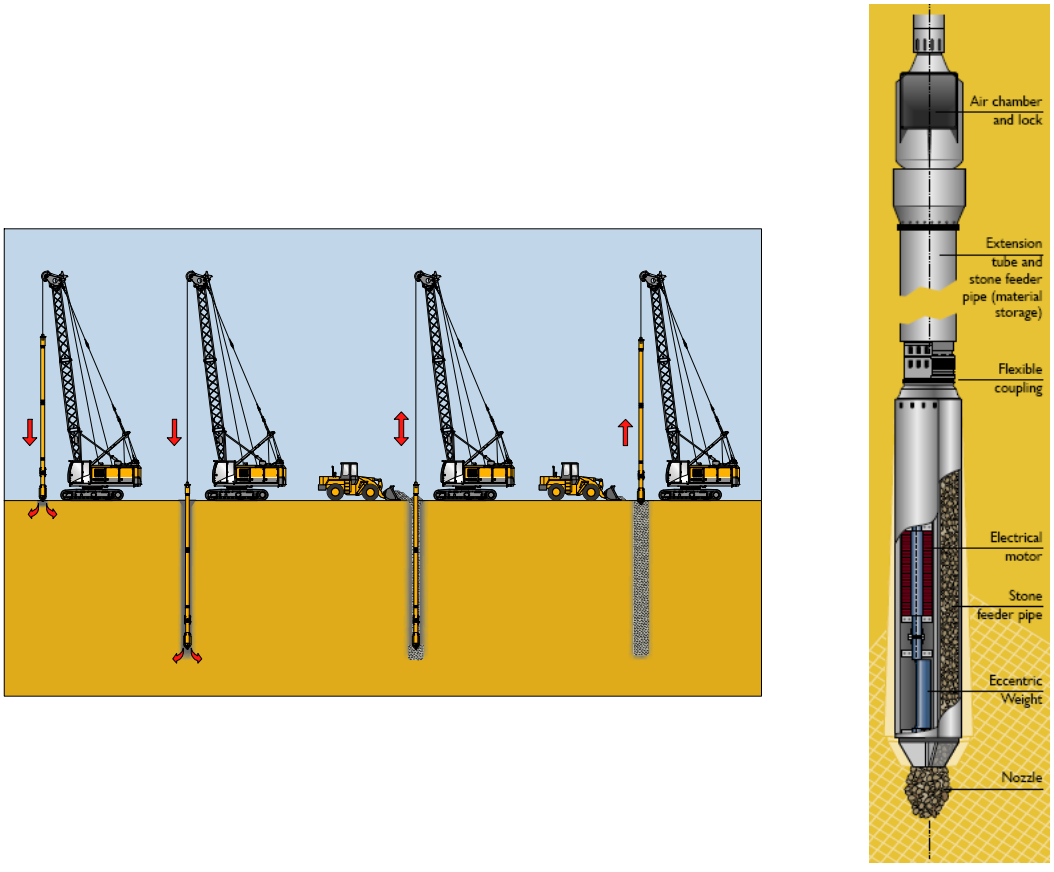

(a) **(b)**

Figure 2.6: **(a)** Construction stages of the bottom feed method (Bauer,2010), **(b)** Cross-section of the rod and the vibrator used in the bottom feed method. (Keller–Ground Engineering Pty, Ltd).

2.2.2 Non-Vibratory methods

Gravel drain installation is possible without vibration, using the casing auger method, as explained below. The casing auger method, although not frequently used in current practice, it is mentioned in the present chapter in order to provide a detailed overview of the available installation methods.

As indicated in **Figure 2.7** the casing auger is first mounted at the center of rotation of the earth auger and perpendicularity is confirmed (phase a). Then, the rotating auger is advanced into the ground, displacing the natural soil, and the gravel or crushed stone is poured into the casing from its upper end (phases b & c). Consequently, the auger is lifted up while discharging the gravel at the bottom and the gravel column is formed (phases d & e). Pressurized water or air is occasionally used to stabilize the lower end of the casing.

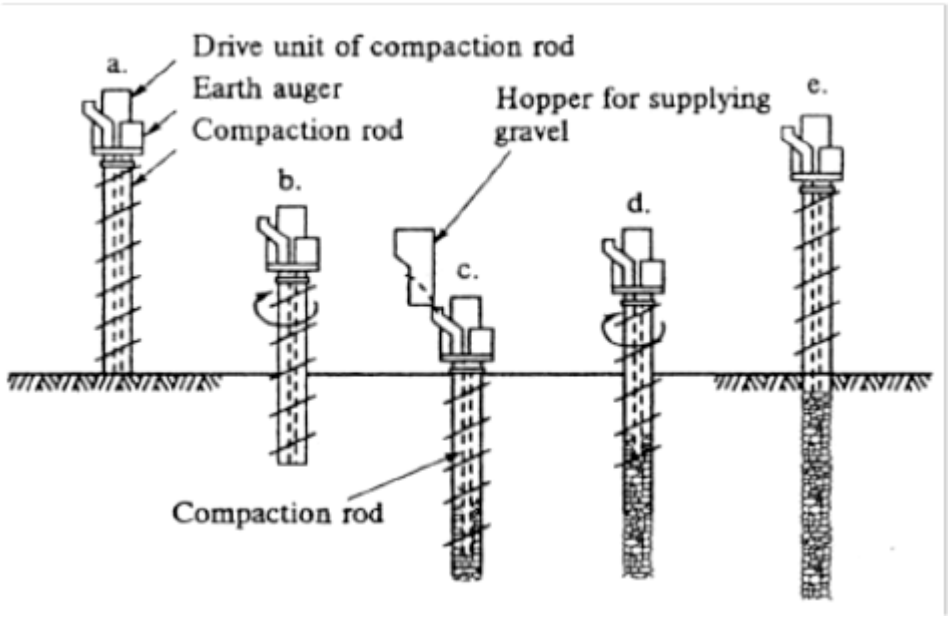

Figure 2.7: Casing auger method (Japanese Geotechnical Society, 1998).

The installation equipment consists of a crawler type driver, an earth auger, a casing with screws for displacing soil and a hopper for supplying the gravel material. **Figure 2.8** presents the installation equipment. Occasionally, the ductility of the column is increased by vibrating the gravel material and the surrounding soil either by a compacting rod at the center of the casing or by vibrating the lower end of the casing. Nevertheless, the achieved densification is very small and is disregarded in design applications.

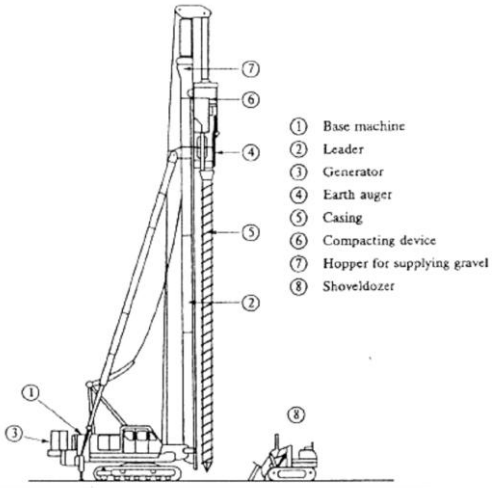

Figure 2.8: Installation equipment used in the casing auger method (PHRI, 1997).

Comparative evaluation of installation methods.- Figure 2.9 provides an overview on the classification of the available installation methods described in the present section. Namely, these are divided into two main categories i.e vibratory and non-vibratory, based on the induced vibration during their installation. The main difference between the two installation techniques concerns the excessive noise and degree of vibration to the surrounding environment. In view of the above observation, the casing auger method causes the least disturbance to the environment and the adjacent structures, compared to the vibratory methods.

In the case where some degree of vibration is required, the selection of the appropriate installation method and equipment depends mainly on the ground conditions as presented in **Figure 2.10**. Obviously, in the presence of fines in the liquefiable stratum, the bottom feed method is recommended for use, by all major contracting companies, whereas in the case of clean sands the top feed method is more suitable.

Additionally, when acceptable vibration and noise levels have to be considered in the selection of the appropriate vibratory drain installation method, it is acknowledged that the bottom feed method induces less noise and vibration. The standard type of vibro-hammer used, has a frequency of 10Hz and force capacity 40t, whereas when more tight noise and vibration restrictions apply, lighter equipment may be selected (20Hz, 25t). In case of soil strata with high penetration resistance heavier equipment (e.g. 10Hz, 88t) is necessary for the gravel column installation. Note that both methods are reported to be inadequate for compaction near the ground surface, thus other methods are recommended.

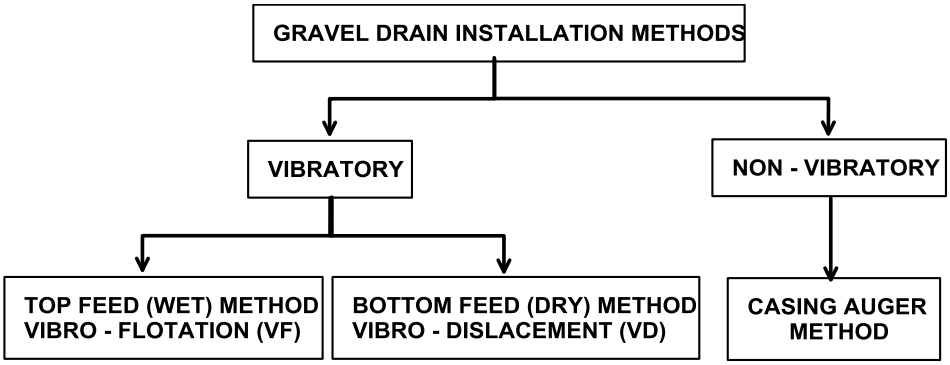

Figure 2.9: Classification of gravel drain installation methods.

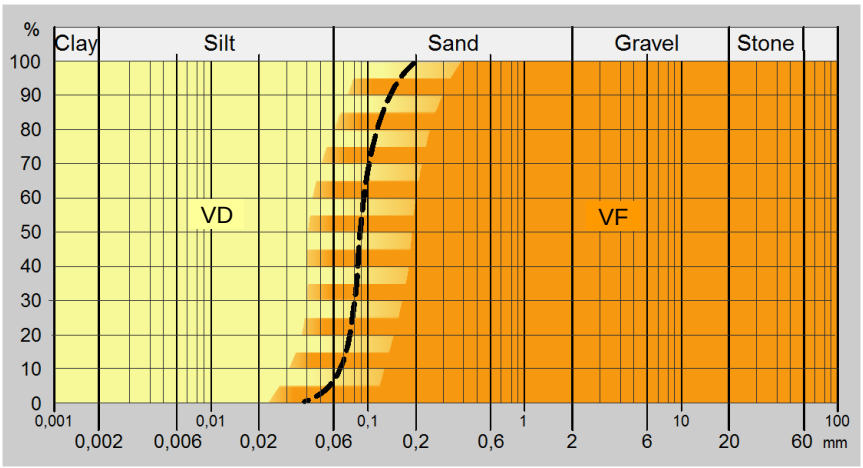

Figure 2.10: Application range for the bottom feed (Vibro-displacement) and top feed (vibro-flotation) methods (Bauer, 2010).

Another major difference between the two categories of vibratory methods concerns the compaction mechanism. In the top feed method, gravel is placed from the surface into the hole, to fill in the voids created in the soil from the induced vibration, therefore the quantity of the fill varies depending on the capacity of the vibrator. Namely, under new installation data, e.g. changing the vibrator's capacity, it is necessary to revise the design method and the quantity of fill to be used. On the contrary, in the bottom feed method the quantity of the inserted material is determined in advance and automatically controlled during installation, as compaction is accomplished by placing the gravel below the ground surface by vibrating the casing.

Two major drawbacks in the application of the top feed method concern the use of water as well as the applied vibration levels. More specifically, the use of water (primarily in the top feed method) may entail environmental hazards, if polluted spoil material is washed inside

the hole and transferred to the surface after constructing the gravel column. Additionally, the locally induced soil liquefaction in combination with the insertion of the gravel material may contaminate the gravel column with finer sand particles and therefore reduce its drainage capacity. In support of the above observation, Boulanger et al. (1998) indicate that the permeability of stone columns, was often two orders of magnitude less than the expected values from laboratory results. Special consideration is therefore required with respect to clogging, which can be avoided with the use of the top feed method, or the non-vibratory methods described below. The main features and limitations of each installation method are reviewed in **Table 2.1.**

Table 2.1: Main features and limitations of vibratory methods.

Installation Method	Maximum Installation Depth (m)	Maximum Fines Content for compaction efficiency	Influence on the surrounding areas	Remarks
Vibro – displacement (Bottom-feed)	20	10 - 15%	Relatively high levels of noise and vibration.	The method is less effective for layers with interpositioned clayey material due to obstacles to the supply of filling material
Vibro – flotation (Top – feed)	8 - 30 depending on the used equipment*.	< 10%	Little noise and vibration compared to vibro-displacement	The method is less effective for layers with interpositioned clayey material due to obstacles to the supply of filling material
Casing auger method (Non vibratory)	Up to 20m	No available data	Low noise and vibration levels	No degree of densification is achieved.

*In Europe the 30HP vibrator allows installation depths of up to 20m.

2.2.3 Evaluation of post – improvement soil properties

The densification of the liquefiable soil surrounding the gravel drains needs to be taken into consideration during drain design, hence it is essential to be able to evaluate the properties

of the improved soil in advance. This is possible with the aid of a number of empirical methods, as described below, based on the design guidelines proposed by the Japanese Geotechnical Society (JGS, 1998):

(a) N – D_r – e relationship for clean sands.- The improved soil's void ratio e_1 is specified from charts such as those appearing in **Figure 2.11**, as a function of the initial void ratio e_o, initial and post-improvement SPT values N_o & N_1 respectively. The replacement ratio α_s is then calculated based on *Equation 2.1*:

$$\alpha_s = (e_o - e_1)/(1 + e_o) \qquad 2.1$$

The effective overburden pressure appearing in the charts is calculated at half or one third of the thickness of the layer.

(b) N – D_r – e relationship considering fines content (f > 5%).- The current procedure is essentially an extension of the previous Method (a), further taking into account the effect of fines content. It is completed in the following steps:

- Determination of maximum and minimum void ratio (e_{max} and e_{min}) as a function of the fines content as presented below:

$$e_{max} = 1.0 + 0.02f\,(\%) \quad \text{and} \quad e_{min} = 0.6 + 0.008f(\%) \qquad 2.2$$

- Calculation of the initial void ratio e_o from the initial relative density, Dr_o, the maximum and minimum void ratio (e_{max} and e_{min}). The initial relative density Dr_o can be obtained from *Equation 2.3* as a function of the SPT blow count N_o and the confining vertical stress σ'_{vo}.

$$D_{ro} = 21\,[N_o/(0.7 + \sigma'_{vo})]^{1/2} \quad (\sigma'_{vo} \text{ in } kg/cm^2) \qquad 2.3$$

- Evaluation of the correction factor β, which depends on the the fines content f(%) as shown in the following equation:

$$\beta = 1.05 - 0.51\log_{10} f(\%) \qquad 2.4$$

- Use of the correction factor for the correction of the SPT blowcount, based on *Equation 2.5*:

$$N'_1 = N_o + (N_1 - N_o)/\beta \qquad 2.5$$

- Determination of the replacement ratio α_s from *Equation 2.1*.

(c) Charts based on empirical data.- Charts from actual projects or full scale experiments are used to determine the post improvement SPT blow count (denoted as N_1 or N_p), as a function of the original SPT blow count N_o and the replacement ratio α_s. The particular

charts, appear in **Figure 2.12**, and are valid for sandy soils with fines content lessr than 20%.

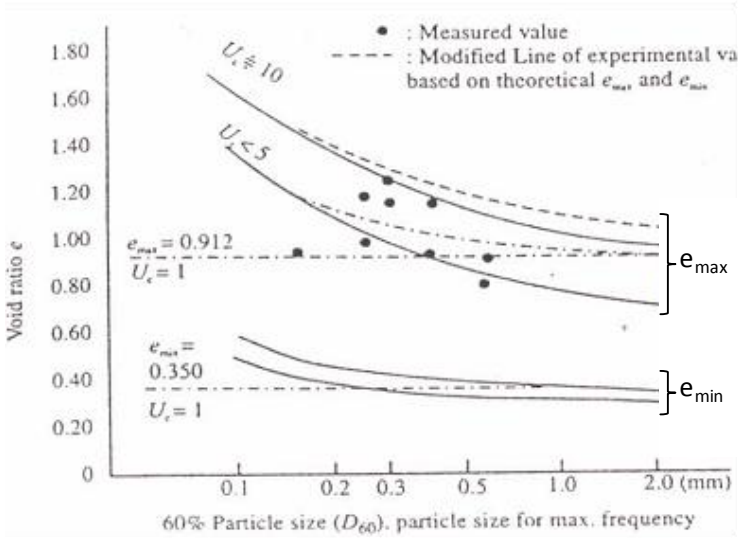

(a) Relationship between particle size – grain size and e_{max}, e_{min}

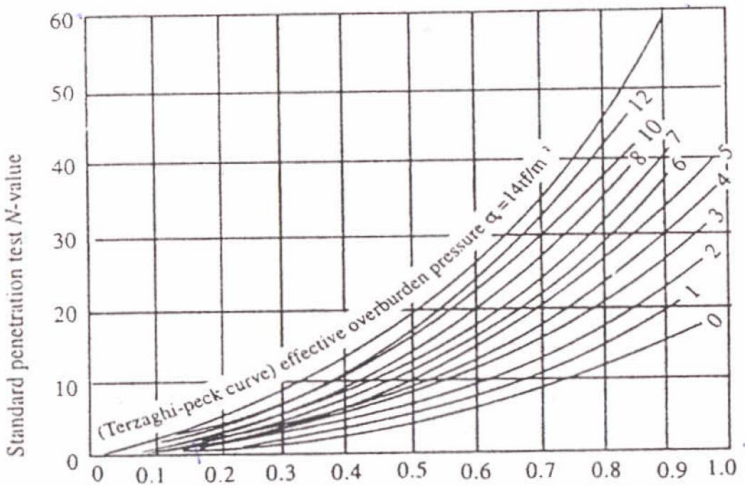

(b) Relationship between relative density D_r and N value.

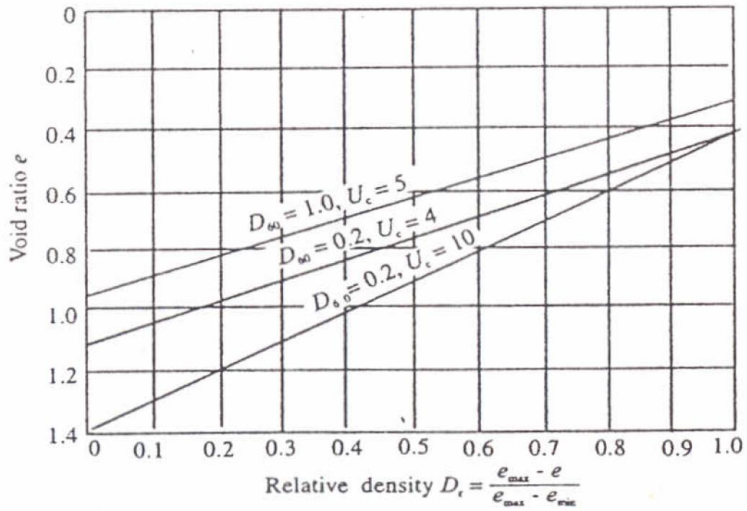

(c) N – D_r – e relation

Figure 2.11: N – D_r – e charts for evaluating improved soil's properties for clean sands.

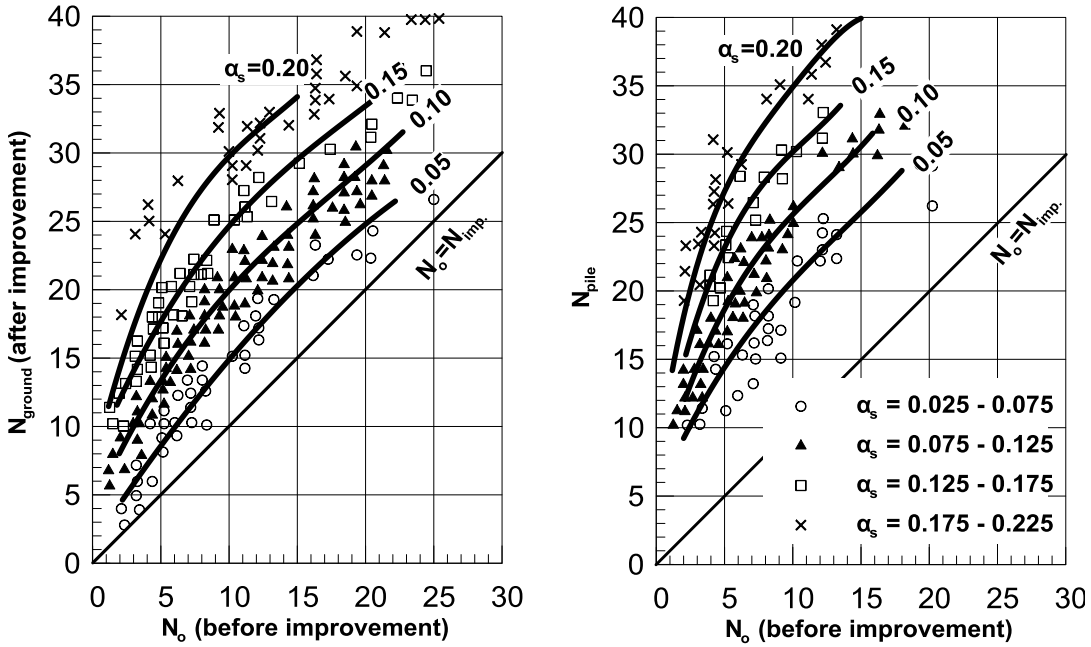

Figure 2.12: Correlation of initial (N_o) and post improvement N-value (N_1 or N_p) to the replacement ratio α_s (JGS, 1998).

2.3 Design parameters

In the present section, the main parameters involved in the design of gravel drains and the means to evaluate them in practice are addressed.

Coefficient of natural soil permeability k_s.- of the natural soil is determined either using permeability tests (in situ or laboratory) or empirical methods. In most current design methodologies, it is assumed that water flow, during an earthquake, occurs in the horizontal direction, hence the coefficient of horizontal permeability, also denoted as k_h, is used in design. For a relatively uniform soil stratum with a coefficient of uniformity $U_c < 5$ and d_{10} = 0.1 to 0.3mm the coefficient of permeability can be obtained from *Equation 2.6* (PHRI, 1997):

$$k_s = 100 \times d^2_{10} \qquad 2.6$$

When the above constraints are not satisfied, the Port & Harbour Research Institute (PHRI, 1997) propose **Tables 2.2** and **2.3**, which can provide a fairly accurate value of permeability.

Table 2.2: Diameter of sand particles (d_{50}) and associated coefficient of Permeability (after PHRI, 1997).

Soil Type	Particle Size (d_{50}) (mm)	Coefficient of permeability (cm/sec)
Very fine sand	0.05 - 0.10	0.001 - 0.005
Fine sand	0.10 - 0.25	0.005 - 0.01
Medium sand	0.25 - 0.50	0.01 - 0.1
Coarse sand	0.50 - 1.00	0.1 - 1.0
Small peebbles	1.00 - 5.00	1.0 - 5.0

Table 2.3: Diameter of sand particles (D_{20}) and associated coefficient of Permeability (after PHRI, 1997).

D_{20} (mm)	k (cm/sec)	Soil type	D_{20} (mm)	k (cm/sec)	Soil type
0.005	3.00×10^{-6}	Coarse clay	0.12	2.6×10^{-3}	Fine sand
0.01	1.05×10^{-5}	Fine silt	0.14	3.8×10^{-3}	
0.02	4.00×10^{-5}	Coarse silt	0.16	5.1×10^{-3}	
0.03	8.50×10^{-5}		0.18	6.85×10^{-3}	
0.04	1.75×10^{-4}		0.2	8.90×10^{-3}	
0.05	2.80×10^{-4}		0.25	1.40×10^{-2}	
0.06	4.60×10^{-4}	Very fine sand	0.3	2.20×10^{-2}	Medium sand
0.07	6.50×10^{-4}		0.35	3.20×10^{-2}	
0.08	9.00×10^{-4}		0.4	4.50×10^{-2}	
0.09	1.40×10^{-3}		0.45	5.80×10^{-2}	
0.1	1.75×10^{-3}		0.5	7.50×10^{-2}	
			0.6	1.10×10^{-1}	Coarse sand
			0.7	1.60×10^{-1}	
			0.8	2.15×10^{-1}	
			0.9	2.00×10^{-1}	
			1	3.60×10^{-1}	
			2	1.8	Fine gravel

Coefficient of volume compressibility m_v.- The coefficient of volume compressibility can be obtained through undrained cyclic triaxial tests by measuring the residual volumetric strain of undisturbed samples. It is estimated using *Equation 2.7* and is usually expressed in units of 1/kPa or cm^2/kgf:

$$m_{v,3} = \frac{\Delta V}{V} \times \frac{1}{u_{max}} \qquad 2.7$$

where ΔV = the change in the specimen's volume during consolidation

V = initial volume

u_{max} = excess pore water pressure at the beginning of consolidation

(usually, consolidation begins when the excess pore pressure ratio u_{max}/σ'_{vo} reaches a specified value, less than 0.5).

However, because such tests are rather complex and require sophisticated laboratory equipment and skilled personnel, $m_{v,3}$ is usually calculated based on published data for sands with different gradation. Typical values of the coefficient of volume compressibility are summarized in **Table 2.4**, provided by the Port & Harbor Research Institute (PHRI, 1997). The associated gradation curves for the tested sands are presented in **Figure 2.13**.

Table 2.4: Diameter of sand particles and associated coefficient of volume Compressibility PHRI, 1997)

Type of sand	Coefficient of volume compressibility (cm^2/kgf)	References (year)
Sacramento river sand	2.00×10^{-3}	Lee et al. (1974)
El Monte sand (D)	2.00×10^{-3}	Lee et al. (1974)
El Monte sand (E)	2.00×10^{-3}	Lee et al. (1974)
Akita Port sand	$3.00 - 4.00 \times 10^{-3}$	Zen et al. (1984)
El Monte sand (C)	4.00×10^{-3}	Lee et al. (1974)
Monterey sand	4.00×10^{-3}	Lee et al. (1974)
Fuji River sand	6.00×10^{-3}	Ishihara et al. (1978)
El Monte sand (B)	8.00×10^{-3}	Lee et al. (1974)
Ogishima sand	10×10^{-3}	Ono et al. (1983)

The coefficient of volume compressibility depends on the mean effective vertical stress σ'_m and the relative density of the soil D_r. For excess pore pressure ratio values (u_{max}/σ'_v) less than 0.5, the dynamic coefficient $m_{v,3}$ can be satisfactorily approximated by the static coefficient of volume compressibility (JGS, 1998), implying that $m_{v,3}$ exclusively depends on the vertical effective stress σ'_v. For that reason, it is noted that the $m_{v,3}$ values in **Table 2.4** were obtained at a confining pressure of σ'_v = 100kPa and excess pore water pressure ratio $r_u < 0.5$. For different levels of confining pressure σ'_v the obtained $m_{v,3}$ values must be multiplied by $1/\sqrt{(\sigma'_{vo}/p_a)}$, where p_a is the atmospheric pressure and σ'_{vo} the ever current vertical effective stress.

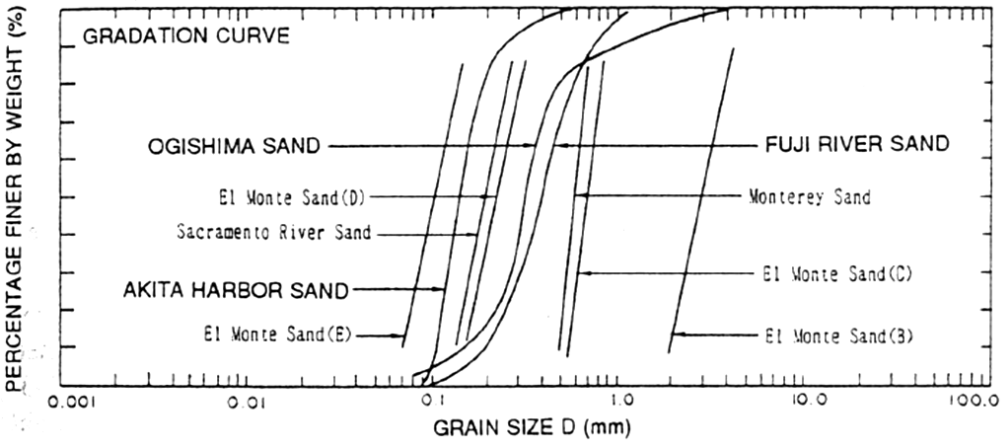

Figure 2.13: Gradation curves for the tested sands presented in **Table 2.4**, for determining their coefficient of volume compressibility (PHRI, 1997).

The coefficient of volume compressibility $m_{v,3}$ can also be correlated to the one-dimensional Young's modulus E_s, considering that

$$m_{v,3} = 1/K \qquad 2.8$$

where K is the bulk modulus for which

$$K = (0.50 \div 0.75)\, E_s \qquad 2.9$$

Table 2.5 is taken from the Japanese Geotechnical Society (1998) and summarizes cuclic triaxial test results on undisturbed samples, in which $m_{v,3}$ values were measured and correlated to the relative density of the samples. The examples clearly indicate an association between the two soil properties; however, a quantitative relationship has not been established yet.

Table 2.5: Coefficient of volume compressibility and relative density (after JGS, 1998).

Type of soil	Relative Density (%)	Coefficient of volume compressibility (cm^2/kgf)
Silty sand	-	0.005 - 0.02
Loose sand	20 - 40	0.005 - 0.01
Medium dense sand	40 - 60	0.002 - 0.005
Dense sand	60 - 80	0.001 - 0.002
Gravel	-	0.0005 - 0.001

Coefficient of drain permeability k_d.- The coefficient of drain material permeability depends primarily on the hydraulic gradient i, the ramming degree achieved during installation as well as the size distribution curve of the material.

The hydraulic gradient i is associated to the developing excess pore pressure ratio r_u, within the improved ground, which may be conservatively considered equal to the allowable excess pore pressure ratio r_{ud}, used in design. Hence, in the case where fast dissipation of the excess pore pressures is required, (namely low r_u values) the permeability k_d of the material needs to be high enough, to create a low hydraulic gradient i. The specific observation is clarified in the upper graph of **Figure 2.14**, which correlates typical permeability values to the hydraulic gradient i, and the densification degree achieved during installation (ramming). In this chart, the term ""*rammed 500 or 1000 times*" *indicates the number of tamping with a 4.5kgf ram".* The lower graph presents the size distribution curves for the same materials.

Gradation of drain material.- In the event of an earthquake, the horizontal water flow may carry along fine sand particles that eventually migrate from the natural soil into the gravel column. This effect, also known as clogging, can significantly reduce the flow capacity of a gravel column, decreasing its initial coefficient of permeability.

To avoid clogging, a series of empirical criteria has been proposed, mainly based on filtering criteria for selecting anti-clogging gravel drain material for earth dams. More specifically, according to the Japanese Geotechnical Society (1998), if D is the diameter of the drain material and d that of the natural soil and under long term seepage flow conditions, clogging is avoided when:

- $D_{15}/d_{85} < 4$ (Terzaghi's criterion)
- $D_{15}/d_{85} < 5$ (Japanese Society of Large Dams)

where D_{15} = grain size of gravel drain material corresponding to 15% finer by

weight

d_{85} = grain size of natural soil corresponding to 85% finer by weight

The Port and Harbour Research Institute in Japan (PHRI, 1997), also provides the following criteria:

- $D_{25}/d_{75} \leq 9.5$ or
- $D_{15}/d_{85} \leq 6.4$

(where D_{25} and d_{75} are similarly defined as noted above for 25% and 75% diameters)

Due to the short duration of an earthquake, materials should also be selected based on results on short seepage flow. For that reason the following criteria appear in the literature:

- $D_{15}/d_{85} < 9$ [Ohno et al. (1984)]
- $20d_{15} < D_{15} < 8d_{85}$ [Nakajima et al. (1985)]

The Department of Defense Handbook on Soil Dynamics and Special Design Aspects (1997) slightly modifies Nakajima's relationship for short-term flow and erosion, which appears in the following form:

- $20d_{15} < D_{15} < 9d_{85}$

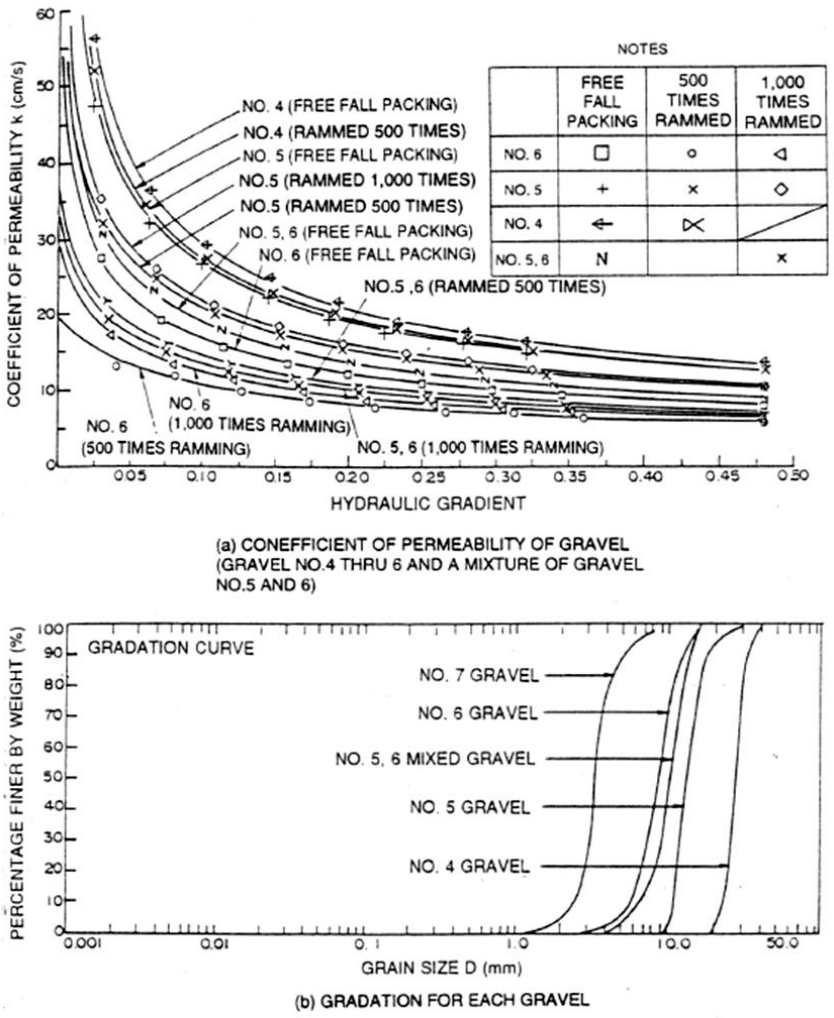

Figure 2.14: Permeability values and associated gradation curves for gravel materials typically used in drain construction (PHRI, 1997).

2.4 Design methods

2.4.1 Basic design considerations

The basic design principle behind the gravel drain method concerns the correlation between the dissipation and generation rates of excess pore water pressures during a seismic event. A gravel drain allows a faster dissipation rate of excess pore pressures compared to their generation rate. Higher pore pressure generation rates occur in loose soils subjected to an intense and sudden earthquake loading. Additionally, higher pore pressure dissipation rates are obtained in highly permeable and non – compressible soils, i.e. having high k_s and low $m_{v,3}$ values.

Many researchers have mathematically expressed the above observations via analytical solutions, having thus quantified the controlling parameters of the phenomenon and have formulated appropriate design charts for practical use. The main theoretical approaches and the related design charts, appearing in the literature, are outlined in this section. The key design parameters involved in all methodologies are explained below:

- The maximum allowable excess pore pressure ratio $r_{u,max}$, is defined as the ratio of the maximum excess pore pressure developing between the gravel drains, u_{max}, over the effective vertical stress σ'_{vo} and is a critical design parameter, in all design methodologies. Seed & Booker (1977) indicated that maximum pore pressure ratio values greater than 0.5, have a significant effect on the coefficient of volume compressibility $m_{v,3}$, as shown in **Figure 2.15**, and can lead to excessive post-earthquake settlements, thus it is recommended to avoid design values greater than 0.6. In practice, typical allowable $r_{u,max}$ values range from 0.2 ÷ 0.6, with the lower boundary values being considered the most conservative.

- The diameter of gravel drains (D) and effective spacing (b), usually corresponding to the effective radius, in most design charts, are determined based on a consolidation analysis, estimating the dissipation of earthquake – induced excess pore pressures with time. Given the effective spacing, the actual center – to – center distance, S, between gravel drains is determined, depending on the selected grid configuration. The relationship determining the drain spacing is as follows:

$$2 \times b = 1.05 \times S \quad \text{for a triangular grid configuration} \qquad \textit{2.10a}$$

$$2 \times b = 1.13 \times S \quad \text{for a square grid configuration} \qquad \textit{2.10b}$$

- Additionally, the area replacement ratio defined as the area of the gravel column over the area of the unit cell affected by the drain, provides a good estimate of the obtained soil improvement. This index denoted as α_s, is computed according to *Equation 2.11*:

$$\alpha_s = \left(\frac{D}{2 \times b} \right)^2 \qquad 2.11$$

Depending on the grid configuration, α_s is estimated as presented in **Table 2.6**, where D is the diameter of the gravel drain and S the center – to – center distance between two consecutive drains.

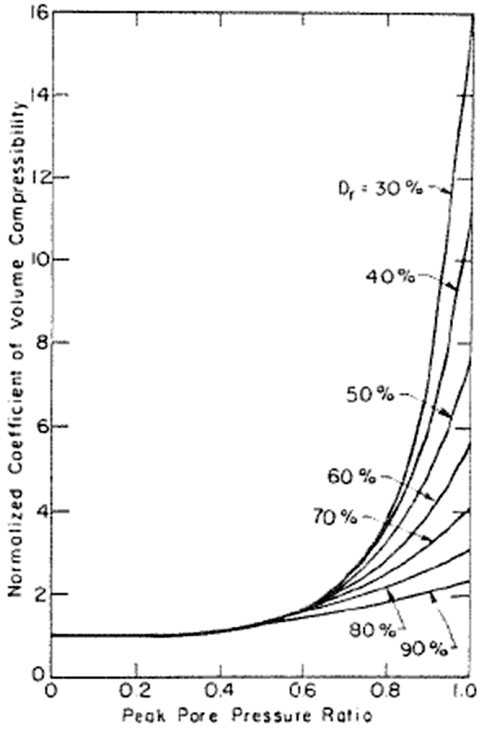

Figure 2.15: Relationship between coefficient of volume compressibility mv and pore pressure built up (Seed & Booker, 1977).

Table 2.6: Replacement ratio (α_s) as a function of the grid pattern and the spacing distance.

Grid	Center - to - center distances	α_s (%)
Triangular	S	$0.91(D/S)^2$
Square	S	$0.785(D/S)^2$
Quadrilateral	S_x, S_y	$0.785D^2/(S_xS_y)$

The design methodologies that follow, have developed around two theoretical approaches. The first assumes a 'perfect' drain, namely a column of infinitely large permeability, and has been proposed by Seed & Booker (1977). The second approach incorporates the drain's resistance to excess pore pressure dissipation and has been proposed by Okita et al. (1986) and Onoue (1988). Most recently, however, Bouckovalas et. al. (2009) revisited the Seed and Booker (1977) theory and proposed new design charts which effectively account for the effect of fabric evolution on $r_{u,max}$.

2.4.2 The Seed & Booker (1977) method

Seed & Booker (1977) first examined the earthquake induced pore pressure build up in liquefiable soils and the dissipation obtained through gravel drains. They generalized the one-dimensional theory of pore – water pressure generation and dissipation developed by Seed, Martin and Lysmer (1975), to the three dimensions and applied it to the analysis of gravel drains under various earthquake conditions. The geometry of the examined problem is presented in **Figure 2.16**, where **a** equals the radius of the gravel drain and **b** the radius of the drain's effective area.

The assumption that water flow is governed by Darcy's law, and the considerations of continuity of flow lead to the following equation*:*

$$\frac{\partial}{\partial x}\left(\frac{k_h}{\gamma_w}\frac{\partial u}{\partial x}\right)+\frac{\partial}{\partial y}\left(\frac{k_h}{\gamma_w}\frac{\partial u}{\partial y}\right)+\frac{\partial}{\partial z}\left(\frac{k_v}{\gamma_w}\frac{\partial u}{\partial z}\right)=\frac{\partial \varepsilon}{\partial t} \qquad 2.12$$

in which u = the excess hydrostatic pore – water pressure

k_v, k_h = coefficients of permeability in the vertical and horizontal directions respectively

γ_w = the unit weight of water

ε = the volume strain, with volumetric reduction being considered positive.

During a time interval of dt, the pore – water pressure in a soil element will exhibit a change du, while it will also be subjected to dN cycles of alternating shear stress, which will cause an additional increase in pore pressure - i.e. $(\partial u_g/\partial N)\times dN$

in which u_g = the pore pressure generated by the alternating shear stresses.

Therefore, considering the change in bulk stress to be negligible, the volume change, dε, of the element in time dt is

$$d\varepsilon = m_{v,3}\left(du - \frac{\partial u_g}{\partial N} dN \right) \qquad 2.13$$

in which $m_{v,3}$ = the coefficient of volume compressibility.

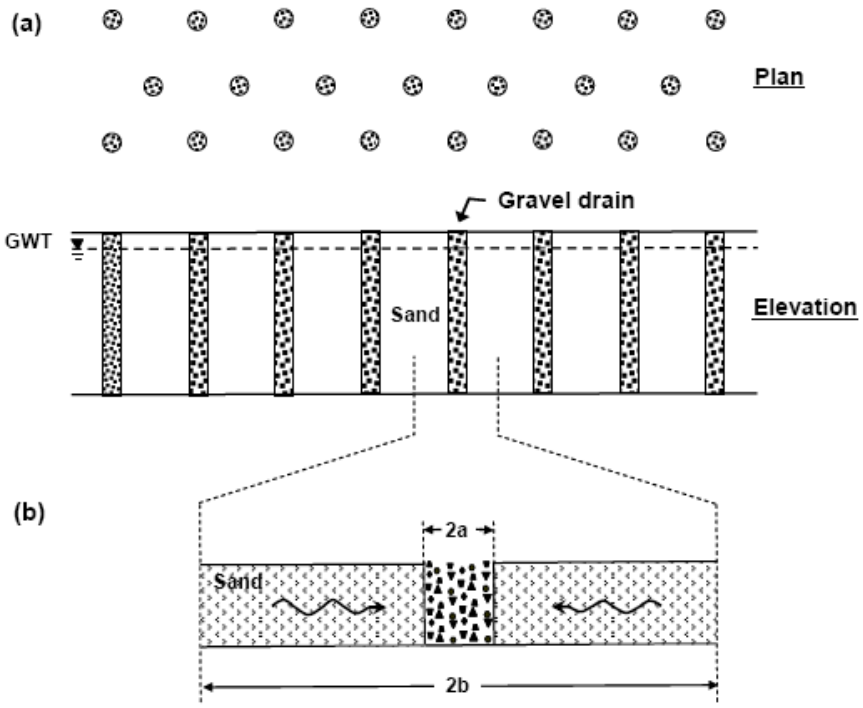

Figure 2.16: Plan arrangement (a) and elevation (b) of the problem geometry (Seed & Booker, 1977).

Combining the previous equations, under the assumption of constant values of the coefficients of permeability k_s and volume compressibility $m_{v,3}$, and for the axisymmetric conditions considered in the examined problem we get:

$$\frac{k_h}{\gamma_w m_{v,3}}\left(\frac{\partial^2 u}{\partial r^2} + \frac{1}{r}\frac{\partial u}{\partial r} \right) + \frac{k_v}{\gamma_w m_{v,3}} \frac{\partial^2 u}{\partial z^2} = \frac{\partial u}{\partial t} - \frac{\partial u_g}{\partial N}\frac{\partial N}{\partial t} \qquad 2.14$$

For purely radial drainage *Equation 2.14* reduces to the following form, i.e. *Equation 2.15*:

$$\frac{k_h}{\gamma_w m_{v,3}}\left(\frac{\partial^2 u}{\partial r^2} + \frac{1}{r}\frac{\partial u}{\partial r} \right) = \frac{\partial u}{\partial t} - \frac{\partial u_g}{\partial N}\frac{\partial N}{\partial t} \qquad 2.15$$

Based on undrained cyclic simple shear tests, Seed, Martin, Lysmer (1975), propose that for many soils u_g and N can be expressed as a function of the vertical effective stress σ'_{vo} and the required number of cycles for liquefaction N_l, as demonstrated in *Equation 2.16*:

$$\frac{u_g}{\sigma'_o} = \frac{2}{\pi}\sin^{-1}\left(\frac{N}{N_l}\right)^{\frac{1}{2A}} \qquad 2.16$$

in which σ'_{vo} = the initial mean bulk effective stress for triaxial test conditions or the initial vertical effective stress for simple shear conditions and

A = an empirical constant that has a typical value of 0.7.

The A = 0.7 value resulted from statistical processing of laboratory data from cyclic simple shear tests as illustrated in **Figure 2.17**.

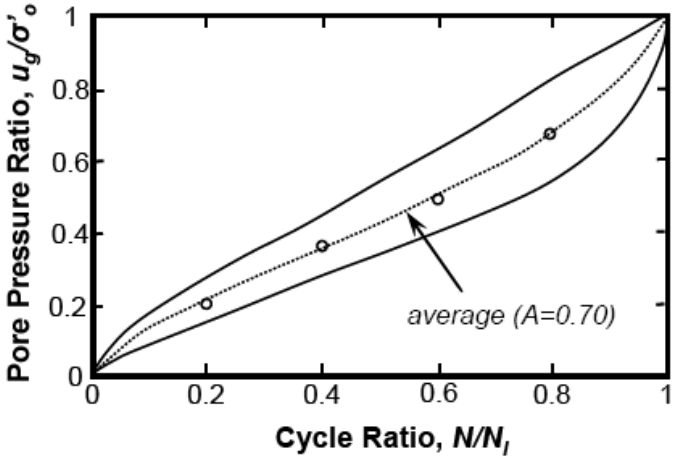

Figure 2.17: Rate of pore pressure built up from cyclic simple shear test (De Alba et al., 1975).

Considering the partial derivative of the generated excess pore pressures, u_g, with respect to the number of cycles N, the previous equation takes the form:

$$\frac{\partial u_g}{\partial N} = \frac{2\sigma'_o}{A\pi N_l}\frac{1}{\sin^{2A-1}\left(\frac{\pi}{2}r_u\right)\cos\left(\frac{\pi}{2}r_u\right)} \qquad 2.17$$

in which $r_u = u/\sigma'_{vo}$ equals the excess pore pressure ratio

For practical purposes, the irregular cyclic loading induced by a seismic excitation can be converted to an equivalent number, N_{eq}, of uniform stress cycles, at a stress ratio of τ_h/σ'_{vo},

occurring in some duration of dynamic time t_d of earthquake shaking. Thus the ∂N/∂t term of the basic *Equation 2.14* is transformed into:

$$\frac{\partial N}{\partial t} = \frac{N_{eq}}{t_d} \qquad 2.18$$

Following a thorough parametric investigation which falls outside the scope of the present analysis, Seed & Booker (1977) propose a set of design charts presenting the variation of the maximum excess pore pressure ratio, $r_{u,max}$, as a function of the spacing ratio a/b, for N_{eq}/N_l equal to 1, 2, 3, 4 and for a wide range of values of a dimensionless time factor T_d. The dimensionless time factor T_d is described as :

$$T_{ad} = \frac{k_s \times t_d}{m_{v,3} \times \gamma_w \times a^2} \qquad 2.19$$

where k_s (m/sec) = the horizontal soil permeability

t_d (sec) = dynamic time

$m_{v,3}$ (1/kPa) = the coefficient of volume compressibility

γ_w (kN/m^3) = water unit weight

a (m) = the radius of the gravel drain

Therefore, for any particular soil, given the gravel drain diameter, shaking intensity (expressed through the N_{eq}/N_l ratio) and drainage capacity T_d, the a/b value corresponding to an allowable excess pore pressure ratio $r_{u,max}$, can be obtained from **Figure 2.18**.

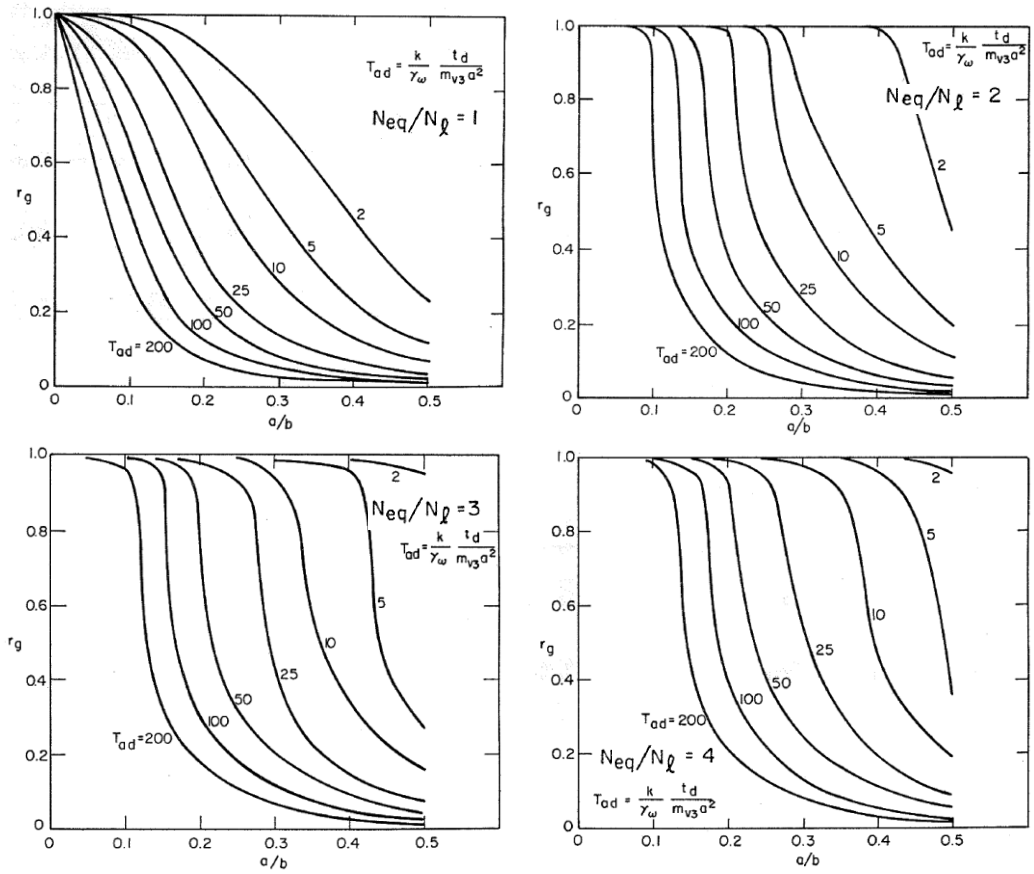

Figure 2.18: The Seed & Booker (1977) design charts.

Note that the Seed & Booker (1977) theory is based on the following simplifying assumptions:

- Purely horizontal drainage is considered to be the dominant mechanism of drainage. Taking into account that the permeability of the sand in the vertical direction is one third of that in the horizontal direction, and that the drain installation creates significantly shorter horizontal drainage paths compared to those in the vertical direction, the above assumption is justified.
- The drain material is assumed to be infinitely permeable, thus disregarding any resistance to water flow imposed from the material inside the drain. Based on parametric analyses, it is reported by Seed & Booker (1977) that "*the drain operates perfectly, provided it has a permeability of the order of 200 times that of the sand*". Based on this observation, medium to fine gravel is judged to be a suitable filling material.
- The natural soil surrounding the drain is considered elastic.

2.4.3 The Okita (1986) and Onoue (1988) methods

Following the pioneering work by Seed & Booker (1977), many geotechnical engineers re-examined the basic assumptions of their theory. Particularly the assumption of the infinitely permeable drain was proven to be inadequate to describe the actual water flow inside the drain. Okita et al. (1986) and Onoue (1988) introduced a new parameter to capture the drain's resistance to flow, denoted as well resistance L (or L_w) and defined through *Equation 2.20*:

$$L = \frac{32}{\pi}\frac{k_s}{k_d}\left(\frac{H}{2a}\right)^2 \qquad 2.20$$

where

k_s (cm/sec) = the coefficient of permeability of the natural soil

k_d (cm/sec) = the coefficient of permeability of the drain material

H (m) = the thickness of the sand layer (equal to the length of the drain)

α (m) = the radius of the gravel drain

Okita et al. (1986) recommended the use of the initial design charts by Seed & Booker (1977) after a correction in the dimensionless time factor T_d, while Onoue (1988) proposed entirely new design charts.

Evidently, the key parameter for the use of methodologies considering well resistance, over the simplified methodology of Seed and Booker (1977), appears to be the coefficient of well resistance L_w. According to the Port Harbour Research Institute of Japan (PHRI, 1997), a drain can be considered infinitely permeable when the coefficient of well resistance is less than or equal to unity. Expressing the above condition with respect to the coefficient of permeability of the drain material k_d it appears that:

$$k_d \geq 0.81 k_s \left(\frac{H}{a}\right)^2 \qquad 2.21$$

where H equals the depth of the drain installation and

a denotes the radius of the drain.

Equation 2.20 clearly indicates that the accuracy of the simplified methodology developed by Seed & Booker (1977) is directly related to the permeability of the drain material. When the above condition is not satisfied, one of the methodologies including well resistance should be applied. In case the drain material permeability decreases to less than the one

given by *Equation 2.21*, the installation spacing is reduced up to the extreme case which leads to total replacement of the natural liquefiable stratum by the gravel drain material.

Okita et al. (1986).- According to the Japanese Geotechnical Society (JGS, 1998), Okita et al. (1986) proposed a method, in which the value of the dimensionless time factor T_d, is decreased to T'_d to incorporate the effect of well resistance. Namely, for a given b value, the corrected time factor T'_d is calculated from *Equation 2.22*:

$$T'_d = T_d \times \frac{[F(n) + 0.8L]}{F(n)} \qquad 2.22$$

where F(n) is given by *Equation 2.23*:

$$F(n) = \frac{n^2}{n^2 - 1}\log(n) - \frac{3n^2 - 1}{4n^2} \qquad 2.23$$

with n = b/a

Given the intensity of the seismic excitation (N_{eq}/N_l ratio), the maximum pore pressure ratio, $r_{u,max}$, is estimated from the design charts proposed by Seed & Booker (1977) as a function of T'_d and the spacing ratio a/b. If the estimated $r_{u,max}$ value is lower than the allowable one, the assumed effective radius of the drain cell b is considered adequate and the center – to – center spacing distance S is evaluated (depending on the grid configuration). In the opposite case, computations are repeated assuming a lower b value.

Onoue (1988).- Even though Okita's methodology is quite straightforward and simple to use, Onoue (1988) stresses out that the related nomograph, incorporating well resistance for reading Seed & Booker's (1977) design charts, is limited to a pore pressure ratio (r_u) equal to 0.5 and coefficient of well resistance equal to unity. Thus, an analytical method is developed, to incorporate well resistance in the basic equations of flow and new design charts are proposed.

The basic equations developed by Seed & Booker (1977) are kept identical and are supplemented by a new continuity equation (*Equation 2.24*) along the drain periphery, initially proposed by Yoshikuni & Nakanodo (1974) for a consolidation analysis.

$$\left(\frac{\partial u}{\partial r}\right)_{r=a} + \frac{a}{2}\frac{k_d}{k_s}\left(\frac{\partial^2 u}{\partial z^2}\right)_{r=a} = 0 \qquad 2.24$$

Equations 2.14, 2.17 and *2.24* are solved as a continuous equation, considering the boundary conditions presented in **Figure 2.19**. The initial condition is u = 0 when t = 0. The coefficients of ground permeability in the horizontal and vertical direction, denoted as k_h and k_v

respectively, are assumed to be equal to k_s, when horizontal flow towards the drain and vertical drainage towards the surface of the sand layer are taken into consideration. In the case where vertical drainage is disregarded, k_v equals zero.

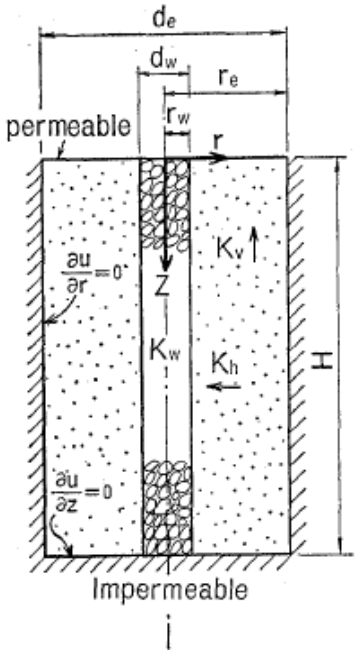

Figure 2.19: Drain well and boundary conditions in Onoue (1988) solution**.**

The design charts generated by Onoue (1988) are presented in **Figure 2.20** and correspond to the case where both horizontal and vertical drainage in the sand layer are considered. The spacing ratio (a/b) is correlated to the coefficient of well resistance L_w, as a function of the allowable maximum excess pore pressure ratio $r_{u,max}$ and the time factor T_d. It is also pointed out that ignoring vertical drainage becomes significant only in the case of N_{eq}/N_l =1, thus an additional design chart is provided in **Figure 2.21** for this case.

The design process using Onoue's design charts is not different than the one described for the Seed & Booker (1977) case. Practically, all steps are repeated, but the design charts presented in **Figure 2.20** & **Figure 2.21** are used for the final evaluation of the spacing ratio a/b.

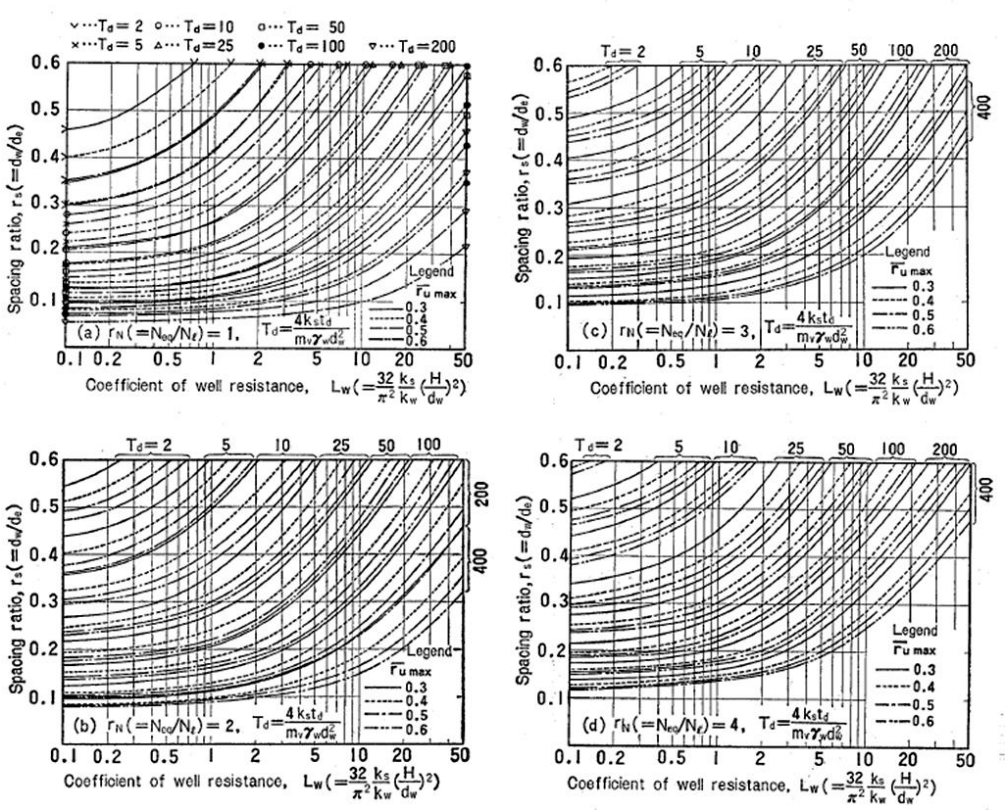

Figure 2.20: Design charts correlating well resistance to spacing ratio for different maximum excess pore pressure ratios and shaking intensities (Onoue, 1988).

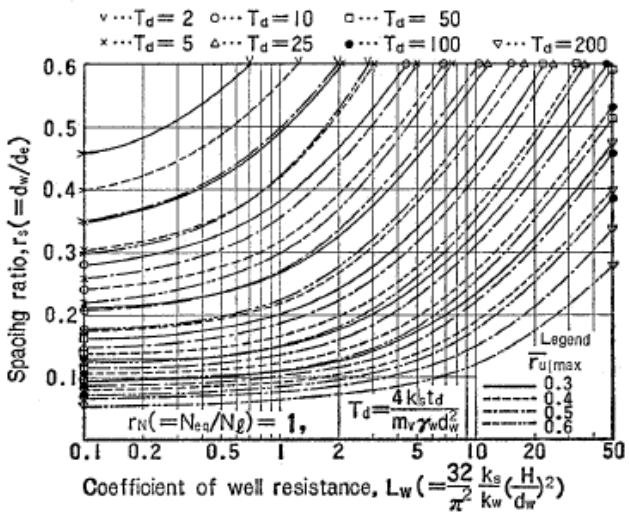

Figure 2.21: Relationship between spacing ration and well resistance in the case where vertical drainage is disregarded (Onoue, 1988).

2.4.4 The Bouckovalas et al. (2009) method

Bouckovalas et al. (2009) re-examined the basic mathematical assumption concerning the earthquake – induced excess pore pressure generation in the Seed & Booker (1977) theory. Namely, the Seed & Booker (1977) theory overlooks the shake – down effect occurring during cyclic loading, thus underestimating the effectiveness of the gravel drain. The new implementation of the equation for the rate of undrained excess pore pressure generation, proposed by Bouckovalas et al. (2009), focuses on the discrimination of two separate terms controlling the excess pore pressure build up. Differentiating Equation (2.16) with respect to N, and expressing it as a function of N_{eq}/N_l, leads us to the following expression:

$$\frac{\partial u_g}{\partial N} = \frac{\sigma_o}{A\pi N_l} F_1 F_2 \qquad 2.25$$

where

$$F_1 = \frac{1}{(N_{eq}/N_l)^{1-1/2A}} \qquad 2.26$$

$$F_2 = \frac{1}{\sqrt{1-(N_{eq}/N_l)^{1/A}}} \qquad 2.27$$

Expressions F_1 & F_2, described in the previous *Equations 2.26* and *2.27* are plotted against the normalized number of cycles N_{eq}/N_l in **Figure 2.22**.

In the present formulation the term F_1 affects the soil response during the initial stages of loading, representing the gradual evolution of the sand fabric towards a more stable state after each loading cycle. The fabric evolution is a process which continues with time and therefore F_1 is expressed as a function of N_{eq}/N_l. Considering that N = t/T, where T is the predominant period of shaking, F_1 is described as follows:

$$F_1 = \frac{1}{(t/TN_l)^{1-1/2A}} \qquad 2.28$$

The term F_2, appears to control the soil response at the final stages of shaking, where the rate of excess pore pressure build up becomes higher with each loading cycle. Therefore, F_2 was preserved as a function of the excess pore pressure ratio r_u, following the Seed & Booker (1977) formulation (*Equation 2.17*). Combining the above expressions with *Equation 2.25*, the final expression for the rate of excess pore pressure build up is formulated:

$$\frac{\partial u_g}{\partial N} = \frac{\sigma'_o}{\pi A N_l} \frac{1}{(t / TN_l)^{1-1/2A} \cos(\frac{\pi}{2} r_u)} \qquad 2.29$$

Consequently, *Equations 2.15*, *2.18* and *2.29* are combined and the resulting expression is expressed in non-dimensional form as presented as follows:

$$T_{ad}(\frac{\partial^2 r_u}{\partial R^2} + \frac{1}{R}\frac{\partial r_u}{\partial R}) = \frac{\partial u}{\partial t^*} - B \qquad 2.30$$

where $$B = \frac{1}{\pi A}(\frac{N_{eq}}{N})^{1/2A} \frac{1}{(t^*)^{1-1/2A} \cos(\frac{\pi}{2} r_u)} \qquad 2.31$$

The parameter T_{ad} is a normalized time factor equal to T_d used in the Seed & Booker (1977) method (*Equation 2.19*). The above *Equation 2.30* is solved, applying the following initial and boundary conditions:

- $r_u(R, t^* = 0) = 0$
- $r_u(R = 1, t^*) = 0$
- $\frac{\partial r_u}{\partial R}(R = b/a, t^*) = 0$

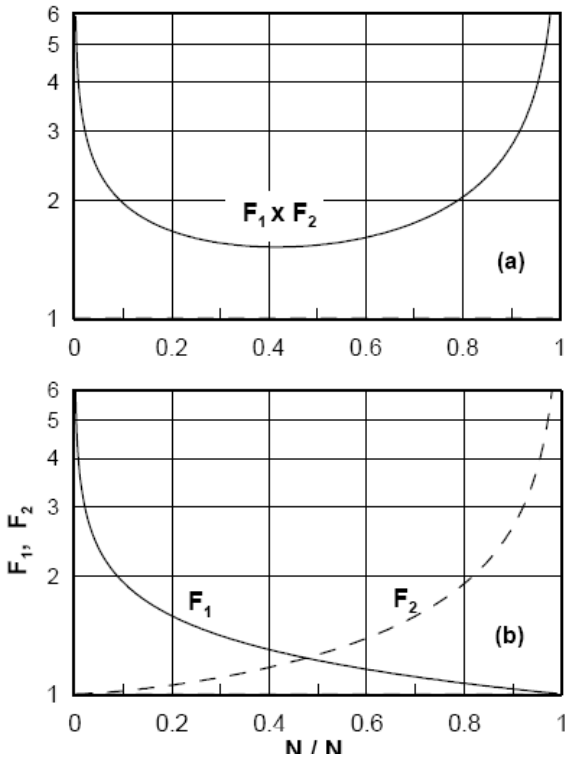

Figure 2.22: Excess pore pressure generation rate with respect to normalized loading cycles from cyclic simple shear tests (Bouckovalas et al., 2009).

The revised design charts for the computation of the maximum excess pore pressure ratio as a function of the spacing ratio (a/b = 0 to 0.5), the shaking intensity (N_{eq}/N_l = 1 to 4) and the dimensionless time factor (T_{ad} = 2 to 200), are presented in **Figure 2.23**.

The implications of the proposed modifications on the design of gravel drain systems are explored in **Figure 2.24a**, considering a maximum allowable excess pore pressure ratio $r_{u,max}$=0.40 and a triangular pile arrangement, rendering α_s equal to $0.91(a/b)^2$. The required replacement ratio α_s is plotted against the dimensionless time factor T_{ad}, for various shaking intensities, for the Seed & Booker (1977) (solid lines) and the revised method described herein (dashed lines). Moreover, **Figure 2.24b** presents the respective variation for the ratio of the revised over the original prediction as a function of T_{ad}. As it is seen, the values predicted by the revised method are systematically lower with respect to the equivalent values predicted by the Seed & Booker (1977) method.

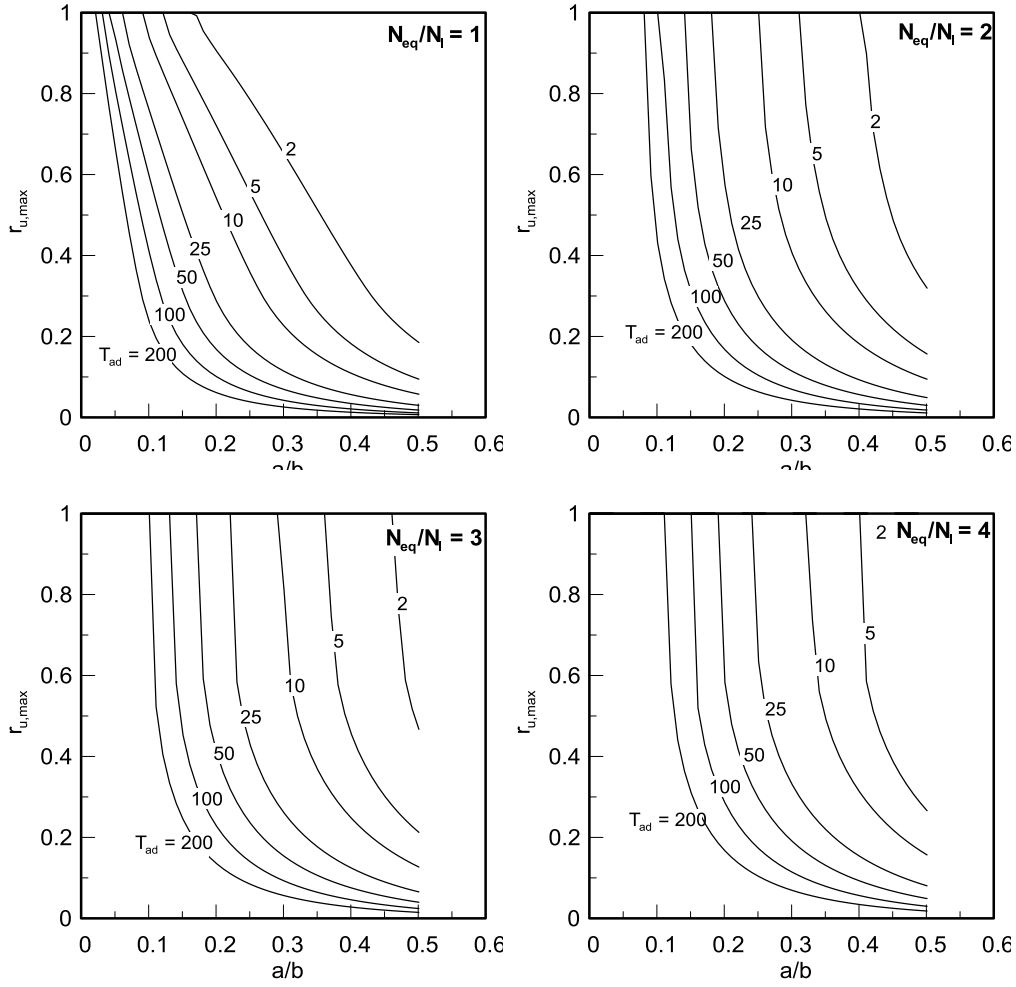

Figure 2.23: New proposed design charts based on the revised methodology by Bouckovalas et al., 2009.

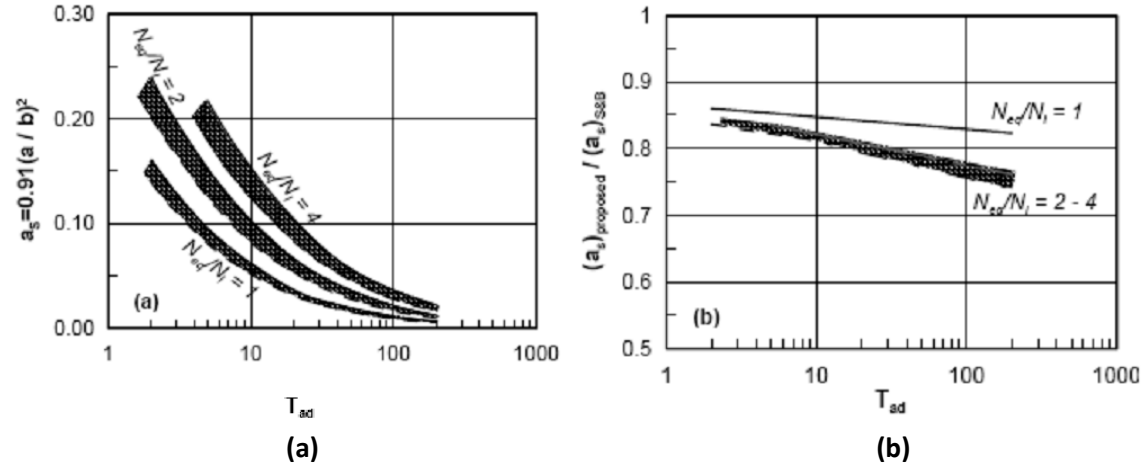

(a) **(b)**

Figure 2.24: **(a)** Replacement ratio α_s with respect to drainage potential (T_{ad}) for an allowable $r_{u,max}$ = 0.40 and various shaking intensities (N_{eq}/N_l) as predicted by Seed &Booker (1977) and Bouckovalas et al. (2009). **(b)** Comparative evaluation of the above predictions [$\alpha_{s,rev.}$ and $\alpha_{s,S\&B}$]. (Bouckovalas et al.,2009).

CHAPTER 3

Composite Drains for Liquefaction Mitigation

3.1 Introduction

Undoubtedly, gravel drains are the most effective liquefaction countermeasure used in current practice. Nevertheless, environmental issues and construction constraints tend to reduce the method's efficiency and level of confidence. Gravel drain installation entails significant traffic disturbance, and depending on the selected installation method, produces considerable amounts of potentially hazardous spoil material. Clogging during installation is an issue typically encountered, especially in the case of the top feed method, and reduces the column's drainage capacity. Additionally, the space and considerable time required for the installation of each column may frequently hinder or even postpone the implementation of the method in various projects, thus urging for alternative liquefaction countermeasures.

In the current chapter, two new innovative types of drains are thoroughly described, in terms of material specifications, installation procedure, equipment requirements and design methodology, which are intended to overcome some of the drawbacks of the gravel drain method, mentioned above. Namely:

- EQ-drains, which were initially developed and have been used in various projects in the U.S.A.
- Screen pipes, which originate and are used in a number of technical projects in Japan.

The effectiveness of the innovative drain types has been tested through laboratory and in-situ tests, which are also presented in the present chapter. Blast and vibration induced liquefaction and centrifuge tests have been carried out to test the performance of EQ-drains. The performance of screen pipes has been tested with shaking table tests and in situ experiments.

3.2 Earthquake (or EQ-) drains

Prefabricated geocomposite drains, also referred to as EQ-drains, have been recently introduced as an alternative to gravel drains for liquefaction remediation projects. EQ-drains consist of a synthetic corrugated pipe, enclosed in geotextile filter fabric and are usually installed with a vibrating mandrel. Their primary role is to provide a path for the immediate and unhindered dissipation of earthquake induced excess pore pressures, while a secondary effect is the soil densification occurring during installation. EQ-drains have been used in a variety of applications such as:

- Highway and railway embankments
- Seismic retrofit of existing buildings and bridge foundations
- Commercial and residential developments

Many companies in the U.S.A. are involved in the design and installation of earthquake drains; the three major being Nilex Corporation, Geo-Technics America Inc. and Ellington Cross. In the following paragraphs material specifications, installation methods and equipment requirements, provided by the above companies, as well as the available design methods are outlined, to provide a detailed description of this new approach in liquefaction remediation.

3.2.1 Design parameters

The main parameters involved in the design of EQ-drains concerning the surrounding soil, are the coefficient of permeability k_s and the coefficient of volume compressibility $m_{v,3}$. The determination of the above parameters does not differ from what was mentioned in the case of gravel drains, and is therefore omitted. In the sequel, specifications regarding the materials used in the manufacturing of EQ-drains are provided.

Pipe requirements.- The corrugated pipe used for the construction of EQ-drains has a typical nominal inside diameter ranging from 75 - 200mm and is composed of high density polyethylene (HDPE). In addition, the pipe has a minimum average wall thickness of 0.042 inches. Typically, for most projects encountered in the literature, the 75mm diameter is used

and recommended by the contracting companies. A sample of the corrugated pipe used in practice is presented in **Figure 3.1a &b.**

(a) **(b)**

Figure 3.1: Corrugated pipe without filter fabric **(a)** and enclosed in filter fabric **(b)** (Nilex Inc.; personal communication).

Filter requirements.- The filter fabric is suggested to be non-woven and made of thermally spun bonded polypropylene with minimum weight of 3.9oz/ft^2 (128g/m^2), maximum apparent opening size (AOS) of 0.21mm and minimum grab strength of 440N (100lbs). It is preferable that the filter fabric is not exposed to sunlight for more than 72 hours. Depending on the drainage application and the soil classification, several geotextiles are available to use. A completed EQ-drain ready for installation is presented in **Figure 3.2**.

Figure 3.2: EQ-drain ready to be installed (after E. Naesgaard; personal communication).

Clogging Criteria.- The Japanese Geotechnical Society (1998) specifies a relationship used to determine the size of the openings in steel pipes. The above relationship is expressed in the following Equation:

- $O_e \leq D_{s85}$ [Chen et al.,1981]

where O_e = the effective size of the opening

D_{s85} = grain size of natural soil corresponding to 85% finer by weight

Nevertheless, there is no reference in the U.S.A. field of practice to clogging issues.

3.2.2 Installation and equipment

EQ-drains are installed both in new projects as well as in the seismic retrofit of existing structures. The installation procedure and associated equipment are mentioned below:

- A tubular steel mandrel, like the one presented in **Figure 3.3**, is positioned over the desired spot and the drain enclosed in the filter material is fed from the bottom, as shown in **Figure 3.4**.
- The mandrel is advanced into the soil to the design depth using a combination of static crowd and vibration, as shown in **Figure 3.5**, from an actual project in the U.S.A.
- When reaching the design depth, the drain is anchored with a specially designed anchor plate (also called shoe or lost point), demonstrated in **Figure 3.6**.

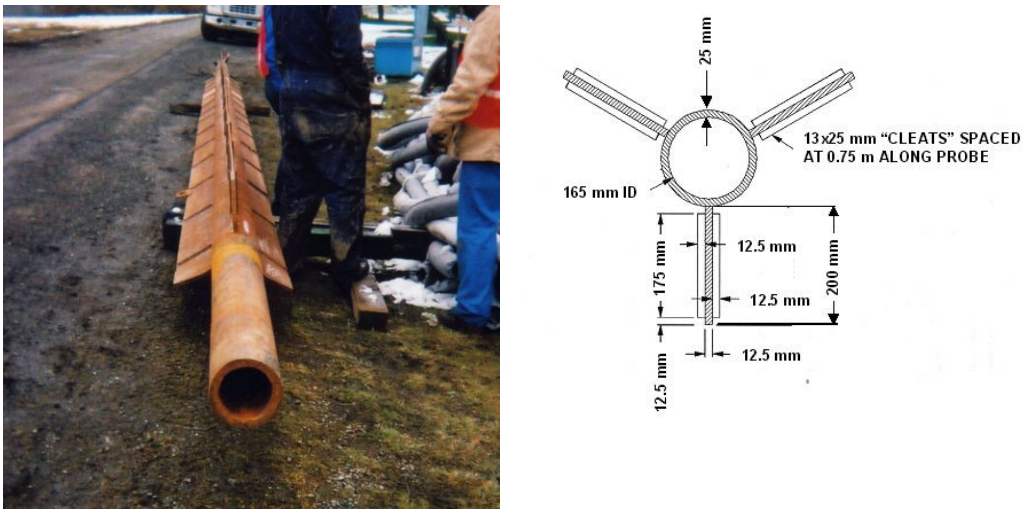

Figure 3.3: Tubular steel mandrel for EQ-drain installation (left figure) and dimension specifications (Nilex Inc.;personal communication).

Figure 3.4: Feeding the EQ-drain into the mandrel (Ellington Cross LLC).

Figure 3.5: Installing EQ-drains at a construction site (Bay bridge project Nilex Corporation).

Figure 3.6: Pre-assembled EQ-drains with the specially configurated anchorplate (Nilex corporation).

- After installation, the mandrel is retracted, protecting the corrugated pipe and filter sock from tears, cuts and abrasions.
- All installed drains are trimmed on the top and a special plastic elbow is attached. All elbows maintain the same orientation, as indicated in **Figure 3.7**.
- Reservoir space is often required to accommodate the expelled water during a seismic event. The reservoir space may take the form of a naturally occurring permeable layer of gravel, on top of the drains. The gravel material is bladed from the closed side of the elbows, to avoid falling into the drains as shown in **Figure 3.8**. Moreover, the natural reservoir is carefully designed to be above the water table.
- In case where an artificial reservoir is formed, individual reservoirs may be constructed at each drain. Usually, in practice, an additional length of drain material is attached to the main drain body, folded and buried at each drain.

Figure 3.7: Finished EQ-drains with all elbows oriented in the same direction (Home Depot Yuma project, Nilex Corporation).

Figure 3.8: EQ-drains installed and reservoir under construction (Bay bridge project Nilex, Corporation).

In cases where vibration is detrimental to existing structures or foundations, EQ-drains are installed with restricted-access drilling equipment, as shown in **Figure 3.9**. The steel casing is drilled to the desired depth and the drain is inserted through the center of the casing. The casing in then withdrawn, leaving the drain in place, as shown in **Figure 3.10**. The pictures appearing in the above figures correspond to the seismic retrofit project of the Historic Charleston Courthouse in the U.S.A., undertaken by Geotechnics America Inc.

The following installation guidelines and specifications are proposed by the main EQ-drain contractors in the U.S.A namely, Nilex Corporation, Geo-Technics America Inc. and Ellington Cross:

- If the rate of mandrel penetration is less than (<) 80mm/sec, under full static force and vibrator output, the drain may be abandoned.
- Falling weight impact hammers are not allowed for installation.
- Water may be used occasionally to facilitate drain anchoring.
- Augering (or other methods) may be used for loosening of stiff upper soil layers prior to installation, unless they extend more than 60cm into the liquefiable stratum.

- In the case of severe obstructions, the drain is completed from the obstruction up to the surface and a new drain is installed within 50cm of the obstructed drain (at the direction of the Engineer). A maximum of 2 attempts are made.
- The equipment must be tested for plumbness and shall not deviate from the vertical by more than 8cm/m during installation.
- Stakes must be preserved by the Contractor and drains' final position must not differ by more than 15cm from the locations indicated by the Engineer. Drains out of proper position may be abandoned in place or removed.
- Trial drains are usually installed to test the available equipment and drain performance.

Figure 3.9: Restricted access drilling equipment and EQ-drain installation (Historic Charleston Courthouse, Geotechnics America Inc.).

Figure 3.10: EQ-drains installed under an existing structure (Historic Charleston Courthouse, Geotechnics America, Inc.).

3.2.3 Design methods

In EQ-drain design, there are still no appropriate design charts formulated for use in current practice in the U.S.A.. The three major EQ-drain contractors in the U.S.A. rely on the use of the finite element program FEQdrain for the analysis and design of the EQdrain grid configuration. The set of design charts, proposed by the Japanese Geotechnical Society (JGS, 1998), is presented herein. Additionally, the Japanese Geotechnical Society (JGS) propose the use of specific design charts also presented in the current section.

FEQdrain (Pestana et al., 1997).- This finite element program is capable of simulating the response of a perforated plastic pipe, either alone or enclosed in geotextile, and computing the excess pore pressures throughout the effective area of the drain. The excess pore pressure flow occurring in the natural ground is simulated according to Darcy's law and the same equation is applied to describe the pore pressure built up as explained in the Seed & Booker (1977) theory. The basic mechanism describing the function of the pipe is based on the non-linear discharge capacity Q_d as a function of hydraulic gradient (dh/dz).

More analytically, the head loss (Δh) for the water entering the drain is expressed as:

$$\Delta h = \frac{v_r}{\psi} + \frac{c_{orf}}{\alpha^2_{orf}} * \frac{v^2_r}{2 * g} \qquad 3.1$$

where v_r = Darcy's discharge velocity in the radial direction at the drain boundary ($r=r_w$)

c_{orf} = is a coefficient describing the entrance loss through the orifices in terms of entrance kinetic energy head. It is used to reduce the amount of flow through the perforations and can range from 0.5 to 2, with the lower end boundary (c_{orf} =0.5) assuming minimum or no head loss through the perforations. FEQdrain user's manual recommends that c_{orf} equals unity.

α_{orf} = is the dimensionless ratio of the orifice area to the lateral surface area of the perforated pipes, defined as $\alpha_{orf} = orf / 2\pi r_w$, where *orf* denotes the area of openings per unit length in the perforated pipe and r_w is the outside radius of the drain.

ψ = is the permittivity of the geofabric [1/t]

g = acceleration of gravity (m/sec^2)

The hydraulic gradient in the vertical direction inside the drain is described by the modified Manning's equation as:

$$\frac{\Delta h}{\Delta z}\Big|_{z,t} = c_1 (Q_d(z,t))^{c2} \quad \text{for } z > z_{res} \qquad 3.2$$

where Q_d = the vertical flow inside the drain and

c_1, c_2 = constants provided by the manufacturer, expressing the discharge capacity of the perforated plastic pipe, when the water level in the pipe is lower than the depth of the reservoir z_{res}.

When the water level is above the depth of the reservoir *Equation 3.3* is derived:

$$\frac{\Delta h}{\Delta z}\Big|_{z,t} = c_3 \left[Q_d(z,t) \right]^{c4} \quad \text{for } z < z_{res} \qquad 3.3$$

where c_3, c_4 = constants provided by the manufacturer, expressing the discharge capacity of the perforated plastic pipe, when the water level in the pipe is higher than the depth of the reservoir z_{res}.

To simulate the flow in the plastic pipe and the flow through the geofabric and pipe orifices, the drain space is divided in two elements: an inner and an outer core, respectively. The flow in the outer core is assumed to be radial, whereas inside the inner core the flow is considered essentially vertical. The above assumptions are better illustrated in **Figure 3.11**.

The two elements are characterized by a linearized equivalent hydraulic conductivity representing the head gradient in the vertical and horizontal directions.

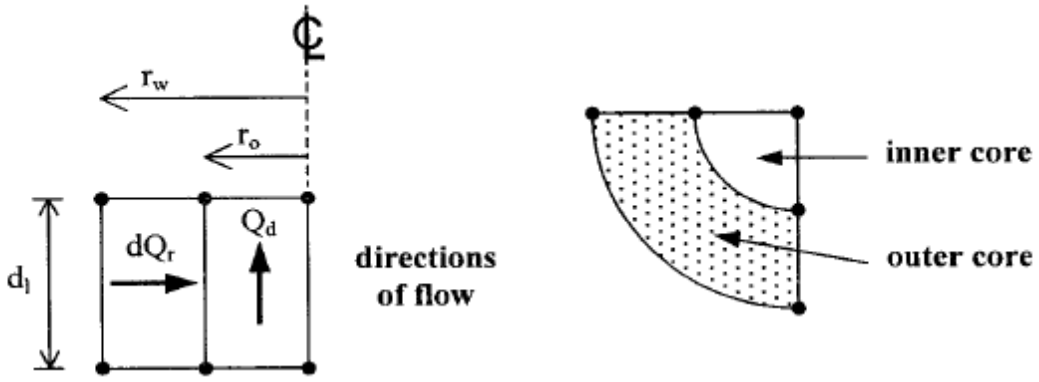

(a) Profile **(b)** Plan view

Figure 3.11: Simulation of flow within drain elements (FEQ-Drain User's Manual).

The radial flow in the outer core element *dQr,* can be expressed as:

$$dQ_r = k_{heq}(t) * A_{surf} * \frac{\Delta h}{r_w \ln\left(\frac{r_w}{r_o}\right)} \qquad 3.4$$

where k_{heq} = is the equivalent horizontal hydraulic conductivity of the outer core element at time *t* and

A_{surf} = the surface area of the axisymmetric element with height *dl*.

The surface area A_{surf} is given based on the following expression:

$$A_{surf} = 2 * \pi * r_w * dl \qquad 3.5$$

The head loss across the outer core can be expressed as a function of the energy loss due to orifice entrance and permeation through the geofabric. In terms of horizontal flow through the outer element the head loss is expressed as:

$$\Delta h = \frac{c_{orf}}{\alpha^2_{orf}} \frac{(dQ_r)^2}{2gA^2_{orf}} + \frac{dQ_r}{A_{surf}\psi} \qquad 3.6$$

where ψ = is the permittivity of the geofabric [1/t]

A_{surf} = the surface area of the axisymmetric element with height *dl*,

The horizontal flow dQ_r, can be rewritten as a function of the average excess pore pressure Δu, across the examined element and the properties of the prefabricated drain. Therefore the previous *Equation 3.6* is transformed as shown below:

$$\frac{dQ_r}{A_{surf}} = \frac{2 * \psi * \frac{\Delta \bar{u}}{\gamma_w}}{1 + \sqrt{1 + \frac{2 * c_{orf}}{g * \alpha^2_{orf}} * \psi^2 * \frac{\Delta \bar{u}}{\gamma_w}}} \qquad 3.7$$

Solving *Equation 3.7* with respect to the equivalent hydraulic conductivity during a time increment Δt, we get:

$$k_{h,eq}(t) = \frac{Q_r}{A_{surf}} * \frac{r_w * \ln(r_w / r_o)}{\Delta \bar{u} / \gamma_w} \qquad 3.8$$

Subsequently, substituting into *Equation 3.4*, the final expression for k_{heq} is given through *Equation 3.9*:

$$k_{h,eq}(t) = \frac{2 * \psi * r_w * \ln(r_w / r_o)}{1 + \sqrt{1 + \frac{2 * c_{orf}}{g * \alpha^2_{orf}} * \psi^2 * \frac{\Delta \bar{u}}{\gamma_w}}} \qquad 3.9$$

Apparently, the equivalent hydraulic conductivity for a specific element is not constant with time, but is related to the average excess pore pressure during Δt. Therefore, the problem is solved iteratively.

Likewise, the average vertical hydraulic conductivity for the inner core is computed based on *Equation 3.10*:

$$Q_d(t) = k_{v,eq}(t) * \pi * r^2_o \frac{dh}{dz} \qquad 3.10$$

where $\frac{dh}{dz} = c_1 Q_d^{c2}$ and in the end, the following expression is derived:

$$k_{v,eq}(t) = \frac{\bar{Q}_d^{(1-c_2)}}{c_1 * (\pi * r^2_o)} \qquad 3.11$$

where Q_d = is the average vertical flow for the examined element

It is important to clarify that the separation of the drain space into inner and outer sections is totally arbitrary and does not relate to the physical dimensions of the geofabric and the

perforated slots of the plastic pipes. For the sake of simplicity, it is assumed that the inner and outer core elements have the same radial dimension (i.e. $r_o = r_d = r_w/2$).

Due to the nonlinearity of the problem, and in order to avoid numerical inaccuracies, the software analytically computes the solution of excess pore pressures for the outer core elements of the pipe, based on *Equations 3.2* and *3.3* and in the sequel applies the solution in the form of transient boundary conditions to the inner core element.

JGS (1998).- The Japanese Geotechnical Society (1998) referring to a similar type of artificial drains, proposes the following process for determining the spacing distance *b*. Following the gravel drain method for the determination of the dimensionless time factor T_{d0}, the coefficient of well resistance and the cycle number ratio (N_{eq}/N_l), the following steps are followed:

- A spacing ratio *a/b* is assumed and the correction factor m is determined from **Figure 3.12** and the corrected time factor T_d is calculated.
- Given the maximum excess pore pressure ratio $r_{u,max}$, the related *b/a* ratio is defined from **Figure 3.13**.
- In case of considerable deviation between the two specified *b/a* values, the process is repeated until convergence.

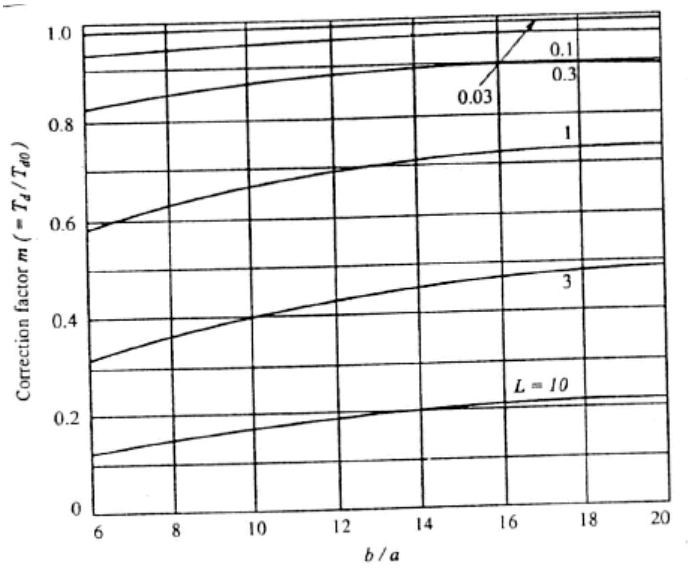

Figure 3.12: Determination of m correction factor (JGS, 1998).

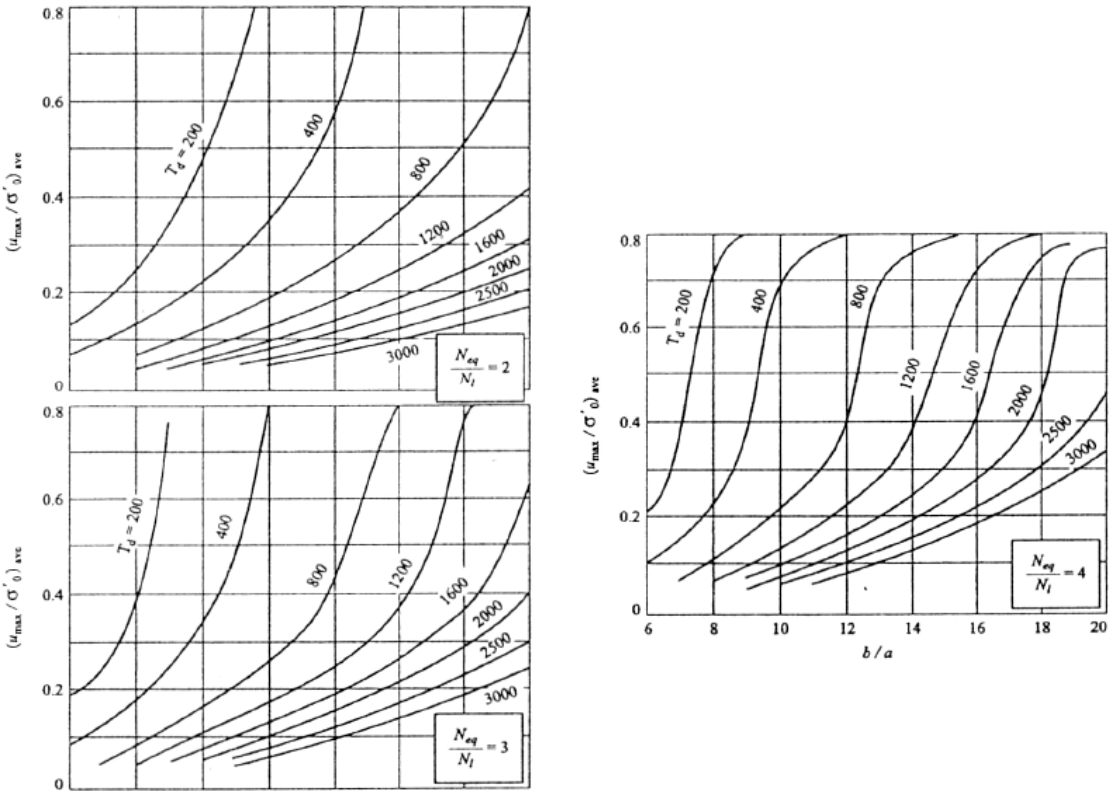

Figure 3.13: Design charts proposed by JGS (1998) for the spacing of artificial drains.

3.3 Screen pipe method

A relatively new technique developed in Japan appears to gain ground in the seismic retrofit of existing structures, especially in cases of very limited working space. The screen pipe method is proposed by Harada (2004, 2006) and includes specially constructed metal pipe drains, which are installed in loose sands with relatively light equipment and the least possible disturbance in the adjacent structures.

3.3.1 Design parameters

The screen pipe is made of equally interspaced metal rods in the axial direction with metal rings surrounding them. The diameter of the screen pipe typically ranges from 50 to 100mm and the opening size between the rings is of the order of 0.1 – 0.3mm. Characteristic details of a screen pipe are demonstrated in **Figure 3.14**. The screen pipe exhibits much greater permeability compared to the natural soil, since it is hollow in the inside. Thus, excess pore water pressures are dissipated much faster, compared to the conventional gravel drains.

Moreover, clogging during seismic excitation is prevented, due to the narrow opening size of the external steel rings.

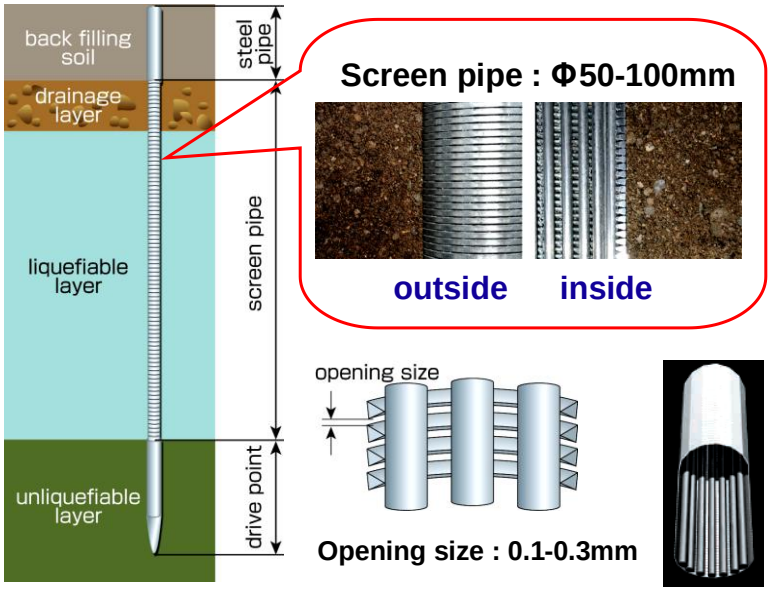

Figure 3.14: Characteristic screen pipe details (Harada et al.,2006).

3.3.2 Installation and equipment

Screen pipes are installed using small machinery, such as boring machines and vibratory pile drivers, as presented in **Figure 3.15**. It is also reported that human power through air hammers may be also applied. A typical air hammer apparatus is demonstrated in **Figure 3.16**. The installation procedure is outlined in **Figure 3.17** and is completed in the following stages:

- The selected machinery is positioned over the correct installation spot
- The screen pipe, which is attached to the rod of the boring machine is inserted into the ground by mechanical blows
- A drain mat is constructed on top of the screen pipe.

The installation interval ranges from 0.5 to 1.5m and drains can be installed vertically or inclined to a pre-determined depth.

Figure 3.15: Application range for the bottom feed (Vibro-displacement) and top feed (vibro-flotation) methods (Bauer, 2010).

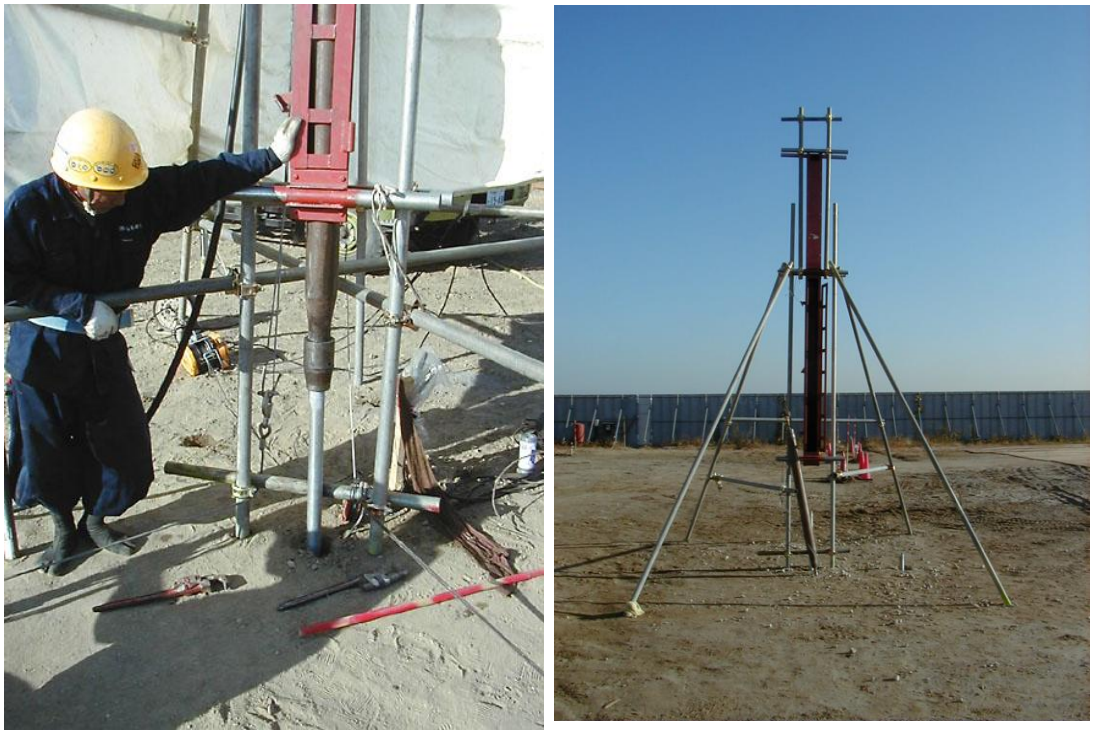

Figure 3.16: Use of Air Hammer for screen pipe installation (Photograph provided by Prof. I. Towhata after personal communication).

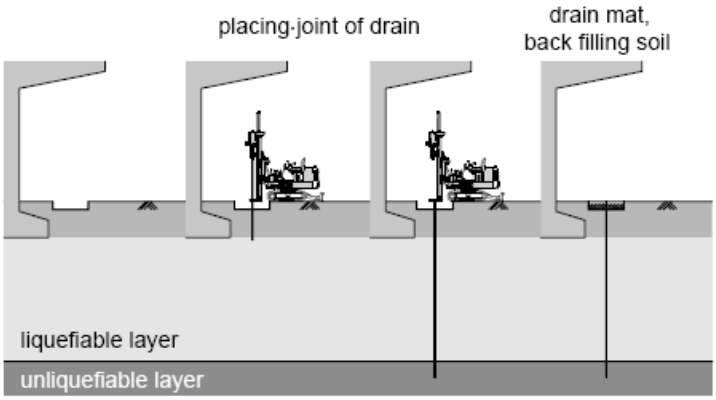

Figure 3.17: Construction sequence of the screen pipe method (Harada et al., 2006).

3.3.3 Design method

The screen pipe method has recently appeared in the international literature and is still experimentally investigated. Research in this field of soil improvement remains active and suitable installation guidelines and design charts are expected in the future. Nevertheless, because the function of screen pipes is essentially the same as that for EQ-drains, their design may be based on FEQ-Drain or even the Seed & Booker (1977), or the Bouckovalas et al. (2009) method for perfect drains (without internal flow).

According to Harada et al. (2006), the main benefits obtained from the screen pipe method are summarized in the following:

- Screen pipes can be used for soil improvement under or in the vicinity of existing structures, especially in cases with serious space limitations.
- The construction procedure is simple and efficient with little time requirements.
- The installation activity causes minor environmental impacts (such as noise and vibration).
- Experimental investigation through shaking table tests and field experiments confirm the method's efficiency in excess pore pressure dissipation, nevertheless, indicate that for strong seismic events (exceeding 200gals) liquefaction may not be prevented. In such cases the use of screen pipes in conjunction with piles may preserve shear strength and mitigate earthquake induced damage to pile supported structures.
- Screen pipes can be inserted at any desired angle.
- The technique is performed without any soil removal.
- The steel pipe configuration prevents clogging phenomena.

3.4 Experimental evaluation of alternative drain types.

3.4.1 EQ-drains

In the absence of actual performance data, from past seismic events, many researchers have conducted laboratory and field tests to evaluate the efficiency of EQ-drains. The most important findings are summarized below.

Rollins et al. (2003).- evaluated the effectiveness of EQ-drains through controlled blasting techniques in two test sites, located in Treasure Island - San Francisco and Vancouver, Canada. The performed blasts investigated the pore pressure dissipation efficiency of EQ-drains, as well as, the obtained densification of the surrounding soil during installation.

Treasure Island, San Francisco Test Site.- EQ-drains were installed in eight separate clusters, each one consisting of seven drains in triangular spacing, incorporating different spacing distances, use of filter fabric and intensity of vibration used for installation.

The test layout is presented in **Figure 3.18**. The soil profile consisted of hydraulically placed fill and native sands to a depth of 4.2m, underlain by silty sand to a depth of 7.5m. Bay mud was encountered at a depth of 7.5m. The water table was located approximately 0.15m below the ground surface.

Soil improvement during installation was evaluated through settlement monitoring and CPT soundings. One week following installation, a CPT sounding performed within the drain cluster indicated an increase of the cone tip resistance in the order of 20 – 35% compared to the initial values, which is translated to a 5 – 10% increase in relative density. A cross section of the soil conditions, along with profiles of CPT cone tip resistance, SPT blow count and associated relative density values before and after installation at the site is presented in **Figure 3.19**. Additionally, the installation induced settlements in the tested site ranged from 20 to 275mm, depending on spacing and amount of vibration.

Dynamic loading consisted of sixteen (16) explosive charges, which were placed around the periphery of two circles, 5m in diameter. The performance of the treated site was compared to the response of an adjacent untreated site, in terms of pore pressure built up and observed settlement accumulation.

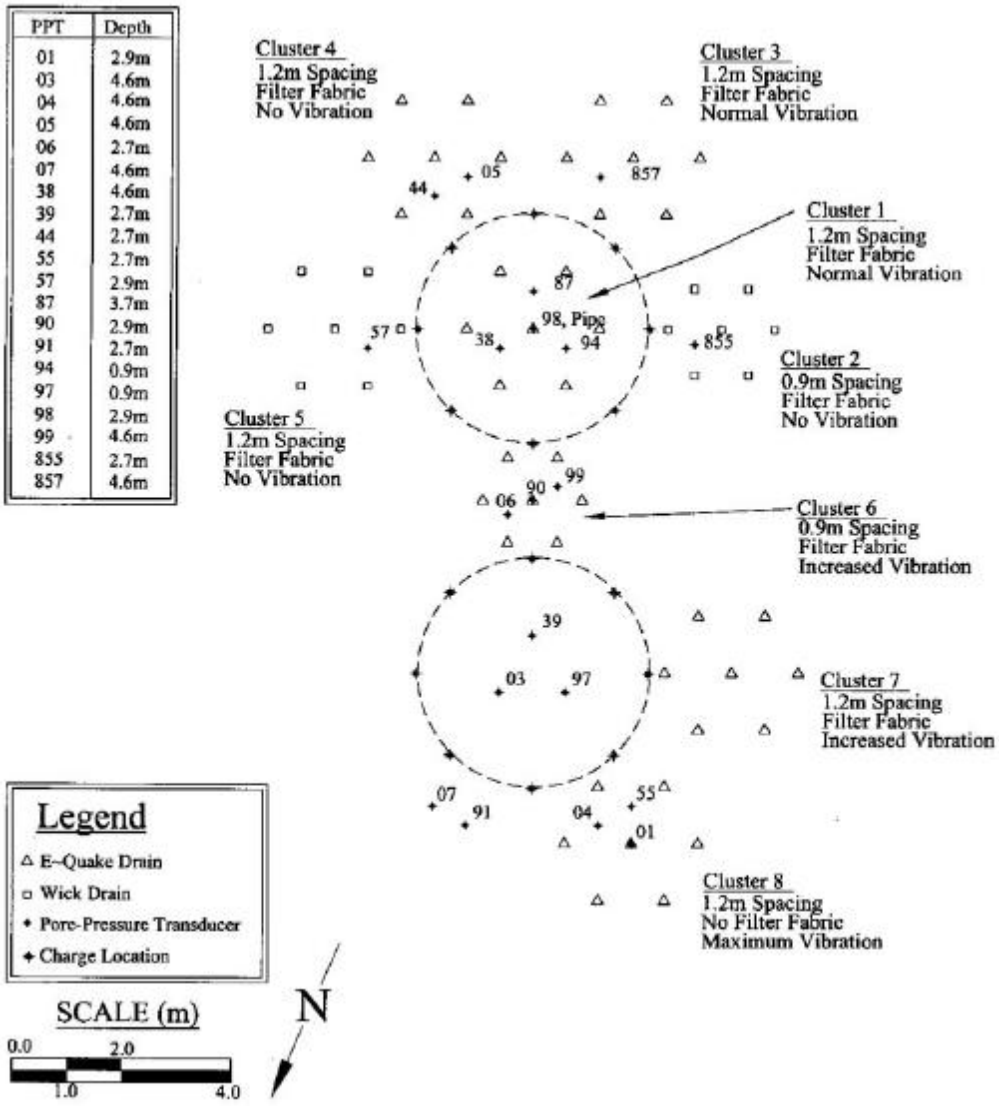

Figure 3.18: Layout of drain clusters, pore pressure transducers and blast charges at test site on Treasure Island in San Francisco (Rollins et al.,2003).

Due to the rapid and abrupt nature of loading, EQ-drains did not prevent liquefaction from occurring, nevertheless, they effectively dissipated excess pore pressures, as indicated in **Figure 3.20.** The Authors note that the rise of r_u values for the treated area from 0.1 to 0.3 before dropping again is attributed to sand infiltration in the drains, despite the fact that the geofabric met all related filter criteria. In terms of blast-induced settlements, about 20 – 40% less settlement occurred in the center of the treated area compared to the untreated site. The maximum amount of settlement in the treated area occurred near the improvement boundaries and was comparable to the maximum settlement in the untreated area.

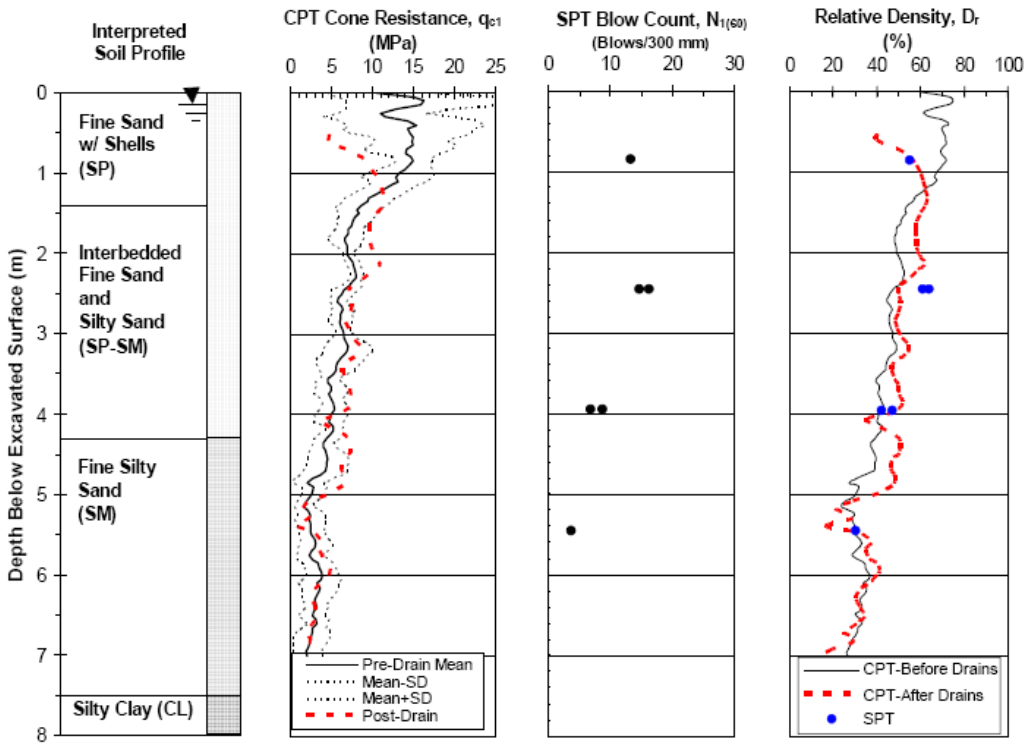

Figure 3.19: Typical soil profile, SPT, CPT and Dr profiles, before and after drain installation from Treasure Island in San Francisco (Rollins et al.,2003).

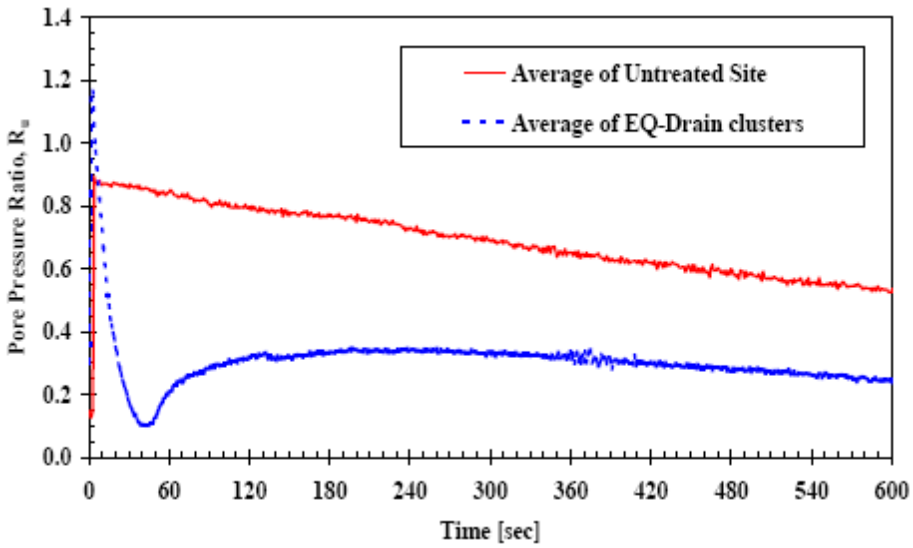

Figure 3.20: Excess pore pressure ratio time history for the treated and the untreated test sites at depth of 2.7m (Rollins et al.,2003).

Vancouver, Canada Test Site.- In the particular site, drain performance was evaluated by installing a single cluster consisting of 35 EQ-drains and comparing the blast induced settlement and pore pressures with regard to an untreated site displaying comparable soil properties.

Soil conditions generally, consisted of silt and clay to a depth of 5m, underlain by loose liquefiable sand to a depth of 15m, with very low CPT values, ranging from 5 – 7 MPa. Based on the CPT measurements, the relative density ranged between 40 – 45%. The water table was located at 2.8m below the ground surface. A cross section of the soil conditions, along with profiles of CPT cone tip resistance and interpreted relative density values before and after installation at the site is presented in **Figure 3.21**.

The drains were spaced at 1.22m (center – to – center distance) in a triangular grid and were installed to a target depth of 12.8m using a steel mandrel. A new, improved filter fabric was used in order to eliminate the clogging issues encountered in the previous test and the end of the fabric tube was tied to further prevent infiltration. During installation, approximately 350mm of settlement occurred near the center of the cluster which gradually decreased to about 50mm along the periphery.

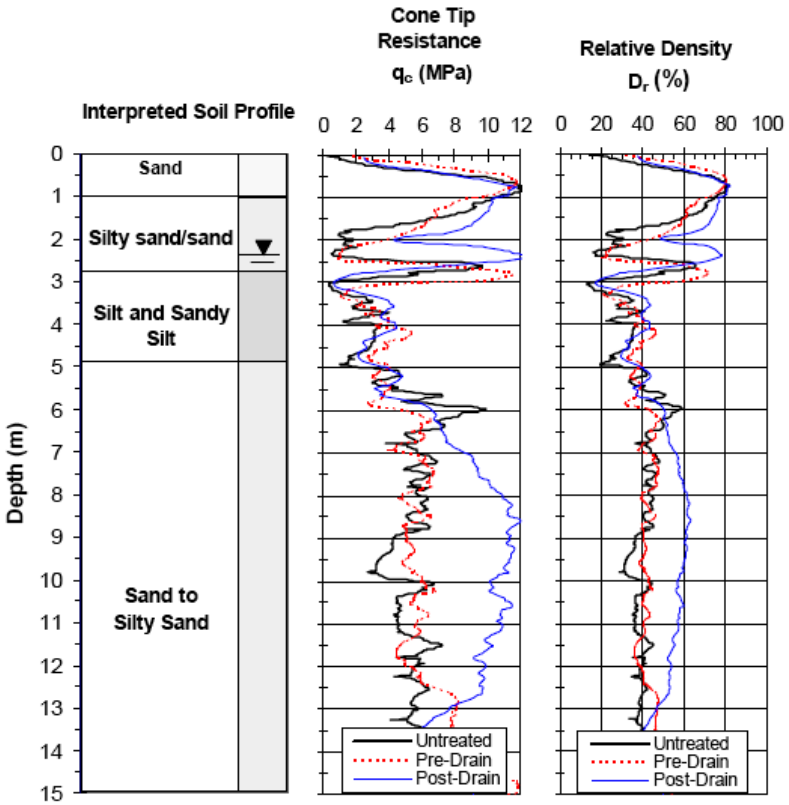

Figure 3.21: Typical soil profile, CPT and relative density (D_r) profiles, before and after drain installation from the Vancouver, Canada test site (Rollins et al.,2003).

Four blast holes were created around the periphery of a circle 5m in diameter and overall, 16 charges were detonated at different depths. The experiment layout along with the positions of the blast holes and the pore pressure transducers is demonstrated in **Figure 3.22**.

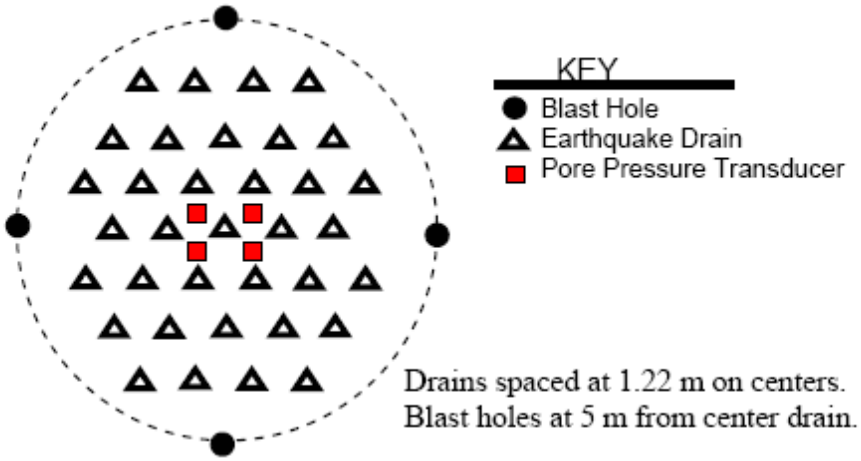

Figure 3.22: Layout of drains, pore pressure transducers and blast hole for the Vancouver test site (Rollins et al.,2003).

Figure 3.23 presents the excess pore pressure ratio time histories from various depths for the treated and the untreated area. The drains did not succeed in preventing liquefaction, however, higher dissipation rates were obtained in the treated areas. Moreover, EQ-drains reduced settlements by 30 – 65% compared to the untreated site, as it is shown in **Figure 3.24**. Note that this reduction may be partly attributed to the increased dissipation rate, since significant densification had already occurred during installation.

According to the Authors, in contrast to actual seismic events, blast induced liquefaction was obtained in 2 – 3 seconds, which leaves very little time for pore pressure built up, therefore diminishing the effectiveness of the drains. Considering this to be the main reason for liquefaction occurrence in the treated sites, numerical simulations using FEQdrain software were carried out to further investigate the EQ-drains' effectiveness. The settlement and excess pore pressure measurements from the blasting test sites were used to calibrate the numerical model's soil properties, and the comparison between the measured and computed excess pore pressure ratio is presented in **Figure 3.25** and **Figure 3.26** respectively. The above calibrated computer model was subsequently tested against various earthquake motions with different intensities and durations and the results are summarized

in **Table 3.1**, in terms of excess pore pressure ratios, r_u, and settlement accumulation. Opposite to the blasting test results, the numerical investigation indicated that properly spaced drains can prevent liquefaction and significantly reduce excess pore pressures and settlements, under properly simulated earthquake loading conditions.

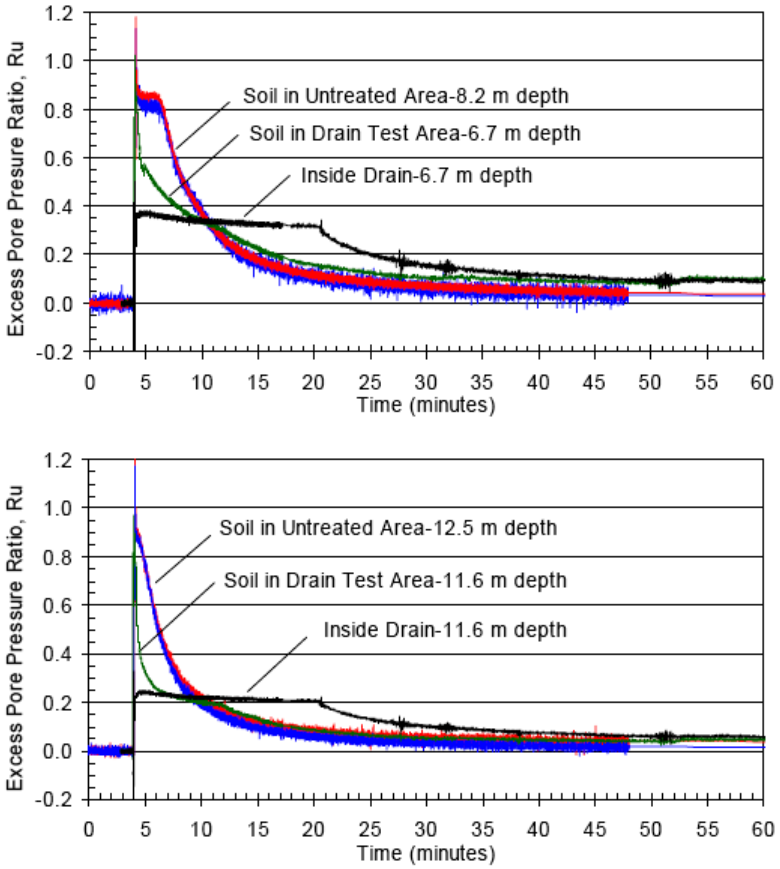

Figure 3.23: Excess pore pressure ratio time histories for the untreated and the treated site at various depths (Rollins et al.,2003).

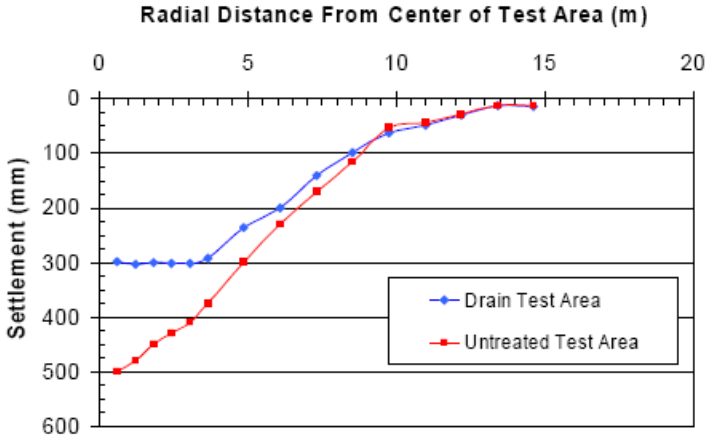

Figure 3.24: Liquefaction induced settlement versus radial distance from the center of the drain for the treated and untreated test areas.

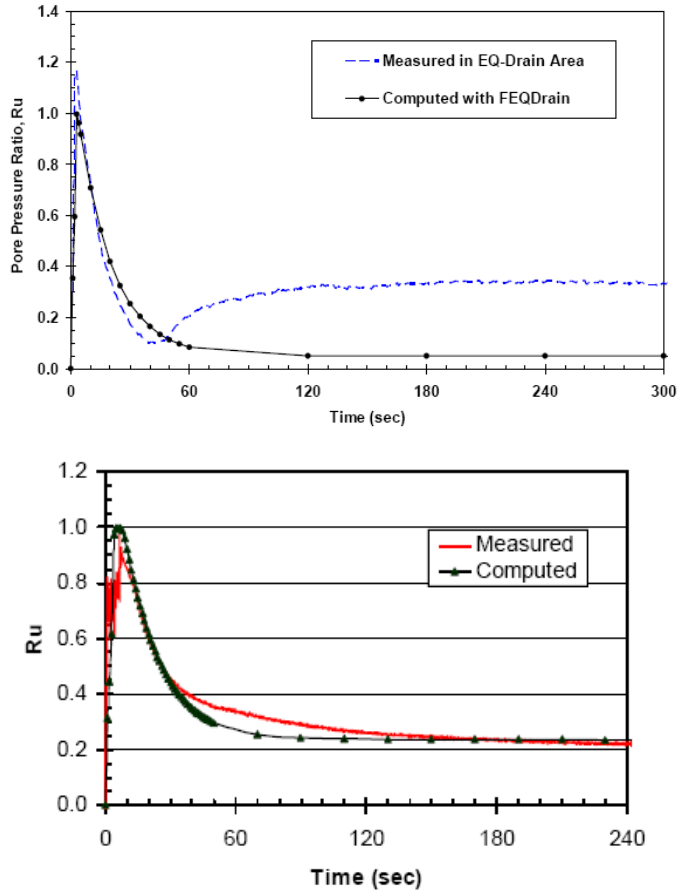

Figure 3.25: Comparison of measured r_u time history with time history computed using FEQ-drain for Treasure Island (upper graph) and Vancouver (lower graph) test site respectively (Rollins et al.,2003).

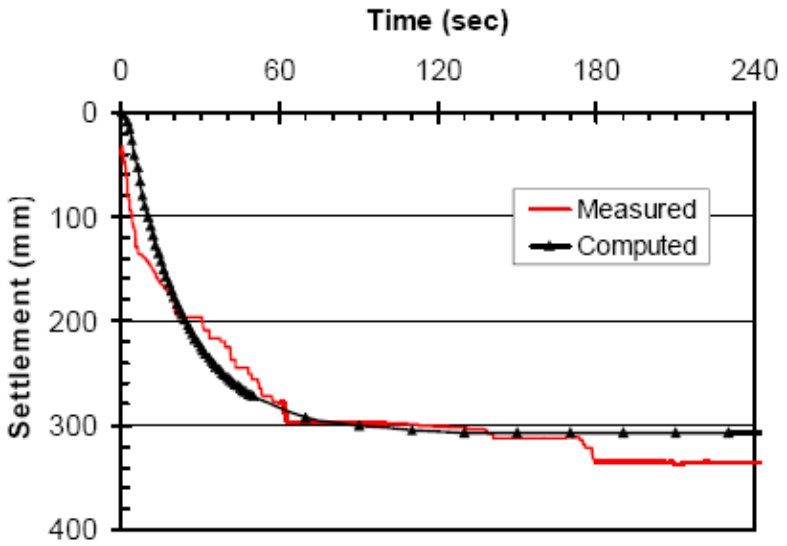

Figure 3.26: Comparison of measured settlements against computed settlements with time using FEQ-drain for Vancouver test site (Rollins et al.,2003).

Table 3.1: Computed values of pore pressure ratios (Ru) and settlement for various earthquake events and drain spacings for the Vancouver test site.

Magnitude	Duration (sec)	N_{eq}/N_l	Drain Spacing (m)	Maximum R_u	Settlement (mm)
Blast	8	4.0	1.22	1.0	310
6.0	8	2.0	0.91	0.40	31
6.75	17	2.0	0.91	0.47	35
6.75	17	3.0	0.91	0.61	48
7.5	35	2.0	0.91	0.65	53

Rollins et al. (2004).- Based on the previous work by Rollins et al. (2003), Rollins & Anderson (2004) further investigated the effect of installation induced vibration to the effectiveness of EQ-drains. They evaluated the behavior of EQ-drains under low and high levels of vibration at the same test site with the previous blasting test, located in Vancouver, Canada. Each test area consisted of a cluster of 35 drains, installed to a target depth of 12.8m, arranged in a triangular grid with a center – to center spacing of 1.22m. The experiment layout is presented in **Figure 3.27**.

In the first test area, drains were installed with a pipe mandrel, in an effort to induce as little densification as possible, thus very little settlement was observed. In the second test area,

drains were installed with a finned mandrel, designed to induce soil densification, leading to significant settlement (volumetric strains of 2.5%). Blast holes were created in a similar manner as described earlier (see **Figure 3.22**). Excess pore pressure ratio time histories are presented in **Figure 3.28** and **Figure 3.29** for the two test areas. The untreated site response is also plotted for comparison purposes.

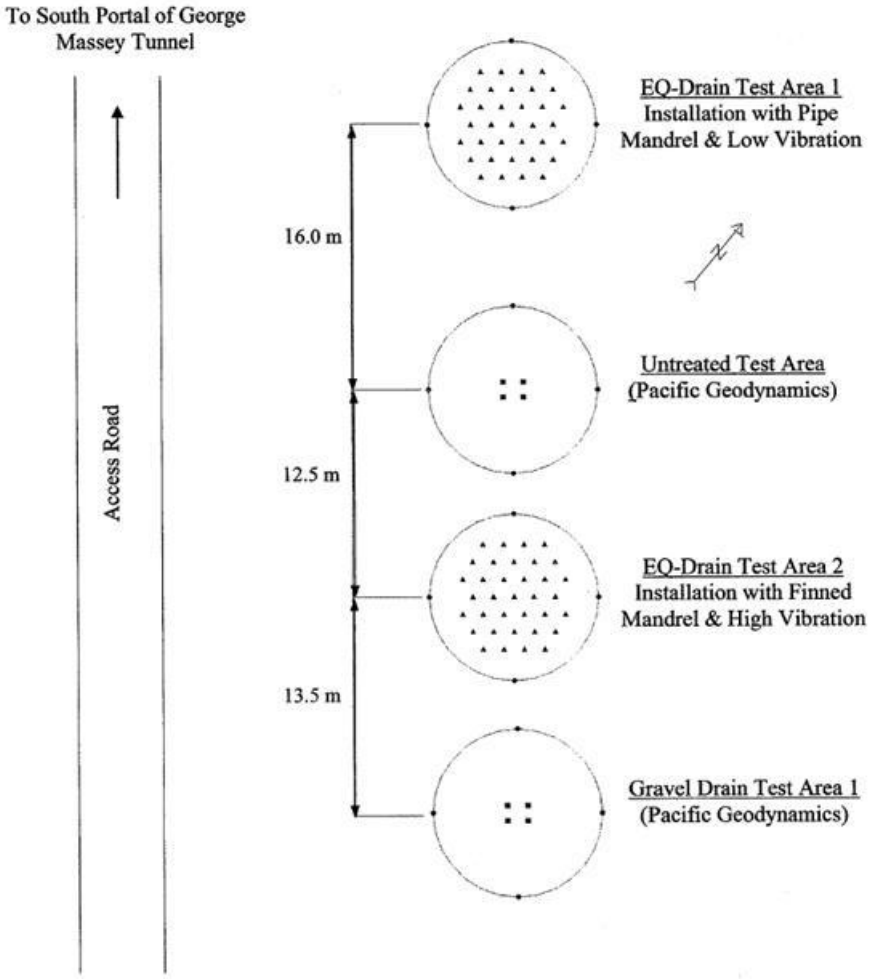

Figure 3.27: Test layout at Vancouver, Canada (Rollins et al, 2004).

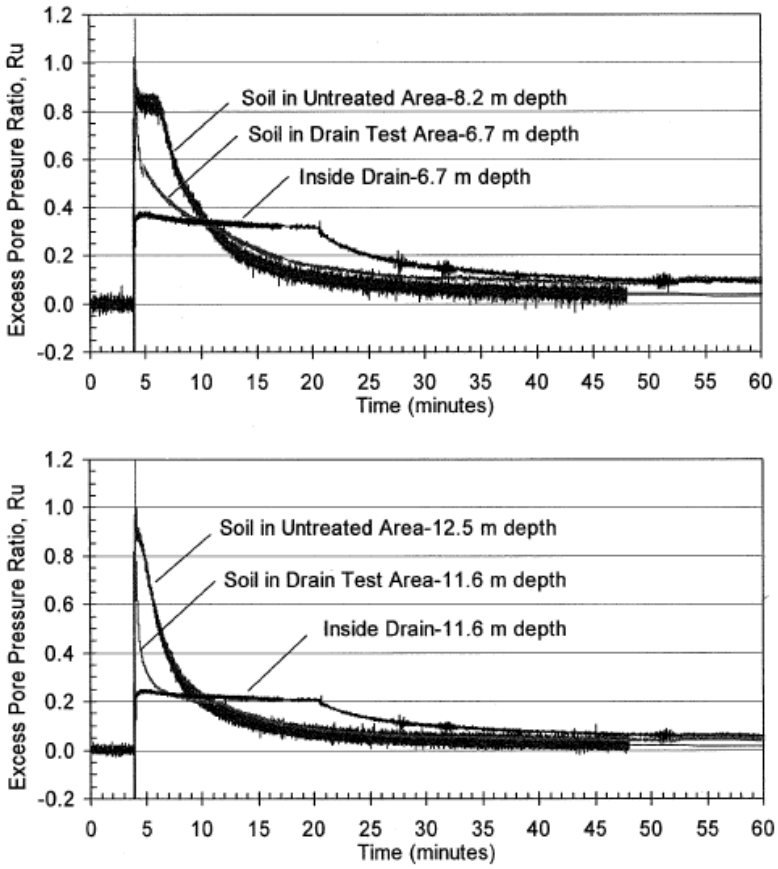

Figure 3.28: Excess pore pressure ratio Ru time histories at various depths in the untreated area and the test Area 2 (high vibration). The time histories for the untreated soil are provided for comparison purposes.

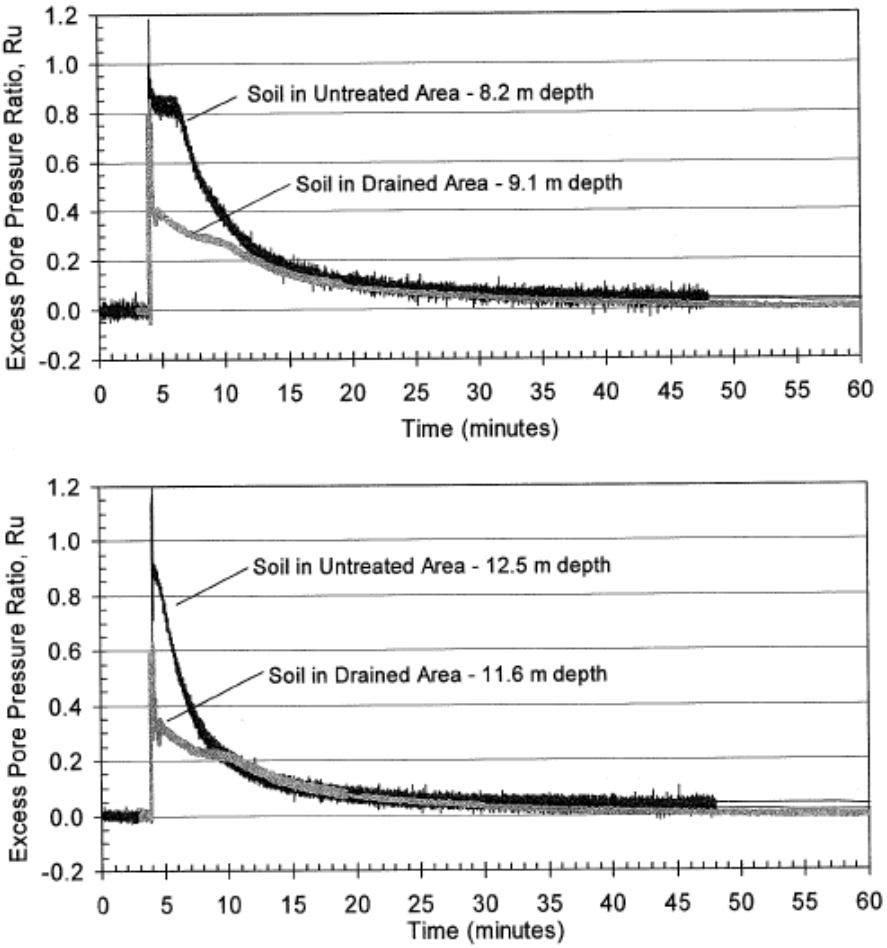

Figure 3.29: Excess pore pressure ratio r_u time histories at various depths in the untreated area and the test **Area 1** (low vibration).

The test results indicated that even though drains did not prevent initial liquefaction during the rapid loading conditions of the blasting test, higher dissipation rates of excess pore pressures were recorded compared to the untreated site. Dissipation rates were alike for the two tested areas, thus the amount of induced vibration did not affect the dissipation rates. CPT soundings performed at the test sites about 2 months later indicated a 20% increase in relative density in the case where drains were installed with high vibration and a 10% increase for the low vibration test area. Additionally, the blast induced settlements are plotted with respect to the radial distance from the center of the test area in **Figure 3.30**, for the untreated site and the two treated sites. The settlements in the high vibration test area were reduced to 60% of the settlements measured in the untreated test site, whereas in the low vibration area the settlement reduction was in the order of 80%.

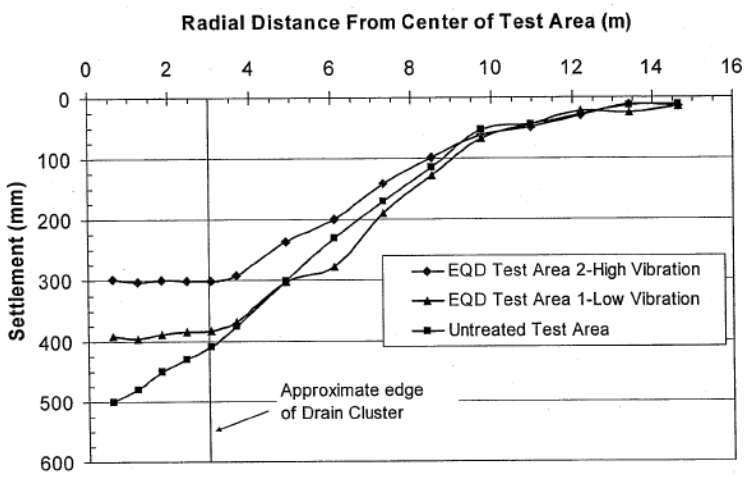

Figure 3.30: Blast induced settlements vs radial distance from center of test area for the untreated site and the two treated cases.

Chang et al. (2004).- In the previously described field tests, vibration during installation induced some densification to the surrounding soil; therefore the effect of drainage to the reduction of pore pressure generation could not be directly assessed. The dynamic in situ liquefaction testing program performed by Chang et al. (2004) aimed at exactly isolating the drainage function of EQ-drains and study its effect to excess pore pressure generation, post – shaking pore pressure dissipation and associated settlements.

The tests were performed at two reconstituted test specimens, of saturated sand, with dimensions 1.2m $\times$ 1.2m $\times$ 1.2m, enclosed in an impervious membrane. The configurations for the untreated and treated specimen are shown in **Figure 3.31.** For the Drain test, the 100mm diameter drain was placed in the one end of the test area, in order to simulate a 200mm diameter drain spaced at 2.4m. Additionally, to avoid any installation-induced vibrations and evaluate solely the drainage function of the drain, the latter was placed inside the test area before the specimen preparation by water pluviation. The liquefiable sand used in the tests, had a relative density of 36% and shear wave velocities between 90 and 115m/sec. Dynamic loading was applied through a vibroseis truck that has been extensively used in the past, as a wave source in geophysical explorations. The vibroseis truck induced vibrations in the vertical direction on a footing constructed in the vicinity of the test area. The test involved staged loading, in which small shaking level was initially applied followed by increasing levels of shaking.

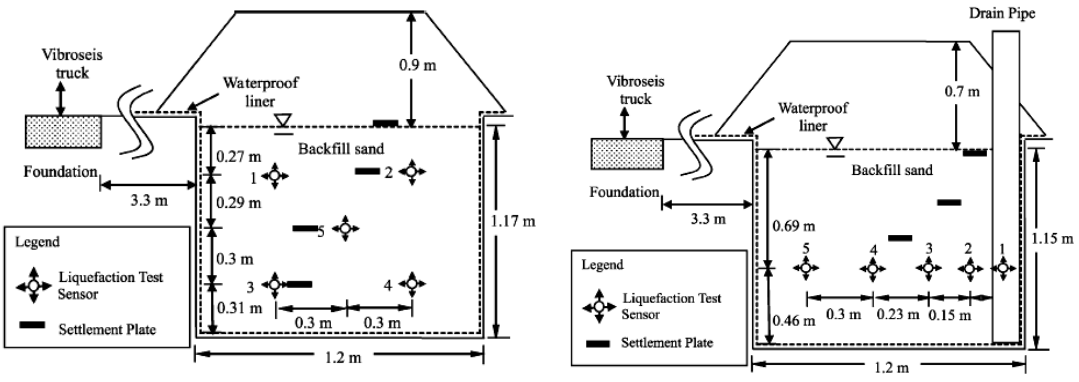

Figure 3.31: Test layout for the untreated **(a)** and the treated **(b)** case.

The shear strain and pore pressure time histories corresponding to the largest loading level are presented in **Figure 3.32** for both test configurations. In the "No drain" case the shear stain amplitude varies throughout the test, as a result of the high excess pore pressures generated during loading. The soil liquefies after approximately 35 loading cycles and 2.5cm of settlement, corresponding to 2.1% of volumetric strain. In the Drain case, shear strain amplitude remains constant during shaking, as a result of the low levels of excess pore pressure ratio, which did not exceed 0.35. Only 0.6cm of settlement occurred, corresponding to 0.5% volumetric strain.

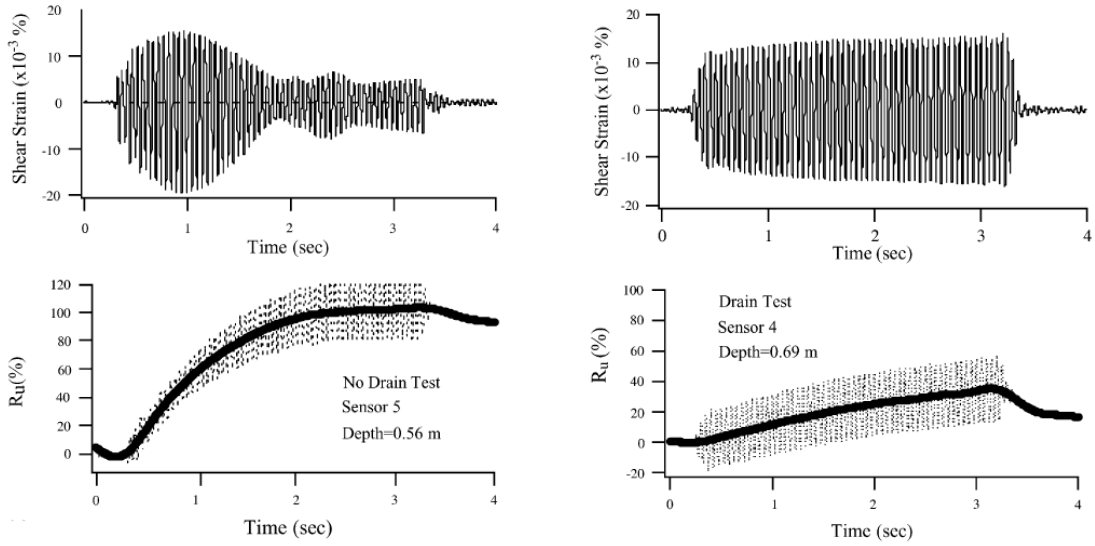

Figure 3.32: Shear strain (*10^{-3}%) and excess pore pressure ratio r_u time histories for the **(a)** No drain and the **(b)** Drain test case, for the greatest loading intensity.

Post shaking pore pressure dissipation rates were also examined and the related time histories for the two tests are presented in **Figure 3.33.** It is concluded that the post – shaking dissipation rate is accelerated due to the presence of the drain in the second test configuration.

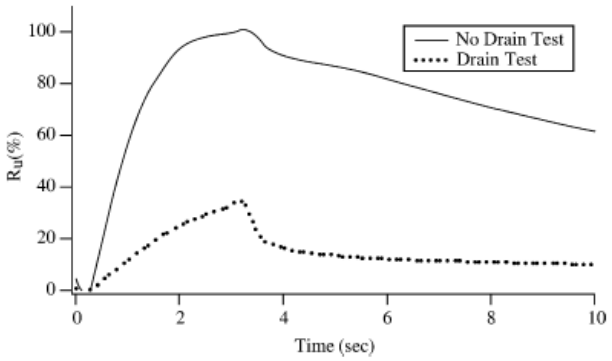

Figure 3.33: Excess pore pressure dissipation rates for the No Drain and the Drain test.

Marinucci et al. (2008).- conducted a series of centrifuge tests to examine the effectiveness of prefabricated drains for liquefaction remediation.

The centrifuge model consisted of sloping ground (approximately 3%) towards a central channel. The soil profile is composed of a 4.8m liquefiable layer of loose Nevada sand (D_r = 40%) overlain by a 1m thick crust of compacted Yolo loam in prototype scale. Soil improvement was applied only on the left side of the channel as presented in **Figure 3.34**. Overall, 58 drains were installed in a triangular pattern, spaced at 1.5m center – to – center in prototype scale (100mm in model scale). The drain, was modeled by a nylon tube and had a diameter of 100mm in prototype (7mm in model scale). It was enclosed in filter fabric to prevent clogging and it is shown in **Figure 3.35**. Due to the relatively small centrifugal acceleration of 15g and the low permeability of Nevada sand, the use of water as pore fluid was justified by the Authors.

Twelve shaking events were applied to the model, each one consisting of 20 cycles of sinusoidal motion at a prototype frequency of 2Hz. The input base acceleration (PGA) varied between 0.01 and 0.28g. The drain performance was evaluated based on the last 5 shaking events with intensities of 0.01g, 0.028g, 0.063g, 0.11g and 0.28g. The experiment instrumentation involved 88 accelerometers, 57 pore pressure transducers, 13 potentiometers as well as vertical and surface markers.

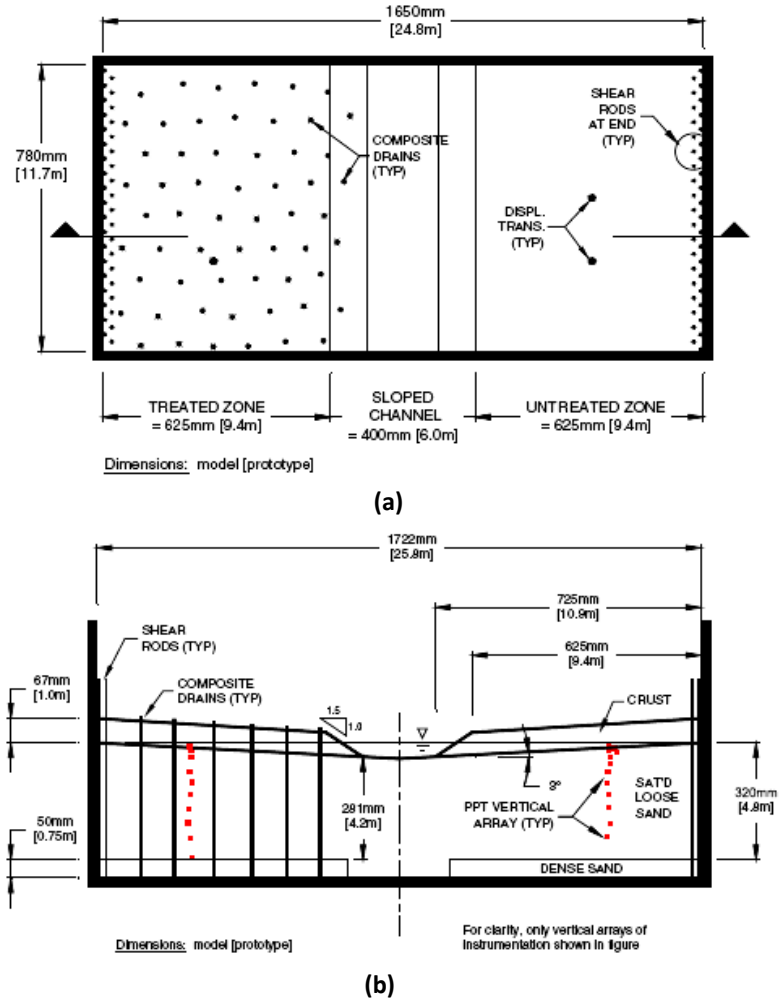

Figure 3.34: Plan arrangement of test set up **(a)** and cross section **(b)**

(a) **(b)**

Figure 3.35: **(a)** 7mm model drain and **(b)** geosynthetic drain (D = 100m) in prototype scale

Typical test results are presented in **Figure 3.36a** & **b** in terms of pore pressure ratio time histories for base PGA equal to 0.28g, for both treated and untreated side of the channel. It appears that even though r_u values greater than 0.5 develop in the treated side, they remain well below unity for depths greater than 3m. The soil on the untreated site liquefies at all depths shortly after the beginning of shaking and large r_u values are maintained, for a long time after the end of shaking.

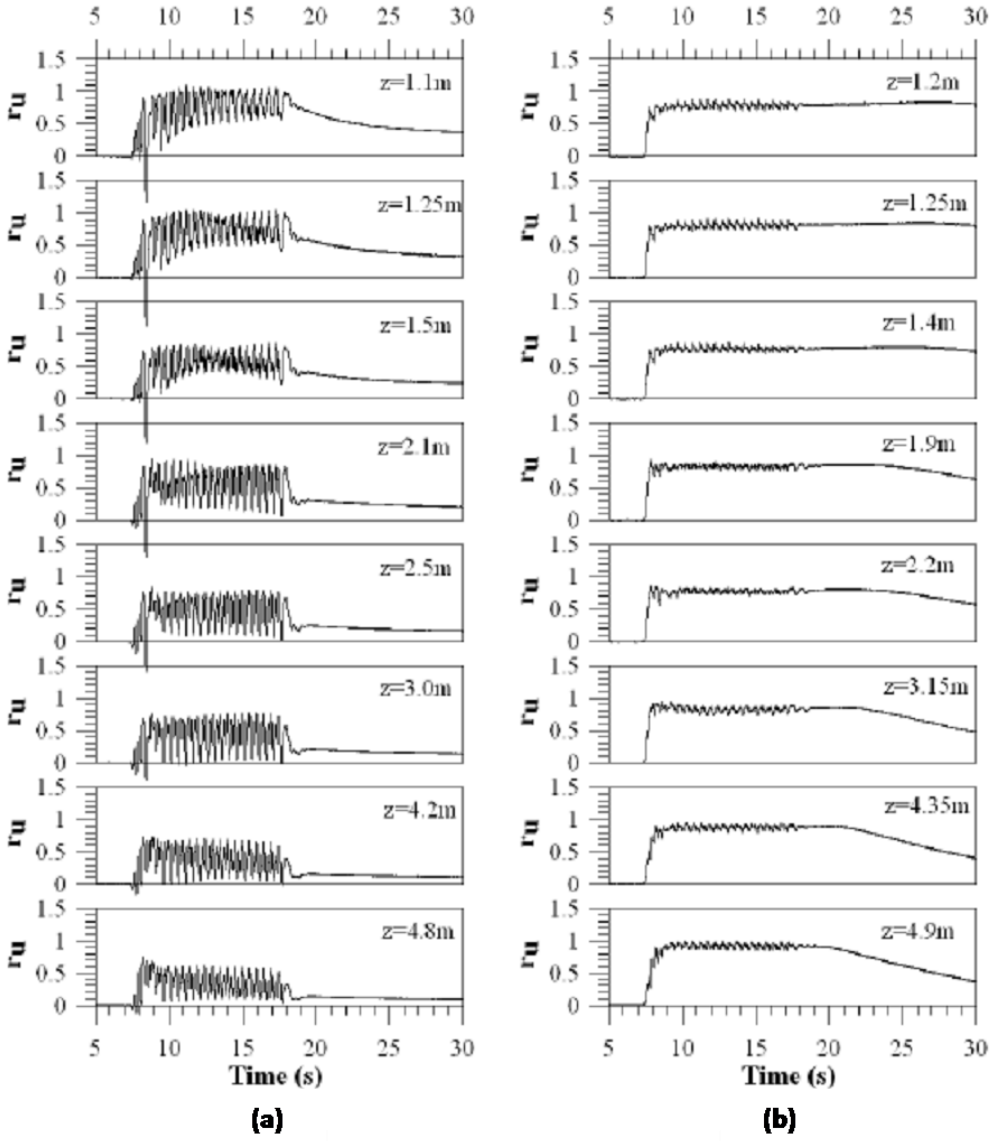

Figure 3.36: Excess pore pressure ratio R_u time histories at selected depths for the **(a)** treated **(b)** non treated site, for PGA = 0.28g.

Horizontal and vertical displacements as a function of time are presented in **Figure 3.37a** & **b** for the main five shaking events. Displacements in both directions are considered negligible for low shaking levels, but increase significantly for the last two events, especially in the case of the untreated side. Overall, permanent horizontal displacements on the treated side were reduced by 80% compared to the equivalent displacement amplitude for the untreated side.

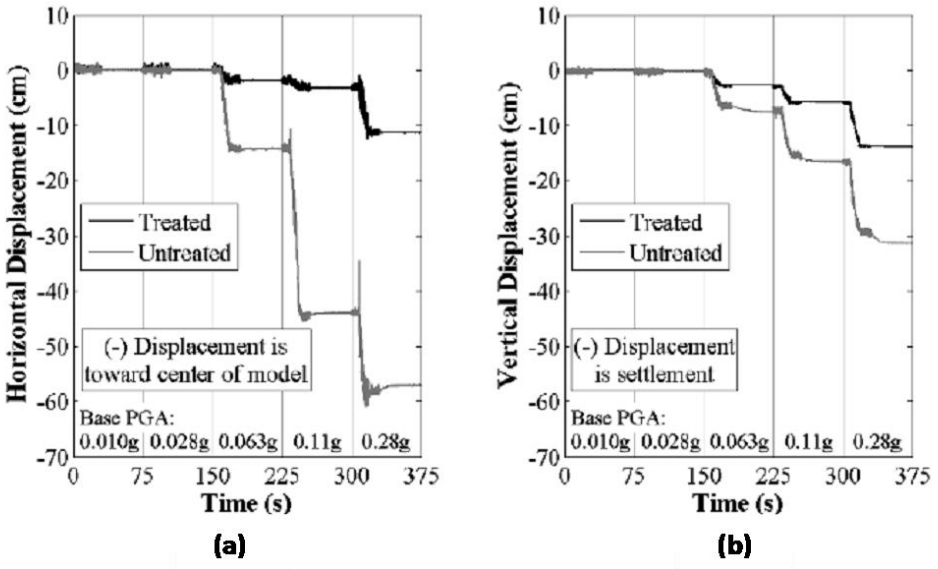

Figure 3.37: Shaking induced displacements in the **(a)** horizontal and **(b)** vertical directions for both examined cases.

3.4.2 Screen Pipes

Shaking Table Tests (Harada et al.,2006).- The behavior and effectiveness of the screen pipe method was evaluated with a series of shaking table tests on a 2×2 pile foundation resting on improved soil. The response of the pile foundation was examined under different drain configurations around the piles and different levels of shaking intensity.

The apparatus used in the experiments is presented in **Figure 3.38**. The shaking table is 3.0 × 2.0m in dimension and is equipped with electrodynamic shakers in the two horizontal directions, able for a maximum acceleration input of 1.2g. The laminar box is 1.0m in width, 0.5m in depth and 1.0m in height and consists of 11 rectangular metal rings of 80mm in thickness. Between the rings, two pairs of chains with bearings 4mm in diameter, ensure that the laminar box follows the soil deformation.

Figure 3.38: Apparatus used in the experimental investigation of the effectiveness of the screen pipe method.

The soil profile consisted of two layers, both made of Silica sand, with different relative densities. The upper liquefiable layer had a relative density of 40% and was created by water pluviation. The lower non – liquefiable layer was created by air-pluviation and had a relative density of 80%. Typical properties for Silica sand are summarized in **Table 3.2.** Both layers were saturated with a cellulose solution with about 11 times higher viscocity than that of water, to abide by the related scaling laws. The excessive dissipation of water on the ground surface was restricted by laying a vinyl sheet on the surface and a thin layer of gravel on top.

Table 3.2: Silica sand properties

Material	G_s	D_{50} (mm)	F_c (%)
Silica sand	2.62	0.18	5

A 2×2 pile foundation with a pile cap at the top was simulated in the experiments at a scale of 1/25 of the prototype. The pile cap weighted 80N, corresponding to a reinforced concrete bridge pier (weighting around 1250kN). The rectangular cross section of the pile (B = 38mm, t = 4.5mm, L = 800mm, EI = 5.90e4kNmm^2) allowed adequate displacement limits during shaking.

The drains were constructed of a screen pipe, 22mm in diameter, with 0.1mm openings. **Figure 3.39** provides a rough comparison between the coefficients of permeability for a gravel pile and a screen pipe as a function of the hydraulic gradient. It is observed that the permeability of the screen pipe can be greater than that of a conventional gravel drain by the order of a magnitude. Before the main experiment, a group of preliminary tests was performed, to investigate the possible inertial effects of screen pipe drains on soil response during shaking. The outline of the preliminary experiments is presented in **Figure 3.40**.

Overall, three cases were examined, each at a shaking intensity of 500gal, and a 100mm square arrangement of pipes, as summarized in **Table 3.3.**

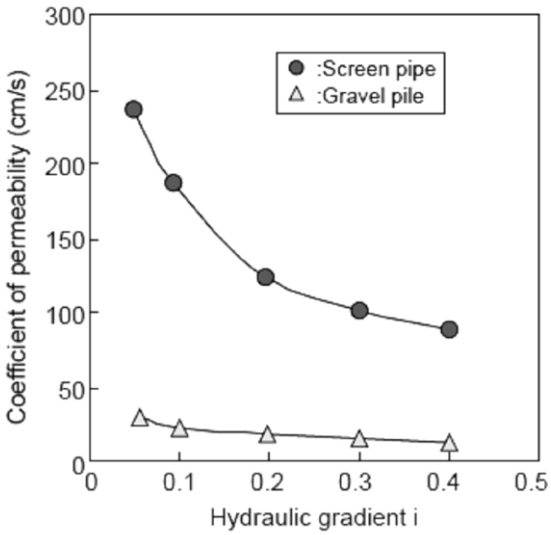

Figure 3.39: Drainage capacity of gravel pile and screen pipe

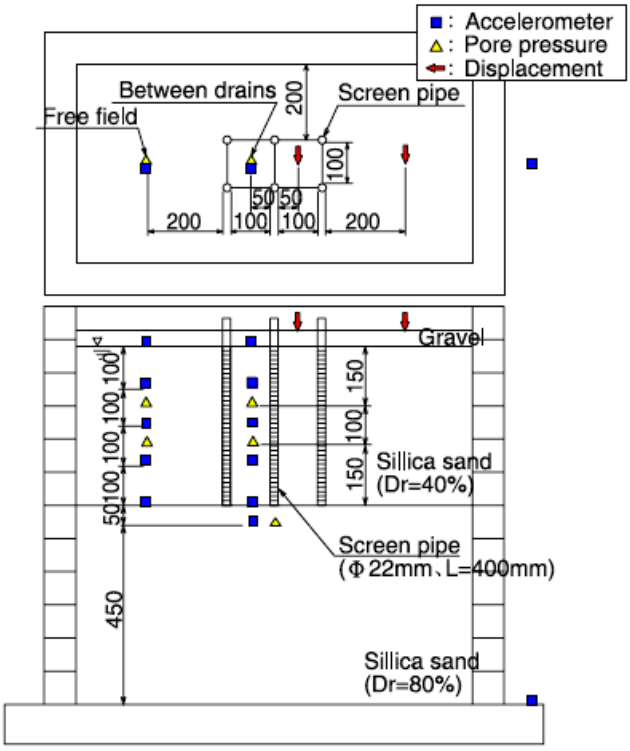

Figure 3.40: Test set up of preliminary test.

Table 3.3: Summary of preliminary experiments

No	Drain Material	Input motion (gal)
1	No drain	500
2	Screen pipe	500
3	Prevention of drainage from embebed pipes, by vinyl tape rolled on top.	500

The response acceleration time histories from the three examined cases are presented in **Figure 3.41**. It is not specified if the above recordings correspond to the ground surface, however, it is concluded that soil response is controlled by the pore pressure dissipation rather than the rigidity of the inserted steel pipes.

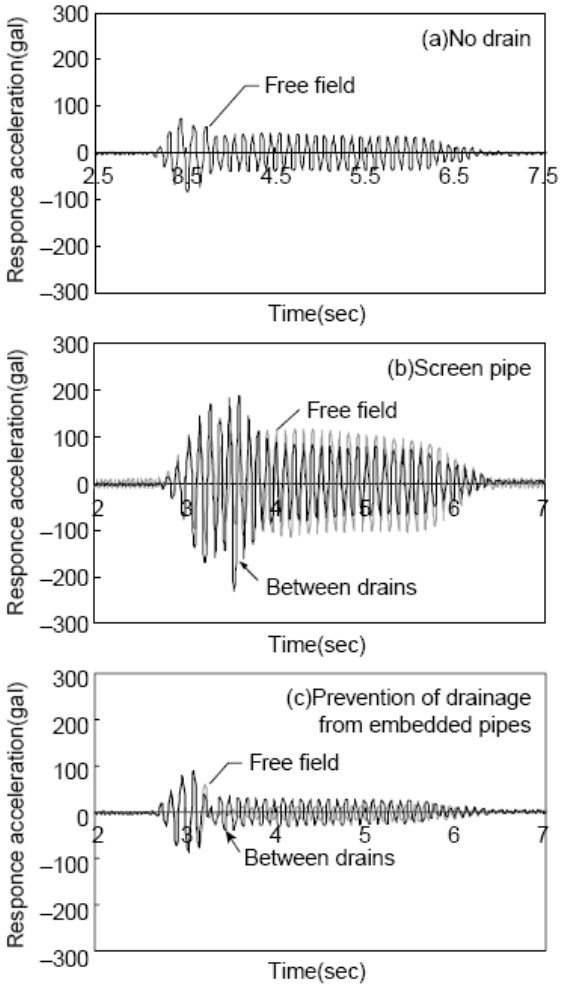

Figure 3.41: Ground acceleration time histories for the preliminary experiment at an input motion intensity of 500gal.

The main experimental sequence included the following arrangements: **Case (1)** No drains present **Case (2)** Sparse arrangement of drains, **Case (3)** dense arrangement of drains and **Case (4)** drains installed around the circumference and outside the footing. The overview and cross section of the experiment set up is presented in **Figure 3.42**.

The models were subjected to harmonic excitation with a frequency of 10Hz. The input motions had intensities of 50, 100, 200, 300, 400, and 500gal, whereas the last test of each case was run with a horizontal load of 60N acting on the pile cap, in an attempt to investigate the drainage effect to the horizontal resistance of the soil. The input motion with an intensity of 300gal is provided in **Figure 3.43**.

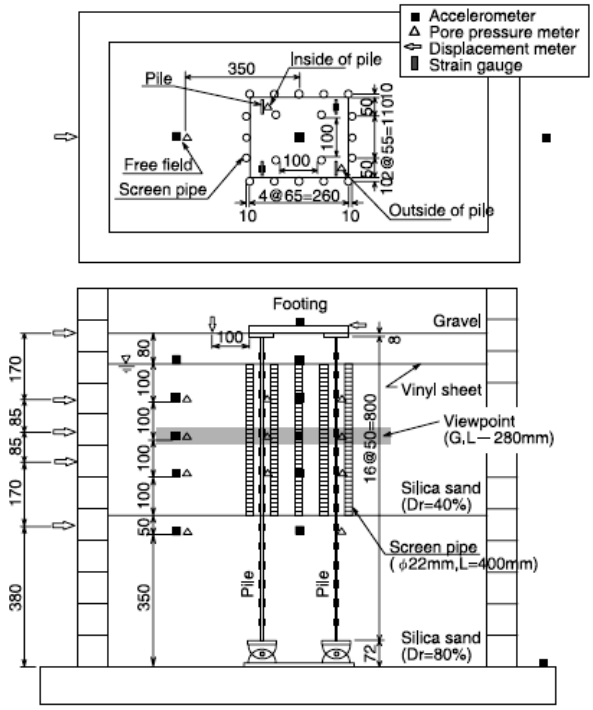

Figure 3.42: Overview and cross – section of the main experiment series.

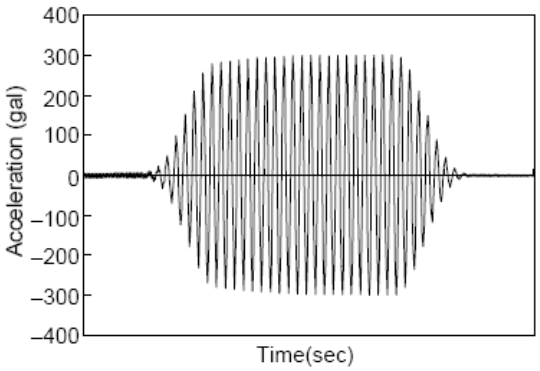

Figure 3.43: Input motion at 300gal.

Accelerometers and pore pressure transducers were placed on selected depths around the pile foundation and far away from it, as indicated in the same **Figure 3.42**. The recording time included the stage of excess pore pressure dissipation after the end of the input motion. Pile bending strain was also measured at 15 locations; however, priority is given here to the drainage capacity of the screen pipe.

The excess pore pressure ratio time histories, recorded for each examined case are presented in **Figure 3.44** for shaking intensity equal to 300gal. The recordings correspond to the mid - depth of the liquefiable layer i.e. the G.L.-280mm view point.

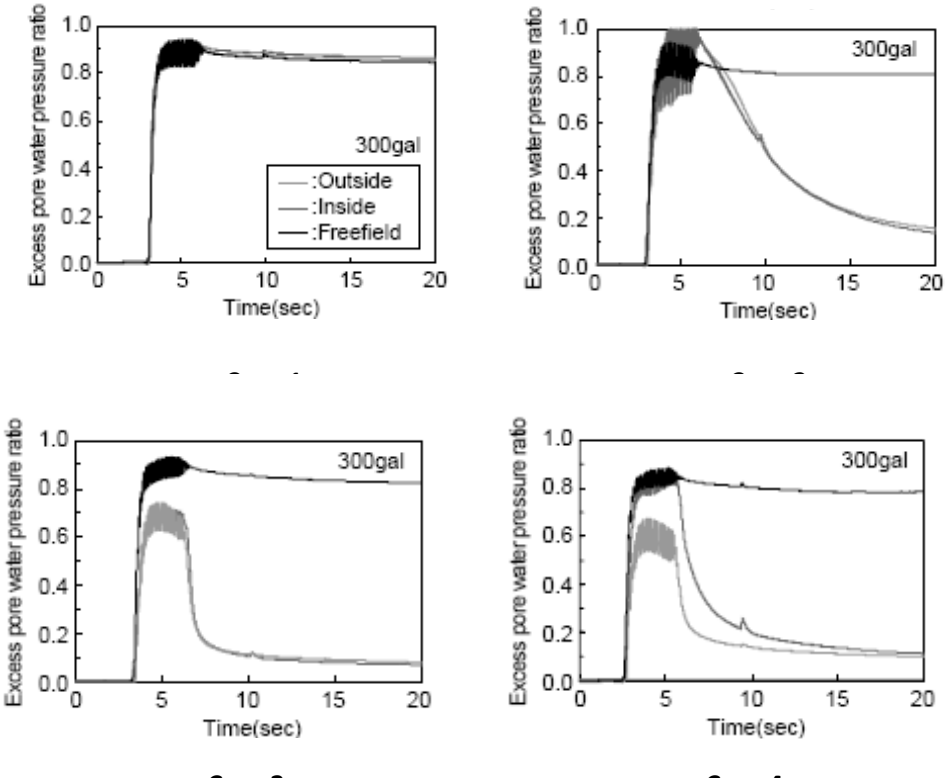

Figure 3.44: Overview and cross – section of the main experiment series.

It is concluded that in the No – drain case (1) the ground liquefies uniformly and remains in a liquefied state for a long time after the end of shaking. The installation of screen pipes and variation of spacing appears to significantly affect the efficiency of steel pipes in pore pressure dissipation. In the sparse pipe configuration (Case 2) the drainage effect of the screen pipes is not significant, since the pore pressure time history near the pile foundation does not differ significantly from the free – field recording. Nevertheless, the screen pipes become more efficient in dissipating the excess pore water pressure, when installed in a dense configuration, as observed in Case 3. Additionally, although screen pipes were not

installed beneath the footing (Case 4) the pore pressure ratio is not significantly affected, compared to Case 3. It is interesting though, that pore pressures outside the footing in Case 4 increased, compared to the equivalent recording in Case 3, due to the lack of the additional drainage capacity provided by the pipes inside the footing.

On-site experiment (Harada et al., 2006).- The efficiency of the new liquefaction mitigation method was also investigated by in-situ liquefaction testing.

The layout (cross – section and plane arrangement) of the on-site test is presented in **Figure 3.45**. On the whole, four different cases were examined, the first without drains and the following three with drains at various spacing intervals (1.5m, 1.0m, and 0.5m respectively). The screen pipes had a diameter of 48.6mm with openings of 0.3mm and extended from the ground surface to the bottom of the liquefiable sand layer. A small boring machine was used for the installation, and shaking induced liquefaction was generated by a steel pipe 508mm in diameter and 12m in length, attached to a vibratory pile driver of 60kW in capacity and frequency of 18.3Hz as presented in **Figure 3.46**.

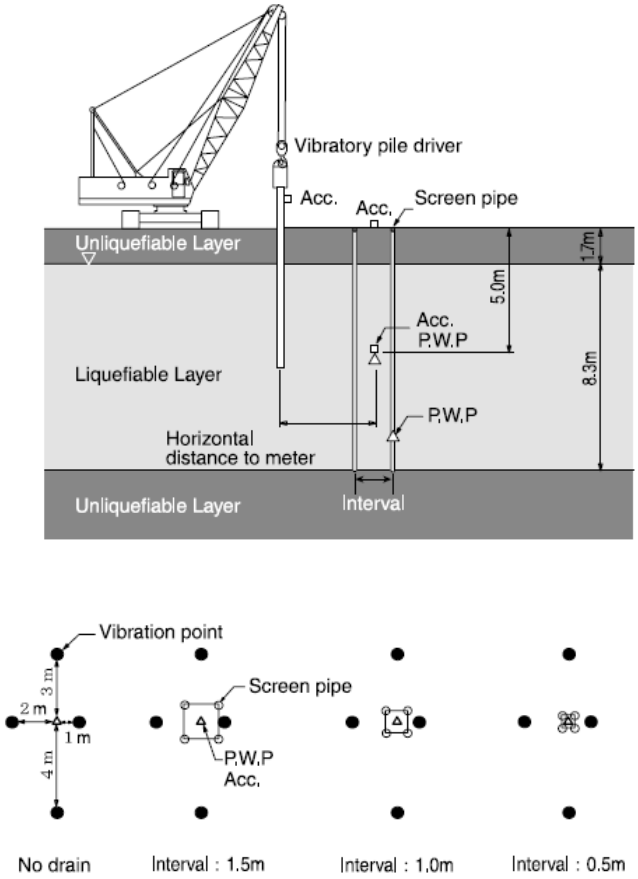

Figure 3.45: Cross section and plane arrangement of in-situ test.

Shaking was induced by penetrating the pile driver into the liquefiable layer to a depth of 8m, at a rate of 1 – 2m/min, vibrating the steel pipe at a constant power. The different shaking intensities were achieved by placing the steel pipe at different horizontal distances with respect to the measuring instrument (4, 3, 2, and 1m respectively), as presented in **Figure 3.47** (same figure as in experiment layout). **Figure 3.47** provides a snap shot taken from the site, for the 1m grid spacing, provided by Prof. Ikuo Towhata, after personal communication.

Steel pipe acceleration, acceleration at the ground surface and excess pore water pressure at a depth of 5m, were permanently recorded during the in-situ experiments. Moreover, the excess pore water pressure in a screen pipe was instrumented to investigate potential clogging phenomena. All instrumentation positions are denoted in **Figure 3.45**.

The tests were conducted at the reclaimed land of Uraysu-shi at Chiba, mainly consisting of loose fine sands, displaying a high liquefaction potential. A cross section of the test area is provided in **Figure 3.48**. The groundwater level is located at a depth of 1.7m and the average N-value is around six.

The time history of excess pore pressures (kN/m^2) for all four cases, when placing the pile driver at a distance of 1m from the measuring instrument, is plotted in **Figure 3.49**. High pore water pressures are quickly generated and maintained for a long time in the case of the unimproved ground (Case 1). On the contrary, pore pressures, in the improved ground, are effectively dissipated through the screen pipes (Cases 2, 3, 4). The dense pipe configuration allowed fast dissipation of excess pore pressures, and consequently the occurrence of lower peak values.

Figure 3.46: Vibratory pile used for shaking induced liquefaction.

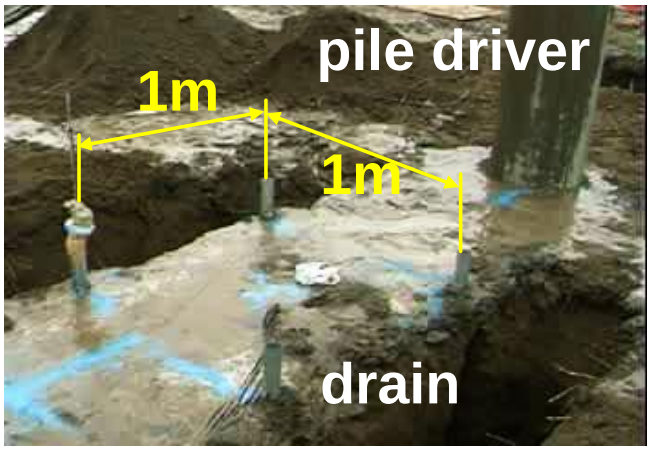

Figure 3.47: Close-view of the screen pipe grid and the pile driver (Photograph provided by Prof. I. Towhata).

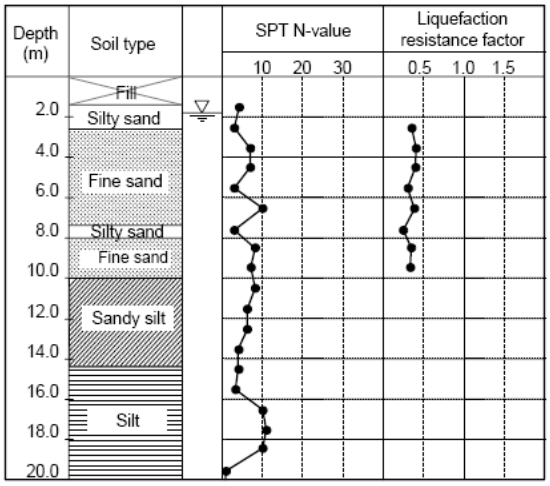

Figure 3.48: Typical soil profile of the examined site.

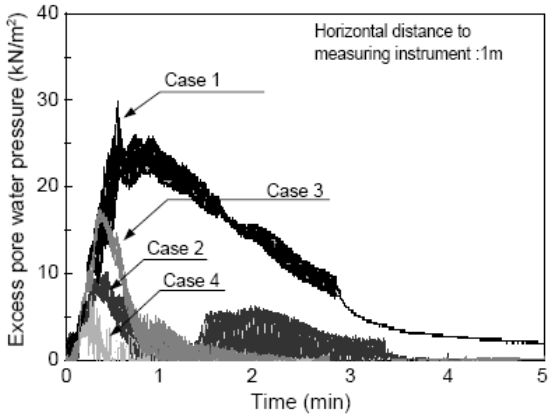

Figure 3.49: Excess pore pressure time history for the 4 examined cases and the most intense induced shaking.

3.5 Comparative evaluation of drain types and design methods.

In the present paragraph, typical design considerations for all three types of drains are summarized and a comparative evaluation of the available design tools is provided in an attempt to assess and compare their results.

Typical design considerations for gravel drains.- Gravel drains are typically spaced at center – to – center distances between 1.8 and 3.0m and have a diameter ranging from 0.6 to 1m. Thus, considering a diameter of 1m and drain permeability of 1cm/sec the flow rate is roughly equal to $6.51*10^{-3}$ m^3/sec. The cost per linear meter is estimated to vary between 60 and 90€ including gravel material and installation costs, while construction time ranges from 15 to 45 minutes per column, depending on installation depth and grid spacing. The major drawbacks of the method include significant traffic disturbance and dust problems at the

construction site, spoil material generated during installation (approximately 1 - 3 m^3 per column) as well as clogging concerns.

Typical design considerations for EQ-drains.- For EQ-Drains, typical center – to – center spacing may range from 1m – 1.5m, depending on the design earthquake magnitude and the soil properties (i.e. relative density and permeability). This is roughly half the spacing required for gravel drains to provide an equivalent level of liquefaction protection. The corrugated pipe has a diameter typically between 75 – 100mm. Given the above data, for D = 100mm, hydraulic gradient i = 0.25, the flow rate is estimated to be in the order of 0.093m^3/sec, significantly greater than the equivalent rate estimated for gravel drains. Cost is also drastically lower, varying between 5 – 10€ per linear meter, including the cost of drains, filter fabric and installation. Installation time is considerably shorter compared to that of gravel drain, ranging from 1 to 3 minutes per drain depending on installation depth and spacing. Moreover, EQ-drains do not generate spoil material and cause only minor environmental disturbance.

Typical design considerations for screen pipes.- In the case of screen pipes, the installation spacing ranges from 0.5 to 1.5m. Unfortunately, there was no available data in the literature in terms of drainage capacity, cost estimate and installation time. Nevertheless, it appears safe to assume that installation time is comparable to the time required for EQ-Drains, given the presented equipment. It is important to stress out that the use of screen pipes does not induce any densification of the surrounding soil, which is something to be considered in design. Moreover, as it was already mentioned, screen pipes prove to be insufficient in preventing liquefaction during strong earthquakes, thus it is suggested to be used concurrently with piles.

Design application.- The performance and efficiency of the available design methods concerning gravel drains, and the comparative evaluation between gravel drains and EQ-drains is presented in the following paragraph.

The comparative evaluation of the various design methodologies was performed in the case of a uniform liquefiable sand layer, possessing the soil properties summarized in **Table 3.4.**

Table 3.4: Soil properties used in the FEQ-Drain analysis.

	Clay	Sand
k_h (m/s)	$3.05*10^{-10}$	$7.60*10^{-5}$
$m_{v,3}$ (m^2/kN)	$4.17*10^{-5}$	$4.17*10^{-5}$

In the present application, the site was treated with gravel drains, 0.06m in radius, arranged in a triangular grid. The design referred to a seismic motion intensity (N_{eq}/N_l) equal to 2, a maximum allowable pore pressure ratio, $r_{u,max}$, equal to 0.5 and several values of the dimensionless time factor T_{ad}, ranging from 2 to 200. The three most popular design methodologies [Seed & Booker (1977), Onoue (1999) and Bouckovalas et al. (2009)) were applied and the resulting area replacement ratio α_s is plotted against the dimensionless time factor T_{ad} in **Figure 3.50**. The method proposed by Onoue (1988) was applied for different well resistance values, L_w, ranging from 1 to 18. Apparently, the incorporation of well resistance into the dominant flow theory slightly increases the required area replacement ratio α_s producing an increasing trend at increasing T_{ad} values. Moreover, there is a distinct improvement in the predicted α_s values between the traditional Seed & Booker (1977) and the revised Bouckovalas et al. (2009) theory, with the latter leading to lower area replacement ratios, this being translated to a more economical design.

The comparison between gravel drains and EQ-drains was performed considering a different soil profile. Namely, the soil profile under examination consisted of a 9.14m (30ft) liquefiable sand layer overlain by a 2.75m (9ft) clay cap. The soil properties are presented in **Table 3.4**. Both gravel drains and EQ-drains had a radius of 0.06m, whereas both analyses were performed for a constant T_{ad} value equal to 647,84. The sand layer was considered to liquefy after 15 cycles of shaking, whereas the seismic excitation consisted of 25 equivalent cycles, rendering a N_{eq}/N_l ratio equal to 1.67 and dynamic time t_d equal to 12.5sec.

The ground water table was initially located at 1.22m (4.0ft) below the ground surface and the resulting maximum pore pressure ratio, $r_{u,max}$, is plotted against the usual range of spacing ratios (a/b) used in current practice as presented in **Figure 3.51**. The above analysis was repeated for different locations of the ground water table [(i.e. -1.68m (-5.5ft), -1.83m (-6.0ft) & -2.13m (7.0ft)) and the resulting curves are also plotted in the above figure. The observed divergence between the initial analysis (ground water table at -1.22m) and the Seed & Booker (1977) solution is consistently reduced in the subsequent analyses, the most probable reason being the hydraulic head which is formed around the circumference of the drain, when the dissipation of the excess pore pressures occurs above the sand layer.

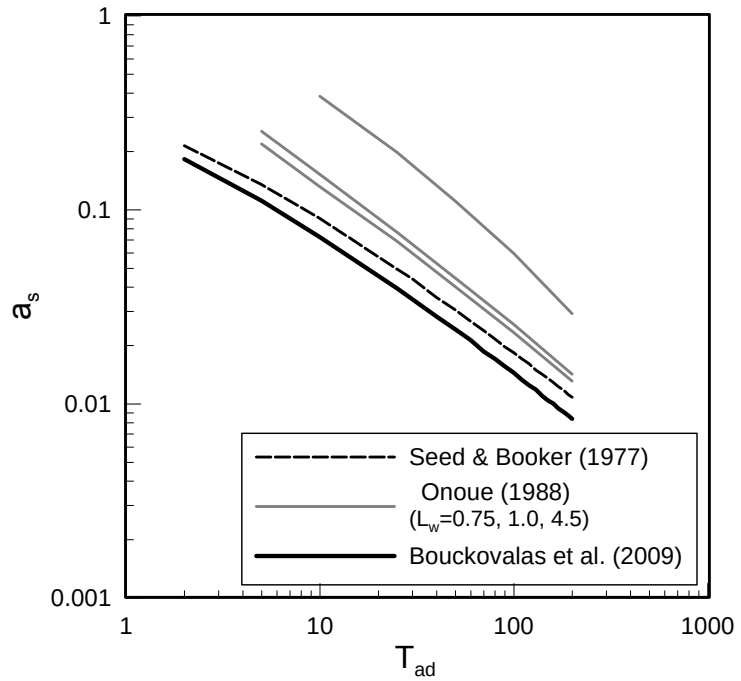

Figure 3.50: Comparative evaluation of the three major design methodologies [Seed & Booker (1977), Onoue (1988), & Bouckovalas et al. (2009)].

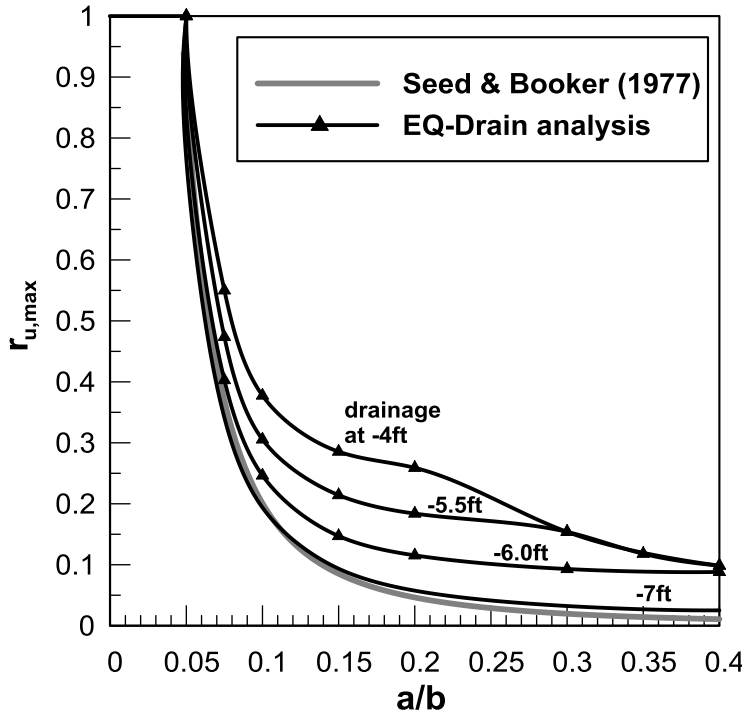

Figure 3.51: Comparison between analysis with EQ-Drains and gravel drains designed according to Seed & Booker (1977) theory.

CHAPTER 4

Performance - Based Criteria

4.1 Introduction

Performance based engineering approaches the design of structures within a predefined seismic performance objective, under established levels of seismic risk. The main concept behind it is, essentially, the extent of damage that the owner/user of a structure is willing to accept, under specific seismic hazard levels, considering a wide range of economic and social issues such as the cost of initial design and repair or the effect on human life in case of severe damage or collapse.

There are essentially three basic steps to be followed for a complete performance based approach: The *Design Seismic Motions* specified for each structure category, essentially set the frame for the seismic design, taking into consideration local seismic conditions as well as the importance of the structure. *Performance Levels & Objectives* describe the service level and the extent of damage in the structure, after the occurrence of each of the design seismic motions defined above, while in the last step, Performance Levels are linked to *Deformation Limits* in order to provide quantitative criteria for the seismic design of new and the retrofitting measures of already existing structures.

In the present chapter the above steps are further explained, based on the specifications of Seismic Design Guidelines and Provisions currently in effect in Europe and other areas, such as the U.S.A. and Japan. The following review is narrowed in structures founded on spread footings, i.e. bridges and buildings.

4.2 Design seismic motions

In specifying Design Seismic Motions, attention is given to the seismicity of the area of interest, which leads to the definition of a set of (typically two) design ground motions, associated with specific levels of hazard and probabilities of occurrence. The lower level ground motion refers to seismic events of moderate intensity that are likely to occur during the life time of the structure, while the upper level ground motion refers to strong seismic events that are less frequent and thus, have a low probability of occurrence during the life span of the structure. This set of design ground motions is assigned different return periods, which serve as a guide for the selection of the appropriate intensity of earthquake motion considering suitable local seismic hazard maps.

In most Design Specifications presented below, design earthquake motions are assigned a Probability of Exceedance (P_E), which essentially expresses the probability of a ground motion to exceed a specific level of intensity, within the life time of a structure. Probability of exceedance (P_E) is assumed to follow a Poisson probability model, where earthquakes of given magnitudes occur randomly in time at an average rate. The occurrence of an earthquake is assumed to have no effect on the timing or probability of a future earthquake. It is given by the following *Equation 4.1*, as a function of the lifetime of the structure (t) and the annual frequency of exceedance of the ground motion amplitude (ν):

$$P_E = 1 - e^{-\nu t_L} \tag{4.1}$$

Since, the annual frequency of exceedance (ν) of the ground motion amplitude is set equal to the inverse of the Return Period (T) i.e. ν = 1/T, *Equation 4.1* may be appropriately transformed, to provide the return period in terms of the probability of exceedance (P_E), and the lifetime of the structure t_L as shown below:

$$T = \frac{1}{1-(1-P_E)^{1/t_L}} \tag{4.2}$$

For instance, for a common building with design life time t_L = 50yrs, the seismic event with P_E = 10% has a return period of $T = \frac{1}{1-(1-0.10)^{1/50}} = 475 yrs$

4.2.1 Design seismic motions for bridges

Eurocode 8 (2003).- The EN1998-2 part of Eurocode-8 presented below, applies to "*the seismic design of bridges in which the horizontal seismic actions are mainly resisted through*

bending of the piers or at the abutments; i.e. of bridges composed of vertical or nearly vertical pier systems supporting the traffic deck superstructure. It is also applicable to the seismic design of cable-stayed and arch bridges, although its provisions should not be considered as fully covering these cases. Suspension bridges, timber and masonry bridges, movable bridges and floating bridges are not covered".

The design seismic action, A_{Ed}, is defined in terms of **(a)** the reference seismic action A_{Ek}, which is linked to a reference probability of exceedance (P_E) in 50 years or a return period T and **(b)** the importance factor γ_I used to take into account the reliability differentiation, as expressed below:

$$A_{Ed} = \gamma_I A_{Ek} \quad 4.3$$

In EC-8 the reference seismic action is assigned a return period T = 475years.

Bridges are categorized in importance classes based on **(i)** the consequences of their failure on human life, **(ii)** their role in maintaining communications especially in the immediate post-earthquake period, and **(iii)** the economic consequences in case of collapse.

Table 4.1 summarizes the three main categories defined in Eurocode 8 as well as the importance factors ascribed for each one of them.

Table 4.1: Importance Classes and associated factors for bridges according to EC-8(2006).

Importance Class	Description	Importance Factor
I	1. Bridge not critical for communications 2. The adoption of either the ref. probability of exceedance P_{NCR} in 50yrs for the design seismic action or of the standard bridge design life of 50yrs is not ecomonomically justified	0.7
II	Bridges on motorways and national roads, railroad bridges	1
III	Bridges of critical importance for maintaining communications especially in the immediate post-earthquake period, bridges the failure of which is associated with a large number of probable fatalities and major bridges for which a design life greater than normal is required.	1.3

Recommended LRFD Guidelines for the Seismic Design of Highway Bridges, Part I: Specifications (ATC – MCEER 2001).- The particular guidelines are applied to bridges of *conventional slab, beam girder, box girder and truss superstructure construction* and are the outcome of the joint venture undertaken by ATC and MCEER to propose updated

performance-based specifications to be incorporated in the AASHTO LRFD Bridge Design specifications.

The proposed seismic performance objective is studied for two levels of design ground motions:

- The *Lower level* seismic event is referred to as Expected Earthquake (EE) and includes motions with 50% probability of exceedance in 75 years or a return period of approximately 109 years. The seismic design should essentially ensure the elastic response of the bridge under the occurrence of the more frequent events.
- The *Upper level* also termed as the Maximum Considered Earthquake (MCE), is assigned a probability of exceedance of 3% in 75 years, rendering a return period equal to 2463yrs.

Next to highly active faults, MCE ground motions are bounded deterministically, so that ground motion levels do not get unreasonably high. Deterministic bound ground motions are calculated assuming the occurrence of maximum magnitude earthquakes on the highly active faults and are equal to 1.5 times the median ground motions for the maximum magnitude earthquake. Also, special consideration is given so that the estimated ground motion accelerations are not less than 1.5g for the short period spectral acceleration plateau and 0.6g for the 1.0 second spectral acceleration. **Figure 4.1** conceptually describes the procedure of incorporating deterministic bounds on MCE maps.

South Carolina Department Of Transportation (SCDOT, 2002).- The particular provisions apply to "*bridges of conventional slab, beam, girder and box girder superstructure construction with spans not exceeding 150m (500ft)"*. The two levels of design ground motions are specified as follows:

The *Functional Evaluation Earthquake* (FEE) is defined as the ground shaking having a 10% probability of exceedance in 50 years or a return period of 474 years.

The *Safety Evaluation Earthquake* (SEE) is a low probability seismic event with 2% probability of exceedance in 50 years, i.e. return period equal to 2.500 years. Such a design motion corresponds to a rare but possible and strong earthquake.

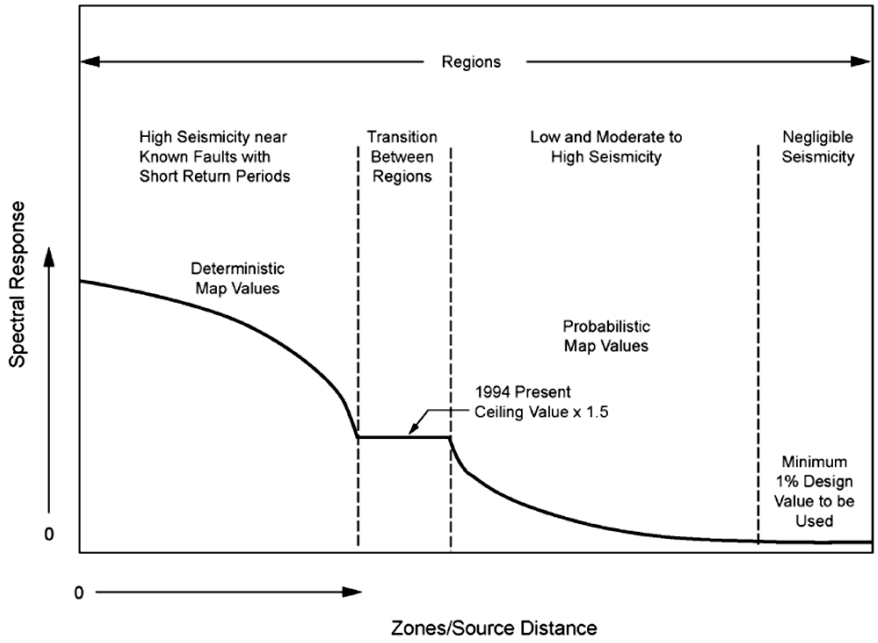

Figure 4.1: Incorporation of deterministic bounds in the Maximum Considered Earthquake (MCE) ground motion map of the 1997 NEHRP Provisions (BSSC, 1998).

Seismic Retrofitting Manual for Highway Structures: Part I: Bridges (MCEER, 2005).- The specific manual contains methods for evaluating and upgrading the seismic resistance of existing "*conventional steel and concrete highway bridges, with spans not exceeding 150m (500ft). Suspension bridges, cable-stayed bridges, arches, long-span trusses and movable bridges are not covered"*. The retrofitting approach is based on principles such as Anticipated Service Life (ASL), Importance and expected Performance Level under a Lower and Upper Level of Ground Motion.

The *Lower Level* ground motion includes frequent ground motions and is assigned a 50% probability of exceedance in 75 years (i.e. return period of approximately 100years).

The *Upper Level* ground motion concerns more rare seismic events and has a probability of exceedance of 7% in 75 years, rendering a return period of approximately 1000 years.

Caltrans Seismic Hazard Practice (1999, 2001).- Seismic Design Criteria issued by Caltrans are intended to aid in the design of new reinforced and pre-stressed concrete bridges constructed with typical superstructure and substructure components traditionally used in California, while steel bridges are not covered. Evaluation Levels in the Caltrans Specifications are defined as follows:

Functional Evaluation Motion: This probabilistically specified ground motion is proposed in the Task 6 Report of NCHRP 20-7(193) Project, conducted by Imbsen & Associates Inc., to have a 60% probability of not being exceeded during the useful life of the bridge. In the latest *Memo to Designers 20-1,* issued by Caltrans in June 2010, the specific hazard level is proposed to be developed in consultation with the Seismic Safety Peer Review Panel. It is also reported that Ordinary Bridges, as will be defined in later sections, are not designed for the Functional Evaluation Seismic Hazard Level.

Safety - Evaluation Ground Motion: The particular ground motion may be specified either deterministically or probabilistically. The probabilistically assessed ground motion is assigned a long return period, of 1.000 to 2.000 years and applies to Important Bridges. For Ordinary bridges, this is the "Design Earthquake" which is defined as follows:

"In general, the Design Earthquake (DE) is defined as the greater of:

(a) A probabilistic spectrum based on a 5% in 50 years probability of exceedance (or a 975yr return period)

(b) A deterministic spectrum based on the largest median response resulting from the maximum rupture (corresponding to $M_{max.}$) of any fault in the vicinity of the bridge site

(c) A statewide minimum spectrum defined as the median spectrum generated by a magnitude 6.5 earthquake on a strike-slip fault located 12 kilometers from the bridge site."

Seismic Design Specifications for Highway Bridges (Japan Road Association 1996, 2002).- The revised seismic design specifications issued by the Japanese Road Association in 2002, incorporate performance-based design concepts by considering two levels of ground motion, without however, providing probabilistic estimations as to the recurrence period of each one of the seismic events. Thus:

Level 1 Earthquake includes moderate ground motions, with the acceleration spectra of **Figure 4.2a**, induced by frequent earthquakes, which essentially corresponds to the most severe ground motion that can be resisted by the bridge with elastic response.

Level 2 Earthquake includes two different types of ground motions: Type-I refers to strong interplate earthquakes, reaching a magnitude of around 8 (like the Tokyo recording during the 1923 Kanto Earthquake) and Type-II motion refers to inland earthquakes with magnitude of around 7, occurring at very short distance, such as the ground motion at Kobe during the

Hyogo-ken-Nanbu earthquake. The proposed acceleration spectra for the particular Types of motion and different soil classifications are shown in **Figure 4.2a, b** and **c**.

4.2.2 Design seismic motions for buildings

Eurocode 8 (2003).- Design seismic actions are defined on the same basis as described for bridges, also applying *Equation 4.3*. Importance factors γ_I take into consideration the type and function of the building and are summarized in **Table 4.2**.

However, for each importance factor, two levels of earthquake motions are defined as follows: the lower level earthquake motion with 10% probability of exceedance in 10yrs, or a return period equal to 95yrs, and the upper level seismic motion with 10% probability of exceedance in 50yrs, thus a return period of 475yrs. Both levels of seismic motions are later associated to specific Performance Levels, mentioned in subsequent sections.

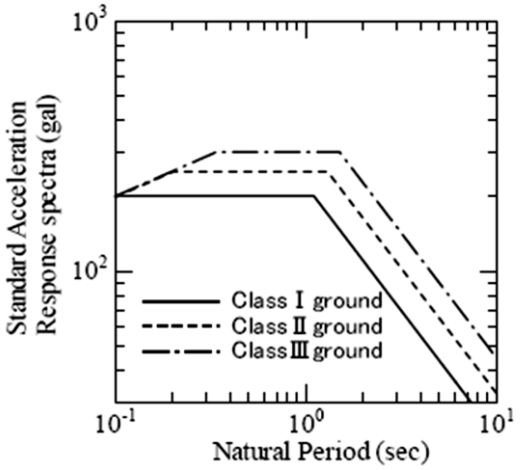

(a) Level 1 earthquake

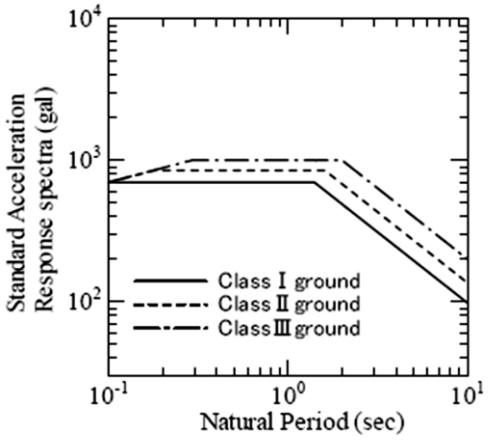

(b) Level 2 earthquake (Type I)

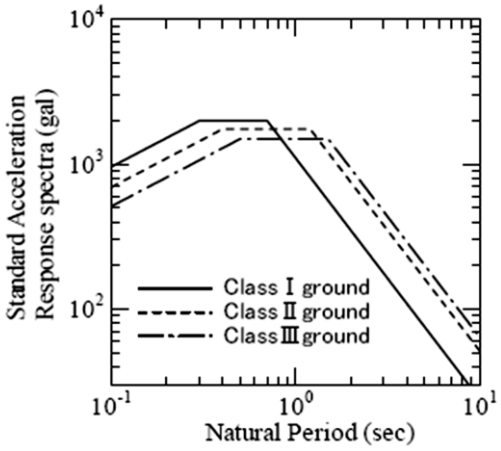

(c) Level 2 earthquake (Type II)

Figure 4.2: Acceleration spectra for corresponding Levels of ground motion, proposed by the Japan Road Association (2002).

Table 4.2: Importance Classes for buildings according to EC-8.

Importance Class	Description	Importance Factor
I	Buildings whose integrity during earthquakes is of vital importance for civil protaction, e.g. hospitals, fire stations, power plants, etc.	1.4
II	Buildings whose seismic resistance is of importance in view of the consequences associated with a collapse, e.g. schools, assembly halls, cultural institutions etc.	1.2
III	Ordinary buildings, not belonging to the other categories	1.0
IV	Buildings of minor importance for public safety, e.g. agricultural buildings, etc.	0.8
For buildings housing dangerous installations or materials, the importance factor should be established in accordance with the criteria set in EN 1998-4		

Structural Engineers' Association of California (SEAOC, 1999).- The SEAOC Blue Book provides a quite extensive analysis of performance criteria, relating seismic hazard levels to corresponding performance levels. A complete, although conceptual, framework is proposed, which can be incorporated into future guidelines and provisions.

In this context, seismic hazard is represented by four levels of probabilistic events, as presented in **Table 4.3**. Note that the Recurrence Interval corresponds to the return period.

Table 4.3: Seismic Hazard Levels according to SEAOC (1999).

Event	Recurrence Interval	Probability of Exceedance
Frequent	43 years	50% in 30 years
Occasional	72 years	50% in 50 years
Rare	475 years	10% in 50 years
Very Rare	970 years	10% in 100 years

Uniform Building Code (1997).- In the Uniform Building Code (1997) design seismic motions are not defined probabilistically, but each area in the United States is classified in seismic zones and assigned a seismic zone factor Z, which is next used in the calculation of earthquake loads. Indicatively, the seismic zone factors specified in the U.B.C. are presented in **Table 4.4.**

Table 4.4: Seismic zone factors Z, according to U.B.C. (1997).

Zone	1	2A	2B	3	4
Z	0.075	0.15	0.20	0.30	0.40

Nevertheless, the performance based design concept is evident in subsequent steps of the seismic design process, where buildings are classified in occupancy categories depending on their function, occupant load of people, materials stored in the building etc. A more analytical presentation is provided in a later section.

4.3 Performance levels and objectives

The second step in Performance based design, concerns the selection of performance objectives, between the client/owner of the facility and the engineer, given the client's expectations and the seismic hazard analysis. Performance objectives result from the combination of an expected performance level given the expected level of ground motion, as defined in the previous section. Performance Levels are typically defined taking into consideration the post-earthquake *service level* of the structure, as well as the *extent of damage* in its structural and non-structural components. In the following paragraphs service and damage levels are defined separately for bridges and buildings.

4.3.1 Performance levels & objectives for bridges.

In most Guidelines, there is a common code as to the definition of Service and Damage Levels, thus the core concepts and definitions will be presented herein and additional observations will be made where necessary.

Service Levels refer to the functionality of the bridge in terms of its use by normal or emergency traffic. Hence, in the ***Immediate* Service Level** access to the bridge by normal traffic is possible after inspection of the bridge, while under the ***Significant Disruption/Impaired*** Level, only limited access (reduced lanes, light emergency traffic) is possible after shoring, while the bridge may have to be replaced.

Damage Level (Extent) is described in terms of structural damage to the components of the bridge and the required effort for repair and is typically separated into a Minimal and a Significant Level as follows:

- ***Minimal Damage:*** There are some visible signs of damage. Minor inelastic response may occur, but post-earthquake damage is limited to narrow flexural cracking to concrete and the onset of yielding in steel. Permanent deformations are not apparent, and any repairs could be made under non-emergency conditions with the exception of superstructure joints which may need removal and temporary replacement.

- ***Significant Damage:*** Although collapse is avoided, the particular damage level includes permanent offsets and damage consisting of cracking, yield reinforcement and major spalling of concrete, extensive yielding and local buckling of steel columns, global and local buckling of steel braces and cracking in the bridge deck slab at shear studs along the seismic load path. The above conditions usually require closure to repair the damage. Beams may be unseated from bearings but no span should collapse. No damage is anticipated in foundations, with the exception of large lateral flows due to liquefaction, in which case inelastic deformation in piles may be evident, and partial or complete replacement of the columns and piles may be necessary. To avoid this scenario, design approaches producing minimal or moderate damage such as seismic isolation should be assessed.

Given the above definitions, the two ***Performance Levels*** usually identified in most Seismic Design Guidelines are described as follows:

- ***Operational Level (Minimization of Damage):*** The sustained damage is minimal and service for emergency vehicles should be immediate after inspection of the bridge. Damage is expected to be repairable without interruption of traffic flow.
- ***Life Safety (No Collapse):*** The sustained damage is significant to such a point that replacement of the bridge may be necessary and service is disrupted, however, life safety is preserved.

The selection of the appropriate Performance Level for the occurrence of each design ground motion largely depends on the importance of the bridge, which is mentioned in all Codes and Specifications with slight variations. In ***EC-8*** for instance, bridge importance is incorporated in the Reference Seismic Action through the Importance Factor γ_I as analyzed earlier. In all other Code Provisions presented below, bridges are classified as either *Important* or *Ordinary*/*Standard* based on the following criteria:

- A bridge is characterized ***Important/Essential*** when: (i) it is expected to provide secondary life safety; for example it provides access to local emergency services such as hospitals, or carries lifelines such as electric power and water supply pipelines, (ii) the time required for restoration of functionality after closure would create a major economic impact (iii) it is formally appointed by a local emergency response plan as critical, because it will potentially enable the immediate response of fire/civil defense departments, or public health agencies to disaster situations.

- All bridges not satisfying one or more of the above criteria are characterized as ***Ordinary*** or ***Standard***.

In the following paragraphs, an overview of the Seismic Performance Criteria is presented from Design Specifications in power in Europe, the U.S.A. and Japan.

Eurocode 8 (2003).- The basic requirements which have to be satisfied in design are outlined below:

No collapse (Ultimate Limit State).- The bridge is generally anticipated to preserve its structural integrity, hold adequate residual resistance in order to avoid total collapse. Considerable damage is expected to occur, mainly in the form of flexural yielding of specific sections (i.e. the formation of plastic hinges) in the piers, which in the absence of seismic isolation is a desirable situation. The bridge deck should in general be designed to avoid damage, except for breakage of secondary components, such as expansion joints and continuity slabs. Also, the bridge deck must be able to accommodate loads from piers experiencing plastic hinging and must not become unseated under extreme seismic displacement. In the case of a design seismic action with high probability of exceedance within the design life of the bridge, the parts of the bridge contributing to energy dissipation are designed to enable emergency traffic and inspections in the post-earthquake period and to be easily repairable.

Minimization of damage (Serviceability Limit State).- A high probability of occurrence seismic scenario may cause only minor damage to secondary components and parts of the bridge contributing to energy dissipation. All other components of the bridge are expected to remain untouched; traffic should not be disturbed and repairs should not be urgent.

The design seismic criteria proposed in EC-8, aim explicitly at satisfying the no-collapse requirement. However, they implicitly cover the damage minimization requirement as well.

Recommended LRFD Guidelines for the Seismic Design of Highway Bridges, Part I: Specifications (ATC – MCEER 2001).- The particular Guidelines initially considered two Performance Objectives i.e. the Operational and the Life Safety objective. However, they were re-examined in 2002, after concerns of undue liability on behalf of stakeholders, to finally consider only the Life Safety Performance Objective. **Table 4.5**, presents the performance matrix currently proposed by the ATC-MCEER specifications.

Table 4.5: Design Earthquakes and Seismic Performance Objectives according to ATC-MCEER (2001,2002).

Earthquake Ground Motion	Performance Level	Performance Objective
		Life Safety
Maximum Considered Earthquake (MCE) 3% PE in 75 yrs (return period 2463yrs) or 1.5 Median Deterministic	Service	Significant Disruption
	Damage	Significant
Expected Earthquake (EE) 50% PE in 75 yrs (return period 109yrs)	Service	Immediate
	Damage	Minimal

South Carolina Department Of Transportation (SCDOT, 2002).- In the present Specifications, Service and Damage Levels are slightly altered, in order to become more thorough. Bridges are classified into three instead of two Importance Categories – namely, Critical, Essential and Normal bridges - described as follows:

Critical Bridges **(I.C. I)** are those expected to remain open to all traffic following inspection after the occurrence of the Functional Evaluation Earthquake (FEE) and be usable by emergency vehicles and for security/defense purposes immediately after the Safety Evaluation design Earthquake (SEE).

Essential bridges **(I.C. II)** should at a minimum remain open to emergency vehicles and for security/defense purposes after the SEE event and open to all traffic within days after the SEE event.

Normal bridges **(I.C. III)** are those that are not classified as either critical or essential.

The *Dual-Level Design* method (i.e consideration of two levels of design ground motion as explained earlier) is applied only in the case of critical bridges. Also, two extra Service Levels and one additional Damage Level are specified, as indicated in **Table 4.6**. Namely, the ***Maintained Service Level*** dictates a necessary short period of closure to public, while the bridge is expected to remain open to emergency vehicles. In the ***Recoverable Service Level*** the short period of closure is dictated only to public traffic, while in the ***Repairable Damage Level*** no collapse occurs and damage consists of concrete cracking, spalling of concrete cover and minor yielding of structural steel. Damage extent is limited and the structure can be restored to its pre-earthquake condition with a minimum risk of losing functionality and without replacement of reinforcement or structural members.

Table 4.6: Seismic Performance Criteria in the SCDOT (2002) Specifications.

Earthquake Ground Motion	Performance Level	Normal Bridges	Essential Bridges	Critical Bridges
Functional Evaluation Earthquake (*FEE*) 10% PE in 50 yrs (return period 474yrs)	Service	Not Required	Not Required	Immediate
	Damage	Not Required	Not Required	Minimal
Safety Evaluation Earthquake (*SEE*) 2% PE in 50yrs (return period 2500yrs)	Service	Impaired	Recoverable	Maintained
	Damage	Significant	Repairable	Repairable

Seismic Retrofitting Manual for Highway Structures: Part I: Bridges (MCEER, 2005).- The following **Table 4.7** summarizes the process of selection of the appropriate Performance Level, considering the seismic hazard analysis, bridge importance and its anticipated life service as specified by the MCEER Manual (2005).

Table 4.7: Performance Levels for retrofitted bridges. (MCEER, FHWA, 2005).

Earthquake Ground Motion	Bridge Importance and Service Life Category					
	Standard			Essential		
	ASL 1	ASL 2	ASL 3	ASL 1	ASL 2	ASL 3
Lower Level Ground Motion 50% PE in 75 years (return period 100yrs)	PL 0	PL 3	PL 3	PL 0	PL 3	PL 3
Upper Level Ground Motion 7% PE in 75 years (return period 1000yrs)	PL 0	PL 1	PL 1	PL 0	PL 1	PL 2

Anticipated Service Life (ASL) refers to the remaining design life of the bridge and is divided into three categories:

- ASL 1: 0 – 15 years
- ASL 2: 16 – 50 years
- ASL 3: >50 years

Also, the required Performance Levels (PL) are defined below:

PL 0: No minimum level of performance is recommended.

PL 1: Life Safety. Significant damage is sustained and service is significantly disrupted, but life safety is preserved. The bridge may need to be replaced after a large earthquake.

PL 2: Operational. The sustained damage is minimal and service for emergency vehicles should be available after inspection and clearance of debris. Bridge should be reparable with or without restrictions on traffic flow.

PL 3: Fully Operational. No damage is sustained and full service is available for all vehicles immediately after the earthquake. No repairs are required.

Caltrans Seismic Hazard Practice (1999, 2001).- The set of seismic performance criteria developed by Caltrans for new bridges, is presented in **Table 4.8**. Definitions of Service and Damage levels are not different from what has been presented in the previous paragraphs.

Table 4.8: Performance matrix specified by Caltrans (1999,2001).

Earthquake Ground Motion	Ordinary Bridges	Important Bridges
Functional-Evaluation Motion 40% PE in the useful life of the bridge	Immediate Service Level Repairable Damage	Immediate Service Level Minimal Damage
Safety-Evaluation Motion 5% PE in 50yrs (return period 975yrs)	Limited Service Level Significant Damage	Immediate Service-Level Repairable Damage

Seismic Design Specifications for Highway Bridges (Japan Road Association 1996, 2002).- Table 4.9 presents the performance matrix proposed in the JRA specifications. In *Seismic Performance Level 1* and for the *Level 1* design ground motion, all bridges (Type-A and Type-B) are expected to behave elastically, without essential structural damage. In the occurrence of extreme ground motions (*Level 2*), critical failure is prevented for Type-A bridges, whereas for Type-B bridges limited damage is anticipated.

Table 4.9: Performance criteria according to the JRA Specifications (1996, 2002).

<table>
<tr><th colspan="2">Earthquake Ground Motion</th><th>Standard Bridges (Type A)</th><th>Important Birdges (Type B)</th></tr>
<tr><td colspan="2">Level 1 Earthquake: Ground motions with high probability to occur</td><td colspan="2">SPL 1: Prevent Damage</td></tr>
<tr><td rowspan="2">Level 2 Earthquake: Ground Motions with Low Probability to Occur</td><td>Interplate Earthquake (Type I)</td><td rowspan="2">SPL 3: Prevent Critical Damage</td><td rowspan="2">SPL 2: Limited Damage for Function recovery</td></tr>
<tr><td>Inland Earthquakes (Type II)</td></tr>
</table>

4.3.2 Performance levels & objectives for buildings.

Eurocode 8 (2003).- As it is shown in **Table 4.10**, two performance levels are specified in the context of Eurocode 8; namely, the Damage Limitation Requirement, which is associated to a 95year event and the No-Collapse Requirement, which is assigned a 475 year event. Definitions and analytical description of the two performance levels is provided below:

- **Damage Limitation Requirement.-** The structure "*is designed and constructed to resist a seismic action with a larger probability of occurrence than the design seismic action, without the occurrence of damage and the associated limitations of use, the costs of which would be disproportionally high in comparison to the costs of the structure itself*". According to EC-8 the design seismic motion for the Damage Limitation Requirement is characterized by a return period of 95yrs.
- **No Collapse Requirement.-** The structure is "*designed and constructed to withstand the design seismic action without local or global collapse, thus retaining its structural integrity as well as a residual load bearing capacity after the occurrence of the seismic events"*. According to EC-8 the design seismic motion for the No Collapse Limit State is characterized by a return period of 475yrs.

Table 4.10: Design Seismic Actions and Performance Requirements (EC-8)

Earthquake Ground Motion	Requirement
Lower Level 10% PE in 10yrs (return period 95yrs)	Damage Limitation
Upper Level 10% PE in 50yrs (return period 475yrs)	No - collapse

Structural Engineer's Association of California (SEAOC, 1999).- Performance Levels reflect both the damage and service level of the building in the post-earthquake period and are described as follows:

- *Fully Operational:* Facility continues to operate with negligible damage.
- *Operational:* Facility continues to operate with minor damage and minor disruption in nonessential services.
- *Life safe:* Life safety is substantially protected and damage is moderate to extensive.
- *Near Collapse:* Life safety is at risk and damage is severe, however structural collapse is prevented.

Figure 4.3, provides a complete description of the above performance levels, in terms of damage extent, while **Table 4.11** through **Table 4.13** provide detailed damage description by Performance Levels and Permissible Structural Damage in structural and non-structural components of a building. Corresponding tables with permissible damage for Architectural elements, Mechanical/Electrical/Plumbing systems and contents (e.g. furniture, book shelves, office equipment and computer systems) are also provided in the Specifications but were here omitted due to their excessive size.

In this context, a set of Minimum and Enhanced Performance Objectives is defined in order to facilitate both the engineer and the owner of the facility in choosing performance criteria in design. The minimum performance objectives are illustrated in **Figure 4.4** and take into consideration the building's importance. The basic objective usually refers to typical new buildings, while the Essential/ Hazardous and Safety Critical Objectives may be applicable to facilities such as hospitals and nuclear facilities respectively. Moreover, Enhanced Objectives may be agreed between the engineer and the client/user of the facility, upon request of the latter, however no further description is provided.

Uniform Building Code (U.B.C., 1997).- In U.B.C. (1997), earthquake resistant design is performed considering, among other parameters (e.g. seismic zoning, site characteristics, building configuration and structural system) the occupancy of each building or structure.

Structures are classified in occupancy categories; each one assigned an importance factor, as provided in **Table 4.15**. Design base shear (the minimum design lateral force) is calculated using Importance Factor I, whereas, the total design seismic forces are calculated using Importance Factor I_P. A short description on the various Groups and associated occupancy description is provided in **Table 4.15**. It should be noted that the particular Code does not provide any information regarding the permissible damage that buildings may sustain during an earthquake. The above importance factors and occupancy categories are used in the estimation of earthquake loads.

Table 4.11: General Damage description by Performance Level and various components of the building (SEAOC, 1999).

	Performance Level				
System Description	**10 Fully 9 Operational**	**8 7 Operational**	**6 5 Life Safety**	**4 3 Near Collapse**	**2 1 Collapse**
Overall Building Damage	Negligible	Light	Moderate	Severe	Complete
Permissible Transient Drift	< 0.2% ±	< 0.5% ±	< 1.5% ±	< 2.5% ±	> 2.5% ±
Permissible Permanent Drift	Negligible	Negligible	< 0.5% ±	< 2.5% ±	> 2.5% ±
Vertical Load-Carrying Element Damage	Negligible	Negligible	Light to moderate, but substantial capacity remains to carry gravity loads	Moderate to heavy, but elements continue to support gravity loads	Partial to total loss of gravity load support
Lateral Load-Carrying Element Damage	Negligible. Generally elastic response; no significant loss of strength or stiffness	Light. Nearly elastic response; original strength and stiffness substantially retained; minor cracking/yielding of structural elements; repair implemented at convenience	Moderate. Reduced residual strength and stiffness, but lateral system remains functional	Negligible residual strength and stiffness; no story collapse mechanisms, but large permanent drifts; secondary structural elements may completely fail	Partial or total collapse; primary elements may require demolition
Damage to Architectural Systems	Negligible damage to cladding, glazing, partitions, ceilings, finishes, etc.; isolated elements may require repair at users convenience	Light to moderate damage to architectural systems; essential and select protected items undamaged; hazardous materials contained	Moderate to severe damage to architectural systems, but large falling hazards not created; major spills of hazardous materials contained	Severe damage to architectural systems; some elements may dislodge and fall	Highly dangerous falling hazards; destruction of components
Egress Systems	Not impaired	No major obstructions in exit corridors; elevators can be restarted perhaps following minor servicing	No major obstructions in exit corridors; elevators may be out of service for extended period	Egress may be obstructed	Egress may be highly or completely obstructed
Mechanical/Electrical/ Plumbing/Utility Services	Functional	Equipment essential to function and fire/ life safety systems operate; other systems may require repair; temporary utility service provided as required	Some equipment dislodged or overturned; many systems not functional; piping conduit ruptured	Severe damage and permanent disruption of systems	Partial or total destruction of systems; permanent disruption of systems
Damage to Contents	Some light damage to contents may occur; hazardous materials secured and undamaged	Light to moderate damage; critical contents and hazardous materials secured	Moderate to severe damage to contents; major spills of hazardous materials contained	Severe damage to contents; hazardous materials may not be contained	Partial or total loss of contents
Repair	Not required	At owner/tenants convenience	Possible; building may be closed	Probably not practical	Not possible
Effect on Occupancy	No effect	Continuous occupancy possible	Short term to indefinite loss of use	Potential permanent loss of use	Permanent loss of use

Table 4.12: Performance Levels and permissible structural damage to Vertical Elements of the building (SEAOC, 1999).

	Performance Level				
Elements	**Type**	**10 Fully 9 Operational**	**8 Operational 7**	**6 Life Safety 5**	**4 Near Collapse 3**
Concrete Frames	Primary	Negligible	Minor hairline cracking (0.02"); limited yielding possible at a few locations; no crushing (strains below 0.003)	Extensive damage to beams; spalling of cover and shear cracking (< 1/8") for ductile columns; minor spalling in nonductile columns; joints cracked < 1/8" width	Extensive cracking and hinge formation in ductile elements; limited cracking and/or splice failure in some nonductile columns; severe damage in short columns
	Secondary	Negligible	Same as primary	Extensive cracking and hinge formation in ductile elements; limited cracking and/or splice failure in some nonductile columns; severe damage in short columns	Extensive spalling in columns (possible shortening) and beams; severe joint damage; some reinforcing buckled
Steel Moment Frames	Primary	Negligible	Minor local yielding at a few places; no observable fractures; minor buckling or observable permanent distortion of members	Hinges form; local buckling of some beam elements; severe joint distortion; isolated connection failures; a few elements may experience fracture	Extensive distortion of beams and column panels; many fractures at connections
	Secondary	Negligible	Minor local yielding at a few places; no fractures; minor buckling or observable permanent distortion of members	Extensive distortion of beams and column panels; many fractures at connections	Extensive distortion of beams and column panels; many fractures at connections
Braced Steel Frames	Primary	Negligible	Minor yielding or buckling of braces; no out-of-plane distortions	Many braces yield or buckle but do not totally fail; many connections may fail	Extensive yielding and buckling of braces; many braces and their connections may fail
	Secondary	Negligible	Same as primary	Same as primary	Same as primary
Concrete Shear Walls	Primary	Negligible	Minor hairline cracking (0.02") of walls; coupling beams experience cracking < 1/8" width	Some boundary elements distress including limited bar buckling; some sliding at joints; damage around openings; some crushing and flexural cracking; coupling beams—extensive shear and flexural cracks; some crushing, but concrete generally remains in place	Major flexural and shear cracks and voids; sliding at joints; extensive crushing and buckling of rebar; failure around openings; severe boundary element damage; coupling beams shattered, virtually disintegrated
	Secondary	Negligible	Minor hairline cracking of walls, some evidence of sliding at construction joints; coupling beam experience cracks < 1/8" width, minor spalling	Major flexural and shear cracks; sliding at joints; extensive crushing; failure around openings; severe boundary element damage; coupling beams shattered, virtually disintegrated	Panels shattered, virtually disintegrated

Table 4.13: Performance Levels and permissible structural damage to walls and foundations of the buildings SEAOC, 1999).

		Performance Level			
Elements	**Type**	**10 Fully Operational 9**	**8 Operational 7**	**6 Life Safety 5**	**4 Near Collapse 3**
Unreinforced Masonry Infill Walls	Primary	Negligible	Minor cracking (<1/8") of masonry infills and veneers; Minor spalling in veneers at a few corner openings	Extensive cracking and some crushing, but wall remains in place; no falling units; extensive crushing and spalling of veneers at corners of openings	Extensive cracking and crushing; portions of face course shed
	Secondary	Negligible	Same as primary	Same as primary	Extensive cracking and crushing; portions of face course shed
URM Bearing Walls	Primary	Negligible	Minor cracking (< 1/8") of masonry infills and veneers; minor spalling in veneers at a few corner openings; no observable out-of-plane offsets	Extensive cracking; noticeable in-plane offsets of masonry and minor out-of-plane offsets	Extensive cracking; face course and veneer may peel off; noticeable in-plane and out-of-plane offsets
	Secondary	Negligible	Same as primary	Same as primary	Same as primary
Reinforced Masonry Walls	Primary	Negligible	Minor cracking (< 1/8"); no out-of-plane offsets	Extensive cracking (< 1/4") distributed throughout wall; some isolated crushing	Crushing; extensive cracking; damage around openings and at corners; some fallen units
	Secondary	Negligible	Same as primary	Crushing; extensive cracking; damage around openings and at corners; some fallen units	Panels shattered, virtually disintegrated
Wood Stud Walls	Primary	Negligible	Distributed minor hairline cracking of gypsum and plaster veneers	Moderate loosening of connections and minor splitting of members	Connections loose, nails partially withdrawn; some splitting of members and panel; veneers shear off
	Secondary	Negligible	Same as primary	Connections loose, nails partially withdrawn; some splitting of members and panel	Sheathing shears off; let-in braces fracture and buckle; framing split and fractured
Foundations	General	Negligible	Minor settlement and negligible tilting	Total settlements <6" and differential settlements <1/2" in 30 feet	Major settlements and tilting

Table 4.14: Performance Levels and permissible structural damage to Horizontal Elements of the building (SEAOC, 1999).

	Performance Level			
Element	**10 Fully Functional 9**	**8 Operational 7**	**6 Life Safety 5**	**4 Near Collapse 3**
Metal Deck Diaphragms	Negligible	Connections between deck units and from deck to framing intact; minor distortions	Some localized failure of welded connections of deck to framing and between panels; minor local buckling of deck	Large distortion with buckling of some units and tearing of many welds and seam attachments
Wood Diaphragms	Negligible	No observable loosening, withdrawal of fasteners, or splitting of sheathing or framing	Some splitting at connections, loosening of sheathing; observable withdrawal of fasteners; splitting of framing and sheathing	Large permanent distortion with partial withdrawal of nails and splitting of elements
Concrete Diaphragms	Negligible	Distributed hairline cracking and a few minor cracks (< 1/8") or larger size	Extensive cracking (<1/4") and local crushing and spalling	Extensive crushing and observable offset across many cracks

Table 4.15: Occupancy Categories and associated Importance factors, U.B.C. (1997).

Occupancy Category	Occupancy or functions of structure	Seismic Importance factor, I	Seismic Importance Factor, I_p
1. Essential Facilities	Group I, Division 1 Occupancies having surgery and emergency treatment areas Fire and police stations Garages and shelters for emergency vehicles and emergency aircraft Structures and shelters in emergency preparedness centers Aviation and control towers Structures and equipment in government communication centers and other facilities required for emergency response Standby power-generating equipment for Category 1 facilities Tanks or other structures containing housing or supporting water or other fire-suppression material or equipment required for the protection of Category 1,2 or 3 structures	1.25	1.50
2. Hazardous structures	Group H, Divisions 1,2,6 and 7 Occupancies and structures therein housing of supporting toxic or explosive chemicals or substances Non-building structures housing, supporting or containing quantities of toxic or explosives substances, that if contained within a building, would cause that building to be classified as a Group H, Division 1,2 or 7 Occupancy	1.25	1.50
3. Special Occupancy structures	Group A, Divisions 1,2 and 2.1 Occupancies Buildings housing Group E, Divisions 1 and 3 Occupancies with a capacity greater than 300 students Buildings housing Group B Occupancies used for college or adult education with a capacity greater than 500 students Group I, Divisions 1 and 2 Occupancies with 50 or more resident incapacitated patients, but not included in Category 1 Group I, Division 3 Occupancies All structures with an occupancy greater than 5.000 persons Structures and equipment in power-generating stations, and other public utility facilities not included in Category 1 or Category 2 above, and required for continued operation	1.0	1.0
4. Standard Occupancy structures	All structures housing occupancies or having functions not listed in Category 1, 2 or 3 and Group U Occupancy towers	1.0	1.0
5. Miscellaneous structures	Group U, Occupancies except for towers	1.0	1.0

Table 4.16: Description of Occupancy according to Groups, U.B.C. (1997).

Group	Description of Occupancy
A	Buildings or portions of buildings having assembly rooms with occupant load from 300 up to 1,000 or more with or without a legitimate stage, including buildings used for educational purposes, stadiums, amusement parks, and reviewing stands.
B	A building or structure, or a portion thereof, for office, professional or service type transactions, including storage of records and accounts; eating and drinking establishments with an occupant load less than 50.
E	Buildings used for educational purposes through the 12^{th} grade of for day-care purposes
F	Low-hazard factory and industrial occupancies including facilities producing non-combustible or non-explosive materials that during finishing, packing or processing do not involve significant fire hazard, or other moderate- hazard factory and industrial occupancies .
H	Occupancies with materials preenting high/moderate/high fire or physical hazard, repair garages, aircraft habgars.
I	Nurseries, health-care centers, nursing homes, mental hospitals, mental sanitariums, prisons and other reformatory institutions.
M	Buildings or structures for the display and sale of merchandise and involving stocks of goods, wares or merchandise, incidental to such purposes.
R	Hotels, apartment houses, congregate residences, lodging houses.
S	Moderate hazard storage occupancies of combustible materials, low-hazard storage occupancies used for storage of non-combustible materials, repair garages where work is limited to exchange of parts and maintenance does not require open flame or welding, open parking garages, aircraft hangars, and helistops.
U	Private garages, carports, sheds, agricultural buildings, fences (over 6ft), tanks and towers.

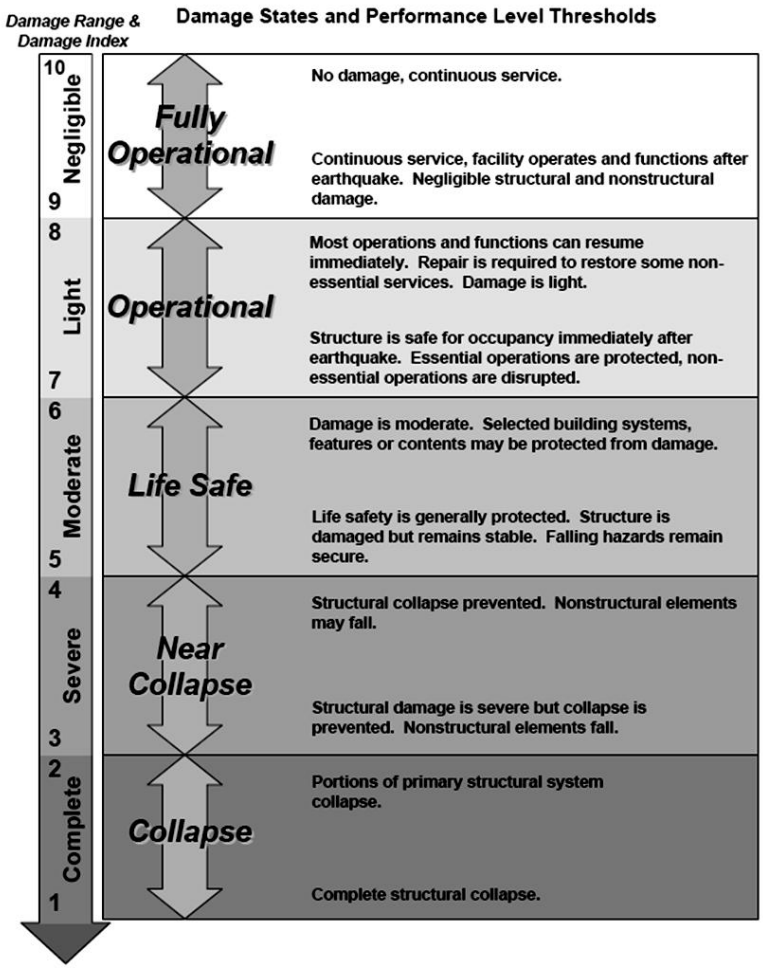

Figure 4.3: Scale of earthquake-induced Damage States and associated Performance Levels.

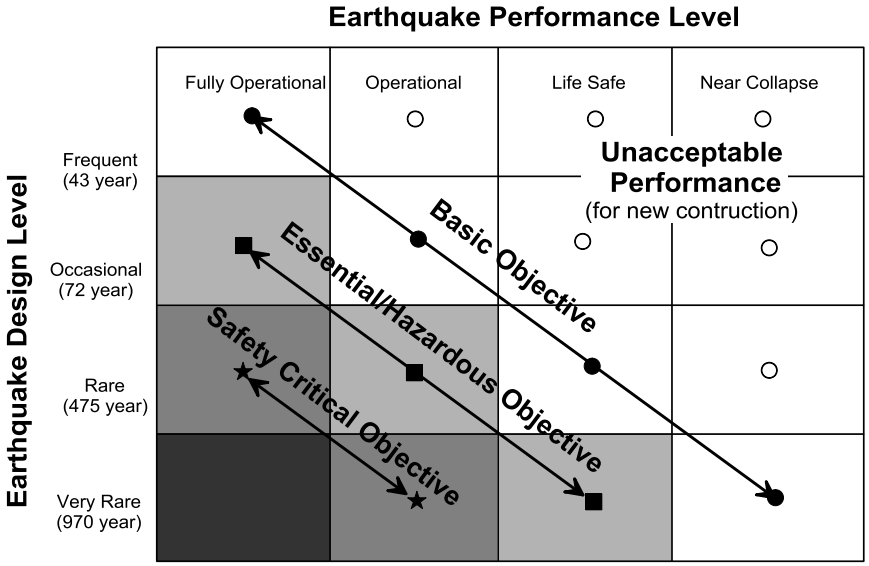

Figure 4.4: Matrix of recommended performance objectives for buildings, (SEAOC,1999).

4.4 Deformation limits

The last phase in the performance-based design approach concerns the association of the previous performance objectives to limiting values of measurable deformations either of the structure or the foundation. Note that the Guidelines and Provisions presented earlier do not correlate Performance Objectives to specific limiting values of deformations, but rather associate different analysis procedures (from elastic to non-linear dynamic analysis) to a certain Seismic Performance Category/Level. Due to the geographically local character of the previously presented Codes, further description of specific analysis methods falls outside the scope of the present chapter and thus will be omitted.

In the absence of limiting values of earthquake-induced deformations to be linked to specific Performance Levels, an overview of the existing allowable values of deformation under static loading is attempted in the following paragraphs. This outline provides useful insight as to the order of magnitude and the type of such deformations as well as, to their effect on the structural integrity of bridges and buildings. In addition it may become a guide for the development of more specific earthquake performance criteria, in the future.

4.4.1 Deformation limits for bridges

Definitions.- Barker et al. (1991) provide the definitions illustrated in **Figure 4.5** concerning possible types of deformations that may occur in bridges. According to their investigation, bridge deformations may appear in the form of *uniform settlement (ρ), uniform tilt (ω)* or *rotation (ϑ)* and *differential settlement (δ)*.

- *Uniform settlement* (ρ) is described as the rather theoretical situation in which each of the bridge foundations settles by the same amount. Even though no distortion of the superstructure occurs, excessive uniform settlement can lead to issues such as insufficient clearance at underpasses, as well as discontinuities at the juncture between approach slabs and the bridge deck, [also referred to as “the bump at the end of the bridge” (Wahls, 1990)] and inadequate drainage at the end of the bridge.
- *Uniform tilt (ω) or rotation (ϑ)* relates to settlements that vary linearly along the length of the bridge. Such type of deformation is most likely to occur in very stiff superstructures and single-span bridges. Usually, no distortion occurs in the superstructure, except in the case of non-monolithic connection between bridge components. In terms of traffic disturbance the same problems (bumps, drainage and clearance height) as mentioned above may occur.

- *Non-uniform settlements* lead to deformation when the superstructure is continuous over three or more foundations, which causes distortion in the superstructure especially in continuous span bridges. It may be either regular or irregular as noted in **Figure 4.5c & d**. A regular pattern in deformation is characterized by a symmetrical distribution of settlement, from both ends of the bridge towards the centre. In the irregular pattern, deformation is randomly distributed along the length of the bridge. Opperational problems caused by non-uniform settlements include bumps at junctures with approach slabs, or between subsequent spans, inadequate drainage and insufficient clearance height at underpasses.
- The non-uniform settlement of bridge foundations is also responsible for the onset of *angular distortion* (β), which affects the structural integrity of the superstructure. It is schematically described in **Figure 4.5d**, and defined as:

$$\beta = \frac{\delta}{S} \qquad 4.4$$

Where β = angular distortion (dimensionless)

δ = differential settlement between two consecutive foundations; in units of length

S = span length expressed in the same length units as the differential settlement.

Movement Criteria.- Limiting values of deformations, as defined above, were assembled from numerous researchers, and are summarized in **Table 4.17** and **Table 4.18** classified by type (vertical settlement, horizontal displacement etc) and in increasing order of magnitude. The damage caused to the superstructure is also cited in the above tables. The limit between tolerable and non-tolerable movement is often difficult to discern, and may depend on factors other than the physical condition of the bridge, such as the cost and practical problems involved in repair and maintenance.

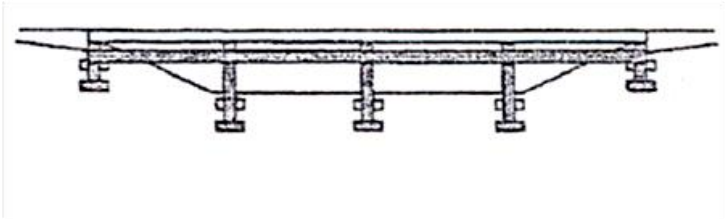

(a) Uniform Settlement (ρ)

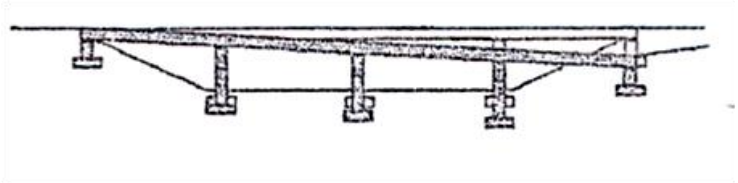

(b) Uniform tilt (ω) or rotation (θ)

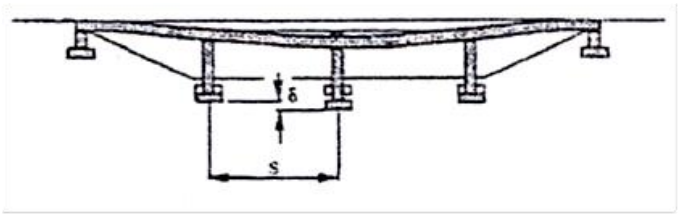

(c) Non uniform settlement (regular pattern of settlement)

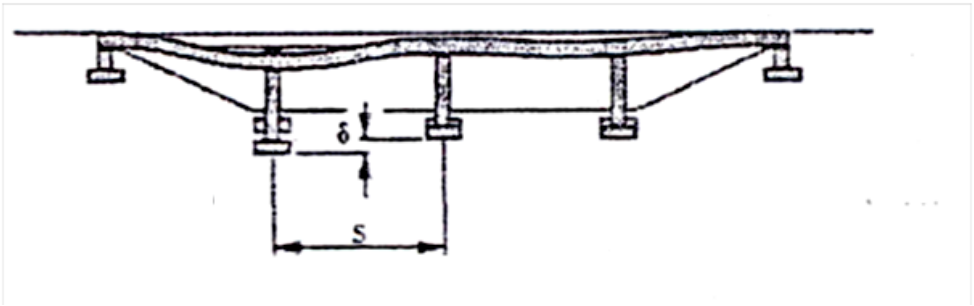

β = Angular Distortion

β = Difference in settlement between foundations/Distance between foundations = δ/S

(d) Non-uniform settlement (Irregular pattern of settlement).

Figure 4.5: Components of settlement and angular distortion in bridges (Barker et al., 1991).

Bozozuk (1978) attempted to distinguish tolerable from non-tolerable displacements for abutments and piers founded on spread footings, as illustrated in **Figure 4.6**. His survey involved 120 cases of spread footings, without specific distinction in terms of type or size. He classified displacements as *tolerable*, when the maintenance needs of the bridge are moderate, despite the magnitude of the displacements and as *non-tolerable* when

considerable maintenance and repair works are required. The work by Bozozuk (1978) was parallel to that of Walkinshaw (1978) and Grover (1978) and was documented via an extensive research on allowable displacements undertaken in the U.S.A. and Canada and published by the Transportations Research Board (TRB). Therefore Bozozuk's definition of tolerable and non-tolerable displacements also applies to the limiting values proposed by Walkinshaw and Grover, cited in **Table 4.17**.

Moulton et al. (1985) adopt the definition for non-tolerable damage proposed by the Transportation Research Board's Committee A2K03 on "*Foundations of bridges and other structures*" based on which: *"Movement is **not** tolerable if damage requires costly maintenance and/or repairs **and** a more expensive construction to avoid this would have been preferable".*

Moreover, Moulton et al. (1985) provide information regarding the possible structural damage induced by excessive vertical and horizontal displacement. According to their definition excessive values of ***vertical displacement*** entail the raising or lowering of the superstructure above or below the planned grade, hence leading to heaving and sagging phenomena respectively. Structures may require shimming or jacking, while truss structures with increased camber are also affected. Excessive ***horizontal displacement*** may cause misalignment between the bearings and the superstructure as well as the jamming of beams against the abutment. Other problems due to horizontal settlement may involve the superstructure extending beyond the abutment, beams requiring to be cut and horizontal movements occurring to the floor system.

The potential effects of distress in the superstructure and damage to bearings are also identified. Thus, ***distress in the superstructure*** consists of cracks or other evidence of excessive stress in beams, girders, struts and diaphragms as well as cracking and spalling of the deck. It also leads to shearing of anchor bolts, opening/closing or damage of deck joints, while the cutting of relief joints may be necessary. ***Damage to bearings*** includes tilting or jamming of rockers as well as cases where rockers have pulled off the bearings, or where movement resulted in an improper fit between bearing shoes and rockers requiring repositioning. Neoprene bearing pads are deformed, anchor bolts in the bearing shoes are sheared and cracking of concrete at the bearings is apparent.

Table 4.17: Allowable values for vertical, horizontal displacements and their combination for bridges.

Type of deformation	Magnitude of deformation	Damage Level	Researcher
Vertical Settlement ρ_V (mm)	< 50	Tolerable or acceptable settlements	Bozozuk (1978)
	51	Not harmful	Bozozuk (1978)
	63	Ride quality	Walkinshaw
	63	Occurrence of structural distress	Poulos (2001)
	> 63	Structural damage	Walkinshaw
	50 ÷100	Harmful but tolerable	Bozozuk (1978)
	> 100	Not tolerable	Bozozuk (1978)
	102	Ride quality and structural damage	Grover (1978)
	102	Harmful but tolerable	Bozozuk (1978)
	>102	Not tolerable	Wahis (1990)
Horizontal displacement ρ_H (mm)	25	Acceptable	Bozozuk (1978)
	< 25	Tolerable or acceptable settlements	Bozozuk (1978)
	25.4 - 50.8 (38.1mm recommended)	Logical tolerable limit on horizontal movements for abutments	Moulton et al. (1986)
	25 ÷ 50	Harmful but tolerable	Bozozuk (1978)
	< 38	Usually acceptable	Moulton et al.
	50	Structural damage	Walkinshaw
	50	Ride quality and structural damage	Bozozuk (1978)
	> 50	Not tolerable	Bozozuk (1978)
Horizontal along with vertical displacements (mm)	< 25	Acceptable	Paikovsky (2005)

Table 4.18: Allowable values for Angular distortion (β) and Differential settlement (Δρ) for bridges.

Type of deformation	Magnitude of deformation	Bridge type	Researcher
Angular Distortion β	0.004, 1/250	Continuous steel/concrete bridges with l ≥ 15.24m (50ft) steel	Moulton et al. (1986)
	0.005, 1/200	Simly supported steel/concrete bridges with l ≥ 15.24m (50ft)	Moulton et al. (1986)
	1/250	Multiple span bridges	Poulos (2001)
	1/200	Single span bridges	Poulos (2001)
	1/800	Usual limit both for continuous decks and simply supported decks.	Hambly (1979)
Differential Settlement Δρ (mm)	L*/1000 (all types of continuous bridges)	Serviceability state	Milan (1989) Current practice in France
	L/500 (slab bridges)	Serviceability state	
	L/250 (or even more for steel decks)	Ultimate Limit state	
	*L being the shortest span		
	< 76.2	Bridge abutment for bridge lifetime (for both steel & concrete bridges)	Moulton et al. (1986)
	< 50.8	Bridge pier for bridge lifetime (for both steel & concrete bridges)	Moulton et al. (1986)
	< 50.8	Bridge abutment following bridge completion (for both steel & concrete bridges)	Moulton et al. (1986)
	< 31.75	Bridge pier following bridge completion (for steel bridges)	Moulton et al. (1986)
	< 38.1	Bridge pier following bridge completion (for concrete bridges)	Moulton et al. (1986)

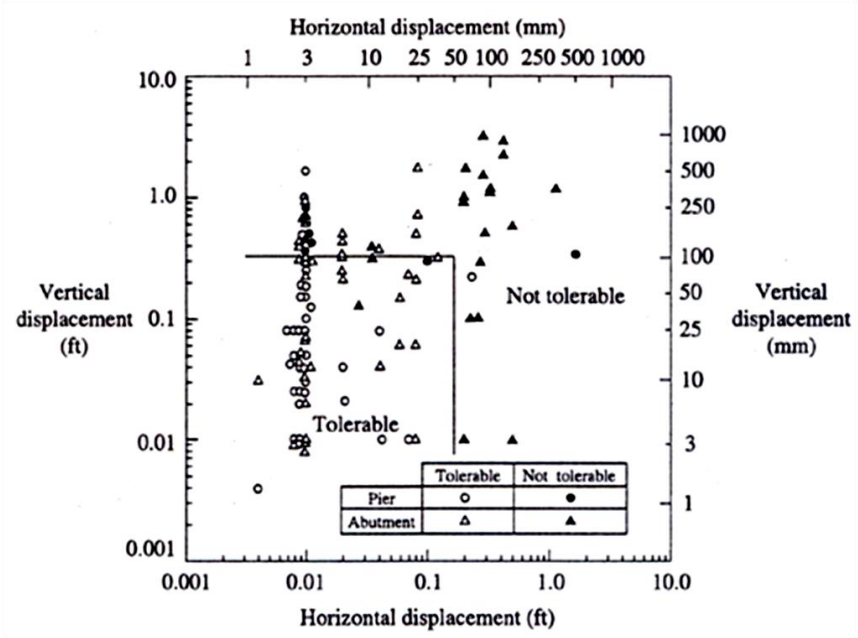

Figure 4.6: Distinction of tolerable and non-tolerable movements for bridge piers and abutments (Bozozuk, 1978).

4.4.2 Deformation limits for buildings.

Definitions.- Burland & Wroth (1974) were perhaps the first to identify and summarize all possible types of deformations, that can cause damage to buildings resting on spread foundations. Their terminology is still in application today and has also been incorporated in *Eurocode – 7*.

Figure 4.7a schematically presents the definitions for *settlement ρ*, maximum *relative settlement* $\delta\rho_{max}$, *rotation* ϑ and *angular strain a*.

- *Rotation (ϑ)* is defined as the change in gradient of a line joining two reference points.
- *Angular strain (a)* is positive when producing "sagging" or upward concavity and negative when it produces "hogging" or downward concavity. For point B angular rotation is estimated as:

$$\beta_B = \frac{\delta\rho_{BA}}{L_{AB}} + \frac{\delta\rho_{BC}}{L_{BC}} \qquad 4.5$$

- *Relative deflection (Δ)* (defined schematically in **Figure 4.7b**) is defined as the displacement relative to the line connecting two reference points at distance L.
- *Deflection ratio* is set equal to the relative deflection divided by the distance L between the two reference points. The sign convention is kept consistent to the convention set for angular rotation. It receives a maximum value when the whole building is either in a sagging or a hogging mode. That is the case for symmetric buildings under symmetric loading in uniform soil, in which the maximum relative deflection is observed at mid span, as illustrated in **Figure 4.8a**. A more complex situation is presented in **Figure 4.8b**, where, part of the foundation experiences sagging and the other part hogging. Reference lines are defined separately for the sagging and the hogging deformation pattern and spans are modified appropriately.
- *Tilt (ω)* (defined schematically in **Figure 4.9**) demonstrates the rotation of a rigid considered structure or of a well defined part of it. In this case, tilt is evaluated assuming that the two points of interest are located on a raft foundation, which implies that the definition is incompatible in the case of frame buildings on spread footings. *Relative rotation* (or *angular distortion β*) is identified as the rotation of the line joining two reference points relative to the tilt.

Settlement Criteria.- Table 4.19 and **Table 4.20**, summarize the allowable values of various types of deformations, as they were defined previously, and proposed by different researchers. Each type of deformation is categorized by type of building, in increasing order of magnitude and, where available, a brief description is provided of the damage degree.

It is interest to note that in Annex H, of Eurocode 7 (2003) the specified range for the occurrence of a serviceability limit state in the structure is considerably wide and ranges from 1/2000 to about 1/300, covering many structure categories, such as open framed structures, infilled frames and load bearing or continuous brick walls. According to EC-7 the recommended limiting value of 1/500 is considered acceptable for many structures, for the serviceability limit state. Moreover, values for both limit states presented in **Table 4.19**, apply to a sagging mode, as illustrated in **Figure 4.7**, while in case of a hogging mode of deformation, values should be halved. It is also stated that "*for normal structures with isolated foundations total settlements up to 50mm are often acceptable*", which is a slightly larger limit compared to Terzaghi & Peck's (1948) specification. Larger settlements may also be tolerable "*provided the relative rotations remain within acceptable limits and provided the total settlements do not cause problems with the services entering the structure or cause tilting etc*". Finally, the above guidelines apply to normal, routine structures under

conditions of uniform loading intensity and therefore should not be applied in structures, falling outside the particular application range.

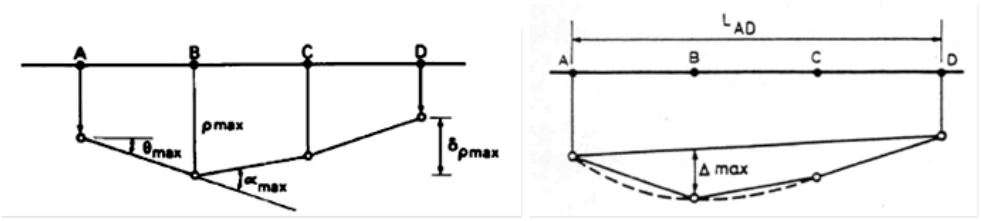

(a) **(b)**

Figure 4.7: Definitions of **(a)** settlement ρ, relative settlement $\delta\rho_{max}$, rotation θ and angular strain α, **(b)** relative deflection Δ and deflection ratio Δ/L.

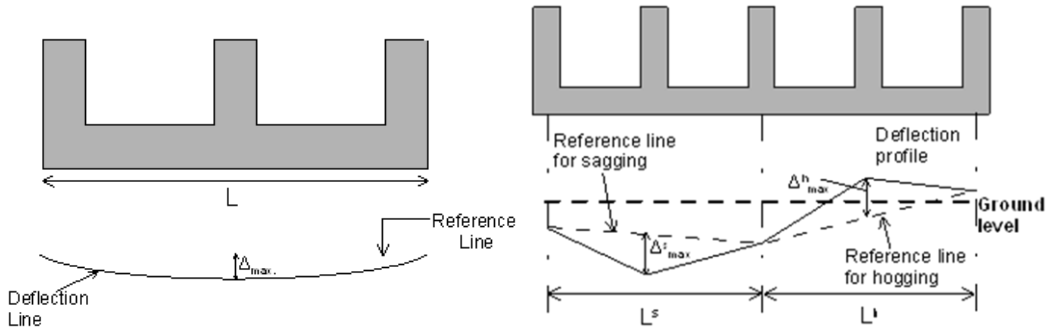

(a) **(b)**

Figure 4.8: Evaluation of deflection ratio in different building configurations **(a)** symmetric building, symmetric loading conditions and uniform soil, **(b)** non uniform conditions.

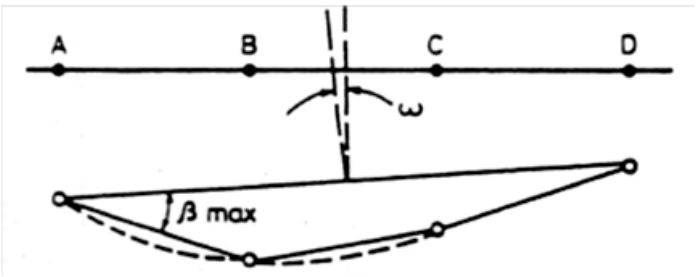

Figure 4.9: Definition of tilt ω and relative rotation (angular distortion) β

The limits of relative rotation β, proposed by Menard (1967) in **Table 4.19**, may appear extremely strict compared to the general trend of the other researchers. The reason is that Menard's criteria are based on settlements determined by the pressuremeter method, which often leads to smaller settlements compared to traditional methods.

Skempton & MacDonald (1956) were among the first to propose a way of estimating tolerable settlements in frame buildings, based on the concept of angular distortion (β). They combined field observations from 98 buildings with laboratory tests on reinforced concrete frames and brick walls subjected to increasing angular distortion until failure, to set the limiting criteria presented in the previous Tables. According to Burland et al. (1977) the Skempton & MacDonald criteria should be applied with careful consideration, since they present a few but important drawbacks:

- The majority of the data are based on indirect evidence in which (i) settlement is reported but not specified in detail, (ii) no settlement damage occurred in the buildings of the database.
- Damage is characterized as “architectural”, “functional” and “structural” with no further classification.
- The limiting values of relative rotation for structural damage in frame buildings were based on elements with average dimensions, therefore no extension can be made to large and stiff beams or columns, where the corresponding angular distortion may be much less.
- Because limiting deformations are based on the criterion of maximum relative rotation, it is implied that damage to buildings is caused exclusively by shear distortion, which is not always the case.

Due to the aforementioned, Burland et al. (1977) suggest that the Skempton & MacDonald (1956) recommendations, particularly regarding differential settlements, to be considered more like “*routine limits*”. Provided deflection ratio and angular distortion are within tolerable limits, greater values of differential and maximum settlement can be adopted.

Polshin & Tokar (1957) developed criteria of allowable deformations based on the concept of relative rotation β and deflection ratio Δ/L applicable to frame buildings, reinforced load-bearing walls and to unreinforced load-bearing walls respectively.

Burland & Wroth (1974) were based on a beam analogy, in which a beam with span L, height H, elastic properties G, E is distorted and loaded in different ways until cracking. Thus, they considered the onset of cracking to be the variable that determines serviceability and ultimate state limits and developed criteria for sagging and hogging mode of deformation, expressed in terms of maximum relative deflection Δ_{max}/L. Note that for the hogging mode of deformation it is assumed that the neutral axis of the beam analog coincides with the bases of the footings.

Figure 4.10, presents the comparison of the three criteria mentioned previously against case histories where different extent of damage was observed (none, slight and substantial). It appears that the limiting values proposed by Skempton & MacDonald (1956) compare reasonably well in the case of frame buildings, while the Polshin & Tokar (1957) standards give satisfactory comparisons in the case of unreinforced (masonry) load bearing walls. The limiting criteria by Burland & Wroth (1974) apply both to frame and masonry buildings under either a sagging or a hogging pattern of deformation.

Since the onset of cracking is frequently assumed to be the controlling factor in the definition of serviceability or ultimate limit states, **Table 4.21** associates cracking width to observed damage and serviceability/safety matters for three categories of buildings (residential, commercial and industrial),thus serving complimentary to the interpretation of the observed damage mentioned in **Table 4.19** & **Table 4.20.**

Table 4.19: Limiting values of relative rotation (β) for buildings.

Type of deformation	Type of Building/Foundation	Magnitude of deformation	Damage Level	Researcher
Relative Rotation or Angular Distortion (β)	Residential Buildings	1/3300 to 1/1500	No description of damage	Menard (1967)
	Industrial constructions	1/1250 to 1/650	No description of damage	Menard (1967)
	Indfilled frames	1/1000	No description of damage	Meyerhoff (1953)
	No specification	1/750	Danger to machinery sensitive to settlement	Wahls (1981) after Bjerrum (1963)
	No specification	1/600	Danger to frames with diagonals	Wahls (1981) after Bjerrum (1963)
	Framed buildings and reinforced load bearing walls	1/500	Onset of cracking in walls and partitions in steel and concrete frame	Polshin & Tokar (1957)
		1/500	Cracking in walls and partitions	Meyerhoff (1956)
		1/500	Cracking in walls and partitions	Bjerrum (1963)
		1/500	Unlikely to lead to eiher SLS or ULS.	Skempton & MacDonald (1956)
		1/500 (1/1000 - 1/1400) for end bays	Cracking in walls and partitions in framed buildings and reinforced	Poulos (2001)
		1/300	Serviceability Limit State: Cracking in walls and partitions observed	Skempton & MacDonald (1956)
		1/250	Onset of structural damage	Meyerhoff (1956)
		1/200	No infill or no danger of damage to	Polshin & Tokar (1957)
		1/150	Development of structural damage	Bjerrum (1963)
		1/150 (or 1/170 according to Salgado, 2007).	Ultimate Limit State: onset of structural damage	Skempton & MacDonald (1956)
		1/150 - 1/250	Onset of structural damage	Poulos (2001) after several authors
		1/2000 to 1/300 (1/500 is acceptable)	Serviceability Limit	EuroCode 7
		1/150	Ultimate Limit State	

Table 4.20: Limiting values of relative deflection (Δ) /deflection ratio (Δ/L), differential settlement ($\delta\rho_{max.}$) and tilt (ω) for buildings.

Type of deformation	Type of Building	Magnitude of deformation	Damage Level	Researcher
Relative Deflection (Δ) / Deflection ratio (Δ/L)	Load bearing walls or continuous brick cladding	1/2000	No description of damage	Meyerhoff (1953)
	Unreinforced load-bearing walls	1/2500	Onset of visible cracking under sagging	Meyerhoff (1956)
		L/H < 3; 1/3300 L/H >5; 1/2000	Onset of visible cracking in structures founded on sand under sagging	Polshin & Tokar (1957)
		L/H < 3; 1/2500 L/H >5; 1/1500	Onset of visible cracking in structures founded on clay under sagging	Polshin & Tokar (1957)
		L/H =1; 1/2500 L/H = 5; 1/1250	Onset of visible cracking in structures under sagging	Burland & Wroth (1975) (Also recommended by Poulos, 2001)
		L/H =1; 1/5000 L/H = 5; 1/2500	Onset of visible cracking in structures under hogging	Burland & Wroth (1975) (Also recommended by Poulos, 2001)
Differential Settlement δρ (mm)	Isolated foundation on sand	20 (berweem adjacent columns)	No particular description of damage	Terzaghi & Peck (1948)
	Isolated foundation on sand	25 (for a relative rotation of 1/500)		Skempton & MacDonald (1956)
	Foundations on clay	40		
Maximum Settlement $\rho_{max.}$ (mm)	Isolated foundation on sand	25	No particular description of damage	Terzaghi & Peck (1948) - Eurocode 7 (1990)
	Raft foundation on sand	50		
	Isolated foundation on sand	40		Skempton & MacDonald (1956)
	Raft foundation on sand	40 - 65		
	Isolated foundation on clay	65		
	Raft foundation on clay	65 - 100		
	Framed buildings and reinforced load bearing walls	50 - 75 (sands) 75 - 135 (clays)	Damage to connection to services	Poulos (2001), after several authors
Tilt (ω)	Framed buildings and reinforced load bearing walls	1/300	Effects on visual appearance	Poulos (2001), after several authors
Tilt after lift installation (ω)	Tall buildings	1/1200 - 1/2000	Effect on operation to lifts and elevetors	Poulos (2001), after several authors

Table 4.21: Cracking width related to observed damage and functionality of three building categories (modified after Thorburn, 1985).

	Degree of Damage			
Crack Width (mm)	**Residential**	**Commercial**	**Industrial**	**Serviceability or safety issues**
< 0.1	None	None	None	None
0.1 - 1	Slight	Slight	Very slight	Cracks may be visible
1 - 2	Slight to moderate	Slight to moderate	Very slight	Possible penetration of humidity
2 - 3	Moderate	Moderate	Slight	Serviceability may be compromised
3 - 15	Moderate to severe	Moderate to severe	Moderate	Ultimate limit states may be reached
> 15	Severe to dangerous	Moderate to dangerous	Severe to dangerous	Risk of collapse
Very slight: Damage is visible on close inspection but is correctable with interior design/decoration tools.				
Slight: external cracks may need to be filled for water-tightness; doors and windows may jam slightly.				
Moderate: replacement of small amount of brickwork is needed, service pipes may be severed and doors and windows are jammed.				
Severe: replacement of portions of walls is needed; window and door frames are distorted, floors may become uneven, service pipes are detached and walls may lean or bulge.				
Dangerous: beams lose bearing, walls may require shoring, windows are broken due to distortion and there is danger of instability.				

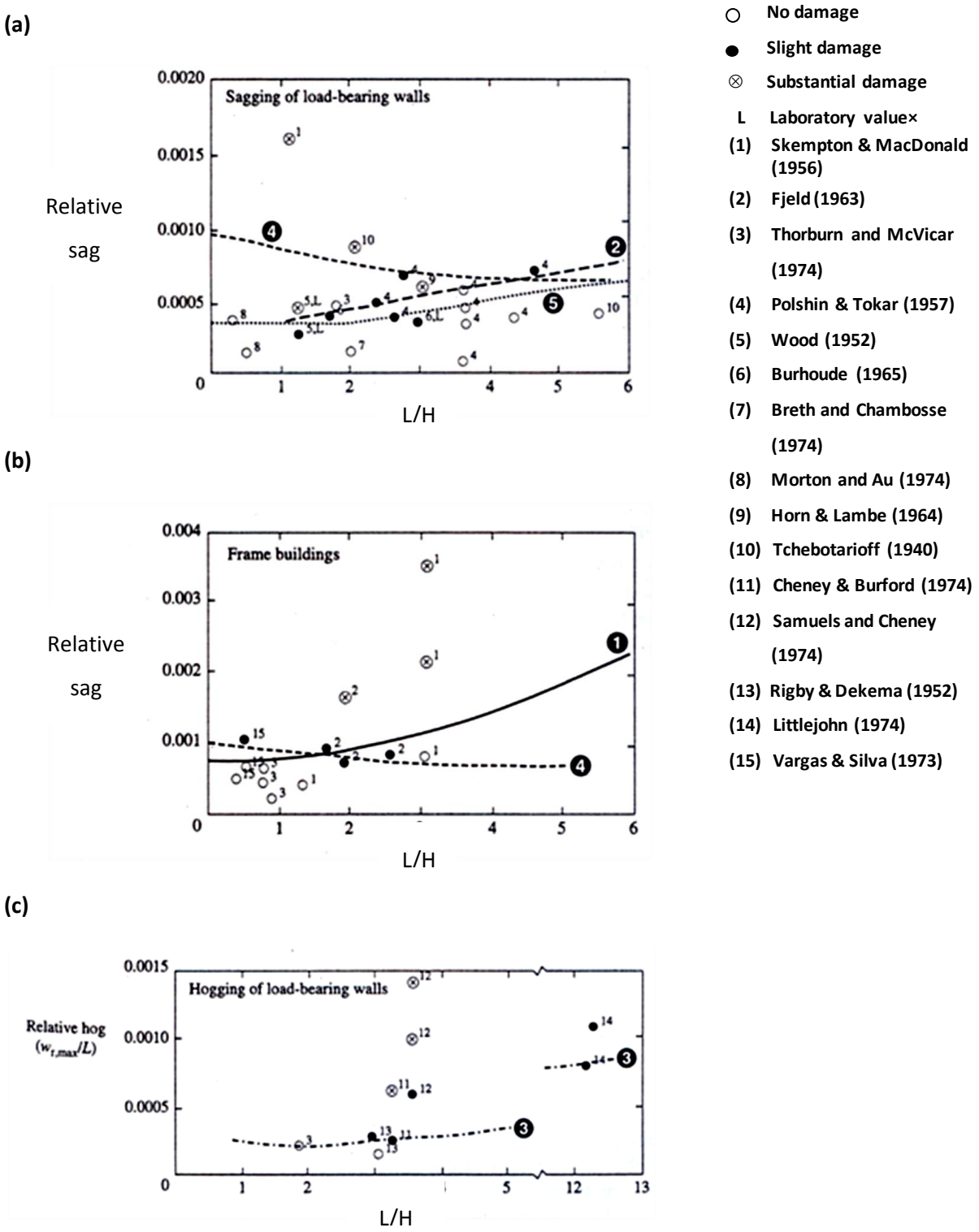

Figure 4.10: Comparison of maximum tolerable settlement criteria against settlement from field observations and laboratory experiments with none, slight or substantial damage. The plots numbered 1 through 5, correspond to: 1 to 3: Burland & Wroth (1974) for frame structures – reinforced masonry buildings, unreinforced masonry buildings in sagging, unreinforced masonry buildings in hogging respectively , 4: Skepmton & MacDonald (1956) and 5:Polshin & Tokar (1957) (after"The Engineering of Foundations",Salgado, 2007).

4.4.3 Methods for evaluation of differential settlement and angular distortion.

Differential settlements between two footings usually appear along with the occurrence of total settlements in the case where *(i)* the foundation soil is not absolutely uniform along the foundation area, *(ii)* the dead-to-live load ratio is different between the two footings or *(iii)* there are discrepancies in the built dimensions of the footings (e.g. a slight not intended eccentricity). Among the above cases, only case (ii) is computationally predictable, while cases (i) and (iii) are accidental and cannot be predicted directly. Hence, due to the complexity and uncertainty involved in their estimation many researchers have correlated differential settlements to maximum absolute settlements.

The correlation between total and differential settlement greatly depends on the type of foundation. In general, stiffer foundations, such as raft (mat) foundations (operating more like a single reinforced-concrete slab), are expected to experience lower differential settlements, compared to isolated foundations (e.g. spread footings which essentially support one single column). The magnitude of differential settlements is also greatly affected by the subsurface soil conditions. Sandy soil profiles present a greater degree of heterogeneity, even within the limits of the same structure; therefore significant differential settlements are more likely to occur. On the contrary, clay deposits are generally more uniform and lower differential settlements are expected, as opposed to sandy soils for a known total settlement.

The proposed correlations by Skempton & MacDonald (1956) between differential and total settlements, as a function of soil and foundation type are summarized in **Table 4.22**. Note however, that the above correlation has received an extensive criticism from Terzaghi (1956), in the case where long-term consolidation in a thick clay layer dominates. Taking this into consideration, it would be advisable to avoid such correlations and estimate each kind of settlement separately and proceed to design considering the excessive values of both.

Table 4.22: Ratio of maximum total settlement to maximum angular distortion $\beta_{max.}$ (modified after Skempton & MacDonald, 1956).

Soil Type	Isolated Foundations	Mat Foundations
Sand/sandy fill	$15L_R$	$20L_R$
Clay	$25L_R$	$30L_R$
L_R = the reference length = 1m = 40in		

Burland et al. (1977) were based on the data by Skempton & MacDonald (1956), as well as Grant et al. (1972) and others to correlate the degree of damage observed in buildings to the maximum settlement and maximum differential settlement. This attempt is presented in **Figure 4.11**, and concerns buildings on isolated or raft foundations, situated on top of seemingly uniform clayey layers, under uniform loading conditions. In parallel, Bjerrum (1963) has presented a similar figure and the suggested upper limit curves for flexible and rigid structures have been incorporated by Burland et al. (1977). Moreover, the dashed arrows specify some maximum average values of settlements permitted by the 1962 USSR Building Code, while the full arrows indicate the design limits proposed by Skempton & MacDonald (1956). Later on, given the differential settlement Δs, Bjerrum (1963) correlated it to the maximum angular distortion $(\Delta s/L)_{max}$, as presented in **Figure 4.12**. This correlation also applies to clayey foundation soils; however no distinction is made as to the type of structure (frame or load bearing building). Equivalent correlations have been proposed by Bjerrum (1963) concerning buildings located on sandy soils, and are presented in **Figure 4.13** & **Figure 4.14**.

More recently, similar correlations were proposed by Justo (1987), based on observations from different researchers. Namely, in **Figure 4.15**, maximum angular distortion β_{max} is plotted against the maximum settlement s_{max} for isolated foundations, located either on clays (**Figure 4.15a**) or sands and fills (**Figure 4.15b**). Likewise, **Figure 4.16**, presents the same correlation for buildings on clays (**Figure 4.16a**) or sands and fills (**Figure 4.16b**).

Day (2000) collected data from various sources concerning the relationship between the absolute value of differential settlement $\Delta\rho_{max}$ and angular distortion Δ/L and verified the relationship initially proposed by Skempton & MacDonald (1956) that is analytically expressed through *Equation 4.6*:

$$\Delta\rho_{\max} = 8900 \times (\Delta s / L)(mm) \qquad 4.6$$

As mentioned earlier, the above limiting deformation criteria refer to static loading conditions, while there is still no complete set of criteria for allowable earthquake-induced deformations. The only relevant study found in the literature is that of Yasuda et al. (2001) who suggest the use of an empirical relationship for the estimation of the angle of inclination due to differential settlement. The proposed empirical relationship correlates the *angle of tilting* ϑ (deg) to the *average settlement* $\rho_{av.}$ (cm), through *Equation 4.7,* and is based on data from tilted buildings after the Kocaeli (1999) and two other earthquakes:

$$\theta = 0.05\rho_{av} \qquad 4.7$$

To further elaborate on the empirical equation provided by Yasuda et al. (2001), it is compared against correlations proposed by Bjerrum (1963) for static loading conditions. Yasuda et al. (2001) correlate the angle of inclination (θ) to the average total settlement, thus, the arctan(θ) provides the angular distortion β and considering different building lengths (L = 5 – 12m), the differential settlement (Δρ) is determined. **Figure 4.17** illustrates the above attempt and incorporates the curves for rigid and flexible structures on clay, proposed by Bjerrum (1963) (also plotted in **Figure 4.11**), as well as the corresponding correlation for structures located on sand (also presented in **Figure 4.13**). With regard to Yasuda et al. (2001), for increasing length of structure the earthquake-induced tolerable differential settlement is apparently greater for a given value of absolute settlement. For small building lengths, the connection between differential and absolute settlements appears to be very close and may be satisfactorily described by the correlations for static conditions. However, it should be stressed out that this is only a preliminary assessment and no conclusive conclusions can be drawn, since there is no information about the soil conditions or the rigidity of the structures that Yasuda et al. (2001) used to formulate *Equation 4.7*.

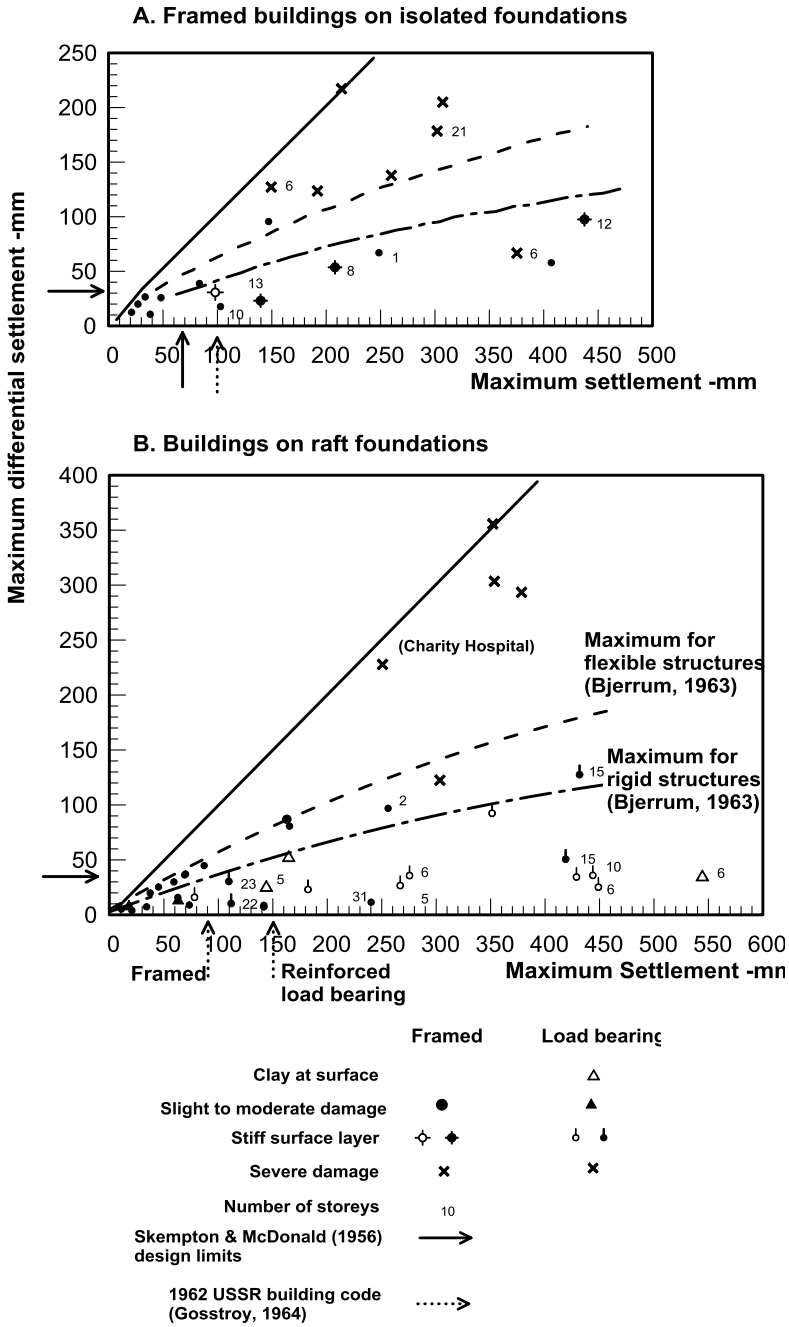

Figure 4.11: Observed maximum and differential settlements in buildings on isolated or raft foundations. (after Burland et al., 1977).

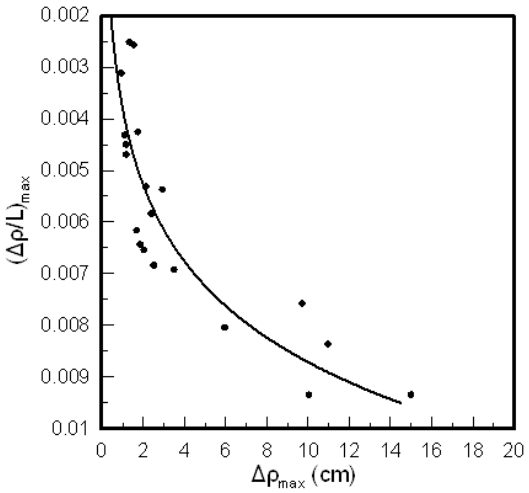

Figure 4.12 Maximum differential settlements and corresponding angular distortion, for clayey foundation soils (after Bjerrum 1963).

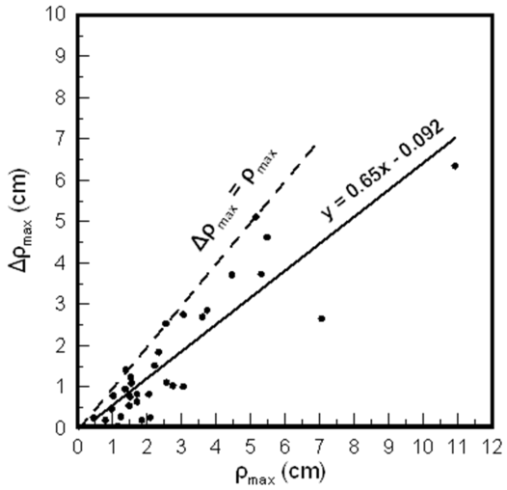

Figure 4.13: Correlation of maximum absolute settlement to maximum differential settlement for buildings on sandy foundation soils (after Bjerrum, 1963).

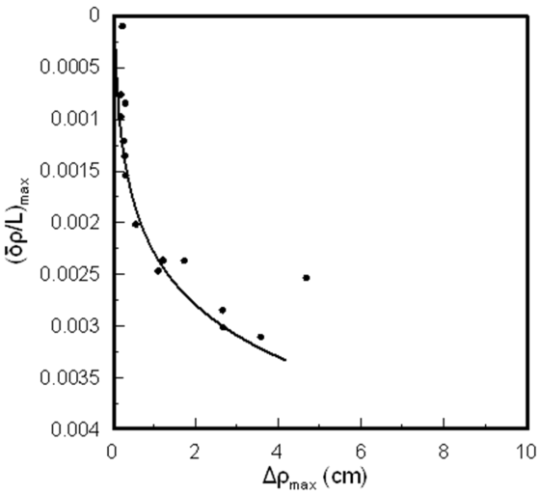

Figure 4.14: Correlation of maximum differential settlement to maximum angular distortion for buildings on sandy foundation soils (after Bjerrum, 1963).

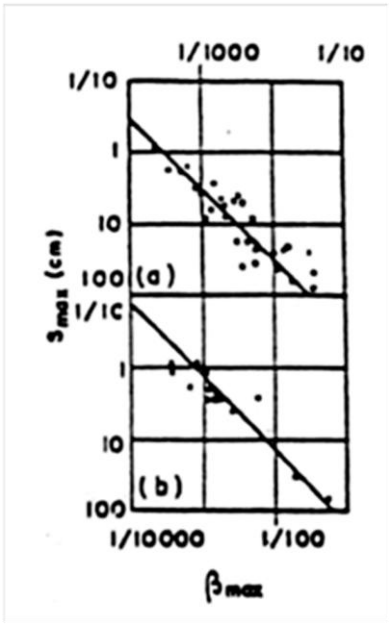

Figure 4.15: Correlation between maximum angular distortion β_{max} and maximum settlement s_{max}, for isolated foundations on **(a)** clays, **(b)** sands and fills (after Justo, 1987, based on several authors).

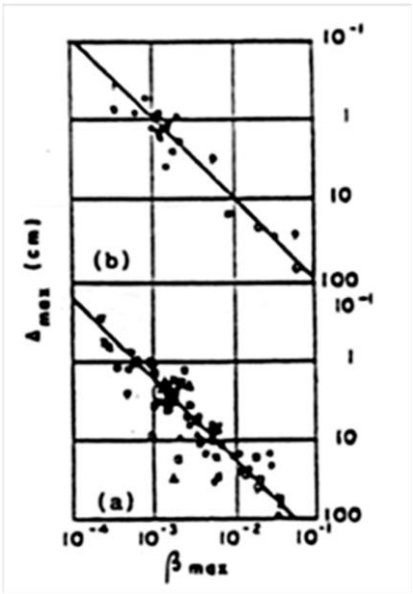

Figure 4.16: Correlation between maximum angular distortion β_{max} and maximum settlement s_{max}, for buildings on **(a)** clays, **(b)** sands and fills (after Justo, 1987, based on several authors).

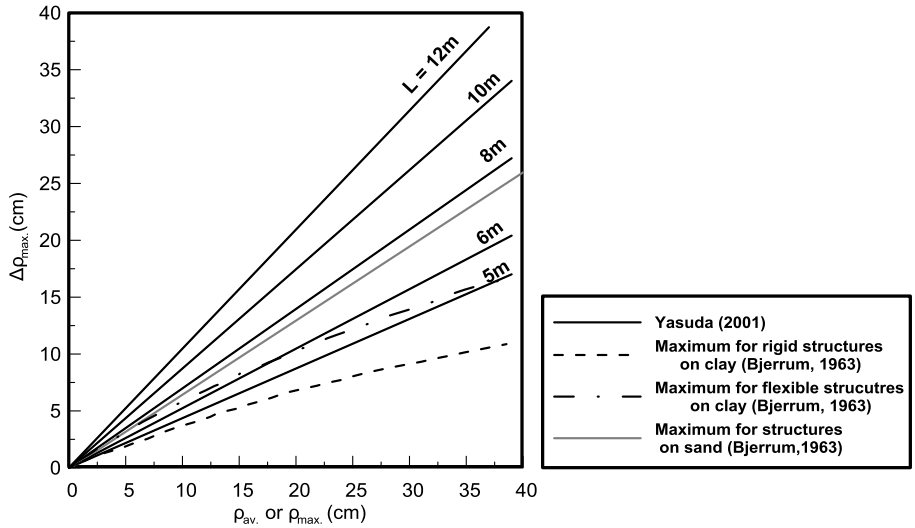

Figure 4.17: Comparative evaluation of the empirical correlation proposed by Yasuda et al. (2001) against correlations for static conditions by Bjerrum (1963).

4.5 Example applications

To obtain insight as to the order of magnitude of allowable deformations of buildings and bridges, typical application examples are provided below. The examined cases refer to three different building types and two structural types of bridges shown in **Figure 4.18** to **Figure 4.21.** Allowable values of settlements will be estimated considering the requirements specified in Eurocode 8, namely two levels of design seismic motions, corresponding to suitable Limit States.

4.5.1 Framed buildings on isolated footings

Problem Outline.- The first application refers to the simplified case of an ordinary one-storey framed building resting on isolated footings. A typical cross – section is provided in **Figure 4.18**, in which the isolated footings are located 12m apart and the maximum height of the building is 4m. According to EC–8 such a building configuration is assigned an importance factor equal to unity. Performance criteria are examined for both clay and sand foundation soil profiles.

Performance Requirements.- In the EC–8 guidelines for buildings two performance Requirements are specified and briefly outlined below:

- **Damage Limitation Requirement.-** The structure "*is designed and constructed to resist a seismic action with a larger probability of occurrence than the design seismic action, without the occurrence of damage and the associated limitations of use, the costs of which would be disproportionally high in comparison to the costs of the structure itself*".

The design seismic motion for the Damage Limitation Requirement is characterized by a return period of 95yrs.

- **No Collapse Requirement.-** The structure is "*designed and constructed to withstand the design seismic action without local or global collapse, thus retaining its structural integrity as well as a residual load bearing capacity after the occurrence of the seismic events"*. According to EC-8 the design seismic motion for the No Collapse Limit State is characterized by a return period of 475yrs.

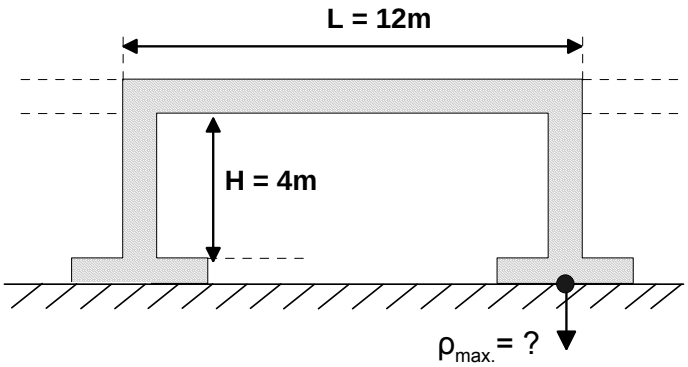

Figure 4.18: Framed building on isolated foundations.

Performance Criteria.- Based on **Table 4.20** the maximum allowable settlement is equal to 2.5 – 4cm for a sand foundation layer and 6.5cm for a clay foundation layer, without any distinction as to the Limit State.

Nevertheless, structural damage such as wall cracking and further loss of serviceability in a building are not caused by uniform settlements, but rather by the differential settlements developing between two footings and the subsequent angular distortion (β). Thus, based on Eurocode 7, which provides a complete design approach regarding performance limit states, and the correlation proposed by Burland et al. (1977), Bjerrum (1963) and Justo (1987), between differential and total maximum settlements the estimated maximum settlements $\rho_{max.}$ are summarized in **Table 4.23**, for both clay and sand foundation soil profiles. More analytically, for the allowable value of angular distortion (β) for each Limit State, dictated by EC-7, the maximum differential settlement ($\delta\rho_{max.}$) is calculated, given the 12m distance (L) between the two footings, from the building configuration presented in **Figure 4.18**. Subsequently, **Figure 4.11**, **Figure 4.13** and **Figure 4.15** are used to estimate the maximum allowable settlement. Note that the estimated values are comparable to the proposed

values by Terzaghi & Peck (1948) and Skempton & MacDonald (1956), provided in **Table 4.20**.

Table 4.23: Limiting values of maximum settlements for two Performance Levels.

Deformation	Serviceability Limit State		Ultimate Limit State		Reference
	Sand/Fills	Clay	Sand/Fills	Clay	
β (=$\delta\rho_{max.}$/L)	1/500		1/150		EC-7
$\delta\rho_{max.}$(cm)	2.4		8		-
$\rho_{max.}$ (cm)	3 - 4	4.5	12.5	19	Burland et al. (1977), Bjerrum (1963)
	≈ 3	6	8	20	Justo (1987)

Considering the uncertainty involved in the assessment of allowable settlements, the ranges of allowable maximum settlements for the above examined case would be as follows:

- *Sand foundation layer:* 3 – 4cm for the Serviceability Limit State and 8 – 12.5cm for the Ultimate Limit State.
- *Clay foundation layer:* 4.5 – 6.0cm for the Serviceability Limit State and 19 – 20cm for the Ultimate Limit State.

4.5.2 Buildings on flexible raft foundation

Problem Outline.- The following application refers to a building of 16m in height and 12 in width, founded on a flexible raft foundation, like the one presented in **Figure 4.19**.

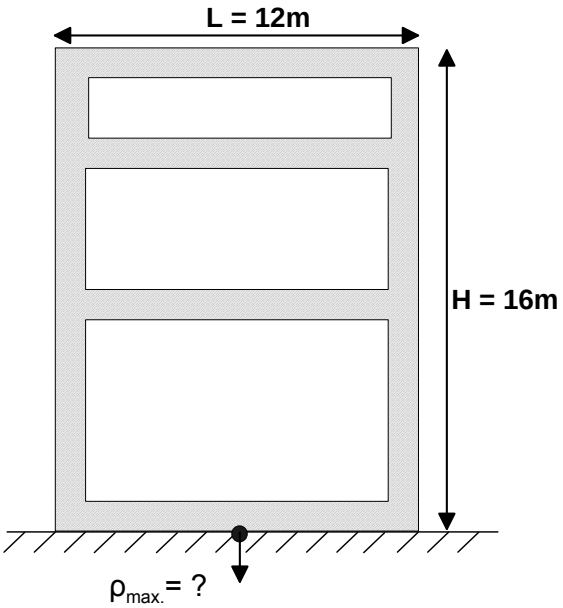

Figure 4.19: Ordinary building resting on a (flexible or rigid) raft foundation.

Performance Requirements.- The two performance Levels and corresponding requirements specified previously are also in effect in this case and will not be further analyzed.

Performance Criteria.- The maximum allowable settlement for this type of building will range from **4** to **6.5**cm, with an average value of **5**cm for a sand foundation layer, [Skempton & MacDonald (1956)], and Terzaghi & Peck (1948) respectively (**Table 4.20**). The equivalent range for a clay foundation layer is from **6.5**cm to **10**cm, according to Skempton & MacDonald (1956).

The allowable limits of angular distortion according to EC-7 and the corresponding differential settlement are the same as discussed in the previous section. Furthermore, based on the correlations proposed by Burland et al. (1977), between differential and maximum settlements, presented in the lower graph of **Figure 4.11**, the resulting values of maximum settlements are summarized in **Table 4.24**.

Table 4.24: Limiting values of maximum settlements for two Performance Levels for the case of a building resting on a flexible raft foundation.

Deformation	Serviceability Limit State		Ultimate Limit State		Reference
	Sand/Fills	Clay	Sand/Fills	Clay	
β (=$\delta\rho_{max.}$/L)	1/500		1/150		EC-7
$\delta\rho_{max.}$(cm)	2.4		8		-
$\rho_{max.}$ (cm)	3 – 4	4	12.5	14	Burland et al. (1977)

Considering the uncertainty involved in the assessment of allowable settlements, the ranges of allowable maximum settlements for the above examined case would be as follows:

- *Sand foundation layer*: 3 – 5cm (or even 6.5cm according to Skempton & MacDonald (1956)) for the Serviceability Limit State and up to 12.5cm for the Ultimate Limit State.
- *Clay foundation layer*: 4 – 6.5cm for the Serviceability Limit State and 10 – 14cm for the Ultimate Limit State.

4.5.3 Buildings on rigid raft foundation

Problem Outline.- The previous case study is now re-evaluated considering the building configuration presented in **Figure 4.19**, which is founded on a rigid raft foundation.

Performance Requirements.- The two performance Levels and corresponding requirements specified in EC 8 and mentioned in the previous paragraphs are also in effect in this case and will not be further analyzed.

Performance Criteria.- According to **Table 4.20,** there is no distinction concerning the rigidity of a raft foundation and the allowable values of maximum settlement. Therefore, for a sand foundation layer the maximum allowable settlements for this type of building will range from **4** to **6.5**cm [Skempton & MacDonald (1956)], with an average value of **5**cm [Terzaghi & Peck (1948)]. The equivalent range for a clay foundation layer would range from **6.5**cm to **10**cm, according to Skempton & MacDonald (1956).

The allowable limits of angular distortion according to EC-7 and the corresponding differential settlement are the same as discussed in the previous sections. Furthermore, based on the correlations proposed by Burland et al. (1977), between differential and maximum settlements for rigid structures, presented in the lower graph of **Figure 4.11**, the resulting values of maximum settlements are summarized in **Table 4.25**. Note that maximum allowable settlements for a rigid raft foundation on sand are not different from what is predicted in the case of flexible foundations.

Table 4.25: Limiting values of maximum settlements for two Performance Levels for the case of a building resting on a rigid raft foundation.

Deformation	Serviceability Limit State		Ultimate Limit State		Reference
	Sand/Fills	Clay	Sand/Fills	Clay	
β (=$\delta\rho_{max.}$/L)	1/500		1/150		EC-7
$\delta\rho_{max.}$(cm)	2.4		8		-
$\rho_{max.}$ (cm)	3 - 4	7	12.5	24	Burland et al. (1977)

In conclusion, the resulting allowable settlements are summarized depending on the foundation layer as follows:

- *Sand foundation layer*: 3 – 5cm for the Serviceability Limit State and up to 12.5cm for the Ultimate Limit State.
- *Clay foundation layer*: 7cm for the Serviceability Limit State and up to 24cm for the Ultimate Limit State.

The following **Table 4.26** summarizes the allowable maximum settlements estimated in the previous applications arranged by type of foundation and foundation layer for the two Limit

States defined in EC-7. All three structures were selected to have the same span (i.e. L = 12m), so that the effect of the type of foundation can be examined independently of the geometrical characteristics of the structure involved in the evaluation of allowable settlements.

It is of particular interest that, for a sandy foundation layer, the type of foundation does not appear to play a major part in the magnitude of tolerable settlements, since only minor differences are observed between different foundation systems. One reason for that, is the use of **Figure 4.13,** proposed by Bjerrum (1963), which does not make any distinction in terms of foundation type in the correlation of differential to maximum total settlements.

For clayey foundation layers, there is obvious distinction in the values of allowable settlements, especially in the settlements required to reach the Ultimate Limit State. It is noteworthy, that a building founded on isolated footings will tolerate larger settlements (19 – 20cm) compared to a building constructed on a flexible raft foundation (10 – 14cm) in the Ultimate Limit State. Also, a rigid raft foundation is expected to perform better than the other two examined cases and withstand larger amount of settlement in both Limit States.

It should also be stressed out that maximum total settlement has been correlated either to the differential settlement $\delta\rho_{max.}$ and then to the maximum angular distortion β_{max}, or directly to the angular distortion β_{max}, (see Justo, 1987). In the second case it seems that the span of the building (L) is not taken into account, or the presented diagrams apply to specific building lengths (L), not clearly stated. In any case, for the 12m length selected here, the results are in accordance to the predictions by Bjerrum (1963). Furthermore, the second figure proposed by Justo (1987), correlating the maximum angular distortion β_{max} to the maximum relative deflection $\Delta_{max.}$ also rises similar questions as to the length of the buildings considered in the research. Assuming a simple framed building resting on two isolated foundations, the resulting maximum relative deflection will be equal to the differential settlement between them. Based on the definition of angular distortion ($\beta_{max.}$) and the same value for both clays and sands (e.g. 10^{-3}), it appears that the graph for sands and fills (**Figure 4.16**) only applies to buildings with L = 10m and the graph for clays applies for buildings with L = 15m. Therefore, attention is required in the application of the graphs presented in **Figure 4.15** & **Figure 4.16,** which provide an order of magnitude of the expected deformations rather than accurate and exact values to use in analysis.

Table 4.26: Summary of limiting total settlements for various foundation types and soil formations (settlements in centimeters).

Type of Foundation (sand layer)	**Serviceability Limit State**	**Ultimate Limit State**
Isolated foundations	3 – 4*	8 – 12.5
Flexible raft	3 – 5 (or even up to 6.5)	12.5
Rigid raft	3 – 5	12.5
Type of Foundation (clay layer)	**Serviceability Limit State**	**Ultimate Limit State**
Isolated foundations	4.5 – 6	19 – 20
Flexible raft	4 – 6.5	10 – 14
Rigid raft	7	24

*Maximum allowable settlements are expressed in centimeters.

4.5.4 Reinforced concrete simply-supported bridges

Problem Outline.- The following case study concerns a reinforced concrete simply supported bridge. The examined bridge is schematically illustrated in **Figure 4.20** and consists of two, L = 40m in length, spans, and a 10m high, central pier, which corresponds to the maximum depth of the valley.

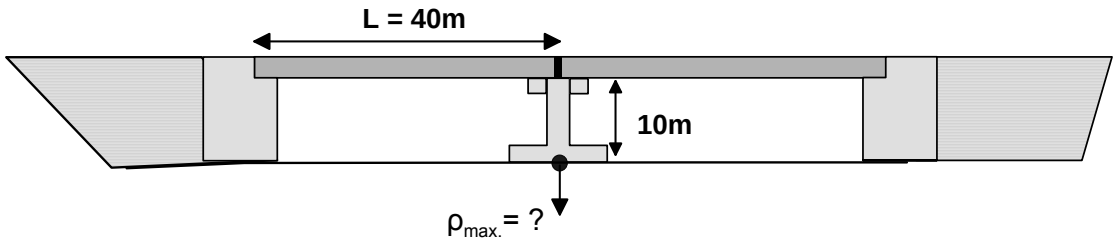

Figure 4.20: Reinforced concrete simply supported bridge.

Performance Requirements.- According to EC-8, the bridge is classified in the second class of importance and therefore assigned an importance factor equal to unity. Performance Criteria are defined as follows:

- **Minimization of Damage (Serviceability Limit State).-** In this lower level performance requirement, "*the design seismic action is assigned a high probability of occurrence and may cause only minor damage to secondary components and to those parts of the bridge intended to contribute to energy dissipation. All other parts of the bridge are expected to remain undamaged"*. The Eurocode 8 provisions do not clearly specify a return period, therefore, for the purposes of the application, it is assumed a return period of

approximately 100yrs, which is adopted by other Specifications mentioned in section **4.2.1**.

- **No – collapse (Ultimate Limit State).-** In the upper level performance requirement, the bridge is generally anticipated to preserve its structural integrity and avoid total collapse. In brief, considerable damage is expected to occur, mainly in the form of flexural yielding of specific sections (i.e. the formation of plastic hinges) in the piers, which in the absence of seismic isolation is a desirable situation. The bridge deck should in general be designed to avoid damage, except for breakage of secondary components, such as expansion joints and continuity slabs. The return period assigned in this specific performance level is 475yrs.

Performance Criteria.- Based on **Table 4.17** & **Table 4.18** with the exception of the limits proposed by Milan (1989) - limiting values of various types of settlements are not associated to observed Limit States of the bridge. Therefore, when attempting to establish limiting values of deformations for specific Limit States, only simplified approaches are possible. For instance, Bozozuk (1978) considers a vertical settlement less than **5cm** to be tolerable or acceptable; which could be considered to be the Serviceability Limit State. Vertical settlements exceeding **5cm** and up to **10cm** are considered harmful but tolerable, roughly corresponding to an Ultimate Limit State condition.

Note that, assuming zero settlement to the abutments of the bridge, estimated differential settlements will correspond to the maximum vertical settlement of the central pier, thus, allowable values of differential settlements must also be included in the following investigation. For concrete simply supported bridges, Moulton et al. (1986) set a limit in the allowable angular distortion equal to 0.005, this being equal to a differential settlement of **20cm**, considering the 40m span of the bridge. Moreover Moulton et al. (1986) specify a differential settlement of less than **3.81cm** to be acceptable for a bridge pier of a concrete bridge following completion, which is a rather conservative value and should not be taken into consideration.

Milan (1989) clearly defines Serviceability and Ultimate Limit State for different types of bridges. Thus, maximum differential settlements for a slab bridge (which essentially corresponds to the examined case) in the Serviceability Limit State will be equal to L/500, or **8cm,** and of the order of L/250, or **16cm**, in the Ultimate Limit State, as summarized in **Table 4.27.**

Table 4.27: Limiting values of maximum settlements for two Performance Levels for the case of a simply supported reinforced concrete bridge.

Deformation	Serviceability Limit State	Ultimate Limit State	Reference
$\delta\rho_{max.}/L$	L/500	L/250	Milan (1989)
$\delta\rho_{max.} = \rho_{max.}$ (cm)	8	16	

Considering the uncertainty involved in the assessment of allowable settlements, the maximum allowable settlements for the Serviceability Limit State would not exceed 8 – 10cm, while in the Ultimate Limit State would be in the order of 16 – 20cm.

4.5.5 Reinforced concrete continuous bridges

Problem Outline.- The previous case study is now re-evaluated, considering a different structural system, namely a continuous reinforced concrete bridge. The bridge is schematically illustrated in **Figure 4.21** and presents the same geometrical characteristics as before.

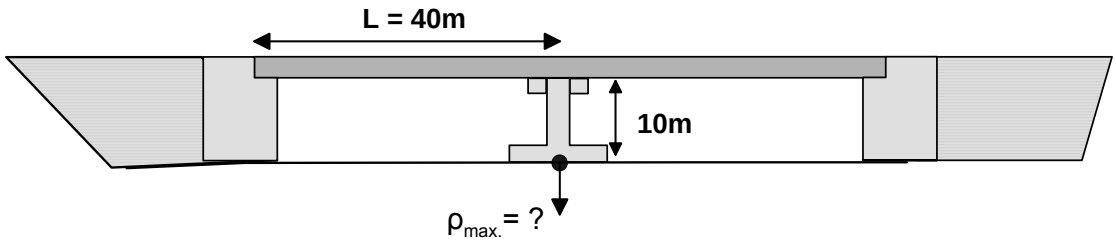

Figure 4.21: Reinforced concrete continuous bridge.

Performance Limit States.- The performance states according to EC-8 are not different from what it was mentioned in the previous paragraph, therefore no further analysis is necessary.

Performance Criteria.- As it was already mentioned, limiting values of various types of settlements are not associated to observed Limit States to the bridge. Therefore, based on **Table 4.17** & **Table 4.18**, Bozozuk (1978) considers a vertical settlement less than **5cm** to be tolerable or acceptable; which could be considered to be the Serviceability Limit State. Vertical settlements exceeding **5cm** and up to **10cm** are considered harmful but tolerable, roughly corresponding to the Ultimate Limit State.

Moreover, considering maximum differential settlements equal to the maximum vertical ones for zero movement of the abutments, Moulton et al. (1986) set a limit in the allowable angular distortion equal to 0.004, this being equal to a differential settlement of **16cm**, considering the 40m span of the continuous bridge. Moreover Moulton et al. (1986) specify

a differential settlement of less than **3.81cm** to be acceptable for a bridge pier of a concrete bridge following completion, which is a rather conservative value and should not be taken into consideration.

Also, Milan (1989) clearly defines Serviceability and Ultimate Limit State for different types of bridges. Thus, maximum differential settlements for a continuous bridge (which essentially corresponds to the examined case) in the Serviceability Limit State will be equal to L/1000, or **4cm,** and of the order of L/250, or **16cm**, in the Ultimate Limit State, as summarized in **Table 4.28**.

Table 4.28: Limiting values of maximum settlements for two Performance Levels for the case of a simply supported reinforced concrete bridge.

Deformation	Serviceability Limit State	Ultimate Limit State	Reference
$\delta\rho_{max.}/L$	L/1000	L/250	Milan (1989)
$\delta\rho_{max.} = \rho_{max.}$ (cm)	4	16	

Considering the uncertainty involved in the assessment of allowable settlements, the maximum allowable settlements for the Serviceability Limit State would not exceed 4 - 5cm and in the Ultimate Limit State would be in the order of 10 - 16cm.

Overall, in the evaluation of limiting values of settlements for bridges, things are more straightforward compared to buildings. **Table 4.29** summarizes the previously estimated settlements, categorized by type of structural system, from which it is concluded that simply supported bridges are more tolerant to settlements as opposed to continuous bridges. Nevertheless, a major drawback in the above criteria by Moulton et al. (1986) & other researchers is the lack of classification of the above criteria with respect to the foundation soil layer (i.e. sand or clay), which would make a significant difference as presented in the case of buildings.

Table 4.29: Limiting values of maximum settlements for different types of bridges.

Structural System	Serviceability Limit State	Ultimate Limit State
Simply Supported Bridges	8 – 10	16 - 20
Continuous Bridges	4 – 5	10 – 16

CHAPTER 5

An Improved Approach for Drain Design

5.1 Introduction

The second main assumption in the Seed & Booker (1977) theory for drain design, concerns the infinitely greater permeability of the drain material, compared to the surrounding ground, thus allowing the unhindered dissipation of the excess pore pressure generated during an earthquake. This, also known as, perfect drain assumption, is preserved in the present chapter, in order to examine the effect of the surrounding soil's properties on the existing design charts initially proposed by Seed & Booker (1977) and lately by Bouckovalas et al. (2009).

New experimental data, which are presented here, suggest a considerable deviation from the empirical correlation between the excess pore pressure ratio r_u and the number of cycles required for liquefaction $N_{L,}$ which may have a considerable influence on the existing design charts. In view of the inadequacy of the attempted modifications on the existing charts to account for the above findings, new design charts are formulated, which improve the predicting capacity of the revised methodology proposed by Bouckovalas et al. (2009) and in parallel highlight the over-conservatism of the traditional theory proposed by Seed & Booker (1977).

5.2 Effect of soil properties on the excess pore pressure ratio

One of the main features in the solution of the basic differential equation in the Seed & Booker (1977) theory is the empirical correlation between the excess pore pressure ratio r_u and the normalized number of cycles N/N_L, where N_L is the number of cycles required for liquefaction. Early cyclic triaxial and cyclic simple shear laboratory tests (Lee & Albaisa, 1974 and De Alba et al., 1975) have shown that the excess pore pressure ratio r_u, when plotted against the cycle ratio N_{eq}/N_L, lies within a relatively narrow range. More specifically, Lee & Albaisa (1974) conducted undrained cyclic triaxial compression tests on different samples of clean saturated sands of various relative densities, coming up with the curves presented in **Figure 5.1**. The cyclic simple shear tests conducted by De Alba et al. (1975) on clean saturated sands, in a range of relative densities (Dr = 54% - 90%), resulted in the curves presented in **Figure 5.2**. The mathematical expression best describing the above experimental data is:

$$\frac{u_g}{\sigma'_o} = \frac{2}{\pi}\sin^{-1}\left(\frac{N}{N_l}\right)^{1/2A} \qquad 5.1$$

where A is on average equal to 0.70.

However, more recent laboratory testing programs provide evidence that parameter A is significantly affected by the soil properties (e.g. relative density and fines content) as well as the test type (e.g. cyclic triaxial or cyclic simple shear test). Namely, typical results from laboratory testing programs (like VELACS and X-SOILS), processed and presented in the following paragraphs, prove that A can receive values greater than 0.70.

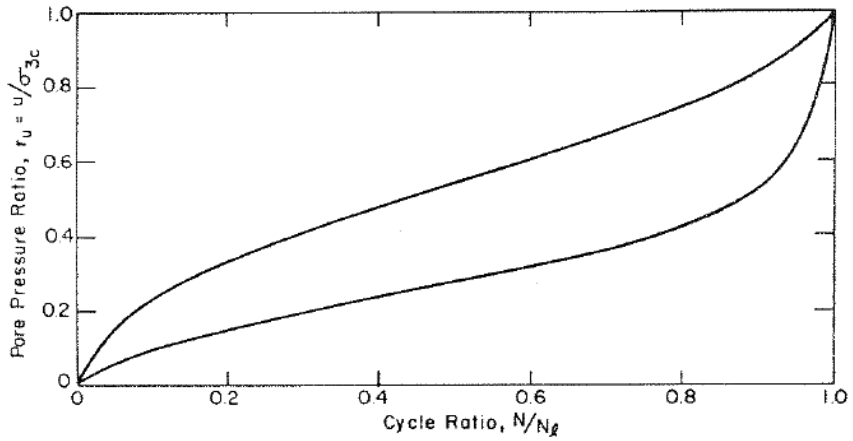

Figure 5.1: Rate of pore pressure built-up in cyclic triaxial tests (after Lee & Albaisa,1974).

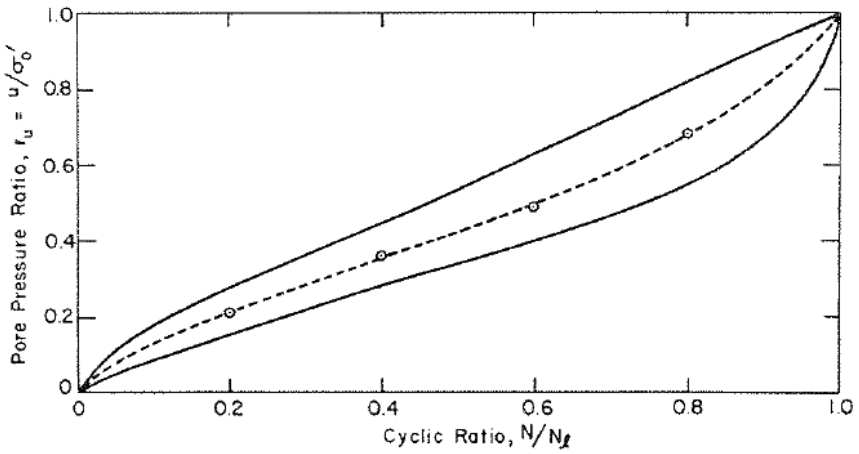

Figure 5.2: Rate of pore pressure built-up in cyclic triaxial tests (after De Alba et al, 1975).

5.2.1 Test Results from the VELACS[1] experimental program

Arulmoli et al (1992) conducted a series of undrained cyclic triaxial and cyclic simple shear tests, with a constant frequency of approximately 1Hz, on clean Nevada sand of relative density 40% and 60% and consolidation stresses ranging from 40 to 160kPa. These tests are reviewed here, focusing on the effect of the specimen's relative density on parameter A. The Nevada sand #120 used in the program possessed the properties summarized in **Table 5.1**.

Table 5.1: Properties of Nevada sand - VELACS testing program

Specific Gravity G_s	Max. dry density $d_{dry,\,max}$ (kN/m^3)	Min. dry density $d_{dry,\,min}$ (kN/m^3)	Maximum void ratio e_{max}	Minimum void ratio e_{min}
2.67	17.33	13.87	0.877	0.511

The laboratory results were grouped according to the relative density of the specimens (40% and 60%) and the type of the test (cyclic triaxial or direct simple shear). The laboratory data are presented in **Figure 5.3** in terms of excess pore pressure ratio, r_u, plotted against the normalized number of loading cycles N to the number of cycles required for liquefaction N_L. The shaded regions correspond to the results from the laboratory tests, while the continuous curves correspond to *Equation 5.1* for different values of A. **Table 5.2** summarizes the resulting A values for the four examined cases.

[1] VELACS: Verification of Liquefaction Analyses by Centrifuge Studies.

Based on the above, it is observed that the value of 0.70 characterizes the looser sand formation examined, and is representative of the undrained cyclic triaxial test results. Parameter A increases with relative density and is consistently greater in the case of the cyclic direct simple shear test results.

Table 5.2: Typical A values for the VELACS laboratory test results

Test Type	A Values	
	Dr = 40%	Dr = 60%
Cyclic TX	0.70	0.80 – 1.00
Cyclic DSS	1.20 – 1.40	1.40 – 1.80

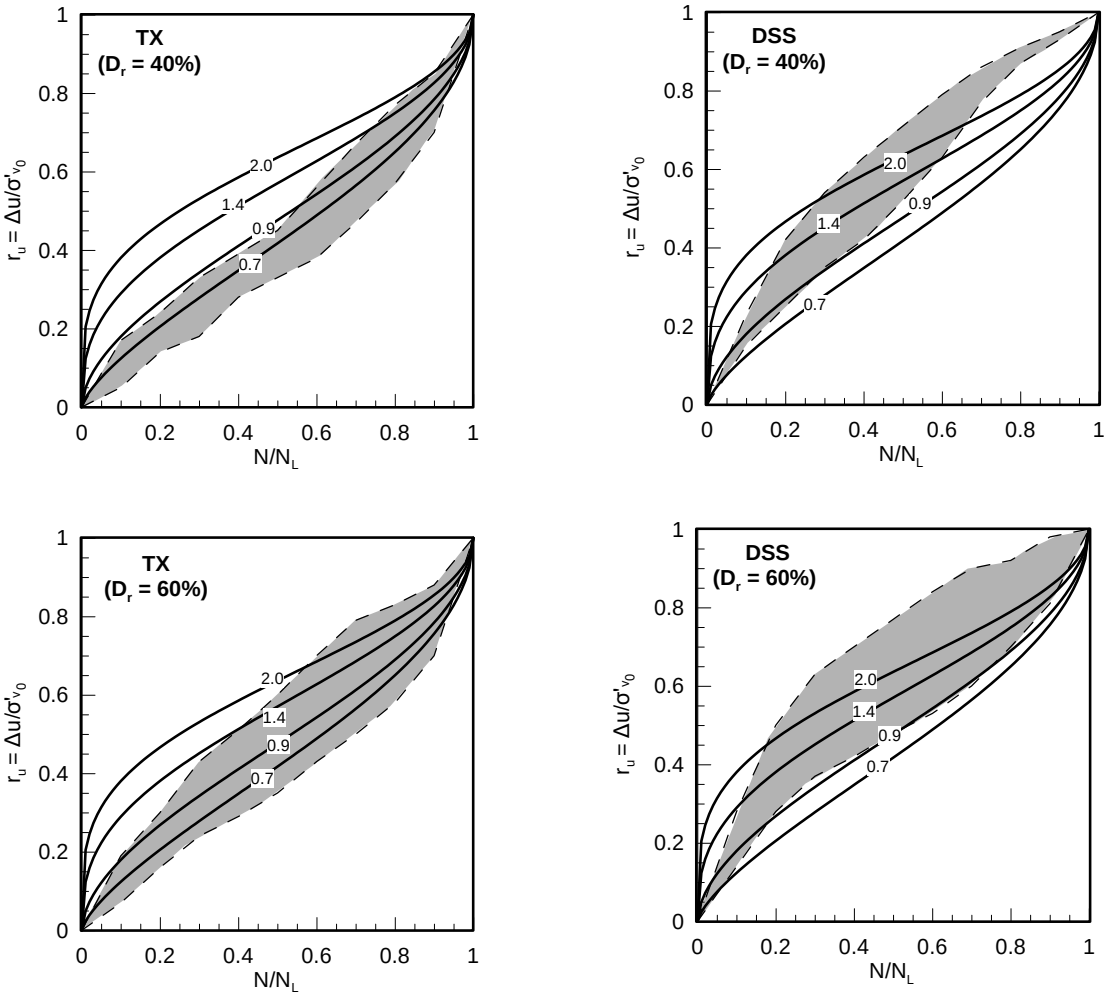

Figure 5.3: Comparison of experimental liquefaction curves from VELACS testing program and analytical solution for various A values.

5.2.2 "X-SOILS" laboratory test results

The second set of laboratory test results is taken from the research program "*X-SOILS: Foundations in seismically sensitive soils undergoing strong earthquake motions*"[2] and concerns the series of undrained cyclic torsional tests on hollow specimens coordinated by Associate Professor of N.T.U.A. V. Georgiannou. The tests were performed on sand M31 with four different values of Fines Content (0, 5, 10, and 15%) and at three different levels of consolidation stress (50, 100 and 300kPa). The specific gravity was found equal to G_s = 2.65 for the clean sand, equal to G_s = 2.66 for the non-plastic silt (NP) and the grain size distribution curve for the two soil formations is presented in **Figure 5.4.** Each specimen was tested under a harmonic excitation with constant amplitude of shear stress and loading cycle period equal to T = 10sec until liquefaction. Detailed information about each test is provided in **Table 5.3**. Note that all these tests were conducted under isotropic initial consolidation stresses (i.e. K_o = 1) and in this respect, they are similar to cyclic triaxial liquefaction tests.

Considering initial liquefaction, when shear strain γ exceeds ±1%, the number of cycles to liquefaction N_L was determined for all tests. Moreover, given the period of each loading cycle, all intermediate cycles were determined and the excess pore pressure ratio was then plotted against the N/N_L ratio, in the same format as the previous laboratory test results from the VELACS project. **Figure 5.5** summarizes the aforementioned plots, where tests are grouped according to the consolidation stress and the Fines Content. In the same plots, *Equation 5.1* is also added for different A values, which best fit the experimental curves.

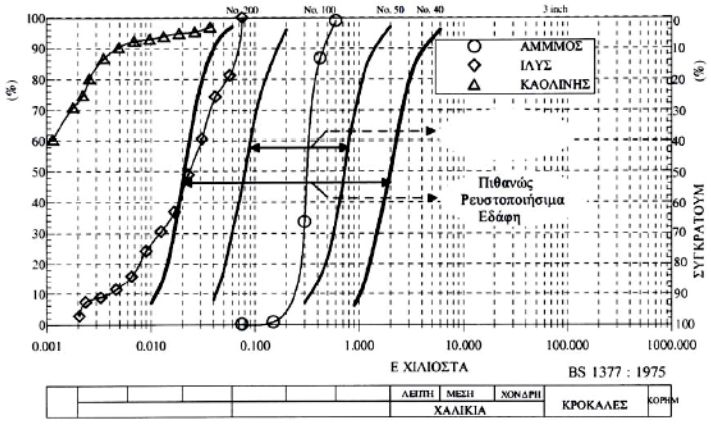

Figure 5.4: Grain size distribution curves for the M31 sand and the Non-Plastic silt used in X-SOILS laboratory testing program.

[2] The "X-SOILS: Foundations in seismically sensitive soils undergoing strong earthquake motions" program was funded from the European Union and the General Secretariat for Research and Technology (GSRT)

The outcome from the above analysis, in terms of the resulting A values, is summarized in **Table 5.4.** It now becomes clear that A equals 0.7 only for the clean sand specimens under the lowest consolidation stress of 50kPa. An increase in the consolidation stress leads to an increase in the value of A, up to twice the value of 0.7, which was initially proposed by De Alba et al. (1974). The fines content (F.C.) appears to influence the A value, in a less consistent trend. At low consolidation stress (50kPa) an increase in the fines content (F.C. = 0 ÷ 15%) leads to an increase in the A value. On the contrary, at large consolidation stresses (100 & 300kPa) a corresponding increase leads to a decrease in the obtained A values.

Table 5.3: Cyclic torsional tests performed at N.T.U.A.

Test Number	Initial Height (mm)	Fines Content - F.C. (%)	Initial void ratio	Consolidation stress (kPa)	Dr (%)	Final Height (mm)	Final void ratio
CY-SH1	138.210	0	0.650	300	65	138.04	0.631
CY-SH3	136.963	0	0.685	300	54	136.833	0.631
CY-SH4	136.703	0	0.678	50	57	136.693	0.675
CY-SH5	136.446	0	0.637	50	69	136.406	0.634
CY-SH6	136.576	0	0.647	50	66	136.556	0.645
CY-SH7	137.353	0	0.641	100	68	137.323	0.635
CY-SH8	137.466	0	0.652	100	65	137.396	0.646
CY-SH9	137.350	0	0.673	100	58	137.29	0.666
CY-SH10	140.256	0	0.674	100	58	140.206	0.667
CY-SH11	137.806	5	0.654	300	-	137.586	0.639
CY-SH12	138.173	5	0.650	300	-	137.933	0.636
CY-SH13	137.323	5	0.631	300	-	137.123	0.619
CY-SH14	137.560	5	0.634	300	-	137.41	0.62
CY-SH15	138.843	5	0.655	50	-	138.843	0.654
CY-SH16	139.646	5	0.712	50	-	139.646	0.709
CY-SH17	139.513	5	0.691	50	-	139.463	0.697
CY-SH18	137.110	5	0.658	100	-	137.06	0.651
CY-SH20	138.046	5	0.667	100	-	138.006	0.66
CY-SH21	136.650	5	0.671	100	-	136.6	0.659
CY-SH24	140.196	15	0.686	300	-	139.966	0.665
CY-SH25	140.180	15	0.723	300	-	139.93	0.7
CY-SH26	139.643	15	0.690	300	-	139.443	0.675
CY-SH28	140.096	15	0.716	100	-	139.996	0.709
CY-SH29	138.730	15	0.663	100	-	138.67	0.653
CY-SH30	137.760	15	0.702	50	-	137.75	0.7
CY-SH35	140.360	10	0.697	300	-	140.1	0.654
CY-SH36	130.167	10	0.648	300	-	129.832	0.631
CY-SH40	132.968	10	0.721	100	-	132.926	0.716

Table 5.4: Typical A values for the N.T.U.A. laboratory test results

Consolidation Stress (kPa)	A Values		
	F.C. 0%	F.C. 5%	F.C. 10 - 15%
50	0.70	0.80	1.00
100, 300	1.20 – 1.40	1.10 – 1.20	0.80 – 1.00

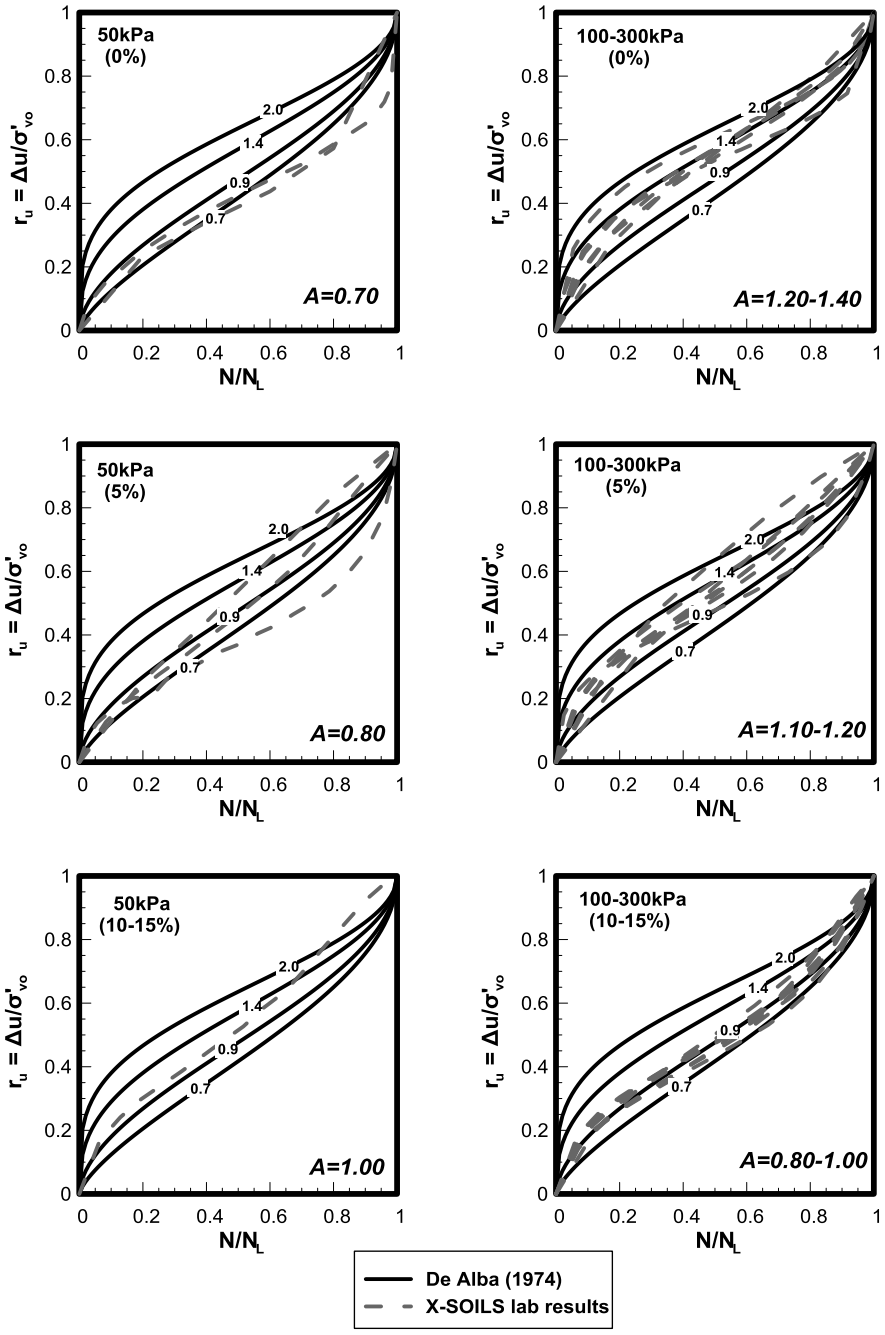

Figure 5.5: Comparison between X-SOILS laboratory liquefaction curves and analytical solution for different A values.

5.3 Investigation of the effect of A on the designparameters of gravel drains

The effect of A on the design of gravel drains is parametrically investigated with the revised method by Bouckovalas et al. (2009) and compared to the Seed & Booker (1977) theory. Both methodologies were programmed in Mathematica (Wolfram Research Inc) allowing the reproduction of the initial design charts by Seed & Booker (1977), as well as the simulation of the revised methodology of Bouckovalas et al. (2009). The overall effect of A was examined with respect to the drain spacing ratio a/b, the maximum excess pore pressure ratio r_{umax}, and the replacement coefficient α_s.

5.3.1 Effect of A on the existing design charts

The design charts proposed by Bouckovalas et al. (2009), for A = 0.70, were regenerated for the new A value of 1.40. For this computation, both initial and boundary conditions were kept identical to those originally introduced by the authors, while the basic problem parameters are summarized in the following **Table 5.5.**

Table 5.5: Basic problem parameters used in the analysis

Horizontal soil permeability k_s (m/sec)	10^{-4}
Initial vertical effective stress σ'_v (kPa)	100
Empirical parameter A	0.70 & 1.40
Coefficient of soil compressibility m_v (m^2/kN)	5×10^{-5}
Gravel drain radius a	0.4

The modified design charts are computed for four levels of seismic motion, expressed through the N/N_L ratio and six values for the dimensionless time factor T_{ad}. More specifically, for a given T_{ad} value, the basic differential equation is analytically solved for an initial a/b value of 0.001 and the procedure is repeated at an interval of 0.005 until the desired range of $0 \leq a/b \leq 0.5$ is covered. At each step, the maximum excess pore pressure ratio is tracked and stored along with the corresponding a/b value in the form of a table. Because this computation is rather complicated, the procedure is repetitive and requires numerous steps to cover the desirable range for the a/b design parameter ($0 \leq a/b \leq 0.5$). To visibly demonstrate the effect of A on the design charts, both sets of diagrams, for A = 0.70 and

1.40 are plotted together in **Figure 5.6**, for N_{eq}/N_L ratio from 1 to 4 and all six T_{ad} values (2, 10, 25, 50, 100 and 200).

It appears from **Figure 5.6**, that A significantly affects the design charts. In particular, for large $r_{u,max}$ values (greater than about 0.35 for all cases), a reduction in the T_{ad} time factor leads to a distinct reduction in the a/b ratio, resulting in a sparser grid of gravel drains. On the contrary, smaller $r_{u,max}$ values lead to an increase in the a/b ratio, thus resulting in a denser grid of gravel drains. The previous effect is reinforced when N_{eq}/N_L ratio increases from 1 to 2, while for values greater than 2, no further offset is noticed. Overall, considering a design range of $r_{u,max}$ between 0.30 ÷ 0.50, it is concluded that A values greater than 0.70, introduce a less conservative approach to the design of gravel drains.

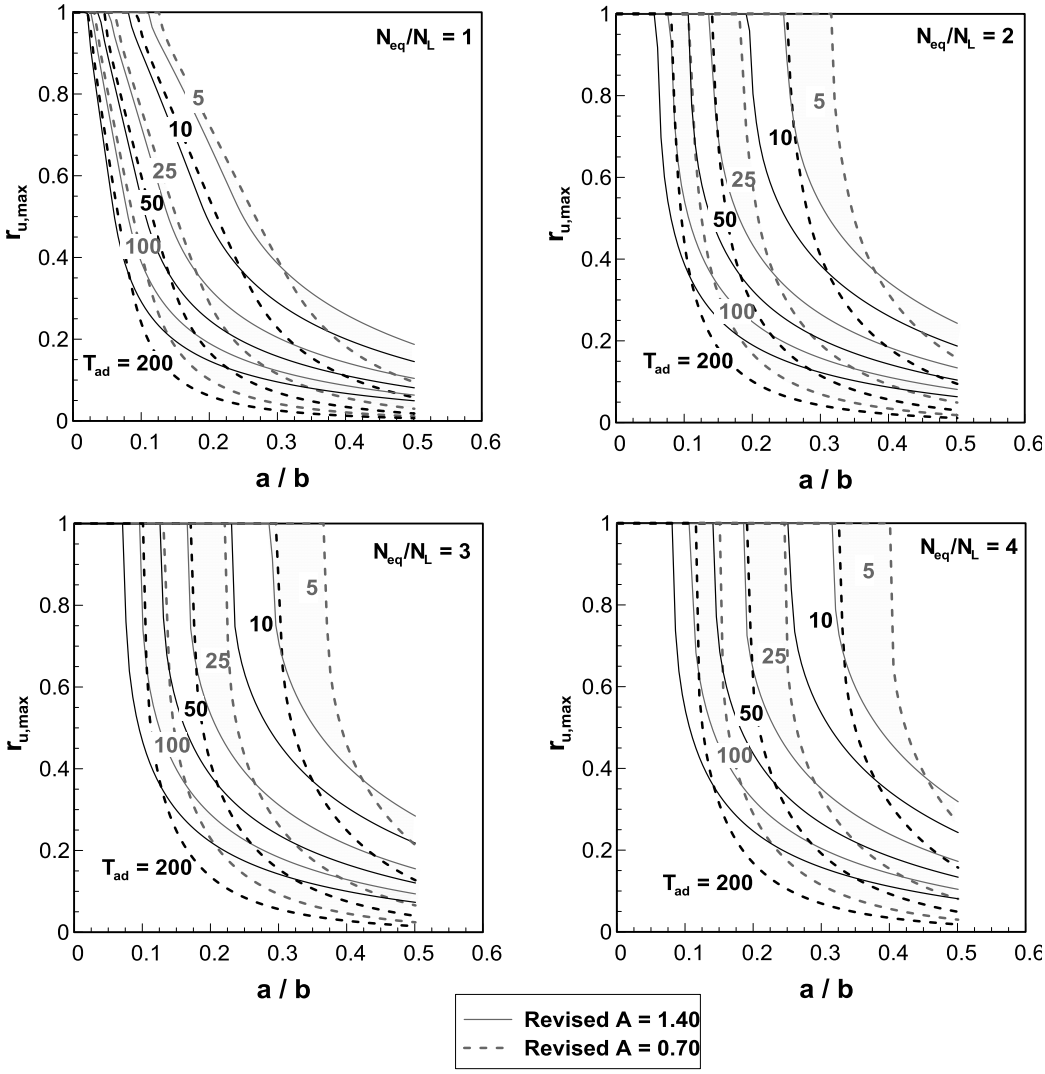

Figure 5.6: Effect of A on the design charts proposed by the revised method by Bouckovalas et al. (2009).

The effect of A is further evaluated through the comparison between the Seed & Booker (1977) design charts for A = 0.70 and the revised charts by Bouckovalas (2009) for A = 1.40, presented in **Figure 5.7**. The above charts concern values of N_{eq}/N_L ratio from 1 to 4 and T_{ad} = 5 ÷ 200. The observation of the two sets of curves reveals the over-conservatism of the Seed & Booker (1977) theory, given the greater a/b ratio, which is consistently obtained for the same $r_{u,max}$ value. This effect becomes even more intense at increased N_{eq}/N_L ratios, causing a reduction in the a/b ratio, leading to a sparser gravel drain grid, of up to 20%, for a common $r_{u,max}$ design value of 0.5, N_{eq}/N_L = 2 and T_{ad} = 5. Note that for N_{eq}/N_L > 2 there is practically no further improvement in the curve offset, therefore the effect of the intensity of the seismic motion is rather limited beyond this threshold. Paradoxically, for $r_{u,max}$ values bellow 0.30, the previously described picture is reversed and the revised design curves by Bouckovalas et al. (2009) for A = 1.40 result in a denser grid. Such low $r_{u,max}$ values though, are not commonly used in design.

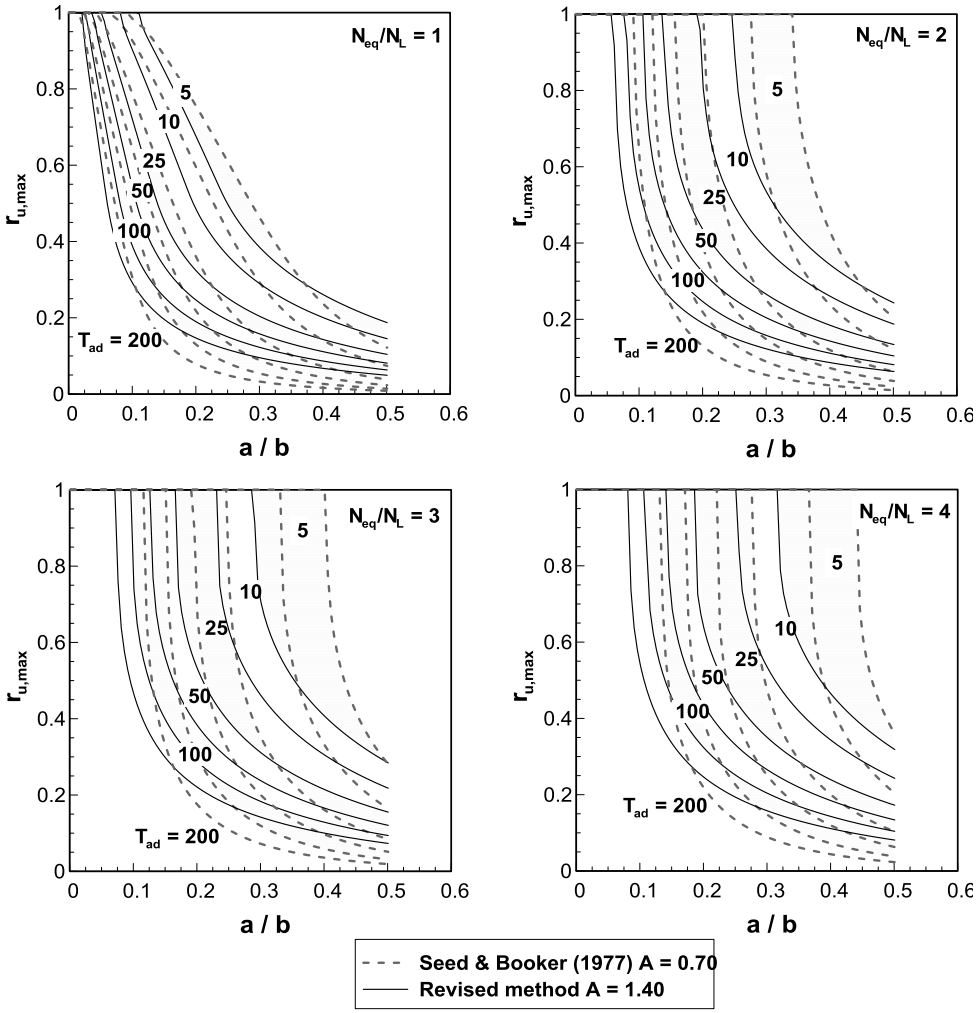

Figure 5.7: Comparative evaluation of the Seed & Booker (1977) and the revised method [Bouckovalas et al. (2009)] design charts.

5.3.2 Effect of A on the allowable excess pore pressure ratio r_{umax}

Proceeding to the effect of A on the excess pore pressure ratio, the $r_{u,max}$ predictions by Bouckovalas et al. (2009) for A = 0.70 and 1.40 are plotted against the a/b ratio for N_{eq}/N_L=1 & 2 and T_{ad} = 5÷200 and presented in **Figure 5.8**. For N_{eq}/N_L = 1, the $(r_{u,Rev.})_{A=1.40}/(r_{u,Rev.})_{A=0.70}$ ratio reaches a minimum at about unity and increases rapidly above a certain a/b threshold, which largely depends on the T_{ad} dimensionless factor. For strong seismic motions (i.e. N_{eq}/N_L=2) the corresponding ratio under examination reaches a minimum at around 0.5, then following a similar pattern to the previous case for increasing values of a/b and decreasing T_{ad}.

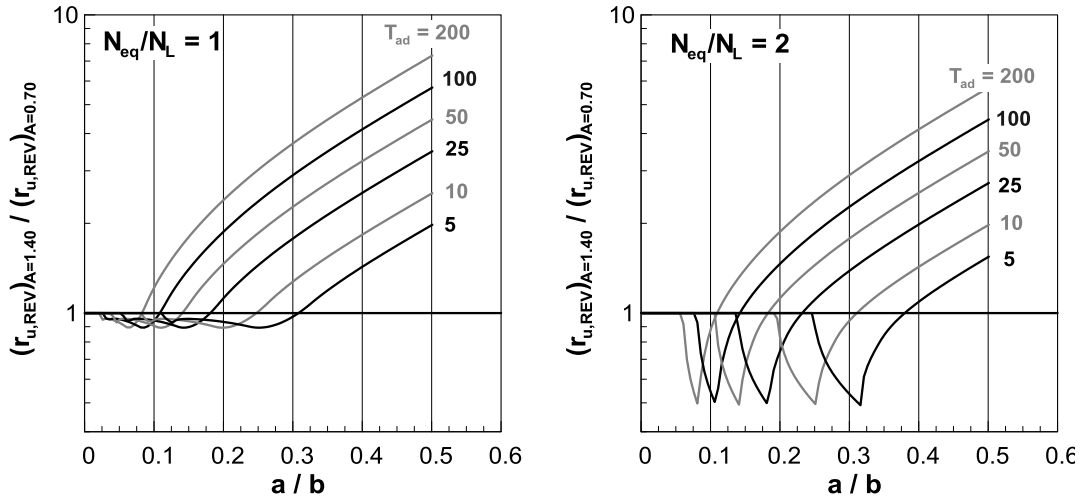

Figure 5.8: Effect of A = 1.40 on the $r_{u,max}$ value, predicted by Bouckovalas et al. (2009), with regard to the gravel drain spacing a/b.

The effect of A on the excess pore pressure ratio is further evaluated by comparing the predictions by Bouckovalas et al. (2009) to the corresponding r_u values predicted by the Seed & Booker theory (1977). The ratio of $(r_{u,Rev.})_{A=1.40}/(r_{u,S\&B.})_{A=0.70}$ is plotted against a/b for N_{eq}/N_L equal to 1 & 2 and T_{ad} = 5 ÷ 200 as presented in **Figure 5.9**. Overall, a similar behavior to **Figure 5.8** is noted, with the main conclusion being that r_u depends mainly on the intensity of the seismic motion expressed through the N_{eq}/N_L term and secondarily on the a/b ratio or the dimensionless factor T_{ad}.

The effect of A on the excess pore pressure ratio becomes even more apparent when eliminating all other parameters involved in the comparison, such as the distance between the drains (a/b ratio) and the T_{ad} factor. For this purpose, in **Figure 5.10** the ratio of the r_u predictions of the revised method introduced by Bouckovalas et al. (2009), for A equal to

0.70 and 1.40, $[(r_{u,Rev.})_{A=1.40}/(r_{u,Rev.})_{A=0.70}]$ is plotted against the excess pore pressure ratio for A equal to 1.40 $(r_{u,Rev.})_{A=1.40}$, taking into account all four levels of seismic motion intensity ($N_{eq}/N_L = 1 \div 4$). The r_u range used in design, (0.25 ÷ 0.50), is indicated by the shaded region.

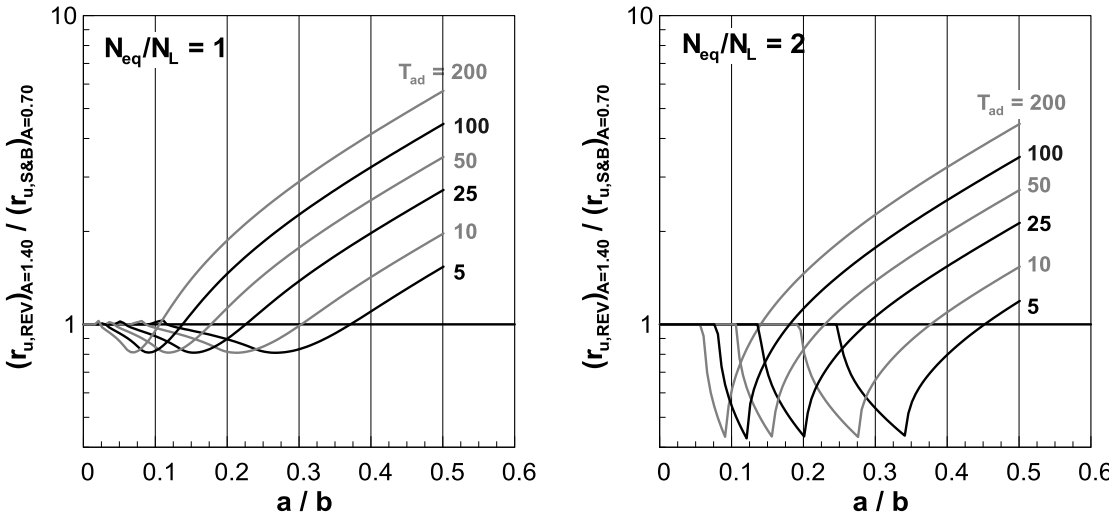

Figure 5.9: Effect of A = 1.40 on the $r_{u,max}$ value, predicted by Bouckovalas et al. (2009), and Seed & Booker (1977) with regard to the gravel drain spacing a/b.

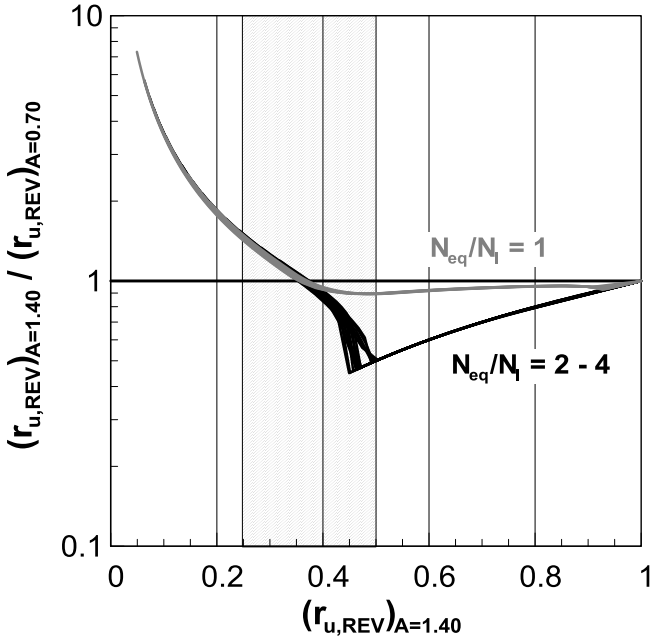

Figure 5.10: Deviation of the excess pore pressure ratio predictions by Bouckovalas et al. (2009) for A = 0.70 and 1.40.

The ratio under consideration $[(r_{u,Rev.})_{A=1.40}/(r_{u,Rev.})_{A=0.70}]$ within the shaded region of interest, is slightly greater than unity for all N_{eq}/N_L values, while the maximum reduction occurs for r_u values between 0.40 and 0.50, which consist the most commonly used values in design. More specifically, in the range of $0.25 \leq (r_{u,Rev.})_{A=1.40} \leq 0.35$ the pore pressure values predicted by Bouckovalas et al. (2009) applied for A = 1.40 $[(r_{u,Rev.})_{A=1.40}]$ are greater up to 1.5 times than the equivalent ones when A equals 0.70. $[(r_{u,Rev.})_{A=0.70}]$, while their ratio remains independent of the intensity of ground motion (N_{eq}/N_L ratio). In the range of $0.35 \leq (r_{u,Rev.})_{A=1.40} \leq 0.50$ the pore pressure values predicted by Bouckovalas et al. (2009) for A = 1.40 $[(r_{u,Rev.})_{A=1.40}]$ are lower than the equivalent ones for A = 0.70 and reach a minimum equal to $[(r_{u,Rev.})_{A=1.40}/(r_{u,Rev.})_{A=0.70}] = 0.9$ for $N_{eq}/N_L = 1$ and 0.5 when $N_{eq}/N_L = 2 \div 4$. Note that a reduction in the ratio under consideration $[(r_{u,Rev.})_{A=1.40}/(r_{u,Rev.})_{A=0.70}]$, implies that for the same a/b ratio, design charts for A = 1.40 lead to a lower excess pore pressure generation. Moreover, all curves for N_{eq}/N_L greater that 2 practically coincide, allowing the reduction of the initially four design charts to two.

A similar comparison is attempted in **Figure 5.11** between the excess pore pressure ratio predicted by the Seed & Booker theory (1977) for A = 0.70 and the corresponding one from the revised methodology for A = 1.40. The ratio of $(r_{u,Rev.})_{A=1.40}$ over $(r_{u,S\&B.})_{A=0.70}$ is plotted with respect to the $(r_{u,Rev.})_{A=1.40}$ for all four N_{eq}/N_L categories. Within the shaded region of interest $[0.25 \leq (r_{u,Rev.})_{A=1.40} \leq 0.50]$ the pore pressure values for the Bouckovalas et al. (2009) method, applied for A = 1.40 $[(r_{u,Rev.})_{A=1.40}]$, are lower than the equivalent ones when A equals 0.70 in the Seed & Booker theory $[(r_{u,Rev.})_{A=0.70}]$, thus resulting in lower excess pore pressures for the revised methodology considering the same grid configuration. It is also clear that the greater excess pore pressure ratio reduction (up to 60%) occurs for $N_{eq}/N_L = 2 \div 4$, also pointing out the detachment of the excess pore pressure built up from seismic motions stronger than $N_{eq}/N_L = 2$.

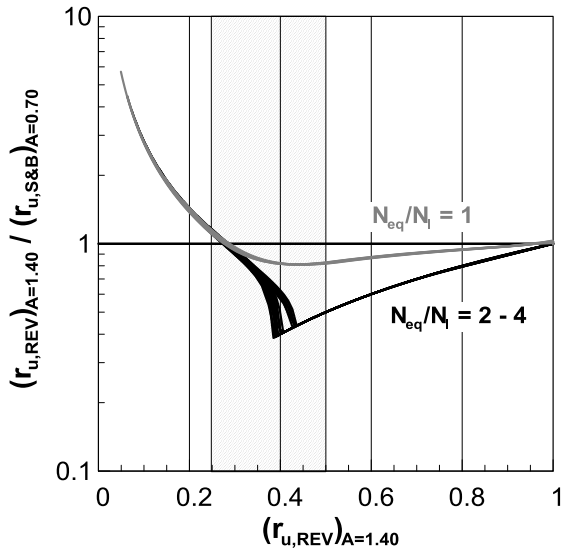

Figure 5.11: Deviation of the excess pore pressure ratio predictions by Bouckovalas et al. (2009) for A = 1.40 and Seed & Booker (1977) for A = 0.70.

5.3.3 Effect of A on the replacement coefficient α_s.

Following the comparisons described previously, the effect of A on the replacement coefficient α_s is examined for both methodologies, for the case of a triangular grid, associating α_s to the distance between the drains as shown below:

$$\alpha_s = 0.91\times (a/b)^2 \qquad 5.2$$

where a = the radius of the gravel drain

b = the center-to-center distance between two consecutive drains

The analysis is performed for a maximum excess pore pressure (r_u) value equal to 0.50, which consists the most commonly used limit in current practice and four levels of seismic motion intensity rendering $N_{eq}/N_L = 1 \div 4$.

In **Figure 5.12a,** the replacement coefficient α_s predicted by the revised method applied for A equal to 0.7 and 1.40 is plotted against the dimensionless time factor T_{ad} for $r_{u,max}$ = 0.50 and $N_{eq}/N_L = 1 \div 4$. It is concluded that, for a given T_{ad} value, the solid curves for A = 1.40 result in lower α_s values. For example, for T_{ad} = 5, A = 1.40 and N_{eq}/N_L = 4 the design r_u value of 0.50 is satisfied, in the case of A = 1.40, at α_s equal to around 0.13, rendering an a/b ratio of 0.38, whereas the use of A = 0.70 requires a ratio of about 0.165 (that is a/b = 0.43), this being translated into a 19% reduction in terms of α_s.

The above conclusion is fully clarified in **Figure 5.12b**, where the ratio of $(\alpha_{s,\,Rev.})_{A=1.40}$ over $(\alpha_{s,\,Rev.})_{A=0.70}$, is plotted with respect to the dimensionless time factor T_{ad}. The examined ratio is

constantly lower than unity, for all four N_{eq}/N_L levels, and follows a reducing trend for increasing T_{ad} values. Therefore, the use of A = 1.40 results in lower α_s values, allowing the configuration of a less dense gravel drain grid, hence leading to a more economical design.

The following two figures present an equivalent comparison between the revised method's predictions for A = 1.40 and the Seed & Booker (1977) theory predictions for A = 0.70. In **Figure 5.13a** the replacement coefficient α_s is plotted against the dimensionless factor T_{ad} for a maximum excess pore pressure ratio of 0.50 and $N_{eq}/N_L = 1 \div 4$. The reduction in the required α_s for the same T_{ad} time factor is more than evident, and more importantly, the plotted curves present a faster reducing trend when compared to **Figure 5.12a**. Following the previous example, according to the revised method, for T_{ad} = 5 A = 1.40 and $N_{eq}/N_L = 4$, the design value of 0.50 is satisfied at a replacement ratio α_s equal to 0.13, rendering a/b = 0.38. Accordingly, the traditional Seed & Booker (1977) theory requires a ratio of about 0.20 rendering a/b = 0.47, this being translated into a 35% reduction in terms of α_s for a triangular grid. The above estimate is significantly higher than the equivalent reduction evaluated in **Figure 5.12a**, providing solid evidence on the over-conservatism of the Seed & Booker (1977) theory. In **Figure 5.13b**, the ratio of $(\alpha_{s,\,Rev.})_{A=1.40}$ over $(\alpha_{s,\,S\&B})_{A=0.70}$, is plotted with respect to the dimensionless time factor T_{ad}. The examined ratio is constantly lower than unity, for all four N_{eq}/N_L levels, and follows a reducing trend at increasing T_{ad} values as was also commented in **Figure 5.12b**. Note that the reducing trend in this case is much faster than in **Figure 5.12b**, highlighting again the conservative approach in the design of gravel drains proposed by Seed & Booker (1977).

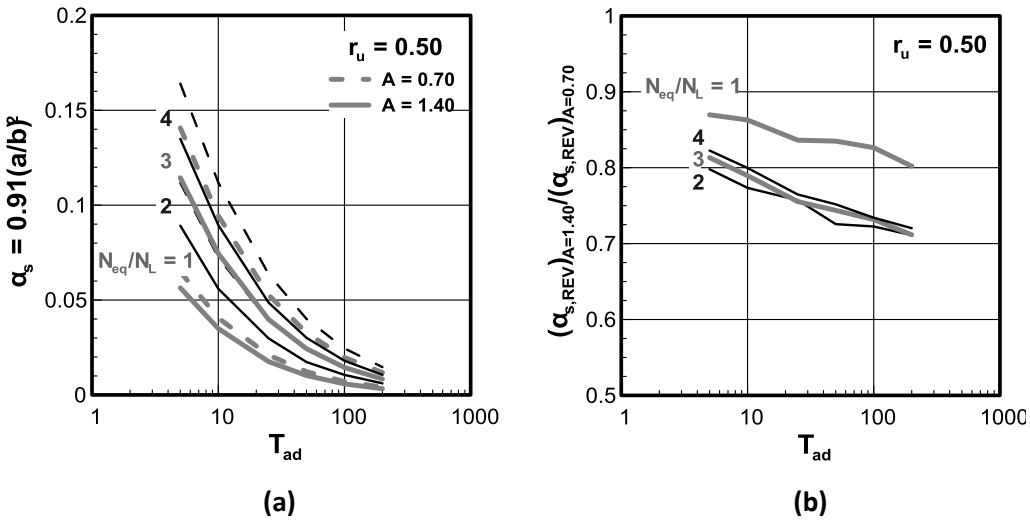

Figure 5.12: Variation of the replacement coefficient α_s predicted by Bouckovalas et al. (2009) with respect to T_{ad} time factor for A = 0.70 & 1.40, $r_{u,max}$ = 0.50, N_{eq}/N_L=1 ÷ 4.

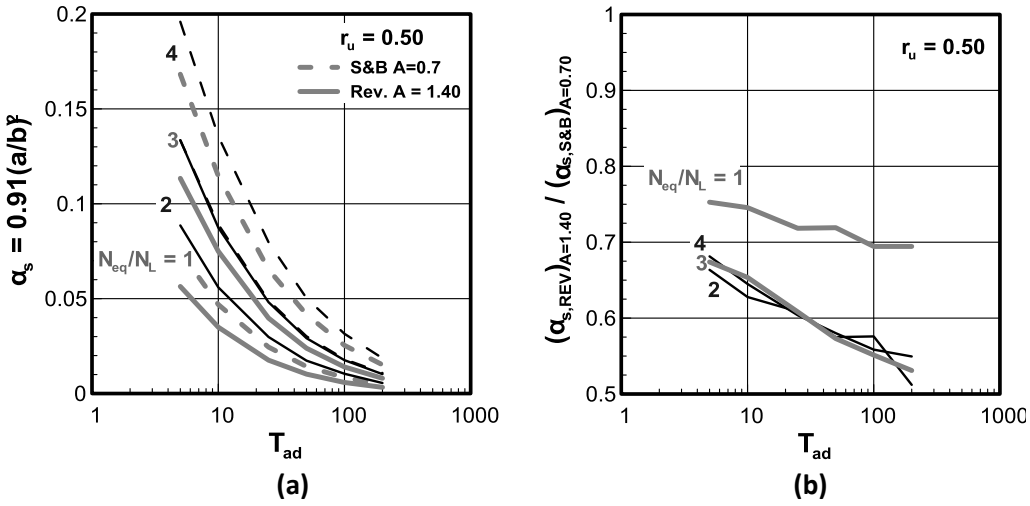

Figure 5.13: Variation of the replacement coefficient α_s predicted by Bouckovalas et al. (2009) and Seed & Booker (1977), with respect to T_{ad} time factor for A = 0.70 & 1.40, $r_{u,max}$ = 0.50, N_{eq}/N_L = 1 ÷ 4.

5.4 Designing for different A values

As pointed out in the previous paragraph, the effect of A cannot be ignored in the design of gravel drains. For that reason, the existing design charts could either be modified or new charts will be generated, incorporating the role of A in the configuration of the gravel drain grid. The modification of the existing design charts was initially attempted based on the allowable excess pore pressure ratio ($r_{u,max}$) and then with regard to the rate of the excess pore pressure generation (($\partial r_u/\partial N$). In the end, given the inadequacy of both attempts new design charts are formulated and incorporated in the revised method proposed by Bouckovalas et al. (2009).

5.4.1 Modification based on the predetermined excess pore pressure ratio (PHRI, 1997)

In the guidelines issued by the Port Harbor Research Institute (1997) the equivalent time to attain liquefaction under undrained conditions t_l is corrected with respect to the excess pore pressure characteristics of the available laboratory tests. In summary, the corrected time is given as:

$$t_l = \frac{(N_u / N_L)}{(N_O / N_L)} \times t_l^* \qquad 5.3$$

where t_l = the equivalent time until liquefaction after the correction

N_u/N_L = the N_{eq}/N_L value corresponding to the allowable excess pore pressure ratio ($r_{u,\ design}$) in the excess pore pressure generation curve obtained from the laboratory test

N_o/N_L = the N_{eq}/N_L value obtained from the pore pressure generation curve from De Alba et al. (1974), where A = 0.70.

Based on the above methodology, for a given allowable excess pore pressure ratio, the liquefaction curve by De Alba et al. (1974) for A^* = 0.70 is modified to fit the experimentally constructed curve, in which A is rarely equal to 0.70, in order to specify a new corrected N_{eq}/N_l value.

Following a similar conception, the existing design charts by Seed & Booker (1977) and Bouckovalas et al. (2009) are modified according to the procedure described below:

1. The allowable excess pore pressure ratio $r_{u,max}$ and the suitable A ($\neq$ 0.70) value best fitting the laboratory data are selected.
2. Given the equivalent number of loading cycles (N_{eq}), the intensity of the seismic motion (i.e. N_{eq}/N_L = 1 - 4) the number of cycles required to liquefaction N_L is determined.
3. The parameters (A and N_L), specified in the previous steps, are now used to determine the number of loading cycles, N, rendering the design $r_{u,max}$ value (from Step 1) through *Equation 5.4* [Seed, Martin & Lysmer (1975)].

$$r_{u,\max} = \frac{2}{\pi}\sin^{-1}\left(\frac{N}{N_L}\right)^{1/2A} \leftrightarrow N = N_L \sin^{2A}\left(\frac{\pi}{2} r_{u,\max}\right) \qquad 5.4$$

4. The same procedure is followed for A^* = 0.70 and the previously determined N, rendering the equivalent number of loading cycles for liquefaction N_L^* for the same $r_{u,max}$ value, now solving *Equation 5.4* for N_L:

$$r_{u,\max} = \frac{2}{\pi}\sin^{-1}\left(\frac{N^*}{N_L}\right)^{1/2A} \leftrightarrow N_L^* = N \sin^{-2A}\left(\frac{\pi}{2} r_{u,\max}\right) \qquad 5.5$$

5. The design methods proposed by Seed & Booker (1977) and Bouckovalas et al. (2009) are solved analytically for A^* = 0.70 and the N_L^* value from step 4, and the two design curves are compared.

The above method was applied for a minimum and a maximum limit of excess pore pressure ratio, commonly encountered in design codes, i.e. $r_{u,max}$ = 0.25 and 0.50, A = 0.70 & 1.40, N_{eq} = 10 and N_{eq}/N_L = 1 & 2.

Application for $r_{u,max}$ = 0.25.- The initial liquefaction curves, for A equal to 0.70 and 1.40 respectively, are plotted in **Figure 5.14** with solid lines. For both N_{eq}/N_L = 1 and 2, the allowable $r_{u,max}$ limit determines the equivalent number of loading cycles N. The initial liquefaction curves for A = 0.70 are subsequently shifted, until they converge to the previously specified combination of N and allowable excess pore pressure ratio $r_{u,max}$. The corrected curves are outlined in the dashed lines and therefore, the equivalent N_{eq}/N_L^* ratio is also specified. The new N_{eq}/N_L^* value is used to analytically generate the design curves of $r_{u,max}$ as a function of the a/b ratio for both methodologies.

The results for the Seed & Booker (1977) theory are summarized in **Figure 5.15**, including the original and the modified design curves for T_{ad} = 10 and 50. It is observed that there is no apparent matching between the A = 1.40 design curve and the approximation for A^* = 0.70 and N_{eq}/N_L^* = 3.84. In fact, the modified curve results in a greater a/b ratio, thus in a less dense grid, than what is initially predicted for A = 1.40.

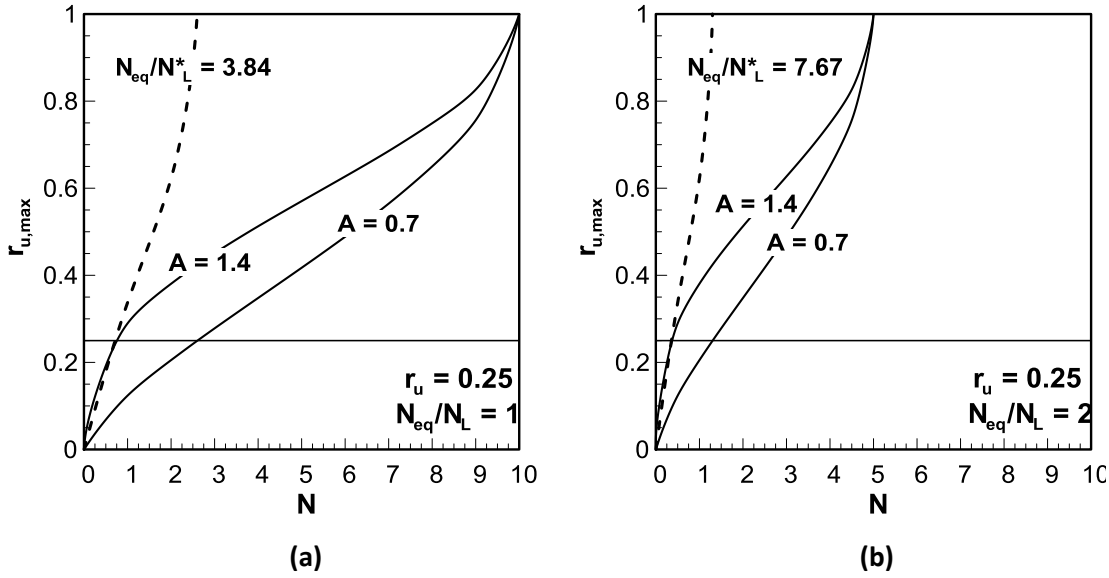

Figure 5.14: Initial and modified liquefaction curves for allowable excess pore pressure ratio $r_{u,max}$ = 0.25.

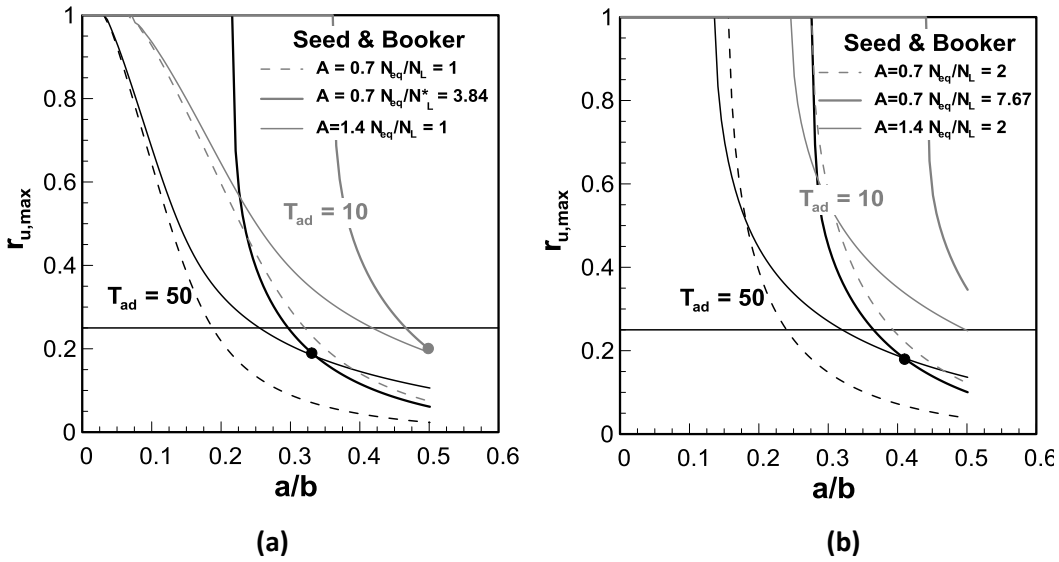

Figure 5.15: Exact (N_{eq}/N_L = 1,2) and modified (N_{eq}/N_L* = 3.84, 7.67 respectively) design curves for the Seed & Booker (1977) theory.

A similar behavior is observed in terms of replacement coefficients, α_s, considering a triangular grid. The correlation between the replacement coefficients for a triangular grid, when using the initial and the modified Seed & Booker (1977) design charts referred to earlier, is plotted on a one-to-one basis in **Figure 5.16a**, for a typical range of T_{ad} from 10 to 100. The values obtained with the modified design curve (noted as α_s^*) are greater by 25% than those obtained with the exact solution (noted as α_s). The convergence between the two replacement coefficient values is not satisfactory, as it is also apparent from **Figure 5.16b**, where the ratio of the α_s values for A = 1.40 over the modified values α_s^* (for A = 0.70 and N_{eq}/N_L^* = 3.84 & 7.67) is plotted with respect to α_s^*. The approximated replacement coefficients are consistently higher than the exact values for A = 1.40 and N_{eq}/N_L = 1 & 2.

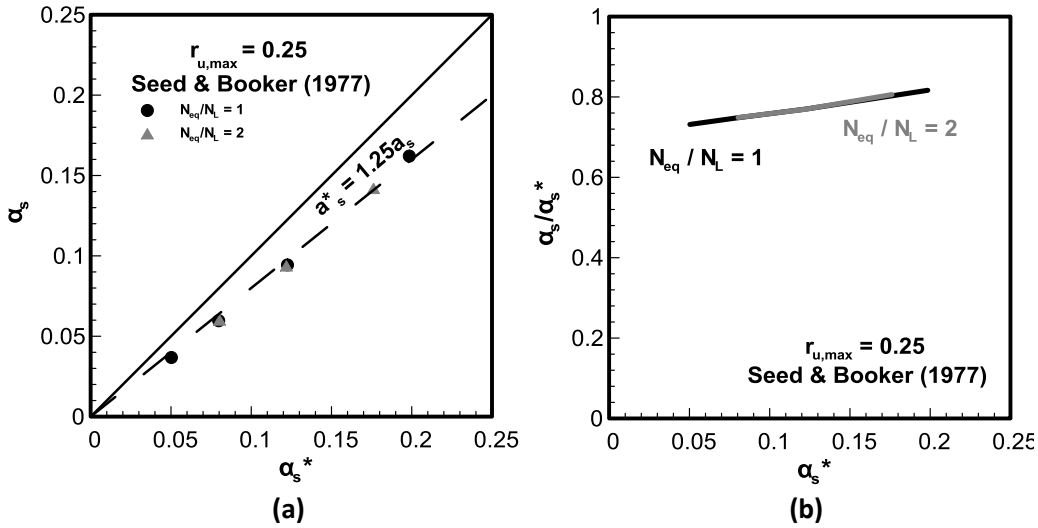

Figure 5.16: Effect of modified Seed & Booker (1977) design curves on the replacement coefficient α_s* for allowable $r_{u,max}$ = 0.25 and T_{ad} = 10, 25, 50, 100 and N_{eq}/N_L = 1 & 2.

Accordingly, the original and the modified design curves for the revised method by Bouckovalas et al. (2009) are presented in **Figure 5.17a&b**, for N_{eq}/N_L = 1 & 2 respectively. Also in this case there is no apparent convergence between the original and the approximated design charts in the initially set allowable excess pore pressure value, but in a much lower one. The effect of the above discrepancy is examined in terms of replacement coefficients, in **Figure 5.18a** & **b**, where it is noted that the modified solution can predict replacement coefficients of up to 65% greater than the exact ones.

Table 5.6 summarizes the predictions of the exact and modified design curves in terms of drain spacing (a/b) and replacement coefficients for four T_{ad} values and N_{eq}/N_L = 1 & 2 for both methodologies.

Therefore, the proposed approximation in the design charts, for such a low allowable excess pore pressure ratio, did not render the desired results, leading to conservative design.

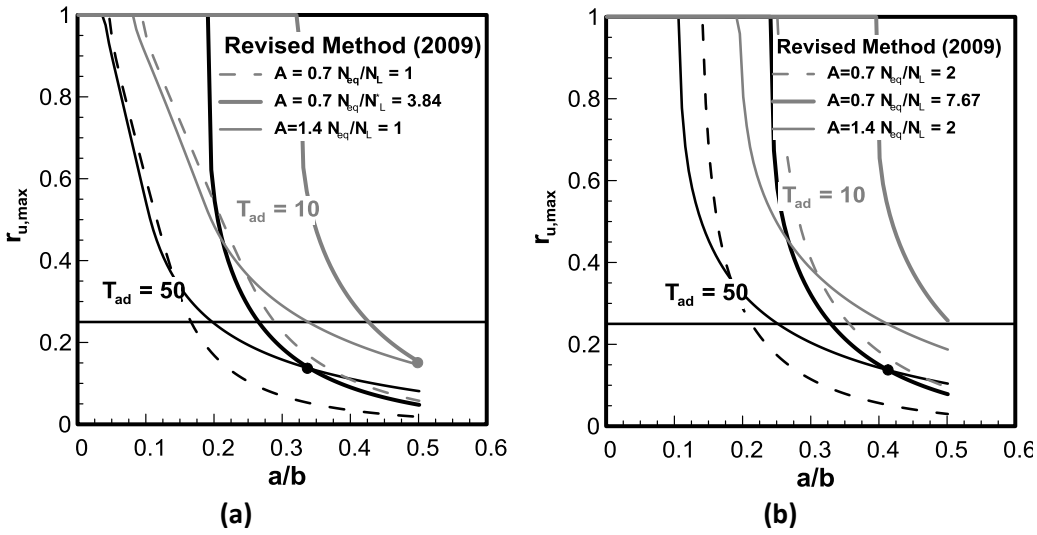

Figure 5.17: Exact (N_{eq}/N_L = 1,2) and modified (N_{eq}/N_L* = 3.84, 7.67 respectively) design curves for the Bouckovalas et al. (2009) revised method.

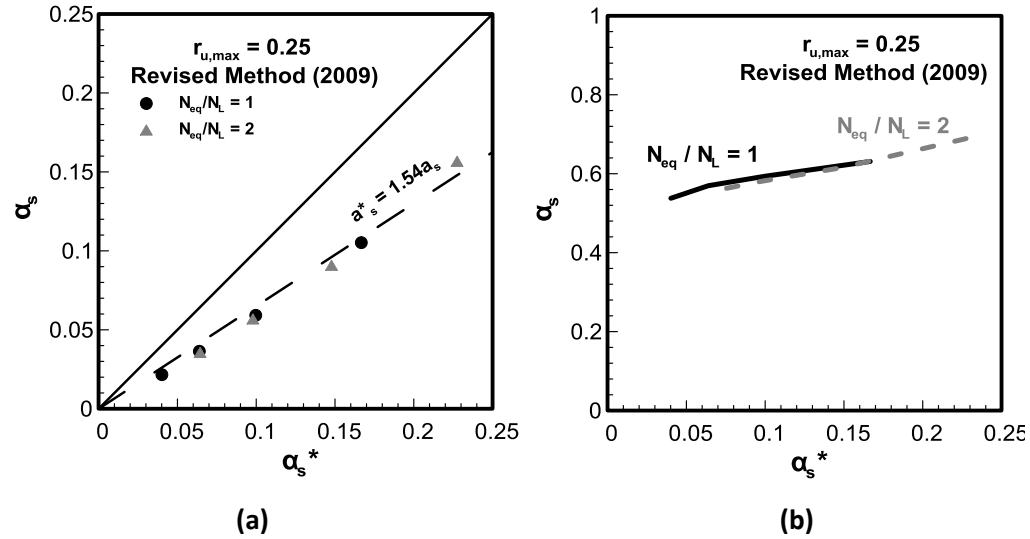

Figure 5.18: Effect of modified design curves by Bouckovalas et al. (2009) on the replacement coefficient α_s^* for allowable $r_{u,max}$ = 0.25 and T_{ad} = 10, 25, 50, 100 and N_{eq}/N_L = 1 & 2.

Table 5.6: Spacing ratios (a/b) and replacement coefficients for $r_{u,max}$ = 0.25.

T_{ad}	Seed & Booker (1977) $r_{u,max}$=0.25							
	N_{eq}/N_l = 1				N_{eq}/N_l = 2			
	A=1.4, N_l		A=0.7, N^*_l		A=1.4, N_l		A=0.7, N^*_l	
	a/b	a_s	a/b	a^*_s	a/b	a_s	a/b	a^*_s
10	0.422	0.162	0.467	0.198	0.500	0.228	0.500	0.228
25	0.322	0.094	0.367	0.123	0.395	0.142	0.440	0.176
50	0.256	0.060	0.296	0.080	0.321	0.094	0.366	0.122
100	0.201	0.037	0.235	0.050	0.257	0.060	0.297	0.080
T_{ad}	Revised Method, Bouckovalas et al. (2009) $r_{u,max}$=0.25							
	a/b	a_s	a/b	a^*_s	a/b	a_s	a/b	a^*_s
10	0.340	0.105	0.428	0.167	0.415	0.157	0.500	0.228
25	0.255	0.059	0.331	0.100	0.316	0.091	0.403	0.148
50	0.200	0.036	0.265	0.064	0.250	0.057	0.328	0.098
100	0.154	0.022	0.210	0.040	0.198	0.036	0.266	0.064

Application for $r_{u,max}$ = 0.50.- The previously described process was applied for an allowable excess pore pressure equal to 0.50, which is the most commonly used design limit. The original and modified liquefaction curves are presented in **Figure 5.19**, rendering N_{eq}/N_L^* = 1.62 and 3.25 respectively for initial N_{eq}/N_L values of 1 and 2.

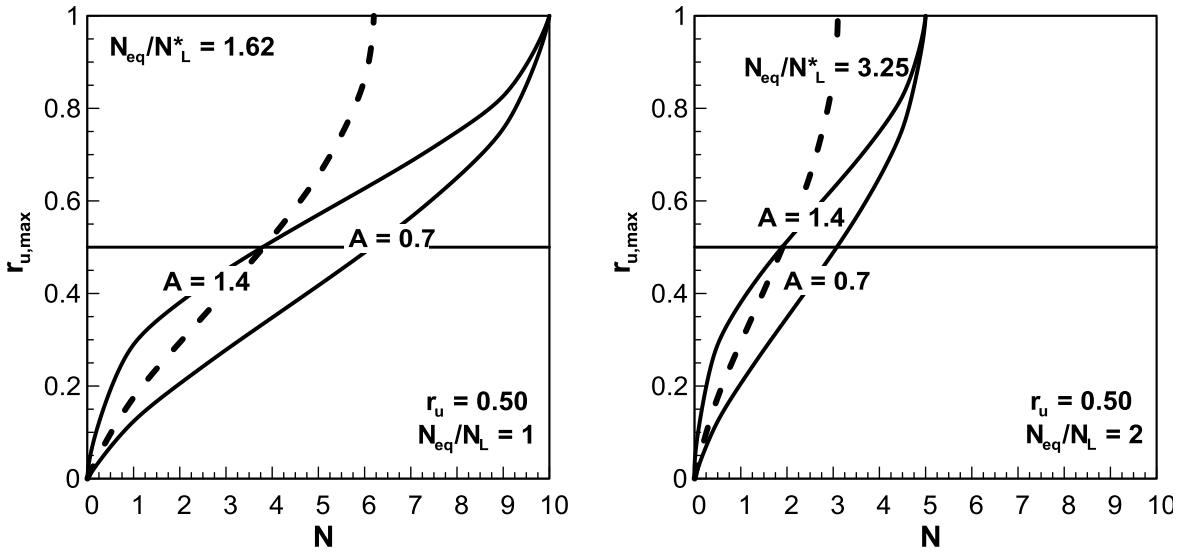

Figure 5.19: Initial and modified liquefaction curves for allowable excess pore pressure ratio $r_{u,max}$ = 0.50.

Consequently, the Seed & Booker (1977) theory for A = 0.70, A = 1.40 and all relevant N_{eq}/N_L values is analytically solved and the resulting design curves for T_{ad} = 10 and 50 are presented in **Figure 5.20a** & **b**. It is observed that the two design curves do not converge in the allowable $r_{u,max}$ design value, but in a much lower one. The modified curves generally result in greater a/b ratios thus in a more conservative approach.

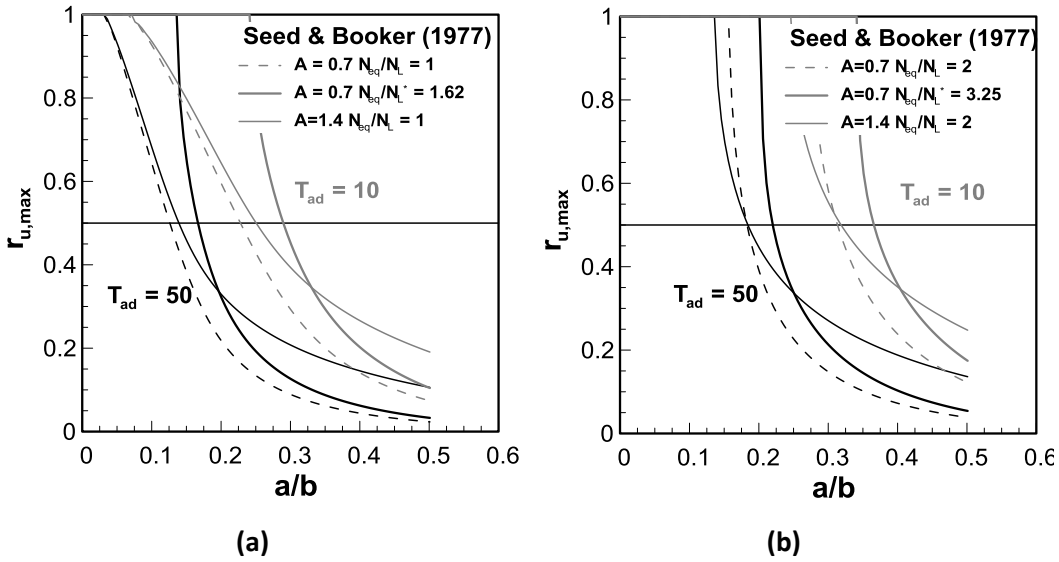

Figure 5.20: Exact (N_{eq}/N_L = 1,2) and modified (N_{eq}/N_L^* = 1.62, 3.25 respectively) design curves for the Seed & Booker (1977) theory.

The initial and modified design curves for the Bouckovalas et al. (2009) revised method are presented in **Figure 5.21**, where yet again the desired convergence is attained at much lower allowable excess pore pressure values. More importantly, the discrepancy between the two sets of design curves appears to be considerable enough when compared to the Seed & Booker (1977) theory.

In terms of replacement coefficients the previously described behavior does not vary much. **Figure 5.22** and **Figure 5.23** indicate that the modified design curves lead to an increase in the replacement coefficients ranging from 40 ÷ 80% for the Seed & Booker (1977) and Bouckovalas et al. (2009) method respectively. Moreover, the ratio of α_s over α_s^* is consistently below unity following a slightly increasing trend at increasing T_{ad} values. **Table 5.7** summarizes the predictions of the exact and modified design curves in terms of drain spacing (a/b) and replacement coefficients for four T_{ad} values and N_{eq}/N_L = 1 & 2 for both methodologies.

Overall, both applications, developed earlier, indicate that modifying the existing design charts with respect to the allowable excess pore pressure ratio $r_{u,max}$ in order to take into account A values greater than the traditional value of 0.70, does not provide satisfactory results. The modified design charts lead to more conservative spacing dimensions (a/b ratio) therefore are not recommended for further use.

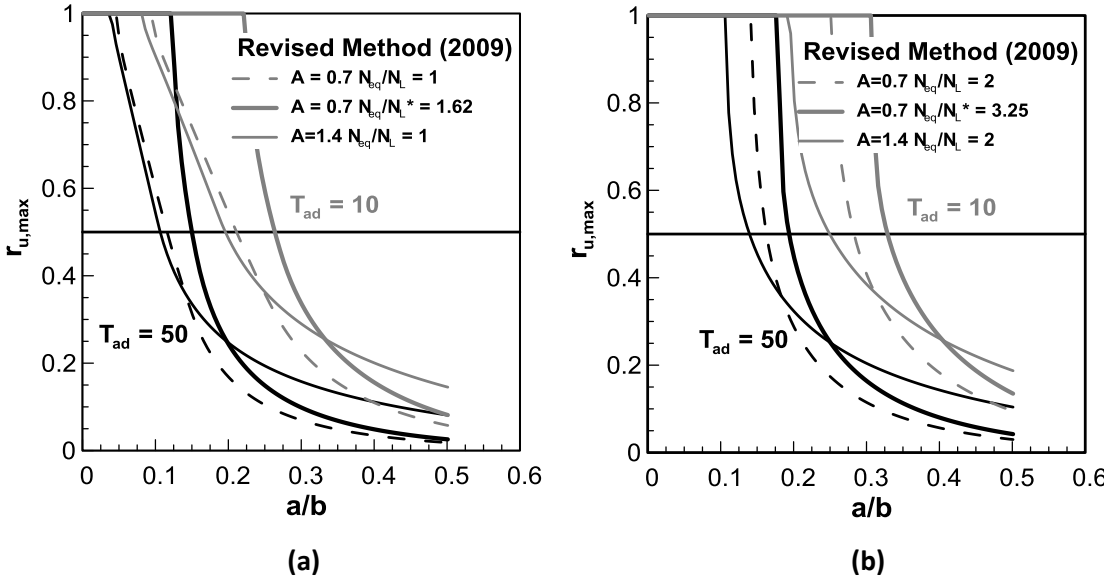

Figure 5.21: Exact (N_{eq}/N_L = 1,2) and modified (N_{eq}/N_L^* = 1.62, 3.25 respectively) design curves for the Bouckovalas et al. (2009) revised method.

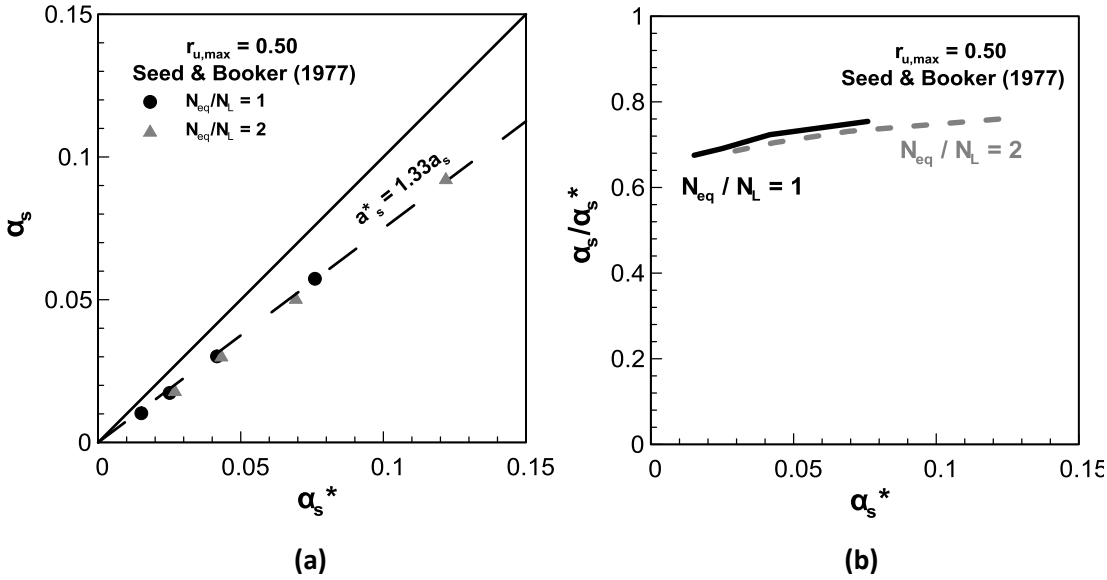

Figure 5.22: Effect of modified design curves by Bouckovalas et al (2009) on the replacement coefficient α_s* for an allowable $r_{u,max}$ = 0.50 T_{ad} = 10, 25, 50, 100 and N_{eq}/N_L = 1 & 2.

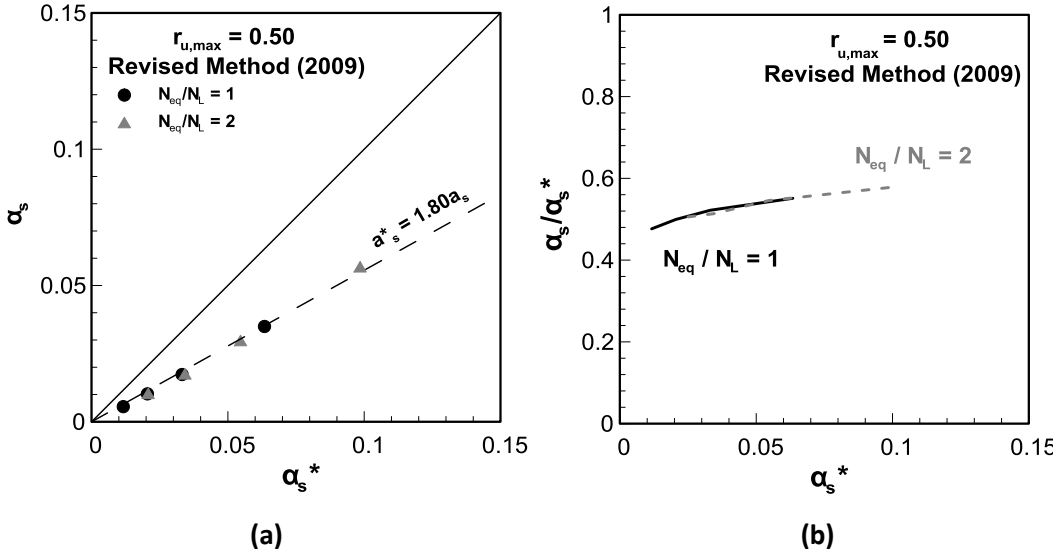

Figure 5.23: Effect of modified design curves by Seed & Booker (1977) on the replacement coefficient α_s^* for allowable $r_{u,max}$ = 0.50 T_{ad} = 10, 25, 50, 100 and N_{eq}/N_L = 1 & 2.

Table 5.7: Spacing ratios (a/b) and replacement coefficients for $r_{u,max}$ = 0.50

T_{ad}	Seed & Booker (1977) $r_{u,max}$=0.50							
	N_{eq}/N_l = 1				N_{eq}/N_l = 2			
	A=1.4, N_l		A=0.7, N^*_l		A=1.4, N_l		A=0.7, N^*_l	
	a/b	a_s	a/b	a^*_s	a/b	a_s	a/b	a^*_s
10	0.251	0.057	0.289	0.076	0.319	0.093	0.366	0.122
25	0.182	0.030	0.214	0.042	0.236	0.051	0.276	0.069
50	0.138	0.017	0.166	0.025	0.183	0.030	0.218	0.043
100	0.106	0.010	0.129	0.015	0.142	0.018	0.172	0.027
T_{ad}	Revised Method, Bouckovalas et al. (2009) $r_{u,max}$=0.50							
	a/b	a_s	a/b	a^*_s	a/b	a_s	a/b	a^*_s
10	0.196	0.035	0.264	0.063	0.250	0.057	0.329	0.098
25	0.138	0.017	0.191	0.033	0.181	0.030	0.245	0.055
50	0.106	0.010	0.150	0.020	0.139	0.018	0.194	0.034
100	0.078	0.006	0.113	0.012	0.107	0.010	0.151	0.021

5.4.2 Modification of design charts with respect to the rate of excess pore pressure built up.

Given the inadequacy of the previous approach, the second method which was applied concerns the modification of the initial liquefaction curves for A = 0.70 with regard to the rate of excess pore pressure ratio built up ($\partial r_u/\partial N$) predicted by the corresponding curves for A = 1.40 at any allowable $r_{u,max}$ value. The above modification is outlined in the following steps:

1. The allowable excess pore pressure value $r_{u,max}$ and the appropriate A value which best fits the available experimental data ($A \neq 0.70$) are selected.
2. The number of cycles for liquefaction N_L is determined based on the equivalent number of cycles N_{eq} and the N_{eq}/N_L value selected for design.
3. Given all previous data the solution of *Equation 5.3* (Seed, Martin & Lysmer, 1975) renders the number of loading cycles N for the allowable excess pore pressure value $r_{u,max}$.
4. The rate of excess pore pressure ratio built up ($\partial r_u/\partial N$) is given as:

$$\frac{\partial r_u}{\partial N} = \frac{1}{A\pi N_l} \frac{1}{\left(N/N_l\right)^{1-1/2A}} \frac{1}{\sqrt{1-\left(N/N_l\right)^{1/A}}} \qquad 5.6$$

5. Consequently, *Equation 5.6* is solved (by trial and error) with regard to the equivalent number of loading cycles to liquefaction N_L^*, for $A^* = 0.70$, and the terms of $\partial r_u/\partial N$ and N determined previously. Thus *Equation 5.7* results:

$$\frac{\partial r_u}{\partial N} = \frac{1}{A^*\pi N^*_l} \frac{1}{\left(N/N^*_l\right)^{1-1/2A^*}} \frac{1}{\sqrt{1-\left(N/N^*_l\right)^{1/A^*}}} \qquad 5.7$$

6. The design methods developed by Seed & Booker (1977) and Bouckovalas et al. (2009) are solved analytically for $A^* = 0.70$ and the N_L^* value from step 5, and the two sets of design curves are then compared.

For consistency purposes, the above process is applied for a minimum and a maximum limit of excess pore pressure ratio, commonly encountered in design codes, $r_{u,max} = 0.25$ and 0.50, A = 0.70 & 1.40, $N_{eq} = 10$ and $N_{eq}/N_L = 1$ & 2.

Application for $r_{u,max} = 0.25$.- Figure 5.24 summarizes Steps 1 through 5 which result in the equivalent number of loading cycles to liquefaction N_L^*. More specifically, the liquefaction curves for A = 0.70 and 1.40 and $N_{eq}/N_L = 1$ & 2, are plotted in the lower part of the graph,

whereas the rate of excess pore pressure built up ($\partial r_u/\partial N$) against the number of loading cycles N is located in the upper-part. The required N_L^* is the number of loading cycles for which the two liquefaction curves for A = 1.40 and A^* = 0.70, present the same gradient, that is the same $\partial r_u/\partial N$ value. Thus, for an allowable excess pore pressure ratio $r_{u,max}$ = 0.25 it is found that the two design methodologies should be now solved for N_{eq}/N_L^* = 1.58 and 3.15 respectively for initial N_{eq}/N_L values of 1 & 2.

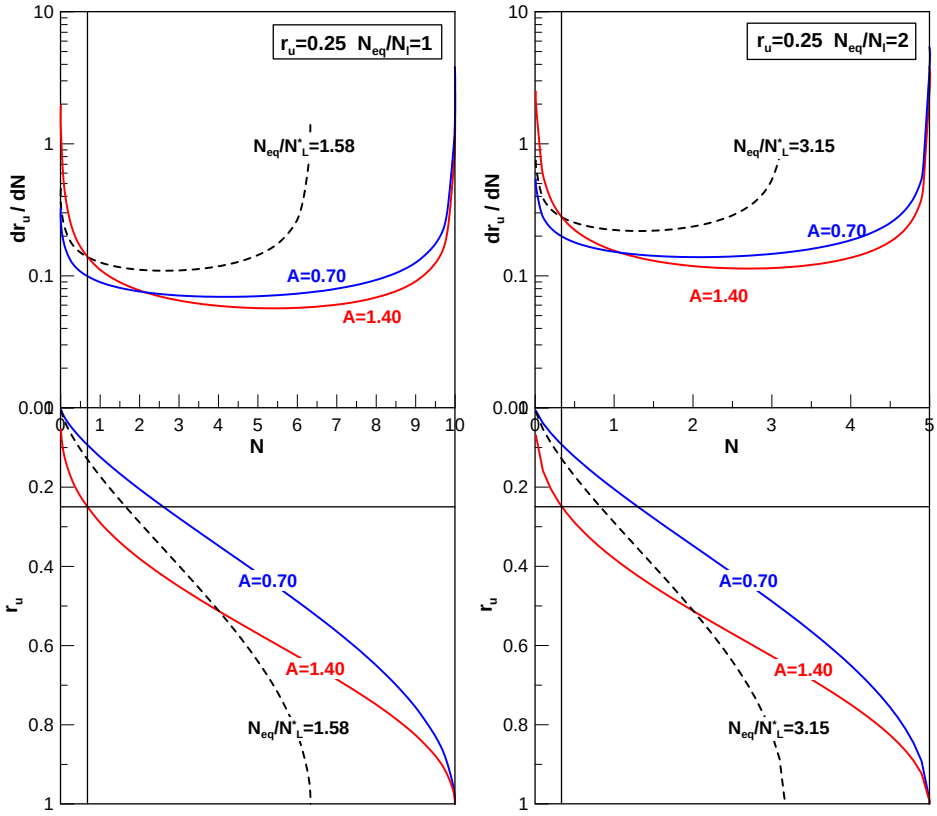

Figure 5.24: Exact and modified liquefaction curves and corresponding rate of excess pore pressure built-up.

The exact and modified design curves, when applying the Seed & Booker method, for T_{ad} = 10 & 50, are presented in **Figure 5.25**. It is observed, once again, that the modified sets of curves are not in good agreement with the exact curves, rendering, in fact, lower spacing dimensions (a/b ratios) for the same allowable excess pore pressure ratio $r_{u,max}$. In terms of replacement coefficient (α_s) the correlation between the exact and the approximated values of α_s presented in **Figure 5.26a**, for a typical range of T_{ad} from 10 to 100, also indicate the above discrepancy. The proposed approximation, results in reduced α_s^* values of up to 20%, hence leading to inadequate design. The previous conclusion is further justified when

looking at the ratio of α_s values when A = 1.40 over the modified values for A^* = 0.70, referred to as α_s^*, in **Figure 5.26b**. The ratio of α_s/α_s^* consistently receives values greater than unity independently of N_{eq}/N_L, following a decreasing trend at increasing T_{ad} values.

Figure 5.27 includes the same group of design curves for the revised method by Bouckovalas et al. (2009). The two sets of curves overlap at the desired excess pore pressure ratio and the convergence between the exact and the modified design curves appears to be independent of the intensity of seismic motion (N_{eq}/N_L) and the dimensionless time factor T_{ad}. Also, from **Figure 5.28a**, both replacement coefficients, plotted on a one-to-one comparison are practically equal in the T_{ad} range examined. Additionally, the ratio of α_s/α_s^* plotted against the replacement coefficient given by the modified design curve (α_s^*), in **Figure 5.28b**, is almost equal to unity, verifying the coincidence observed earlier between the two design curves. **Table 5.8** summarizes the predictions of the exact and modified design curves in terms of drain spacing (a/b) and replacement coefficients for four T_{ad} values and N_{eq}/N_L = 1 & 2 for both methodologies.

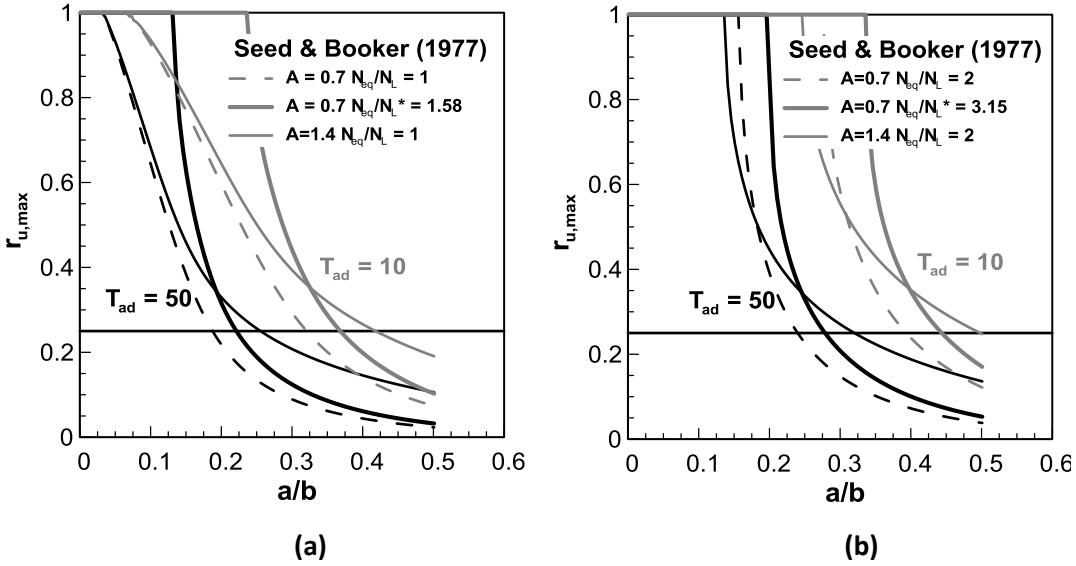

Figure 5.25: Exact (N_{eq}/N_L = 1,2) and modified (N_{eq}/N_L* = 1.58, 3.15 respectively) design curves for the Seed & Booker (1977) theory.

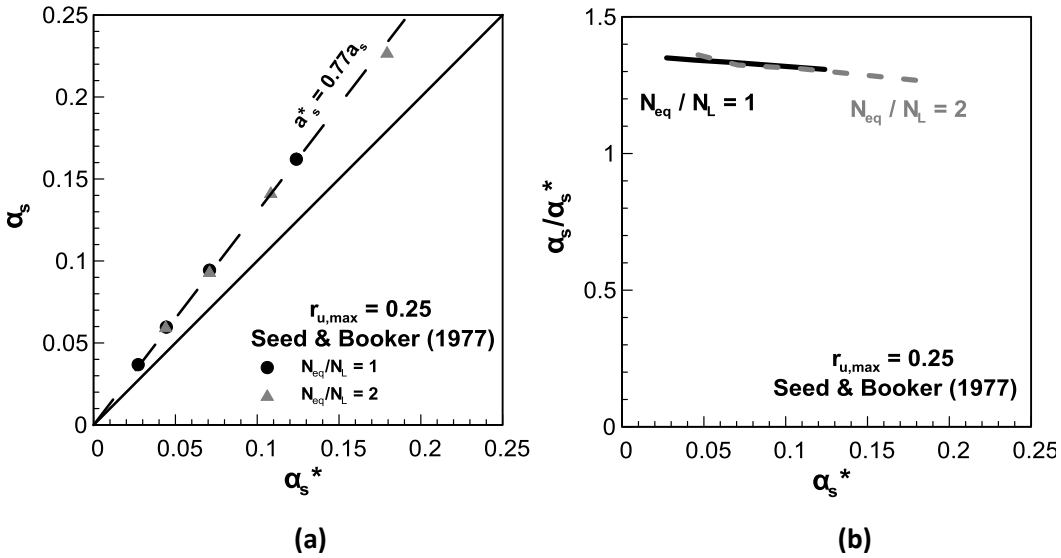

Figure 5.26: Effect of modified design curves by Bouckovalas et al (2009) on the replacement coefficient α_s* for an allowable $r_{u,max}$ = 0.25, T_{ad} = 10, 25, 50,100 and $N_{eq}/_{NL}$ = 1 & 2.

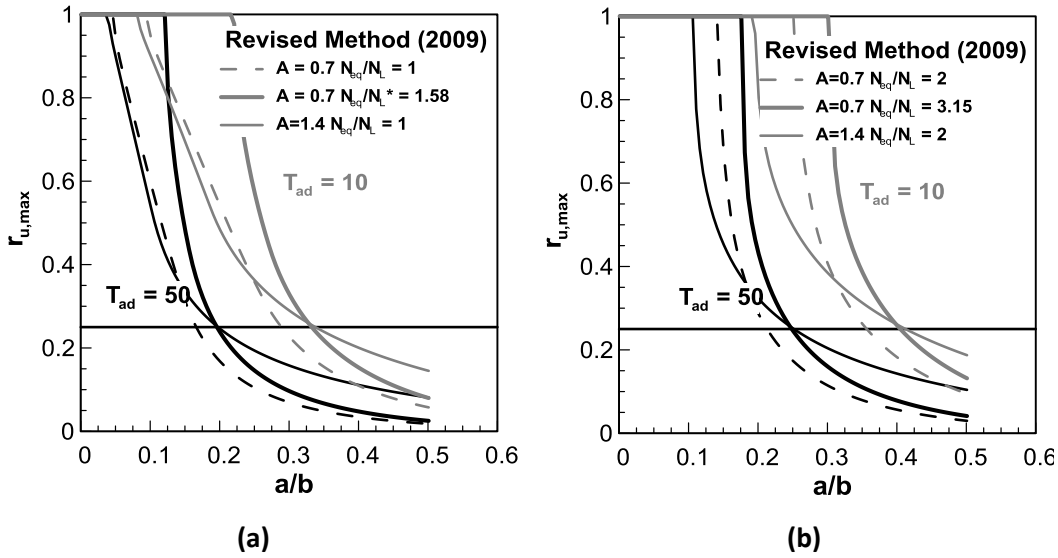

Figure 5.27: Exact (N_{eq}/N_L = 1,2) and modified (N_{eq}/N_L* = 1.58, 3.15 respectively) design curves for the Bouckovalas et al. (2009) revised method.

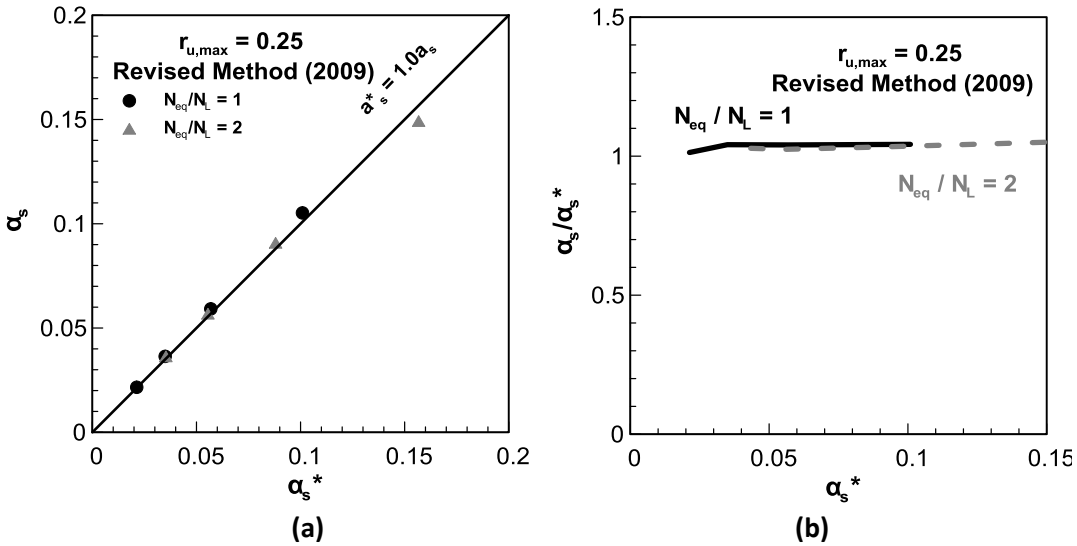

Figure 5.28: Effect of modified design curves by Bouckovalas et al. (2009) on the replacement coefficient α_s* for allowable $r_{u,max}$ = 0.25, T_{ad} = 10, 25, 50, 100 and $N_{eq}/_{NL}$ = 1 & 2.

Table 5.8: Spacing ratios (a/b) and replacement coefficients for $r_{u,max}$ = 0.25.

T_{ad}	Seed & Booker (1977) $r_{u,max}$=0.25							
	N_{eq}/N_l = 1				N_{eq}/N_l = 2			
	A=1.4, N_l		A=0.7, N^*_l		A=1.4, N_l		A=0.7, N^*_l	
	a/b	a_s	a/b	a^*_s	a/b	a_s	a/b	a^*_s
10	0.422	0.162	0.369	0.124	0.500	0.228	0.444	0.179
25	0.322	0.094	0.279	0.071	0.395	0.142	0.345	0.108
50	0.256	0.060	0.221	0.044	0.321	0.094	0.279	0.071
100	0.201	0.037	0.173	0.027	0.257	0.060	0.220	0.044
T_{ad}	Revised Method Bouckovalas et al. (2009) $r_{u,max}$=0.25							
	a/b	a_s	a/b	a^*_s	a/b	a_s	a/b	a^*_s
10	0.340	0.105	0.333	0.101	0.415	0.157	0.405	0.149
25	0.255	0.059	0.250	0.057	0.316	0.091	0.311	0.088
50	0.200	0.036	0.196	0.035	0.250	0.057	0.247	0.056
100	0.154	0.022	0.153	0.021	0.200	0.036	0.197	0.035

Application for $r_{u,max}$ = 0.50.- The previous set of figures was regenerated for an allowable excess pore pressure ratio of $r_{u,max}$ = 0.50. The initial (A = 0.70 & 1.40) and modified liquefaction curves are presented in **Figure 5.29**, from which the required N_{eq}/N_L^* ratio is found equal to 0.86 and 1.71 for initial values of N_{eq}/N_L of 1 and 2 respectively. The Seed & Booker (1977) initial and modified design curves are plotted in **Figure 5.30** for T_{ad} = 10 & 50. Note that the approximated curves do not start from unity, since the N_{eq}/N_L^* ratio is lower

than unity and no liquefaction occurs. The convergence between the exact and the proposed approximation is not satisfactory, since the latter lead to lower a/b values, thus in inadequate design. The above discrepancy is also obvious when looking into the replacement coefficient α_s^* required for a triangular grid. The one-to-one comparison between the two solutions is presented in **Figure 5.31a**, followed by the plot of the ratio of α_s/α_s^* with regard to α_s^* in **Figure 5.31b**. The correlation between the two replacement coefficients is expressed by the following *Equation 5.8*, implying that the proposed approximation leads to values about 20% lower, than those originally predicted by the exact solution. Moreover, the ratio of α_s/α_s^* receives values consistently higher than unity, especially for $N_{eq}/N_L = 1$, further supporting the previous observation.

$$\alpha_s^* \approx 0.80 \times \alpha_s \qquad 5.8$$

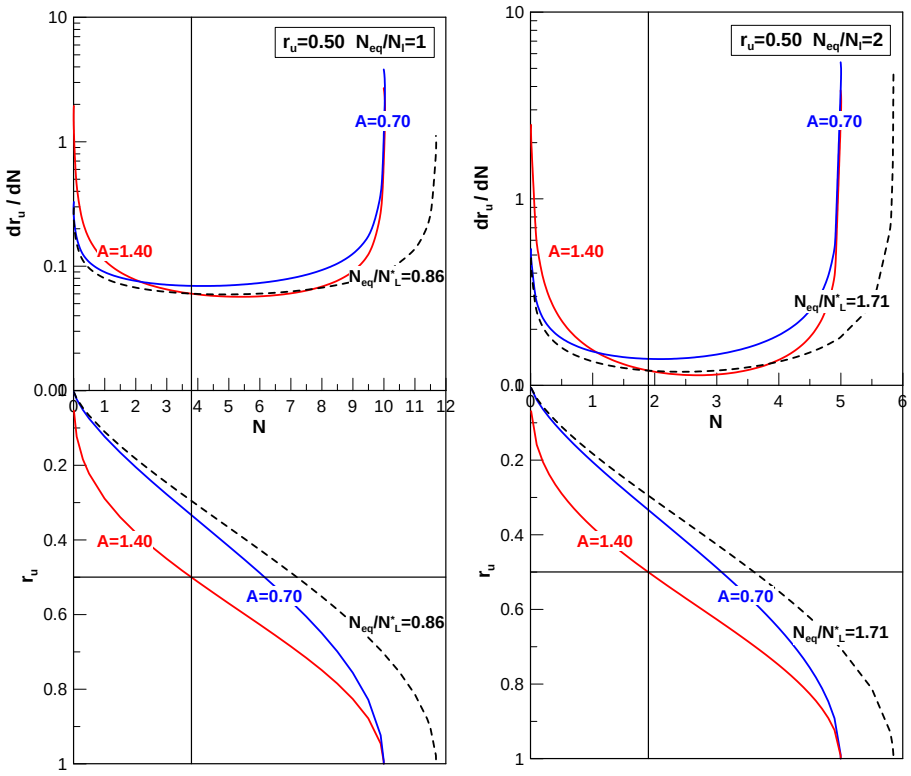

Figure 5.29: Exact and modified liquefaction curves and corresponding rate of excess pore pressure built-up.

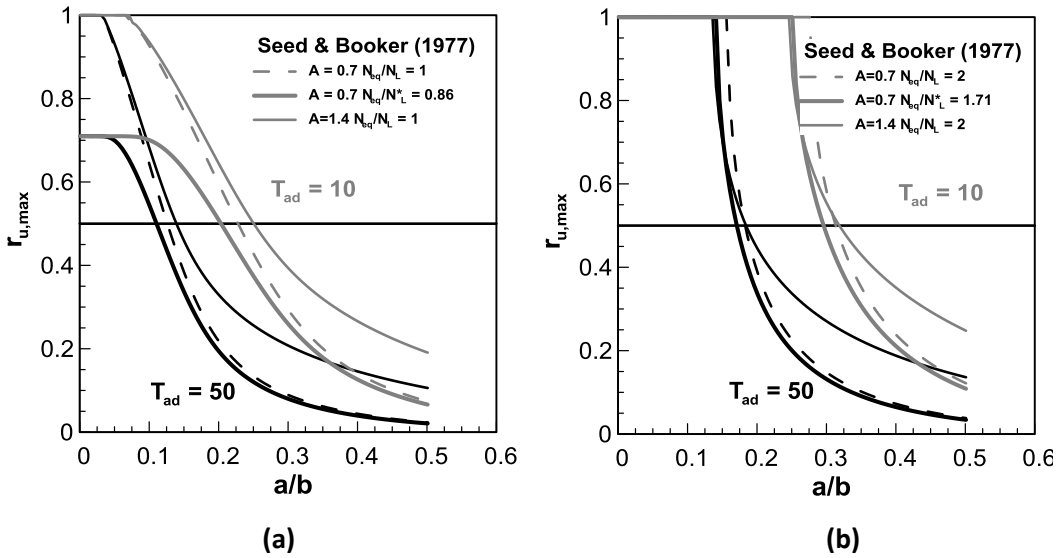

Figure 5.30: Exact (N_{eq}/N_L = 1,2) and modified (N_{eq}/N_L* = 0.86, 1.71 respectively) design curves for the Seed & Booker (1977) theory.

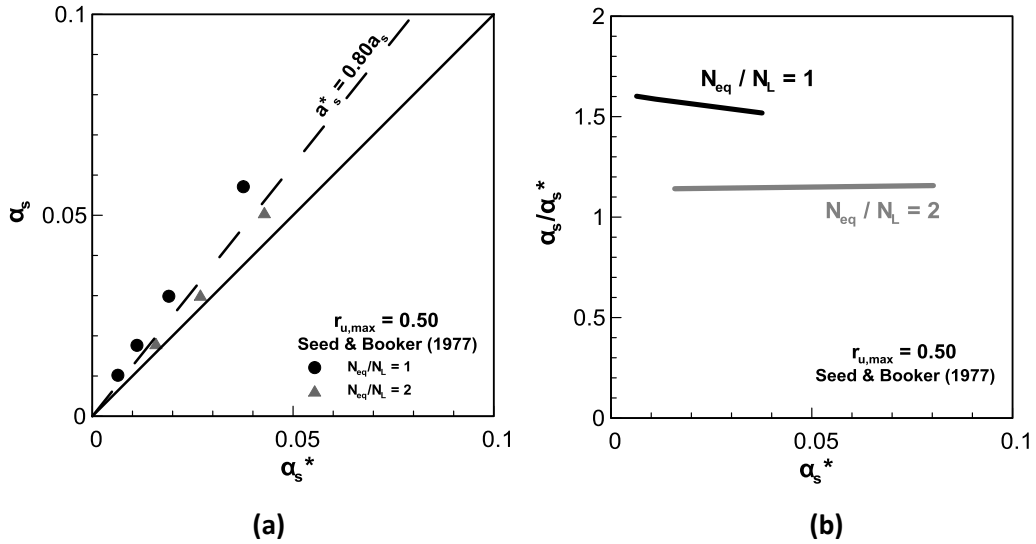

Figure 5.31: Effect of modified design curves by Seed & Booker (1977) on the replacement coefficient α_s* for allowable $r_{u,max}$ = 0.50, T_{ad} = 10, 25, 50, 100 and N_{eq}/N_L = 1 & 2.

The proposed approximation appears to be more efficient in the case of the revised Bouckovalas et al. (2009) method as shown in **Figure 5.32**. The good agreement observed in the design chart for N_{eq}/N_L = 1 is slightly disturbed for N_{eq}/N_L = 2, resulting in greater a/b values than those expected for A = 1.40. The replacement coefficient α_s^* given by the proposed modification, considering a triangular grid is also in good agreement with the equivalent coefficient α_s, given by the exact solution with A = 1.40. **Figure 5.33a** visualizes

the above observation with a one-to-one comparison between the two coefficients. Additionally, the ratio of α_s/α_s^* plotted against the modified coefficient α_s^*, in **Figure 5.33b**, is quite close to unity, for both N_{eq}/N_L values examined. The ratio of α_s/α_s^* slightly deviates from unity, for $N_{eq}/N_L = 2$, underestimating the required a/b ratio.

Overall, the proposed modification, based on the rate of excess pore pressure generation ($\partial r_u/\partial N$), did not match the exact values predicted for A = 1.40 in the case of the Seed & Booker (1977) theory, underestimating the required a/b ratio, as opposed to the modification based on the allowable excess pore pressure ratio $r_{u,max}$, developed by PHRI (1997), which overestimated the corresponding ratio.

On the contrary, it appears that the revised method by Bouckovalas et al. (2009) is adequately approximated for $N_{eq}/N_L = 1$ and more importantly, independently of the allowable $r_{u,max}$ value used in design. The accuracy of the proposed modification is questioned though for $N_{eq}/N_L = 2$, given that for increasing $r_{u,max}$ design values, there is a deviation of about 15 – 20%, compared to the exact solution. **Table 5.9** summarizes the predictions of the exact and modified design curves in terms of drain spacing (a/b) and replacement coefficients for four T_{ad} values and $N_{eq}/N_L = 1$ & 2 for both methodologies.

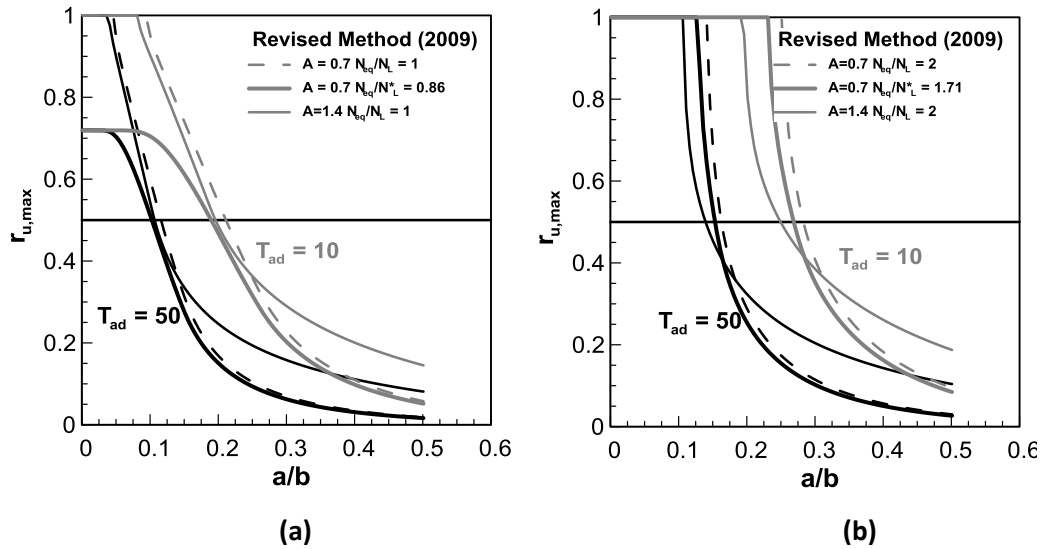

Figure 5.32: Exact (N_{eq}/N_L=1,2) and modified (N_{eq}/N_L*=0.86, 1.71 respectively) design curves for the Bouckovalas et al. (2009) revised method.

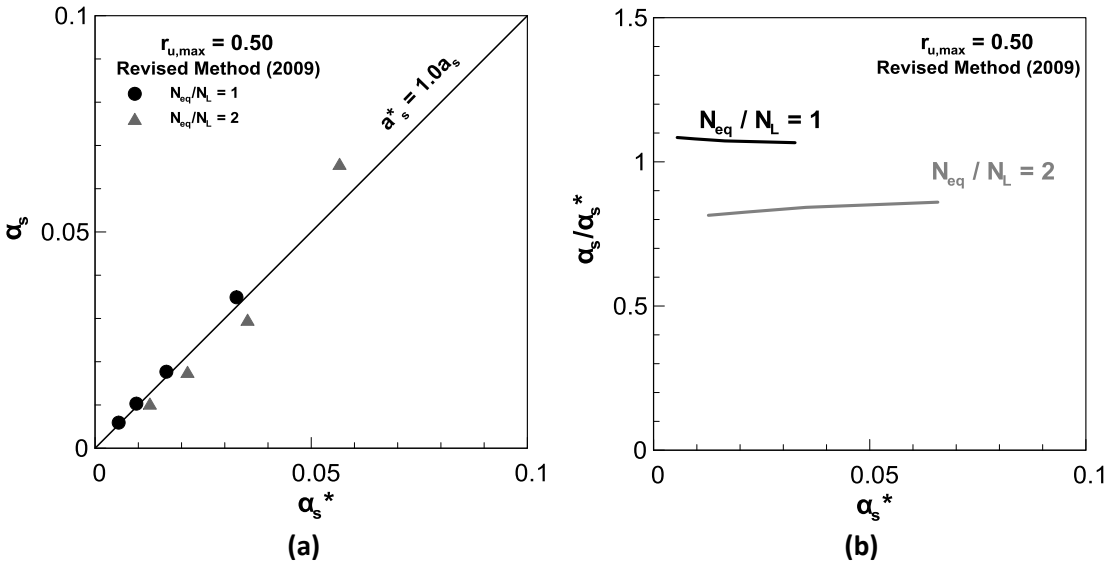

Figure 5.33: Effect of modified design curves by Bouckovalas et al (2009) on the replacement coefficient α_s* for an allowable $r_{u,max}$ = 0.50 T_{ad} = 10, 25, 50, 100 and N_{eq}/N_L = 1 & 2.

Table 5.9: Spacing ratios (a/b) and replacement coefficients for $r_{u,max}$ = 0.50.

T_{ad}	Seed & Booker (1977) $r_{u,max}$=0.50							
	N_{eq}/N_l = 1				N_{eq}/N_l = 2			
	A=1.4, N_l		A=0.7, N^*_l		A=1.4, N_l		A=0.7, N^*_l	
	a/b	a_s	a/b	a^*_s	a/b	a_s	a/b	a^*_s
10	0.251	0.057	0.203	0.038	0.318	0.092	0.297	0.080
25	0.181	0.030	0.145	0.019	0.236	0.051	0.217	0.043
50	0.139	0.018	0.111	0.011	0.182	0.030	0.172	0.027
100	0.106	0.010	0.084	0.006	0.141	0.018	0.132	0.016
T_{ad}	Revised Method Bouckovalas et al. (2009) $r_{u,max}$=0.50							
	a/b	a_s	a/b	a^*_s	a/b	a_s	a/b	a^*_s
10	0.196	0.035	0.190	0.033	0.249	0.057	0.269	0.066
25	0.139	0.018	0.135	0.016	0.181	0.030	0.197	0.035
50	0.106	0.010	0.102	0.010	0.139	0.018	0.153	0.021
100	0.081	0.006	0.077	0.005	0.107	0.010	0.118	0.013

5.4.3 New design charts for different A values

Given the inadequacy of the previous attempts to modify the existing design charts, the revised method by Bouckovalas et al. (2009) is analytically solved for different A values so that new design charts are proposed. In the formula for the dimensionless factor T_{ad}, given by *Equation 5.9*, the dynamic time (t_d) is replaced by the time required for liquefaction t_l, leading to *Equation 5.10* below:

$$T_{ad} = \frac{k_h t_d}{m_{v,3} \gamma_w a^2} \qquad 5.9$$

$$T_{al} = \frac{k_h t_l}{m_{v,3} \gamma_w a^2} \qquad 5.10$$

Therefore, the new proposed design charts will now be solely a function of the soil properties, eliminating the effect of the duration of the seismic motion. The two dimensionless time factors (T_{ad} & T_{al}) are linked through the following relationship (*Equation 5.11*):

$$\frac{N_l}{t_l} = \frac{N_{eq}}{t_d} \leftrightarrow \frac{N_l}{T_{al}} = \frac{N_{eq}}{T_{ad}} \leftrightarrow T_{al} = \frac{T_{ad}}{N_{eq} / N_l} \qquad 5.11$$

The new design charts are presented in **Figure 5.34** for A values 0.70, 1.00, 1.40 and 2.00 and T_{al} values 5, 10, 25, 50 and 100 and are generated for three levels of intensity of seismic motion (that is N_{eq}/N_L = 1, 1.50 & 2), since as it has been pointed out earlier, there is not much accuracy added to the design for seismic motions of greater intensity.

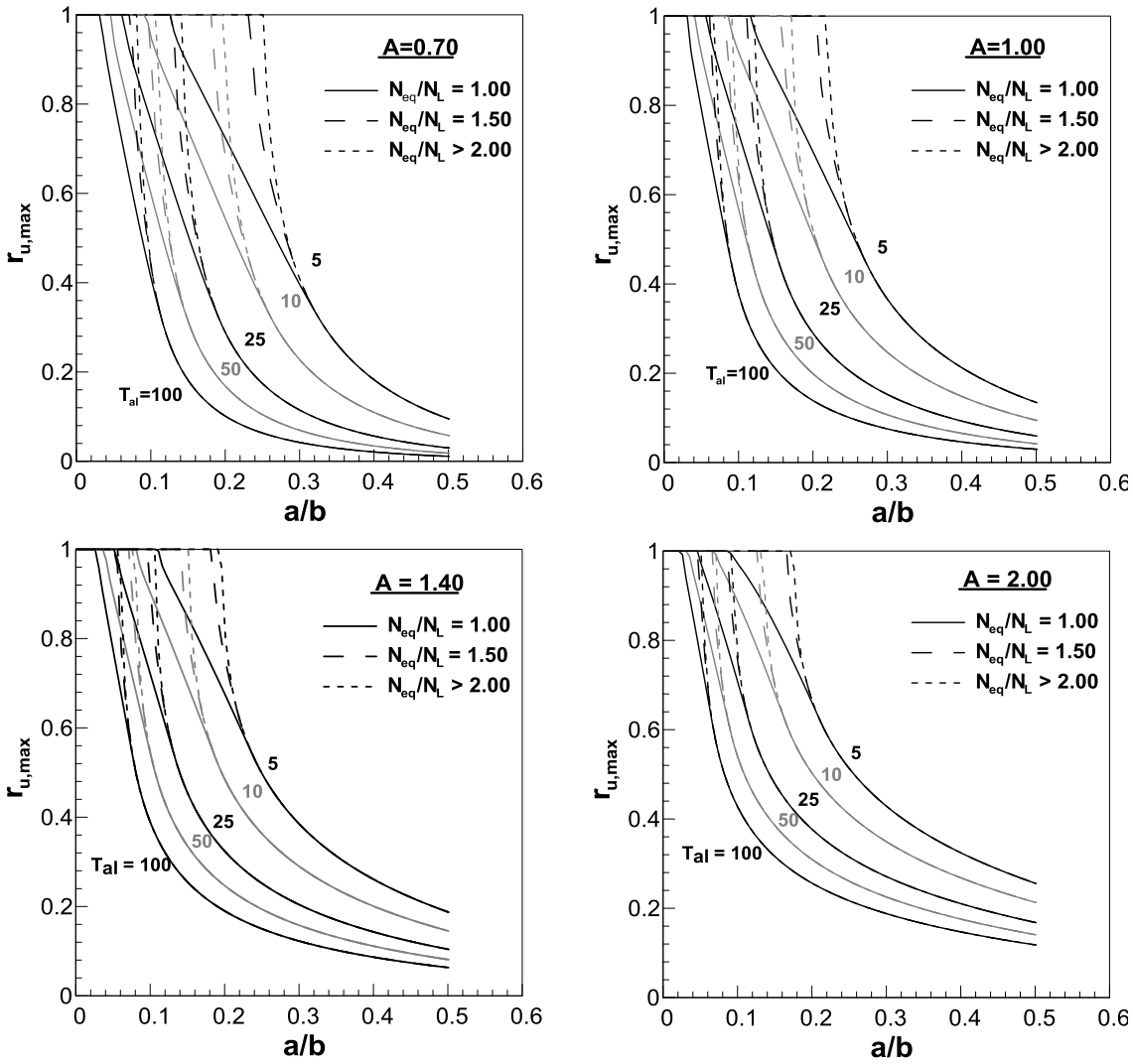

Figure 5.34: New design charts for the revised method by Bouckovalas et al. (2009) for A=0.70, 1.00, 1.40, 2.00 and N_{eq}/N_L=1.00, 1.50, 2.00**.**

More importantly, the effect of the seismic motion intensity becomes important for $r_{u,max}$ values greater than about 0.50, since all design curves for any T_{al}, converge for $r_{u,max}$ values below 0.50. Therefore, the above design charts are further simplified, and are presented in a range of $r_{u,max}$ 0 – 0.50, in **Figure 5.35**. Following a different presentation mode, the design charts presented in **Figure 5.36** are based on the allowable excess pore pressure ratio value $r_{u,max}$. The a/b ratio is plotted with regard to the dimensionless time factor T_{al}, for $r_{u,max}$ values of 0.20, 0.30, 0.40 and 0.50 and the previously mentioned range of A values.

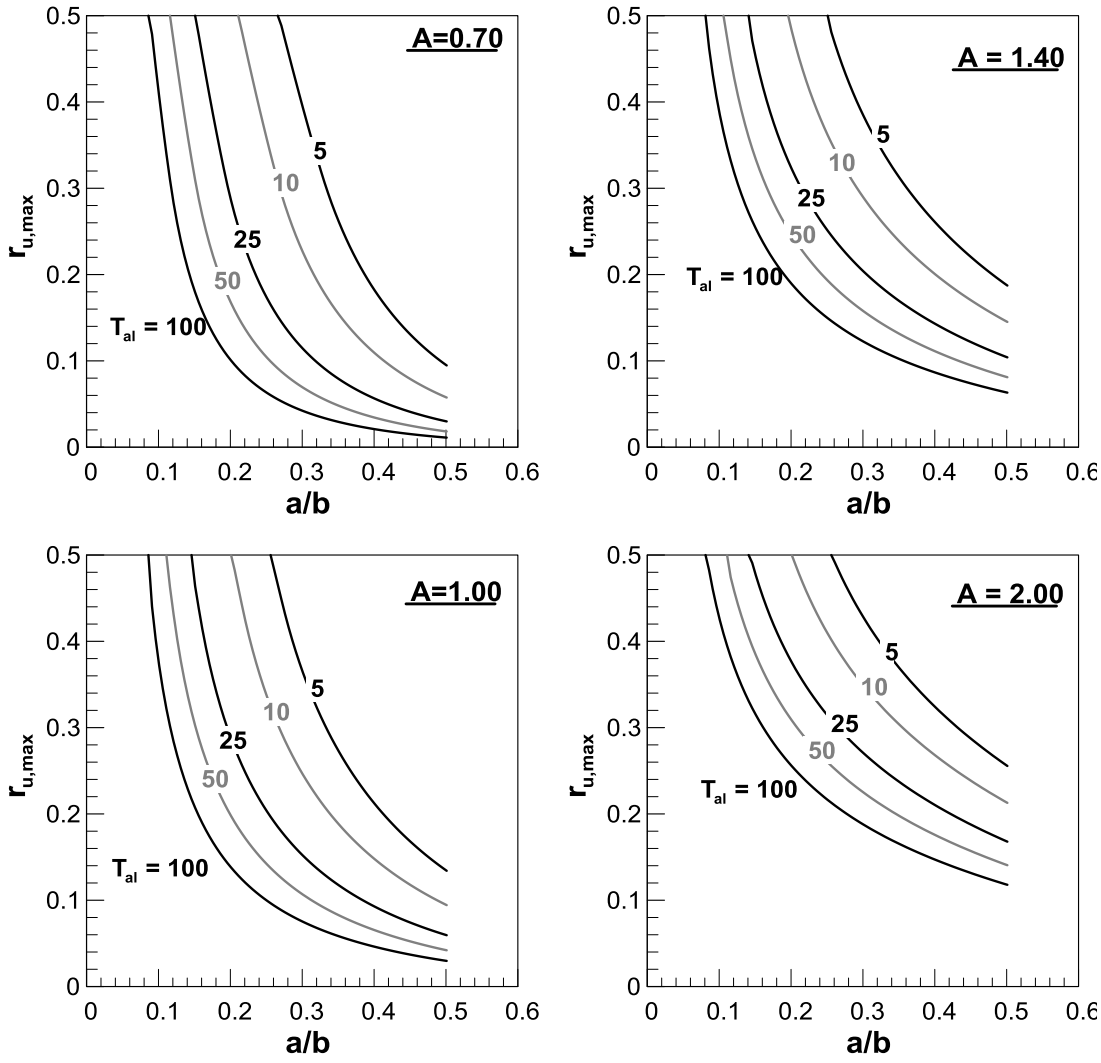

Figure 5.35: New design charts for the revised method by Bouckovalas et al. (2009) for A=0.70, 1.00, 1.40, 2.00 maximum $r_{u,max}$=0.50 and one single N_{eq}/N_L intensity.

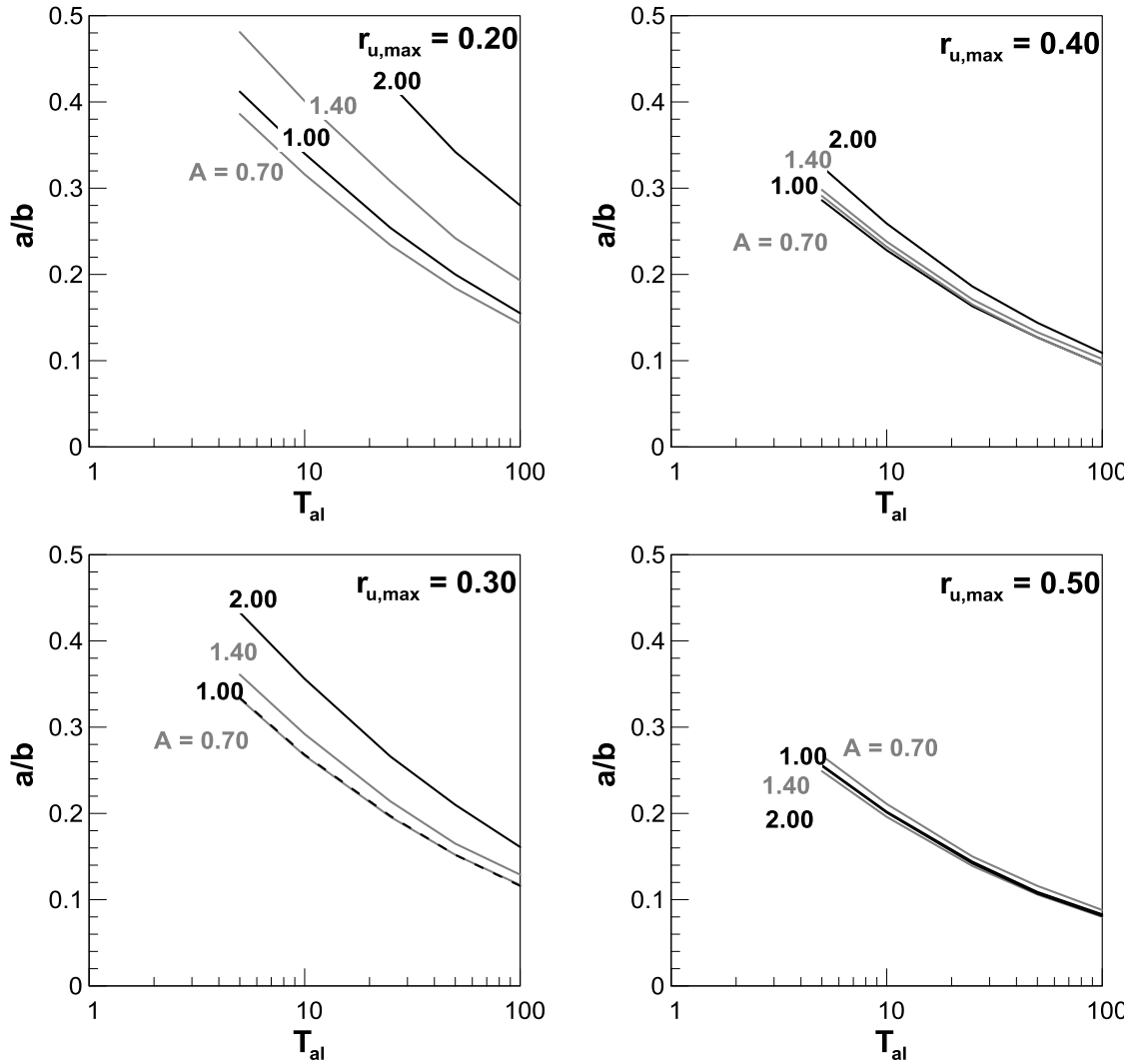

Figure 5.36: Design charts for the revised method by Bouckovalas et al. (2009) for fixed allowable excess pore pressure ratio values and A = 0.70, 1.00, 1.40, 2.00.

CHAPTER 6

Numerical Simulation of Gravel Drain Performance

6.1 Introduction

The present chapter focuses on the drainage function of gravel piles under seismic loading, which is numerically simulated using sophisticated numerical tools such as FLAC3D. Starting from the free field response, the presence of gravel piles within the liquefiable sand layer is then examined, considering the effect of the number of piles, their arrangement in the grid, their stiffness relatively to the sand layer, and their relative permeability to the sand layer. Moreover, effects not directly related to the drains, such as the grid discretization and the boundary conditions are also examined. The particular numerical analyses are evaluated primarily in terms of excess pore pressure Δu and excess pore pressure ratio r_u, built up and secondarily in terms of horizontal acceleration response.

The most numerically stable and computationally effective arrangement is selected and subsequently used in the numerical verification of the analytically derived design charts proposed in the design methodology by Bouckovalas et al. (2009). The particular verification focuses initially on the appropriate fitting of the epp built-up relationship proposed by De Alba et al. (1975), under undrained conditions and then the matching of the numerically derived epp ratio (r_u) time histories to the analytically derived curves, under drained conditions. Due to the lack of information as to a suitable $m_{v,3}$ value to be used in the analytical methodology, the last stage of the verification is performed through back-fitting of the analytical solution for specific $m_{v,3}$ values.

Given the uncertainty in the selection of an appropriate $m_{v,3}$ value, particular effort is dedicated in the specification of a suitable range for the particular parameter. To achieve this, the back-calculated values are evaluated against **(i)** numerically obtained $m_{v,3}$ values, referring to the gravel drain – soil system and the element level soil response and **(ii)** the associated $m_{v,3}$ values proposed in the literature.

6.2 Numerical simulation

6.2.1 Basic assumptions

The numerical analyses presented in the present chapter are performed with the finite difference code FLAC 3-D, which is described in detail in Appendix A. All the common characteristics of the performed numerical analyses are outlined below, followed by additional information on each grid configuration.

Soil Profile & Grid Configuration.- The examined soil profile consists of a 0.50m thick liquefiable sand layer encased between two practically impermeable, 0.45m thick, clay layers. Besides the free field arrangement, three additional grid configurations, including two and four gravel piles arranged either in one or two rows, are examined in order to evaluate the effect of the drain number and their arrangement. Subsequently, the optimum grid set up is selected to proceed to the analysis of the drainage capacity of gravel piles. The particular configurations are described below

- **Free – field (ff) configuration.-** In the particular case, a 5.60m×1.40m×1.0m soil profile is considered, also presented in **Figure 6.1**. The mesh consists of 27 zones of 0.20m, in the x-direction while in the z-direction the clay layer is divided into three zones of 0.15m each and the sand layer into 5 zones of 0.10m. In the y-direction only one zone was considered, since for the free field conditions, no differentiation along the particular direction is expected. Excess pore pressures and acceleration time histories are computed along the mid-depth of the sand layer.

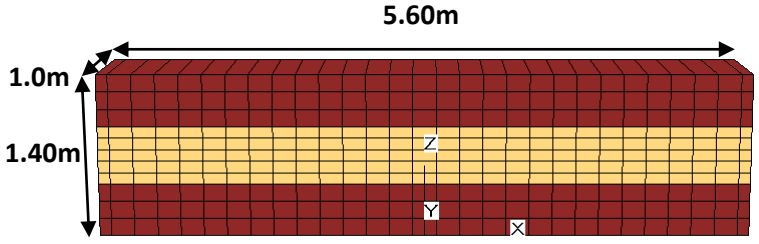

Figure 6.1: Free-field configuration (ff).

- **Two-pile configuration.-** Preserving the soil profile described above, two gravel drains are considered along the total height of the mesh. The total dimensions of the configuration are 5.60m in length and 1.40m in the other two directions. The two gravel drains are 1m(=2a) in diameter, situated at a 2.80m(=b) center – to – center distance, rendering a ratio a/b = 0.5/1.4 = 0.357. Due to the symmetry of the problem, only half the drains are simulated. **Figure 6.2** presents a detailed view of the grid configuration which is composed of 4 1.30m×1.40m×1.40m "radial cylinder" blocks, such as the one illustrated in **Figure 6.3**, appropriately oriented to simulate vertical cylindrical surfaces. For optimum discretization each block is divided into 6 zones in the horizontal direction and 11 zones in the vertical direction. As a result, the clay layer is divided into 0.20m×0.15m zones, the sand layer into 0.20m×0.10m and the gravel drain into 0.25m×0.15m elements within the clay layer and 0.25m×0.10m elements within the sand layer.

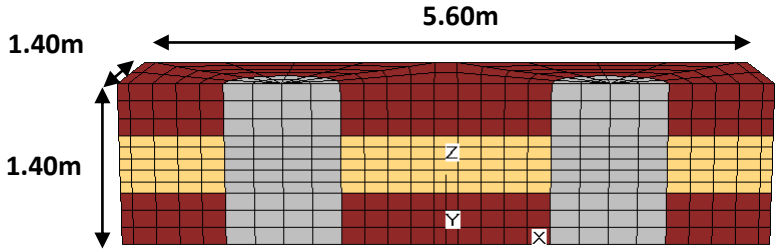

Figure 6.2: 2-pile configuration (2p)

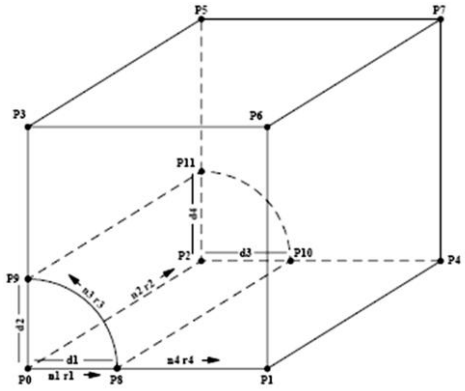

Figure 6.3: Radially graded mesh around cylindrical shaped area – **radcylinder.**

- **Four-pile in one single row (4p).-** The specific configuration includes four gravel piles located in one single row, presenting the same geometrical features with the

previous grid configuration, in terms of drain dimensions and replacement coefficient α_s. The total length of the grid is 11.20m in the horizontal direction and 1.40m in the other two directions and the mesh is composed of the same "radial cylinder" blocks presenting the same discretization with the two-pile configuration. The above are demonstrated in **Figure 6.4.**

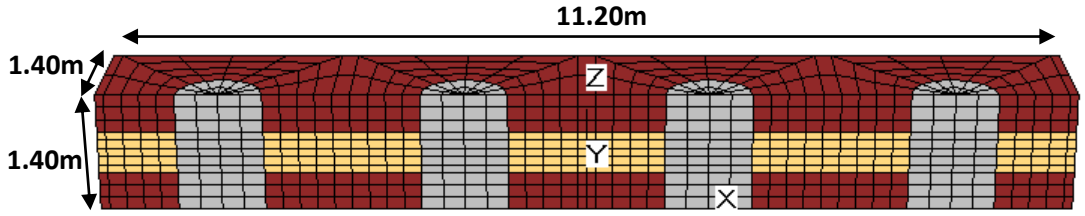

Figure 6.4: 4-pile configuration in single row (4p).

- **Four-piles in two rows (4psq).-** The last configuration consists of four gravel drains arranged in a two rows of two drains each, essentially forming a square arrangement. The main geometrical features are preserved, using the same "radial cylinder" blocks, exhibiting the same mesh discretization. **Figure 6.5** displays a detailed view of the specific grid.

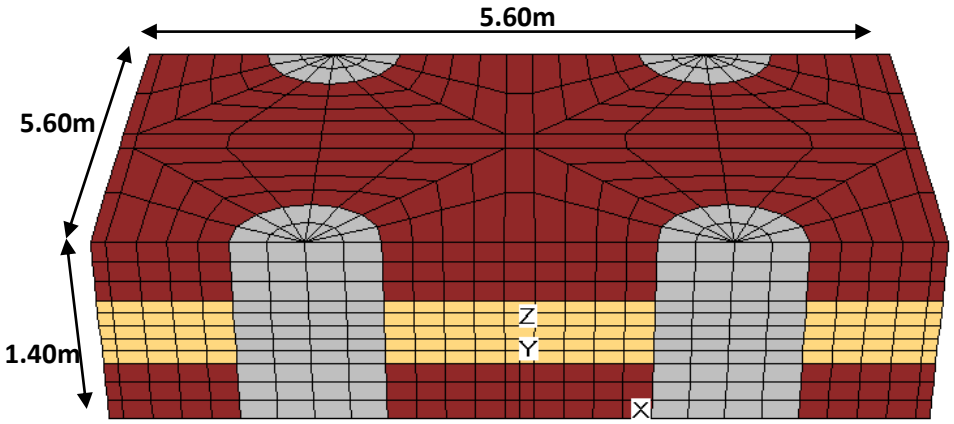

Figure 6.5: 4-pile configuration in square arrangement (4psq).

Soil Properties.- Initial stresses are calculated considering a dry density ρ_ξ = 1.607Mgr/m^3 and a saturated density ρ_{sat} = 2Mgr/m^3. The resulting effective vertical stress in the middle of the sand layer is selected to be equal to 100kPa to facilitate the numerical computations of the excess pore pressure ratio r_u, in the particular depth. Given the shallow depth of the configuration, the 100kPa effective vertical stress in the mid-depth is achieved be applying a

uniform vertical pressure of 186kPa and a pore pressure of 93kPa on top of the grid, thus ensuring the continuous saturation of the soil deposit throughout the applied excitation.

Damping.- During dynamic loading local non-viscous damping is applied to all materials. For the sand, under small shear strain amplitude, a damping value of 2% is selected, which is in accordance to the minimum value reported by Vucetic & Dobry (1991). For larger shear strain amplitudes, hysteretic damping is simulated by the non linear response of the constitutive model itself. The clay layers are assigned a damping value equal to 10%, which is representative of shear strains less than 0.1% for soils with a plasticity index of PI = 15%, according to Vucetic & Dobry (1991). The gravel pile material is also assigned a damping value equal to 10%, corresponding to shear strains in the order of 0.01% for sands and gravels.

Cyclic soil response.- Soil response is simulated based on the constitutive model described in **Appendix A**, using the parameters corresponding to Nevada sand. The initial void ratio is equal to e_o = 0.661, corresponding to porosity n = 0.398 and a relative density of D_r = 60%. Note here, that the externally applied stress essentially ensures the function of the constitutive model in the sand layer, within a uniform stress field with small gradient, avoiding the occurrence of different stress conditions, i.e. contractive and dilative behavior, within the same layer. The clay crusts and the gravel drains were simulated using the elastic linear model, assigning a shear modulus equal to G = 60MPa and bulk modulus equal to K = 130MPa. Poisson's ratio is set equal to ν = 0.33 in both constitutive models.

Excitation.- The seismic excitation is applied at the base of the model and is essentially sinusoidal, consisting of 12 cycles with period T = 0.20sec and peak acceleration α_{max} = 0.08g (**Figure 6.6**). A cycle of smaller amplitude is added at the beginning and at the end of the time history to ensure a gradual increase of the input acceleration and eliminate erroneous numerical results that could result due to an abrupt change in loading conditions.

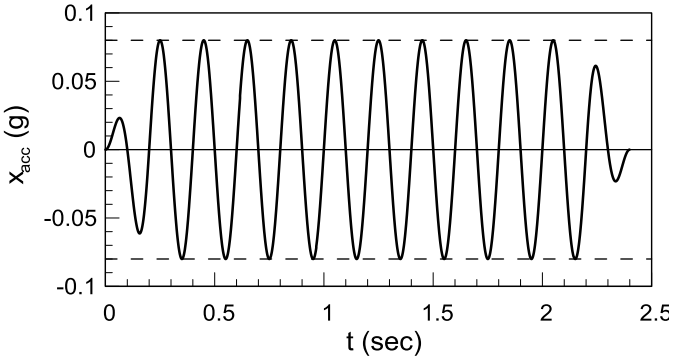

Figure 6.6: Seismic excitation applied at the base.

Boundary Conditions.- In all cases, tied node boundary conditions are imposed at the boundary grid-points of the model, along the y-direction, in order to ensure the same horizontal and vertical displacements at the two borders of the configuration. The particular type of boundary conditions proves more efficient in reproducing the deformation pattern of the free field for level ground conditions.

6.2.2 Effect of r_u computation method

Excess pore pressure ratio is computed based on two different methodologies, namely directly from FLAC 3-D and analytically.

In FLAC 3-D , the built-in computation, is performed through the definition of two extra variables, which correspond to the excess pore pressure Δu and the excess pore pressure ratio r_u respectively. More specifically, in each zone the hydrostatic pore pressure is computed and stored in the memory and subsequently, in each calculation step it is subtracted from the total pore pressure so that the excess pore pressure due to cyclic loading (Δu) is estimated. Then, Δu is divided by the initial effective vertical stress of each zone and the excess pore pressure ratio r_u is calculated.

In the analytical computation, excess pore pressure ratio is calculated dividing Δu, with the current effective vertical stress during cyclic loading, as it is below:

$$r_u = \frac{\Delta_u}{\sigma_{zz} - u_o} \qquad 6.1$$

where σ_{zz} = the current total vertical stress (kPa)

u_0 = the initial hydrostatic pore pressure at the corresponding depth of the sand layer, which in all examined zones herein corresponds to the mid-depth of the sand layer, namely 99.5kPa.

To assess the effectiveness of the different computational approaches of r_u, the response of equivalent zones from the free-field and the 2-pile configurations is examined in terms of excess pore pressures Δu, excess pore pressure ratio (r_u) and effective vertical stress time histories.

Free field.- Excess pore pressures and corresponding epp ratios (r_u) from zones 1 through 5 (horizontal distance from the axis of symmetry **x = 0, 0.6, 0.8, 2.0, 2.4m** respectively), located in the mid-depth and along the liquefiable sand layer, are plotted versus time in **Figure 6.7 & Figure 6.8.** Taking advantage of the grid symmetry, zones only on the one side of the arrangement are examined. **Figure 6.7** presents the excess pore pressure (Δu) time

histories from zones 1 through 5, as computed by FLAC 3-D, from which it is concluded that the response is practically uniform for zones 1 to 3, but as approaching to the tied node boundaries, zones 4,5 develop higher excess pore pressures and reach liquefaction (i.e. $\Delta u = \sigma'_{vo} = 100kPa$) earlier, compared to the middle zones of the arrangement.

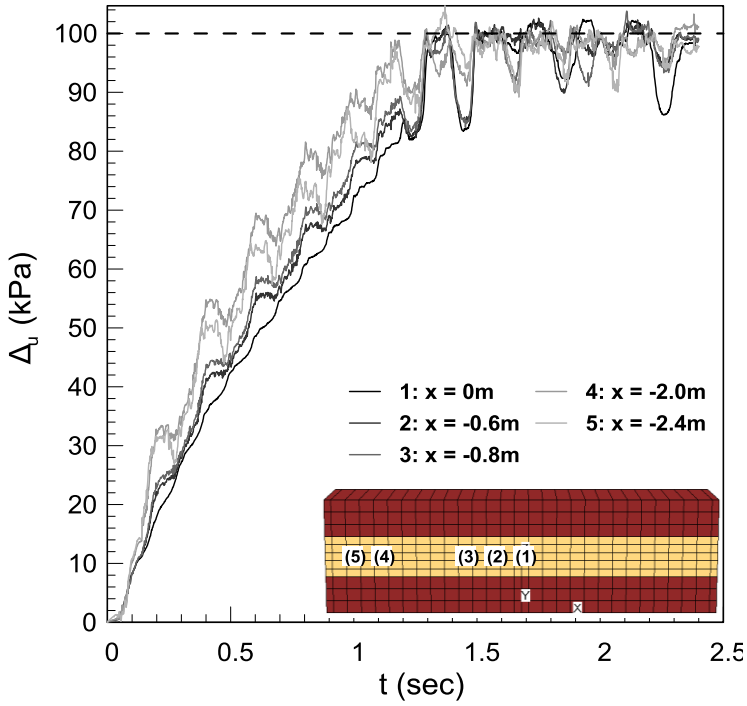

Figure 6.7 Excess pore pressure for the free-field configuration.

The excess pore pressure build up in zones 1 through 5 is also assessed in terms of r_u time histories provided in **Figure 6.8a & b**. Based on **Figure 6.8a**, it is observed that approaching the boundaries of the model, r_u values significantly deviate from the expected behavior, resulting especially in the case of zone 5, in r_u values lower than unity. This indicates the non occurrence of liquefaction, despite the time history of excess pore pressures, which dictates differently. When computing r_u analytically, (**Figure 6.8b**) the behavior is improving, since zones 4 & 5 give a very comparable response with regard to each other as well as with regard to the middle zones of the model.

The reason for this divergence becomes evident when examining the vertical effective stress time history for the particular zones, illustrated in **Figure 6.9**. Vertical effective stresses were manually calculated by subtracting the pore pressure value (pp) from the total vertical stress (σ_{zz}), as the last was computed by FLAC 3-D. Indeed, the zone close to the boundaries is numerically affected, since they are not assigned the same effective vertical stresses

compared to the other zones, for static conditions. Namely, zone 5 (x = -2.4m) has initial vertical stresses equal to σ'_{vo} = 112kPa.

In the case where r_u is routinely computed from FLAC 3-D (i.e. $r_u = \Delta u/\sigma'_{vo}$), the higher Δu values developing in **zone 5** are divided by a higher effective vertical stress (σ'_{vo} = 112kPa), and from t = 0 to 1.2sec (corresponding to 6 loading cycles) those two competing effects appear to become counterbalanced, rendering r_u values, which are comparable to the other zones. After the occurrence of liquefaction (at approximately 6 – 7 cycles) and till the end of shaking, Δu values are practically the same in all zones under examination. Hence, the effect of higher initial effective vertical stresses becomes obvious, and leads to lower r_u values, (0.85 instead of 1) for zone 5, as illustrated in **Figure 6.8a**. In the alternative method used for the assessment of excess pore pressure ratio [i.e. $r_u = \Delta u/(\sigma_v - u_o)$] the response of all zones (**Figure 6.9**) is practically uniform, in terms of the reduction rate of σ'_v, therefore the influence of the effective vertical stress divergence is eliminated and a more uniform response is achieved.

2-pile configuration (2p).- Excess pore pressure (Δu) time histories, from zones located at the same horizontal distance from the axis of symmetry as in the free-field configuration, are plotted and presented in **Figure 6.10**. It is observed that again **zone 5** presents a discrepancy with regard to **zones 1** & **2**, developing excess pore pressures at a faster rate and reaching liquefaction (i.e. $\Delta u = \sigma'_{vo}$ = 100kPa) at approximately one loading cycle earlier. Moreover, **zones 3** & **4**, which are in contact with the gravel pile, also deviate from the anticipated behavior of the first two zones, reaching liquefaction with a slight delay. The particular behavior is attributed to the presence of the pile, which could hinder a uniform response along the horizontal direction of the grid, but the particular effect will be further studied in later sections.

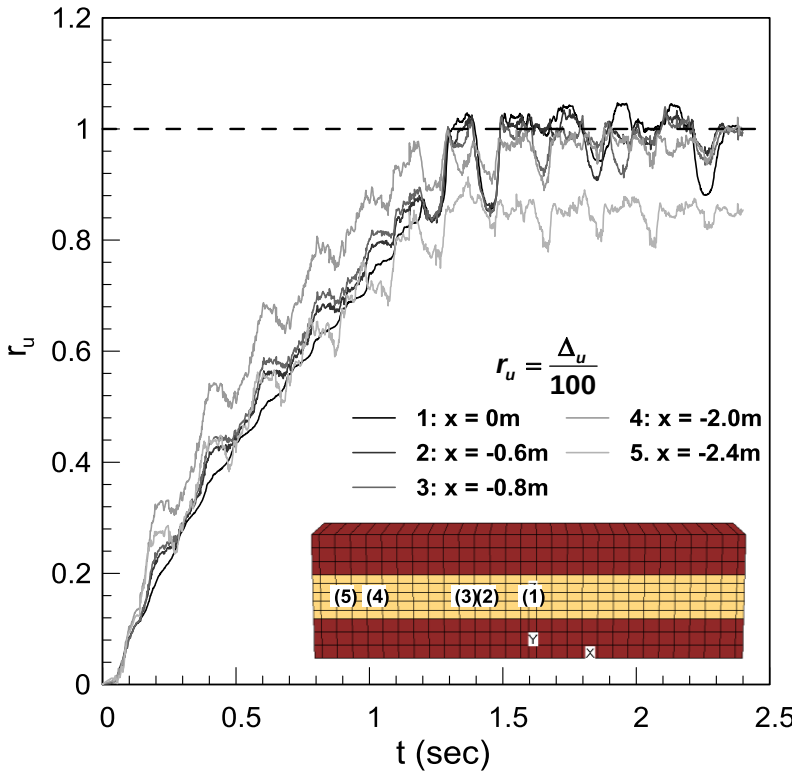

(a)

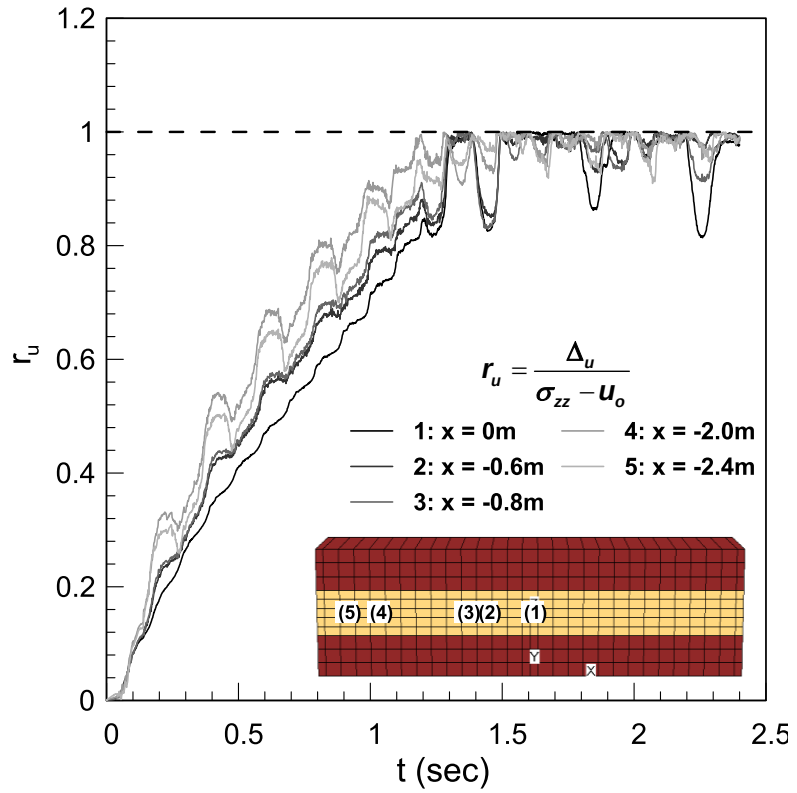

(b)

Figure 6.8: **(a)** Built-in excess pore pressure ratio (r_u) for ff configuration **(b)** Manually calculated excess pore pressure ratio (r_u) for ff configuration.

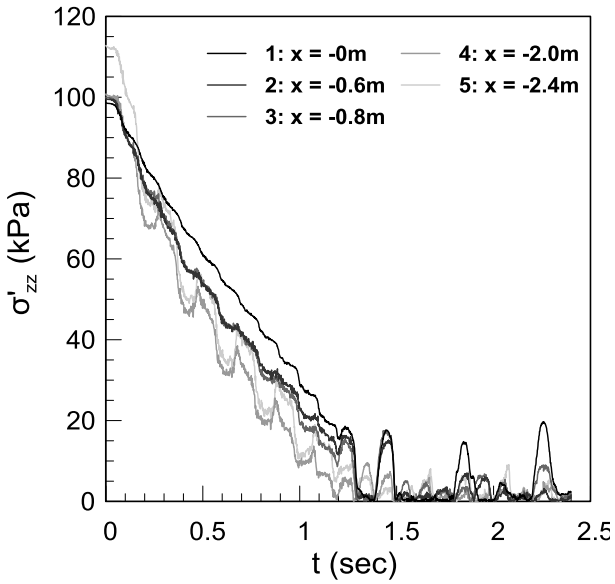

Figure 6.9: Effective vertical stress time histories for ff configuration.

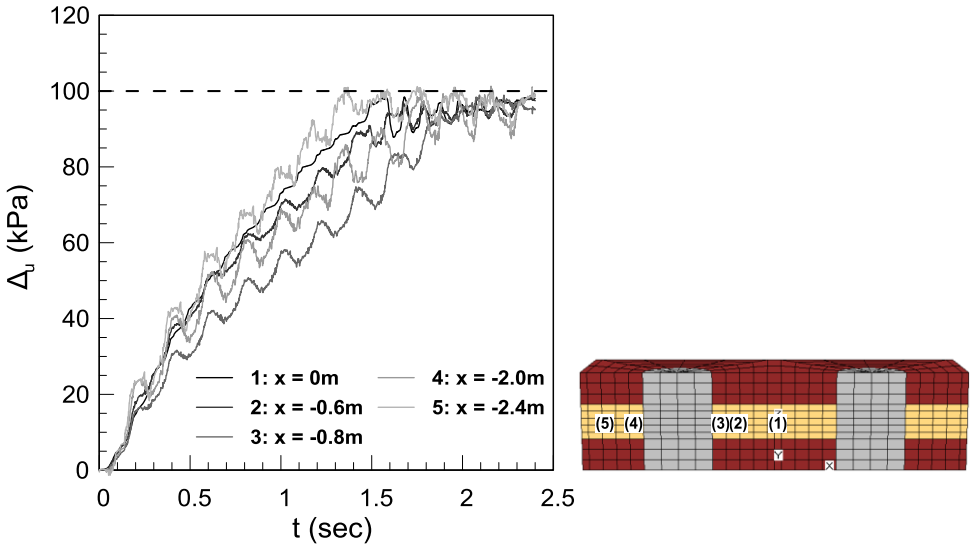

Figure 6.10: Excess pore pressure (Δu) time histories at selected zones for 2-pile (2p) configuration.

Figure 6.11 presents a one – to – one comparison of the excess pore pressure ratio (r_u) time histories computed based on the two different approaches, for the equivalent zones examined in the free field configuration. The two alternative means of r_u assessment, have very little effect in the excess pore pressure built up of zones 1, 2 & 3, nevertheless there is some effect in the case of zones 4 & 5, due to their proximity to the boundaries of the model.

Based on the above analysis, it is concluded that the built-in r_u computation presents a satisfactory performance especially for zones located far from the boundaries. In locations close to the boundaries the particular approach should be utilized with caution, and cross-checked with the excess pore pressure Δu values, since it may have – only – minor effects and lead to underestimated excess pore pressure ratio values. In all the comparisons performed in the sequel, only zones located between the two piles are considered. Therefore, to facilitate and speed up the required comparisons the built-in r_u computation is adopted.

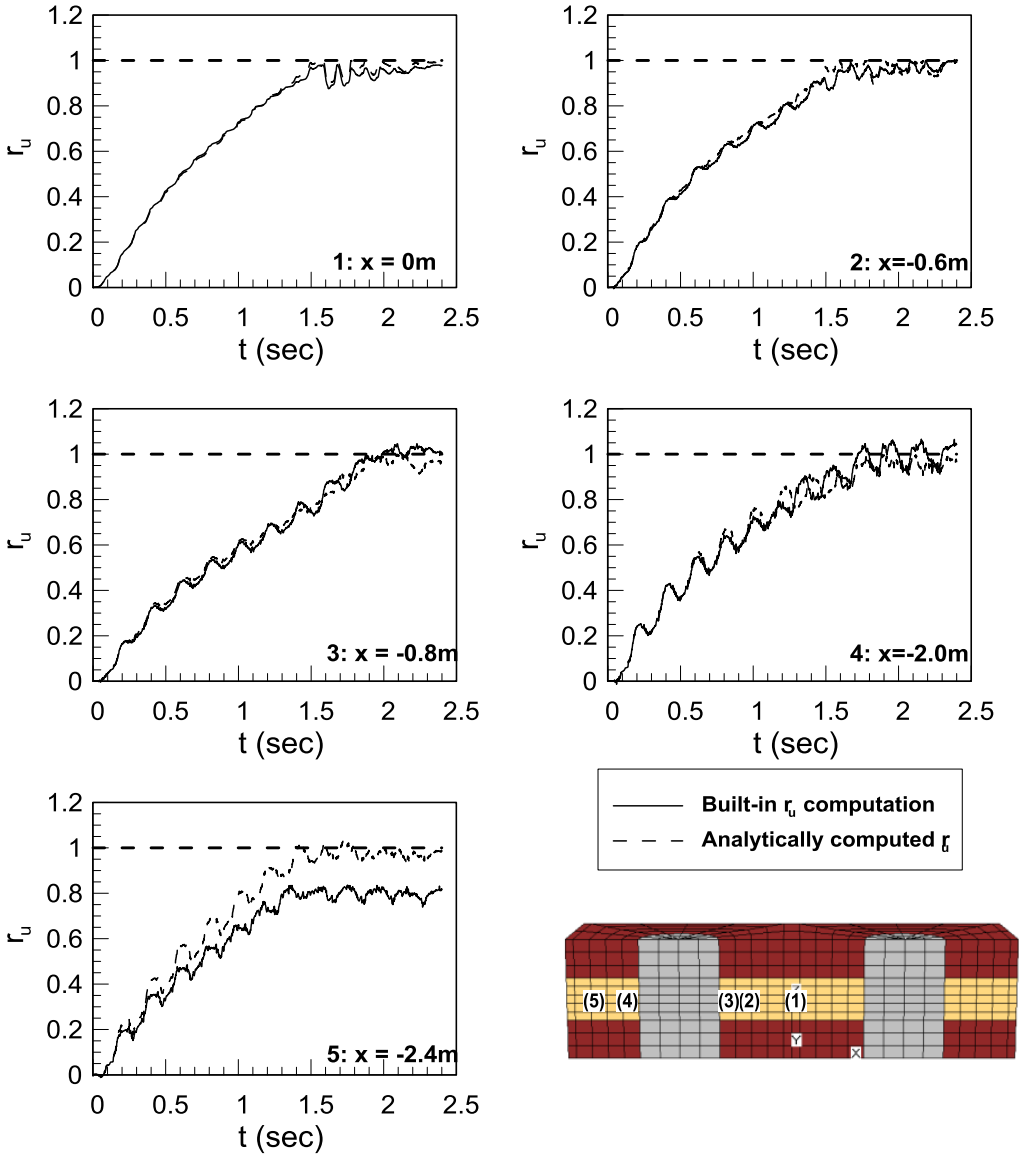

Figure 6.11: Effect of r_u computation method at selected zones for the 2-pile (2p) configuration.

6.2.3 Effect of number of piles

The effect of the number of piles on the excess pore pressure built-up and the response of the system in terms of horizontal accelerations is studied through three different 3-D configurations. Namely, the free-field configuration and arrangements of two and four gravel piles both positioned in one single row. Comparisons are performed for undrained conditions and in terms of excess pore pressure ratio and acceleration time histories.

Excess Pore Pressure Ratio (r_u) time histories.- Excess pore pressure ratio time histories from the middle zone of the free field simulation and the mid-distance between two consecutive gravel drains are plotted in **Figure 6.12**. The black continuous line corresponds to the free field simulation, the gray line to the 2-pile configuration and the light gray line to the row of four gravel piles. In the last case, time histories from zones 1a and 1b as noted in the attached grid to verify the alleged symmetry along the horizontal distance of the configuration.

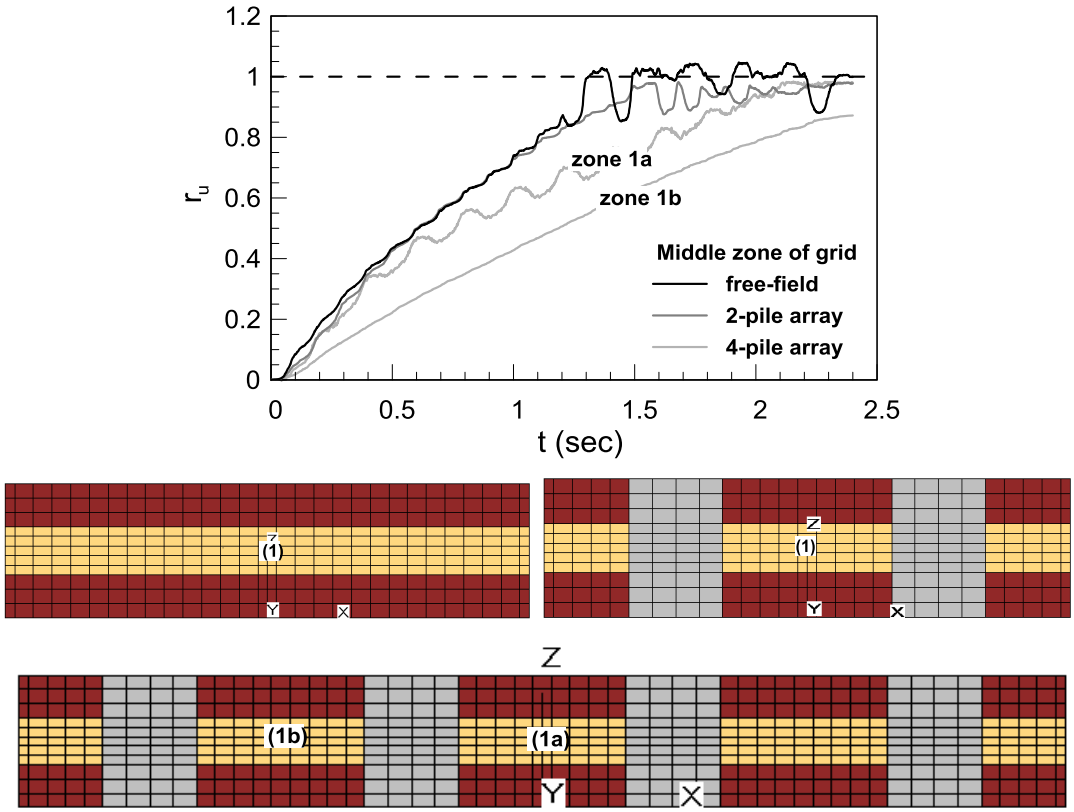

Figure 6.12 Effect of number of piles on the excess pore pressure (r_u) time histories in the central zone for the ff, 2p and 4p configurations.

The 2-pile configuration appears to give comparable results to the free field conditions, reaching liquefaction with a time offset of the order of 0.2sec, corresponding to one loading cycle. On the contrary, the 4-pile configuration presents a totally different excess pore pressure ratio built-up behavior, also exhibiting significant discrepancy between zones located at the mid-distance of two consecutive gravel drains, which were expected to give equivalent results. More specifically, zone 1a reaches liquefaction approximately at the end of shaking, while zone 1b does not liquefy at all and excess pore pressures continue to build up till the end of shaking. The particular effect is attributed to the overall stiffness of the configuration which affects the excess pore pressure built up and renders a different behavior in geometrically symmetrical zones.

Figure 6.13 summarizes excess pore pressure ratio time histories computed at the mid-distance between the left gravel drain and the boundary of the arrangement, for all three cases. Note that epp ratio here is computed analytically avoiding the observed discrepancies mentioned in the previous section and capture the actual epp built up response. Line format is preserved the same for consistency purposes. Once more, the free field and the 2-pile models present very comparable behavior, with the second displaying slightly reduced excess pore pressures at the end of each loading cycle, but reaching analogous and time-synchronized r_u values by the end of shaking. The 4-pile arrangement presents a higher and faster pore pressure built up at the early stages of shaking reaching liquefaction, with a time offset of about two loading cycles earlier compared to the free field case.

Based on the above analysis, it appears that the two-pile configuration approaches the most the free field response, hence it is chosen over the four piles situated in one single row.

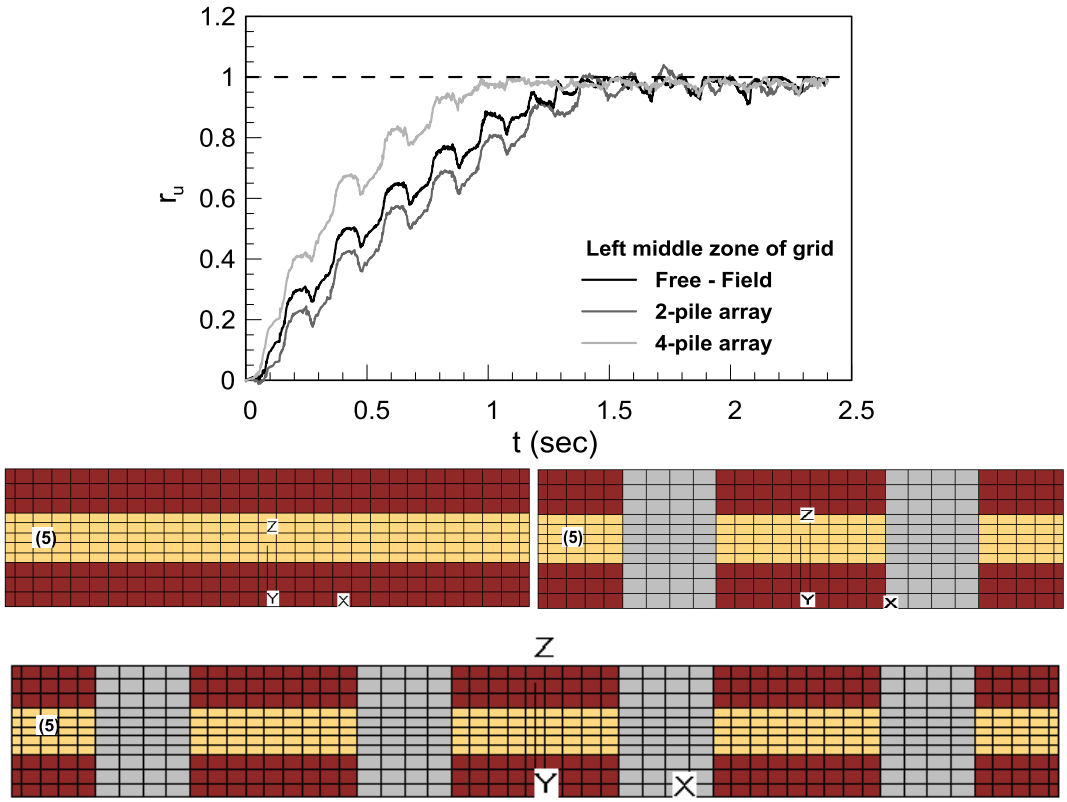

Figure 6.13: Effect of number of piles on the excess pore pressure (r_u) time histories in the left central zone for the ff, 2p and 4p configurations.

Horizontal acceleration (x_{acc}) time histories.- Figure 6.14 summarizes horizontal acceleration time histories computed at the base, the mid-height and the top of the three examined arrangements. The 2-pile arrangement renders a very comparable response to the free field simulation, with equal mean horizontal acceleration values (i.e. 0.20g), recorded on the mid-height, inside the liquefiable sand layer. On the contrary, the 4-pile simulation appears to overdamp the seismic motion, reducing the expected mean acceleration to the middle of the sand layer up to 50%, thus becoming clear that the 2-pile configuration renders comparable results to the free field simulation in terms of mean horizontal acceleration.

Moreover, even though liquefaction occurs in terms of epp ratio values, proof of liquefaction is not observed in the obtained acceleration time histories. Namely, the significantly high acceleration values at the top of the grid imply that the liquefied ground does not act as a natural seismic isolation, as expected. To explain the particular phenomenon, the thickness of the sand layer is compared against the wave length of the imposed excitation. Particularly, for a relative density Dr=60%, the shear wave propagation velocity in the sand ranges between 150 – 200m/sec, with an average value of 175m/sec being considered a

satisfactory approximation. In a liquefied state the shear wave propagation velocity significantly decreases and may reach 50 – 70m/sec (Theocharis, 2011). Therefore, given the period of the excitation (T=0.2sec), the sand layer should be (50÷70)*0.2 = 10÷14m thick to satisfactorily capture evidence of liquefaction in terms of acceleration time history recordings.

In our case, the sand layer is only 0.5m thick; therefore the observed response is justified. Moreover, while it is generally suggested that layer thicknesses should range from 8-10 times the wavelength of the imposed excitation, for the non-liquefied sand, this was not applied in the particular case. The reason lies in the extreme computational cost involved for each analysis, especially for the consolidation analyses presented later, which required some days to complete, even for the considered lay-out. Besides, as it is proved subsequently, numerical results are adequately verified by the corresponding analytical, well established predictions.

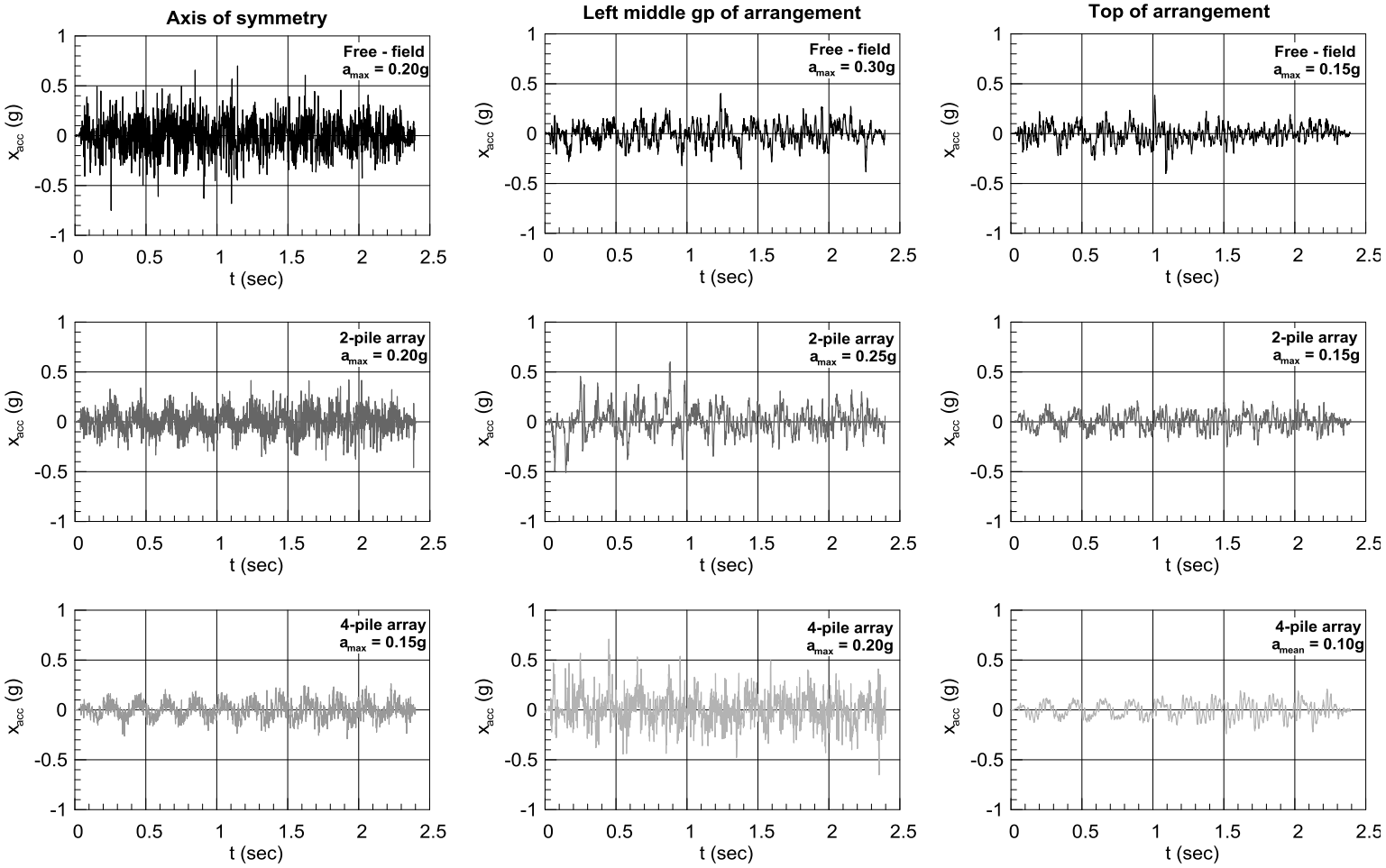

Figure 6.14: Effect of number of piles on horizontal acceleration time histories at the base, mid-height and top of the ff, 2p and 4p configurations.

6.2.4 Effect of pile arrangement

The effect of the number of rows of gravel piles on the system response is examined in the following paragraph. The two arrangements consist of one and two rows of piles and are simulated and analyzed preserving the same problem parameters mentioned in earlier sections.

Excess Pore Pressure Ratio (r_u) time histories.- Figure 6.15, summarizes the excess pore pressure ratio time histories at zones 0 through 5, on a one-to-one basis. Note that zone 0 is located at the middle of the arrangement of the double row of drains and in the mid-depth of the sand layer. Moreover, for zone 5, epp ratio is computed both internally from FLAC 3-D (using a user-defined subroutine in FISH) and analytically (plotted with the dashed lines), as described in previous section, to get a clear view of the actual epp ratio, undisturbed from any potential boundary effects. In all zones examined herein, epp built up appears to be synchronized and liquefaction is achieved concurrently within the imposed loading time history, i.e. at approximately 7 – 8 loading cycles. Note again the delay in the epp built up in zones 3 & 4, which will be analyzed in subsequent paragraph.

Horizontal acceleration (x_{acc}) time histories.- Figure 6.16, displays the horizontal acceleration time histories computed at the base, the mid-depth and mid-length of the sand layer and the top of the clay layer of each configuration. The consistency observed between the two models is also obvious, rendering equivalent maximum acceleration values and time histories. Overall, the response between the two models is consistent and only minor differences are observed in terms of epp ratio peak values. The major drawback in the case of the double row of gravel piles is the overall size of the grid and the time required to perform each numerical analysis. Therefore, due to the increased computational load, the particular arrangement was abandoned and the 2-pile configuration is finally selected for the execution of the main body of numerical analyses.

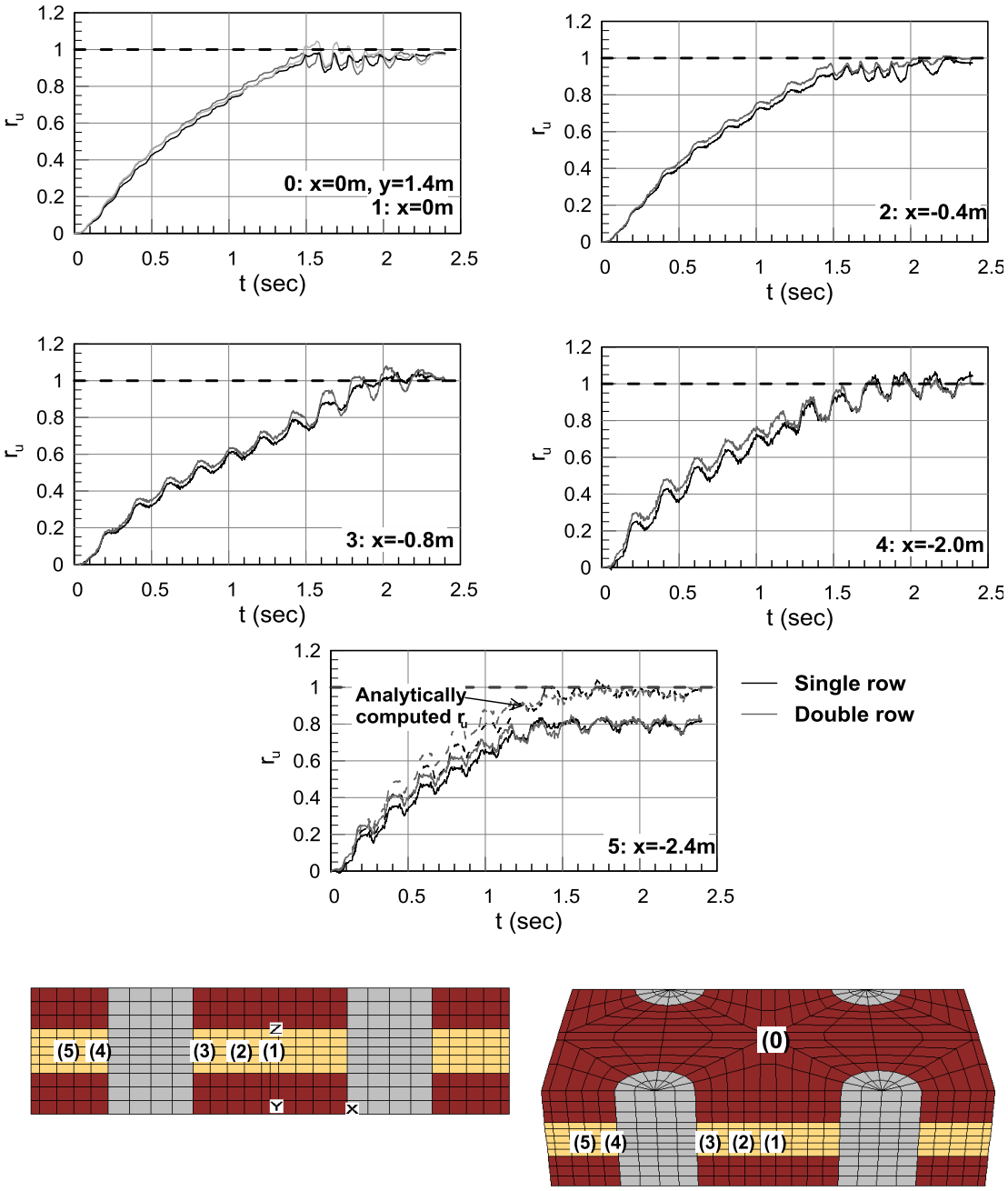

Figure 6.15: Effect of pile arrangement on excess pore pressure ratio (r_u) time histories for the 2p and 4psq configurations.

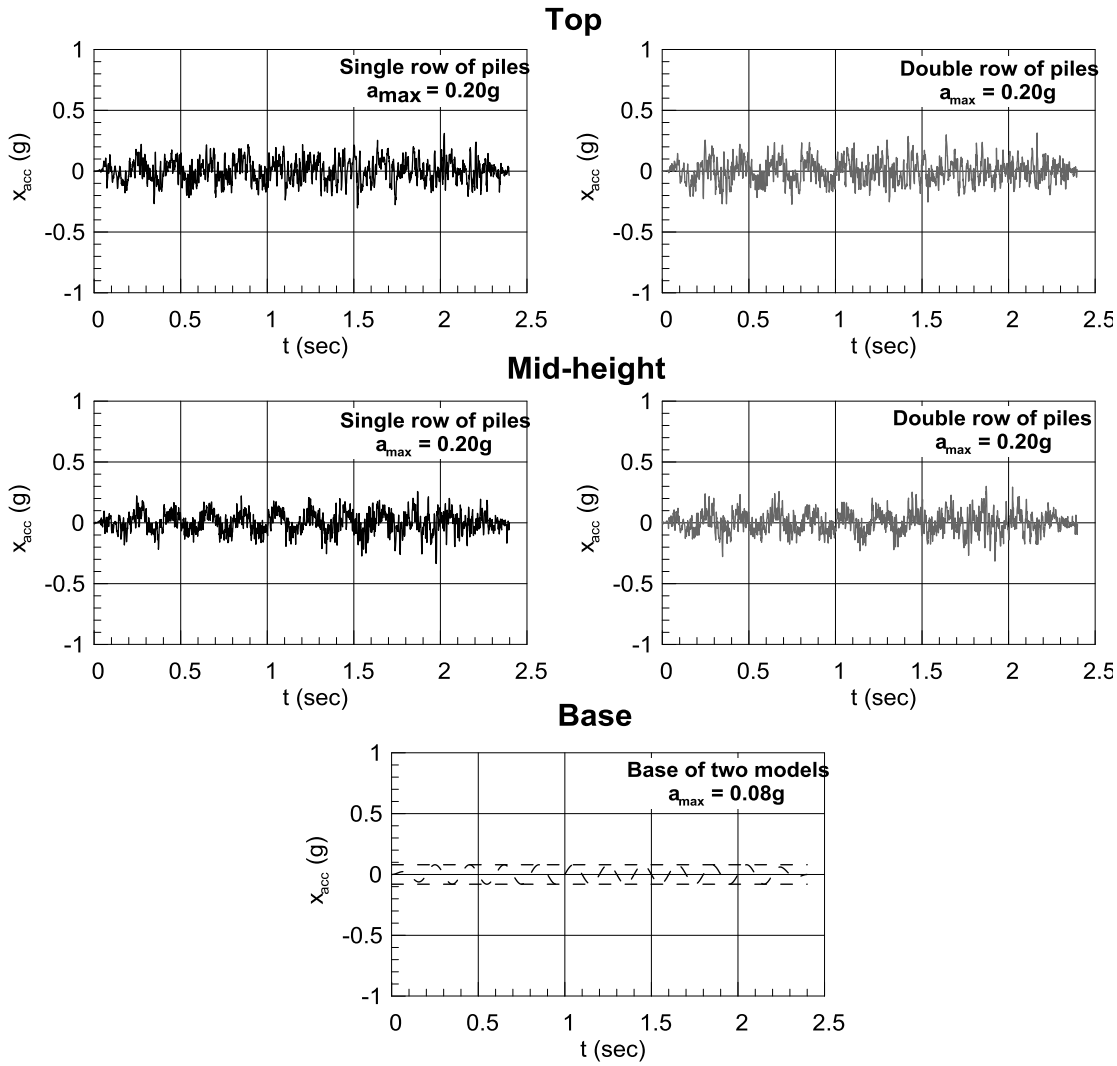

Figure 6.16: Effect of pile arrangement on horizontal acceleration time histories at the base, mid-height and top of the 2p and 4psq configurations.

6.2.5 Effect of drain permeability

Both basic design methodologies namely the first proposed by Seed & Booker (1977) and the suggested revision published by Bouckovalas et al. (2009) assume that the drain material is 200 times more permeable than the sand material. On the other hand, in the finite difference code FLAC 3-D the time step required in each computational cycle significantly increases for a low permeability coefficient, thus proportionally affecting the required computational time. In the following section the above assumption (i.e. $k_{drain} = 200*k_{sand}$) is revisited and is attempted to reduce k_{drain} by half, aiming in reducing the required computational time with negligible effects in the accuracy of the predictions.

The 2-pile configuration is examined under partially drained loading conditions, initially considering the permeability coefficients reported previously (i.e. $k_{sand} = 10^{-5}$ m/sec and k_{drain}

= $2*10^{-3}$m/sec) and subsequently, reducing by half the permeability coefficient of the drain, i.e. k_{drain} = 10^{-3}m/sec. The two separate analyses are compared in terms of excess pore pressure time histories in equivalent zones, summarized in **Figure 6.17**. Apparently, there is very little effect by the performed change in the permeability coefficients; therefore in subsequent analyses, the reduced permeability for the gravel drain material will be applied.

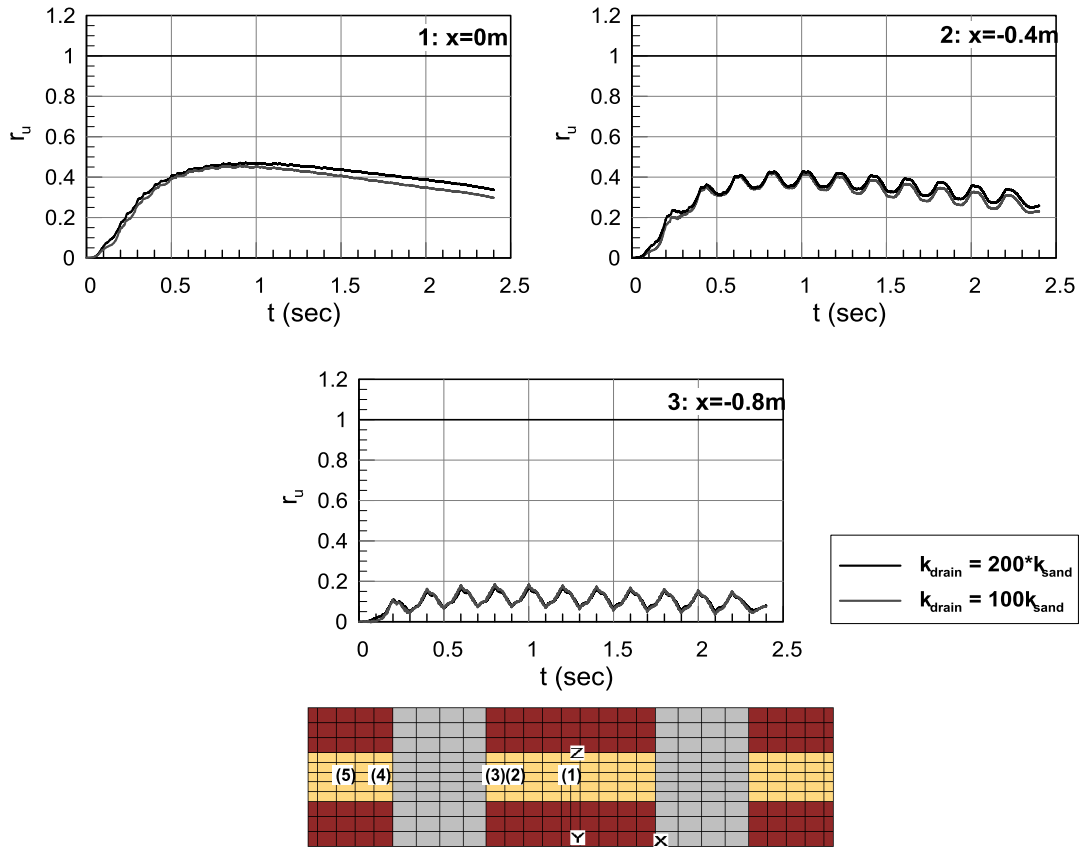

Figure 6.17: Effect of drain permeability on excess pore pressure ratio (r_u) time histories for the 2p configuration.

6.2.6 Effect of pile stiffness

Returning to the discrepancy observed in the excess pore pressure ratio response of the zones in contact to the gravel pile, the following parametric analyses aim at clarifying whether the particular behavior, may be attributed to the stiffness of the pile. Zones 3 & 4 are most affected exhibiting very comparable epp ratio built up response. Among the two, focus will be given on zone 3, which is later used in the calculation of the compressibility coefficient $m_{v,3}$.

In the basic analysis the elastic parameters (bulk and shear modulus) of the clay layers and the gravel material are set equal to K=130,000kPa and G=60,000kPa respectively. Based on the relationships of elasticity, the above parameters render a Young's modulus equal to E_{drain}=156,000kPa and a 1-D compression modulus equal to D_{drain}=210,000kPa, which remains constant throughout the analysis. For the sand layer, the maximum shear modulus (G_{max}) is expressed through *Equation 6.2*, namely the well-established relationship proposed by Hardin (1978)

$$G_{\max} = \frac{B \times p_a}{0.3 + 0.7 \times e} \sqrt{\frac{p}{p_a}} \qquad 6.2$$

where: B model parameter

e the void ratio

p isotropic effective stress

p_a atmospheric pressure (=98.1kPa)

Thus, for the mid-depth of the sand layer, a relative density D_r = 60% (i.e. e = 0.661) and a ratio of effective stresses K_o = 0.5, the maximum shear modulus G_{max} is equal to 79.700kPa. Considering a Poisson's ratio equal to ν = 0.33, the maximum Young's modulus is E_{max}=268,128kPa and the respective 1-D Compression Modulus in the order of D_{sand}=315.000kPa. Note that the ratio of the gravel pile to the sand layer permeability coefficient was set equal to 100.

The parametric investigation included four additional cases, in which the pile stiffness is reduced to different portions of G_o, namely G = 0.75, 0.50, 0.25 and 0.08G_o (G_o=60.000kPa) respectively. The obtained results are compared in terms of excess pore pressure built up under undrained conditions, focusing on the response of zones 1 and 3, as demonstrated in **Figure 6.18.** It is observed that the reduction of the pile stiffness does not significantly affect the excess pore pressure ratio built up, and the discrepancy in the response of the examined zones is preserved even in the case where the gravel pile stiffness is reduced to 0.08G_{max}, namely to about 5.000kPa.

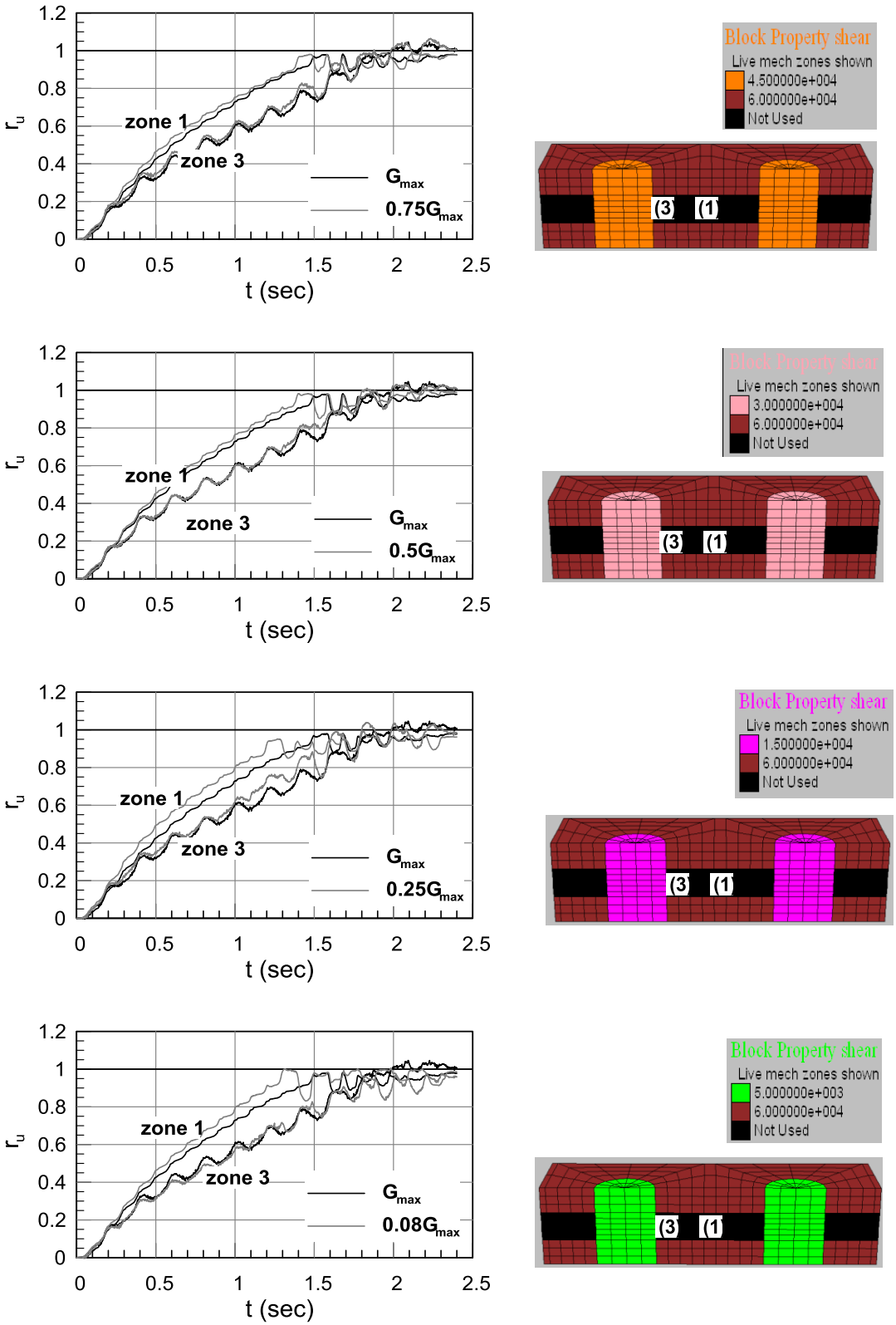

Figure 6.18: Effect of drain permeability on excess pore pressure ratio (r_u) time histories for the 2p configuration.

6.2.7 Effect of mesh descritization

The response of the gravel drain – soil system is evaluated under a differently discretized grid, in order to eliminate potential numerical - induced effects. Hence, the new grid exhibits a denser discretization around the interface area of the gravel pile and the soil, as illustrated in **Figure 6.19**. In particular, beginning from the axis of symmetry of the pile the zone width is reduced by half and then increased at a ratio of 1:1.5 till the center of the grid arrangement. The analysis is executed under the same problem parameters, in order to be able to evaluate the effect of the increased grid density and preserving the low gravel pile stiffness (0.08Gmax = 5000kPa).

Figure 6.20, presents the response of zones 1 through 6, whose location is marked in the attached grid, in terms of excess pore pressures Δu, and excess pore pressure ratio r_u. It is interesting to note that the response of zone 6 exhibits a fast rate of excess pore pressure ratio built up, comparable to the response of the other zones, also reaching liquefaction within the same loading cycle, as opposed to the behavior detected previously. Overall, the system response is judged to be satisfactory in terms of excess pore pressure ratio built up.

The proposed grid refinement is also evaluated against the original configuration and the free field response in **Figure 6.21a** & **b**. **Figure 6.21a** summarizes the excess pore pressure ratio time histories derived for the central zone of each case, from which it is concluded that the refinement effect is not so significant, since in both cases the free field response is satisfactorily captured. **Figure 6.21b** presents the corresponding epp ratio time histories for the zone in contact to the pile for the 2-pile configuration, or the zone at the equivalent horizontal distance from the axis, for the free field configuration. Clearly, the proposed refinement leads to an acceleration of the excess pore pressure ratio built up, and creates a more uniform response in terms of excess pore pressures, adequately capturing the free field response. Given the above, the refined grid is going to be adopted in the the assessment of the drainage capacity of the gravel drains presented in the following sections.

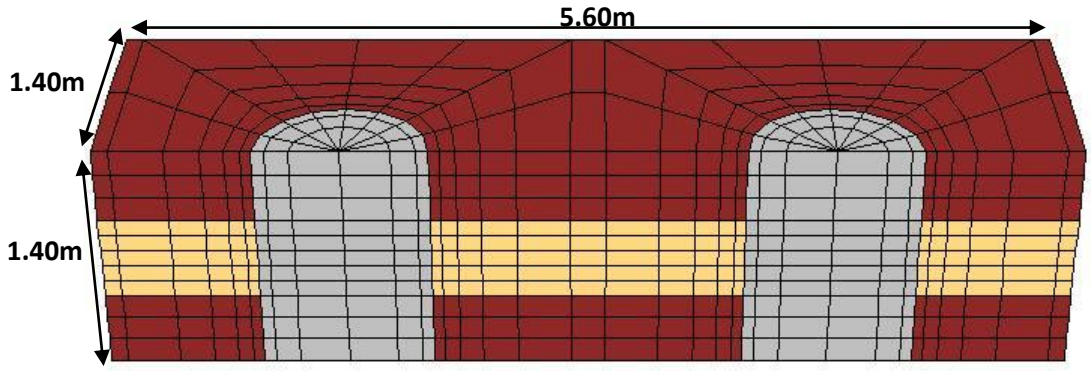

Figure 6.19: New proposed refined grid.

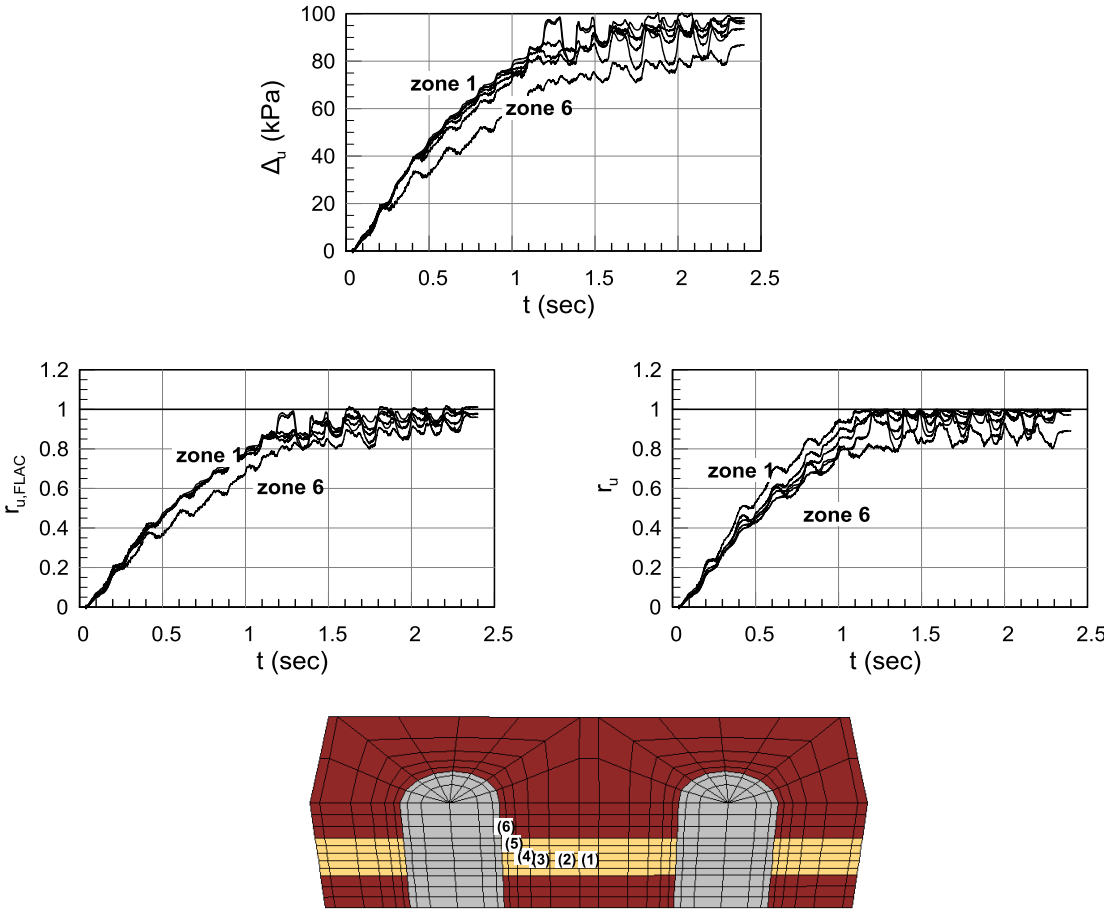

Figure 6.20: Excess pore pressure Δu and epp ratio (r_u) time histories for selected zones of the refined grid.

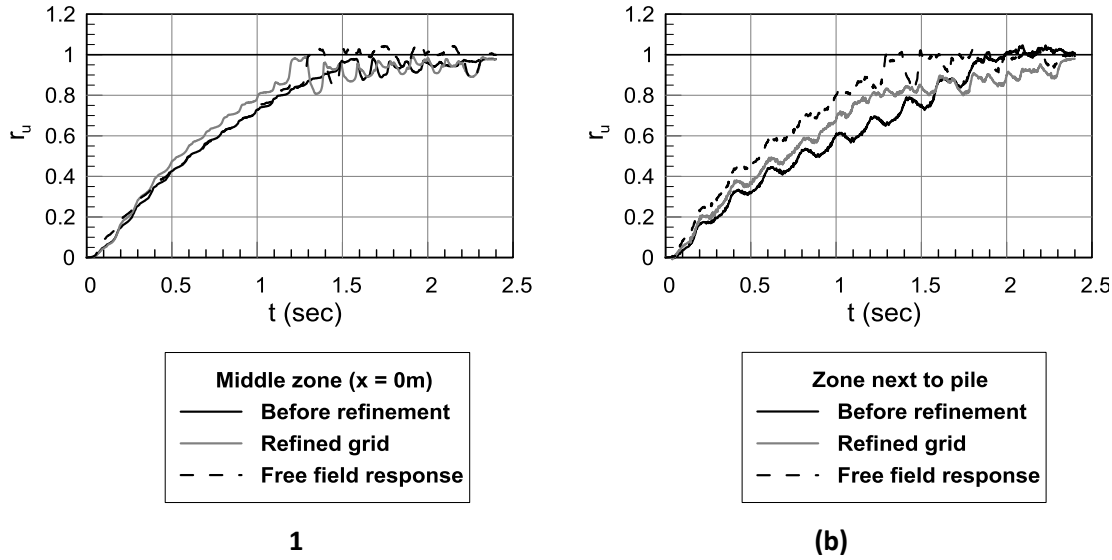

Figure 6.21: Excess pore pressure ratio (r_u) time histories for **(a)** central zone and **(b)** adjacent zone to pile for ff, original 2p grid and proposed refinement.

6.3 Numerical verification of the new analytical approach

6.3.1 Analytically computed $m_{v,3}$

To check the validity of the revised analytical approach by Bouckovalas et al. (2009) for drain design, a number of numerical analyses were performed, in which the coefficient of sand permeability varied from k_{sand} = 0 (undrained conditions) to $1*10^{-4}$m/s, as shown in **Table 6.1**. In all analyses the coefficient of drain permeability was 100 times that of k_{sand}.

The results of these analyses are presented in **Figure 6.22** in the form of excess pore pressure time histories. The first thing to observe is that the curves in **Figure 6.22** show the characteristic shape of the revised analytical predictions, where a peak is attained at intermediate stages of shaking, followed by a smooth decrease, while shaking persists.

The second thing requiring checking is whether the numerical predictions may be fitted with a unique set of soil parameters, excluding the permeability coefficient, which varied as in **Table 6.1.** The first step was to fit the numerical predictions for undrained shaking (i.e. k_{sand} = k_{drain} = 0), which was achieved by trial and error as it is shown in **Figure 6.23**. Namely, **Figure 6.23** includes numerically derived (under undrained conditions) epp ratio (r_u) time histories from 22 zones around the gravel pile as well as analytical predictions of epp ratio built-up, based on *Equation 5.1,* (Seed, Martin & Lysmer, 1975) for three distinct values of A, namely 0.70, 1.40 and 2.00 and three representative t_l values, namely t_l=1.2,1.3 & 1.4sec. Note that

the analytical predictions begin with a time offset of 0.2 sec, to disregard the first loading cycle of increasing magnitude, (see also **Figure 6.6**) and the following conclusions are drawn:

- The comparison between numerical results and analytical predictions, essentially confirms the ability of the numerical analysis to simulate the analytically predicted epp ratio built up, hence providing a solid numerical background for the study of the gravel drain-soil system response under drained conditions.
- The recommendation made in chapter 4 concerning the use of an A value, in the analytical relationship by De Alba et al. (1975), equal to 1.40 is now further justified and will be adopted in the subsequent steps.
- The required time for liquefaction ranges from t_l=1.20 to 1.40sec, rendering 5, 5.5 and 6 cycles to liquefaction for T=0.2sec, respectively. The most representative value of t_l=1.3sec will be adopted in the following sections.

Table 6.1: Values of permeability coefficient (m/sec).

Name of Analysis	Sand Permeability coefficient (m/sec)	Gravel drain permeability coefficient (m/sec)
a.	10^{-4}	10^{-2}
b.	$5*10^{-5}$	$5*10^{-3}$
c.	$2*10^{-5}$	$2*10^{-3}$
d.	10^{-5}	10^{-3}
e.	$5*10^{-6}$	$5*10^{-4}$
f.	$2*10^{-6}$	$2*10^{-4}$

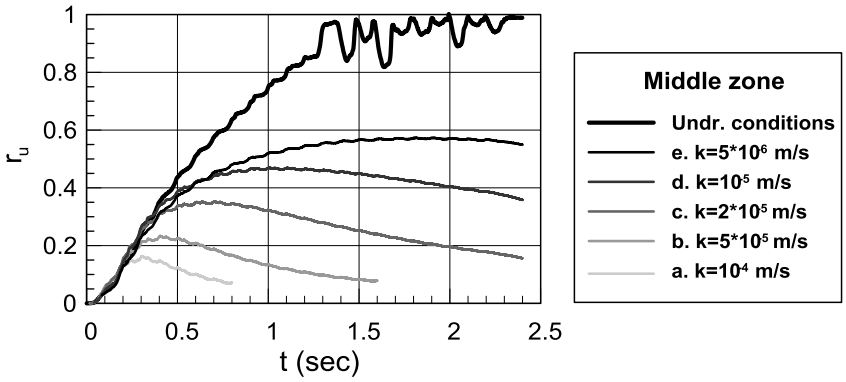

Figure 6.22: Numerically derived excess pore pressure ratio (r_u) time histories in the central zone for different permeability coefficients.

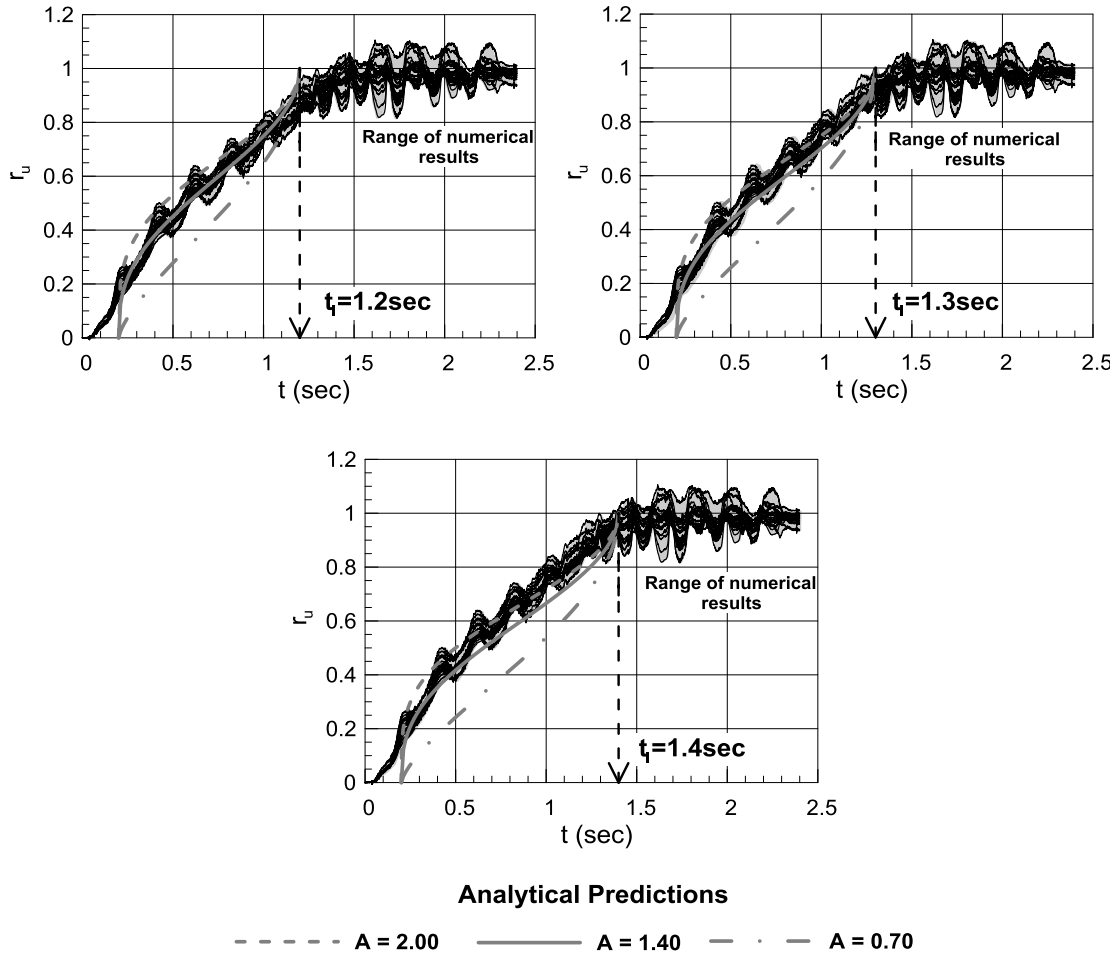

Figure 6.23: Numerically derived r_u time histories and analytical predictions for different A values.

Having specified t_o, A, and t_l, the second step includes the fitting of the analytical predictions to the numerically predicted r_u time histories, by changing the volume compressibility coefficient $m_{v,3}$. The associated comparisons are shown in **Figure 6.24** through **Figure 6.27**. Namely, **Figure 6.24** presents all the zones starting from the zone in contact with the pile, to the axis of symmetry of the configuration, in which $m_{v,3}$ is computed. The obtained values are summarized in **Figure 6.24** for one of the numerical analyses (c. k=2*10-5m/sec) . The specific values are practically constant, independently of the distance b.

For all numerical analyses, back calculation of $m_{v,3}$ is performed based on two different convergence criteria and for the middle zone of the configuration. According to the first criterion, the back-calculated $m_{v,3}$ values must render the same peak $r_{u,max}$ value to the numerical simulation whereas according to the second one, $m_{v,3}$ values produce the maximum $r_{u,max}$ value at the same moment of dynamic shaking as the numerical simulation. The analytically computed liquefaction curves based on the Bouckovalas et al. (2009)

methodology are plotted along with the numerically computed time histories in **Figure 6.26.** The set of numerical and analytical predictions for undrained conditions is also plotted for consistency purposes with the thicker lines. The resulting $1/m_{v,3}$ values are summarized in **Table 6.2**. Considering a small permeability coefficient ($k=2*10^{-6}$m/s), convergence is hardly obtained based on both criteria. Hence, the specific analysis is not considered in the back-fitting of the Seed & Booker (1977) methodology nor included in the subsequent sections. **Figure 6.27** presents a comparison between the analytical methodology proposed by Seed & Booker (1977) and the numerical predictions. The comparison is performed for A=0.70 and 1.40, following the first convergence criterion.

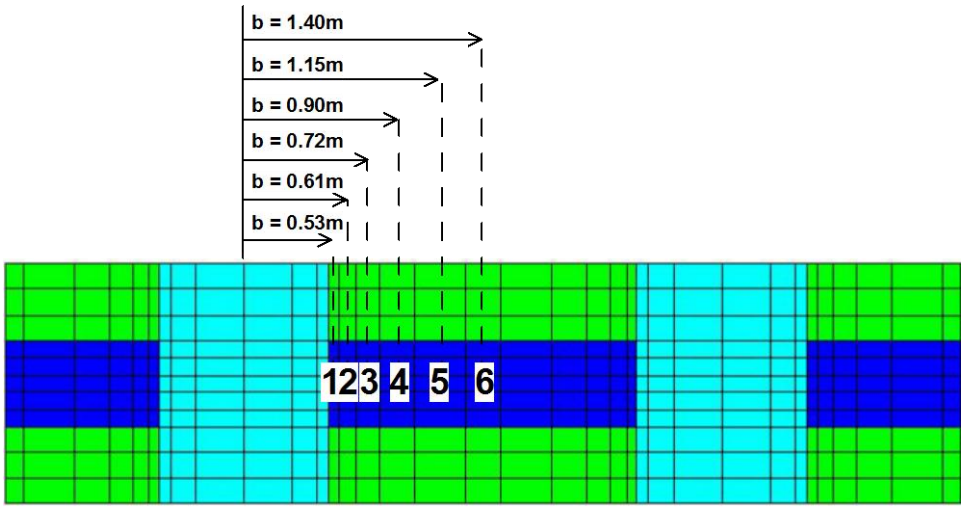

Figure 6.24: Horizontal distances (b) from the center of the pile.

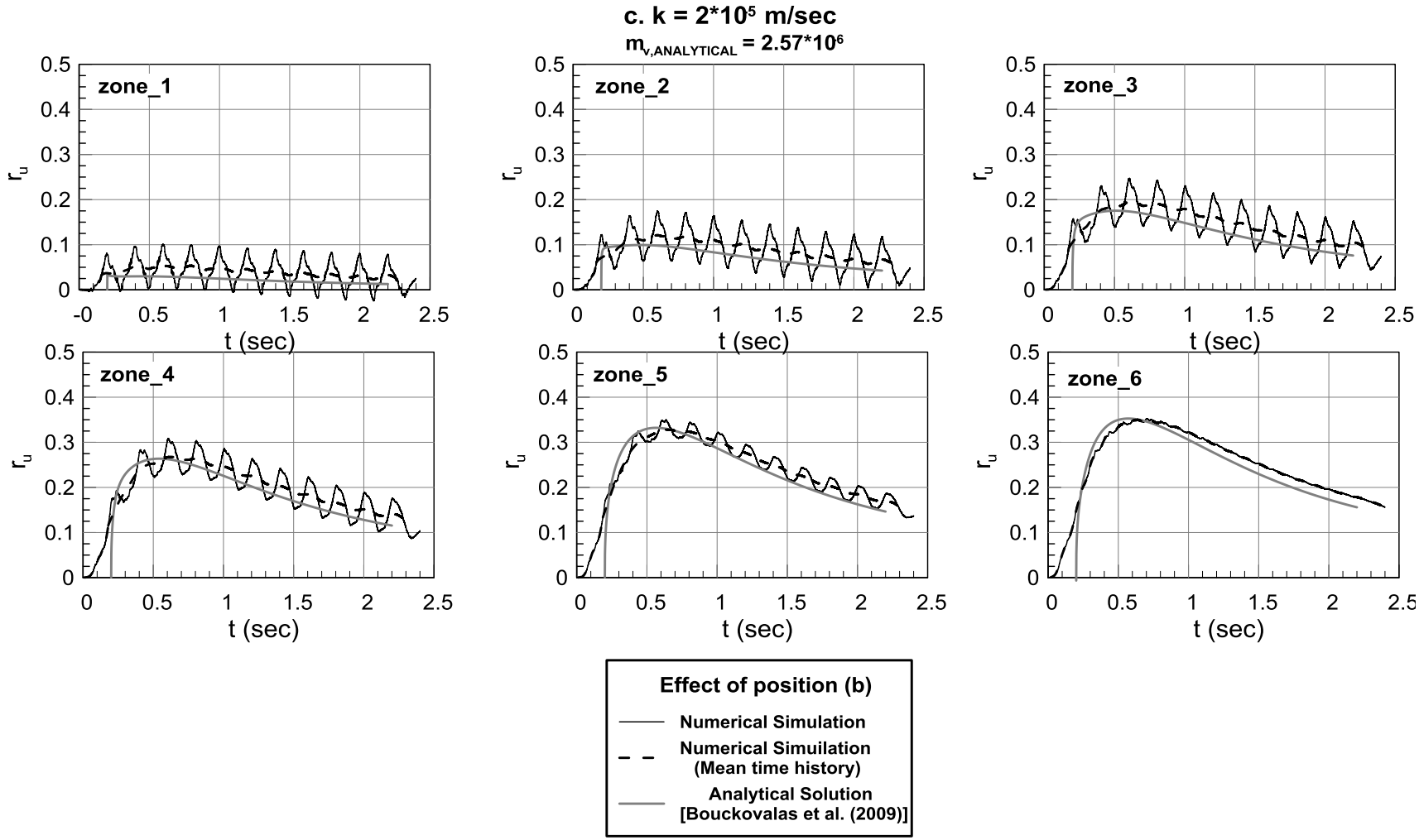

Figure 6.25: Numerical verification of analytical solution.

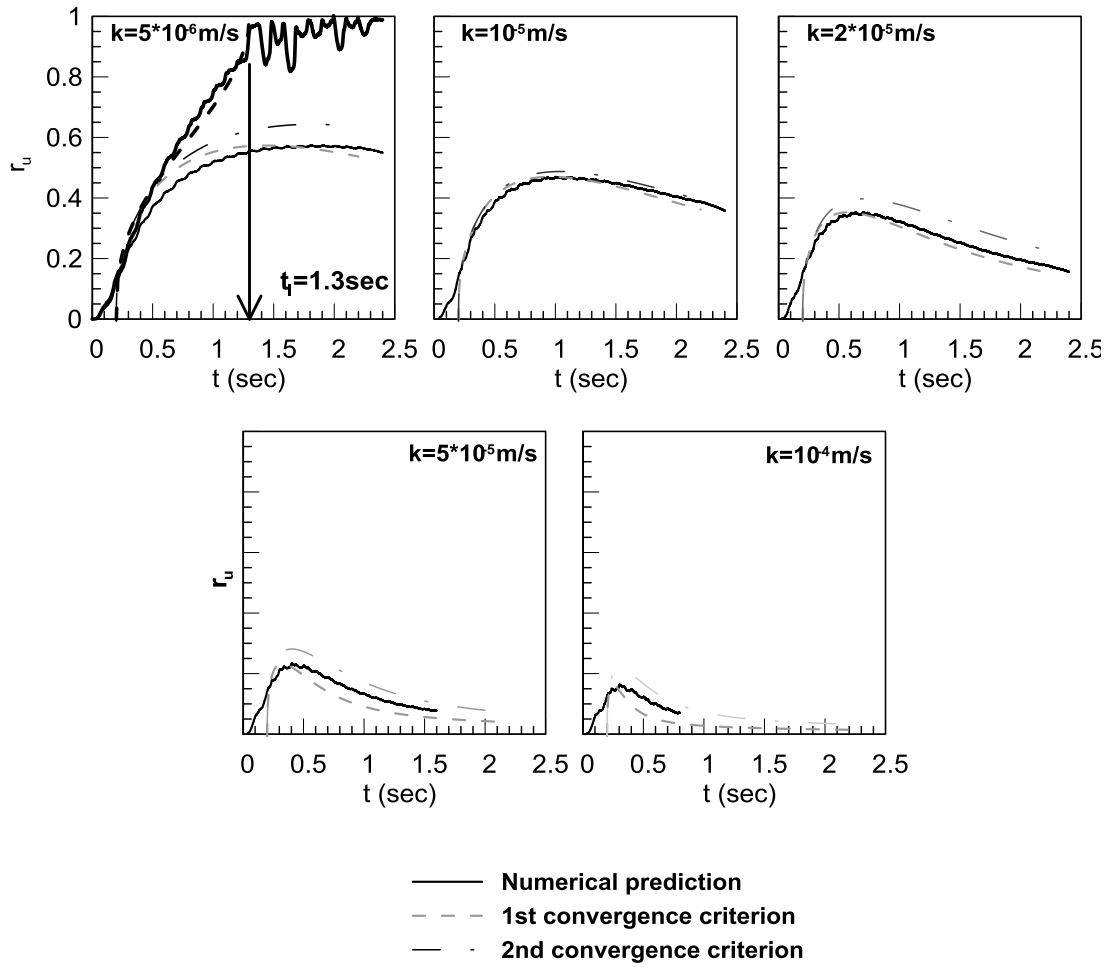

Figure 6.26: Back-fitting of the Bouckovalas et al. (2009) methodology for A=1.40, to numerical predictions for two criteria of convergence for tl=1.3sec and different values of permeability coefficient k.

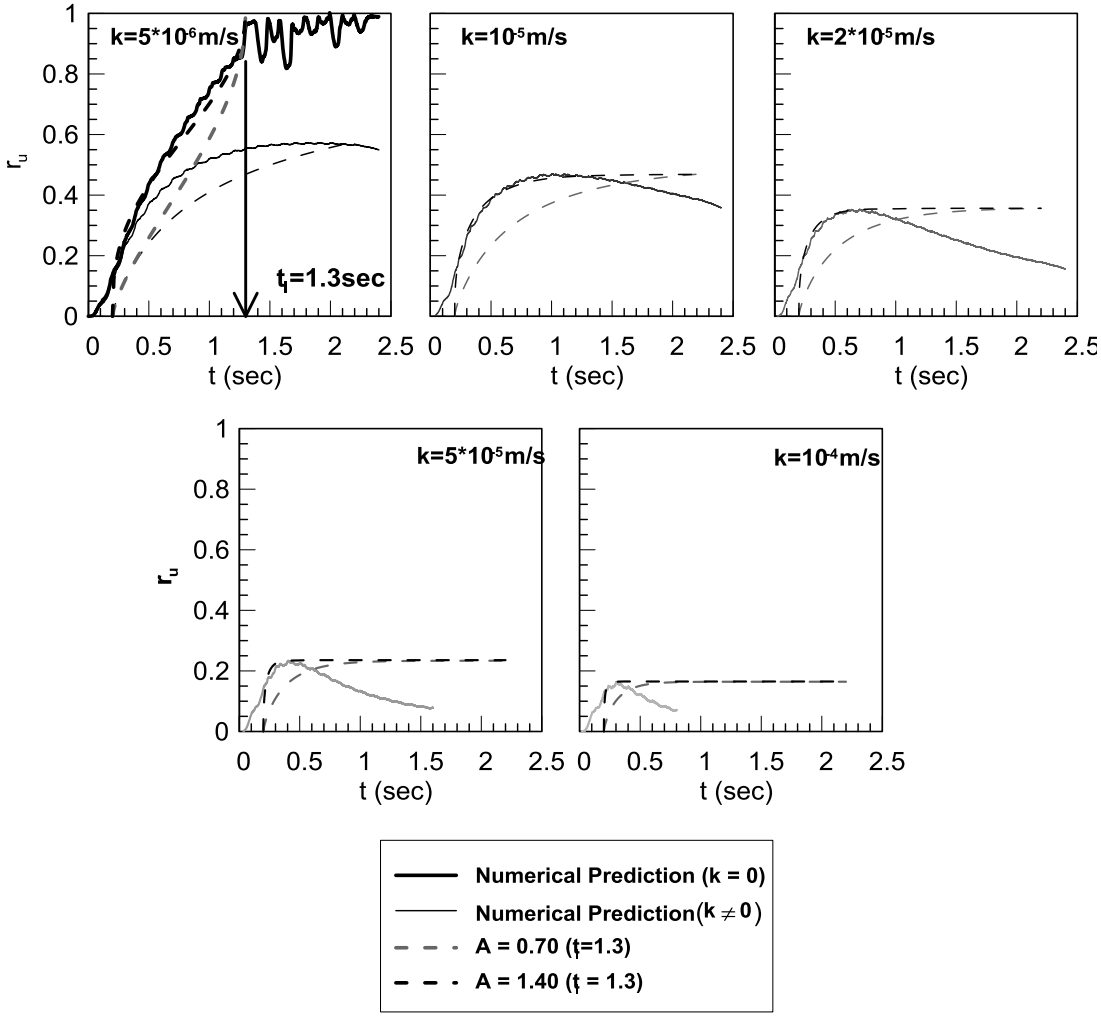

Figure 6.27: Back-fitting of the Seed & Booker (1977) methodology for A=0.7, to numerical predictions, based on $r_{u,max}$ for t_l=1.3sec and different values of permeability coefficient k(m/s).

Table 6.2: Back-calculated $1/m_{v,3}$ values for the Bouckovalas et al. (2009) methodology and two convergence criteria.

Bouckovalas et al. (2009) – A=1.40								
1st Convergence criterion					2nd Convergence criterion			
k (m/sec)	$m_{v,3}$ ($*10^{-6}$)	$1/m_{v,3}$ ($*10^{5}$)	$r_{u,max}$	T_{ad}	$m_{v,3}$ ($*10^{-6}$)	$1/m_{v,3}$ ($*10^{5}$)	$r_{u,max}$	T_{ad}
10^{-4}	2.05	4.88	0.17	39.02	3.80	2.63	0.17	21.05
$5*10^{-5}$	2.95	3.39	0.26	13.56	3.66	2.73	0.26	10.93
$2*10^{-5}$	3.26	3.07	0.39	4.91	3.40	2.94	0.39	4.71
10^{-5}	2.92	3.42	0.51	2.74	2.65	3.77	0.51	3.02
$5*10^{-6}$	2.10	4.76	0.63	1.90	2.13	4.69	0.63	1.88
$2*10^{-6}$	5.80	1.72	0.47	2.76	-	-	0.47	-

Based on **Figure 6.25** the following conclusions are drawn:

- Coefficient of volume compressibility $m_{v,3}$ is practically constant, independently of the distance b from the gravel drain.
- Assuming the appropriate $m_{v,3}$ value, the analytical solution agrees with the numerical results, hence implying that a fully dynamic problem can be adequately captured by a pseudostatic approach, adopted in the Seed & Booker (1977) analytical methodology.

The $m_{v,3}$ values which were used to fit the numerical predictions are plotted against the maximum r_u value of each analysis in **Figure 6.28.** Observe that for $r_{u,max}$ values within 0.2 – 0.5, which is the useful range for drain design, $1/m_{v,3}$ values remain practically constant independently of the sand permeability. Moreover, for a given permeability coefficient the numerical predictions change slightly from one zone to the other, with the central zone having about 40% larger $1/m_{v,3}$ than the zone adjacent to the pile. Finally, taking into account that the fitting procedure is rather gross and approximate it may be concluded that $m_{v,3}$ can be indeed assumed to be constant (r_u independent) for r_u = 0.2 – 0.5 as it is assumed by the original as well as the revised analytical method for drain design.

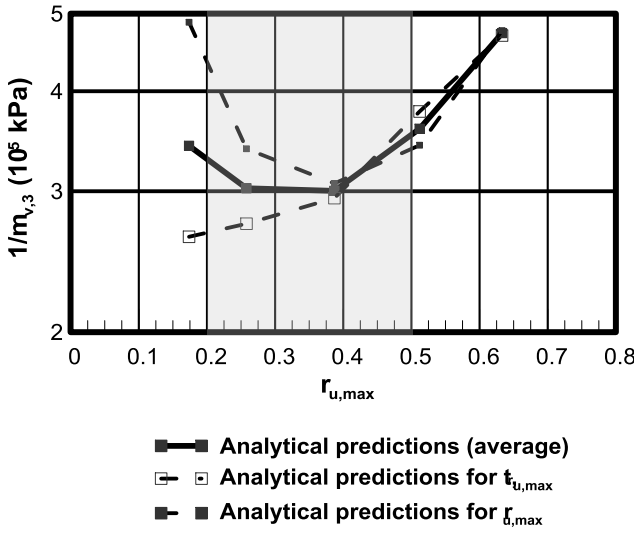

Figure 6.28: Back-fitted $m_{v,3}$ values for the useful $r_{u,max}$ range in drain design.

6.4 Numerical evaluation of the volumetric compressibility coefficient $m_{v,3}$

From the entire evaluation of the drain performance presented in this chapter as well as in the previous Chapter 5, it is realized that drain design is mostly dependent on the correct choice of the volume compressibility index $m_{v,3}$. Unfortunately, this soil parameter cannot be directly measured from conventional soil mechanics tests (e.g. such as the soil permeability coefficient k_r) and is mostly derived on the basis of published experimental data from undrained cyclic triaxial tests (PHRI, 1997).

Hence to gain insight to the proper $m_{v,3}$ values that need to be used in drain design, the back-calculated values presented earlier are compared against three independent sets of $m_{v,3}$ values. Namely:

Numerically predicted $m_{v,3}$ values.- obtained from the simulation of the post-shaking consolidation of the liquefied ground. To obtain this set of data, the definition of the coefficient of volume compressibility, expressed through *Equation 6.3*, is used. Namely, the time of the maximum excess pore pressure $\Delta_{u,max}$ occurence is located and a consolidation analysis is initiated until total dissipation of excess pore pressures.

$$m_{v,3} = \frac{\Delta \varepsilon_{vol}}{\Delta u_{\max}} \qquad 6.3$$

where $\Delta_{u,max}$ = the maximum excess pore pressure

$\Delta\varepsilon_{vol}$ = the volumetric strain developing during consolidation

The consolidation analysis is performed by removing the seismic excitation, zeroing all velocities in the grid and allowing enough time for epp dissipation. The epp ratio time histories up to the maximum excess pore pressure development, followed by the consolidation part are presented in **Figure 6.29.** Volumetric strains are monitored throughout the consolidation analysis and the relative volumetric strain to the time of initiation of consolidation is considered in the calculations. $1/m_{v,3}$ values are determined for all the zones of the grid, starting from the axis of symmetry to the zone in contact with the gravel drain.

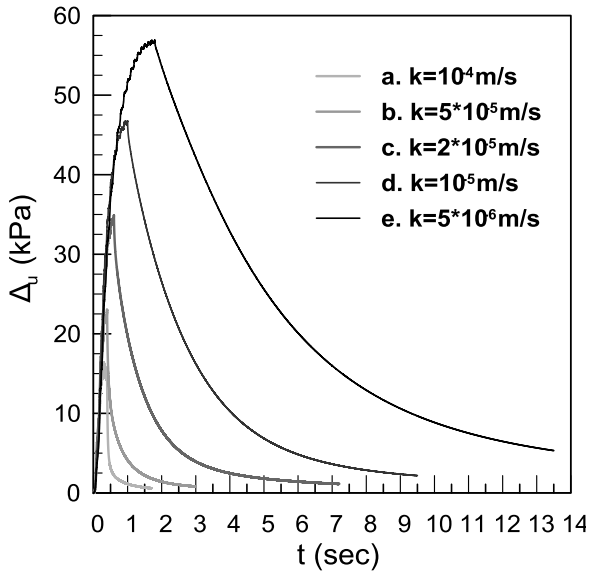

Figure 6.29: Typical excess pore pressure built-up and dissipation time histories for the performed numerical analyses.

Numerically predicted $m_{v,3}$ based on DSS & CTX tests.- To obtain this set of data, laboratory test simulations (cyclic triaxial and direct simple shear) are performed with FLAC 3D, also using the same constitutive model for the liquefiable sand. Coefficient of volume compressibility is measured and computed following the same definition as above.

The cyclic isotropic triaxial test, which is also proposed by Seed & Booker (1977) as the appropriate laboratory test to estimate $m_{v,3}$, was simulated considering a 1m×1m×1m cubic element of liquefiable sand at an initial effective confining stress of 100kPa. Velocities were considered to be constant in all boundaries and loading conditions included applying a cyclic deformation along the vertical direction z, of constant magnitude, and cyclic deformations along directions x and y, having half the magnitude of the vertical deformation. The overall set-up, loading and boundary conditions are demonstrated in **Figure 6.30**. The element response analysis was repeated for several epp ratio (r_u) values (i.e. 0.10, 0.20, 0.30, 0.40, 0.50) and then followed by a one-dimensional consolidation analysis, performed by zeroing all nodal velocities and imposing an adequately small velocity at the top boundary of the element, until total reconstitution of the initial effective stresses. Consequently, $m_{v,3}$ was computed following the procedure described in previous sections.

For the direct simple shear test the same grid layout was assumed, with the same boundary conditions and constitutive model. Loading conditions involved a constant vertical stress and a cyclic shear stress both imposed at the top boundary of the element, as illustrated in **Figure 6.31**. Analyses were performed following the same procedure described for the cyclic

isotropic TX test. The resulting $1/m_{v,3}$ values from the two test simulations are summarized in **Table 6.3**, for the different $r_{u,max}$ levels.

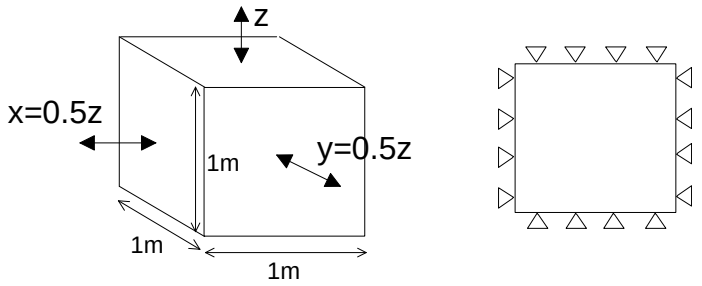

Figure 6.30: Set-up and boundary conditions for the cyclic triaxial (TX) test simulation performed with FLAC3D.

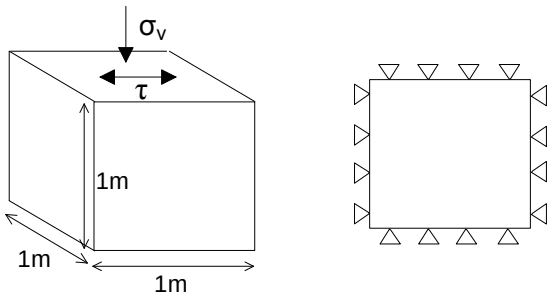

Figure 6.31: Set-up and boundary conditions for the direct simple shear (DSS) test simulation performed with FLAC3D.

Table 6.3: Summary of $1/m_{v,3}$ values from laboratory test simulations.

$r_{u,max}$	Cyclic Triaxial Test (TX)	Direct Simple Shear Test (DSS)
	$1/m_{v,3}$ ($*10^5$ kPa)	$1/m_{v,3}$ ($*10^5$ kPa)
0.1	2.17	2.88
0.2	2.11	2.86
0.3	2.01	2.76
0.4	1.95	2.59
0.5	1.83	2.49

Analytically back-calculated $1/m_{v,3}$ values for t_l=1.30sec, as well as numerically computed $1/m_{v,3}$ values from all examined zones, are assembled and plotted as a function of the corresponding maximum epp ratio $r_{u,max}$ in **Figure 6.32.** The analytical predictions by Bouckovalas et al. (2009) correspond to both convergence criteria, plotted with the dashed lines and the average value, plotted with the continuous line. Numerical results are plotted for each performed analysis, each time extracting a representative average $1/m_{v,3}$ value. The

$1/(m_{v,3})_{avg}$ is calculated as $1/(m_{v,3})_{avg}= 1/(\Sigma m_{v,3i})/n$, where n the number of the zones under consideration. Overall, the analytically determined $1/m_{v,3}$ values appear in good agreement with the numerical results, especially in the range between 0.20 – 0.50 of $r_{u,max}$, which consists the typically encountered range in current practice. Especially the use of the first convergence criterion renders the most satisfactory results, further validating the revised methodology. The fitting to the time increment of the $r_{u,max}$ occurrence does not compare as well to the numerical results and therefore will be disregarded from the following analysis. Moreover, the DSS element test results appear to better describe the above range of $1/m_{v,3}$ values, while the TX tests show a clear $1/m_{v,3}$ underestimation. Thus, it is evident that the Seed & Booker (1977) suggestion concerning the use of TX test results for the determination of $m_{v,3}$ may lead to conservative design, compared against the use of DSS laboratory tests, which render more realistic values of coefficient of volume compressibility.

Experimental values reported in the literature (PHRI,1997).- for sands of different gradation, summarized in **Table 6.4.** The specific values are mentioned both by the Japanese Geotechnical Society (JGS, 1998) as well as by the PHRI, (1997) to result after cyclic triaxial liquefaction tests. The specific values are obtained at an initial confining pressure of 100kPa and r_u<0.5. The comparison for the specific case is presented in **Figure 6.33.** The related gradation curves for each sand material are plotted in the lower part of **Figure 6.33**, where the curve for Nevada sand, simulated in the numerical analyses, is also plotted.

Given the similarity in terms of gradation profile between Nevada sand and Akita Port Sand, it is concluded that the inverse of coefficient of volume compressibility should result in the range between 0.3-0.4*10^5kPa. The discrepancy between the laboratory obtained values and the numerical results is approximately one order of magnitude and is mainly attributed in the very different volumetric strains developing during the consolidation numerical analysis, both in the boundary value problem and the element test simulations. This observation led to an extensive investigation of a number of reasons, which could be responsible and are listed in the following paragraph.

Table 6.4: Typical values of coefficient of vol. compressibility of sands (PHRI, 1997).

Type of sand	Coefficient of volume compressibility (cm^2/kgf)*	References (year)
Sacramento River Sand	$2*10^{-3}$	Lee et al. (1974)
El Monte Sand (D)	$2*10^{-3}$	Lee et al. (1974)
El Monte Sand (E)	$2*10^{-3}$	Lee et al. (1974)
Akita Port Sand	$3\sim4*10^{-3}$	Zen et al. (1984)
El Monte Sand (C)	$4*10^{-3}$	Lee et al. (1974)
Monterey Sand	$4*10^{-3}$	Lee et al. (1974)
Fuji River Sand	$6*10^{-3}$	Ishihara et al. (1978)
El Monte Sand (B)	$8*10^{-3}$	Lee et al. (1974)
Ogishima Sand	$10*10^{-3}$	Ono et al. (1983)

*Measured at $u/\sigma'_c<0.5$, **σ'_c=1kgf/cm^2 = 98.06kPa**

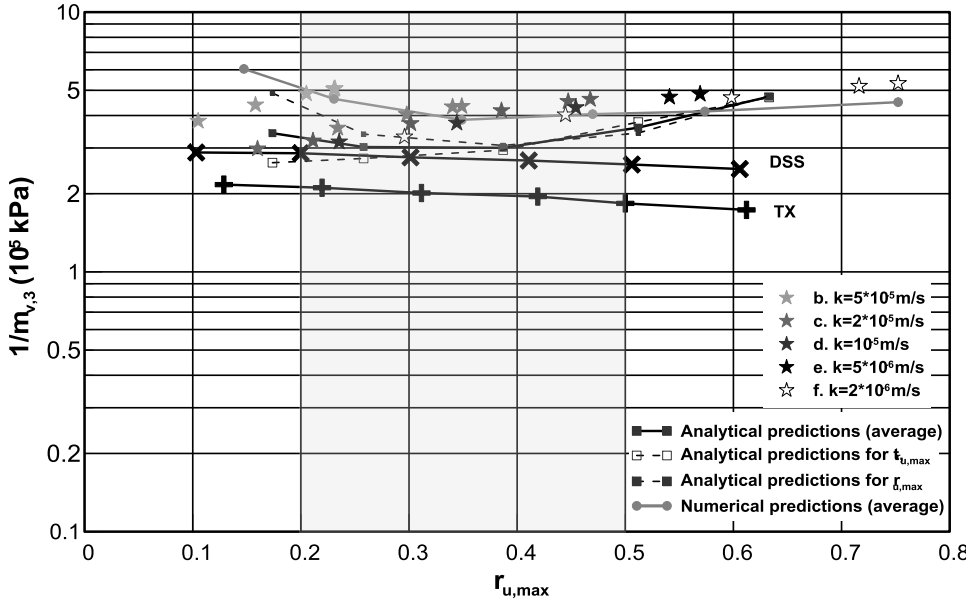

Figure 6.32: Numerically derived and analytically back-calculated $1/m_{v,3}$ values for the performed drained analyses.

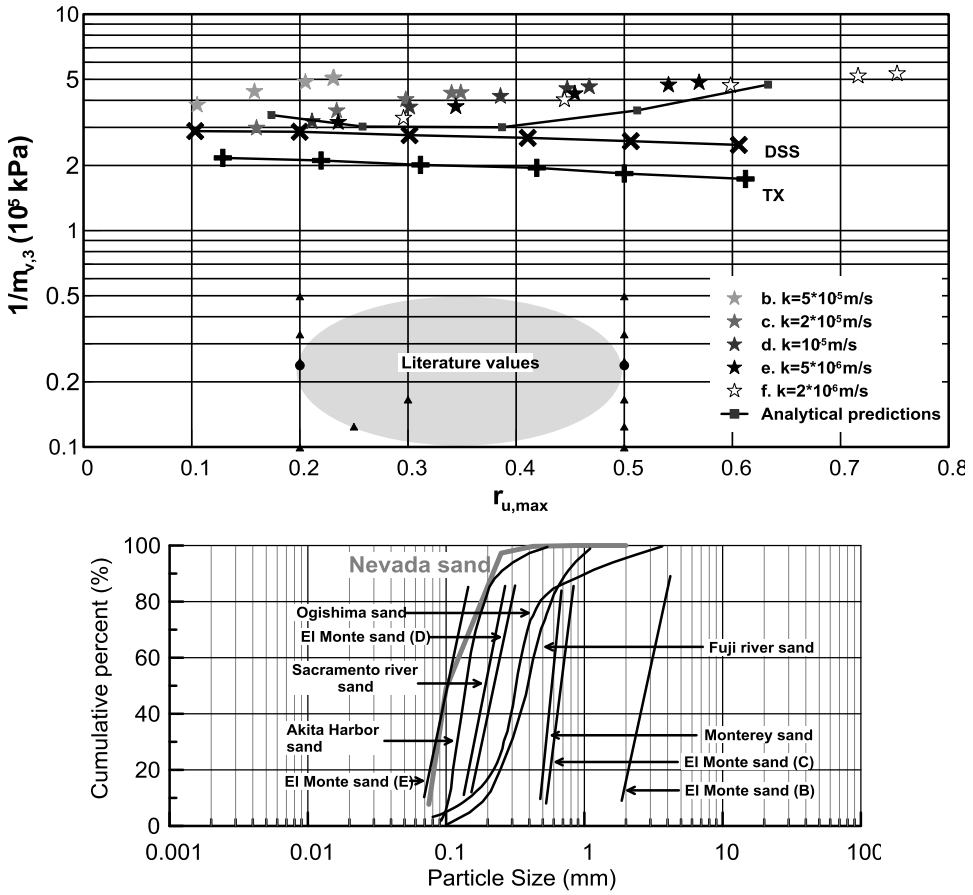

Figure 6.33: Comparison of numerical & analytical $1/m_{v,3}$ values against literature proposed values.

6.5 Analysis of the volumetric strain development mechanism

Volumetric Strain Measurement.- Before any investigation, it was crucial to guarantee that the correct volumetric strain was derived from FLAC 3D. The accuracy of the numerically computed volumetric strains was checked by applying nodal displacements of known magnitude on one element and measuring the resulting deformations. It was indeed found that the numerically derived volumetric strain was equal to the manually calculated one (i.e the sum of e_{xx}, e_{yy} and e_{zz} strains), providing absolute confidence in the numerical computations.

It was also noted that due to drained conditions, volumetric strains developed already from the dynamic loading part in the boundary value problem. On the contrary, in the laboratory tests simulation cyclic loading is applied under zero volume change and volumetric strains start developing only during consolidation. Including the dynamically induced volumetric strains in the $1/m_{v,3}$ calculation would undoubtedly improve the consistency between

numerically derived and the literature proposed values, nevertheless such a calculation would not be consistent to the initial definition of $1/m_{v,3}$. Additionally, if the dynamic loading part of the numerical analysis is performed under undrained conditions, thus under zero volumetric strains, followed by a typical consolidation analysis, the resulting volumetric strains due to consolidation do not significantly change, rendering similar $1/m_{v,3}$ values.

Effect of Constitutive Model's Parameters.- So far, the constitutive model for the liquefiable sand is applied for the set of dynamic parameters (B and a_1) proposed by Andiranopoulos et al. (2010). More specifically maximum shear modulus, G_{max}, is computed based on the mathematic expression proposed by Hardin (1978) for a model parameter value B equal to 600 and the parameter expressing the non linearity of "elastic" shear modulus, a_1, is set equal to 0.6. Taking into account the monotonic character of a consolidation analysis, the related model parameters are re-considered. Therefore, for the element test simulations, B value was switched from 600 to 180 and then to 100, corresponding to development of greater strain amplitudes and the model constant a_1[3], is set from 0.6 to 1.0, essentially simulating a linear behavior. The system response analyses are also re-evaluated, nevertheless, due to the significant computational load of each one of them, only the B value equal to 100 is examined.

The outcome of the above re-evaluation is illustrated in **Figure 6.34.** The element level response is depicted for 3 different sets of model parameters (B,a_1), namely (600, 0.6), (180,1.0) and (100, 1.0) and the system response behavior for two sets i.e. (600, 0.6) and (100, 1.0). In the case of the element test simulations volumetric strains are significantly affected, rendering $1/m_{v,3}$ values up to 80% lower for the same $r_{u,max}$ levels, which compare very well with the literature proposed values for Nevada sand, located in the upper boundary of the shaded region. In fact, the increase in volumetric strains is greater when considering a lower B value, thus justifying the B value reduction by 6 times, instead of the range of 2-4 times, proposed by Andrianopoulos et al. (2010). For the boundary value problem, volumetric strains are not proportionally affected by the model parameter change, resulting in a 30 - 40% reduction in $1/m_{v,3}$ values, hence the discrepancy with the literature proposed values is maintained.

[3] Model parameter a_1 is the ratio of the secant shear modulus to the maximum shear modulus for a characteristic value of γ_1. Values of a_1 less than unity correspond to non-linear response, while for a_1=1, behavior is independent of γ_1 and purely hypo elastic. Model constant γ_1 essentially determines the point beyond which any further shear degradation is due to development of plastic strains.

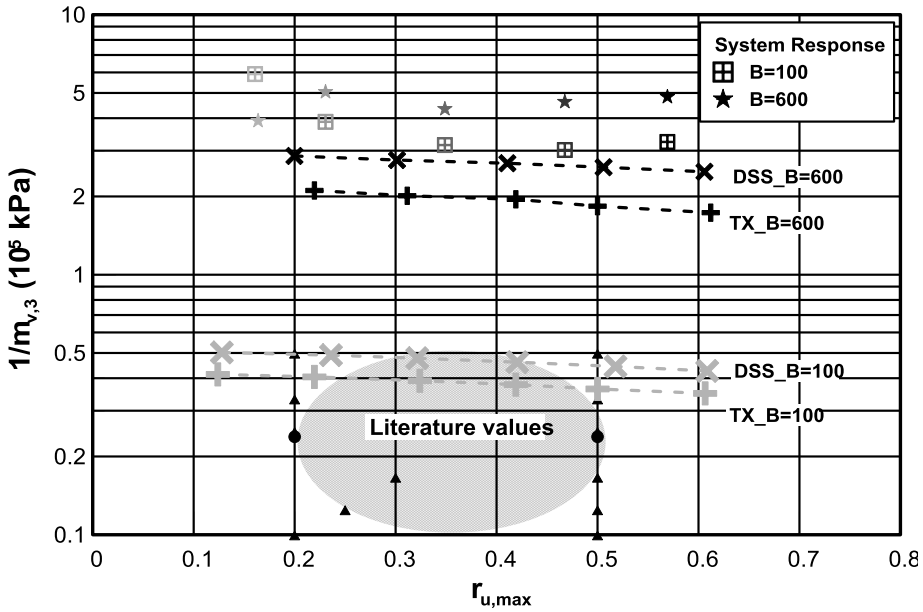

Figure 6.34: Effect of B value on $1/m_{v,3}$ values.

Obviously, the boundary value problem exhibits a much stiffer behavior, which does not allow for the development of large volumetric strains. The particular aspect is going to be further evaluated in the subsequent sections. In an attempt to reduce excessive computational load all analyses that follow were executed considering the monotonic model parameters and for one value of permeability coefficient, $k=10^{-5}$m/sec.

Effect of y-Discretization.- The imposed boundary conditions restrict any deformation in the out of xz plane direction, thus potentially confining the development of vertical displacements. For that purpose, two additional analyses were performed, in which discretization along the y-axis was increased. **Figure 6.35** presents the two configurations, in which the first involves 3 zones in the middle part, and the second, 4 zones, followed by the related increase in the radial cylinder elements.

The increase of discretization did not have any effect in the development of volumetric strains, essentially rendering very similar results with the less dense discretization examined earlier.

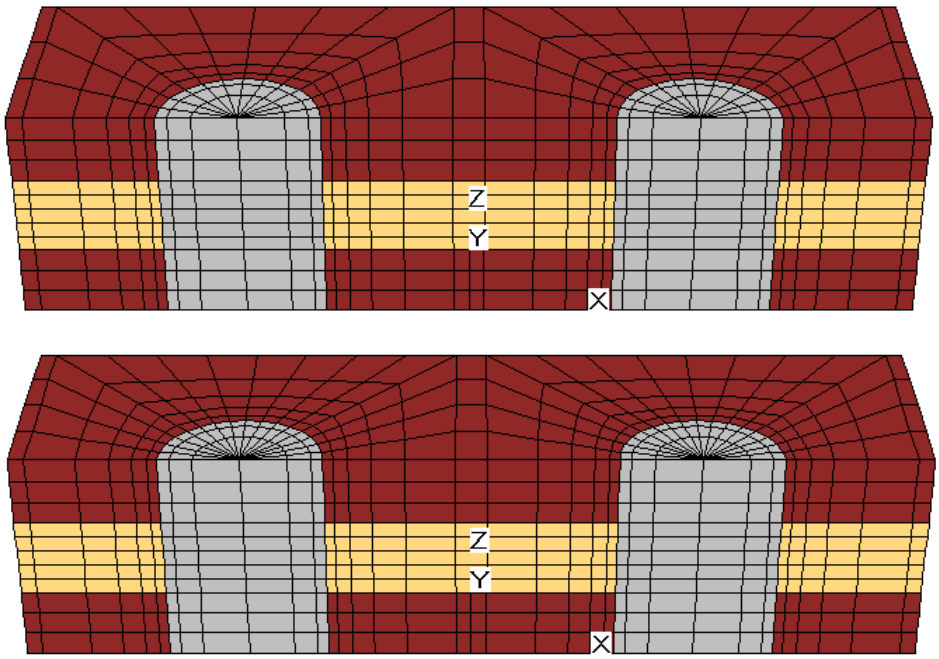

Figure 6.35: Consideration of denser discretization along y-axis.

Effect of Permeability Coefficient Increase.- All numerical analyses reported previously, are carried out assuming the same coefficient of permeability in both stages, namely the dynamic loading part and the consolidation analysis that follows. Nevertheless, according to field investigations (Ishihara 1994, Schofield 1981), laboratory tests (Jafarzadeh & Yanagisawa, 1995) and analytical studies (Arulanandan & Sybico, 1992) soil permeability increases significantly during seismically induced pore water pressure generation. Hence, the consideration of a constant coefficient of permeability throughout a liquefaction analysis may lead to an underestimation.

To account for the permeability increase in the numerical simulation of liquefaction, researchers usually multiply the initial "static" value of permeability by a constant factor. More specifically, Arulanandan & Sybico (1992) propose a factor of 3.67, Balakrishan (2000) consider a factor of 4 and Taiebat et al. (2007) consider the "dynamic" value of permeability to be one order of magnitude greater. Even more recently, Shahir, Pak, Taiebat & Jeremic (2009) suggest that permeability should not be considered constant during excess pore pressure generation and dissipation processes. They propose a relationship in which permeability varies at each stage (i.e. built-up stage, liquefied stage and dissipation stage) and is expressed as a function of the ever-current excess pore pressure ratio r_u. As it is also noted by the authors, because the proposed relationship still requires further investigation,

in the present analysis the method of the "constant increased permeability coefficient" is adopted.

To investigate the potential effect of permeability in the obtained values of $m_{v,3}$ a consolidation analysis was performed, considering a permeability coefficient equal to $k=10^{-4}$m/sec, i.e. 10 times greater than the "static" value of permeability. The gravel drain permeability was increased proportionally. Still, volumetric strains remained unaffected by the increase in permeability, rendering pretty much equivalent $1/m_{v,3}$ values. In that case, it may be possible that because excess pore pressure ratio does not exceed 0.5, actual permeability is not affected.

Effect of Modelling Approach.- The liquefiable sand layer is simulated using the constitutive model developed in NTUA (Papadimitriou, 2001, Andrianopoulos, 2010) and the gravel piles are considered elastic. It is thus alleged that the potential interaction between one sophisticated constitutive model to the elastic may be responsible for the low volumetric strains developing during consolidation. To evaluate this possibility, the component of the gravel pile located within the sand layer, is simulated by the NTUA-SAND constitutive model, preserving the pile's permeability coefficient. Both dynamic and consolidation analyses were performed; nevertheless, only minor effects were observed, essentially producing almost identical results.

Effect of Interface Surface.- Another factor obstructing the development of settlements was claimed to be the presence of the two elastically simulated, undistorted piles, which could restricting the undisturbed settlement of the improved soil layer. To eliminate any potential pile-soil interaction phenomena and to allow the undisturbed development of settlements within the soil, the external stack of zones of the gravel piles was assigned different elastic properties during the consolidation analysis.

The interface area is depicted in **Figure 6.36** and it is intended to provide very low resistance in shearing and an adequately high bulk modulus value to avoid squeezing towards the pile. After an extensive parametric investigation shear modulus G was set equal to 30kPa and bulk modulus K equal to 130e4kPa. The particular properties were also verified considering a totally elastic grid, with a much softer sand layer compared to the piles and the clay caps, producing uniform volumetric strains and settlements along the sand layer. Concurrently, the gravel pile's elastic properties were increased by an order of magnitude (i.e. K=130e4kPa, G=60e4kPa) to avoid shear deformation and squeezing from the periphery to the centre of the pile. Settlement contours from the reference case (without the interface)

and the current analysis are provided in **Figure 6.37** and are very descriptive of the interface area benefit. The influence proves to be very limited, mainly affecting vertical displacements in the vicinity of the gravel piles, producing a more uniform distribution of settlements between them.

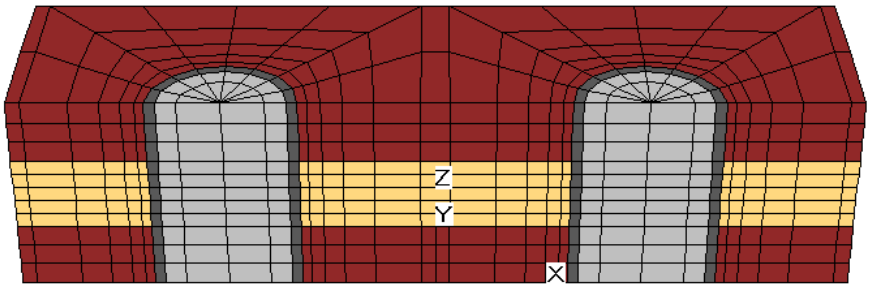

Figure 6.36: Introduction of an interface zone between liquefiable ground and gravelpiles.

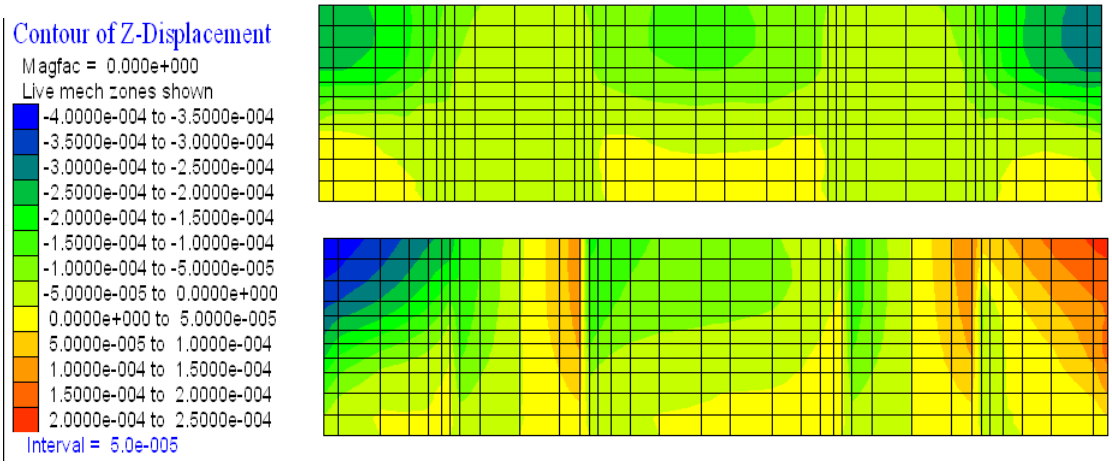

Figure 6.37: Vertical displacement contours for the reference case (upper graph) and the interface consideration, at the end of consolidation.

Figure 6.38 summarizes the $1/m_{v,3}$ values derived after each attempted modification, described in the present paragraph, and compared against the corresponding values of the reference case. Note that the introduction of the interface area actually leads to greater $1/m_{v,3}$ values, which do not correspond to the expected outcome and the expected uniformity in terms of volumetric strain distribution. Hence, despite the attempted modifications the resulting $1/m_{v,3}$ values remain unaffected.

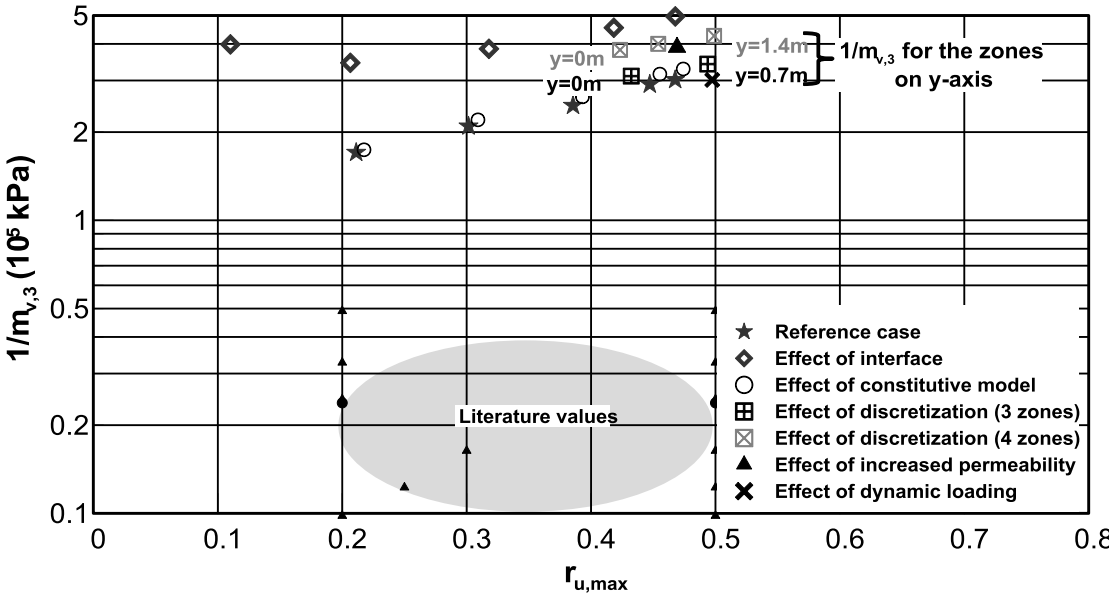

Figure 6.38: Effect of the examined interventions on the final $1/m_{v,3}$ for the central zone.

CHAPTER 7

Simulation of Footing Response

7.1 Introduction

In the present study it is assumed that the top, non liquefiable crust has the same initial consistency as the liquefied sand and has been created using vibrocompaction or vibro-replacement. In both methods, along with the creation of gravel drains which accelerate excess pore pressure dissipation and thus will mitigate liquefaction, the natural soil is considerably densified. This combined intervention creates a quite complex pattern regarding the density distribution, the shear strength and the excess pore pressure dissipation mechanism in the crust of the improved ground. Namely:

- The relative density of gravel piles is different than that of the surrounding soil. Moreover, due to the densification created by vibrocompaction the relative density of the densified soil decreases radially from the axis of the gravel drain and outwards.
- The shear strength of the gravel pile is also different than that of the surrounding sand, even if the aforementioned radial variation in relative density is not considered.
- The excess pore pressure dissipation mechanisms in the improved ground differ than those in the liquefied sand. More specifically, the improved ground drains both in the radial and the vertical directions while the underlying liquefied sand drains practically vertically towards the gravel drains installed on top of it.

It is definitely possible to simulate these mechanisms based on the present numerical capabilities offered by FLAC and FLAC3D and the advanced constitutive model that has been implemented to it for the simulation of complex seismic soil response problems. Nevertheless, the time required for such analyses would be restrictive for performing an extensive parametric study. Furthermore, a number of the input data required for such analyses e.g. permeability coefficient, as well as mechanical parameters of gravel drains under monotonic and cyclic loading are not known with accuracy, thus reducing the accuracy of the analyses despite any elaborate numerical computations.

In view of the above objective difficulties, the detailed numerical simulation of the liquefied ground response in the presence of a surface crust of improved ground, becomes cumbersome and outside the scope and the extent of this study. Consequently, this study will proceed using the concept of "*Equivalent Uniform Improved Ground*", also noted hereafter as *E.U.I.G.*, which is widely accepted in practice when desinging geostructures and foundations on weak soil improved with gravel piles. According to this, the improved ground layer is considered uniform with appropriately computed unique soil parameters, which take into account the properties of the natural ground, the properties of the gravels, as well as the extent of ground improvement. Possible means of estimating the related properties of the improved surface crust are described in the first part of the present chapter.

Subsequently, the accuracy of the applied numerical methodology is verified against well-established centrifuge experiments performed by Liu & Dobry (1997), in terms of the accumulating seismic settlements. Particular consideration is dedicated to the suitable coefficient of permeability introduced in the numerical analyses, while in parallel, the effects on the overall system response are extensively discussed.

7.2 Equivalent Uniform Improved Ground

7.2.1 Relative density of improved ground

Based on the initial relative density of the liquefiable sand, and the replacement ratio α_s[4] of the gravel drain geometry (ground improvement scheme), the relative density of the improved ground may be derived from the empirical charts of **Figure 7.1**.

[4] Replacement ratio, a_s, is defined as the ratio of the plan view area of the gravel drain, over the area of the influence zone around the drain.

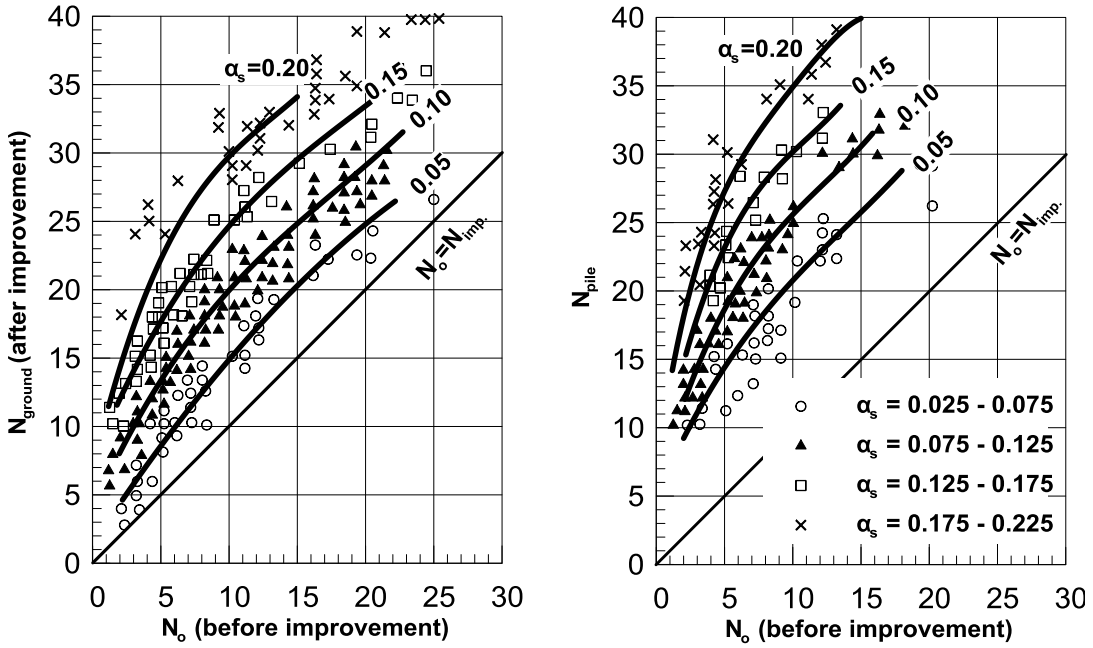

Figure 7.1: Design chart applicable to sandy ground (JGS, 1998).

According to the guidelines accompanying these figures, provided by the JGS (1998), given the corrected N_{SPT} value for the natural soil, which is equal to $N_o=N_{SPT}*C_N$, and the replacement ratio (α_s) of the applied ground improvement, the corrected N_{SPT} value in the improved ground is computed based on the following expression:

$$N_{imp.} = \alpha_s N_{pile} + (1-\alpha_s) N_{ground} \qquad 7.1$$

where N_{pile} is the corrected N_{SPT} blow count value corresponding to the location of the gravel pile (**Figure 7.1**) and

N_{ground} the corrected N_{SPT} blow count value obtained at the mid-distance between two consequtive gravel drains (**Figure 7.1**).

The above practice is followed for natural soil deposits with initial relative density Dr_o = 35, 40, 45, 55, 65 & 70% and replacement ratios α_s = 5, 10 15 & 20%. Relative density was related to the corrected N_{SPT} blow count through the following empirical equation proposed by Tokimatsu & Seed (1987), as expressed below:

$$(N_1)_{60} = 44 Dr^2 \qquad 7.2$$

where $(N_1)_{60}$ = the corrected with depth, applied pressure and fines N_{SPT} blow count

D_r(%) = relative density

The results are summarized in **Table 7.1** for the range of initial relative densities mentioned above.

Table 7.1: N_{SPT} values in the improved ground (according to JGS, 1998) and related relative density values (based on Tokimatsu & Seed, 1987) for six initial relative density scenarios.

Dr_o (%)	35				Dr_o (%)	40			
N_o	5.5				N_o	7			
a_s	N_{ground}	N_{pile}	N_{imp}	Dr_{imp} (%)	a_s	N_{ground}	N_{pile}	N_{imp}	Dr_{imp} (%)
0.05	9	15	9	46	0.05	11	17	12	51
0.1	14	19	14	57	0.1	16	22	17	62
0.15	18	24	19	66	0.15	21	27	22	70
0.2	23	28	24	74	0.2	26	31	27	78

Dr_o (%)	45				Dr_o (%)	55			
N_o	9				N_o	13			
a_s	N_{ground}	N_{pile}	N_{imp}	Dr_{imp} (%)	a_s	N_{ground}	N_{pile}	N_{imp}	Dr_{imp} (%)
0.05	14	20	14	56	0.05	19	24	19	65
0.1	19	24	19	66	0.1	23	29	24	74
0.15	23	29	24	74	0.15	28	33	29	81
0.2	29	33	29	82	0.2	33	38	34	88

Dr_o (%)	65				Dr_o (%)	70			
N_o	18.5				N_o	21.5			
a_s	N_{ground}	N_{pile}	N_{imp}	Dr_{imp} (%)	a_s	N_{ground}	N_{pile}	N_{imp}	Dr_{imp} (%)
0.05	24	30	24	74	0.05	26	33	26	77
0.1	28	33	29	81	0.1	31	35	31	84
0.15	33	36	33	86	0.15	35	39	36	89
0.2	37	38	37	93	0.2	38	40	38	98

It is important to note that for the initial relative density scenario of D_r=70%, the use of the empirical figures provided by the Japanese Geotechnical Society (**Figure 7.1**) is rather marginal, since the initial N_{SPT} value, according to Tokimatsu & Seed (1987), i.e. N_{SPT} = 21.5, falls outside the designated range of N_{SPT} values. Therefore, to correctly simulate such cases, it became inevitable to make an extrapolated use of the suggested empirical graphs. Nevertheless, the particular issue concerns a rather limited number of cases and does not affect the overall trend of the numerical results, as it is observed in the following paragraphs.

7.2.2 Permeability coefficient of the improved ground

The permeability coefficient of the improved ground layer is an essential input parameter for the numerical analyses, but it is also the most difficult to compute using the concept of *E.U.I.G.*. As a first approximation, flow through the improved crust may be considered

vertical so that, a weighted average of the permeabilities for the natural soil and the gravel drains might be used, as described below:

$$k_{eq.} = \alpha_s k_{drain} + (1 - \alpha_s) k_{sand} \qquad 7.3$$

Taking into account that k_{drain}/k_{sand} must be greater than about 200 and also that a_s ranges from 0.05 to 0.20 it comes out that $k_{eq.} > (11 \div 41)k_{sand}$.

It is also well known that the permeability coefficient under seismic loading is initially less than the equivalent static value but may increase in proportion to r_u. Parametric analyses performed by Chaloulos (2012) for the simulation of centrifuge tests of a pile into liquefied and laterally spreading ground revealed that the static value of permeability is a reasonable average for liquefied and non liquefied states and can be used for the numerical computations without significant loss in accuracy. According to Arulmoli et al. (1992), the static value of the permeability coefficient differs with relative density, and more particularly the proposed values are summarized in **Table 7.2**.

Table 7.2: Permeability coefficient values and relative density for the liquefiable sand layer (Arulmoli et al., 1992).

Dr (%)	k_{sand} (*10^{-5}m/s)
40	6.6
60	5.6
90	2.3

The variation of the coefficient of permeability with relative density is plotted in **Figure 7.2**, from which it is concluded that the permeability coefficient remains essentially constant and equal to 6.6*10^{-5} m/s for relative densities up to 40-50%. Therefore, for initial values of relative density (35, 40 & 45%) the permeability coefficient is set equal to 6.6*10^{-5} m/s, whereas for the three remaining values (55, 65 & 70%) , it is set equal to 5.8, 5.2 and 4.5(*10^{-5}) m/s respectively. Also, following *Equation 7.3* the values of the equivalent coefficient of permeability for the improved crust are summarized in **Table 7.3.**

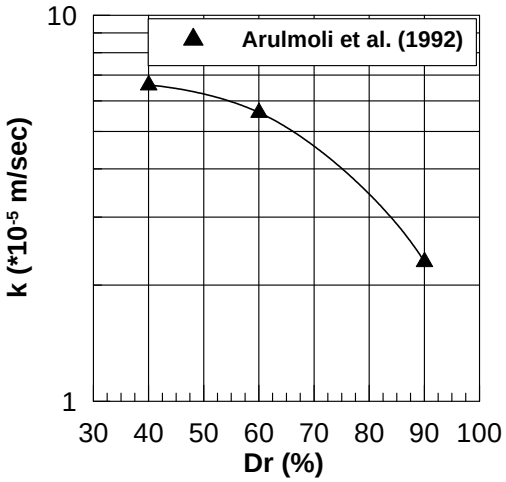

Figure 7.2: Change in the permeability coefficient with regard to relative density for Nevada sand, as proposed by Arylmoli et al. (1992).

Table 7.3: Equivalent permeability coefficient for the improved layer.

Dr_o (%)	35, 40, 45	
k_{sand} (m/s)	6.60E-05	
a_s	k_{drain} (m/s)	$k_{eq.}$ (m/s)
0.05	1.32E-02	7.23E-04
0.1		1.38E-03
0.15		2.04E-03
0.2		2.69E-03

Dr_o (%)	55		Dr_o (%)	65		Dr_o (%)	70	
k_{sand} (m/s)	5.80E-05		k_{sand} (m/s)	5.20E-05		k_{sand} (m/s)	4.50E-05	
a_s	k_{drain} (m/s)	$k_{eq.}$ (m/s)	a_s	k_{drain} (m/s)	$k_{eq.}$ (m/s)	a_s	k_{drain} (m/s)	$k_{eq.}$ (m/s)
0.05	1.16E-02	6.35E-04	0.05	1.04E-02	5.69E-04	0.05	9.00E-03	4.93E-04
0.1		1.21E-03	0.1		1.09E-03	0.1		9.41E-04
0.15		1.79E-03	0.15		1.60E-03	0.15		1.39E-03
0.2		2.37E-03	0.2		2.12E-03	0.2		1.84E-03

7.3 Numerical analysis outline

Mesh discretization.- The seismic performance of a shallow foundation is investigated under plane strain conditions, through 2-dimensional numerical analyses. The general outline of the arrangement is illustrated in **Figure 7.3**. Starting from a uniform liquefiable sand layer of total thickness equal to 20m, three potential improvement depths were considered, namely 4, 6 & 8 meters. As illustrated in **Figure 7.3**, in the vicinity of the footing, and around the axis

of symmetry of the configuration, 1.0×1.0m zones are generated and the zone-width is gradually increased to 1.5×1.0m and 2.0×1.0m, at the boundaries of the configuration.

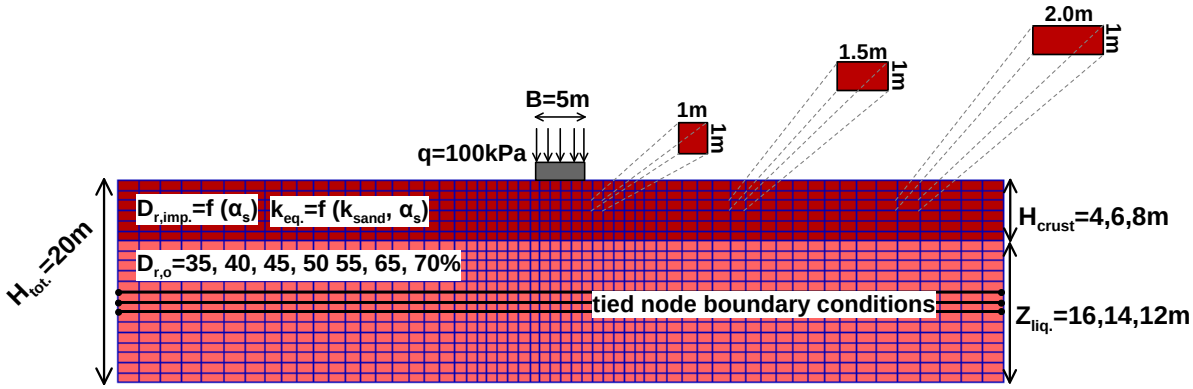

Figure 7.3: Mesh used in the 2-D numerical analyses.

Excitation.- The 2-layer soil profile is subjected to a harmonic sinusoidal excitation, consisting of 12 cycles with period T=0.35sec and peak acceleration α_{max} = 0.15g, (**Figure 7.4**). A cycle of smaller amplitude is added at the beginning and at the end of the time history to ensure a gradual increase of the input acceleration and eliminate erroneous results due to an abrupt change in the loading conditions.

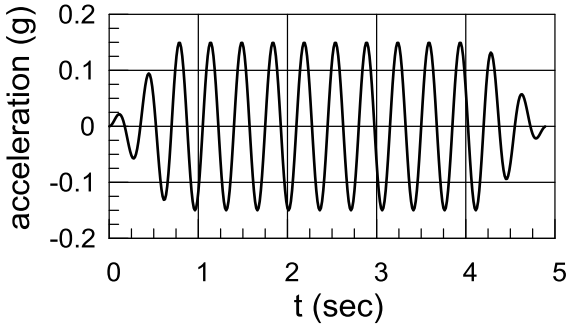

Figure 7.4: Input acceleration time history in the basic numerical analysis

Constitutive Model.- The liquefiable sand response under the imposed dynamic loading is simulated using the NTUA-SAND constitutive model, which is re-calibraed to fit the special conditions of the problem at hand. Additional information on the neccessity for re-calibration and the procedure which was applied are provided in Appendix B.

The improved crust is initially simulated using the Mohr-Coulomb constitutive model. The required input strength parameters included the friction angle ϕ, the cohesion c, and the

dilation angle ψ. Subsequently, the same analysis is repeated considering the NTUA-SAND model throughout the soil profile, paying attention to the equivalence in the required strength parameters inntroduced in both constitutive models. It is found that the Mohr-Coulomb model may adequately capture the response of the partially liquefied crust, provided a suitable value for the dilation angle is selected. Nevertheless, there is great uncertainty involved in the assessment of dilation angle ψ, as opposed to friction angle, which discouraged the use of the Mohr-Coulomb model. Hence, the critical state NTUA-SAND constitutive model is applied in the entire mesh

Boundary conditions.- Different Boundary Conditions are used for static and dynamic loading conditions. For static loading, and for the application of initial geostatic stresses, horizontal displacements are restrained in the lateral boundaries, whereas along the vertical direction only the bottom boundaries are restrained, allowing the system to settle freely. Moreover, the bottom boundaries are allowed to move horizontally, to avoid the generation of parasitic shear stresses.

During dynamic loading, tied-node boundary conditions are considered for the lateral boundaries, which are imposed by connecting gridpoints of the same altitude through rigid elements, thus compelling them to develop equal horizontal displacements. The philosophy behind the development of the specific type of boundary conditions, is to simulate the response of a laminar box during seismic loading, which is widely used in centrifuge and shaking table laboratory tests. The main drawback of the particular type of boundary conditions is that horizontally propagating seismic waves are reflected back into the main area of interest and may affect the numerical outcome. Nevertheless, in highly non-linear problems, such as the liquefation phenomena studied here, the elasto-plastic behavior of the materials produces enough hysteretic damping, which in combination with the initially assigned local damping, absorb reflected waves. This reduction is more efficient when boundaries are located far away.

Water level.- Water level is considered to be 1m above the ground surface. This is simulated by applying a vertical stress equal to 9.81kN/m^3, over the entire ground surface.

Footing.- The 5m wide strip footing is simulated on top of the improved crust applying a uniform contact pressure equal to q. The footing is considered to have zero mass, to avoid the generation of inertia effects. Horizontal and vertical displacements of the gridpoints corresponding to the footing are restricted by considering a connecting rigid beam element. Bearing stresses are applied over four (4) zones simulating a 4×1.00m=4.00m wide footing.

Nevertheless, according to ITASCA (2005), bearing pressure is simulated through vertical velocity applied at specific gridpoints. This velocity varies linearly from the value at the last gridpoint upon which it is applied, to zero at the adjacent gridpoint. Therefore, half the width of the adjacent zones should be added to the actual footing width, thus resulting to a 5m wide strip footing.

Loading Sequence.- All analyses are conducted in three separate phases, which are schematically presented in **Figure 7.5** and outlined below**:**

Phase 1: Initial geostatic stresses are generated and the foundation load under static conditions is incrementally applied at increments of 5kPa until the desired contact pressure q is reached (branch a-b).

Phase 2: A fully-coupled effective stress dynamic analysis is executed, subjecting the soil-foundation system to a harmonic excitation,with parallel pore water flow throughout the grid. During this phase, excess pore pressures develop and dynamic settlements accumulate under constant load Q (branch b-c). Note that seismic settlements may become large and even exceed the static ones.

Phase 3: After the end of shaking, the static load Q is increased until bearing capacity failure, while the undelying un-improved layer remains liquefied (branch c-d). Branch c-d in the figure, practically renders a degraded bearing capacity of the footing, compared to the initial static value (branch b-b'), as the subsoil remains liquefied and its shearing resistance has practically vanished. The post-shaking stage is performed under drained conditions, nevertheless, to account for the effects of liquefaction, excess pore pressures generated during shaking are maintained constant. This is achieved by prohibiting water flow and setting the water bulk modulus to a very small value (1kPa instead of 2×10^{6}kPa) so that pore pressures are not affected by the applied static loading. The additional load application was performed by fixing the gridpoints corresponding to the foundation in both (horizontal and vertical) directions and applying an adequately small velocity of 10^{-7}m/sec, which has proven to provide a pretty stable response, with minor unbalanced forces. The related load was computed by summing up the vertical resistance forces at the fixed nodes.

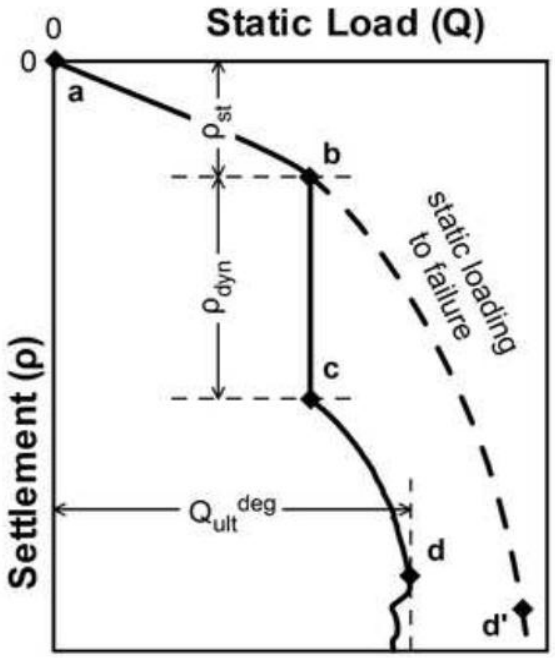

Figure 7.5: Typical load-displacement curve.

Damping.- Non-hysteretic damping is introduced in order to reproduce the energy loss in a natural system when subjected to dynamic loading. The two main damping options suggested by FLAC for dynamic simulations are briefly described herein. Also, their effect on the numerical outcome is assessed for the case of a shallow footing on top of an improved crust in terms of excess pore pressure builtup, soil response and associated dynamic settlement accumulation. The numerical analysis considered a 20m thick soil layer of initial relative density of $D_{r,o}$=65%, improved over the first 8 meters, considering a replacement ratio equal to α_s=0.10.

Rayleigh Damping.- It was originally used in the analysis of structures and elastic continua to damp the natural oscillation modes of the system. The related equations are expressed in the form of a matrix C, which is proportional to the mass (M) and stifness (K) matrices, as shown below:

$$C = aM + \beta K \qquad 7.4$$

where α=the mass-proportional damping constant

β= the stiffness-proportional damping constant

For a multiple degree of freedom system, the critical damping ratio ξ_i, at any angular frequency of the system ω_i, is given in the following equation:

$$\xi_i = \frac{1}{2}\left(\frac{\alpha}{\omega_i} + \beta\omega_i\right) \qquad 7.5$$

The variation of the normalised critical damping ratio with angular frequency ω_i is presented in **Figure 7.6**, as the mass and stifness component and the sum of both components. The curve representing the sum of both components attains a minimum of $\xi_{min} = (\alpha\beta)^{1/2}$ at $\omega_{min} = (\alpha/\beta)^{1/2}$.

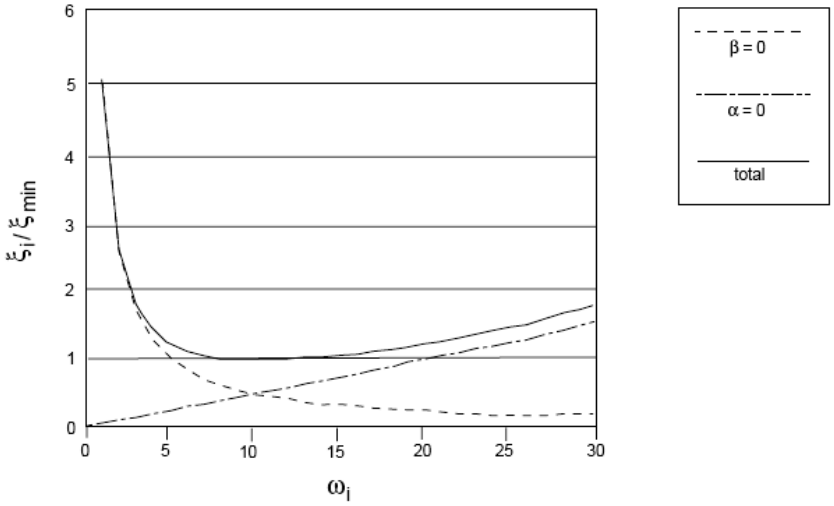

Figure 7.6: Variation of normalized critical damping ratio with angular frequency.

From the above figure, it is concluded that this particular damping option is largely frequency dependent. More specifically, mass-proportional damping is dominant at the lower angular-frequency ranges, while stifness-proportional damping dominates at higher angular frequencies. Also, at frequency ω_{min}, (or f_{min}) mass damping and stifness damping each supply half of the total damping force. Despite the above frequency dependence, there is a "flat" region, spanning at about one third of the frequency range, in which damping becomes frequency-independent. The specific range essentially forms the area of interest in a dynamic analysis, in which f_{min} (or ω_{min}) is appropriately adjusted so that its 3:1 range coincides with the range of predominant frequencies of the problem. Hence frequency dependenty effects are canceled out at the frequencies of interest. By the term "predominant frequencies" both the input frequencies and the natural modes of the system are considered. The term ξ_{min} is adjusted to coincide with the desired value of the damping ratio.

In the present research, the liquefiable soil element response is simulated with the use of an advanced constitutive model, suitably formulated to describe the highly hysteretic behavior of liquefiable sands under cyclic loading. Still, there is a need for a viscous damping componenet of the order of 2-4%. However, with the NTUA-SAND model, no stiffness component is defined. Hence, the damping matrix can only be composed of the mass component and the Rayleigh damping equations are appropriately adjusted. The requested parameters are set equal to ω_{min}=10Hz, ξ_{min}= 2% which correspond to the minimum damping value reported by Vucetic & Dobry (1991) for very small cyclic shear strain amplitudes (0.001%).

Local damping.- was initially designed as a means to equilibrate static simulations, hence it presents certain features that make it attractive for dynamic simulations by providing an approximate way to introduce damping. Local damping operates on a gridpoint or structural node, by adding mass, whenever the velocity changes sign or substracting mass, when velocity passes a maximum or minimum point. Special consideration is given to overall mass preservation throughout a full cycle of oscillation. In addition, the use of local damping is much simpler than Rayleigh damping, because no frequency-independent area needs to be specified. The main drawback of local damping is that it becomes increasingly unrealistic with the complexity of the waveform. In our case, local non-viscous damping was assigned an initial value of 2%, corresponding to the minimum damping value reported by Vucetic & Dobry (1991) for very small cyclic shear strains (0.001%). For greater shear strain amplitudes, hysteretic damping is simulated by the non-linear behavior of the NTUA-SAND constitutive model.

Results of the performed analyses are summarized in **Figure 7.7**, in the form of excess pore pressure timehistories obtained at different depths of the arrangement and two locations, namely under the footing and away from it. It is concluded that minor variations are observed between the two damping options and that there is essentially no significant effect of the considered damping on the generated excess pore pressures at any depth.

Figure 7.8, illustrates the acceleration time histories derived at the ground surface, again under the footing and away from it. It is observed that minor variations are again observed especially at the later stages of shaking, which do not however hold up in favor of the one or the other option. The obtained dynamic settlements are plotted in **Figure 7.9**, from which it is concluded that the use of Rayleigh damping leads to slightly increased settlements, thus implying the underdamping of the seismic motion. Nevertheless, compared to the complexity involved in the definition of Rayleigh damping the particular deviation is not

judged to be significant, so that local non-viscous damping can be considered in all subsequent analyses.

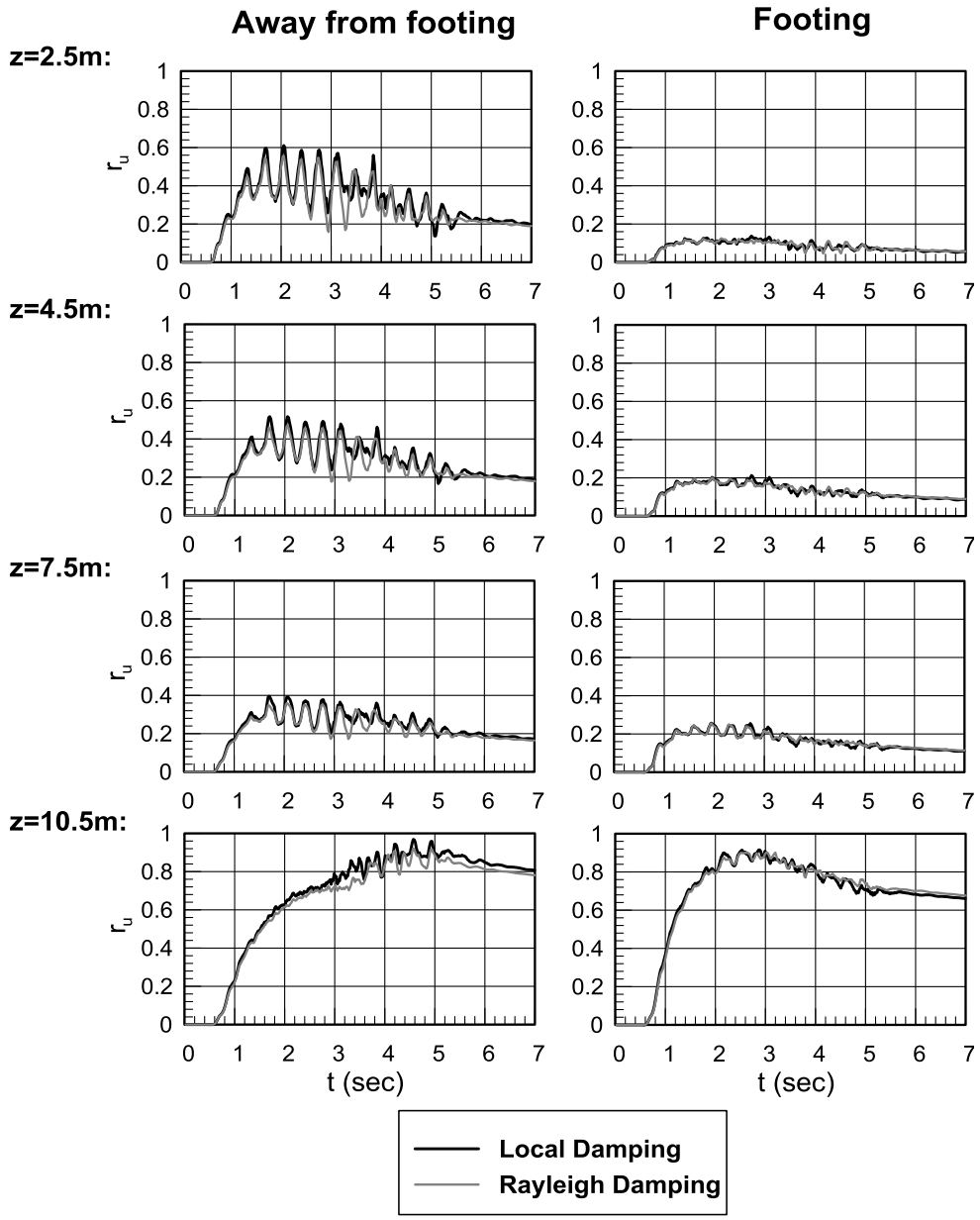

Figure 7.7: Effect of damping on excess pore pressure generation in different depths of the configuration.

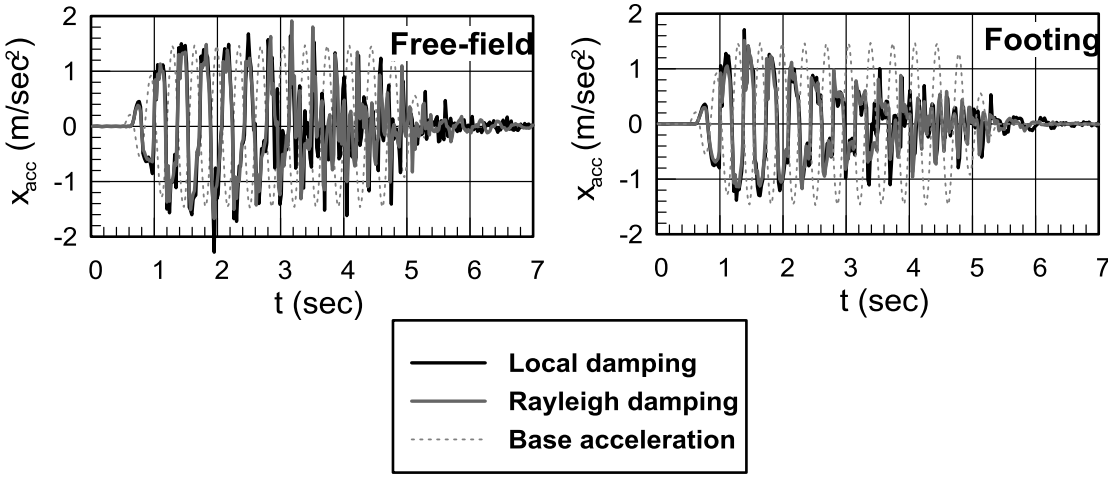

Figure 7.8: Effect of damping on soil response at the free-field and the footing.

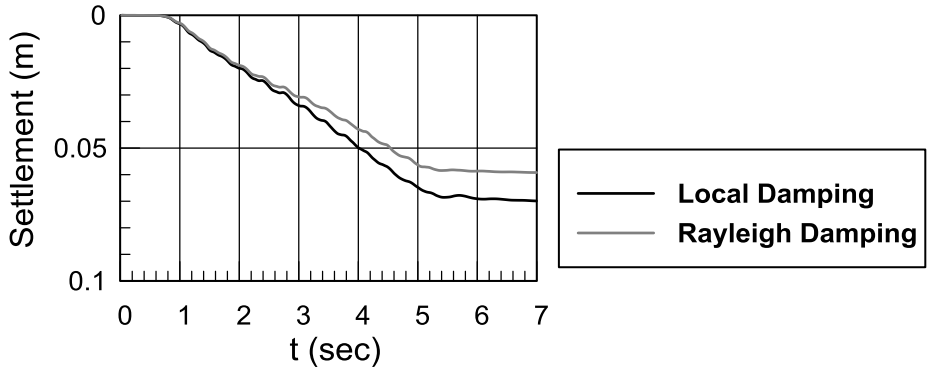

Figure 7.9: Effect of damping on the footing settlements.

Lateral Dimensions.- Particular attention is given to the total width of the configuration and its effect on the seismic performance of the shallow footing under examination. According to DIN 4017 the static failure mechanism of a surface footing resting on top of a relatively stiff cohesionless soil may extend up to 8.51 times the footing width B, for a friction angle of ϕ=40^o, as exhibited in **Figure 7.10**. Thus, for the 5m wide stip footing examined herein, an 85m wide configuration would be at minimum requested.

Additionally, due to the performed improvement, the relative density of the top crust significantly increases and is expected to reach up to 85-90%, always depending on the selected replacement ratio α_s and the initial relative density $D_{r,o}$(%) of the remediated soil. The use of the recalibrated NTUA-SAND constitutive model in the simulation of the particularly dense sand, leads to the prediction of friction angle values greater than 40 degrees, especially under simple shear conditions. This particular observation, in combination with **Figure 7.10**, implies that even wider grid configurations may be necessary

for the free and unobstructed development of the post-shaking failure mechanism and the determination of the degraded bearing capacity of the footing.

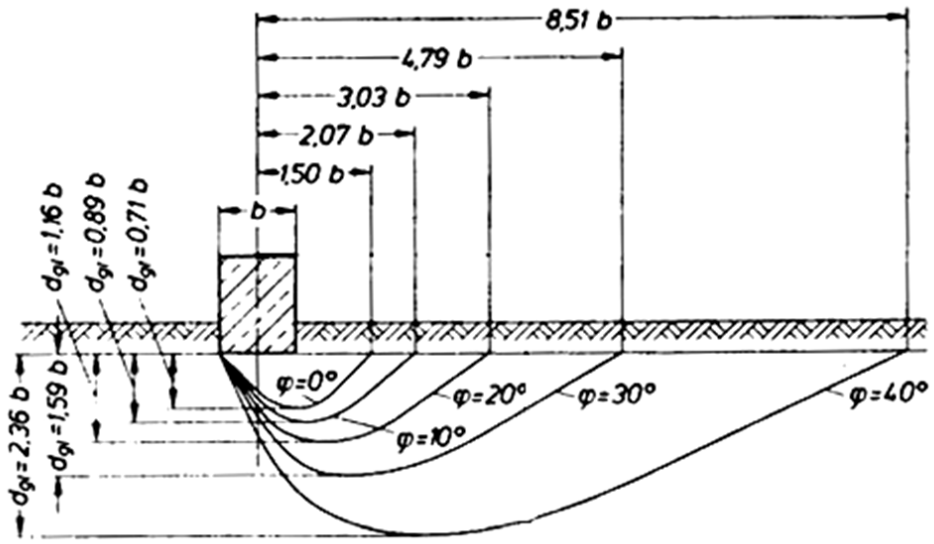

Figure 7.10: Bearing failure wedge sizes for strip footings on cohesionless soils, with different friction angles ϕ, (DIN4017).

The lateral sufficiency of the considered grid is parametrically investigated for a 20m thick sand layer of initial relative density equal to $D_{r,o}$=65%, three depths of improvement, namely $H_{imp.}$=4, 6, & 8m and an average relative density in the improved crust equal to 85%. Initially, four grid arrangements are tested for each scenario, considering L_x/B ratios equal to 12, 16.8, 21.2 and 24.8, rendering total horizontal dimensions equal to L_x=60, 84, 106 and 124 meters, respectively. Later on, additional analyses are executed in the case of $H_{imp.}$=6 & 8m, for L_x=140 meters, to fully visualize the observed trend between the width of the grid - L_x(m) -and the load required to reach failure, $q_{ult.}$ (kPa).

Three of the overall five different grid configurations are summarized in **Figure 7.11**. The narrowest grid considered in the particular investigation (L_x=60m) consists of 42×20=840 zones, with dimensions varying from 1.0×1.0m around the axis of symmetry to 1.5×1.0m and 2.0×1.0m, as approaching the boundaries of the configuration. The 84×20m grid arrangement resulted after increasing the number of zones in the x-direction to 58, thus generating 58×20=1160 zones, preserving at the same time the same discretization pattern. The next grid arrangement (L_x=106m) is discretized in 72×20=1440 zones, the L_x=124m mesh in 84×20=1680 zones and the widest mesh (L_x=140m) in 96×20=1920 zones, always preserving the discretization outline of the initial configuration.

Figure 7.12 summarizes the effect of the grid width on dynamic settlements. The three different curves correspond to the three different improvement depths, $H_{imp.}$(m). The observed effect is particularly minor and practically independent of the width of the considered configuration for L_x/B values greater than about 15.

Figure 7.13, exhibits the effect of the mesh width on the post-shaking degraded bearing capacity of the foundation, again with regard to the normalized width L_x/B. It is observed that unlike the previous figure, the load to failure ($q_{ult.}$) significantly decreases with increasing grid-width L_x(m), disclosing the major boundary effects that take place in the narrower grid arrangements, regardless of the improvement depth. The particular observation essentially implies that unless the grid is wide enough, the failure mechanism during the post-shaking phase cannot fully develop because the grid-boundaries provide substantial lateral resistance, hence leading to false and considerably non-conservative estimates of the post-shaking load required to failure. Additionally to the above, it appears that the grid demands are higher for deeper improvement schemes, considering that for $H_{imp.}$=8m the derived curve levels off after L_x/B=25. Based on the previous remarks, all analyses with $H_{imp.}$=4 & 6m will be performed hereafter with L_x=106m while for $H_{imp.}$=8m the width will be increased to L_x=124m to eliminate potential boundary induced effects.

An untimely but important observation is that, provided the optimum grid width is used, the thickness of the improved crust has a distinct effect on both the dynamic-induced settlements and the post-shaking bearing capacity. Indeed, dynamic-induced settlements greatly diminish from 0.13m to 0.10 and 0.08m after increasing the improvement depth from 4 to 6m and then to 8 meters respectively. The opposite trend is observed for the post-shaking bearing capacity, which increases with increasing depth of improvement. Namely, after doubling the thickness of the improved crust from 4 to 8meters, the post-shaking bearing capacity increases by a factor of 3, i.e. from 100kPa to 300 kPa. All the above, disclose the controlling role of the thickness of the performed improvement, on the seismic performance of a shallow foundation, which is going to be thoroughly examined in subsequent chapters.

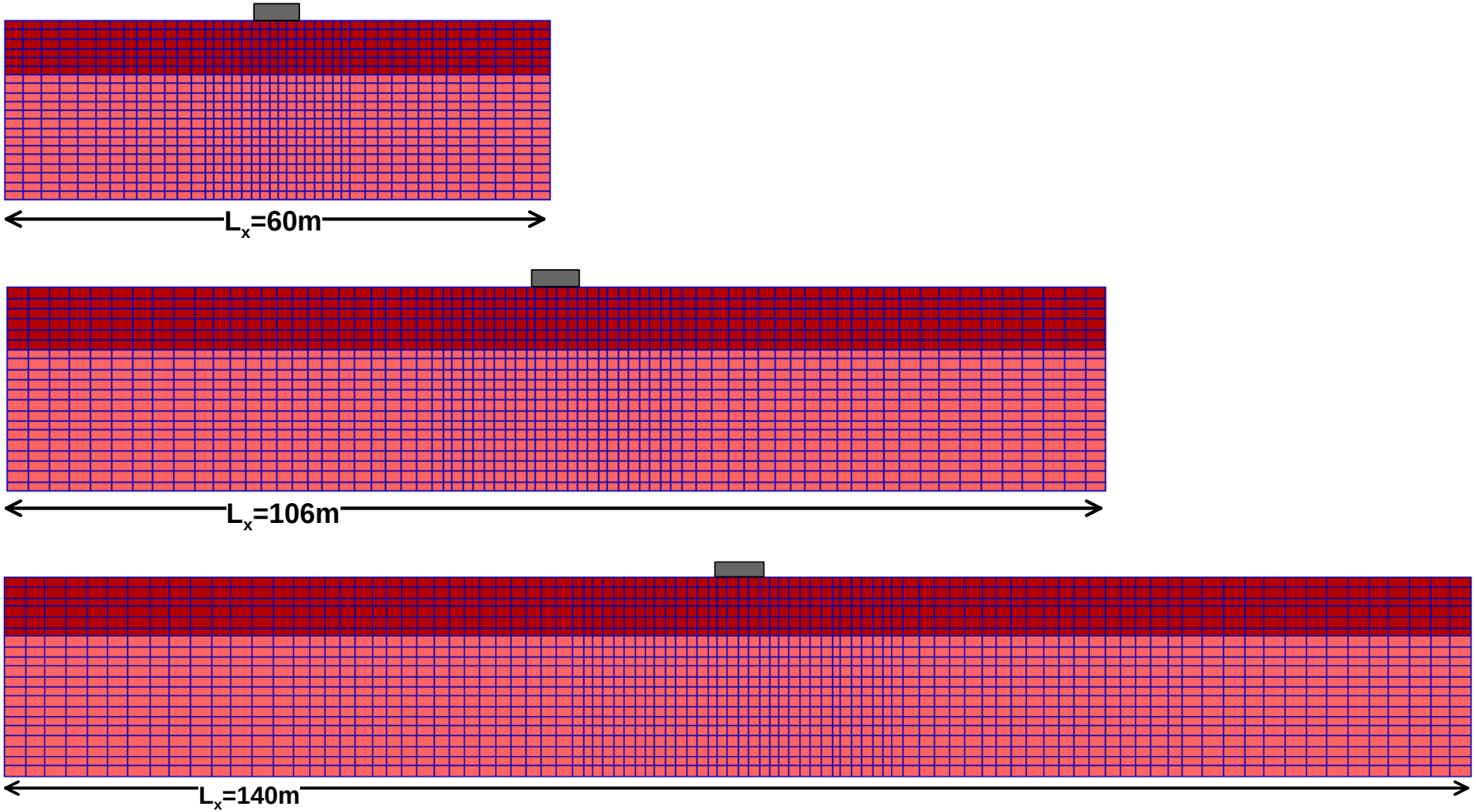

Figure 7.11: Parametric investigation of grid width for the execution of the 2-D analyses. Typical grid configurations for L_x=60, 106 & 140m.

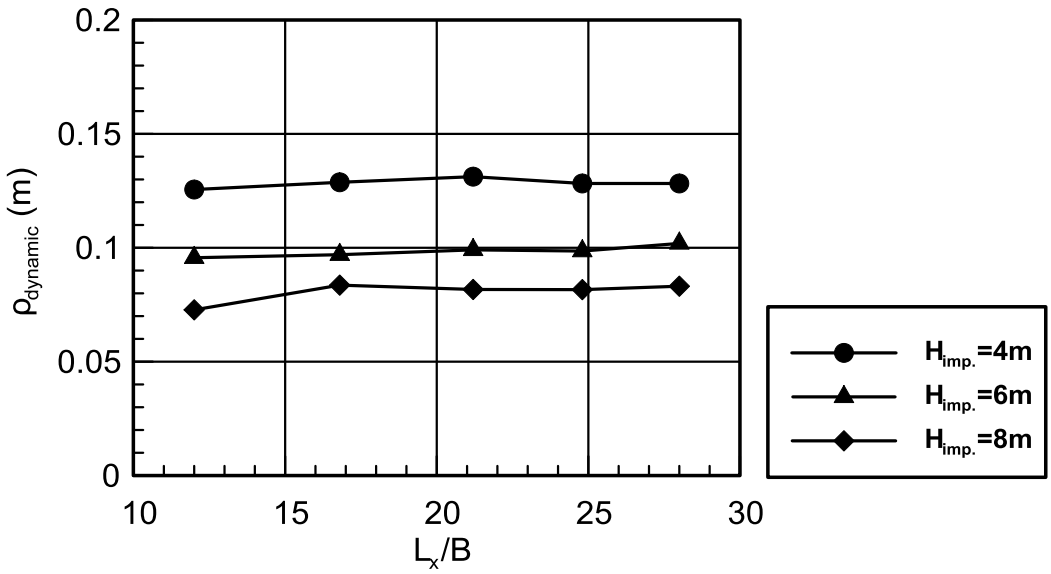

Figure 7.12: Dynamic settlements as a function of width L_x(m) normalized by the footing width B(m).

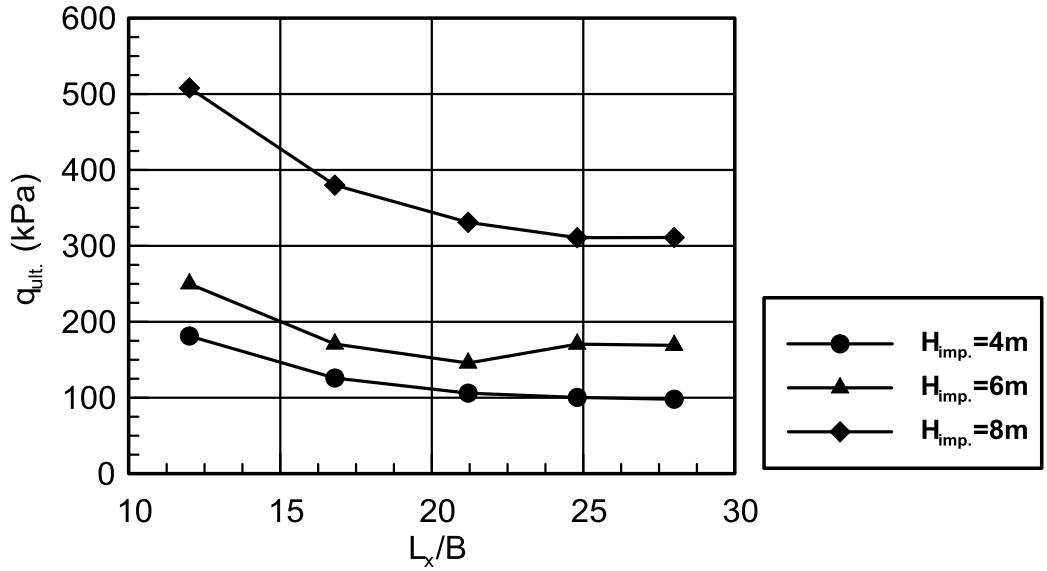

Figure 7.13: Ultimate bearing capacity $q_{ult.}$ (kPa) as a function of width L_x(m) normalized by the footing width B(m).

7.4 Typical numerical results.

The reference analysis, depicted in **Figure 7.14**, refers to a 20m thick liquefiable sand layer, with initial relative density $D_{r,o}$=45% and initial coefficient of permeability $k_{sand}=6.6*10^{-5m}$/s, improved at the top 4 meters at a replacement ratio equal to α_s=0.07. The improved crust is attributed a relative density equal to $D_{r,imp.}$=60% and a coefficient of permeability $k_{eq.}=9.85*10^{-4}$m/s. The shallow foundation on top of the above soil profile applies a contact pressure equal to q=75kPa. All other associated assumptions involved in the numerical analysis have already been described previously.

The comparisons will be performed regarding the mechanisms of excess pore pressure generation, the accumulations of seismic-induced settlements as well as the degradation of the footing's bearing capacity due to liquefaction of the under-laying sand.

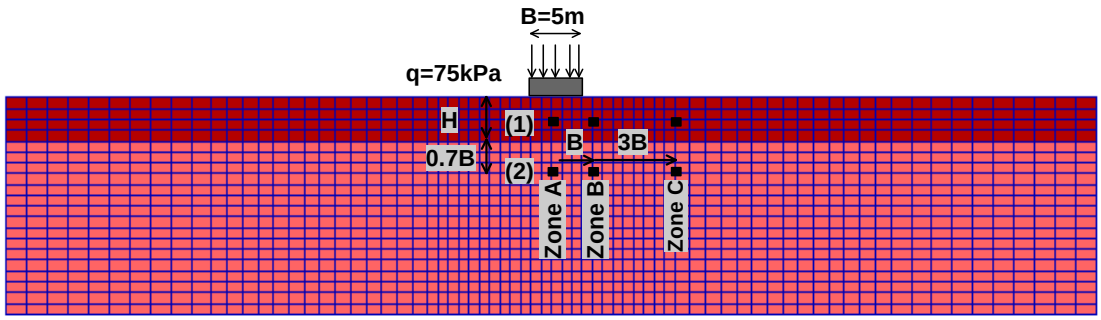

Figure 7.14: Location of characteristic zones

7.4.1 Excess pore water pressure generation

The mechanisms of excess pore pressure generation and evolution during shaking as well as the post-shaking behavior of the partially or entirely liquefied soil are going to be examined in the present paragraph. For that purpose, **Figure 7.15** and **Figure 7.16,** summarize the excess pore pressure and excess pore pressure ratio time-histories in three different zones, namely underneath the footing (A), at the corner (B) and in the free field (C), and at two distinct depths, namely inside the improved crust (A1, B1, C1) and the liquefiable ground (A2, B2, C2).

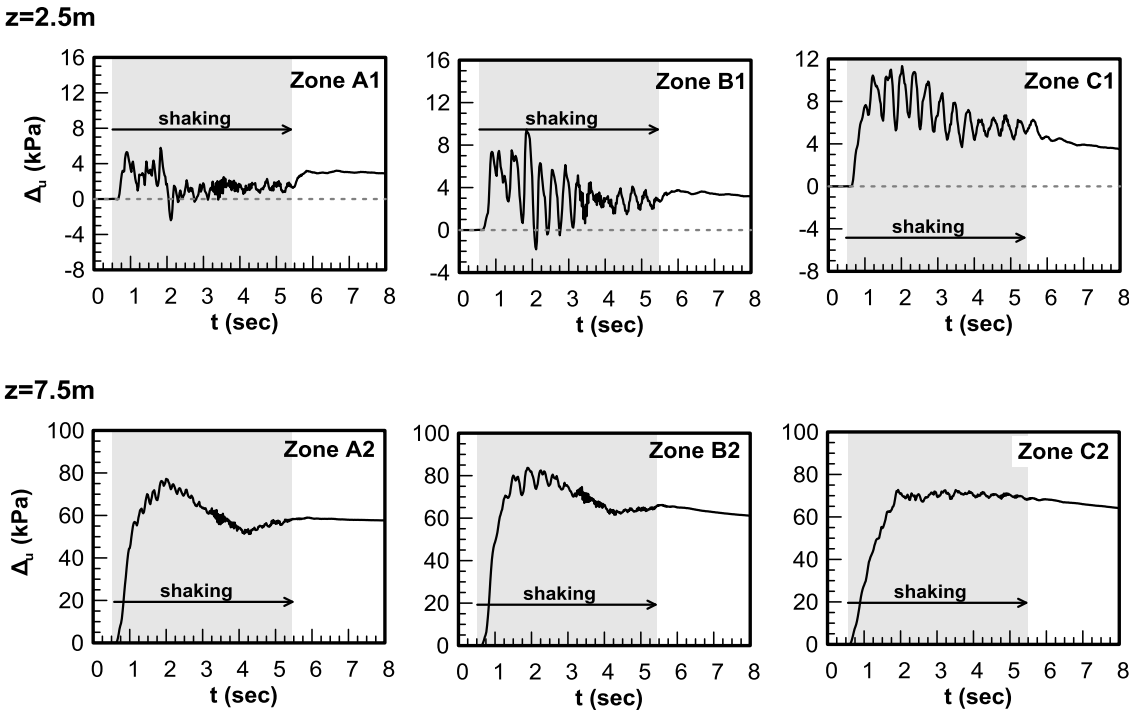

Figure 7.15: Excess pore pressure time-histories.

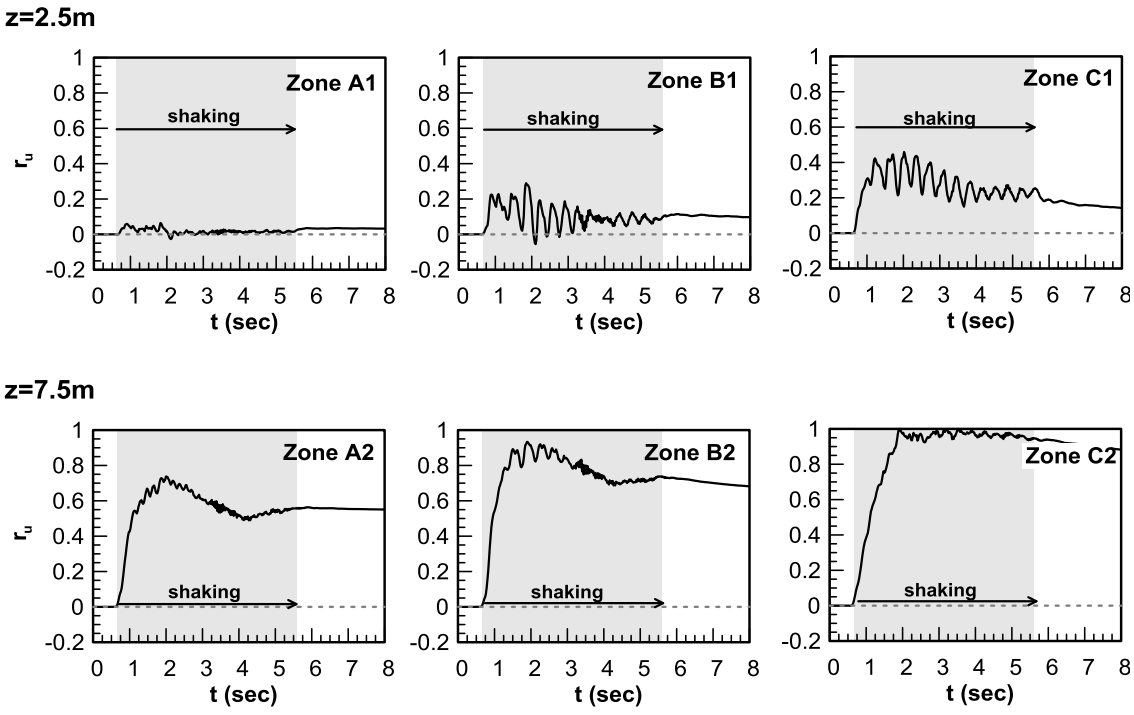

Figure 7.16: Excess pore pressure ratio time-histories.

One of the main observations that stand out is the fact that the soil underneath the footing experiences lower excess pore pressures compared to the soil in the free-field, regardless of elevation. The explanation behind the above behaviour, focuses on the foundation-induced static deviatoric stresses, preventing excess pore pressures under the foundation to reach or exceed the free-field values. The particular observation was originally noticed by Yoshimi & Tokimatsu (1977) in their field observations after the Niigata earthquake in 1964. Shaking table tests performed by themselves as well as additional shaking table and centrifuge experiments performed by other researchers [e.g. Liu & Dobry (1997), Kawasaki et al. (1998), Adalier et al., (2003) and Coelho et al., (2004)] provided additional support to the particular remark.

The previous pattern is repeated in the excess pore pressure ratio time histories, which are lower underneath the footing and increase with increasing distance from the footing (zones A2, B2, C2). The explanation to the particular effect lays in the definition of the excess pore pressure ratio itself, also noted by Karamitros et al. (2013). Taking into account the additional vertical stress applied by the footing, it is mathematically established that the excess pore pressure ratio under the footing will be defined as:

$$r_{u,foot} = \frac{\Delta u_{foot}}{\sigma'_{vo,foot}} = \frac{\Delta u_{foot}}{\sigma'_{vo,ff} + \Delta\sigma'_{v,foot}} \tag{7.6}$$

Nevertheless, as mentioned above, due to the foundation-induced static deviatoric stresses the excess pore pressures developing in the free field are greater than the ones underneath the footing. Particularly, under liquefaction, excess pore pressures will equal the effective vertical stresses, i.e. $\Delta u_{,ff} = \sigma'_{vo,\,ff} = \sigma'_{vo,\,foot}$. Therefore the above expression is transformed as follows:

$$r_{u,foot} \leq \frac{\Delta u_{ff}}{\sigma'_{vo,ff} + \Delta\sigma'_{v,foot}} = \frac{\sigma'_{v,o,foot}}{\sigma'_{vo,ff} + \Delta\sigma'_{v,foot}} = \frac{1}{1 + \Delta\sigma'_{v,foot} / \sigma'_{vo,ff}} \tag{7.7}$$

The above methematical expression also explains the gradual increase of excess pore pressure ratio values with depth (zones A1-A2 & B1-B2). Namely, the additional vertical stress applied by the footing gradually decreases with depth, therefore, the resulting excess pore pressure ratio will increase.

Lower excess pore pressure ratios developing underneath the footing have also been mentioned by Liu & Dobry (1997), after performing centrifuge tests to examine the mechanism of liquefaction-induced settlement of a shallow foundation, as well as the effect

of sand densification in a specified area under a shallow footing. They attributed the lower excess pore pressure ratios to the dilative response of the soil, induced by the applied static shear stresses. Moreover, Adalier et al. (2003) observed that excess pore pressures increased with depth and distance from the footing and that the footing values did not exceed the excess pore pressures in the free field. They attributed this behavior to the inability of the liquefied free-field soil to provide sufficient lateral resistance beyond its initial vertical effective stress.

Regarding locations C1 and C2, it is inferred that the obtained excess pore pressure ratio within the crust (zone C1) barely exceeds $r_{u,max}$=0.4, as a result of the performed improvement. On the other hand, within the unimproved sand layer, liquefaction occurs already from the early stages of loading, as indicated by the excess pore pressure ratio which becomes equal to $r_u=\Delta_u/\sigma'_{vo} = 1$.

Another interesting characteristic concerns the excess pore pressure generation pattern in the vicinity of the footing and inside the improved crust, namely locations A1 & B1. The excess pore pressure time-history in location A1, essentially verifies the observation by Coelho et al. (2004) about positive peaks of Δu, gradually evolving to intense negative peaks as a result of soil dilation. The negative peaks though are not preserved for long, due to the groundwater flow arriving to the specific location from the surrounding area. Moreover, at the edge of the footing, the previously reported positive spikes appear more intense up to about 2secs and consequently reduce to negative values. At the later stages of loading the particular effect is smoothed, probably due to the groundwater flow taking place in the permeable crust. The decrease in the excess pore pressure time histories in the deeper location of the configuration is explained on the same basis of soil dilation. The main difference is that the footing-induced static stresses are lower at greater depths and therefore greater excess pore pressures are allowed to develop.

The post-shaking increase of excess pore pressures under the footing, evident in the presented time-histories, is explained on the basis of groundwater flow occuring upwards as well as from the free field towards the footing. This is also verified by the groundwater flow vectors at the end of shaking illustrated in **Figure 7.17**. Note that the post-shaking increase of excess pore pressures within the crust is substantially greater, compared to locations within the liquefiable sand, as a consequence of the greater permeability of the drain improved upper layer. Liu & Dobry (1997) noted the post-shaking increase in the excess pore pressures under the footing as well, which was also attributed to a substantial groundwater

flow from the surrounding areas towards the footing. The particular observation is also mentioned by Adalier et al. (2003), and Kawasaki et al. (1998).

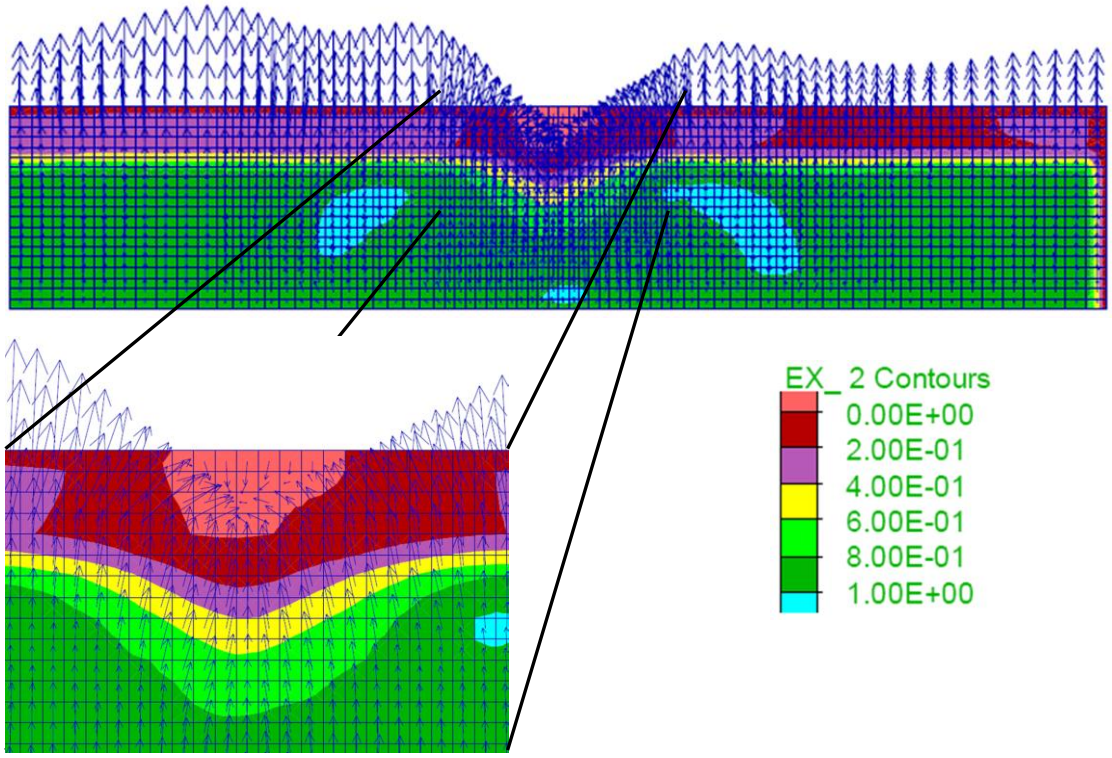

Figure 7.17: Excess pore pressure ratio contours and flow vectors under the footing area at the end of shaking.

7.4.2 Settlement accumulation

The seismic settlement time-history of the footing is illustrated in **Figure 7.18**. It is observed that settlements accumulate linearly with time and mainly develop during shaking, with only a minor part being added post-shaking, probably due to excess pore pressure dissipation. The specific pattern has also been observed by Liu & Dobry (1997), Adalier et al. (2003) as well as Dashti et al., (2010) in centrifuge experiments examining the seismically induced settlements of shallow foundations on different configurations of improved densified ground.

Moreover, the deformed mesh at the end of shaking and associated displacement vectors are exhibited in **Figure 7.19**. Evidently, at the footing location, displacement vectors are totally vertical, as a result of the consideration of a rigid beam element, as exlained previously. More importantly, the footing's settlement accumulation, leads to significant lateral flow of the liquefied underlying sand towards the partially liquefied surface. The

particular deformation pattern has also been obseved in centrifuge tests performed by Adalier et al. (2003) and Dashti et al. (2010).

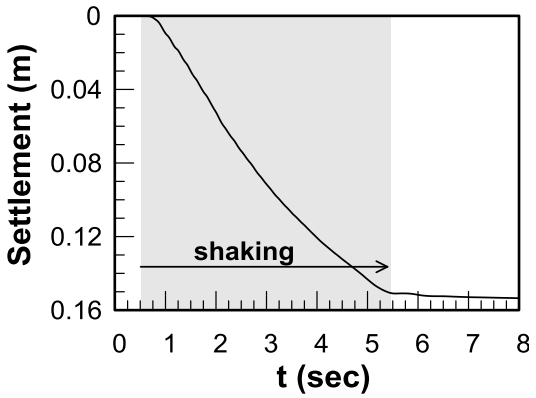

Figure 7.18: Footing settlement accumulation time-history.

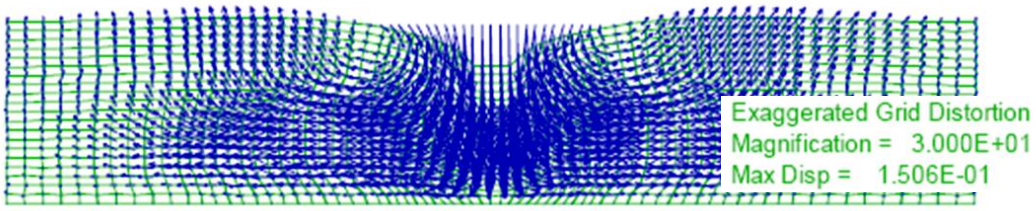

Figure 7.19: Deformed mesh and displacement vectors at the end of shaking.

To further analyze the mechanisms behind settlement accumulation, **Figure 7.20**, summarizes the horizontal and vertical components of the footing's motion including acceleration, velocity and displacement time-histories. The particular time-histories refer to the baseline case described in the previous section. It is observed that the onset of liquefaction leads to a significant de-amplification of the horizontal motion without any significant horizontal displacement. On the other hand, the much smaller in magnitude, vertical component of motion does not reduce its amplitude and presents a ratio of 2:1 regarding the predominant frequency of the vertical over the horizontal acceleration, as it has also been observed by Coehlo et. (2004). More importantly, from the above figure it is implied that the "plateau-shaped" velocity time-history is responsible for the linear accumulation of settlement with time, plotted beneath.

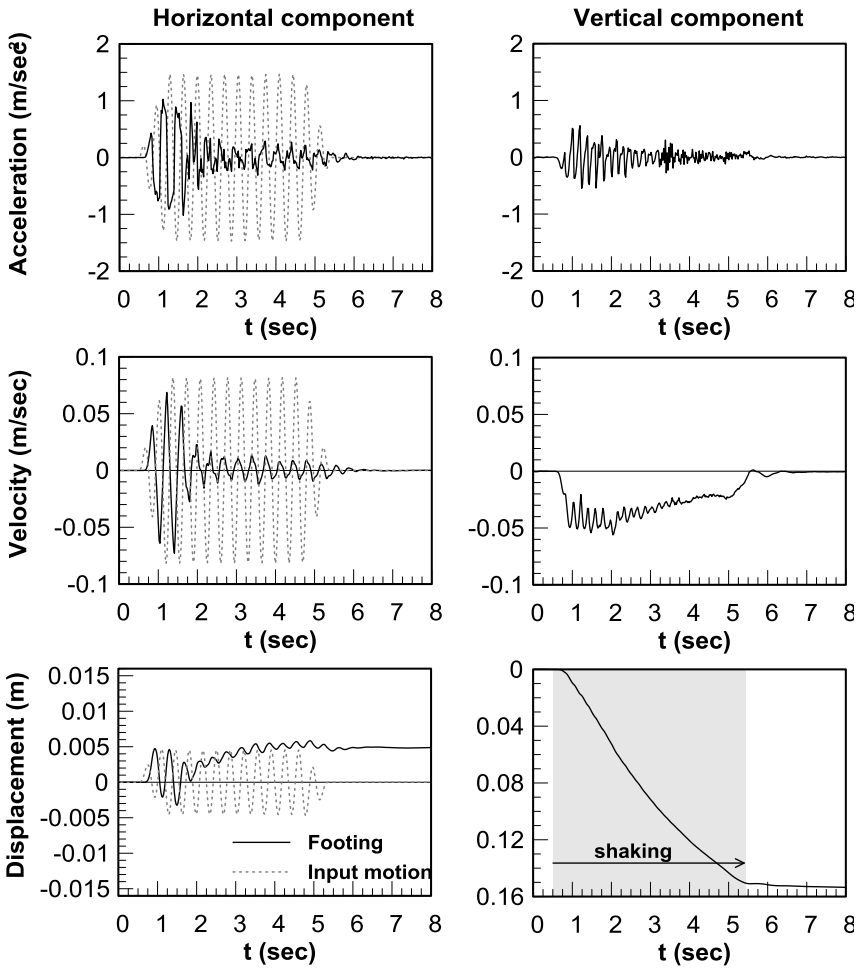

Figure 7.20: Horizontal and vertical acceleration, velocity and displacement time-histories at the footing and comparison to the input motion.

The particular pattern was initially identified by Richards et al. (1993), who employed the Richards & Elms (1979) sliding-block approach for retaining walls to calculate seismic displacements of foundations on uniform dry sand. Namely, they considered a simplified Coulomb active-passive wedge failure mechanism, which is activated every time the critical acceleration level is exceeded. As a result, the active wedge underneath the footing moves downward and sideways, while the passive wedge is displaced laterally. Hence, displacements accumulate incrementally during shaking and may be easily computed as a function of the excitation characteristics and the seismic counterpart of the active critical angle of rupture (ρ_{AE}).

The above work by Richards et al. (1993) may be extended to describe the liquefaction – induced settlement accumulation of shallow foundations in saturated liquefiable sands. **Figure 7.21** illustrates the velocity vectors and shear strain rate contours occurring within one loading cycle and more specifically at the time of the maximum acceleration at each

direction, to justify the above mechanism. More specifically, the combination of the footing's bearing pressure along with the developing horizontal inertia forces in the subsoil trigger the activation of the same one-sided wedge-type failure mechanisms. The particular wedge system develops twice within one loading cycle, one on each side of the footing and opposite to the ever-current direction of the input motion. As a result, during one total loading cycle, one vertical and two opposite and equal - therefore cancelling - horizontal footing displacements occur. The above observations are also verified by Karamitros et al. (2013), who examined the relevant issue of a shallow foundation on liquefiable soil with a clay crust.

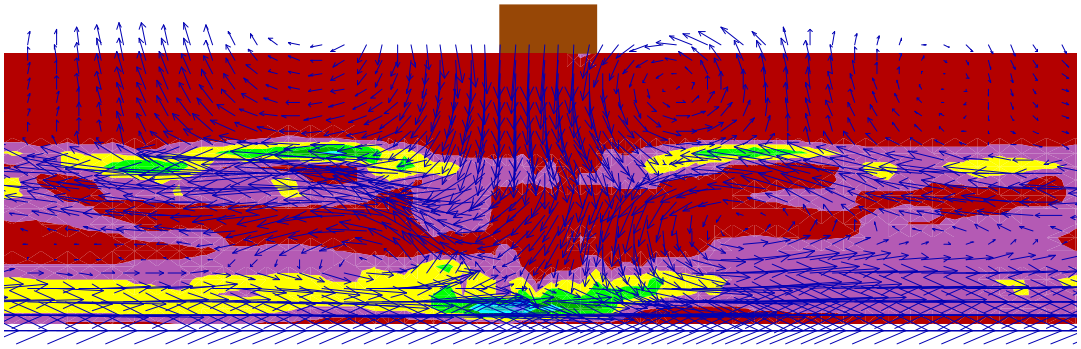

(a)

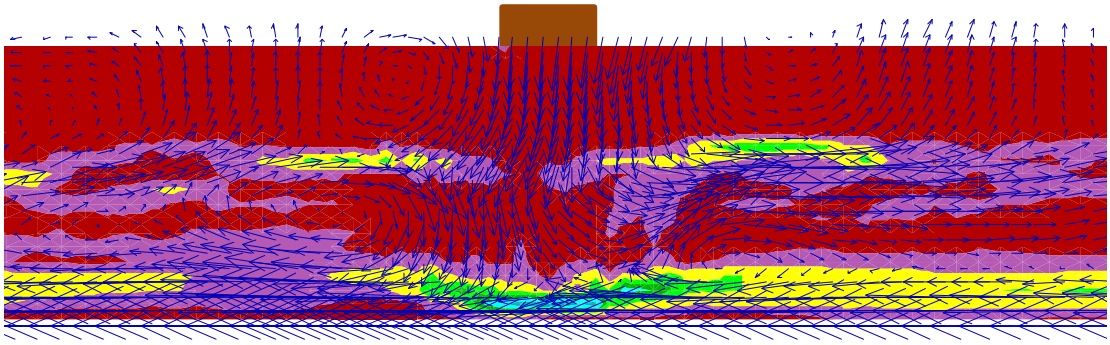

(b)

Figure 7.21: Shear strain rate contour and velocity vectors within one loading cycle **(a)** maximum applied acceleration to the right **(b)** maximum applied acceleration to the left.

7.4.3 Post-shaking bearing capacity degradation

The onset of subsoil liquefaction apart from the accumulation of dynamic settlements causes total loss of shear strength in the unimproved soil and partial loss of shear strength inside the improved crust, due to the inevitable but controled development of excess pore pressures. The particular effect leads to the degradation of the shallow foundation's bearing capacity, for a specific period of time, defined as the time required for the total excess pore pressure dissipation. As a result, the allowable post-shaking factor of safety may become much lower than the conventional values for static loads.

Figure 7.22a & **b**, exhibit shear strain rate contours and velocity vectors at failure developing for static non-liquefied conditions and the liquefied state respectively, providing a useful insight to the developing mechanisms. It is evident that under static conditions, failure occurs within a very confined area within the crust. On the contrary, in the case of liquefaction occurrence, the footing appears to punch through the partially liquefied crust, into the liquefied subsoil whose shearing resistance has practically minimized as a consequence of the excess pore pressure generation. The specific failure pattern is also referred to as "punching shear failure" (Vesic, 1973) and is encountered in cases of fairly loose soils.

The developing failure pattern is very similar to the mechanism proposed by Meyerhoff & Hanna (1978) for shallow foundations on layered soil profiles, illustrated in **Figure 7.23a** & **b**. In the proposed methodology, it is specified that punching shear failure (**Figure 7.23a**) occurs in relatively thin top layers, thus depending on the H/B ratio, in which H is the thickness of the upper layer, and B the width of the footing. In cases where H is relatively large, the failure surface develops entirely within the top stronger layer, as illustrated in **Figure 7.23b**.

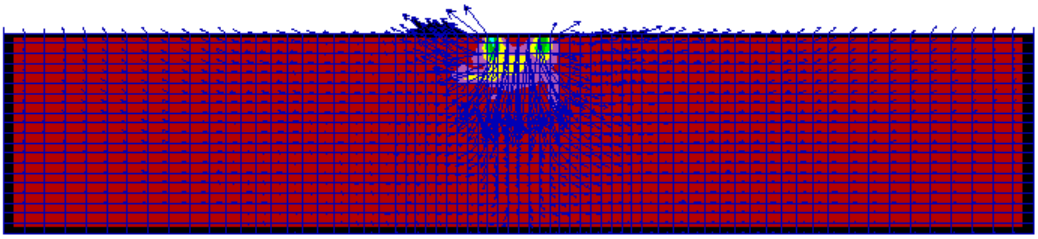

(a) Static load failure mechanism

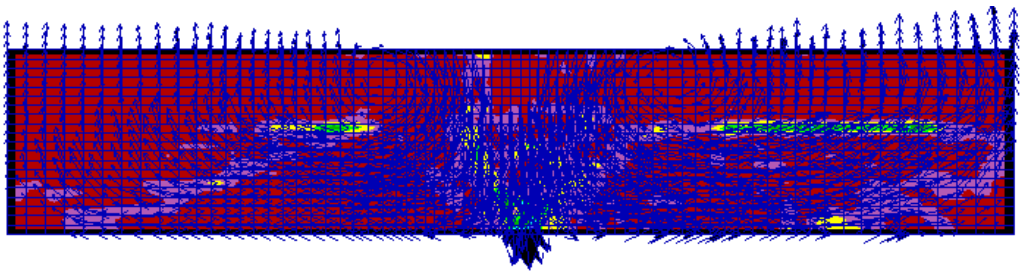

(b) Post-shaking failure mechanism

Figure 7.22: Shear strain rate contour and velocity vectors related to **(a)** static and **(b)** post-shaking bearing capacity failure.

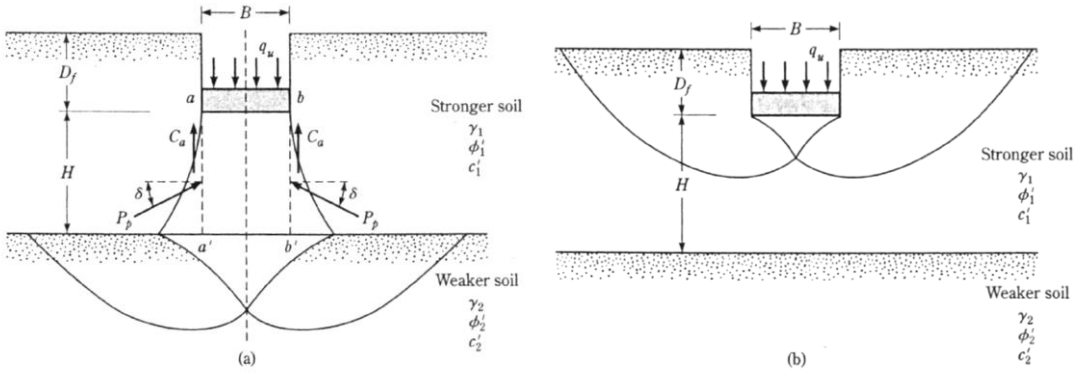

Figure 7.23: Bearing capacity of a continuous foundation on layered soil (Meyerhof & Hanna, 1978).

Figure 7.24, ehxibits the load-displacement curves for static loading and the post-shaking part of the reference analysis (*Phase 3* as mentioned previously). The static bearing capacity failure was numerically simulated by incrementally increasing the footing's contact pressure (*Phase 1*) up to the failure load of 1550kPa. The theretically derived ultimate bearing capacity of a 2-layer sand formation was estimated between q_t=1410 and 1660kPa, therefore, essentially verifying the numerical prediction. As a result, the factor of safety under static conditions is estimated to be equal to $F.S._{stat.}$=1550/75=20.6. The post-shaking bearing capacity was computed to be slightly above 90kPa, reducing the safety factor to

F.S.deg.=90/75 ≈ 1.20, indicating a marginal avoidance of total structural failure, due to the onset of liquefaction in the subsoil.

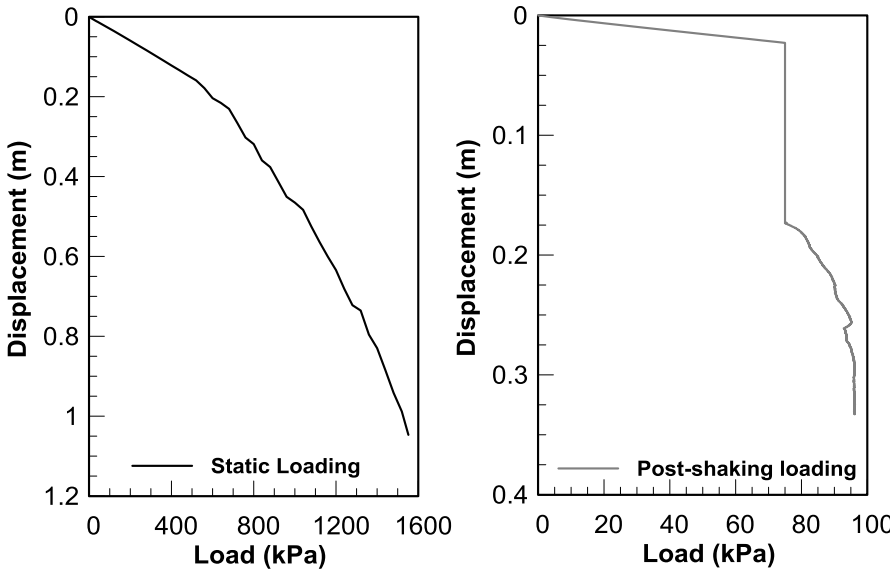

Figure 7.24: Load-displacement curves for initial static loading and post-shaking loading.

7.5 Verification of numerical methodology [Liu & Dobry (1997)].

The subsequent verification will focus on the effectiveness of the methodology to accurately predict the seismically induced excess pore pressure generation and the associated dynamic settlements. The selected data are obtained from a series of centrifuge tests performed by Liu & Dobry (1997). In brief, Liu & Dobry (1997) investigated the mechanism of liquefaction-induced settlement of a shallow foundation, as well as the effectiveness of sand densification by vibrocompaction in a cylindrical area under a shallow footing. Overall, eight centrifuge experiments were performed at the centrifuge facility of the Rensselaer Polytechnic Institute (RPI), Troy, NY, considering a circular footing placed on top of a medium dense saturated sand layer overlying an impervious rigid base. The first series of tests focused on the effect of the depth of compacted soil under the foundation on the footing's acceleration and settlement. The second group consisted of three tests in which the effect of soil permeability on excess pore pressure built up and footing settlement is investigated, without any performed densification. For the purposes of the specific verification, the first group of five tests was considered.

7.5.1 Test description and numerical simulation

Model Configuration and Instrumentation Layout.- The rigid foundation is a circular footing of prototype diameter 4.56m applying an average contact pressure of q=100kPa (in prototype scale, for a centrifugal acceleration field of 80g). The soil used in all tests is a fine, uniform Nevada #120 sand with initial relative density Dr = 52±3% and a total thickness equal to 12.5m in prototype scale (**Figure 7.25a**). The vibro-compacted zone extends to a area of about 1.6 times the width of the footing, as illustrated in **Figure 7.25b**, while the compaction depth varies from Z_c = 0 to 2.76B, essentially covering to the full thickness of the soil statum. The relative density of the compacted zone was estimated around 90%. The different testing parameters are summarized in **Table 7.4** for all five models. The average relative density of the compacted cylindrical soil in test C1 was computed equal to $D_{r,c}$=106%, which according to Liu & Dobry (1997), is probably due to errors in estimating the compacted soil volume.

Table 7.4: Soil properties of series C tests (Liu & Dobry, 1997).

Test	$D_{r,ini}$ (%)	Z_c (m)	Zc/B	$D_{r,c}$ (%)
C0	54	0	0	-
C1	51	3.22	0.71	>100
C2	55	6.72	1.47	88
C3	49	9.45	2.07	91
C4	51	12.58	2.76	89

The permeability of Nevada #120 sand tested in the laboratory at 1g is reported to be equal to the dynamic value, i.e. k=0.0021cm/s. The pore fluid used in the particular test series is water, therefore, according to the applying scaling laws, the permeability of the prototype soil will be n times larger than that obtained in the laboratory test at 1g. Hence, at 80g n equals 80 and the permeability coefficient is equal to k=80*0.0021=0.168cm/s, corresponding to a coarse sand.

Figure 7.26 shows the model configuration and instrumentation of the tests. Three horizontal accelerometers were installed, the first at the model base, α_i, the second on the soil surface away from the footing, α_s, and the third on the footing itself, α_f. Settlements were monitored at the center of the footing (S_f) and the free field (S_s), with vertical linear voltage differential transformers (LVDT). Also, seven pore pressure transducers were placed in the soil at different depths under the center of the footing (locations PC1, PC2 and PC3), close to the edge of the footing (location PE) and away from the footing (locations PF1, PF2

and PF3). The specific configuration was constructed in a rigid rectangular bucket with dimensions 454×204×241mm^3. All test configurations were subjected to the same 10-cycle uniform sinusoidal excitation with frequency equal to f=1.5Hz and an average acceleration amplitude of 0.2g.

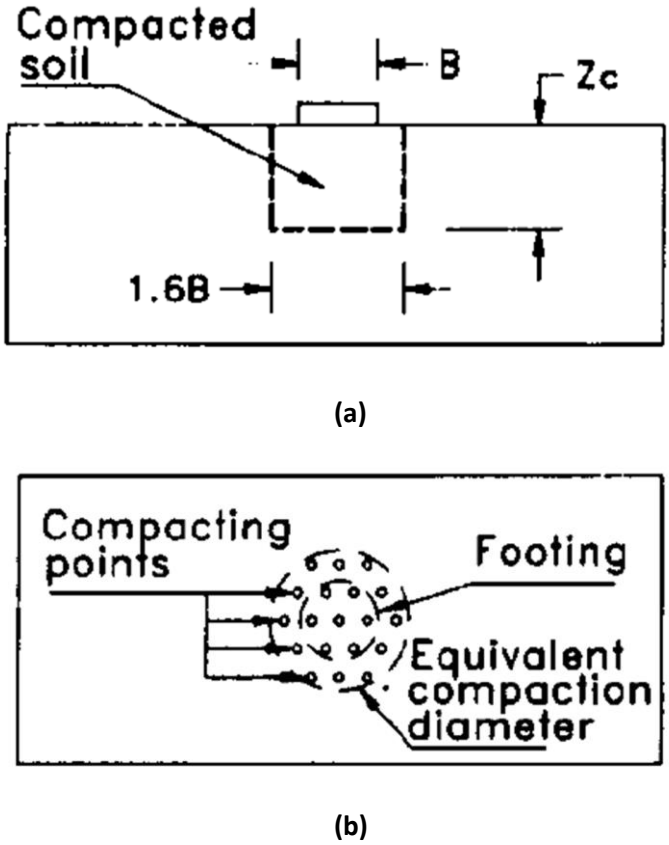

Figure 7.25: Centrifuge test soil compaction: **(a)** profile **(b)** plan view.

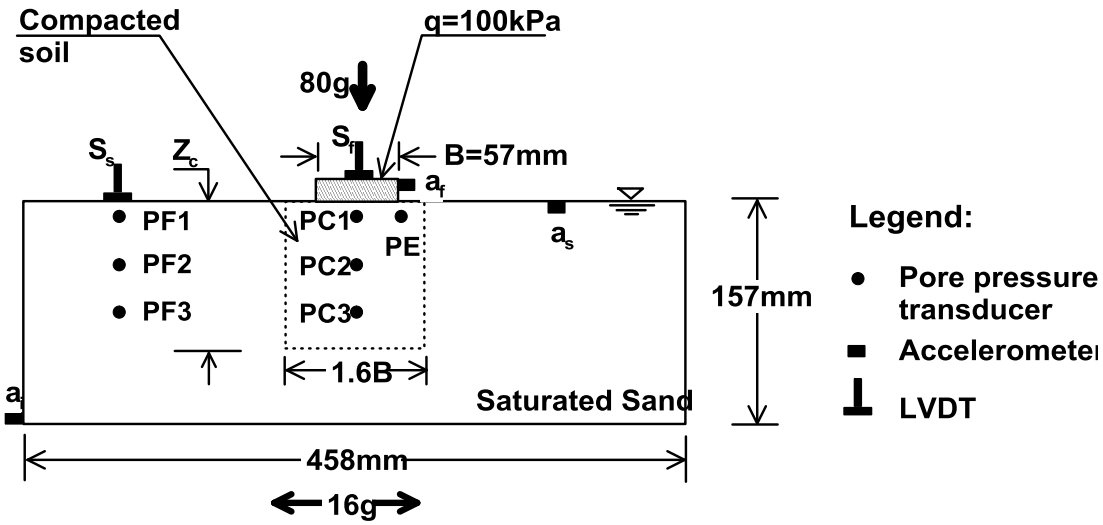

Figure 7.26: Model configuration and instrumentation of test series.

Model Preparation and Test Procedure.- The model sand deposit was suitably deposited to a relative density of $D_{r,o}$=52% using the dry pluviation process with the help of a sand rainer. Pore pressure transducers and accelerometers were placed in the model during the deposition process. After the construction of the uniform sand layer, the densified zone around the assumed footing locaion was constructed with a vibrating tube, 6.4mm in diameter (0.50m in prototype), which was inserted in 19 locations over a circular area of about 1.6 the diameter of the footing. The depth of compaction differs between the tests and it was assumed to reach about 1.5 tube diameters below the tip of the tube. During the densification process some settlement in the area occurred but the soil was leveled by adding additional sand at the ground surface to preserve its initial elevation.

Following compaction, the container was sealed and de-aired by applying a negative vacuum pressure of 101kPa for one hour. De-aired water was then inserted very slowly to the bottom of the model in order to achieve fully saturated conditions. When the water reached 10mm above the free soil surface, vacuum was removed and the model was loaded on the centrifuge platform to be spun at 80g. After consolidation, at the geostatic stresses, the centrifuge was stopped and the model footing was placed on the soil surface. The soil-foundation system was spun back at 80g until the stabilization of all output data of the instruments and the dynamic excitation was applied.

Numerical Simulation.- Due to the three-dimensional nature of the above test series, the numerical analyses are performed with the finite difference code FLAC-3Dv4.0. According to Liu & Dobry (1997) the rigid rectangular bucket has plan dimensions 454×204mm^2, this corresponding to prototype dimensions of 36.64×16.32m^2 and the sand layer measures a thickness of 12.5m. Also, the dynamic loading is applied along the x-direction, thus the system's response is symmetrical along the y-direction. To take advantage of this symmetry, only half the footing was modeled, by generating a 36.80×8×12.5m^3 grid as presented in **Figure 7.27**. The specific grid is discretized at 0.8×0.8×0.5m^3 brick zones, thus creating a total of 11500 zones.

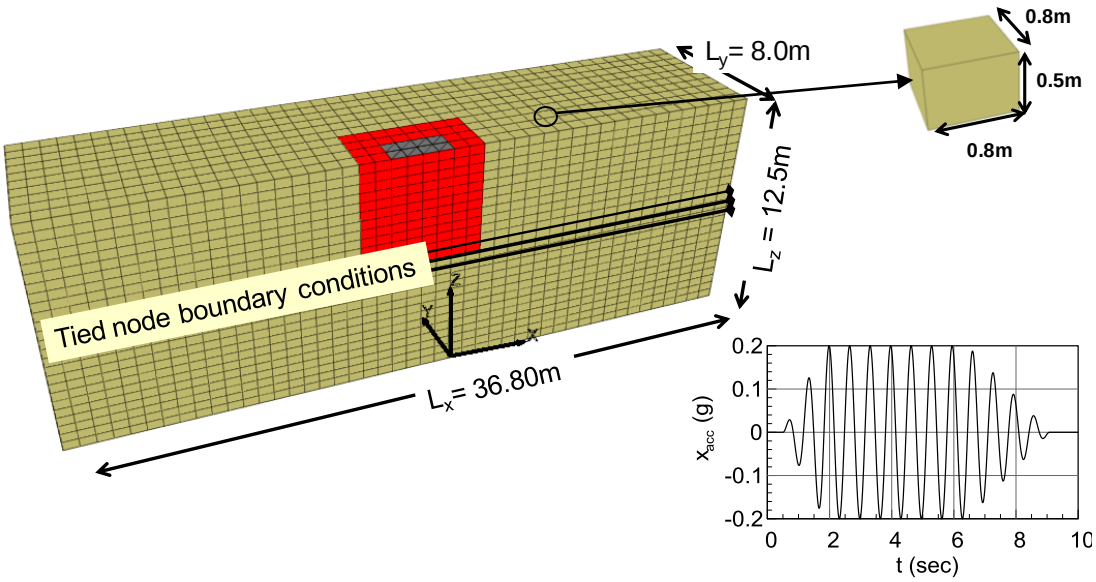

Figure 7.27: Model simulation in FLAC3D – grid configuration and excitation applied at the base.

Footing simulation.- It is reminded that in FLAC, the bearing pressure of a foundation is simulated through vertical velocity applied at specific gridpoints. This velocity varies linearly from the value at the last gridpoint upon which it is applied, to zero at the adjacent gridpoint. Therefore, in such problems, half the width of the adjacent zones should be added to the actual footing width. Based on the above and the brick-zone discretized grid, it turned out that the application of velocity on a group of gridpoints corresponding to a circular footing would lead to very approximate simulations, which would introduce significant deviations. Therefore to maintain the configuration outline as accurate as possible, it was decided to consider a square footing with an equivalent width B, so that the same contact pressure of q=100kPa-or a load of Q=100×π×R^2≈1600kN- is applied. Based on this simplifying approach, the width of the equivalent square footing is computed equal to B=√(1600/100)=4.0m. The square foundation is simulated through shell elements, because rigid elements are not supported by FLAC3D. To appropriately reproduce the symmetrical conditions, the rotational degree of freedom around the x-axis of the shell nodes laying on the symmetry plane, is fixed. The shell elements were assigned the elastic properties of concrete, namely Young's modulus E=30MPa and Poisson's ratio v=0.20.

Nevada #120 sand.- is simulated using the advanced constitutive model NTUA-SAND, which has already been described in previous sections. For static loading, and the application of initial stresses, horizontal displacements are restrained in the lateral boundaries, whereas

along the vertical direction only the bottom boundaries are restrained, allowing the system to freely settle. Moreover, the bottom boundaries are allowed to move horizontally, to avoid the generation of parasitic shear stresses.

Permeability Coefficient.- As mentioned earlier, the permeability coefficient does not remain constant during seismic loading, but fluctuates proportionally to the ever-current excess pore pressure ratio, r_u. Also, according to Chaloulos (2012), the static value of permeability can be considered to be a reasonable average between liquefied and non-liquefied states. In the present problem, two different sets of analyses are performed, the first considering the dynamic value of permeability, which is also reported by the Authors, and the second, setting the permeability of the sand equal to k=80*0.0066 = 0.528cm/s, corresponding to the static value of permeability for Nevada sand, as proposed by Arulmoli et al. (1992). The third option of a varying permeability coefficient was excluded, due to the excessively large computed permeability values. Such (prototype scale) values were dramatically decreasing the required numerical time-step set by FLAC3D and increased the computational time, rendering the particular analyses practically unfeasible.

Boundary conditions.- The centrifuge model is reported to have been constructed in a rigid container. Additionally, even though it is quite usual in such containers to apply a soft, flexible dux-seal material at the interior, the Authors do not specify whether such a material was used. The purpose of such a material aims at disengaging the container oscillation from the soil response as well as minimizing wave reflections from the rigid boundaries towards the soil.

Numerically, the simulation of a rigid box was performed by allowing all motion across the x-direction and applying the uniform sinusoidal excitation plotted in **Figure 7.27**, at the base as well as the lateral boundaries of the configuration. Reference test C_0, was initially performed without considering a dux-seal material and the outcome indicated extended motion amplification in the ground surface. Slightly lower levels of excess pore pressures, presenting intense fluctuations throughout shaking were recorded and almost twice footing settlements developed, compared to the centrifuge recordings.

Andrianopoulos (2006), in the numerical simulation of VELACS centrifuge test No12, examined the response of a rigid footing on top of a thin non-plastic silt underlain by liquefiable sand. He particularly examined the effect of boundary conditions –rigid against flexible container and rigid with elastic boundaries - on the particular test results. The consideration of an elastic material, at the boundaries of the configuration, essentially

corresponded to the use of dux-seal material in the centrifuge test. He concluded that there is a distinct but somehow restricted effect of the considered boundary conditions on the numerical results, particularly noticeable in the soil ground surface acceleration timehistories and accumulating seismic settlements. He also suggested that the flexible, laminar box type of boundary conditions, provided the most efficient approach to the numerical simulation of liquefaction related problems.

Following, a numerical analysis was performed, considering a lateral zone of elastic flexible material with significantly low Young's modulus. The obtained results indicated a definite improvement regarding the acceleration time histories and accumulated settlements being in satisfactory comparison with the centrifuge recordings. Nevertheless, the elastic properties and thickness of the potentially used dux-seal material are not known, therefore the particular solution could not be firmly established. To resolve the boundary conditions issue, also based on the previous detailed investigation by Andrianopoulos (2006), tied node boundary conditions were finally selected in all five simulations. The particular type essentially allows the unconfined soil oscillation during the applied excitation and, as stated above has systematically proven to effectively and accurately simulate the actual soil behavior.

7.5.2 Interpretation of numerical results

Reference test C_0.- Typical results in prototype units from the reference test are summarized in **Figure 7.28**. In brief, the results presented below refer to the analysis with the static value of permeability. Both sets of numerical results are evaluated in the subsequent section, against the overall influence of the densification depth, where the effect of permeability became more tangible. The available centrifuge data are plotted with black colour and include **(i)** acceleration time histories at the free-field (a_s), and the footing (a_f), **(ii)** excess pore pressure time histories at selected locations, as well as **(iii)** settlement accumulation at two locations, namely underneath the footing and away from the footing, thus corresponding to free field conditions. The numerically obtained results at the same locations are plotted with gray colour.

Acceleration time histories.- Satisfactory agreement is obtained between the centrifuge recordings and the numerical results, with minor deviations relative to the magnitude of the measured acceleration, as exhibited in **Figure 7.28**. Note in both cases, how the magnitude of the horizontal acceleration in the ground surface (a_s) is drastically reduced already from the 2nd loading cycle, implying the occurrence of extensive liquefaction in the lower parts of

the sand layer, which restrains the propagation of the seismic motion to the upper parts of the configuration. The same phenomenon is also observed underneath the footing (a_f), where the motion cut-off is slighlty delayed and occurs at the end of the 4^{th} cycle, as a consequence of the higher initial vertical effective stresses induced by the footing.

Excess pore pressure built-up.- The numerically derived results, presented in **Figure 7.28**, are in good accordance with the centrifuge recordings, with the exception of perhaps location PC_1, in which the numerical predictions underestimate the developped excess pore pressure. Nevertheless, it should be stressed out that during spinning of the container, and as the soil surrounding the transducer liquefied, it is possible that the pore pressure transducer located at position PC_1 slipped and sunk deeper into the ground, thus measuring pore pressures at a deeper location than the one originally assigned. The particular observation becomes even more crucial when comparing the pore pressures recorded at locations PC_1 and PC_2, which are very similar to each other. Apart from the above inconsistency, it is concluded that excess pore pressures are realistically simulated by the numerical model developed herien.

Settlement accumulation.- Seismic induced settlements under the footing and in the free field are plotted in **Figure 7.28**. Settlements are slightly underestimated up to the first 5sec of loading but the rate of settlement accumulation is accelerated and renders a total settlement of 0.67m by the end of shaking, (at about 9sec), as opposed to the 0.56m measured at the centrifuge test. Overall, it is concluded that the settlement evolution with time is satisfactorily described by the applied numerical methodology.

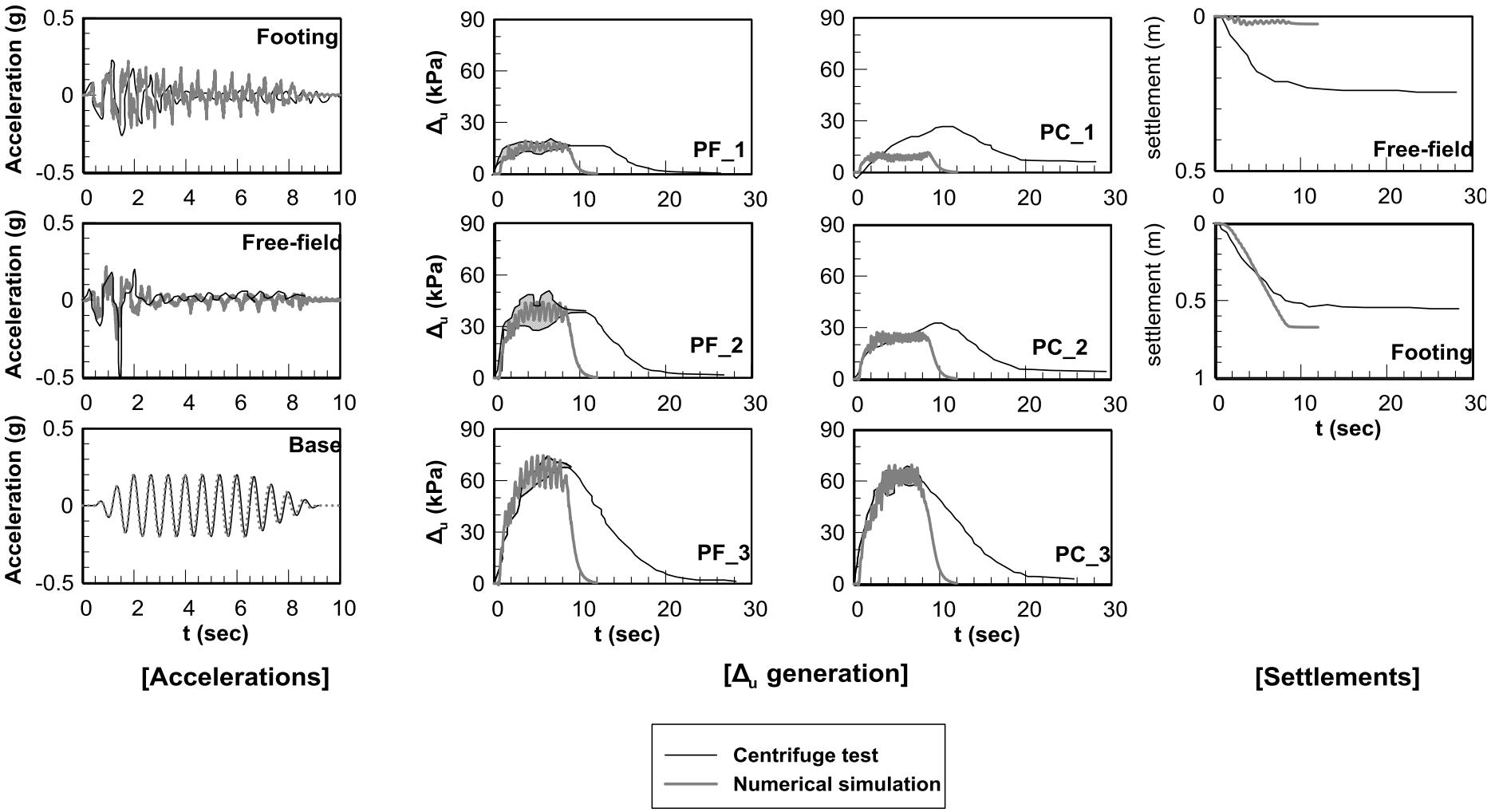

Figure 7.28: Typical results for test C_0.

The ground surface settlement in the free field is numerically computed equal to 0.03m, and in contrast to the centrifugal value of 0.25m is substantially underestimated, as it is also illustrated in the corresponding figure. The particular inconsistency may be explained with reference to the arrangement which is usually employed to monitor the seismic induced settlements in the free-field. **Figure 7.29** illustrates a typical arrangement used in the majority of centrifuge tests. The depicted configuration was used in a series of centrifuge tests performed at the centrifuge facility of the University of Cambridge, UK, by the research team of Prof. Bouckovalas in the context of the TNA project entitled "Experimental Verification of Shallow Foundation Performance under Earthquake-Induced Liquefaction". The arrangement consists of a vertical Linear Voltage Differential Transformer (LVDT) which is connected to a specially-made small footing used to acquire the required data during flight. In the present case, under the centrifugal acceleration of 80g, the prototype weight of the small footing is scaled by a factor of 80 and therefore may become significant. The particular remark, in combination with the triggering of liquefaction already from the 2nd loading cycle, in the underlying sand, may have induced the settlement of 0.25m. Thus, the measured settlement reported in the experiment could be the product of the above mechanism, which of course cannot be numerically predicted.

Figure 7.29: LVDT arrangement, typically used in centrifuge tests (Bouckovalas et al., 2011).

Tests C_0 ÷ C_4.- The evaluation of the obtained numerical predictions against the experimental results, for all five tests, will be performed with regard to:

i. The dynamic settlement of the footing and its correlation to all considered densification depths Z_c.

ii. The excess pore pressure distribution with depth and its variation during the seismic excitation.

iii. The effect of the densification depth to the propagation of the seismic motion towards the soil surface

The accumulated dynamic settlements of the footing and their variation with the improvement depth Z_c is illustated in **Figure 7.30.** The centrifuge data are plotted with the black squares while the numerical predictions with different shades of gray, corresponding to the effect of the dynamic and static value of permeability respectively. The use of the static value of permeability appears to slightly over-estimate the dynamic footing settlements, as opposed to the set of analyses assuming the dynamic permeability coefficient ($k=1.68*10^{-3}$m/s). At an average, both sets of analyses capture the centrifuge results rather well, up to Z_c/B = 1.5, by forming an upper and lower boundary. For Z_c/B greater than about 1.5, both approaches over-estimate the footing settlements. Apart from the above quantitative differentiations, in both cases, the numerical outcome confirms the experimentally observed reducing trend of the footing settlements with increasing depth of densification Z_c.

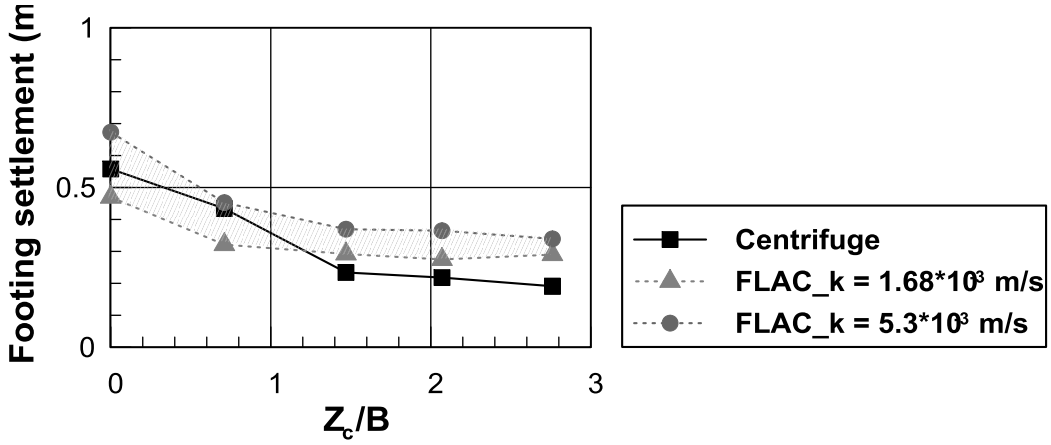

Figure 7.30: Footing settlement $S_{foot.}$ versus densification depth Z_c normalized with the footing width B.

The excess pore pressure distribution with depth and its change with time for both permeability coefficients is presented in **Figure 7.31 - Figure 7.35.** The results are obtained at t=3.5sec and the end of shaking, and two different locations, namely under the footing and away from it. The dashed black lines without symbols correspond to the initial vertical effective stresses as they were calculated in the free field and under the footing as $\sigma'_{vo}=\gamma_b+\Delta\sigma'_v$, where $\Delta\sigma'_v$ the effect of the foundation load estimated using the elastic theory.

As a general interpretation of the obtained response, it is stated that under free field conditions, the numerical analyses verify the propagation of the liquefaction front from the shallower towards the deeper loactions extending to depths ranging from 6 to 8meters. Under the footing, liquefaction is also systematically prevented since the developping excess pore pressures are substantially lower than the effective vertical stresses.

Focusing on the use of the dynamic coefficient of permeability, ($k=1.68*10^{-3}$m/s) higher excess pore pressures than the experimentally reported, are numerically predicted principally in the deeper locations of the configuration, as a result of the limited drainage capacity at the specific depths. Moreover, the influence of the permeability coefficient becomes even more obvious for increasing thickness of the performed densification (Z_c) as observed in the case of test C_4. The related excess pore pressures clearly indicate the triggering of liquefaction throughout the improved depth already from the early stages of loading.

The consideration of the static value of permeability ($k=5.3*10^{-3}$m/s) in the numerical analyses, significantly improves the previous numerical predictions in both considered time instants. Especially at the deeper locations, excess pore pressures are reduced and the liquefaction front does not propagate as deep as previously, thus rendering a very reasonable agreement to the centriguge data as well. Especially in the case of test C_4, there is still an obvious divergence nevertheless the distribution of excess pore pressures with depth indicates the successful mitigation of liquefaction in the improved area of the sand layer.

The effect of the depth of improvement Z_c normalized against the footing width B, on the propagation of the seismic motion to the ground surface, expressed as the footing/base acceleration is summarized in **Figure 7.36**. Again the results from both sets of analyses are plotted and compared against the reported centrifuge data, preserving the same line and symbol layout as above.

Notice that the use of the dynamic coefficient of permeability systematically leads to lower amplification ratios, compared to the centrifuge results. It is of particular interest that for the maximum considered ratio $Z_c/B=2.76$ the numerically computed amplification ratio separates from the previously established trend and drops. The particular behavior, is explained on the basis of the high developing excess pore pressures along the soil column underneath the footing, provided previously. Namely, as a result of the insufficient drainage capacity the high excess pore poressures drastically reduce the sand's shear strength and the related shear wave velocity, impeding the propagation of the seismic motion to the top.

The successful liquefaction mitigation illustrated in the previous figures, for the static value of permeability ($k=5.3*10^{-3}$m/s), provides the necessary justification to the improved amplification ratio predictions, plotted in **Figure 7.36**. Indeed the increase of the coefficient of permeability by about 5.28/1.68 = 3 times considerably improves the observed motion transmission to the top, as a result of the generation of lower excess pore pressures with depth.

In the last two tests (C_3 & C_4) still a noticeable deviation is observed, which may attributed to resonance effects, as subsequently explained. Focusing on test C_4, a soil column of thickness H=12.5m, relative density Dr=89% and average mean effective pressure p=40kPa, is estimated to roughly have a shear wave velocity equal to 200m/sec, this being calculated to an elastic period T, equal to T=4*H/Vs = 0.25sec and $T_{soil}/T_{exc.}=0.25/0.67=0.37$. Based on a conservative estimate, as a result of the performed densification, the average excess pore pressure over depth, during shaking, under free field conditions, is not expected to rise above $r_{u,avg}=0.80$, which is going to reduce the soil's shear wave velocity to $Vs_{liq}=\sqrt[4]{1-r_u}*Vs_{,o}$= 130m/sec. In that case, the period of the soil column is going to climb up to T=0.40sec, therefore $T_{soil}/T_{exc.}=0.40/0.67=0.60$. The increase in the $T_{soil}/T_{exc.}$ ratio implies that the soil column moves closer to resonance ($T_{soil}/T_{exc.}=1$) and higher amplification ratio values are obtained.

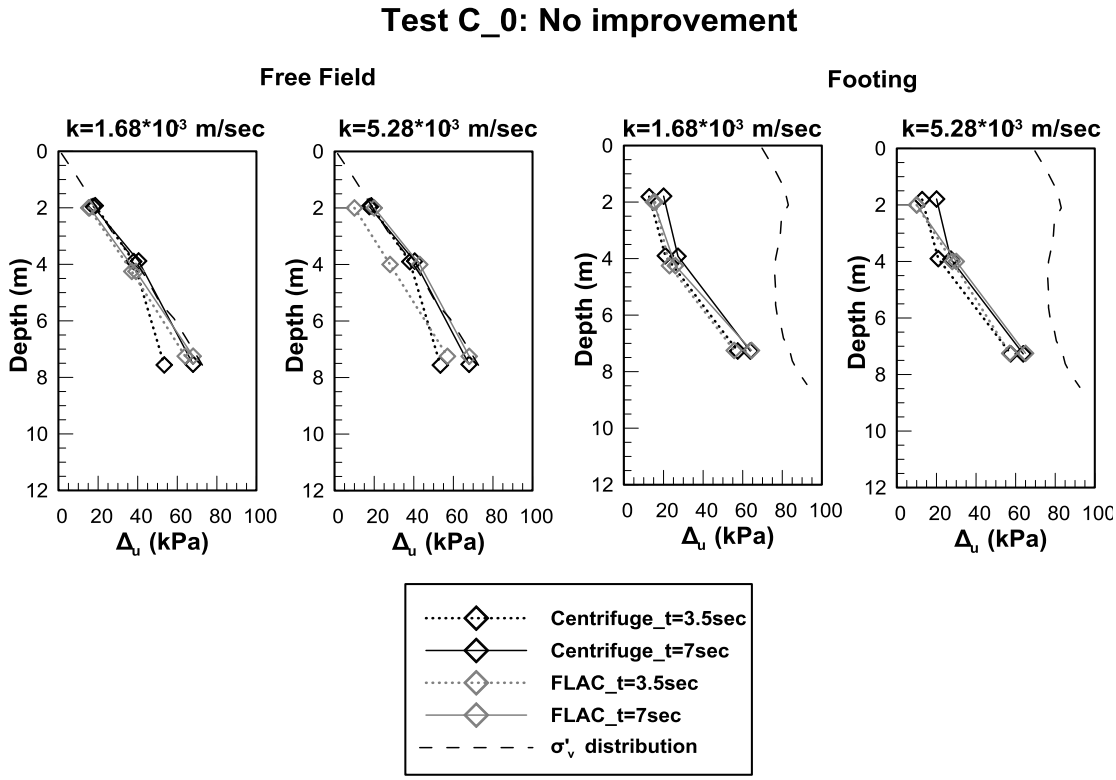

Figure 7.31: Excess pore pressures distribution with depth for test C_0.

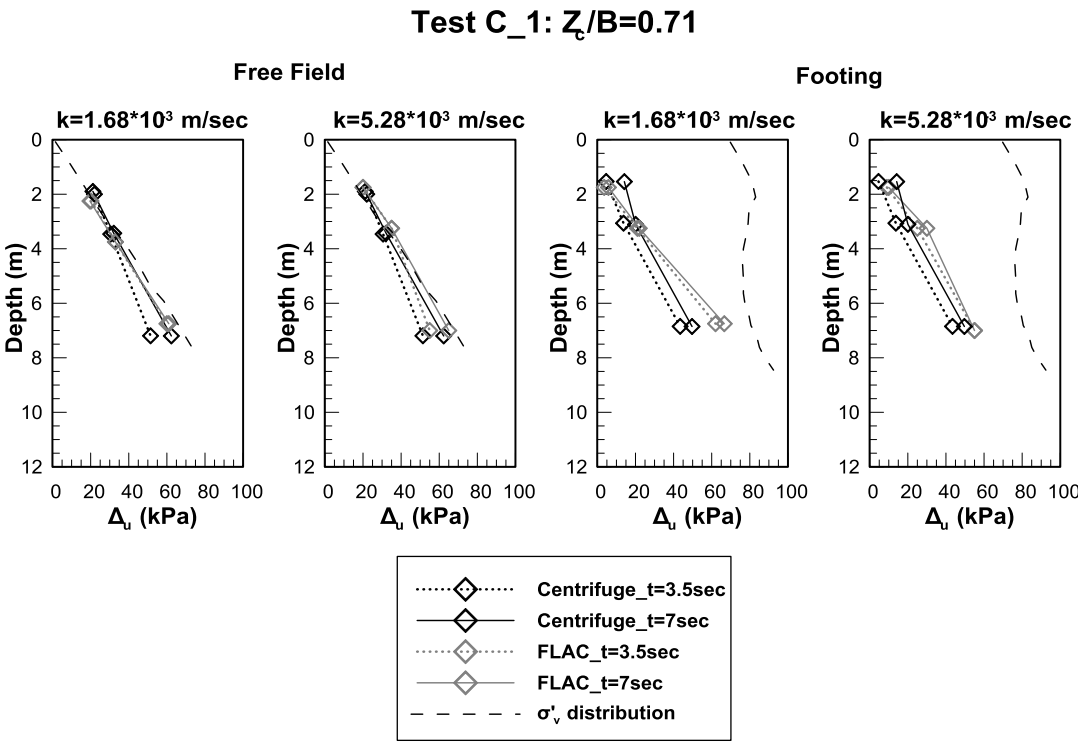

Figure 7.32: Excess pore pressures distribution with depth for tests C_1.

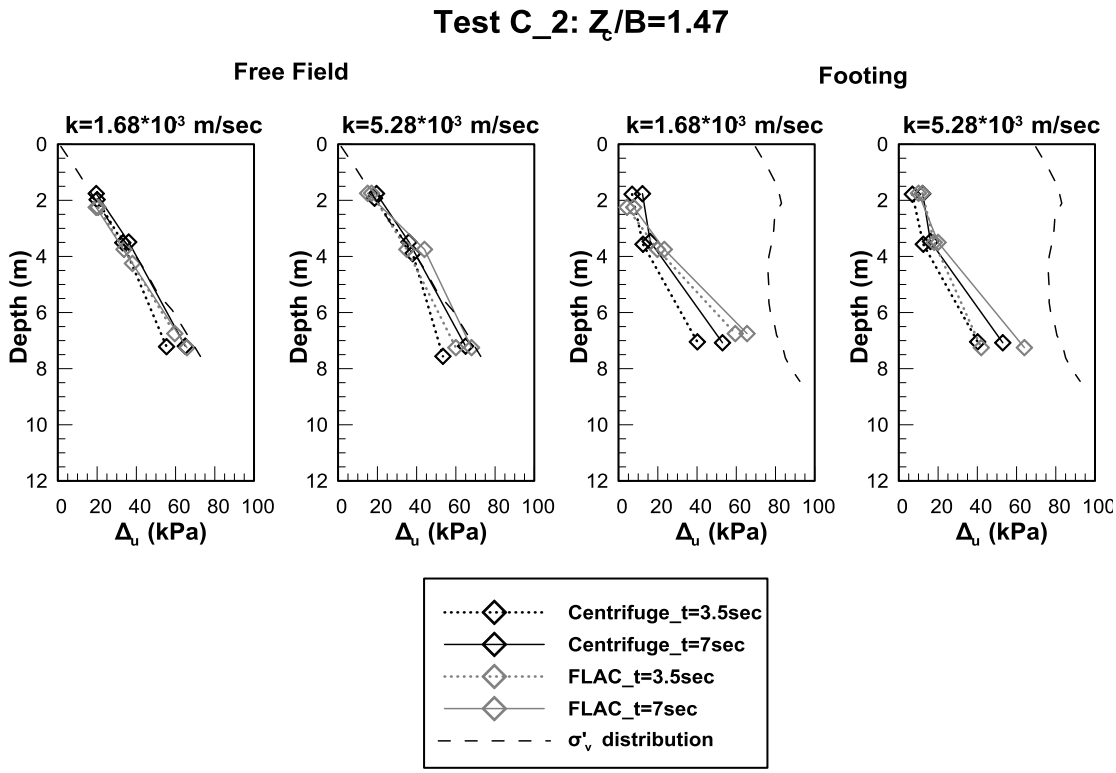

Figure 7.33: Excess pore pressures distribution with depth for test C_2.

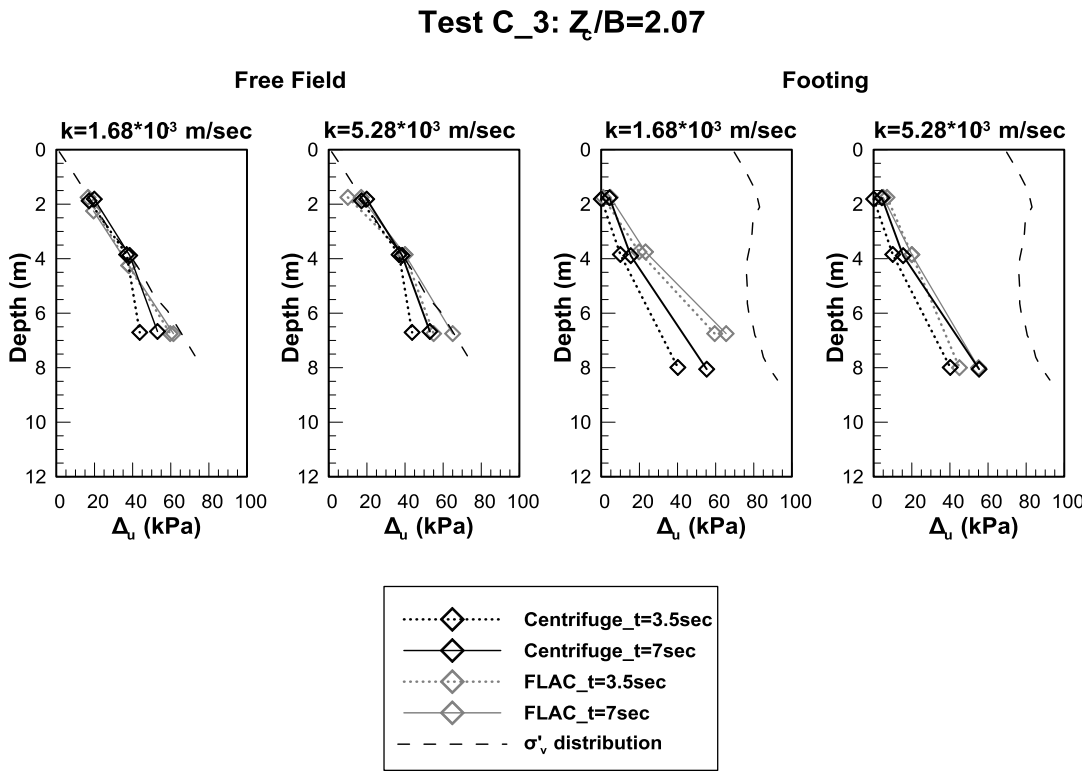

Figure 7.34: Excess pore pressures distribution with depth for test C_3.

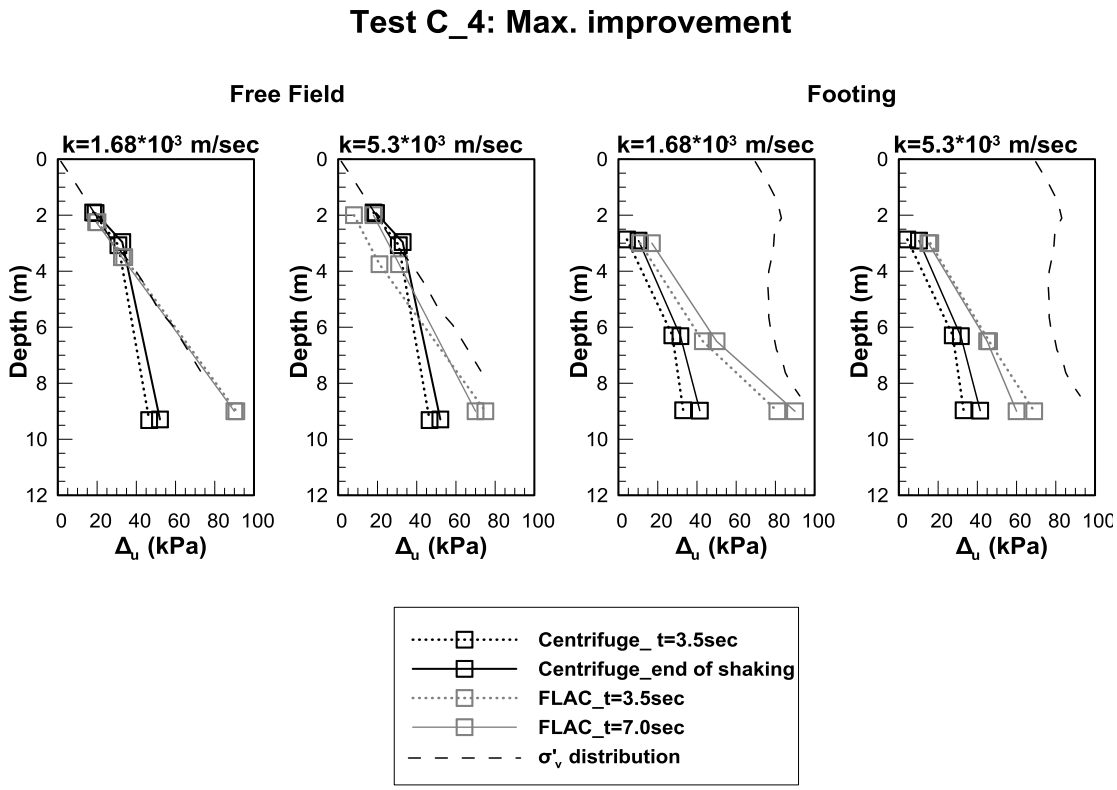

Figure 7.35: Excess pore pressures distribution with depth for test C_4.

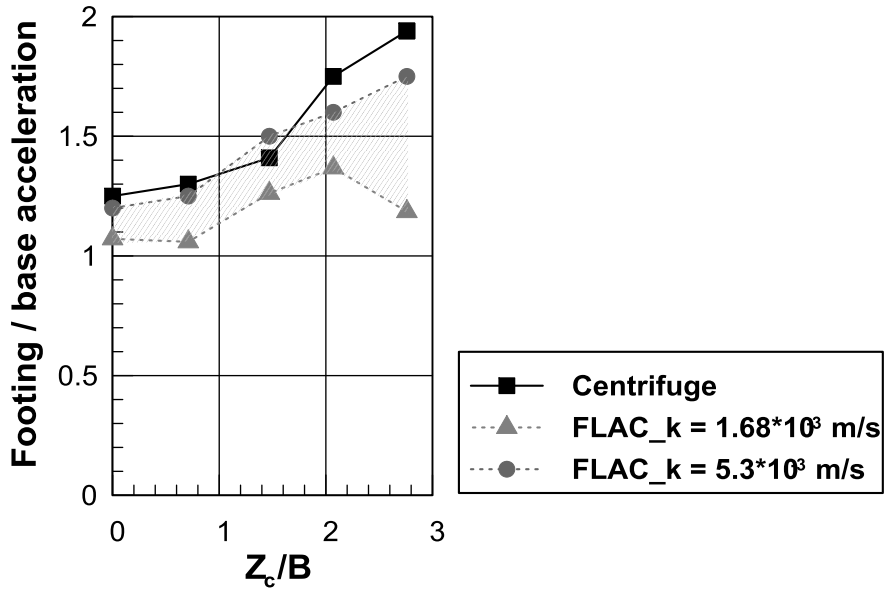

Figure 7.36: Footing/base acceleration versus Z_c/B for all five centrifuge test.

CHAPTER 8

Parametric Analyses of Footing Response

8.1 Introduction

The simplified concept of "*Equivalent Uniform Improved Ground*", thoroughly described in the previous chapter, essentially led to a 2-layer configuration with the following basic characteristics:

a. A liquefiable sand layer of given uniform density and relatively large thickness, covered by a non-liquefiable surface layer, of the same origin as the liquefiable one but with larger relative density (due to the vibrocompaction) and larger overall permeability due to the presence of the gravel drains.

b. Following the current design practice, the average over-depth excess pore pressure ratios in the top layer should not exceed a safe value, well below 1 (e.g. $\overline{r}_{u,\,max} = 0.3 \div 0.5$)

In relation to the above objectives, it is first necessary to specify a methodology to predict beforehand the developing excess pore pressures in the improved crust. For that purpose, a number of 1-D numerical analyses is performed, simulating the free-field response of the improved ground. The ultimate intention is to identify the replacement ratio α_s which is required in order to restrain excess pore pressure development in the improved ground within the target range of $\overline{r}_{u,\,max} = 0.30 - 0.50$.

Following, a number of 2D parametric analyses is performed in order to examine the seismic response of a shallow footing on the above specified soil profile. Additionally, a separate set of analyses is performed to examine the effect of the lateral extent of improvement on the

seismic response of the shallow footing. The basic problem parameters are identified and a detailed description of the plan of the parametric investigation is provided in the corresponding sections.

8.2 Free field numerical analyses.

To evaluate the appropriate replacement ratio α_s required to restrain the average excess pore pressure ratios within the desired range, of $\overline{r}_{u,\,max}$ = 0.30 – 0.5, a series of 1-D free-field numerical analyses is performed. The particular numerical investigation is performed for a wide range of initial relative densities (i.e. $D_{r,o}$=35, 40, 45, 55, 60, 65 & 70%) and related permeability coefficients.

The grid configuration initially consisted of a 28m wide and 20m thick uniform liquefiable sand layer, as illustrated in **Figure 8.1**. Overall, 24×20=480 zones were generated, with dimensions varying from 1.0×1.0m around the axis of symmetry to 1.5×1.0m, at the boundaries of the configuration. With the initial relative density being the controlling parameter, three different depths of improvement were considered in each case, i.e. 4, 6 and 8m, as well as four different replacement ratios – α_s = 0.05, 0.10, 0.15 and 0.20. In total, 72 numerical analyses were performed.

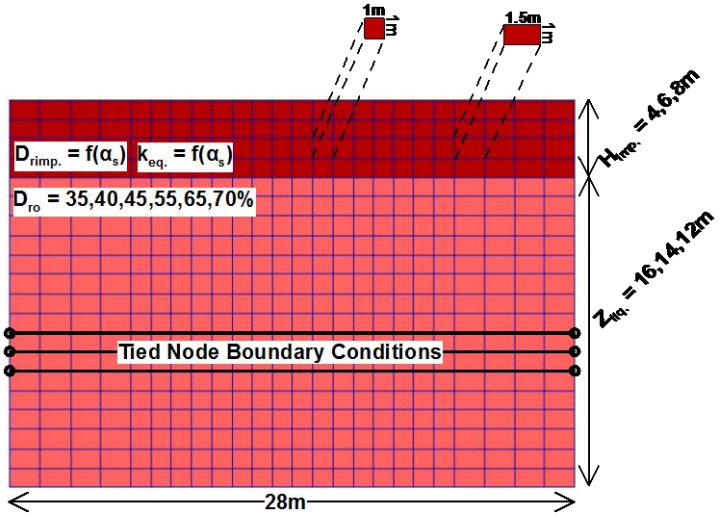

Figure 8.1: Grid configuration used in the 2-dimensional free-field numerical analyses.

The associated assuptions of the 1-D numerical analyses regarding the applied excitation, type of damping, imposed boundary conditions, constitutive model, and water level are the same as in the reference case of a surface footing on top of the 2-layered profile and will not

be repeated herein. Hence, the rest of this section is devoted to the investigation concerning the lateral dimensions of the grid configuration.

Lateral dimensions.- The tied-node boundary conditions during dynamic loading combined with the high permeability coefficient used for the improved crust, were found to generate significant boundary effects, concerning the excess pore pressure ratio distribution within the improved crust and the associated flow during shaking. The particular effect became more intense in the case of increased improvement thickness. For instance, **Figure 8.2** illustrates the excess pore pressure ratio distribution and flow vectors at the end of the 4th cycle for the case of a soil layer with initial relative density of $D_{r,o}$=65%, improved at the maximum considered depth and with the highest replacement ratio, i.e. $H_{imp.}$=8m & α_s=0.20. Excess pore pressure ratio distribution appears highly non-uniform and flow vectors indicate pretty much irregular flow taking place across the improved crust.

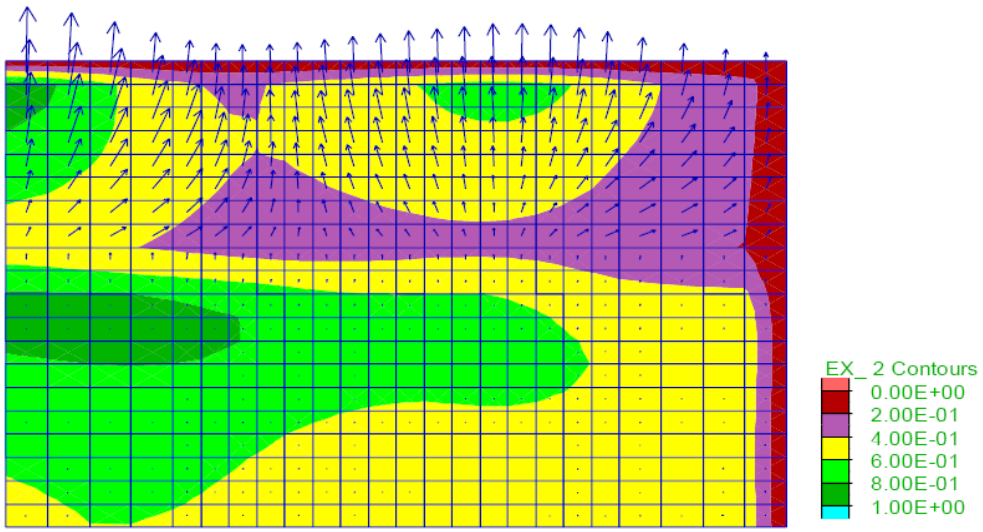

Figure 8.2: Non-uniform excess pore pressure ratio distribution and associated flow vectors at the end of the 4th loading cycle for $Dr_{,o}$=65%, H_{imp}=8m, α_s=0.20.

To achieve a uniform field of excess pore pressure ratios and pure vertical flow towards the surface, a parametric investigation is performed by laterally extending the boundaries of the grid from 28m, to 60m and subsequently to 84 meters. The outcome of the above analyses is summarized in **Figure 8.3**, presenting r_u time histories derived inside the crust and the axis of symmetry, for the three different cases. Moreover, snapshots of excess pore pressure ratio contours and flow vectors at the end of the 4th loading cycle are presented in **Figure 8.4**. It is observed that increasing the lateral dimension of the grid diminishes and confines the

irregularity in the r_u distribution around the edges of the configuration, thus leaving the central area unaffected. Moreover, vertical flow is evident around the axis of symmetry, with localized fluctuations at the boundaries. As a result, to ensure a uniform excess pore pressure field development and pure vertical flow, across the improved crust, the wider grid configuration of 84 meters is selected to perform the following 1-D free-field numerical investigation.

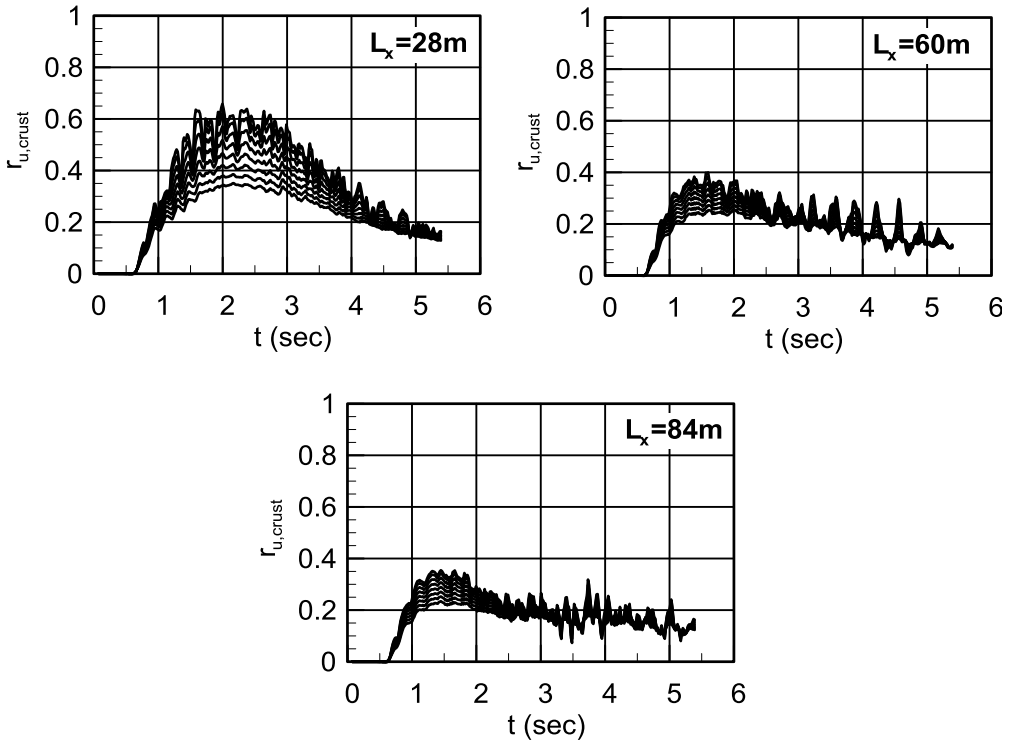

Figure 8.3: Parametric investigation of lateral grid dimensions - epp ratio timehistories inside the crust.

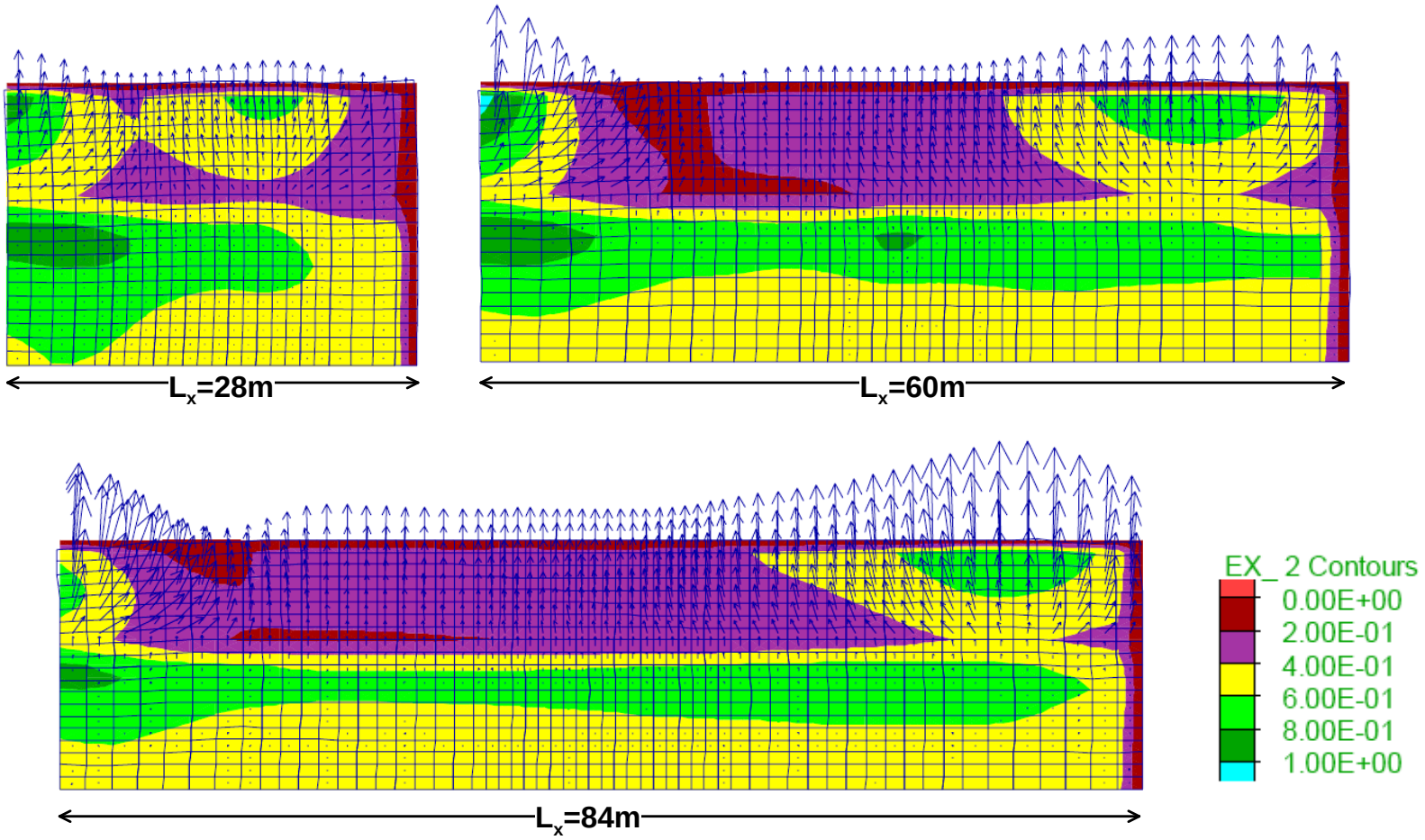

Figure 8.4: Parametric investigation of lateral grid dimensions- epp ratio contours at the end of the 4th loading cycle.

8.3 Evaluation of 1-D numerical predictions.

Due to the large number of parametric analyses, three typical cases are selected and presented below, reflecting the response of a loose (Dr_o=40%), medium dense (Dr_o=55%) and dense (Dr_o=70%), but still liquefiable, sand under seismic loading. In all three examples different replacement ratio (α_s) values are selected, achieving to restrain the average in-crust excess pore pressure ratio to acceptable levels, i.e $\overline{r}_{u,\,max} = 0.3 \div 0.4$. The above analyses will be assessed, in terms of:

1. the excess pore pressure ratio (r_u) distribution with depth at the axis of symmetry. The particular distributions are plotted for two different time moments **(i)** the time of the maximum r_u occurrence within the improved crust and **(ii)** the end of shaking.
2. the excess pore pressure ratio time histories at different depths of the grid, namely 3m, 7m, 12m and 16m and
3. the excess pore pressure ratio time histories within the improved crust.

Predictions for Dr_o=40%.- Figure 8.5a,b & **c**, summarize the outcome for the case of initial relative density of 40% and improvement depth 4m. From the distribution of excess pore pressure ratios with depth, (**Figure 8.5a**) it is obvious that the underlying sand develops much higher r_u values, which gradually increase from the interface of the two layers down to the bottom of the configuration. By the end of the imposed shaking, liquefaction is evident and extends practically to an area starting 2-3 meters below the interface of the two layers, up to the bottom of the configuration. As a result, the thickness of the performed improvement ($H_{imp.}$) decisively controls the extent of the liquefied area underneath, by delaying or even preventing the occurrence of liquefaction. This indirect advantage is translated to extra shear strength, contributing to the shear strength provided by the overlying denser crust and is going to be appropriately taken into consideration in the development of the analytical methodology in subsequent chapters.

Figure 8.5b summarizes r_u time histories derived from selected depths of the configuration. It is of particular interest that the r_u time history derived at 7 meters clearly indicates liquefaction already from the 3rd loading cycle. However, there is a very limited drainage effect present, which prevails over the rate of r_u built up at the later stages of loading and causes a slight lowering of the r_u values. The specific effect indicates the beneficial action of the top improved crust which restrains excess pore pressures beyond the improvement limits, as it is also illustrated in the following cases.

Moreover, excess pore pressure ratio values within the improved crust, illustrated in **Figure 8.5c**, are confined within the pre-defined desirable range of $\bar{r}_{u,max} = 0.3 \div 0.4$. To achieve this, the performed mitigation against liquefaction is materialised for a replacement ratio equal to α_s=0.10. The slightly increased r_u values which are recorded at the shallower zones of the grid configuration are attributed to the vertical drainage occuring from the deeper parts of the crust towards the surface, thus increasing the excess pore pressure (Δu) at the specific depths.

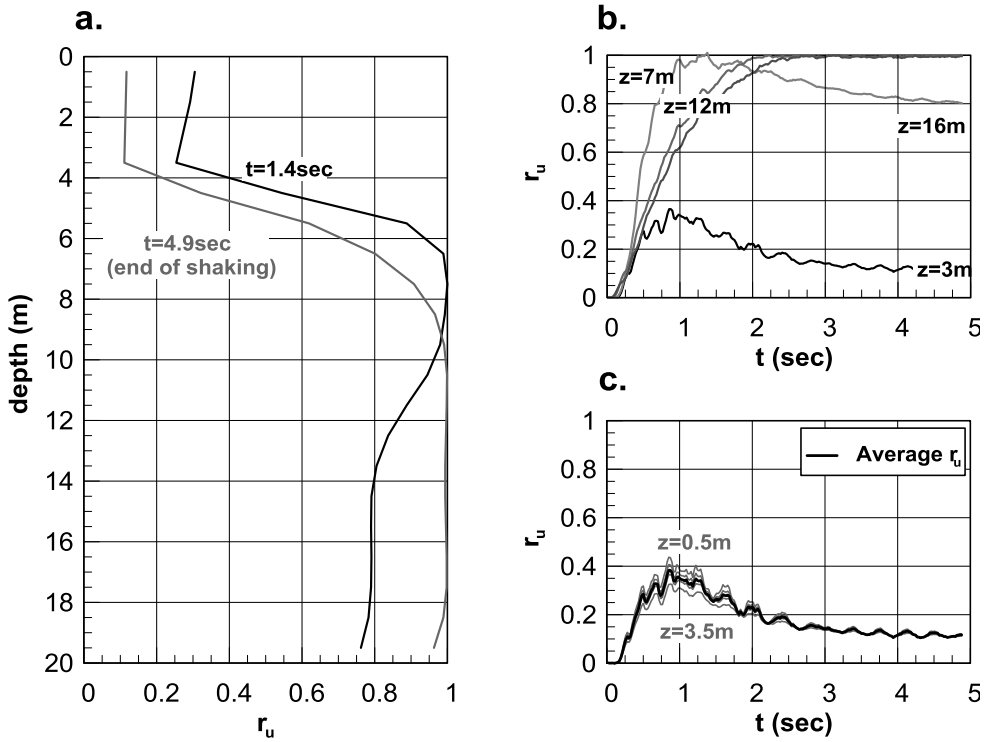

Figure 8.5: Typical results for Dr_o=40%, improvement depth H_{imp}=4m and α_s=0.10 **a.** r_u distribution with depth at t=1.4 and t=4.9sec, **b.** r_u time histories at selected depths of the configuration and **c.** r_u time histories within the improved crust-gray lines and derived average-thick black line.

Predictions for Dr_o=55%.- Figure 8.6a,b & **c**, summarize the outcome for the case of initial relative density of 55% and improvement depth equal to 8m. The r_u distribution with depth (**Figure 8.6a**) attains an average value of r_u=0.35, at the mid-depth of the improvement, which fluctuates from 0.27 at the deepest locations to 0.40 at the shallow parts of the improved layer, at the end of the 3rd cycle of the excitation. **Figure 8.6b** summarizes excess pore pressure time histories at selected depths of the configuration. In this example the improved crust extends up to 8meters, therefore the corresponding time history derived at

7meters indicates a successful liquefaction mitigation. Moreover, excess pore pressure ratio values within the improved crust, illustrated in **Figure 8.6c**, are confined within the pre-defined desirable range of $\overline{r}_{u,\,max} = 0.3 \div 0.4$. To achieve this, the performed mitigation against liquefaction was materialised for a replacement ratio equal to α_s=0.15. The slightly increased r_u values which are recorded at the shallower zones of the grid configuration are attributed to the vertical drainage occuring from the deeper parts of the crust towards the surface, thus increasing the excess pore pressure (Δ_u) at the specific depths.

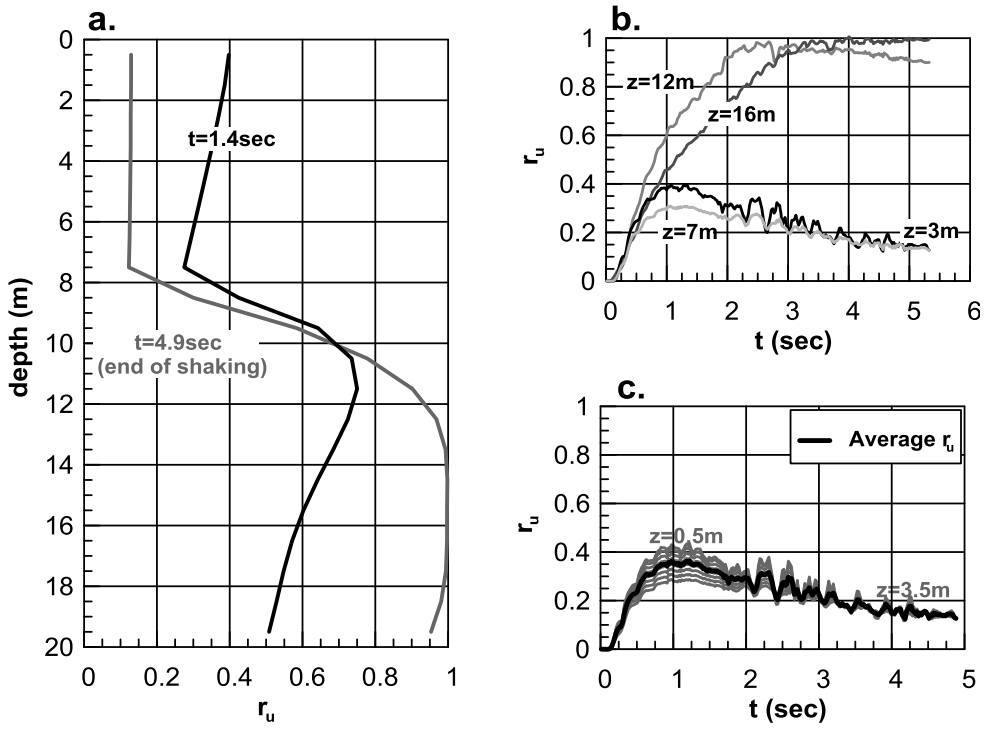

Figure 8.6: Typical results for Dr_o=55%, improvement depth H_{imp}=8m and α_s=0.15 **a.** r_u distribution with depth at t=1.4 and t=4.9sec, **b.** r_u time histories at selected depths of the configuration and **c.** r_u time histories within the improved crust-gray lines and derived average-thick black line.

Predictions for Dr_o=65%.- The particular example refers to the remediation of a 65% initial relative density sand layer by improving the top 6 meters. **Figure 8.7a,b** & **c,** indicate that the desired response is obtained for a replacement ratio equal to α_s=0.20. Maximum excess pore pressures attain roughly $r_{u,max}$=0.25, especially in the shallower parts of the improved crust, while, at an average, maximum excess pore pressure values reach approximately $\overline{r}_{u,max} = 0.23$. **Figure 8.7b**, proves the beneficiary effect of the improvement which affects

the excess pore pressure built up beyond its actual thickness. Proof of this is the r_u time history derived at a depth of 7 meters which remains well below liquefaction triggering.

Overview of reults.- To fully visualize the replacement ratio value (α_s) required to achieve an acceptable level of excess pore pressure built-up, for all the examined combinations of initial relative density (D_{ro}-%) and depth of improvement ($H_{imp.}$) a set of figures, which summarize the excess pore pressure ratio time histories within the improved crust for all the executed numerical analyses is generated. For each case of initial relative density Dr_o (%), and all four examined replacement ratio (α_s) values, namely α_s=0.05, 0.10, 0.15 and 0.20, excess pore pressure ratio time histories, are derived at increments of 0.5m starting from the ground surface and proceeding to the bottom of the improved crust. To avoid interrupting the flow of the analysis at hand, the particular time histories are plotted in **Figures C-1** to **C-18** of **Appendix C**.

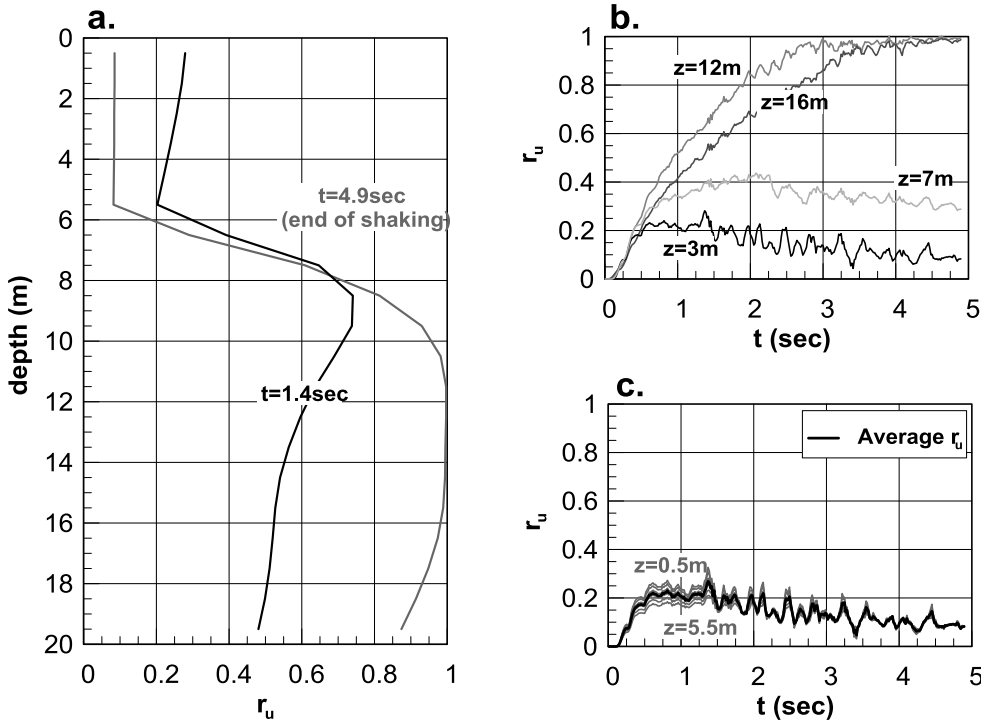

Figure 8.7: Typical results for Dr_o=65%, improvement depth $H_{imp.}$=6m and α_s=0.20 **a.** r_u distribution with depth at t=1.4 and t=4.9sec, **b.** r_u time histories at selected depths of the configuration and **c.** r_u time histories within the improved crust-gray lines and derived average-thick black line.

Set of Proposed Design Charts.- The average maximum excess pore pressure ratio within the improved crust is plotted with regard to the corresponding replacement ratio α_s in an attempt to provide an easy-to-use design chart. The outcome is exhibited in **Figure 8.8**, for all six different initial relative density scenarios and three depths of improvement. The particular figure essentially illustrates the effectiveness of every examined combination of initial properties of the sand layer and considered improvement depth.

Following, **Figure 8.9** summarizes the replacement ratio α_s required for every initial relative density value D_{ro} (%) and three distinct average $\overline{r}_{u,\max}$ values expected to develop within the improved crust, namely 0.30, 0.40 & 0.50. Additionally, depending on the replacement ratio α_s obtained from the above figure, the properties of the improved crust, i.e. relative density $D_{r,imp}$ (%) and equivalent coefficient of permeability $k_{eq.}$ (m/sec) may be easily obtained through **Figure 8.10a** & **b**. More specifically, **Figure 8.10a** correlates replacement ratio α_s to the relative density of the improved crust through seven different curves, each one for an initial relative density $D_{r,o}$ (%). **Figure 8.10b**, associates the replacement ratio α_s to the equivalent coefficient of permeability $k_{eq.}$ (m/sec) as a function of the permeability of the natural sand layer.

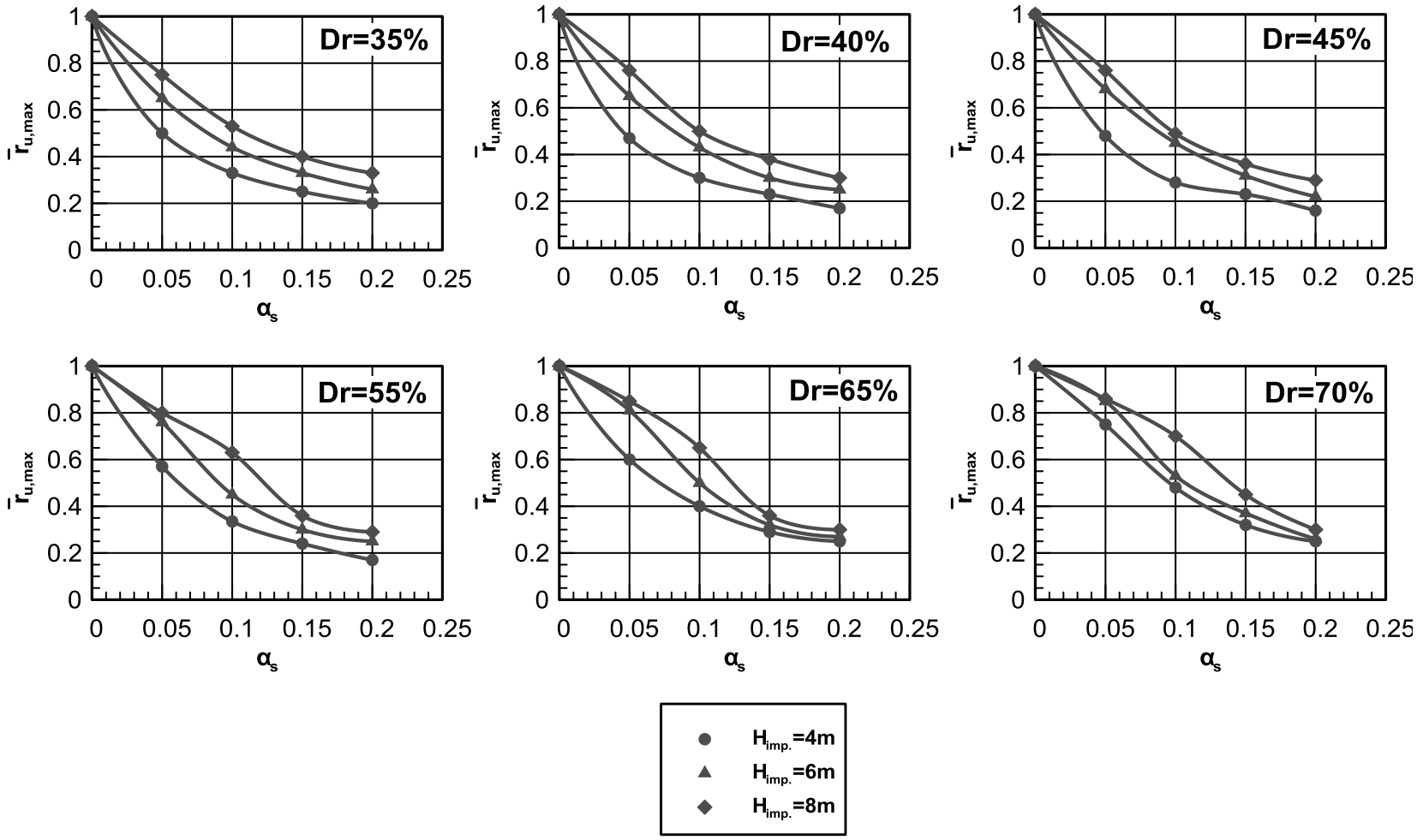

Figure 8.8: Average r_u within the improved crust as a function of replacement ratio α_s, for all examined scenarios of initial relative density and improvement thicknesses.

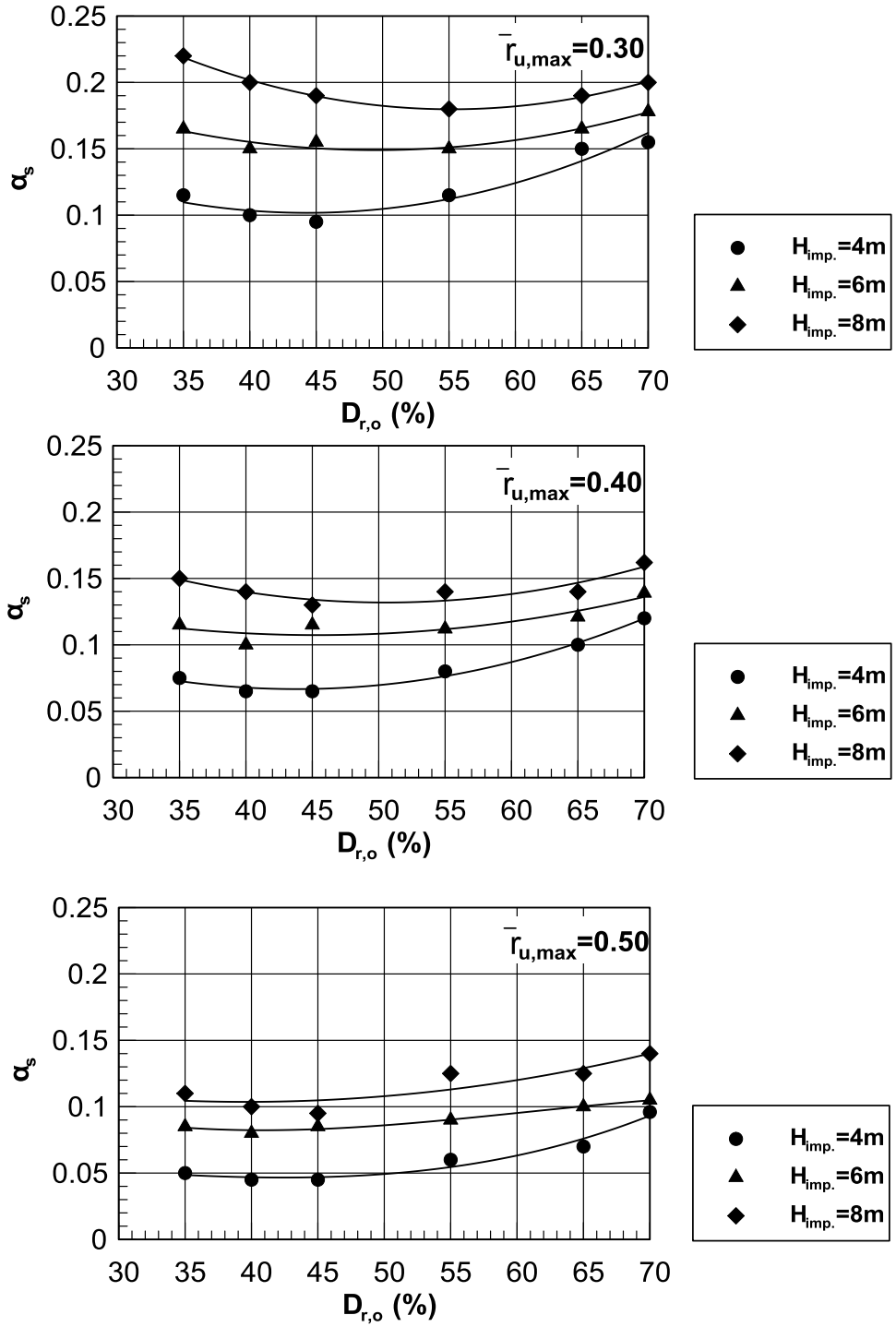

Figure 8.9: Required replacement ratio α_s with regard to initial relative density $Dr_{,o}$(%) and three allowable levels of $r_{u,max}$.

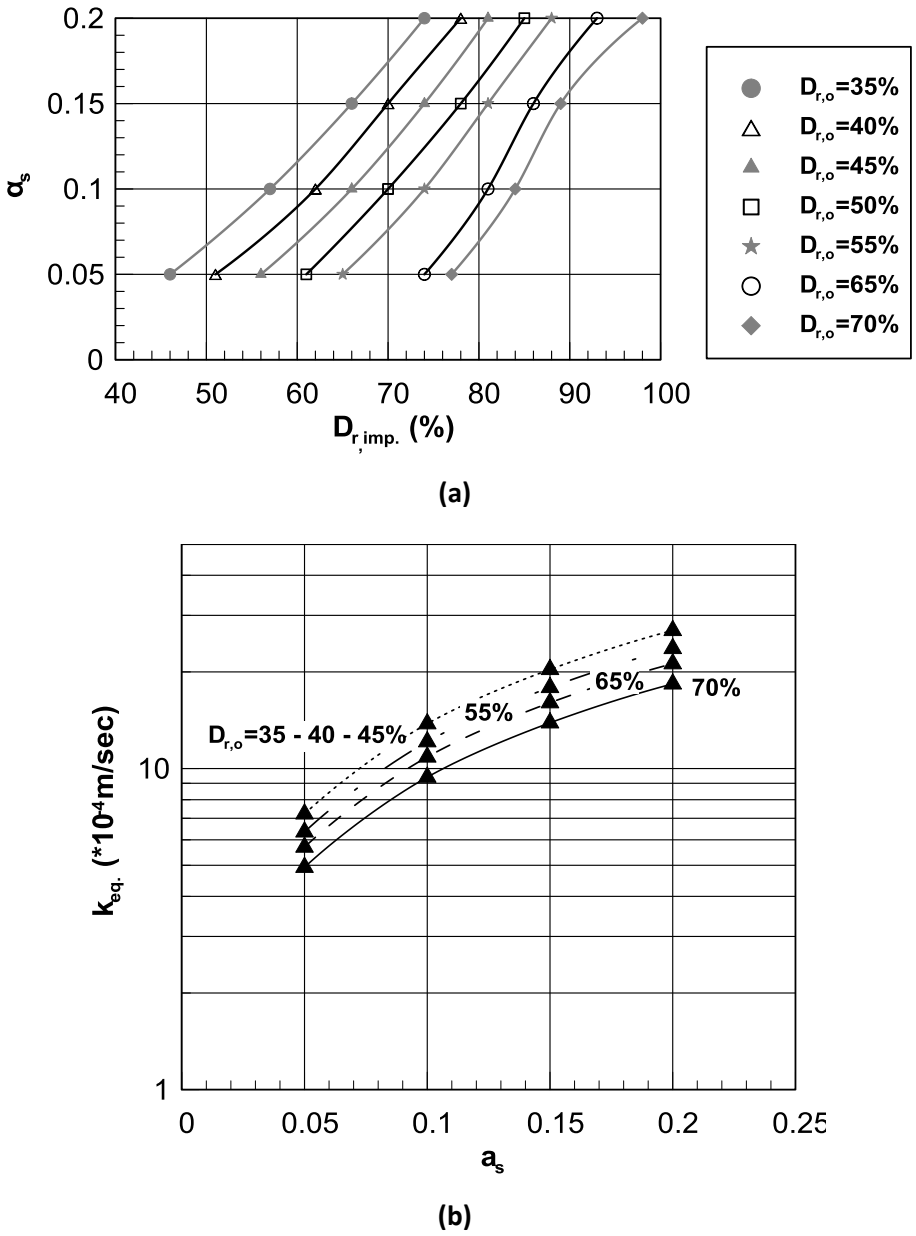

Figure 8.10: Assessment of the improved properties **(a)** relative density $Dr_{,imp}$(%) and **(b)** permeability $k_{eq.}$(m/sec), as a function of replacement ratio α_s.

8.4 Parameter identification

Following the numerical methodology developed in Chpater 7, the liquefaction performance of a strip foundation is parametrically investigated focusing on two main objectives:

- the seismically induced footing settlements ρ_{dyn} (m)
- the degraded post-shaking bearing capacity of the footing $q_{ult.}$ (kPa)

The performed numerical analyses are classified in two categories, based on the lateral extent of the performed improvement, namely “infinite” and “finite” width of improvement as it is further explained in the subsequent sections.

8.4.1 “Infinitely” extending improvement

To simplify the problem at hand, it is initially assumed that the improved zone extends up to the limits of the considered grid. Hence, the liquefaction response of the footing is initially examined under conditions of “infinite” improvement. Within the above contect, the sliding-block mechanism identified in the dynamic settlement accumulation mechanism in the previous chapter, also recognized by Karamitros (2010) and subsequently Karamitros et al. (2013), allows the recognition of two groups of basic problem parameters:

Loading and strength parameters.- They are associated to the activated failure mechanism and include: **(i)** the average foundation bearing pressure q, **(ii)** characteristics of the drain-improved crust, namely the normalized thickness H_{imp}/B, the friction angle $\phi_{improved}$, as well as **(iii)** properties of the liquefiable sand layer, including the normalized thickness Z_{liq}/B and the relative density $D_{r,o}$.

Excitation characteristics.- These parameters control the amount of accumulated settlement, and include: the peak bedrock acceleration α_{max}, the peak bedrock velocity v_{max} and the number of significant loading cycles N. The peak bedrock velocity v_{max} may be alternatively incorporated in the parametric investigation through the predominant excitation period T.

Note that the shear strength of the crust is expressed through the improved relative density $D_{r,imp.}$, which is directly linked to the initial relative density of the underlying liquefiable sand, through the replacement ratio α_s. Additionally, the improved crust allows the dissipation of excess pore pressures and consequently the formation of a flow front propagating upwards from the deepest to the shallower locations. The permeability of the crust is practically related to the permeability of the original sand layer again through the selected replacement ratio α_s, as described in Chapter 7. Also, as suggested by the design charts provided in **Figure 8.9,** replacement ratio α_s, is directly controlled by the maximum excess pore pressure ratio $r_{u,max}$ expected to develop under free field conditions within the improved crust. Hence, it is concluded that the key-parameter controlling the properties assigned in the improved crust is the maximum anticipated excess pore pressure ratio $r_{u,max}$, which is set equal to 0.4 for the majority of the numerical analyses.

The parametric analyses plan is summarized in **Table 8.1** and consists of 82 analyses. The range of each parameter included in the parametric investigation is summarized below. Note that the effect of each parameter was examined separately, with the other parameters being given the reference values provided in the parentheses:

- Average contact pressure applied by the foundation q=52, 60, 70, 75, 80, 90, 100, 110kPa (52, 100kPa)
- Relative density of the liquefiable sand layer $D_{r,o}$=35, 45, 55, 65% (45%)
- Thickness of the liquefiable layer $Z_{liq.}$=6, 8, 10, 12, 14, 16m (16m)
- Depth of the performed improvement $H_{imp.}$=4, 5, 6, 7 & 8m (4m)
- Width of the foundation B=3, 5, 7, 9m (5m)
- Peak input acceleration, applied at the base of the liquefiable layer α_{max}=0.10, 0.15, 0.20, 0.25, 0.30, 0.35g (0.15g)
- Number of cycles of the sinusoidal motion N=5, 10, 12, 15 (10)
- Excitation period T=0.15, 0.20, 0.25, 0.35, 0.50sec (0.35sec)
- Maximum excess pore pressure ratio inside the crust $r_{u,max}$=0.15, 0.20, 0.30, 0.40 (0.40).

To isolate the influence of the improved relative density from the concurrent change in the permeability, a separate set of analyses is performed. Namely, the improved crust is assigned the appropriate relative density resulting from the design charts but different values for the permeability the natural sand are applied. Also, the effect of the relative density of the liquefiable sand was separately examined, by preserving the properties ($D_{r,imp.}$ & $k_{eq.}$) of the crust and altering only $D_{r,o}$ (%). Moreover, the ultimate bearing capacity for crust thicknesses $H_{imp.}$=6 & 8m is investigated, by increasing the initial contact pressure q up to immediate post-shaking failure.

The first set of parametric analyses is performed for an average contact pressure equal to q=100kPa and the parameter combination summarized in case No7 of **Table 8.1.** Nevertheless, it turns out that the specific arrangement is located in a meta-stable area, with regard to parameter Z_{liq}/B, as illustrated in **Figure 8.11**. In other words, for $Z_{liq.}$/B=3.2 (Z_{liq} = 16m) the degraded factor of safety is well above unity, but for lower $Z_{liq.}$/B values the footing has experienced post-shaking failure. For that reason, a second set of analyses is performed, with a considerably reduced average contact pressure, equal to q=52kPa, ensuring that the particular arrangement is far from post-shaking failure.

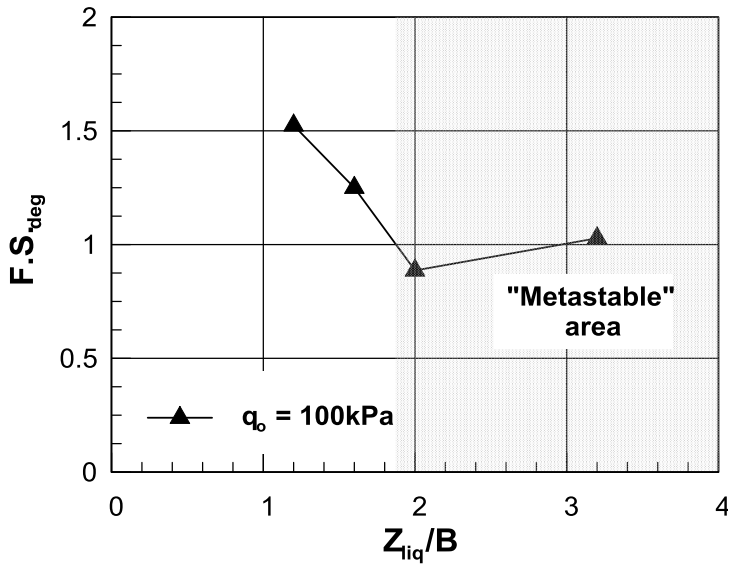

Figure 8.11: Variation of the degraded bearing capacity $F.S._{deg}$ versus Z_{liq}/B for constant footing presure q = 100kPa and footing width B = 5m.

The discovery of a meta-stable area in the post-shaking response of the shallow footing is particularly interesting. It is possible that the thickness of the liquefiable layer, which determines the depth of liquefaction occurrence, plays a key role in the particular phenomenon. The meta-stable area is also observed, when incrementally increasing the footing pressure, q (kPa), independently of the thickness of the improved crust and the other parameters of the configuration. Namely, the increase of the applied pressure did not provide a continuously reducing degraded factor of safety, but rather its fluctuation around unity. The particular observation may be attributed to secondary dilation phenomena in the vicinity of the footing, which locally increase the shear strength of the improved crust. The observed meta-stable cases are excluded from the statistical processing regarding the degraded bearing capacity of the footing.

Table 8.1: Summary of parametric analyses plan.

No	Analysis Name	q (kPa)	$D_{r,o}$ (%)	$Z_{liq.}$ (m)	$r_{u,max}$	$H_{imp.}$ (m)	B (m)	a_{max}(g)	T	N	$k_{eq.}$ ($*10^{-4}$m/s)	$D_{r,imp}$ (%)	$L_{imp.}$ (m)
1	q=52kPa	**52**	45	16	0.4	4	5	0.15	0.35	10	$f(\alpha_s)$	$f(\alpha_s)$	inf.
2	q=60kPa	**60**	45	16	0.4	4	5	0.15	0.35	10	$f(\alpha_s)$	$f(\alpha_s)$	inf.
3	q=70kPa	**70**	45	16	0.4	4	5	0.15	0.35	10	$f(\alpha_s)$	$f(\alpha_s)$	inf.
4	q=75kPa	**75**	45	16	0.4	4	5	0.15	0.35	10	$f(\alpha_s)$	$f(\alpha_s)$	inf.
5	q=80kPa	**80**	45	16	0.4	4	5	0.15	0.35	10	$f(\alpha_s)$	$f(\alpha_s)$	inf.
6	q=90kPa	**90**	45	16	0.4	4	5	0.15	0.35	10	$f(\alpha_s)$	$f(\alpha_s)$	inf.
7	q=100kPa	**100**	45	16	0.4	4	5	0.15	0.35	10	$f(\alpha_s)$	$f(\alpha_s)$	inf.
8	Dr_o (%)-35	52	**35**	16	0.4	4	5	0.15	0.35	10	$f(\alpha_s)$	$f(\alpha_s)$	inf.
9	Dr_o (%)-55	52	**55**	16	0.4	4	5	0.15	0.35	10	$f(\alpha_s)$	$f(\alpha_s)$	inf.
10	Dr_o (%)-65	52	**65**	16	0.4	4	5	0.15	0.35	10	$f(\alpha_s)$	$f(\alpha_s)$	inf.
11	$Z_{liq.}$=14m	52	45	**14**	0.4	4	5	0.15	0.35	10	$f(\alpha_s)$	$f(\alpha_s)$	inf.
12	$Z_{liq.}$=12m	52	45	**12**	0.4	4	5	0.15	0.35	10	$f(\alpha_s)$	$f(\alpha_s)$	inf.
13	$Z_{liq.}$=10m	52	45	**10**	0.4	4	5	0.15	0.35	10	$f(\alpha_s)$	$f(\alpha_s)$	inf.
14	$Z_{liq.}$=8m	52	45	**8**	0.4	4	5	0.15	0.35	10	$f(\alpha_s)$	$f(\alpha_s)$	inf.
15	$Z_{liq.}$=6m	52	45	**6**	0.4	4	5	0.15	0.35	10	$f(\alpha_s)$	$f(\alpha_s)$	inf.
16	$r_{u,max}$=0.30 (α_s=0.09)	52	45	16	**0.3**	4	5	0.15	0.35	10	$f(\alpha_s)$	$f(\alpha_s)$	inf.
17	$r_{u,max}$=0.20 (α_s=0.175)	52	45	16	**0.2**	4	5	0.15	0.35	10	$f(\alpha_s)$	$f(\alpha_s)$	inf.
18	$r_{u,max}$=0.15 (α_s=0.20)	52	45	16	**0.15**	4	5	0.15	0.35	10	$f(\alpha_s)$	$f(\alpha_s)$	inf.
19	$H_{imp.}$-5	52	45	15	0.4	**5**	5	0.15	0.35	10	$f(\alpha_s)$	$f(\alpha_s)$	inf.
20	$H_{imp.}$-6	52	45	14	0.4	**6**	5	0.15	0.35	10	$f(\alpha_s)$	$f(\alpha_s)$	inf.
21	$H_{imp.}$-7	52	45	13	0.4	**7**	5	0.15	0.35	10	$f(\alpha_s)$	$f(\alpha_s)$	inf.
22	$H_{imp.}$-8	52	45	12	0.4	**8**	5	0.15	0.35	10	$f(\alpha_s)$	$f(\alpha_s)$	inf.
23	B=3m	52	45	16	0.4	4	**3**	0.15	0.35	10	$f(\alpha_s)$	$f(\alpha_s)$	inf.
24	B=7m	52	45	16	0.4	4	**7**	1.15	0.35	10	$f(\alpha_s)$	$f(\alpha_s)$	inf.
25	B=9m	52	45	16	0.4	4	**9**	2.15	0.35	10	$f(\alpha_s)$	$f(\alpha_s)$	inf.
26	B=3m	52	45	16	0.4	**5**	**3**	0.15	0.35	10	$f(\alpha_s)$	$f(\alpha_s)$	inf.
27	a_{max}=0.10g	52	45	16	0.4	4	5	**0.10**	0.35	10	$f(\alpha_s)$	$f(\alpha_s)$	inf.
28	a_{max}=0.20g	52	45	16	0.4	4	5	**0.2**	0.35	10	$f(\alpha_s)$	$f(\alpha_s)$	inf.
29	a_{max}=0.25g	52	45	16	0.4	4	5	**0.25**	0.35	10	$f(\alpha_s)$	$f(\alpha_s)$	inf.
30	a_{max}=0.30g	52	45	16	0.4	4	5	**0.30**	0.35	10	$f(\alpha_s)$	$f(\alpha_s)$	inf.
31	a_{max}=0.35g	52	45	16	0.4	4	5	**0.35**	0.35	10	$f(\alpha_s)$	$f(\alpha_s)$	inf.
32	T=0.15sec	52	45	16	0.4	4	5	0.15	**0.15**	10	$f(\alpha_s)$	$f(\alpha_s)$	inf.
33	T=0.25sec	52	45	16	0.4	4	5	0.15	**0.20**	10	$f(\alpha_s)$	$f(\alpha_s)$	inf.
34	T=0.50sec	52	45	16	0.4	4	5	0.15	**0.25**	10	$f(\alpha_s)$	$f(\alpha_s)$	inf.
35	T=0.50sec	52	45	16	0.4	4	5	0.15	**0.50**	10	$f(\alpha_s)$	$f(\alpha_s)$	inf.
36	N=5 cycl.	52	45	16	0.4	4	5	0.15	0.35	**5**	$f(\alpha_s)$	$f(\alpha_s)$	inf.
37	N=12 cycl.	52	45	16	0.4	4	5	0.15	0.35	**12**	$f(\alpha_s)$	$f(\alpha_s)$	inf.
38	N=15 cycl.	52	45	16	0.4	4	5	0.15	0.35	**15**	$f(\alpha_s)$	$f(\alpha_s)$	inf.

Table 8.1: Summary of parametric analyses plan (cont.).

	Analysis Name	q (kPa)	$D_{r,o}$ (%)	$Z_{liq.}$ (m)	$r_{u,max}$	$H_{imp.}$ (m)	B (m)	a_{max}(g)	T	10	$k_{eq.}$ (m/sec)	$D_{r,imp}$ (%)	$L_{imp.}$ (m)
39	$D_{r,o\text{-}ind}$ = 35%	52	**35**	16	0.4	4	5	0.15	0.35	10	**10.87**	**82**	inf.
40	$D_{r,o\text{-}ind}$ = 45%	52	**45**	16	0.4	4	5	0.15	0.35	10	**10.87**	**82**	inf.
41	$D_{r,o\text{-}ind}$ = 55%	52	**55**	16	0.4	4	5	0.15	0.35	10	**10.87**	**82**	inf.
42	$D_{r,o\text{-}ind}$ = 65%	52	**65**	16	0.4	4	5	0.15	0.35	10	**10.87**	**82**	inf.
43	k_{sand}=6.6*10^{-6}m/s (α_s = 0.23)	52	45	16	0.4	4	5	0.15	0.35	10	**3.09**	86	inf.
44	k_{sand}=1*10^{-5}m/s (α_s = 0.2)	52	35	16	0.4	4	5	0.15	0.35	10	**4.08**	82	inf.
45	k_{sand}=1*10^{-4}m/s (α_s = 0.06)	52	55	16	0.4	4	5	0.15	0.35	10	**12.9**	58	inf.
46	Dr_o (%)-35	100	**35**	16	0.4	4	5	0.15	0.35	10	f(α_s)	f(α_s)	inf.
47	Dr_o (%)-55	100	**55**	16	0.4	4	5	0.15	0.35	10	f(α_s)	f(α_s)	inf.
48	Dr_o (%)-65	100	**65**	16	0.4	4	5	0.15	0.35	10	f(α_s)	f(α_s)	inf.
49	$Z_{liq.}$=10m	100	45	**10**	0.4	4	5	0.15	0.35	10	f(α_s)	f(α_s)	inf.
50	$Z_{liq.}$=8m	100	45	**8**	0.4	4	5	0.15	0.35	10	f(α_s)	f(α_s)	inf.
51	$Z_{liq.}$=6m	100	45	**6**	0.4	4	5	0.15	0.35	10	f(α_s)	f(α_s)	inf.
52	$r_{u,max}$=0.30	100	45	16	**0.3**	4	5	0.15	0.35	10	f(α_s)	f(α_s)	inf.
53	$r_{u,max}$=0.20	100	45	16	**0.2**	4	5	0.15	0.35	10	f(α_s)	f(α_s)	inf.
54	$r_{u,max}$=0.15	100	45	16	**0.15**	4	5	0.15	0.35	10	f(α_s)	f(α_s)	inf.
55	$H_{imp.}$-5	100	45	15	0.4	**5**	5	0.15	0.35	10	f(α_s)	f(α_s)	inf.
56	$H_{imp.}$-6	100	45	14	0.4	**6**	5	0.15	0.35	10	f(α_s)	f(α_s)	inf.
57	$H_{imp.}$-7	100	45	13	0.4	**7**	5	0.15	0.35	10	f(α_s)	f(α_s)	inf.
58	$H_{imp.}$-8	100	45	12	0.4	**8**	5	0.15	0.35	10	f(α_s)	f(α_s)	inf.
59	B=3m	100	45	16	0.4	4	**3**	0.15	0.35	10	f(α_s)	f(α_s)	inf.
60	B=3m_H_{imp}=5m	100	45	15	0.4	5	**3**	0.15	0.35	10	f(α_s)	f(α_s)	inf.
61	B=3m_H_{imp}=6m	100	45	14	0.4	6	**3**	0.15	0.35	10	f(α_s)	f(α_s)	inf.
62	a_{max}=0.10g	100	45	16	0.4	4	5	**0.10**	0.35	10	f(α_s)	f(α_s)	inf.
63	a_{max}=0.25g	100	45	16	0.4	4	5	**0.25**	0.35	10	f(α_s)	f(α_s)	inf.
64	a_{max}=0.35g	100	45	16	0.4	4	5	**0.35**	0.35	10	f(α_s)	f(α_s)	inf.
65	T=0.15sec	100	45	16	0.4	4	5	0.15	**0.15**	10	f(α_s)	f(α_s)	inf.
66	T=0.25sec	100	45	16	0.4	4	5	0.15	**0.25**	10	f(α_s)	f(α_s)	inf.
67	T=0.50sec	100	45	16	0.4	4	5	0.15	**0.50**	10	f(α_s)	f(α_s)	inf.
68	N=5 cycl.	100	45	16	0.4	4	5	0.15	0.35	**5**	f(α_s)	f(α_s)	inf.
69	N=12 cycl.	100	45	16	0.4	4	5	0.15	0.35	**12**	f(α_s)	f(α_s)	inf.
70	N=15 cycl.	100	45	16	0.4	4	5	0.15	0.35	**15**	f(α_s)	f(α_s)	inf.
71	$D_{r,o\text{-}ind}$ = 35%	100	**35**	16	0.4	4	5	0.15	0.35	10	**10.87**	**82**	inf.
72	$D_{r,o\text{-}ind}$ = 45%	100	**45**	16	0.4	4	5	0.15	0.35	10	**10.87**	**82**	inf.
73	$D_{r,o\text{-}ind}$ = 55%	100	**55**	16	0.4	4	5	0.15	0.35	10	**10.87**	**82**	inf.
74	$D_{r,o\text{-}ind}$ = 65%	100	**65**	16	0.4	4	5	0.15	0.35	10	**10.87**	**82**	inf.
75	$H_{imp.}$-6	**124**	45	14	0.4	**6**	5	0.15	0.35	11	f(α_s)	f(α_s)	inf.
76	$H_{imp.}$-6	**152**	45	14	0.4	**6**	5	0.15	0.35	12	f(α_s)	f(α_s)	inf.
77	$H_{imp.}$-6	**176**	45	14	0.4	**6**	5	0.15	0.35	13	f(α_s)	f(α_s)	inf.
78	$H_{imp.}$-6	**200**	45	14	0.4	**6**	5	0.15	0.35	14	f(α_s)	f(α_s)	inf.
79	$H_{imp.}$-8	**152**	45	14	0.4	**8**	5	0.15	0.35	15	f(α_s)	f(α_s)	inf.
80	$H_{imp.}$-8	**200**	45	14	0.4	**8**	5	0.15	0.35	16	f(α_s)	f(α_s)	inf.
81	$H_{imp.}$-8	**250**	45	14	0.4	**8**	5	0.15	0.35	17	f(α_s)	f(α_s)	inf.
82	$H_{imp.}$-8	**300**	45	14	0.4	**8**	5	0.15	0.35	18	f(α_s)	f(α_s)	inf.

8.4.2 Effect of lateral extent of improvement (L_{imp})

In real applications, the improved crust is going to be artificially manufactured around the shallow foundation, disclosing a major independent problem parameter, namely that of the extent of the performed improvement, L_{imp}. For that purpose, an additional set of analyses is executed, considering various widths of improvement in order to evaluate the observed effect on the previously established liquefaction performance of the footing.

The influence of lateral extent of improvement is investigated comparatively to the footing response for conditions of “infinite” improvement. Namely, out of the parametric analyses plan presented above, twelve (12) characteristic cases are selected, which exhibit different soil, excitation and geometric characteristics. In each set of analyses, the “infinitely” extending improved layer is the reference analysis. Subsequently, the width of the improved layer (L_{imp}) is progressively reduced down to nearly the width of the footing itself. A detailed description of the particular set of parametric analyses as well as the conclusions of the statistical processing of the numerical results are provided in the relevant Chapter 10.

CHAPTER 9

Analytical Relations for Seismic Settlements & Degraded Bearing Capacity: Infinite Improvement Width

9.1 Introduction

The present chapter is devoted to the statistical processing of the numerical results obtained from the parametric analysis described earlier. The aim of the statistical evaluation is first to identify the parameters controlling the accumulation of dynamic settlements (ρ_{dyn}) and the post-shaking degraded factor of safety ($F.S._{deg.}$) and consequently to quantify their effect. As a result, analytical expressions are established for the prediction of seismic settlements of the shallow foundation, at the end of shaking, as well as the associated degraded bearing capacity $q_{ult.}$ and factor of safety $F.S._{deg}$.

9.2 Earthquake-induced foundation settlements

9.2.1 Newmark-based analytical expression

Systematic examination of the numerical results, combined with observations from relevant cetrifuge and large-scale experiments published in the literature, suggests that dynamic settlement accumulation of shallow foundations is not the result of sand densification, but rather that of the activation of a Newmark-type sliding block failure mechanism. Namely, as it has been thoroughly explained in Chapter 8, settlement accumulation is associated with

the activation of two one-sided wedge type failure mechanisms, occuring twice during one full loading cycle.

The correlation of dynamic settlement accumulation to a failure mechanism, may potentially lead to its association with the degraded factor of safety, also referred to as $F.S._{deg}$. Hence, to investigate this option, the effect of the different groups of examined problem parameters (i.e.loading, excitation, geometry and soil characteristics) are jointly evaluated for both, the footing settlements and the inverse degraded factor of safety, as shown in **Figure 9.1** through **Figure 9.4**. This parallel evaluation discloses that contact pressure q, as well as all geometry and soil characteristics have qualitatively the same effect on both $\rho_{dyn.}$ and $1/F.S._{deg.}$. Hence, dynamic settlements may be directly related to the inverse of the degraded factor of safety, thus reducing the total number of the independent variables for estimating $\rho_{dyn.}$. It is also evident that this is hardly the case when examining the effect of the excitation characteristics on $\rho_{dyn.}$ and $1/F.S._{deg}$, presented in **Figure 9.2**. Hence, the specific parameters will be handled as separate variables, following the formulation justified below.

For the simple case of harmonic loading, the sliding block mechanism results in displacement accumulation, which is proportional to *Equation 9.1:*

$$\frac{v^2_{max}}{a_{max}} N = a_{max} T^2 N \qquad 9.1$$

Where v_{max} is the maximum velocity of the applied excitation

a_{max} the maximum acceleration magnitude of the applied excitation

T the period of the applied excitation

N the number of cycles

It can be further shown from *Equation 9.2* that:

$$a_{max} T^2 N = \pi^2 \int_{t=0}^{t=N*T} abs(v(t))\,dt \qquad 9.2$$

where v(t) is the applied velocity time history.

The main advantage stemming from the use of such an expresion is that an analytical relation for ρ_{dyn}, initially developed for harmonic motions can be subsequently extended to any type of input motion.

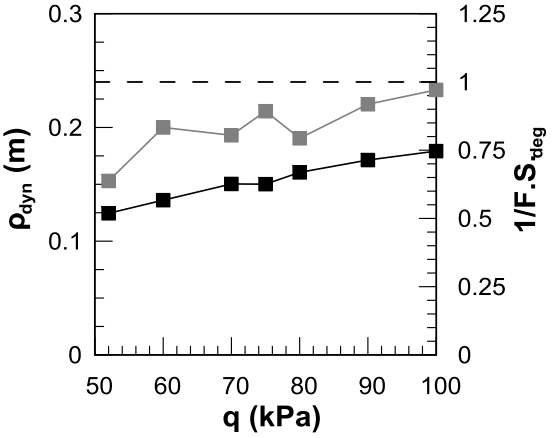

Figure 9.1: Effect of contact pressure q, in ρ_{dyn} and $1/F.S._{deg}$.

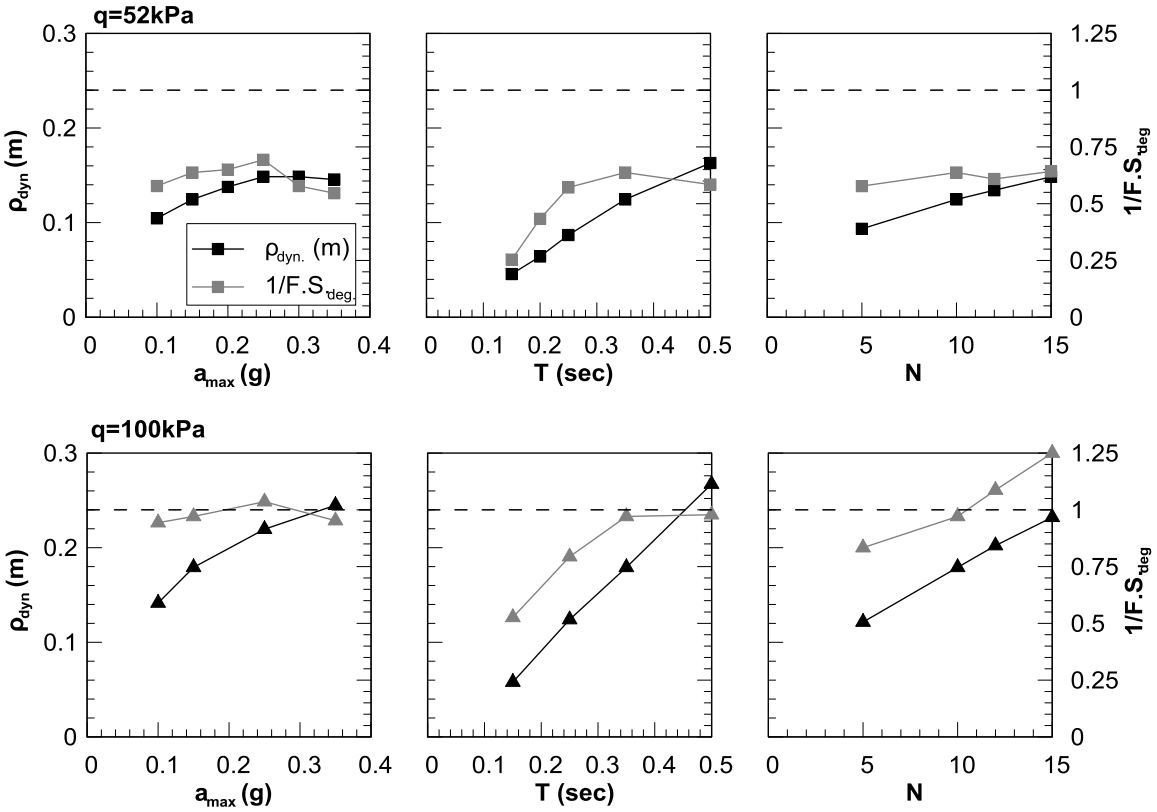

Figure 9.2: Effect of excitation parameters in ρ_{dyn} and $1/F.S._{deg}$ for two loading levels (52 and 100kPa).

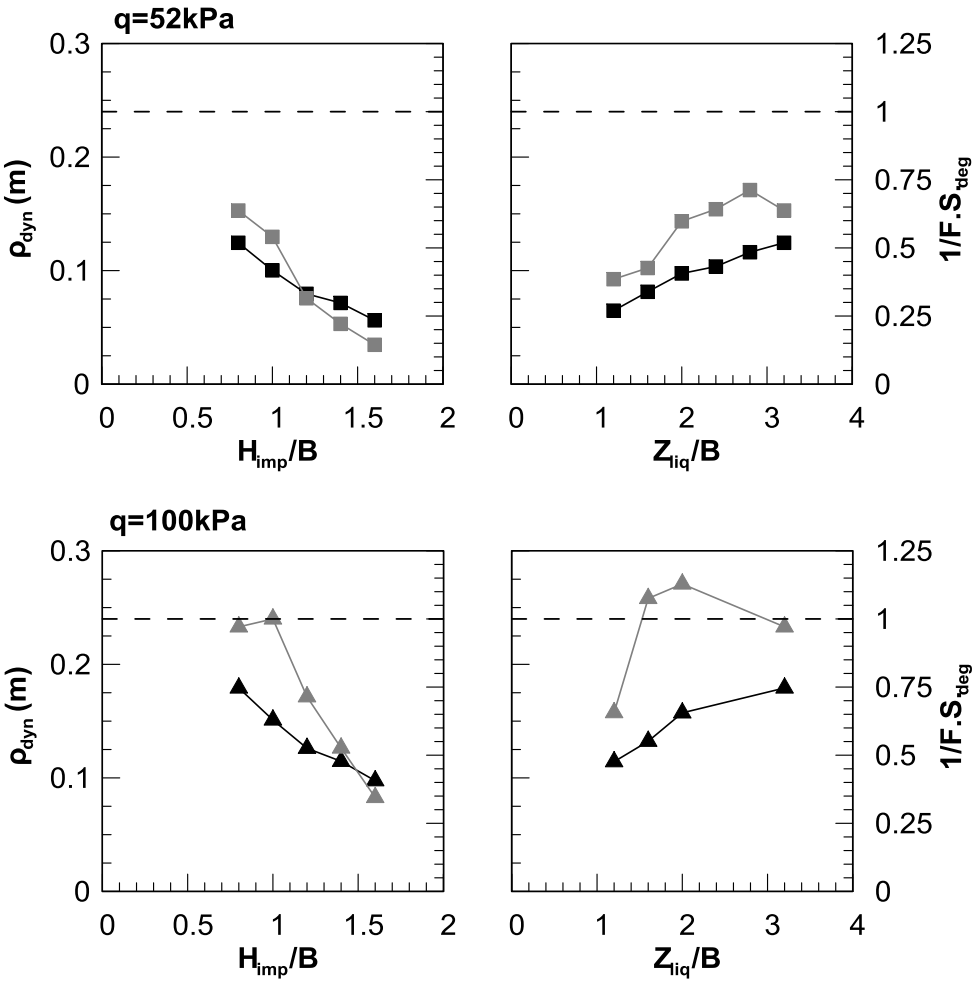

Figure 9.3: Effect of geometry parameters in ρ_{dyn} and $1/F.S._{deg}$ for two loading levels (52 and 100kPa).

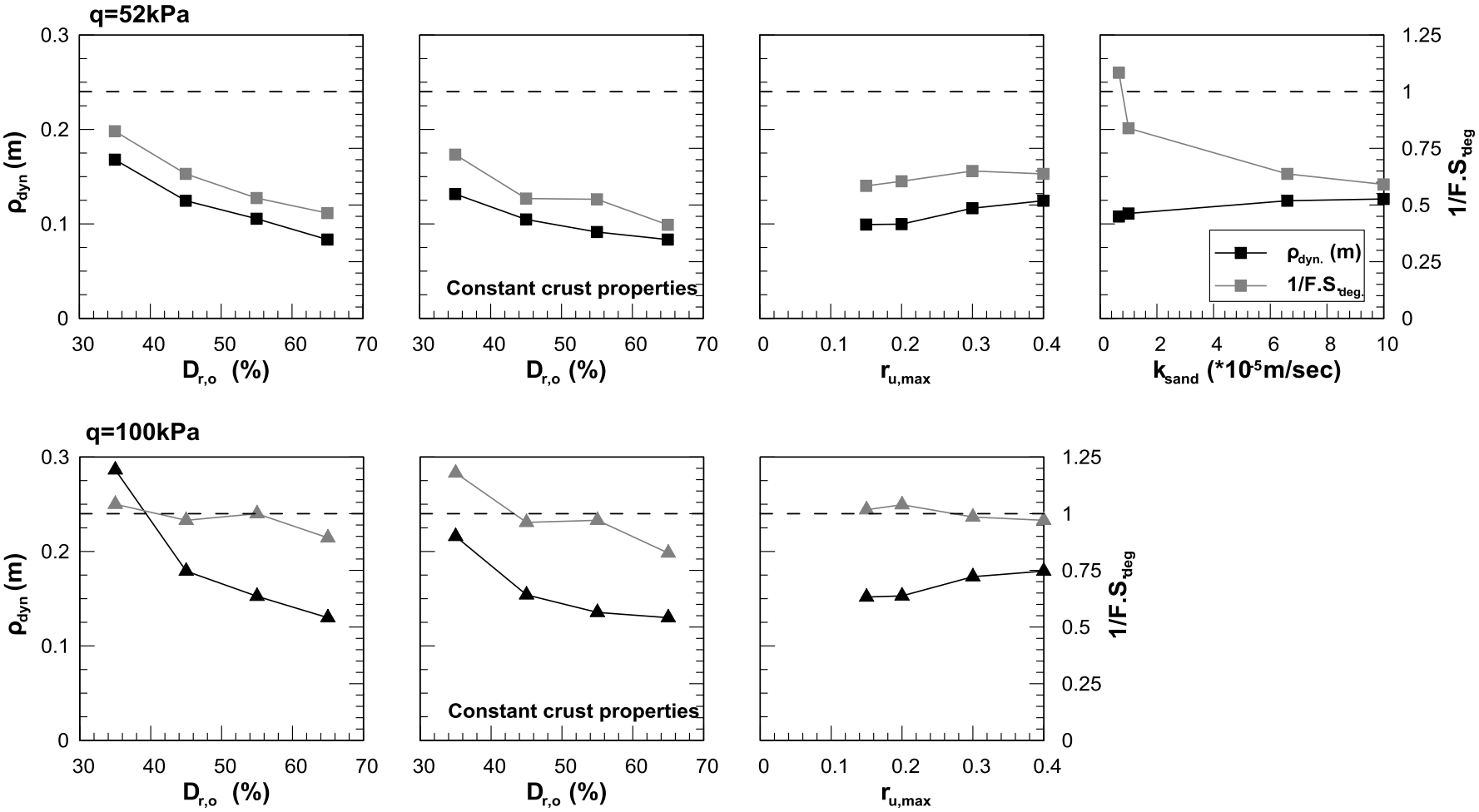

Figure 9.4: Effect of soil parameters in ρ_{dyn} and 1/F.S.$_{deg}$ for two loading levels (52 and 100kPa).

Integration of the applied velocity time-history in the performed numerical analyses was found equal to $\alpha_{max}T^2(N_o+2)$, where N_o is the number of significant cycles of the motion. The total number of loading cycles is increased by two, to account for the additional cycles of varying amplitude, added at the beginning and at the end of the applied excitation.

In extend of the above, the numerically predicted ρ_{dyn} values were normalized against $\alpha_{max}T^2(N_o+2)$ and correlated to the inverse of the degraded factor of safety. This correlation is illustrated in **Figure 9.5**. Observe that there is a consistent trend of the data points, expressed analytically as:

$$\frac{\rho_{dyn}}{a_{\max}T_{exc}{}^2(N_o+2)}=0.06*\left(\frac{1}{F.S._{\deg}}\right)^{0.45}*\left[1+0.3*\left(\frac{1}{F.S._{\deg}}\right)^5\right] \qquad 9.3$$

but the associated scater is considerable and may limit the use of *Equation 9.3* in practical applications. This is mainly attributed to the fact that soil amplification effects, during propagation of the seismic motion from the base to the ground surface, where the settlements accumulate, are overlooked. Namely, while the seismic motion parameters (v_{max}, α_{max}, T) should refer to the base of the "sliding block", in the present application they refer to seismic excitation at the base of the soil column. To account for this mandatory drawback a number of theory-inspired modifications were applied as described below.

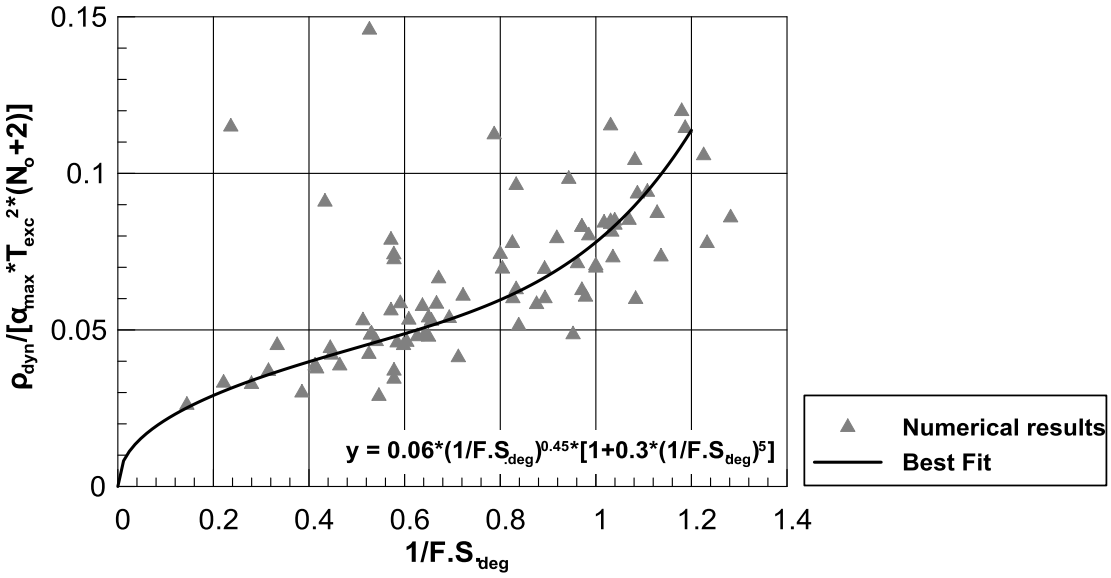

Figure 9.5: Correlation of normalized settlements ρ_{dyn} against $1/F.S._{deg.}$ considering the Newmark approach.

Incorporation of the fundamental soil period T_{soil}.- To reduce the scatter in **Figure 9.5**, the excitation period was averaged with the elastic soil period T_{soil}, the later being expressed as:

$$T_{soil} = \frac{4H_{crust}}{V_{S,crust}} + \frac{4H_{sand}}{V_{S,\text{sand}}} \qquad 9.4$$

where $V_S = \sqrt{\frac{G_{max}}{\rho}}$ denotes the shear wave velocity and the maximum shear modulus G_{max} is approximately computed according to the following equation (Hardin et al., 1978):

$$G_{\max} = 600 \frac{p_{atm}}{0.3+0.7\times e^2} \sqrt{\frac{p}{p_{atm}}} \qquad 9.5$$

in terms of the void ratio of the sand (e), the atmospheric pressure (p_{atm} = 100kPa) and the mean effective pressure (p in kPa) at the mid-depth of each encountered layer (i.e. improved crust and natural sand layer) (kPa).

In more detail, *Equation 9.3* was rewritten in a more general form with T_{exc} replaced by (T_{exc} + a×T_{soil}):

$$\rho_{dyn} = c_1 \alpha_{\max} \left(T_{exc} + aT_{soil}\right)^2 \left(N_o + 2\right) \left(\frac{1}{F.S._{deg}}\right)^{c_2} \left[1 + c_3 \left(\frac{1}{F.S._{deg}}\right)^{c_4}\right] \qquad 9.6$$

In the sequel, a non-linear regression analysis was performed leading to the following values of the coefficients in *Equation 9.6*: **c_1=0.019**, **c_2=0.45**, **c_3=0.25 c_4=4.5** and **a=0.633**. The correlation of the normalized seismic settlements with the inverse degraded factor of safety is shown in **Figure 9.6**.

The scatter of the data points is now significantly reduced, verifying the beneficial effect of introducing the fundamental soil period. Based on the one-to-one comparison of **Figure 9.7**, between numerical and analytical predictions of ρ_{dyn} it is further observed that about *83.3%* of the predictions with *Equation 9.6* lay within a range of ±25% of the numerical results. The relative error, expressed as the ratio of (Predicted – Observed)/Observed values, is presented in **Figure 9.8** with regard to the observed values of dynamic settlements, ρ_{dyn}^{num}(m). The uniform scatter around zero is indicative of the good and unbiased predictive accuracy of the proposed *Equation 9.6,* which is further verified by the Standard deviation of relative error calculated equal to about 21%.

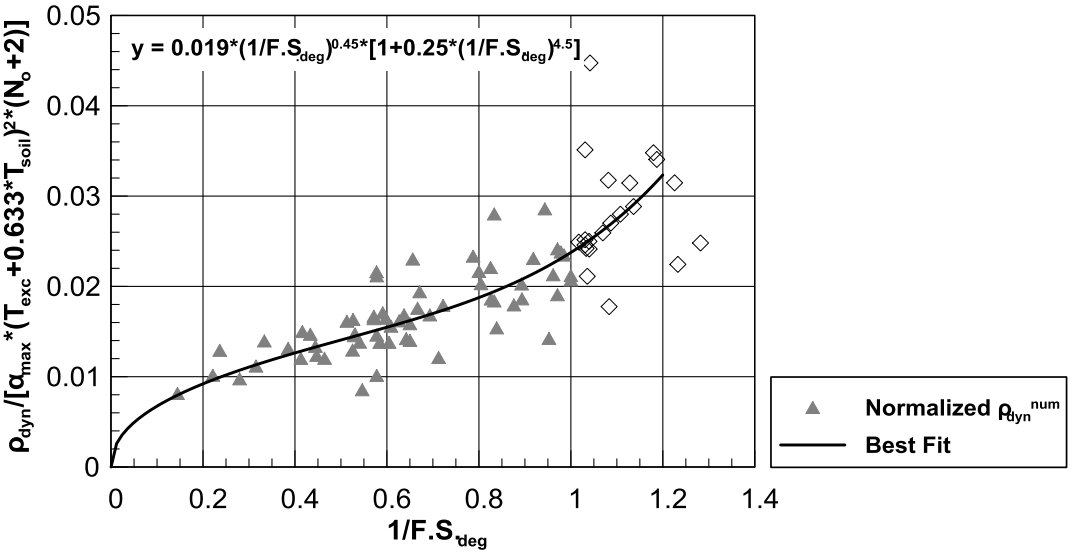

Figure 9.6: Correlation of normalized settlements ρ_{dyn} against 1/F.S.$_{deg.}$ considering the Newmark approach, incorporating the period of the soil column T_{soil}.

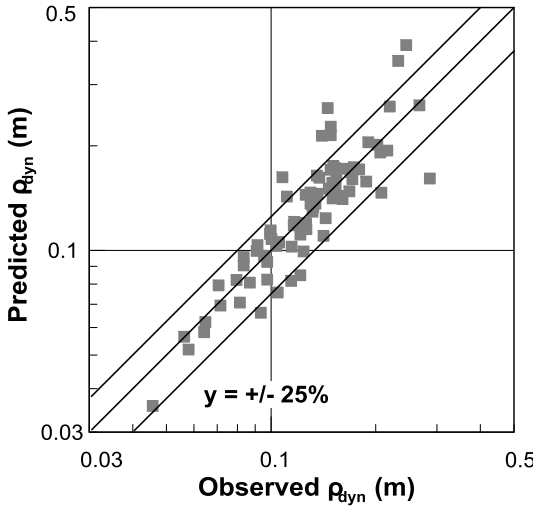

Figure 9.7: Numerical versus predicted values.

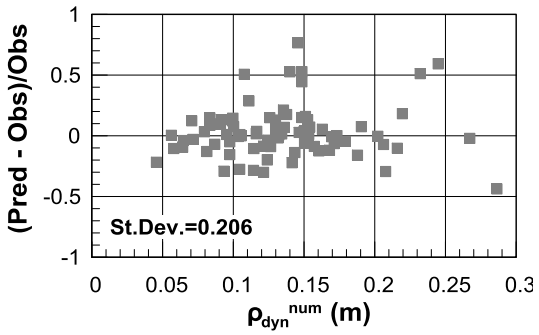

Figure 9.8: Relative error plotted against the numerically derived values of settlement ρ_{dyn}^{num} (m).

9.2.2 Unit-dependent analytical expression

The purpose of the following investigation is to explore whether there is hidden bias in the analytical predictions obtained from the use of *Equation 9.6,* and appropriately modify it, in order to improved its accuracy. To achieve this goal, the ratio of the Observed (numerical) over the Predicted (analytical) values of ρ_{dyn} is plotted against each one of the four basic variables appearing in *Equation 9.6*, and presented in **Figure 9.9**.

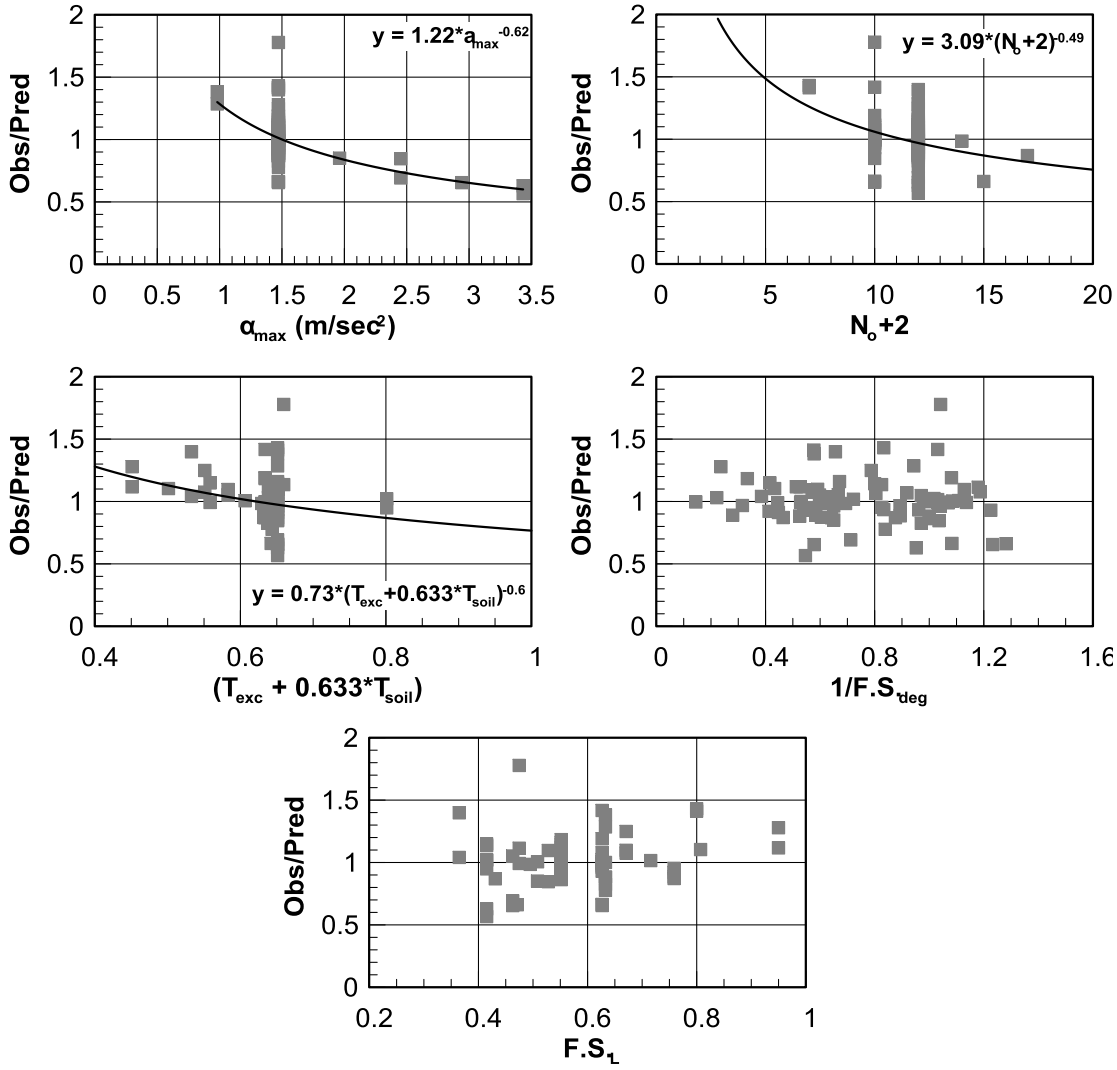

Figure 9.9: Introduced bias for the involved variables and the number of cycles to liquefaction N_L, expressed through $F.S._L$.

The last chart summarizes the ratio of Obs./Pred. values plotted against the factor of safety against liquefaction $F.S._L$. This particular figure is generated because the correlation of seismic-induced settlements to the total number of loading cycles implies that the onset of liquefaction coincides with the onset of seismic shaking, which is not entirely true. Also, the introduction of the inverse of the degraded factor of safety ($1/F.S._{deg.}$) into the analytical expression for the dynamic settlements is not conclusive whether it appropriately captures any possible effect of the "delayed" liquefaction. Hence, to explore this skepticism, the ratio of observed over predicted values of ρ_{dyn} is plotted against the factor of safety against liquefaction $F.S._L$, computed based on *Equation 9.7* below (Bouckovalas, 2013; personal communication):

$$F.S._L = \frac{N^{0.35}+3.3}{N^{0.35}+3.3\dfrac{N}{N_L}} \qquad 9.7$$

where N is the total number of cycles and N_L is the number of cycles required to initiate liquefaction, at the mid-depth of the soil configuration, obtained from free-field numerical analyses (for r_u>0.90).

Based on **Figure 9.9**, it is found that the analytical predictions are indeed biased with regard to all three seismic excitation parameters, as opposed to the inverse relation with the degraded factor of safety, as well as the factor of safety against liquefaction $F.S._L$, where the predictions are evenly scattered around the observed values. This observation does not necessarily revoke the validity of the assumed sliding block mechanism, but essentially reveals that merely introducing the elastic soil period was not adequate in order to account for soil effects on seismic excitation characteristics. Hence, the power functions describing the bias of each variable in **Figure 9.9,** are introduced in *Equation 9.6*, and a new non-linear regression analysis was performed to define coefficients $c_1 \div c_4$. Thus, the empirical relation for the computation of seismic settlements now becomes:

$$\rho_{dyn} = c_1 \alpha_{max}^{0.40} \left(T_{exc} + 0.633 T_{soil}\right)^{1.40} \left(N_o + 2\right)^{0.50} \left(\frac{1}{F.S._{deg}}\right)^{c_2} \left[1 + c_3 \left(\frac{1}{F.S._{deg}}\right)^{c_4}\right] \qquad 9.8$$

with $\mathbf{c_1=0.06}$, $\mathbf{c_2=0.45}$, $\mathbf{c_3=0.4}$ and $\mathbf{c_4=2}$. The correlation of the normalized seismic settlements with the inverse degraded factor of safety is illustrated in **Figure 9.10**. The scatter of the data points is further reduced, verifying the beneficial effect of introducing the correction factors mentioned above.

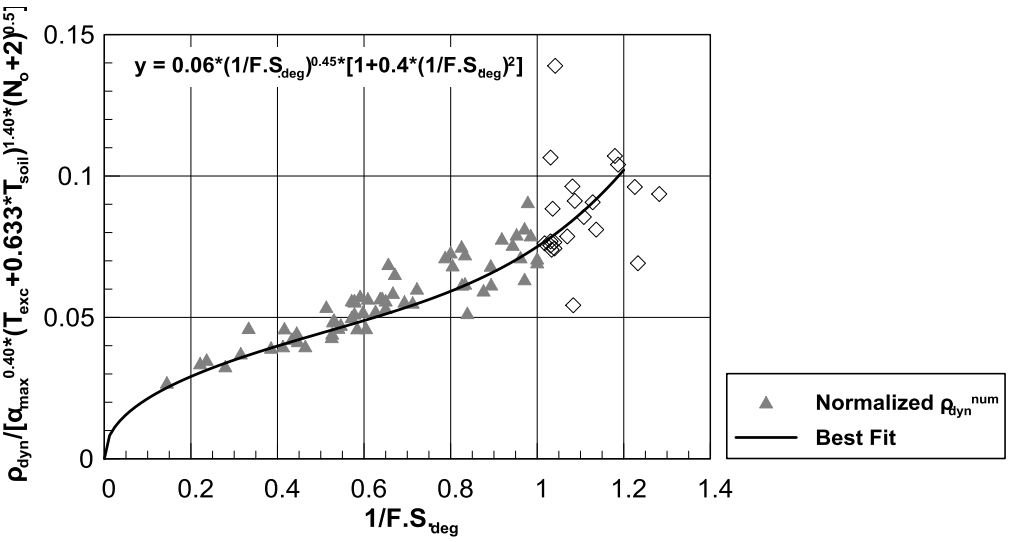

Figure 9.10: Correlation of normalized settlements ρ_{dyn} against $1/F.S._{deg}$ considering bias corrections.

The updated one-to-one comparison between numerical and analytical predictions is shown in **Figure 9.11**. Observe that the scatter of the data points has been considerably reduced, with *95%* of the predictions laying within a ±25% range from the numerical results and 91.6% of the predictions within a ±20% range, as shown in the corresponding figure. The relative error is evaluated in **Figure 9.12** with regard to the observed values of dynamic settlements, ρ_{dyn}^{num}(m). The even more uniform scatter around zero is indicative of the good and unbiased predictive accuracy of *Equation 9.8,* which is further verified by the reduced Standard deviation of relative error calculated equal to 14%.

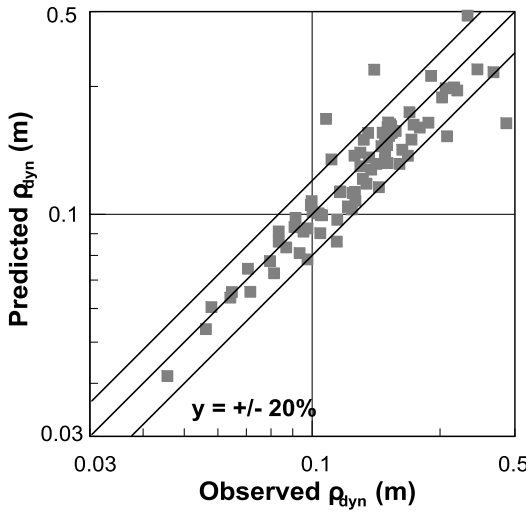

Figure 9.11: Observed versus analytically predicted values after the bias correction

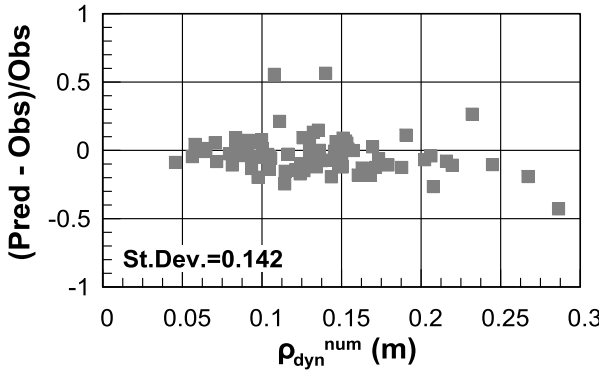

Figure 9.12: Relative error plotted against the numerically derived values of settlement ρ_{dyn}^{num} (m).

9.3 Post-shaking degraded bearing capacity

9.3.1 Theoretical background and modifications

The second part of the proposed analytical methodology focuses on the post-shaking bearing capacity of the surface foundation, which has substantially degraded compared to the initial value under static conditions, due to liquefaction of the unimproved natural soil. For that purpose, an analytical relationship for the evaluation of the degraded bearing capacity $q_{ult.}^{deg}$ (kPa) is formulated, based on theory as well as on the results of the numerical analyses.

The proposed analytical methodology is based on a modified version of the Meyerhof & Hanna (1978) analytical solution for the bearing capacity of shallow foundations on two-layered cohesionless soil profiles. According to this methodology, the bearing capacity of shallow foundations located on top of a two-layered sand formation (without embedment) is evaluated as:

$$q_{ult,deg} = \min\left\{\begin{array}{c} \frac{1}{2}\gamma_1' B N\gamma_1 \\ \gamma_1' H_1^{\,2} K_s \frac{\tan\phi_1}{B} - \gamma_1' H_1 + \frac{1}{2}\gamma_1' B N_{\gamma 2} + \gamma_1' H_1 N_{q2} \end{array}\right\} \qquad 9.9$$

where $N_q = \tan^2(45+\phi/2)e^{\pi\tan\phi}$ *9.9a*

$N_\gamma = 2(N_q+1)\tan\phi$

9.9b

The coefficient ***K_s*** in *Equation 9.9* is evaluated based on the chart of **Figure 9.13**, as a function of the q_2/q_1 ratio, and the friction angle of the upper layer ϕ_1. Bearing capacities q_1

and q_2 refer to the top and the underlying layers respectively, and they are computed based on the first line of *Equation 9.9a.* Assuming the same unit weight for both layers, the q_2/q_1 ratio is reduced to $N\gamma_2/N\gamma_1$.

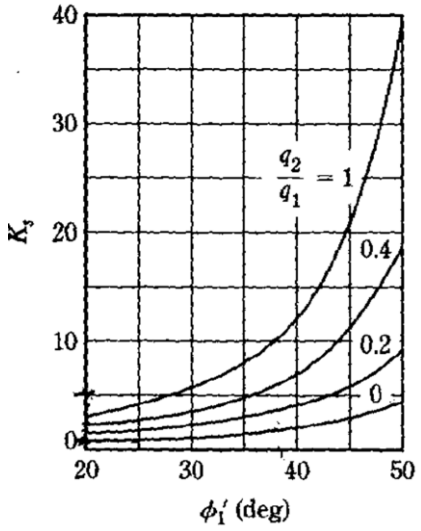

Figure 9.13: Chart for estimating the K_s coefficient in the Meyerhof & Hanna (1978) analytical methodology.

In the problem at hand, it has been noticed that at the end of shaking a transition zone of non-liquefied natural ground (with $0< r_u < 1.0$) is formed between the improved crust and the liquefied sand, as a result of the fast dissipation of the seismic induced excess pore pressures towards the much more permeable improved crust (see also **Figure 9.14**). This transitional zone acts as a secondary crust and essentially causes the Prandl-type failure surface to develop underneath it. If the thickness of the aforementioned layer is expressed as a portion α of the thickness of the improved soil crust, and the unit soil weight is considered uniform ($\gamma_1=\gamma_2=\gamma$), the Meyerhof & Hanna (1978) analytical expression is modified as follows:

$$q_{ult,deg} = \min\left\{\begin{array}{c} \frac{1}{2}\gamma' B N_{\gamma_1} \\ \gamma' H_1^2 K_s \frac{\tan\phi_1}{B} + \gamma'\cdot[(1+\alpha)^2-1]\cdot H_1^2 K_s \frac{\tan\phi_2}{B} - \gamma'(1+\alpha)H_1 + \\ + \frac{1}{2}\gamma' B N_{\gamma 3} + \gamma'(1+\alpha)H_1 N_{q3} \end{array}\right\} \qquad 9.10$$

Note that the friction angles appearing in *Equation 9.10* above should be appropriately reduced in order to account for the excess pore pressure build up that is anticipated at the end of seismic shaking. To this extent, it will be approximately assumed that:

$$\phi_i = \tan^{-1}[(1-U_i)\tan\phi_{i,ini}] \qquad 9.11$$

where the subscript "ini" denotes the friction angle of the ground at the beginning of shaking, while i= 1 for the improved crust, 2 for the transition zone and 3 for the liquefied sand.

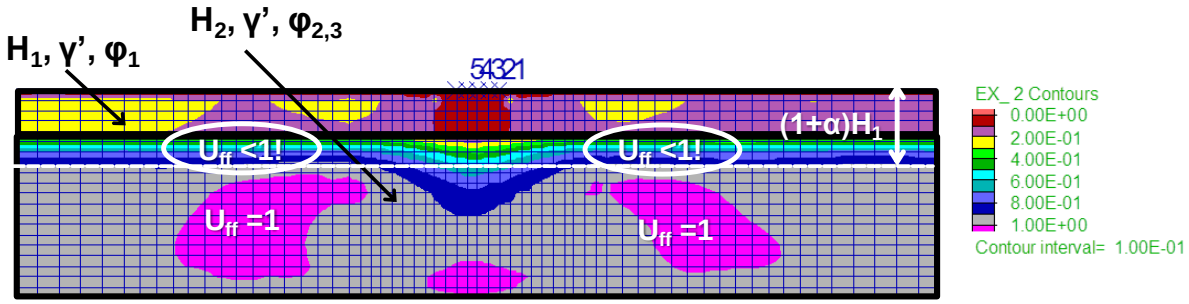

Figure 9.14: Excess pore pressure ratio contours at the end of shaking, indicating the formation of the non-liquefied layer of natural ground.

9.3.2 Calibration of necessary parameters

Coefficient *α*._ The thickness of the transition crust (*αH*) has been defined as the thickness of the natural ground over which the free field at the end of shaking is lower than 0.90. The variation of coefficient ***α*** against each one of the examined problem parameters is provided in

Figure 9.15. Based on that, it is concluded that ***α*** mainly depends on the properties of the improved layer ($H_{imp.}$, $k_{eq.}$) and the features of the applied excitation (T, N). Furthermore, **Figure 9.16** shows that a more or less unique trend is formed when "***α***" is related to the combined parameter $k_{eq}TH/H_{imp}$. Namely, "***α***" may be written as:

$$\alpha = C_\alpha \left[\frac{k_{eq}TN}{H_{imp}}\right]^{0.256} \qquad 9.12$$

The coefficient C_α receives an average value equal to 3.76 with a Standard Deviation equal to St.Dev.=±0.50. The minimum and maximum values are equal to $C_{\alpha,min}$=3 and $C_{\alpha,max}$=4.5 respectively.

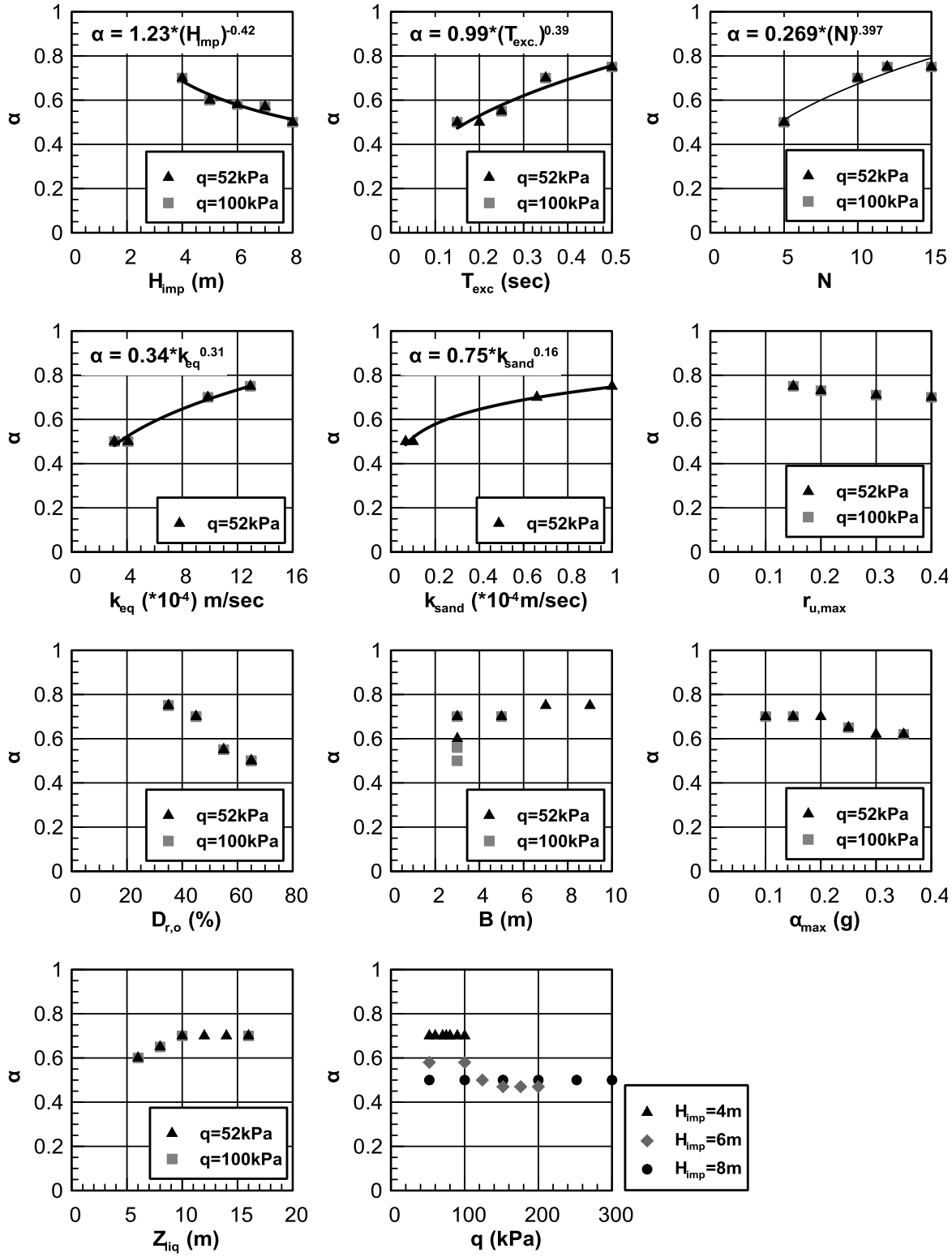

Figure 9.15: Variation of parameter α against each problem parameter.

Note that the permeability of the natural soil, k_{sand}, was not included in *Equation 9.12* for two reasons: the particular effect is indirectly included in the equivalent coefficient of permeability (k_{eq}), while the associated correlation shown in

Figure 9.15 is rather weak.

The accuracy of *Equation 9.12*, for the average value of C_{α}=3.76, is evaluated in **Figure 9.17a** & **b**. In **Figure 9.17a** the numerically derived values of ***α*** are one-to-one compared to the analytical predictions, while the relative prediction error is plotted against the numerical observations in **Figure 9.17b**. It is observed that the scatter of the data points is narrow whereas the relative error is less than ±20% for the majority of the observed values. Additionally, the proposed analytical expression is checked for potential bias with regard to each separate problem parameter in **Figure 9.18.** It is thus observed that in all cases, the observed (numerical) over predicted (analytical) ***α*** ratio receives values close to unity, without exhibiting any significant and consistent trend.

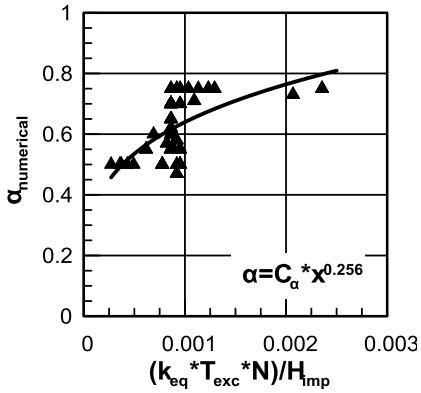

Figure 9.16: Numerical values of coefficient α against the term $(k_{eq.}TN)/H_{imp.}$ and the fitting power function.

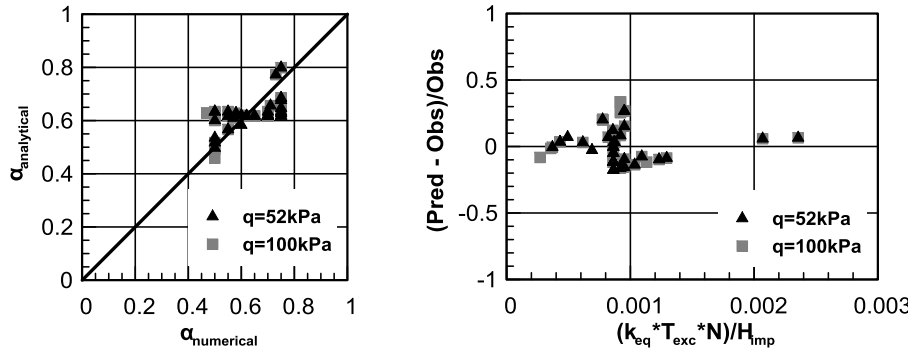

Figure 9.17: **(a)** One-to-one comparison of analytically computed against numerically derived ***α*** values **(b)** Relative error of predicted values.

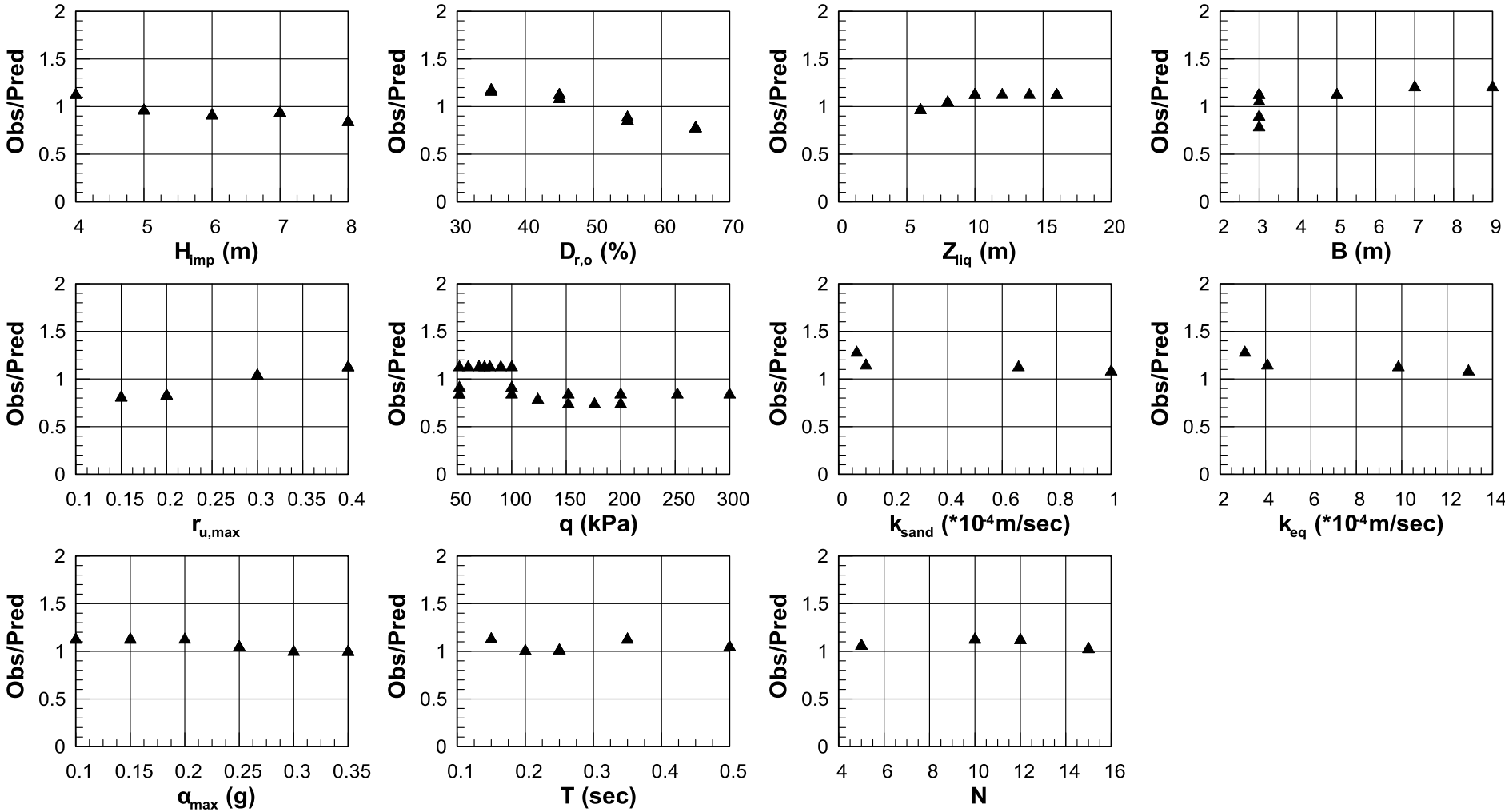

Figure 9.18: Sensitivity analysis for the mathematical expression for α coefficient.

Excess pore pressure ratio U_1 in the improved crust.- The average epp ratio $\boldsymbol{U_1}$ refers to free field conditions and at the end of shaking. To facilitate the performed comparisons, $\boldsymbol{U_1}$ will be expressed hereafter as a portion of the design excess pore pressure ratio, $\boldsymbol{U_{design}}$, determined from the relevant charts formulated and presented in Chapter 9. The variation of ratio $\boldsymbol{\beta=U_1/U_{design}}$ against the various problem parameters is summarized in **Figure 9.19**.

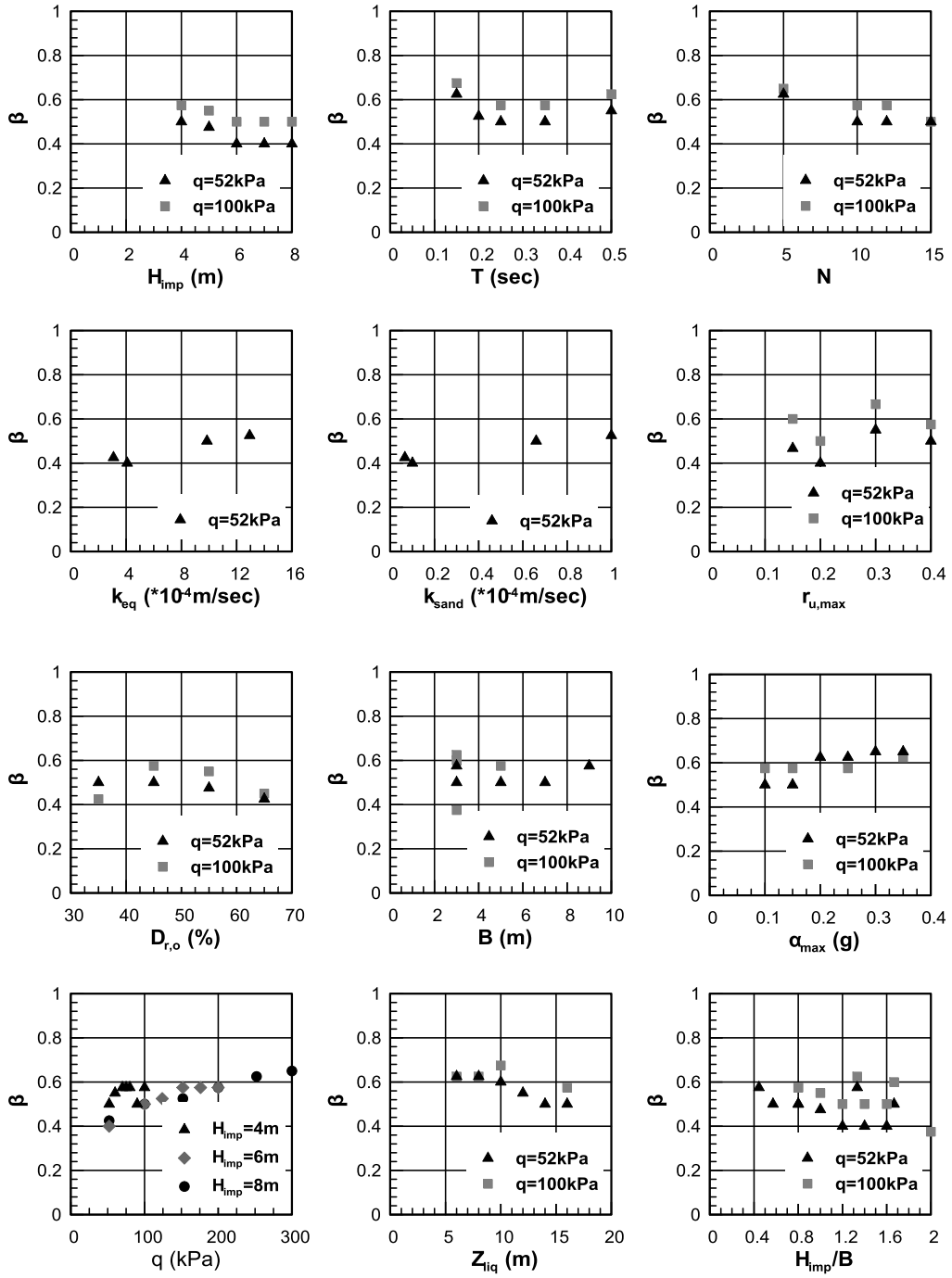

Figure 9.19: Variation of parameter β against each problem parameter.

It is thus concluded that the examined problem parameters have relatively little effect on the obtained ***β*** values. Hence, ***β*** is not expressed through another analytical expression, but instead the average value from all numerical analyses will be considered. To gain more insight regarding the range of variation of the specific parameter, **Figure 9.20** summarizes all the numerically obtained ***β*** values plotted against the ultimate degraded bearing capacity q_{ult}^{num}(kPa). Based on that, ***β*** is set equal to:

$$\beta = 0.54 \pm 0.08 \qquad 9.13$$

The minimum and maximum values are equal to β_{min}=0.375 and β_{max}=0.675 respectively.

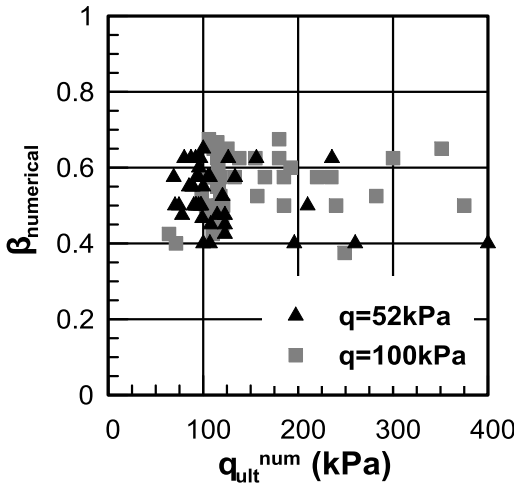

Figure 9.20: Range of variation of parameter β against the numerically derived values of degraded bearing capacity $q_{ul.t}^{num}$ (kPa).

Excess pore pressure ratio in the transition zone U_2.- Parameter U_2, corresponds to the average excess pore pressure ratio in the transitional non-liquefied zone of the natural ground and is estimated as the average between U_1 and the excess pore pressure ratio in the liquefied soil, which equals unity. Thus, U_2 is equal to:

$$U_2 = \frac{(1+U_1)}{2} = \frac{(1+\beta U_{design})}{2} \qquad 9.14$$

Initial Friction angle for each layer $\varphi_{i,ini}$.- Since the seismic response of the soil profile is described with the use of the NTUA-SAND constitutive model, the initial friction angle values assigned to each layer are chosen based on the model's predictions. The NTUA-SAND model friction angle predictions under TX-Compresion, TX-Extension and DSS loading conditions are

summarized in **Figures B.52** to **B.54** of Appendix B, for three different initial vertical stress levels and the entire range of encountered relative densities. Note that, the particular predictions refer to both drained and undrained conditions. Since loading and drainage conditions are not uniform across the activated failure surface, initial friction angle values for both layers are estimated, based on *Equation 9.15,* considering the average among TX Compresion, TX Extension and Direct Simple Shear loading under undrained and drained conditions.

$$\phi_{i,ini} = \frac{\phi_{i,TX-C} + \phi_{i,TX-E} + \phi_{i,DSS}}{3} \qquad 9.15$$

Coefficient K_s.- This parameter reflects the shear strength mobilized across the partially liquefied improved and transitional soil zones, below the edges of the footing. The developing mechanism is schematically demonstrated in **Figure 9.21.**

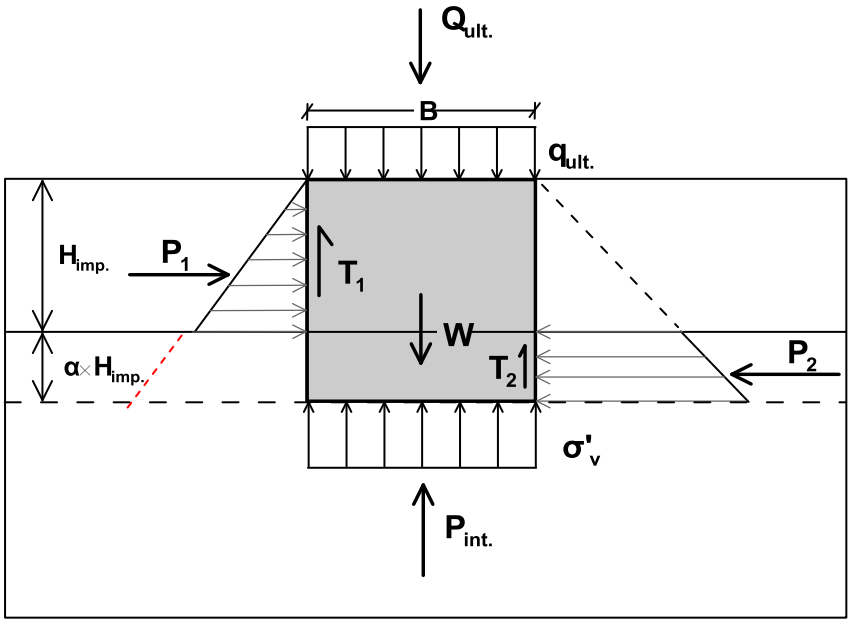

Figure 9.21: Punch through mechanism and developing forces for the determination of coefficient K_s.

The forces appearing in the figure are explained below:

- $Q_{ult.}$(kN/m) is the ultimate load to cause post-shaking failure of the shallow foundation and is computed based on *Equation 9.16* :

$$Q_{ult.} = q_{ult}^{num} B \qquad 9.16$$

where q_{ult}^{num}(kPa) = the numerically derived ultimate bearing capacity of the foundation

B(m) = the width of the footing

- Weight (W) of the soil is estimated as follows:

$$W = \gamma' \times (1+\alpha) H_{imp} \times B \qquad 9.17$$

where γ'=the effective unit weight of the soil

$H_{imp.}$(m) = the thickness of the improved layer

α = the portion by which the thickness of the improved layer is increased in order to account for the development of the transition zone

B(m) = the width of the footing

- $P_{int.}$(kN/m) is the force developing at the interface between the transition zone and the totally liquefied soil underneath the footing. It is computed using *Equation 9.18*:

$$P_{int} = \sigma'_v B \qquad 9.18$$

where σ'_v(kPa) = the numerical effective vertical stresses measured at the specific depth

- Shear force T is composed of two components (T_1 and T_2) corresponding to the shear strength developing across the sides of the improved layer and the transition zone respectively. It can be readily shown that the particular forces are computed based on the following *Equations 9.19* and *9.20* respectively:

$$T_1 = K_s P_1 = \frac{1}{2}\gamma' H_{imp}^2 K_s \tan\phi_{1,deg} \qquad 9.19$$

$$T_2 = K_s P_2 = \frac{1}{2}\gamma' H_{imp}^2 K_s [(1+\alpha)^2 - 1]\tan\phi_{2,deg} \qquad 9.20$$

Applying force equilibrium in the vertical direction, it comes out that:

$$P_{int.} + 2\times T = W + Q_{ult.},$$

yielding the following analytical expression for K_s:

$$K_s = \frac{W + Q_{ult.} - P_{int.}}{\gamma' H_{imp}^2 \left\{ \tan\phi_{1,deg} + \left[(1+\alpha)^2 - 1 \right] \tan\phi_{2,deg} \right\}} \qquad 9.21$$

To gain insight regarding the magnitude of K_s, and derive a suitable analytical expression, K_s was estimated according to *Equation 9.21* for 27 cases, which are summarized in **Table 9.1**. The degraded values of the required friction angles, $\varphi_{deg,i}$ which depend on the excess pore pressure ratios U_1 and U_2, defined earlier, as well as coefficient α were considered equal to the numerically derived values for each numerical analysis. It was thus found that K_s depends mainly on the normalized thickness of the improved zone $H_{imp.}/B$, as well as on the bearing pressure q(kPa). These effects are graphically shown in **Figure 9.22a** & **b**, which also explain the following analytical expression for the computation of K_s:

$$K_s = C_{K_s}\left(\frac{q}{p_\alpha}\right)^{-0.30}\left(\frac{H_{imp}}{B}\right)^{-0.50} \qquad 9.22$$

where p_α = 98.1kPa is the atmospheric pressure.

Coefficient C_{Ks} takes an average value equal to 1.00 with a Standard Deviation equal to St.Dev.=±0.15. The minimum and maximum values were estimated equal to $\mathbf{C_{Ks,min}=0.75}$ and $\mathbf{C_{Ks,max}=1.30}$ respectively.

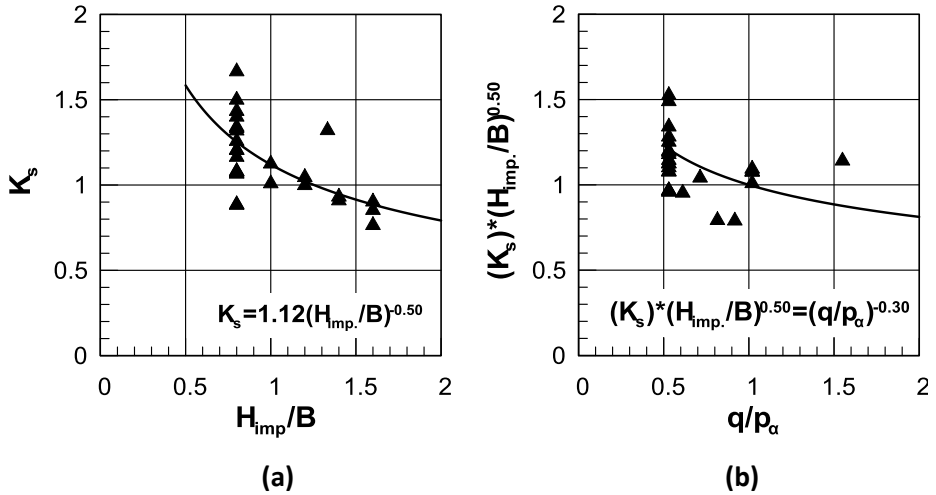

Figure 9.22: Variation of **(a)** K_s coefficient against H_{imp}/B ratio and resulting power fitting (with the black line) **(b)** $K_s/(H_{imp}/B)0.50$ against contact pressure q normalized against the atmospheric pressure p_α=98.1kPa and resulting power fitting (with black line).

The accuracy of *Equation 9.22*, for the average value of C_{Ks} = 1.00, is evaluated in **Figure 9.23a** & **b**. The numerically derived values of K_s are plotted on a one-to-one basis against the analytically predicted ones in **Figure 9.23a,** while the relative error is plotted against the

analytical predictions in **Figure 9.23b**. It can be observed that the scatter of the data points is rather narrow (±30% of the numerical predictions), with only a few cases overestimating K_s. This particular observation was taken into account when proposing minimum and maximum C_{Ks} values.

Table 9.1: Analyses considered for the evaluation of the K_s coefficient.

	H_{imp}	B (m)	q (kPa)	q_{ult} (kPa)	$F.S._{deg}$	$D_{r,o}$ (%)	Z_{liq} (m)	T (sec)	α_{max} (g)	N	K_s
1	4	5	52	82	1.57	45	16	0.35	0.15	10	1.08
2	**5**	5	52	96	1.85	45	16	0.35	0.15	10	1.12
3	**6**	5	52	165	3.17	45	16	0.35	0.15	10	1.05
4	**7**	5	52	235	4.52	45	16	0.35	0.15	10	0.93
5	**8**	5	52	360	6.92	45	16	0.35	0.15	10	0.76
6	4	**3**	52	116	2.24	45	16	0.35	0.15	10	1.32
7	4	5	**60**	72	1.20	45	16	0.35	0.15	10	1.07
8	4	5	**70**	87	1.24	45	16	0.35	0.15	10	1.16
9	4	5	**80**	100	1.25	45	16	0.35	0.15	10	0.89
10	4	5	**90**	98	1.09	45	16	0.35	0.15	10	0.88
11	**6**	5	**100**	150	1.50	45	16	0.35	0.15	10	1.00
12	**8**	5	**100**	300	3.00	45	16	0.35	0.15	10	0.85
13	**8**	5	**152**	174	1.14	45	16	0.35	0.15	10	0.90
14	**5**	5	**100**	100	1.00	45	16	0.35	0.15	10	1.01
15	**7**	5	**100**	195	1.95	45	16	0.35	0.15	10	0.91
16	4	5	52	98	1.88	**55**	16	0.35	0.15	10	1.07
17	4	5	52	112	2.15	**65**	16	0.35	0.15	10	1.20
18	4	5	52	75	1.44	45	**14**	0.35	0.15	10	1.34
19	4	5	52	83	1.60	45	**12**	0.35	0.15	10	1.43
20	4	5	52	87	1.67	45	**10**	0.35	0.15	10	1.67
21	4	5	52	125	2.40	45	**8**	0.35	0.15	10	1.50
22	4	5	52	135	2.60	45	**6**	0.35	0.15	10	1.40
23	4	5	52	91	1.75	45	16	**0.25**	0.15	10	1.08
24	4	5	52	90	1.73	45	16	**0.5**	0.15	10	1.21
25	4	5	52	73	1.40	45	16	0.35	**0.25**	10	1.33
26	4	5	52	95	1.83	45	16	0.35	**0.35**	10	1.26
27	4	5	52	85	1.64	45	16	0.35	0.15	**12**	1.32

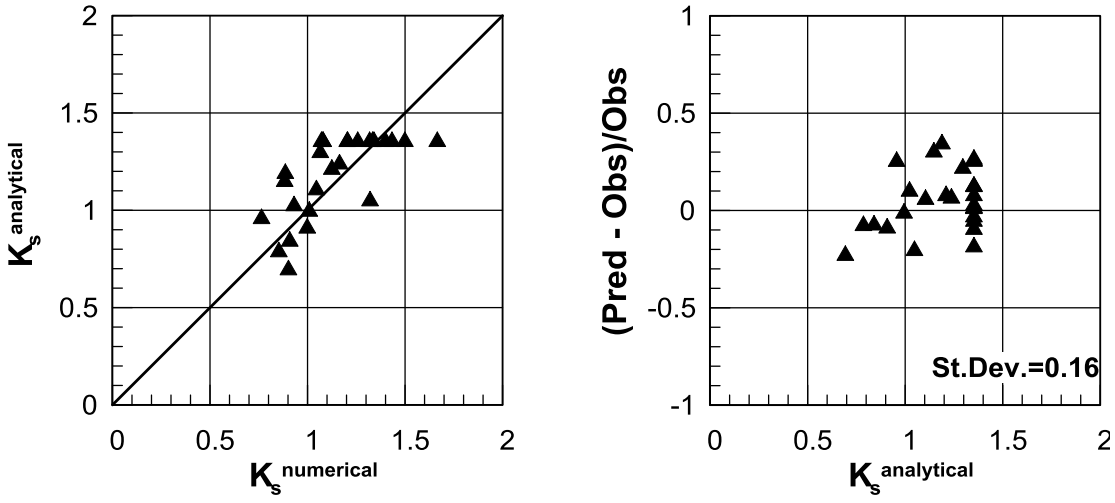

(a) **(b)**

Figure 9.23: **(a)** One-to-one comparison of predicted K_s against numerically computed values **(b)** Relative error of predicted values and standard deviation.

Excess pore pressure ratio in the liquefied ground *U_3*.- The excess pore pressure ratio ***U_3*** refers to the liquefied ground, over a representative area underneath the footing and below the improved crust. To gain insight regarding the variation of U_3, its value has been back-calculated considering the numerically derived values for ***α***, ***U_1***, (and hence ***U_2***) and q_{ult} and the initial values for the friction angles ***$\varphi_{ini1,2}$*** described earlier.

Following a sensitivity analysis on the ***U_3*** dependence on the various problem parameters, it was concluded that the various effects could be collectively represented through a composite problem variable, namely the degraded ultimate bearing capacity $q_{ult.}$ at the end of shaking. This is shown in **Figure 9.24**, where the back-calculated values of ***U_3*** are related to the ultimate bearing capacity ratio q_{ult}/p_a. Observe that all data points form a narrow band fitted by the following average analytical relation:

$$U_3 = C_{U_3}\left(\frac{q_{ult}}{p_\alpha}\right)^{-0.18} \leq 1.00 \qquad 9.23$$

The average C_{U3} coefficient is equal to 0.86 with a Standard Deviation equal to ±0.03, while the minimum and maximum values are **$C_{U3,min}$=0.81** and **$C_{U3,max}$=0.95**.

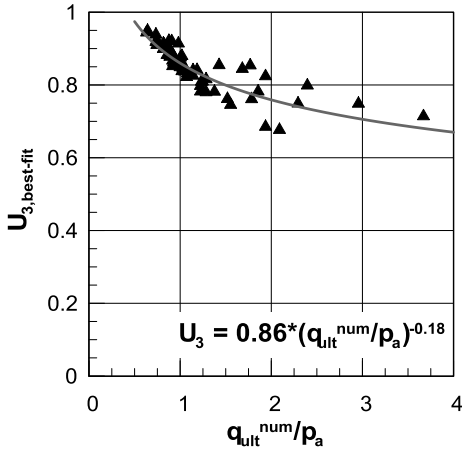

Figure 9.24: Back-calculated values of U_3 plotted against the numerically obtained values of degraded bearing capacity $q_{ult.}^{num}$ normalized against the atmospheric pressure p_a=98.1kPa.

The accuracy of *Equation 9.23* is evaluated in **Figure 9.25a** & **b**. Namely, the back-calculated values of U_3 are plotted in **Figure 9.25a** against the analytical predictions, in a one-to one comparison, while the relative prediction error is plotted against the numerically derived ultimate bearing capacity ratio $q_{ult.}^{num}/p_\alpha$ in **Figure 9.25b.** It is observed that the scatter of the data points is relatively narrow, and the relative error is less than ±10% (St.Dev. = 4%).

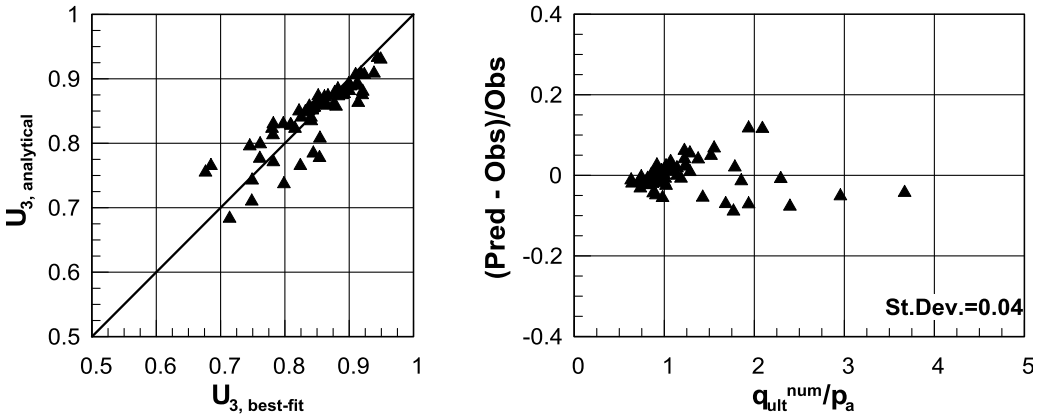

Figure 9.25: (a) One-to-one comparison of analytically predicted versus back-calculated U_3 values (b) Relative error of predicted values against $q_{ult.}^{num}/p_\alpha$.

9.3.3 Analytical computation of q_{ult}^{deg}

Following the analytical definition of the parameters required for the computation of the degraded bearing capacity, the associated relationships will be applied for all *parametric* numerical analyses in order to evaluate the overall accuracy of the proposed methodology. It is noted in advance that, due to the dependence of $\boldsymbol{U_3}$ on q_{ult} the relevant equations (*Equations 9.10* and *9.23)* are solved concurrently. Two different iterative procedure are used for this purpose, as explained below.

Simplified itterative solution.- The associated analytical expressions are programmed in an Excel spreadsheet and, based on the available input data, all necessary parameters are evaluated. In the sequel, the proposed methodology is solved iteratively, following the Steps outlined below:

Step 1: An initial value for $\boldsymbol{U_{3,i}}$ is assumed and the ultimate bearing capacity $q_{ult.}^{analyt}$ is computed from *Equation 9.10*.

Step 2: The above value of $q_{ult.}^{analyt}$ is introduced to *Equation 9.23* and a new excess pore pressure ratio $\boldsymbol{U_{3,i+1}}$ is calculated

Step 3: The relative error between the values of $\boldsymbol{U_3}$ obtained in Steps 1 & 2 is calculated as follows:

$$U_{3,rel.err.} = \frac{\left|U_{3,i+1} - U_{3,i}\right|}{U_{3,i}} \qquad 9.24$$

Step 4: If the resulting relative error is greater than 0.001, the average of the computed values of $\boldsymbol{U_3}$ (i.e $U_{3,i}$ and $U_{3,i+1}$) is derived and Steps 1 to 3 are repeated. The constraint of $U_{3i+2} \leq 1.00$ also applies in the current calculation step.

The iterative procedure is repeated, separately for each parametric nuumerical analysis, until the relative error becomes less than 0.001.

Automated iterative solution.- To facilitate and speed up the calculation process, the iterative solution may also be performed using the Solver Add-In, which is a built-in tool for Excel spreadsheet computations. The particular application is based on the optimization method of Lagrange multipliers, "*which is a strategy for finding the local maxima or minima of a function subject to equality constraints".* In its generalized form, the particular optimization method requires two different functions, namely f(x,y) and g(x,y), which are somehow interrelated. For example, the minimization of function f(x,y) may be requested,

while function g(x,y) is subject to a specific condition i.e. g(x,y)=c. To satisfy the requested condition, the method is based on deriving the gradients of the two functions, therefore for the application of the specific method the functions f(x,y) and g(x,y) need to have continuous first partial derivatives. In the optimization process a new extra variable (λ), called Lagrange multiplier, is introduced and defined as:

$$\Lambda(x,y,\lambda)=f(x,y)+\lambda[g(x,y)-c] \qquad 9.25$$

The auxiliary function presented above is solved by adding or subtracting the Lagrange multiplier λ to satisfy the following condition:

$$\nabla_{x,y,\lambda}\Lambda(x,y,\lambda)=0 \qquad 9.26$$

In our case, the solution process follows the steps outlined below:

Step 1: A starting value for U_3 is assumed and the ultimate bearing capacity $q_{ult.}^{U3}$ is computed from *Equation 9.10*.

Step 2: Considering the same starting value for U_3 the ultimate bearing capacity $q_{ult.}^{analyt}$ is computed from *Equation 9.23*.

Step 3: The relative error between the two obtained values of $q_{ult.}$ is calculated based on *Equation 9.27*:

$$q_{ult.rel.err.}=\frac{\left|q_{ult.}^{analyt.}-q_{ult.}^{U3}\right|}{q_{ult.}^{analyt.}} \qquad 9.27$$

Step 4: In the sequel, U_3 is automatically altered until satisfaction of the requested convergence condition. The convergence critetion is specified by the user and in the particular case is set to $q_{ult.rel.err.}$ = 0.001

Additionally, throughout the iterative procedure U_3 is constrained to be less than or equal to unity, i.e $U_3 \leq 1.0$.

Evaluation of analytical predictions.- Considering the average values of the C_i coefficients in *Equations 9.12*, *9.13*, *9.22*, and *9.23* both convergence approaches, described above, were applied for the assessment of excess pore pressure ratio U_3 and the associated post-shaking ultimate bearing capacity $q_{ult}^{analytical}$. Obtained **U_3** values with the two approaches turned out to be indentical for the majority of the numerical analyses outlined in the previous Chapter. In some cases though, Solver Add-In did not converge to a feasible solution which satisfied the convergence condition dictated in *Equation 9.27*. This occured for large values of **U_3**,

close to unity, where *Equation 9.23* does not have a continuous first partial derivative, as required by the Lagrange multiplier method. To deal with this particular inconsistency, it was decided to preserve the Solver Add-In result for relative error values less than 5% and adopt the result from the simplified method in the remaining cases (namely set $\mathbf{U_3}$ equal to unity and obtain a convervative prediction for the ultimate degraded bearing capacity $q_{ult}^{analytical}$).

The resulting analytical predictions for the ultimate degraded bearing capacity $q_{ult}^{analytical}$, the degraded Factor of Safety $F.S._{deg}^{analytical}$, and the inverse of the degraded Factor of Safety $1/F.S._{deg}^{analytical}$ are evaluated in

Figure 9.26**.** Additionally, the inverse of the degraded Factor of Safety $1/F.S._{deg}^{analytical}$ is plugged into *Equation 9.6* for the computation and the subsequent evaluation of seismic settlement ratio $\rho_{dyn}^{analytical}/B$. The grey data points in all graphs, correspond to the non-converging cases according to the conditions discussed previously. The left column of figures summarizes the one-to-one comparison between the analytical predictions against the numerically observed values, while the right column plots summarize the relative error in the prediction of the above quantities in relation to the analytically derived values.

Observe that, despite the caution exercised in calibrating the analytical methodology for the computation of $q_{ult.}$, it becomes strikingly over-conservative for low values of $q_{ult.}$ (< 150 kPa), whereas it is consistently under-conservative for larger $q_{ult.}$values. The above observation has an immediate effect on the derived degraded factor of safety $F.S._{deg}$, as well as on seismic settlements computation $\rho_{dyn.}$

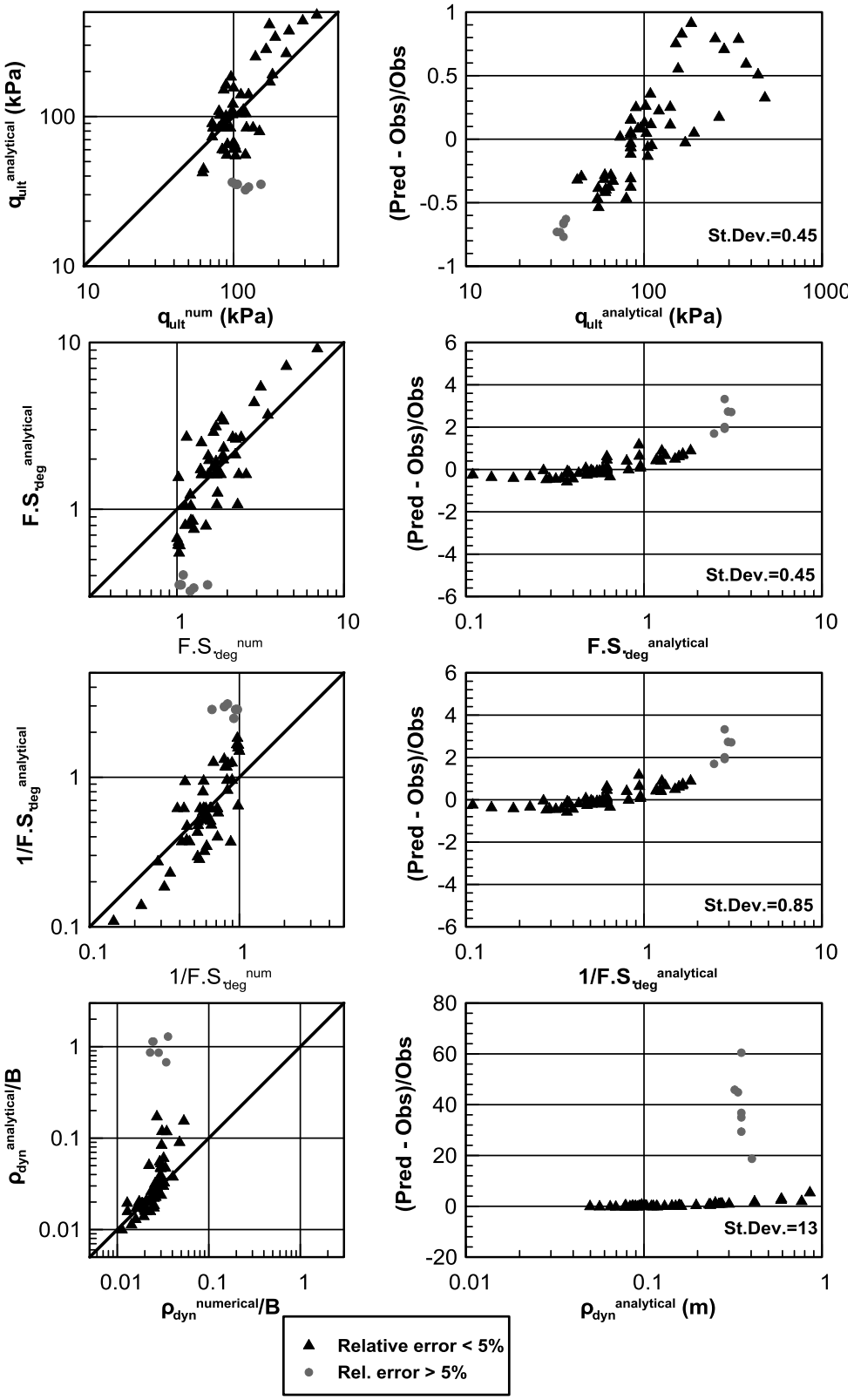

Figure 9.26: Overall evaluation of analytical predictions in terms of q_{ult}, $F.S._{deg}$, $1/F.S._{deg}$ and ρ_{dyn}/B.

9.3.4 Correction of the degraded Factor of Safety F.S.deg

To improve the accuracy of the proposed methodology, the analytically obtained value of $F.S._{deg}$ is corrected, in view of the relative error in predicted q_{ult}, shown in **Figure 9.27**. Namely, the degraded factor of safety obtained analytically, based on the Meyerhof and Hanna failure mechanism is considered as a "bearing capacity index" and is hereafter referred to as $F.S._{deg}^{*}$. In the sequel, the "actual" value of the degraded Factor of Safety $F.S._{deg}$ is re-evaluated by applying the depicted mathematical expressions, each one corresponding to a different level of conservatism. Namely, the equation plotted with the black line corresponds to a best-fit approach, and when solving for the Observed value, the following *Equation 9.28* results:

$$F.S._{deg} = \frac{F.S._{deg}^{*}}{0.05 + 0.60\left(F.S._{deg.}^{*}\right)^{0.85}} > 0.60F.S._{deg}^{*} \qquad 9.28$$

The above correction is applied to all analytical predictions and the final outcome is summarized and evaluated in **Figure 9.28**, preserving the layout described in **Figure 9.26**. Evidently, the corrected analytical predictions for the degraded bearing capacity qult. have improved, presenting a significantly narrower scatter around the diagonal. Note that the corrected analytical predictions appear to slightly overestimate $q_{ult.}$, nevertheless the obtained relative error has been considerably reduced as proven by the Standard Deviation, which is estimated equal to St.Dev.=0.22. Additionally, the predictions for the degraded Factor of Safety, $F.S._{deg.}$, are in very good agreement with the numerical observations. Indeed, the specific parameter no longer receives values less than unity, indicating post-shaking failure of the foundation, which did not occur in any of the performed numerical analyses. Moreover, the obtained relative error is decreased compared to the initial prediction, ranging roughly between ±40% with a reduced Standard Deviation equal to St.Dev.=0.22.

The previous satisfactory agreement is preserved with respect to the inverse $F.S._{deg.}$, and the predicted dynamic settlements. Indeed, the $\rho_{dyn}{}^{analyt.}/B$ ratio compares consistently well with the associated numerical predictions. Namely, the data points appear evenly distributed around the diagonal, with a minor tendency to underestimate dynamic settlements in the higher range of ρ_{dyn}/B. Moreover, as a result of the appropriate estimation of $1/F.S._{deg.}$, dynamic settlements are satisfactorily predicted by ±22%, as dictated by the standard deviation in the relative error.

Conservative (Upper bound) predictions.- The previous approach, provided the best-fit evaluation of the degraded factor of safety $F.S._{deg.}^{analytical}$ and the associated seismic settlements ρ_{dyn}. Taking into account the complexity of the problem analyzed herein, and the associated uncertainties in the proposed soil-foundation model, *Equation 9.29*, also plotted in **Figure 9.27** with the grey line, provides a reasonable upper bound (conservative) prediction for the degraded factor of safety:

$$F.S._{deg} = \frac{F.S._{deg}^{*}}{0.20 + 0.60\left(F.S._{deg.}^{*}\right)^{0.85}} > 0.55 F.S._{deg}^{*} \qquad 9.29$$

The conservative analytical predictions according to *Equation 9.29* are presented in **Figure 9.29**, following the same layout as in **Figure 9.26** and **Figure 9.28**. It is now observed that the analytical methodology overall underestimates the degraded bearing capacity $q_{ult.}$(kPa) throughout the examined range of $q_{ult.}$, with only few exceptions. The calculated relative error is reduced and appears to be restrained between -50% and +20%, with a Standard Deviation equal to St. Dev. = 0.19. Additionally, the degraded Factor of Safety $F.S._{deg}$ also appears to be underestimated in most cases, as opposed to the best-fit solution, whereas the obtained relative error is also reduced with a Standard Deviation equal to St. Dev. = 0.19.

The above observation is not verified in the case of the inverse of $F.S._{deg.}$, which appears slightly overestimated, with the associated relative error ranging between -20% and +50% with a higher Standard Deviation equal to St. Dev. = 0.29, compared to the best-fit solution. This has an immediate impact on the obtained dynamic settlements, ρ_{dyn}, which present a clear tendency for overprediction in the majority of cases. This is also evident in the obtained relative error. Indeed, standard deviation of relative error has increased from St. Dev.=0.22 to St. Dev.=0.54.

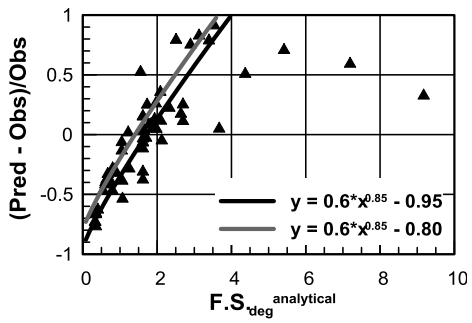

Figure 9.27: Correction factors applied upon the analytically computed degraded factor of safety $F.S._{deg}$.

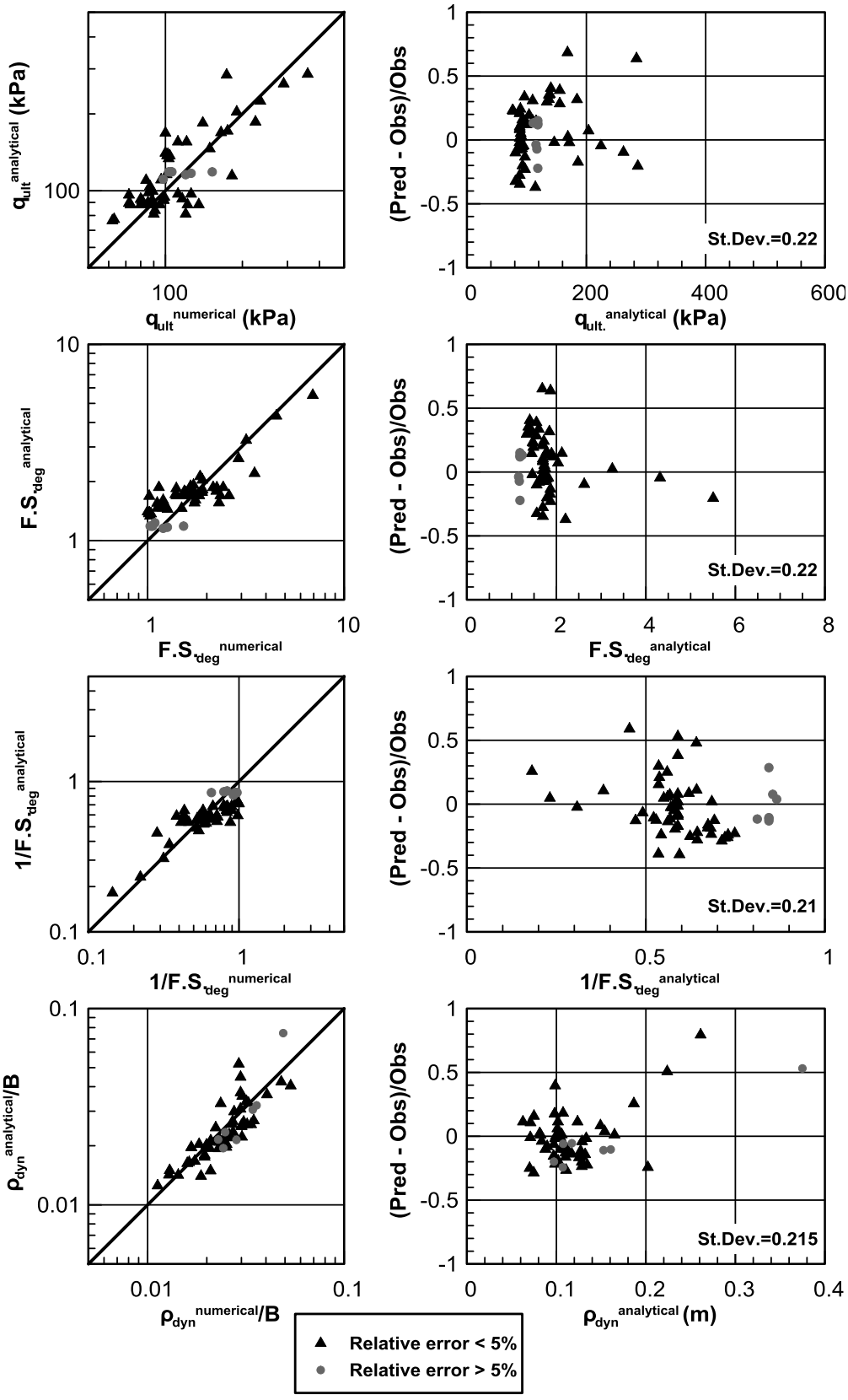

Figure 9.28: Overall evaluation of analytical predictions after the $F.S._{deg}$ correction in terms of q_{ult}, $F.S._{deg}$, $1/F.S._{deg}$ and ρ_{dyn}/B.

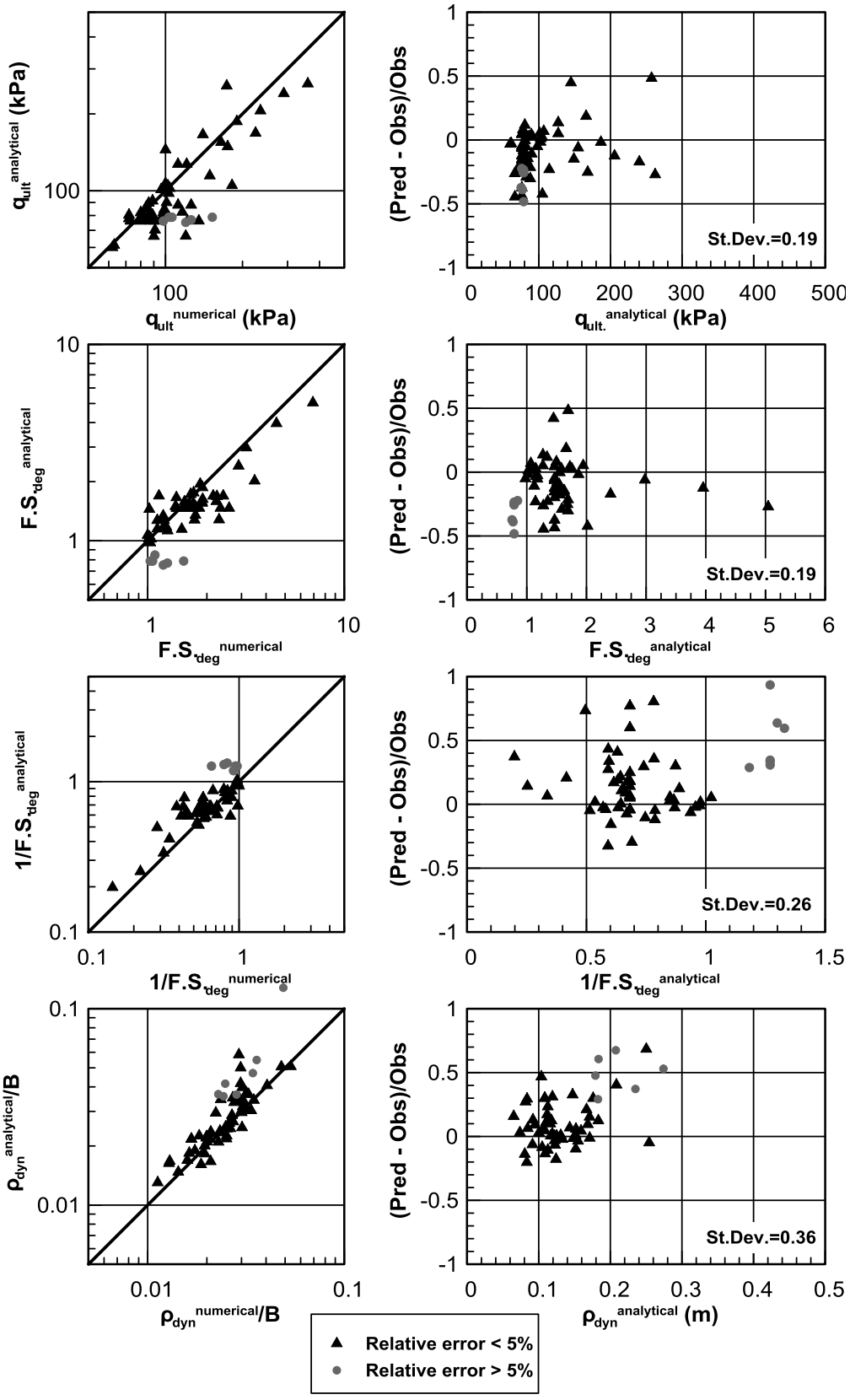

Figure 9.29: Overall evaluation of analytical predictions after the upper bound $F.S._{deg}$ correction in terms of q_{ult}, $F.S._{deg}$, $1/F.S._{deg}$ and ρ_{dyn}/B.

CHAPTER 10

Effect of Ground Improvement Dimensions

10.1 Introduction

The analytical methodology developed in the previous chapter is applicable to "infinitely" extending two-layered soil profiles, hence it does not incorporate the influence of the lateral extend of the performed improvement (L_{imp}). The specific parameter is necessary in the design of the required improvement scheme, and is generally determined in accordance to the ground improvement method.

In the following, the available guidelines are summarized for determining the soil improvement area when using the ground compaction method. Note that, in all guidelines, the depth of improvement extends down "*to the deepest part of the liquefiable soil layer*", following standard practice procedures. Furthermore they do not provide quantitative means for evaluating the foundation performance in the case of a smaller or a larger area is improved.

Japanese Fire Defense Agency (1978).- The JFDA guidelines for oil tanks recommend that the soil improvement area, in excess to the footing width, also denoted as SL, equals two thirds of the improvement depth and must be within 5m < SL < 10m, as illustrated in **Figure 10.1**.

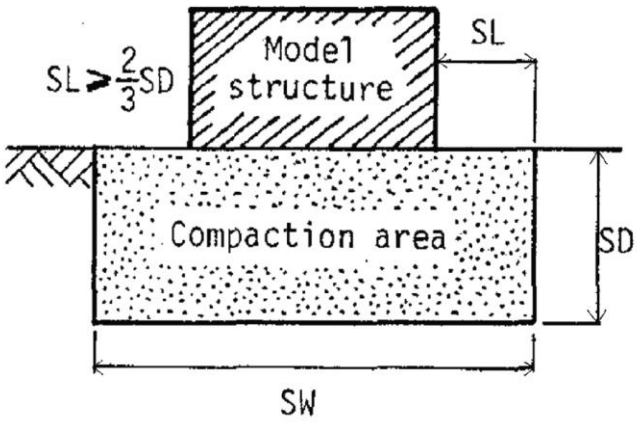

Figure 10.1: Design of soil improvement area of tank foundation.

Thuchida et al. (1976).- recommends that the improvement width around a slightly embedded structure is correlated to the friction angle (ϕ) of the soil as presented in **Figure 10.2**. Specifically, α_1 is the passive failure angle and α_2 the active failure angle, also defined in the figure. SD is the depth of improvement, which, as stated earlier, equals the total thickness of the liquefiable layer.

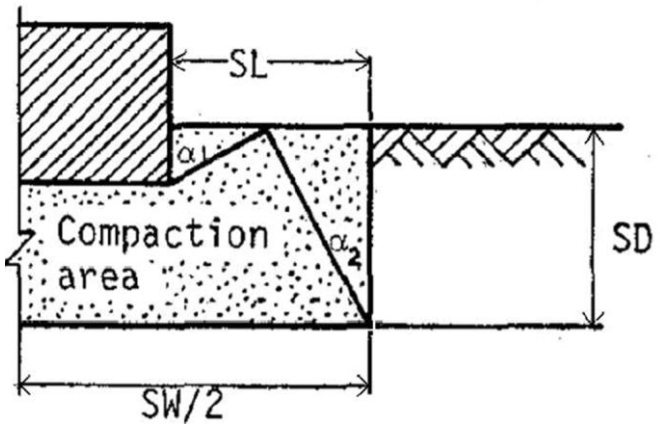

α_1: Passive failure angle = $45^o + \phi/2$

α_2: Active failure angle= $45^o - \phi/2$

Figure 10.2: Specification of lateral extent of improvement based on the friction angle of the soil (Thuchida et al.,1976).

PHRI (1997).- The Port & Harbour Research Institute widely refers to the work performed by Iai et al. (1991) covering the required improvement extend for various types of structures. In the specific study, the excess pore pressure ratio r_u appears to be the controlling design parameter. Namely, based on undrained cyclic loading laboratory test results, excess pore pressure ratio values r_u below 0.5 induced practically negligible loss of strength in the sand specimen. On the contrary, for r_u values above 0.5, the cyclic shearing led to significant shear strength loss in the soil and should be accounted for in the design.

According to Iai et al. (1991), the shear strength of the liquefied un-improved soil should be considered totally lost, especially for loose to medium sands. Moreover, they indicated that the area in which r_u exceeds 0.5 is adequately described by the area ACD in **Figure 10.3**. Therefore, the particular area does not contribute to the bearing capacity of the soil, which depends only on the shear resistance mobilized along the surface EFG. Hence, given the depth of improvement, the extent of the improvement area is associated to the above surface, which provides the necessary shear resistance to ensure the stability of the foundation. Moreover, pressures from the liquefied sand may also be included in the stability analysis of the structure. The specific static pressure corresponds to an earth pressure coefficient K_o=1 after subtracting the dynamic earth pressures. The particular pressures are applied upon the GG' surface.

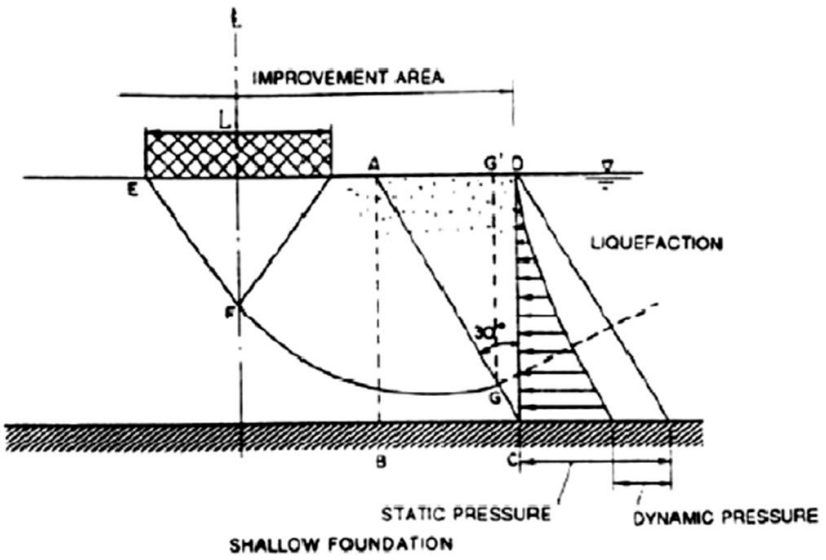

Figure 10.3: Schematic figure to determine improvement area against liquefaction for a shallow foundation (Iai et al., 1991).

Based on the above, it appears that there are relatively few experimental studies that examine the effect of the improvement width on the seismic response of shallow foundations, so that the limits, given by regulations, define a simple extend for common applications. Moreover, all guidelines assume the treatment of the entire thickness of the liquefiable soil, which may potentially lead to over-conservative and costly improvement solutions.

In the above context, the influence of the lateral extend of the applied improvement is numerically investigated through a separate set of analyses, which are presented in section **10.2** below. Namely, the effect of the improvement width (L_{imp}) on the dynamic settlements (ρ_{dyn}) and the degraded Factor of Safety ($F.S._{deg}$) is quantified with reference to the results for "infinite" ground improvement (i.e. $L_{imp} \rightarrow \infty$), discussed extensively in the previous chapter. Particular modifications are further compared to the existing guidelines mentioned earlier and an updated set of design charts is developed for application.

10.2 Description of numerical analyses

The plan of parametric analyses is summarized in **Table 10.1** and consists of 12 different sets, which exhibit different soil, excitation and geometric characteristics. Each set examines the effect of an individual parameter, the value of which appears in the second column of the table. The remaining problem parameters are given the values of the reference analysis, namely: q = 52kPa, $D_{r,o}$ = 45%, Z_{liq} = 16m, H_{imp} = 4, B = 5m, a_{max} = 0.15g, N = 5, and T = 0.35s. Moreover, in each set, the infinitely extending improved layer is considered the reference analysis, and subsequently, the width of the improved layer (L_{imp}) is progressively reduced down to nearly the width B of the footing itself. The different values of L_{imp} normalized against the footing width B, are listed in the last column of the table. **Figure 10.4** presents the basic symbol definitions associated with the geometry of the examined problem.

The assumptions of the numerical methodology, as well as the three distinct phases of the loading sequence, have been thoroughly explained in Chapter 8, and are maintained in the present numerical investigation. It is observed that the L_{imp}/B ratio systematically receives values greater than unity. The particular observation is attributed to numerical reasons and particularly to the simulation approach of the shallow footing. As mentioned in Chapter 8, the numerical simulation of the bearing pressure q of the shallow footing is performed through applying vertical velocity at specific gridpoints. This velocity varies linearly from the value at the last gridpoint upon which it is applied, to zero at the adjacent gridpoint. Hence,

half the width of the adjacent zones should be added to the actual footing width. On the other hand, soil properties are assigned to zones, implying that the width of the improved zone is always going to be at least equal to the number of zones upon which the bearing stresses are applied, further increased by two, one at each side of the footing.

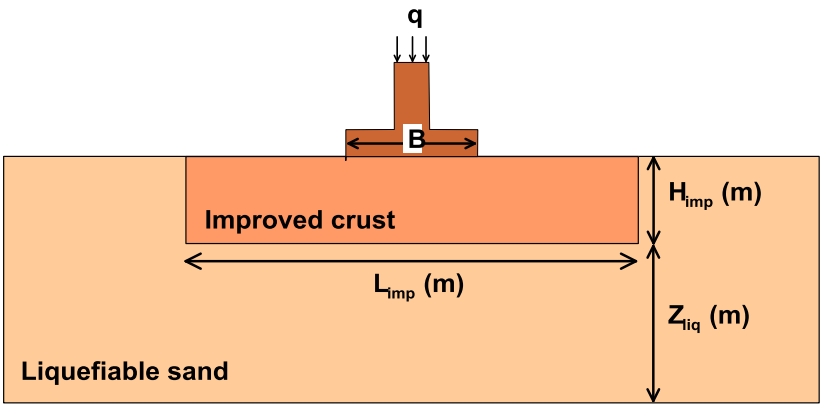

Figure 10.4: Definition of basic symbols.

Table 10.1: Overview of numerical analyses.

Case No.	Examined Parameter	L_{imp}/B
1	q= 52Kpa	1.2, 2, 5.4, 7.8, 10.2, 12, 13.2, 14.8, 17.2, 19.6, 21
2	B=3m	1.3, 4, 7.3, 12.33, 17,21
3	D_{ro}= 55%	1.2, 2, 5.4, 7.8, 10.2, 12, 13.2, 14.8, 17.2, 19.6, 21
4	Z_{liq} = 8m	1.2, 2, 5.4, 10.2, 13.2, 14.8, 17.2, 19.6
5	Z_{liq} = 12m	1.2, 2, 5.4, 10.2, 13.2, 14.8, 17.2, 19.6, 21
6	a_{max}= 0.30g	1.2, 2, 5.4, 7.8, 10.2, 12, 13.2, 14.8, 17.2, 19.6, 21
7	N= 5	1.2, 2, 5.4, 10.2, 13.2, 14.8, 17.2, 19.6, 21
8	T= 0.50sec	1.2, 2, 5.4, 7.8, 10.2, 12, 13.2, 14.8, 17.2, 19.6, 21
9	H_{imp}=6m	1.2, 2, 5.4, 10.2, 13.2, 14.8, 21
10	H_{imp}= 8m	1.2,2, 5, 5.4, 9.8, 13.4, 15.2, 20, 24.8
11	H_{imp}=6m (a_{max}=0.30g)	1.2, 2, 5.4, 10.2, 13.2, 14.8, 21
12	H_{imp}= 8m (a_{max}=0.30g)	1.2, 2, 5, 5.4, 9.8, 13.4, 15.2, 20, 24.8

10.3 Effect of L_{imp} on earthquake-induced foundation settlements ρ_{dyn} (m).

To visualize the effect of the lateral extent of the improved zone (L_{imp}) on the accumulation of dynamic settlements (ρ_{dyn}), **Figure 10.5** summarizes the obtained dynamic settlements (ρ_{dyn}) from the entire group of analyses, plotted against L_{imp}/B ratio. In each set of analyses the obtained dynamic settlements appear normalized against the corresponding value for conditions of "infinite" improvement (ρ_{dyn}^{inf}). The black colour corresponds to the baseline analysis (case No. 1 in **Table 10.1**), while the data sets examining the effect of the different problem parameters are plotted with different tints of grey.

Based on the particular plot, it is concluded that, among the examined parameters, only the thickness of the improved zone (H_{imp}) is significantly influencing the accumulation of dynamic settlements for different L_{imp} configurations. All other parameters have a relatively minor effect, which may be initially neglected in the formulation of the corresponding analytical expression for ρ_{dyn}. Hence, the effects of the width (L_{imp}) and depth (H_{imp}) of the improved zone are independently examined for the formulation of a suitable analytical expression as described in the following sections. To produce a dimensionless expression, both parameters (L_{imp} and H_{imp}) are normalized hereafter against the footing width B.

Effect of L_{imp}/B.- Based on **Figure 10.3**, the trend of the inverse of the normalized dynamic settlement ($\rho_{dyn}^{inf}/\rho_{dyn}$) ranges between zero and unity as the ratio of L_{imp}/B ranges between zero to "infinite" improvement. The particular trend is mathematically expressed below:

$$\frac{\rho_{dyn}^{inf}}{\rho_{dyn}} = 1 - \exp\left[-C_1 \left(\frac{L_{imp}}{B} \right)^{C_2} \right] \qquad 10.1$$

To visualize the effect of L_{imp}/B on the ratio of dynamic settlements $\rho_{dyn}^{inf}/\rho_{dyn}$, *Equation 10.1* is re-arranged, as described in *Equation 10.2*, and plotted in a logarithmic axis-system as illustrated in **Figure 10.6**.

$$-\ln\left(1 - \frac{\rho_{dyn}^{inf}}{\rho_{dyn}} \right) = C_1 \left(\frac{L_{imp}}{B} \right)^{C_2} \qquad 10.2$$

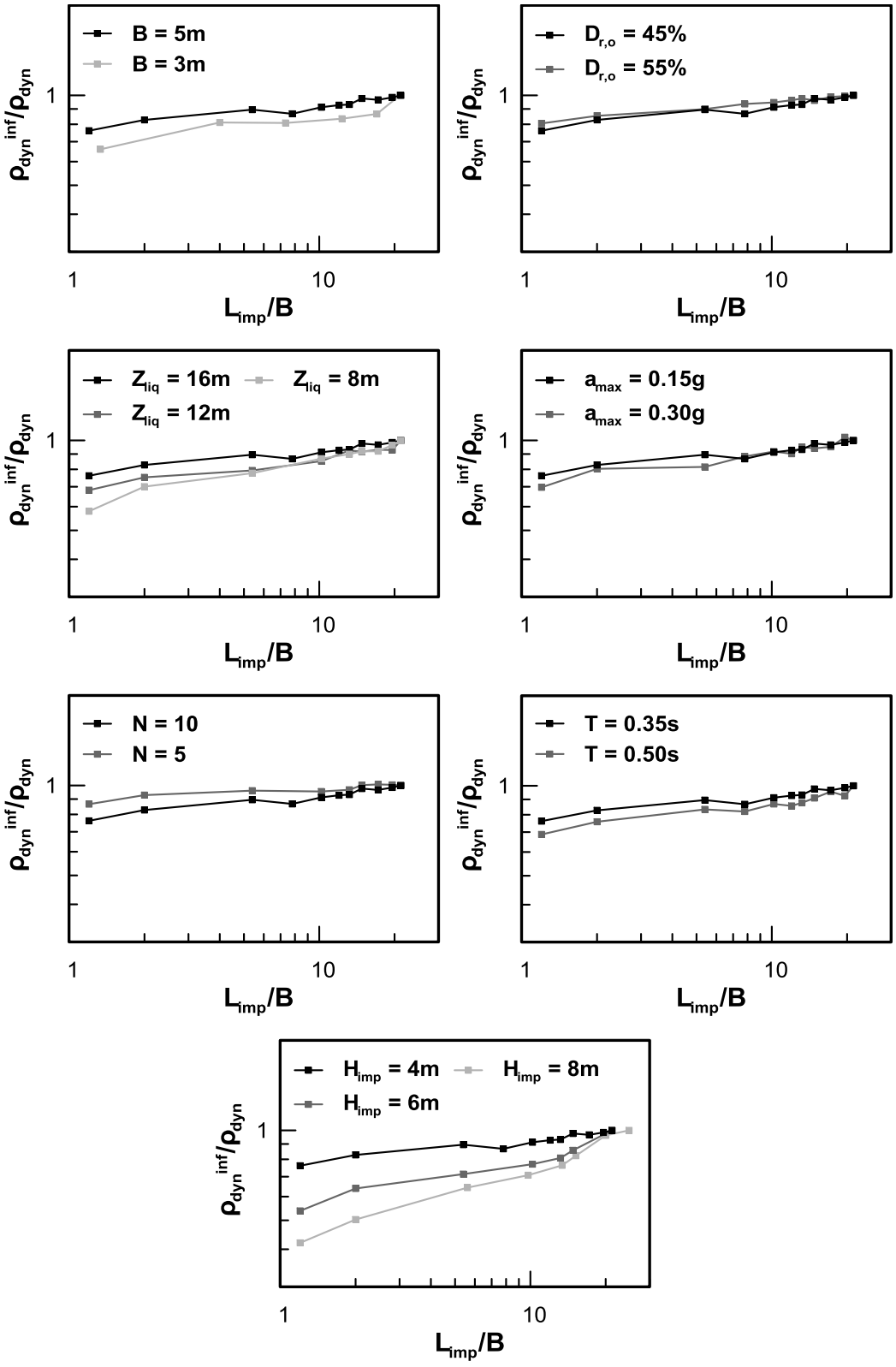

Figure 10.5: Effect of different problem parameters on dynamic settlements ρdyn normalized against the "infinite" value (ρdyn,inf) versus Limp/B.

The solid lines correspond to sets of analyses with different H_{imp}/B values with all other parameters preserved constant, namely Cases 1, 2, 3, 9 and 10 of **Table 10.1**. It is observed that each data set is satisfactorily described through a power function, also plotted with the thicker lines. This essentially verifies the validity of the selected formulation. With regard to coefficient C_1, it equals $-\ln(1-\rho_{dyn,inf}/\rho_{dyn})$ when the width of improvement equals the footing width ($L_{imp}/B = 1$), exhibiting a wide range of variation depending on the ever-current H_{imp}/B ratio.

Coefficient C_2, corresponds to the inclination of the thick lines in **Figure 10.6**, displaying a narrower range of variation for different H_{imp}/B values. Based on the particular observation C_2 is taken as the average of the eight different values obtained from the fitting curves and it is set equal to $C_2 = 0.30$.

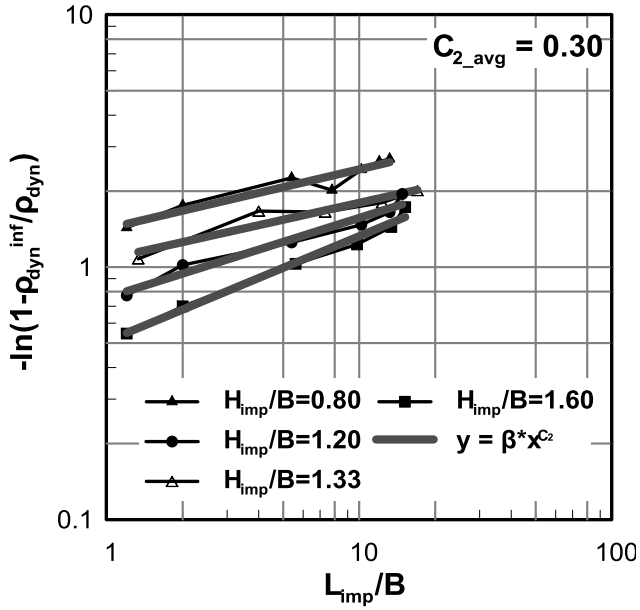

Figure 10.6: Effect of L_{imp}/B on the normalized dynamic settlements $\rho_{dyn,inf}/\rho_{dyn}$ for five different H_{imp}/B values – evaluation of coefficient C_2.

Effect of H_{imp}/B.- To further investigate the observation that coefficient C_1 depends on the ever-current H_{imp}/B ratio, the effect of the thickness of the improved crust, H_{imp}, on the ratio of $\rho_{dyn}^{inf}/\rho_{dyn}$ is appraised in **Figure 10.7** for different L_{imp}/B values. Indeed, the increase of the earthquake-induced settlements ρ_{dyn}, becomes more prominent and the corresponding ratio of $\rho_{dyn}^{inf}/\rho_{dyn}$ decreases significantly with increasing thickness of the improved zone H_{imp}. Nevertheless, the particular observation does not imply that more settlements will

accumulate, for thicker improved zones and decreasing L_{imp}/B values. As thoroughly exhibited in Chapter 9, under "infinite" improvement conditions the selection of a thicker improved zone results in drastically reduced settlements, ρ_{dyn}^{inf}. Therefore, the ratio of $\rho_{dyn}^{inf}/\rho_{dyn}$ may be lower for increasing H_{imp}/B values but it is still possible to obtain the same or even a lower amount of settlement, for greater H_{imp} values, depending on the selected L_{imp}/B value.

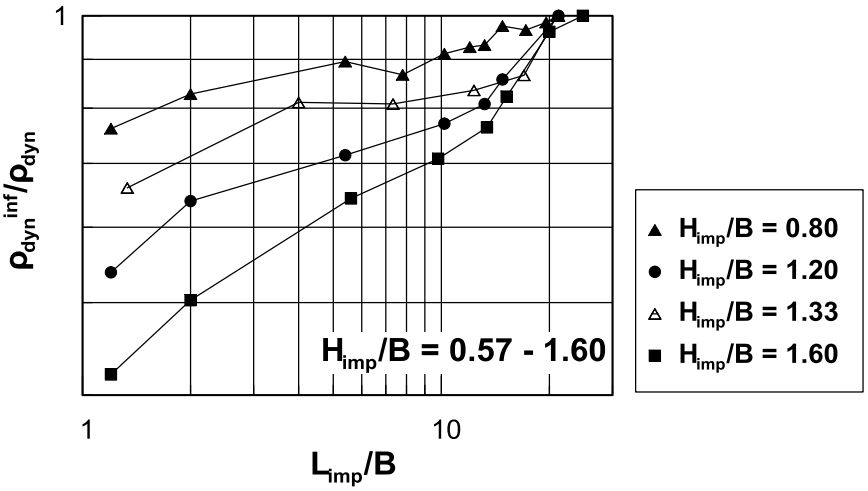

Figure 10.7: Effect of Himp/B on the normalized dynamic settlements ρdyn,inf/ρdyn for different Limp/B values.

Based on the above, the effect of the crust thickness ratio H_{imp}/B, is going to be incorporated in the final analytical expression and specifically in the formulation of coefficient C_1. To achieve this, *Equation 10.2* is solved for coefficient C_1, after setting coefficient C_2 equal to 0.30:

$$C_1 = \frac{\ln\left(1-\frac{\rho_{dyn}^{inf}}{\rho_{dyn}}\right)}{\left(\frac{L_{imp}}{B}\right)^{0.30}} \qquad 10.3$$

The different C_1 values obtained from *Equation 10.3* for each L_{imp}/B value are plotted with regard to the specific H_{imp}/B case in **Figure 10.8** with the black symbols. The grey rhombuses correspond to the average C_1 values obtained from the different data sets. The power function drawn among the above symbols renders the following adopted analytical expression:

$$C_1 = 0.944\left(\frac{H_{imp}}{B}\right)^{-1} \qquad 10.4$$

Hence, the final analytical expression for the conservative lowr-bound estimation of the dynamic settlements for different widths of improvement is provided through the following expression:

$$\frac{\rho_{dyn}^{inf}}{\rho_{dyn}} = 1 - \exp\left[-0.944\left(\frac{H_{imp}}{B}\right)^{-1}\left(\frac{L_{imp}}{B}\right)^{0.30}\right] \qquad 10.5$$

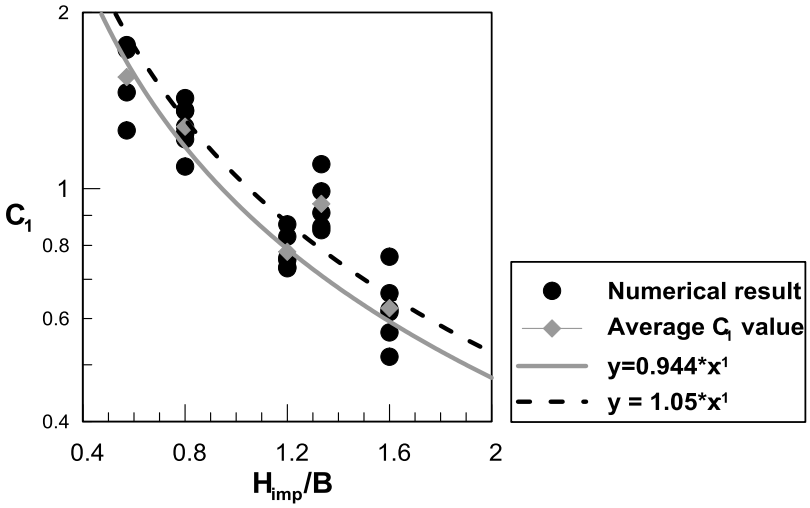

Figure 10.8: Effect of H_{imp}/B on coefficient C_1.

Effect of other problem parameters.- So far, the proposed analytical expression incorporates only the effect of the geometry of the improved area, namely the thickness H_{imp} and lateral width of the improved zone L_{imp}. The effect of the excluded parameters may be accounted for by appropriately modifying the constant factor 0.944. Namely, *Equation 10.5* is re-arranged as presented below:

$$Y = \frac{-\ln\left(1 - \frac{\rho_{dyn}^{inf}}{\rho_{dyn}}\right)}{\left(\frac{H_{imp}}{B}\right)^{-1}\left(\frac{L_{imp}}{B}\right)^{0.30}} \qquad 10.6$$

and subsequently, Y is estimated for all the numerical analyses having L_{imp}/B ratio less than or equal to $L_{imp}/B \leq 15$. Typical results from the analyses so far excluded from the statistical processing 0are summarized in **Figure 10.9.** The fitting curve in each figure corresponds to

the average Y values obtained for each set of analyses. Based on **Figure 10.8,** the average value of Y**,** turned out equal to Y=1.05 and the final analytical expression is modified accordingly:

$$\frac{\rho_{dyn}^{\ inf}}{\rho_{dyn}} = 1 - \exp\left[-1.05 \left(\frac{H_{imp}}{B} \right)^{-1} \left(\frac{L_{imp}}{B} \right)^{0.30} \right] \qquad 10.7$$

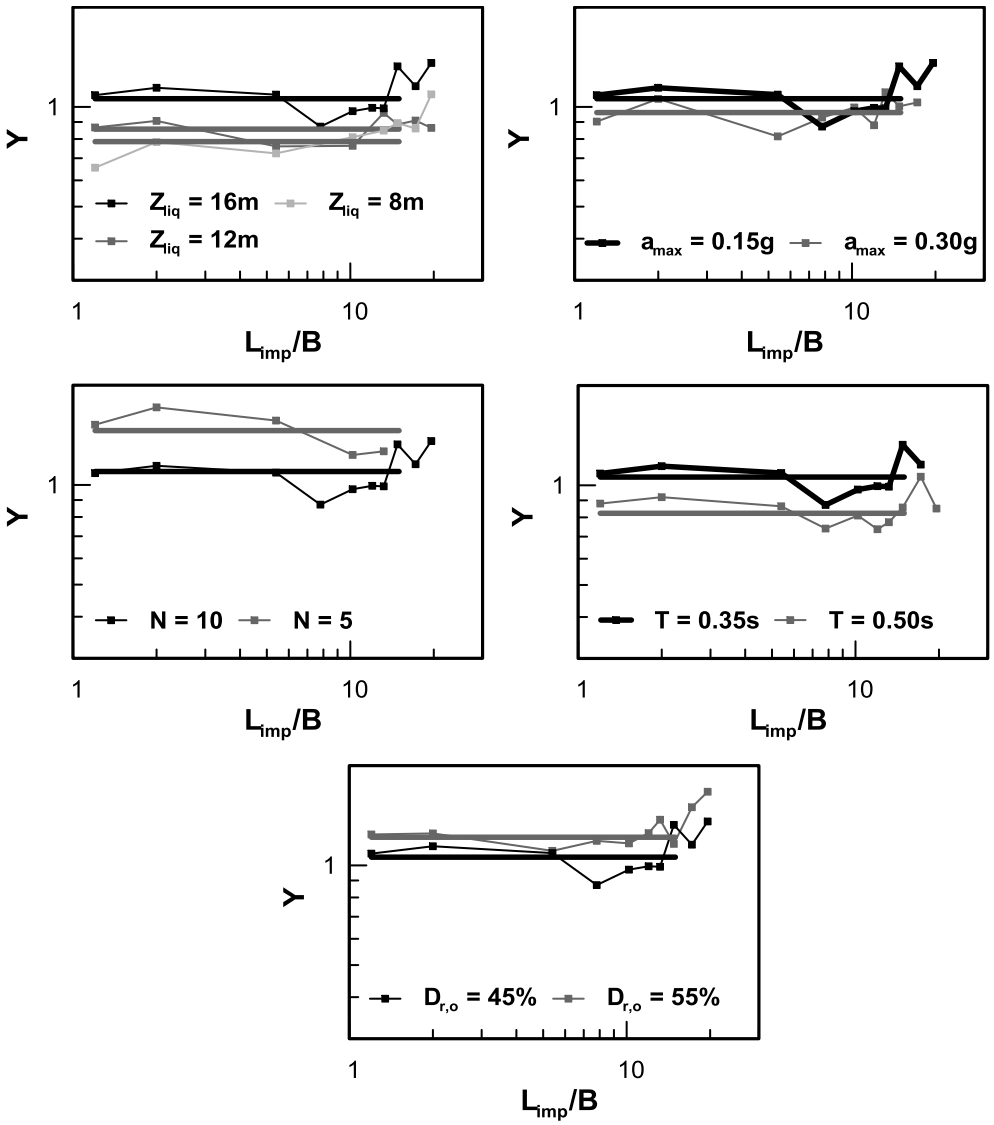

Figure 10.9: Effect of Z_{liq}(m), α_{max}(g), T(sec), N, $D_{r,o}$(%) on the ratio of $-\ln(\rho_{dyn,inf}/\rho_{dyn})$ normalized against $(H_{imp}/B)^{-1}(L_{imp}/B)^{-0.30}$, versus different widths of improvement (L_{imp}) normalized against the footing width B.

Evaluation of analytical expression.- The analytical predictions obtained from *Equation 10.7* are compared against the numerical results in terms of the inverse of the normalized settlement, i.e. ($\rho_{dyn}^{inf}/\rho_{dyn}$) in **Figure 10.10a**. The relative error between numerical and analytically obtained values of the above ratio is also plotted with regard to the numerical results in **Figure 10.10b**. The black symbols correspond to the numerical results used in the formulation of the proposed analytical relation (i.e $L_{imp}/B \leq 15$), whereas, the white symbols represent the excluded numerical analyses with L_{imp}/B ratio greater than $L_{imp}/B > 15$. It is observed that the proposed analytical expression predicts with relatively good accuracy the inverse of the seismically induced settlement for "limited" improvement widths, normalized against the corresponding value for "infinite" improvement conditions. The specific satisfactory behavior is observed even for the excluded cases, which do not deviate significantly from the main group of datapoints. Particularly, the proposed analytical expression under-predicts the specific $\rho_{dyn}^{inf}/\rho_{dyn}$ values by approximately 20%, which essentially corresponds to the maximum obtained relative error. The latter ranges between ±20% with a standard deviation equal to St. Dev.=0.10.

The predictive accuracy of the proposed analytical relation is further verified from **Figure 10.11a & b**, in terms of the obtained settlements for given extent of improvement L_{imp}, preserving the same format considering the color of the used symbols. The specific values of ρ_{dyn}, as well as the associated relative error, are calculated based on the numerical values of $\rho_{dyn,}^{inf}$ and *Equation 10.7*. Hence, **Figure 10.8a** allows the evaluation of the proposed relation, independently of the introduced error stemming from the analytical expression used in the evaluation of ρ_{dyn}^{inf}, presented in Chapter 9. Also, based on **Figure 10.8b**, the particular relative error ranges between ±20% and exhibits a standard deviation equal to St. Dev.=0.7.

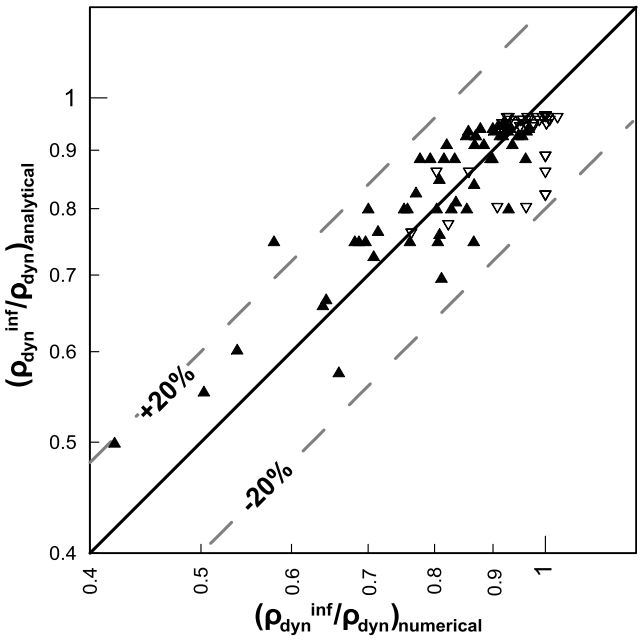

(a)

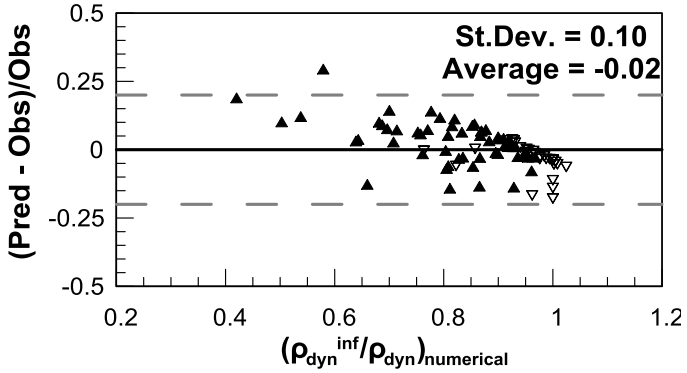

(b)

Figure 10.10: **(a**) Evaluation of the proposed analytical relation with regard to the ratio of $\rho_{dyn}^{inf}/\rho_{dyn}$ for limited lateral improvement, on a one-to-one basis, **(b)** Obtained relative error plotted against the numerically derived ratio of $\rho_{dyn}^{inf}/\rho_{dyn}$.

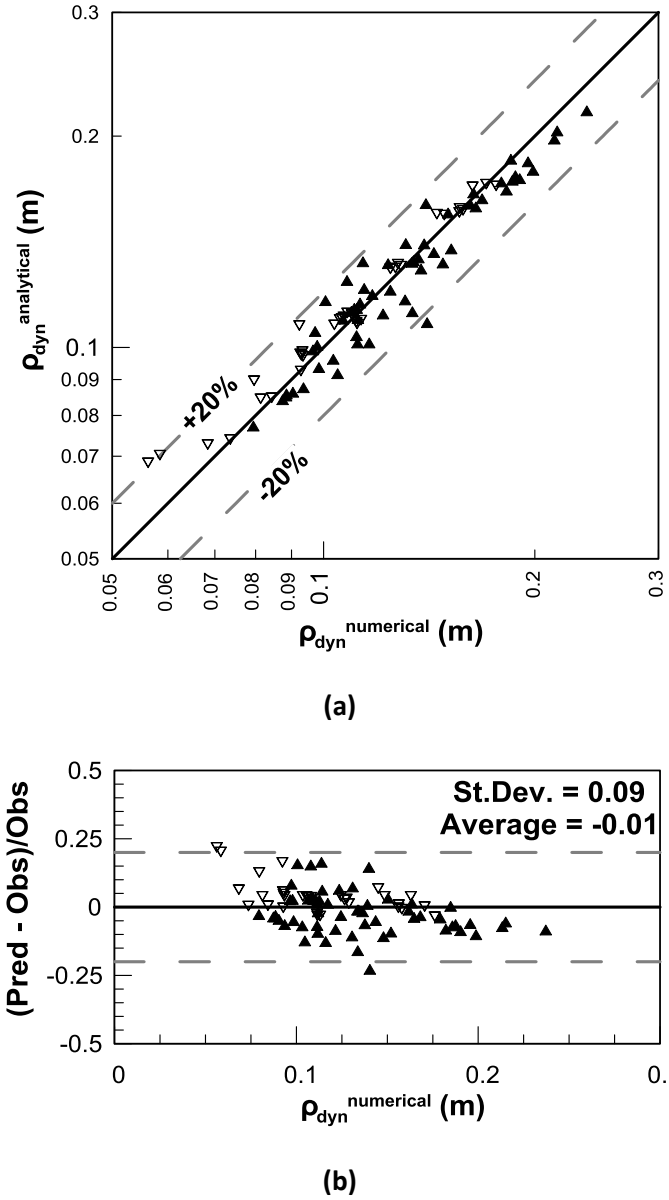

Figure 10.11: **(a)** Evaluation of the proposed analytical relation with regard to the obtained value of dynamic settlement ρ_{dyn}, on a one-to-one basis **(b)** Obtained relative error plotted against the numerically derived value of ρ_{dyn} (lower chart).

In the sequel, *Equation 10.7* is applied for different improvement geometries in order to produce a practical design chart. The outcome is presented in **Figure 10.12** in which both dimensions, i.e. lateral extent (L_{imp}) and thickness (H_{imp}) of the improved zone are expressed as a portion of the footing width (B). Namely, the thickness of the improved crust (H_{imp}) ranges from 0.5B to 2.00B, whereas the lateral extent (L_{imp}) starts from 30B and narrows down to 1B.

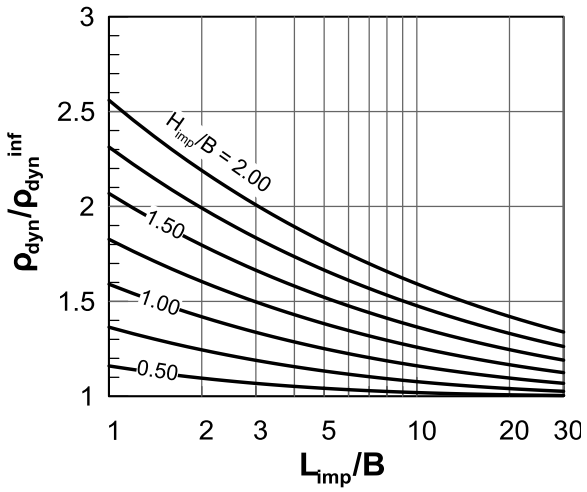

Figure 10.12: Design chart for the evaluation of the amount of dynamic settlement ρ_{dyn} (m), given the geometry of the improvement scheme, described through the width (L_{imp}) and thickness (H_{imp}) of the crust, normalized against the footing width (B).

There are two worthy observations in the particular figure. The first is that dynamic settlements decrease steadily with increasing width of the improved zone. In other words, there is not a certain width in terms of L_{imp}/B ratio, beyond which dynamic settlements stabilize to their minimum value. The second observation is that a fairly extensive improvement may be required in order to get the total benefit of ground improvement. For instance, in the common case of $H_{imp}/B = 1.00 – 1.50$, a L_{imp}/B ratio equal to $L_{imp}/B = 20 – 40$ is required to reduce settlement values that are only 10% higher, compared to the theoretical low for infinite improvement.

10.4 Effect of L_{imp} on the post-shaking degraded Factor of Safety $F.S._{deg}$.

The effect of the improvement width ratio L_{imp}/B, on the post-shaking degraded factor of safety, $F.S._{deg}$, is depicted in **Figure 10.13**, for all the examined cases. It is observed that, opposite to the uniformity of the data regarding the dynamic settlements, the scatter in the obtained values of $FS._{deg}$ is considerably larger.

Regarding the numerical aspect of the problem, it is mentioned that the last stage of the loading sequence, i.e. the evaluation of the degraded bearing capacity $q_{ult.}$(kPa), is performed based on an analysis under static conditions. Also, according to Itasca (2005), in FLAC, a static solution is reached by artificially damping the relevant equations of motion, when the rate of change in kinetic energy in a model approaches a negligible value,. Hence,

even though the magnitude of the applied velocity upon the corresponding grid-points of the footing is very small, numerical instabilities are still likely to occur, even in areas of the grid far away from the footing. Different approaches to locate and resolve the particular issue were investigated, with minor effects on the obtained results. Moreover, the consideration of applying an even smaller magnitude of vertical velocity was abandoned, given the required excessive computational time, which would prohibit the execution of a broad parametric investigation. It is indicatively mentioned that the post-shaking static analysis required on average 4 days for the "infinite" improvement scheme and 2 days for different L_{imp}/B values (with FLAC v5.0).

Due to the considerable scatter of numerical predictions, the development of a suitable analytical expression for evaluating $F.S._{deg}$ followed a different approach compared to the procedure for the dynamic settlements. More specifically, settlements in *Equation 10.7* were expressed in terms of the degraded factor of safety, for infinite and for limited ground improvement, using the general *Equation 9.6* derived in Chapter 9. In the sequel, the resulting relationship was solved for the $F.S._{deg}/F.S._{deg}^{inf}$ ratio and used to express the desired effects of ground improvement dimensions. Note that, for this approach to be valid, it is essential that the ρ_{dyn} – $F.S._{deg}$ relationship of Chapter 9 is unique, i.e. it applies regardless of ground improvement dimensions. Hence, this issue was given priority to the following investigation. The data sets exhibiting a widespread scatter, i.e. Cases 6, 10, 11 & 12, as well individual data points with $F.S._{deg}$ less than $F.S._{deg} < 1.15$ were considered unstable analyses and hence were excluded from the statistical evaluation. The particular cases are marked with white symbols in **Figure 10.13.** Overall, out of the 96 performed numerical analyses only 48 were used for the statistical processing presented in the subsequent paragraphs.

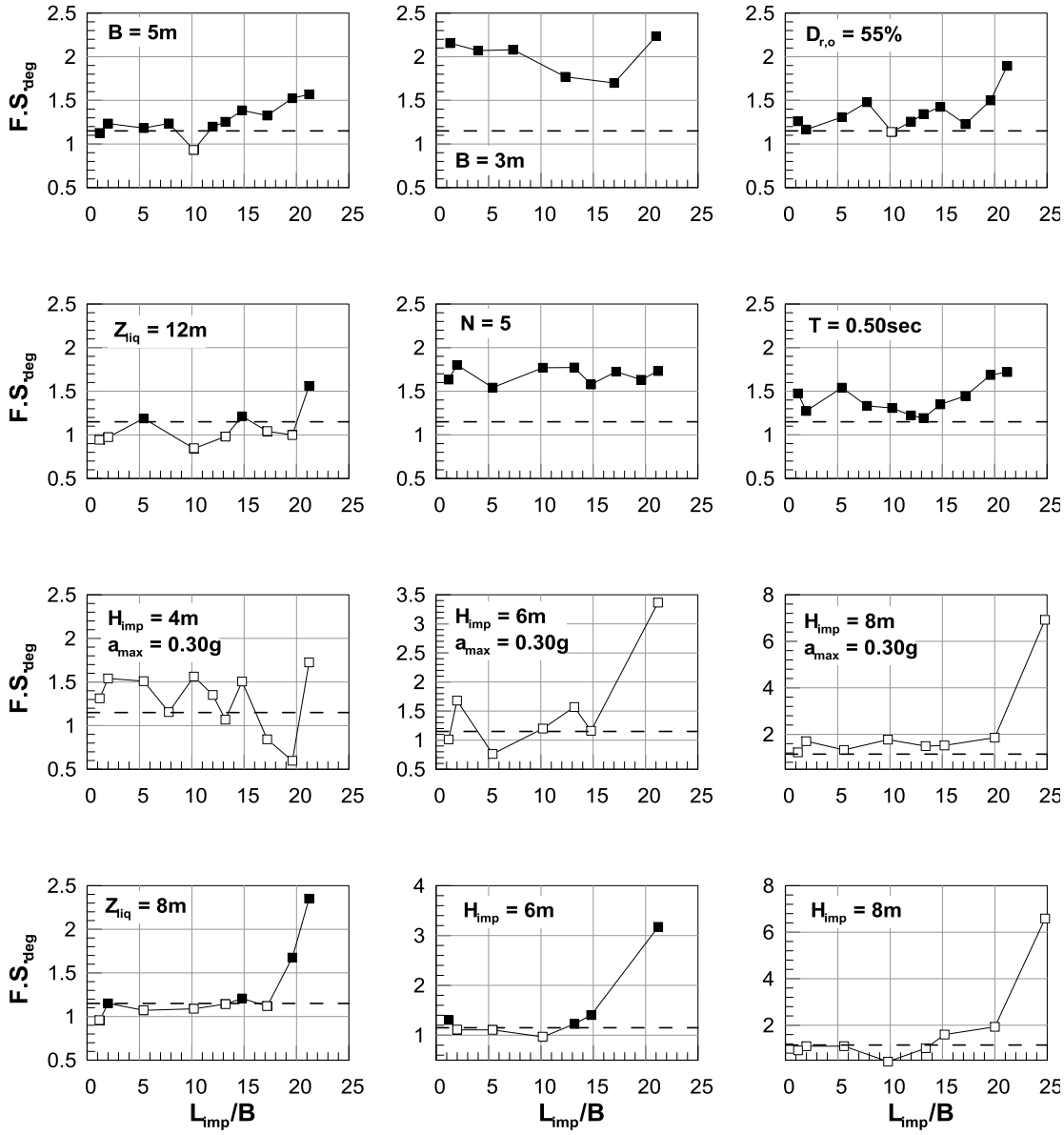

Figure 10.13: Summary of numerical results of degraded Factor of Safety and excluded "toxic" cases (white symbols).

ρ_{dyn} and F.S.$_{deg}$ relationship- In Chapter 9, dynamic settlements are expressed as a function of the degraded Factor of Safety F.S.$_{deg}$. In the current paragraph it is examined whether the above relation can be extended to describe the dynamic settlement accumulation in the case of "limited" improvement width. Hence, *Equation 9.6* is applied for stable numerical analyses with F.S.$_{deg}^{num}$ > 1.15, considering the associated numerically derived degraded factor of Safety F.S.$_{deg}$. The dynamic settlements obtained in this way are summarized in **Figure 10.14**. The numerical results and analytical predictions are plotted in the gray and

black symbols respectively. Based on the above figure it is concluded that the two data sets are in fairly good agreement.

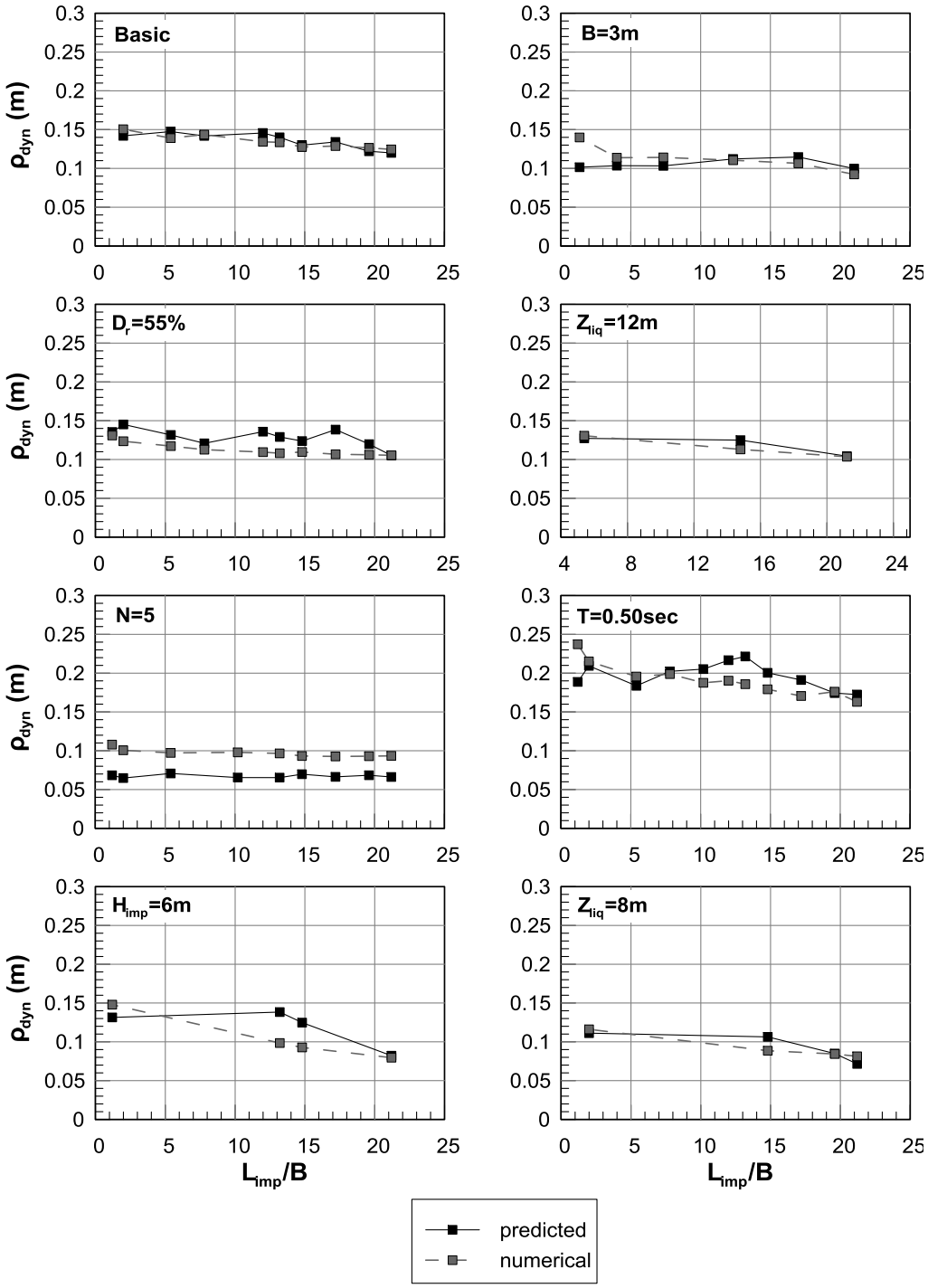

Figure 10.14: Comparison between numerically derived dynamic settlements (grey symbols) and analytical predictions based on the analytical expression for conditions of "infinite" improvement (black symbols).

The above satisfactory agreement is better appraised in **Figure 10.15a**, presenting the analytically predicted dynamic settlements against the numerical results on a one-to-one basis. **Figure 10.15b** provides the relative error plotted against the analytically computed dynamic settlements from which it is concluded that the relative error of the analytical predictions ranges between ±25% and the standard deviation of relative error is equal to St. Dev. = 0.19.

Based on the above, it is concluded that the proposed correlation between dynamic settlements and degraded factor of safety for "infinite" ground improvement apples to cases of finite improvement dimensions as well.

Analytical expression for the degraded factor of safety.- Given the applicability of *Equation 9.6* for cases of "limited" improvement, it is used in the formulation of an analytical expression for the computation of the associated degraded factor of safety. Particularly, *Equation 9.6* is applied once for conditions of "infinite" improvement and secondly for "limited" improvement width. In the sequel, the resulting equations are divided against each other, leading to the following analytical expression for the dynamic settlement ratio:

$$\frac{\rho_{dyn}}{\rho_{dyn}^{inf}} = \left(\frac{F.S._{deg}}{F.S._{deg}^{inf}}\right)^{-0.45} \frac{\left(F.S._{deg}^{inf}\right)^{4.5} + 0.25\left(\frac{F.S._{deg}}{F.S._{deg}^{inf}}\right)^{-4.5}}{\left(F.S._{deg}^{inf}\right)^{4.5} + 0.25} \qquad 10.8$$

In the sequel, the combination of *Equations 10.7* and *10.8*, and the rearrangement of the expression with regard to the ratio of $F.S._{deg}/F.S._{deg}^{inf}$, results to the following non-linear equation for its computation:

$$\left(\frac{F.S._{deg}}{F.S._{deg}^{inf}}\right)^{0.45} = \left\{1 - \exp\left[-1.05\left(\frac{H_{imp}}{B}\right)^{-1}\left(\frac{L_{imp}}{B}\right)^{0.30}\right]\right\} \frac{\left(F.S._{deg}^{inf}\right)^{4.5} + 0.25\left(\frac{F.S._{deg}}{F.S._{deg}^{inf}}\right)^{-4.5}}{\left(F.S._{deg}^{inf}\right)^{4.5} + 0.25} \qquad 10.9$$

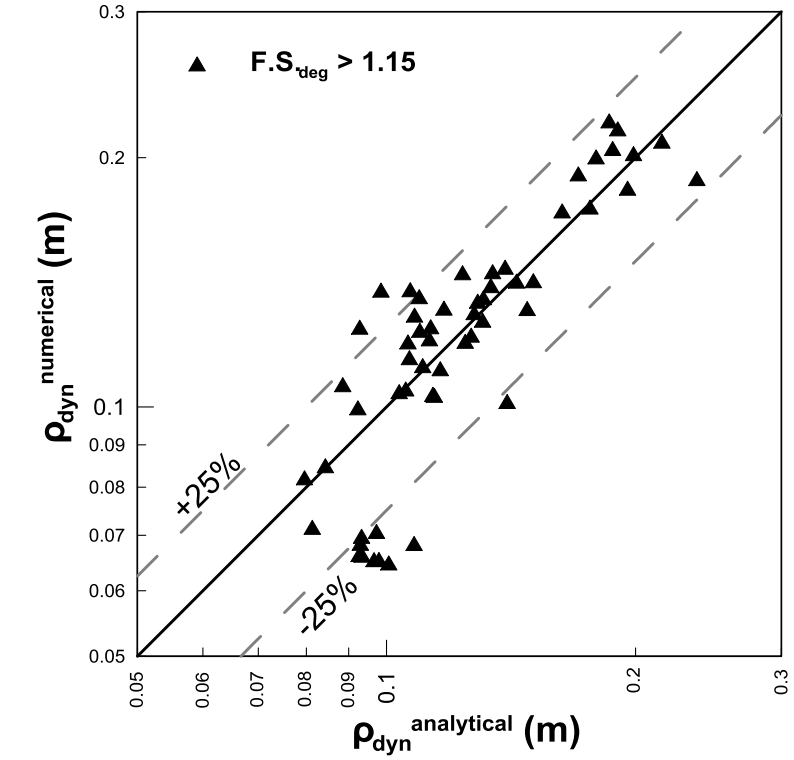

(a)

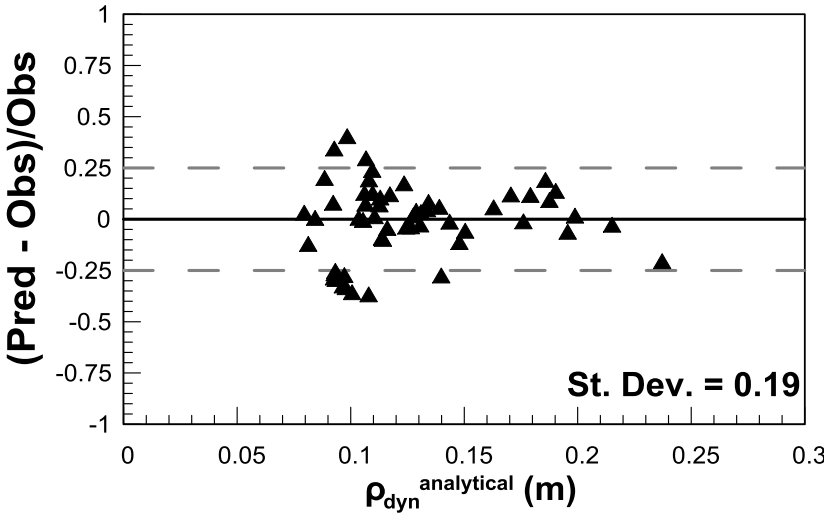

(b)

Figure 10.15: **(a)** Evaluation of the analytical relation for conditions of "infinite" improvement with regard to the obtained value of dynamic settlement ρ_{dyn}, on a one-to-one basis **(b)** Obtained relative error plotted against the analytically computed value of ρ_{dyn}.

The above analytical expression correlates the geometric features of the improved area, (thickness H_{imp} and width L_{imp}) to the degraded factor of safety for "infinite" improvement conditions $F.S._{deg}^{inf}$, as well as to the ratio of the degraded factor of safety for "limited" over that for "infinite" improvement conditions, i.e. $F.S._{deg}/F.S._{deg}^{inf}$. Note that the $F.S._{deg}/F.S._{deg}^{inf}$ ratio appears in both sides of *Equation 10.9,* meaning that an iterative solution is required.

The predictive accuracy of *Equation 10.9* is appraised in **Figure 10.16a & b**, in terms of the ratio of the degraded factor of safety for "limited" over the corresponding value for "infinite" improvement. In **Figure 10.16a** the comparison is performed against the numerical predictions on a one-to-one basis, and refers to the numerically stable analyses. Note that the numerically derived value of $F.S._{deg}^{inf}$ is plugged into the ratio of the analytical predictions, so that the efficiency of the current analytical expression is evaluated independently of the generated error due to the analytical expression proposed for the computation of $F.S._{deg}^{inf}$ presented in Chapter 9. The relative error is plotted against the analytical predictions in **Figure 10.16b**. Based on the above figures it is observed that, with minor exceptions, *Equation 10.9* predicts with substantial accuracy the degraded factor of safety F.S.deg, with a deviation ranging between ±25%. Relative error of the predictions ranges between ±25% with a standard deviation equal to St. Dev. = 0.25.

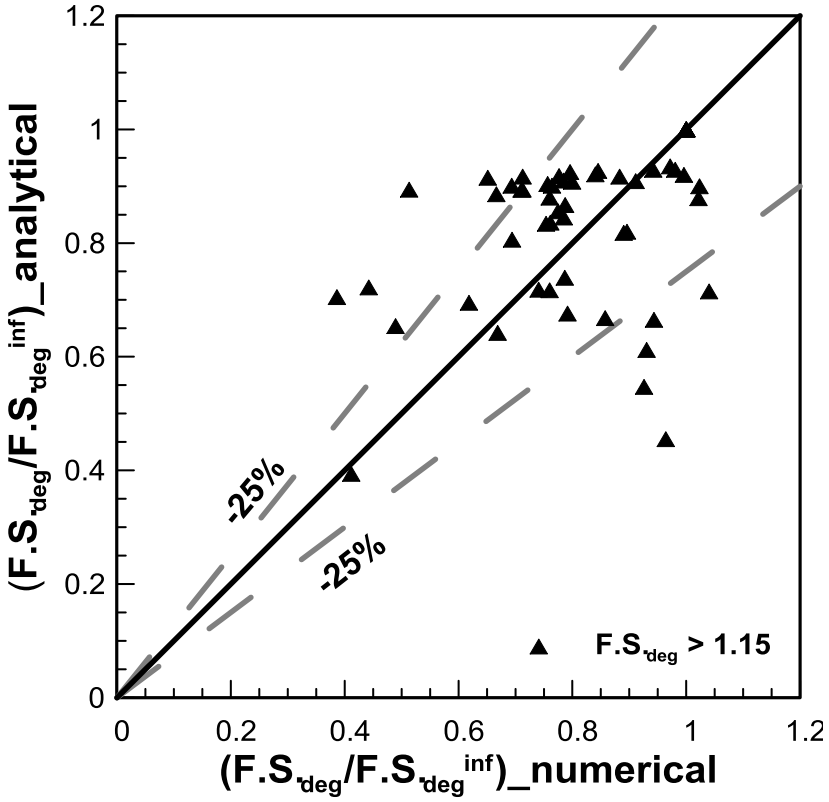

(a)

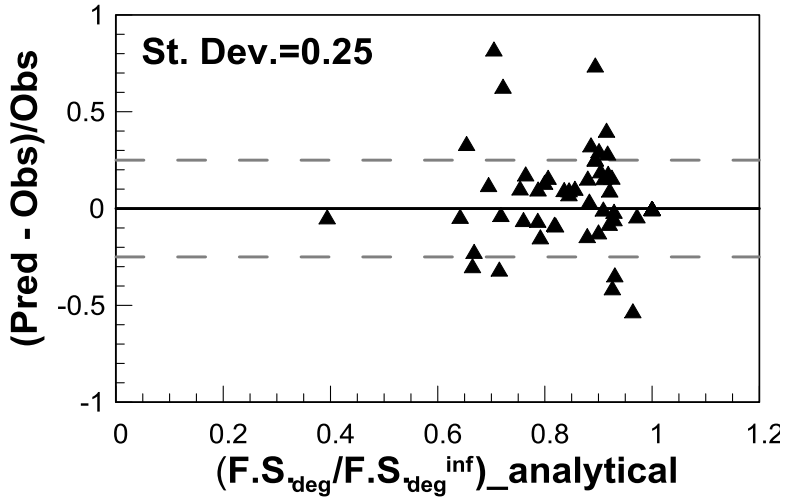

(b)

Figure 10.16: **(a)** Evaluation of the analytically obtained ratio of $F.S._{deg}/F,.S._{deg}^{inf}$ with regard to the numerically derived ratio, on a one-to-one basis **(b)** Obtained relative error plotted against the numerically derived ratio of $F.S._{deg}/F,.S._{deg}^{inf}$.

To facilitate the use of the complex analytical expression presented above, *Equation 10.9* is solved for four different values of H_{imp}/B (= 0.5, 1.0, 1.5, 2.0) and three different values of the degraded factor of safety for "infinite" improvement conditions, namely $F.S._{deg}^{inf}$ = 1.0, 2.0 & 3.0. The outcome is presented in the form of design charts in **Figure 10.17**. It is interesting to note that for increasing values of crust thickness, the influence of the degraded factor of safety for "infinite" improvement conditions, $F.S._{deg}^{inf}$, becomes more pronounced, disclosing the sensitivity of the results at thicker improvement schemes. Moreover it turns out that the effect of $F.S._{deg}^{inf}$ is not excessive, even for the cases of very thick crust, i.e. H_{imp}/B = 2.0. Hence, in view of the overall uncertainties in determining $F.S._{deg}$, discussed in previous sections, it is permissible to overlook the effect of $F.S._{deg}^{inf}$ in *Equation 10.9,* assuming an average value of $F.S._{deg}^{inf}$ = 2.0. The resulting simplifications are discussed next.

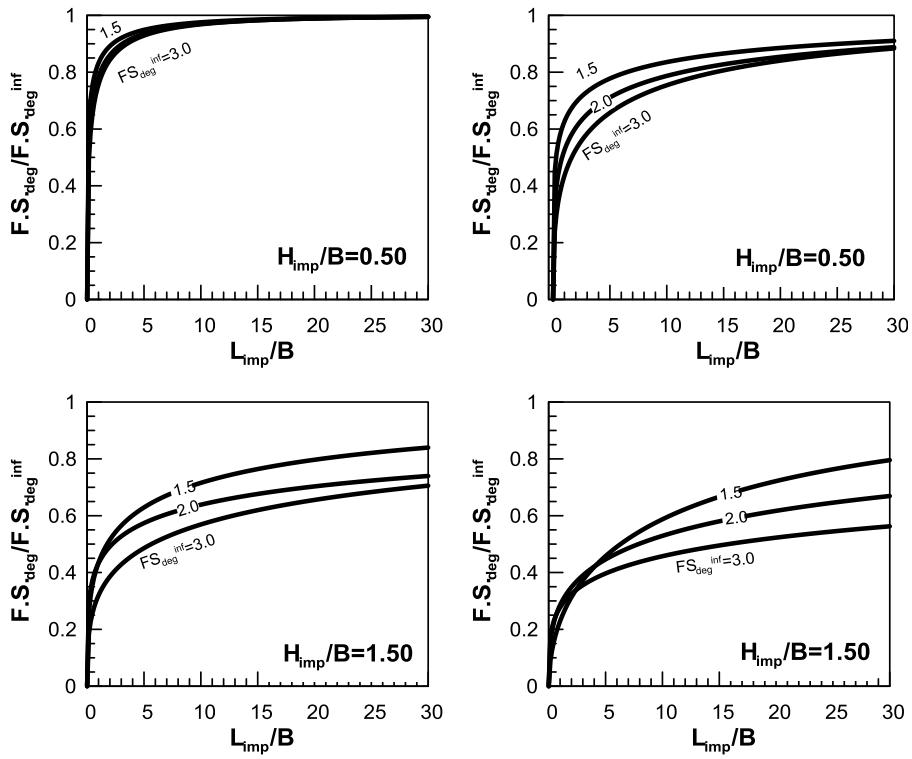

Figure 10.17: Design charts relating the $F.S._{deg}/F.S._{deg}^{inf}$ ratio to the normalized - against the footing width B - lateral width of improvement (L_{imp}/B) for four distinct H_{imp}/B values.

Simplified analytical expression.- Given the drawbacks in the use of *Equation 10.9*, in the present paragraph a simplified analytical expression is formulated, which enables the direct evaluation of the degraded factor of safety $F.S._{deg}$ for "limited" improvement conditions. In its generalized form, this simplified relation is described in the form of *Equation 10.10*:

$$\frac{F.S._{deg}}{F.S._{deg}^{inf}} = 1 - \exp\left[-C_3 \left(\frac{L_{imp}}{B} \right)^{C_4} \right] \qquad 10.10$$

where coefficients C_3 and C_4 will have to be appropriately specified.

To facilitate the evaluation of coefficients C_3 and C_4 the above expression is transformed into *Equation 10.11*:

$$-\ln\left(1 - \frac{F.S._{deg}}{F.S._{deg}^{inf}} \right) = C_3 \left(\frac{L_{imp}}{B} \right)^{C_4} \qquad 10.11$$

The cases included in the statistical processing, exhibit a degraded factor of safety under conditions of "infinite" improvement, on average, equal to two. Hence, coefficients C_3 and C_4 are calculated based on *Equation 10.11*, setting $F.S._{deg}^{inf}$ equal to two and different H_{imp}/B ratios, i.e. H_{imp}/B = 0.5, 1.0, 1.5, 2.0. The resulting curves are summarized in **Figure 10.18** plotted against the lateral width of improvement, L_{imp}, normalized against the footing width B, in a double logarithmic axis system.

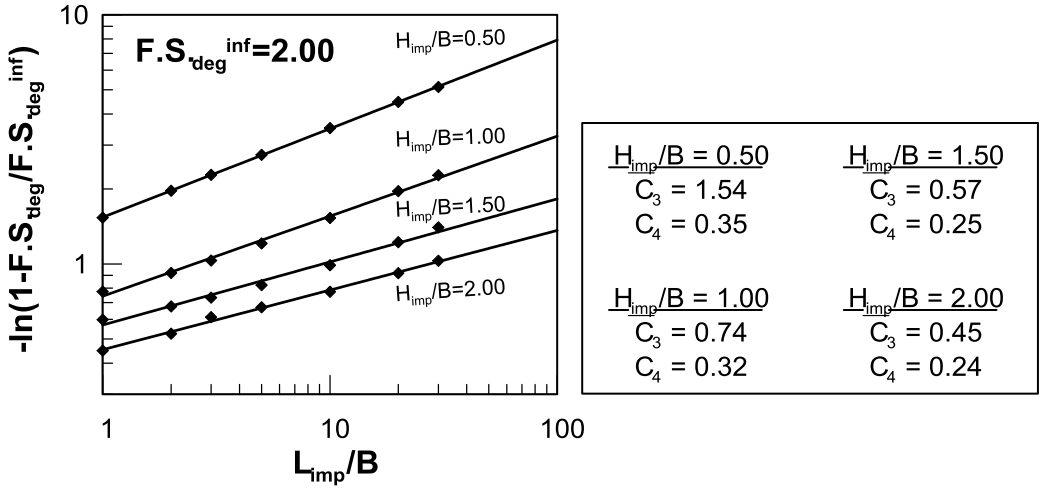

Figure 10.18: Evaluation of coefficients C_3 and C_4 for four distinct values of H_{imp}/B.

Coefficient C_4.- Given the form of the resulting curves, coefficient C_4 corresponds to the inclination of each one of them, which is independent of the L_{imp}/B ratio and may be considered constant and, at an average, equal to **C_4 = 0.29**.

Coefficient C_3.- corresponds to the value of $-\ln(F.S._{deg}/F.S._{deg}^{inf})$ for L_{imp}/B equal to unity and it turns out that it depends on the thickness of the improved zone, H_{imp}, normalized against the footing width B. Substituting C_4 with the previously specified value and rearranging *Equation 10.11*, C_3 can be evaluated as follows:

$$C_3 = \frac{-\ln\left(1-\frac{F.S._{deg}}{F.S._{deg}^{inf}}\right)}{\left(\frac{L_{imp}}{B}\right)^{0.29}} \qquad 10.12$$

The application of *Equation 10.12* for different values of L_{imp}/B (= 1, 2, 3, 5, 10, 20, 30) and the four different H_{imp}/B ratios mentioned earlier, leads to the different values of C_3 plotted in **Figure 10.19** with regard to H_{imp}/B. The power function drawn amongst the presented data points is described by *Equation 10.13* and is hereafter going to be used for the evaluation of C_3:

$$C_3 = 0.82\left(\frac{H_{imp}}{B}\right)^{-1.03} \qquad 10.13$$

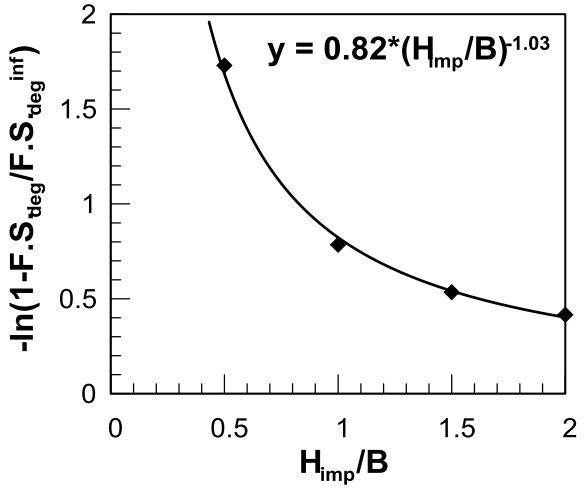

Figure 10.19: Dependence of coefficient C_3 on the considered H_{imp}/B range and best-fitting power function**.**

In the above context, the simplified expression for evaluating $F.S._{deg}$ for "limited" improvement width is transformed as follows:

$$\frac{F.S._{deg}}{F.S._{deg}^{inf}} = 1 - \exp\left[-0.82 \left(\frac{H_{imp}}{B} \right)^{-1.03} \left(\frac{L_{imp}}{B} \right)^{0.29} \right] \qquad 10.14$$

Note that *Equation 10.14* is formulated considering a degraded factor of safety for "infinite" improvement width equal to $F.S._{deg}^{inf} = 2.0$ and applies over a specific range of H_{imp}/B values, namely $H_{imp}/B = 0.5 \div 2.0$. **Figure 10.20a** presents the comparison between the obtained analytical predictions and the numerical results, exhibiting $F.S._{deg}^{inf}$ values within a slightly wider range, i.e. $F.S._{deg}^{inf} = 1.5 \div 2.5$. It is thus concluded that, *Equation 10.14* can be applied with substantial accuracy for a slightly wider range of $F.S._{deg}^{inf}$. The obtained relative error, plotted against the analytical predictions, is presented in **Figure 10.20b**, from which it is concluded that it ranges between ±25% with a standard deviation equal to St. Dev. = 0.23.

Given the predictive efficiency of the above analytical expression, the particular process is repeated for two additional values of $F.S._{deg}^{inf}$, i.e. $F.S._{deg}^{inf} = 3.0$ & 4.0. The resulting analytical expressions are provided below in the form of *Equations 10.15* and *10.16* respectively:

$$\frac{F.S._{deg}}{F.S._{deg}^{inf}} = 1 - \exp\left[-0.64 \left(\frac{H_{imp}}{B} \right)^{-1.30} \left(\frac{L_{imp}}{B} \right)^{0.34} \right] \qquad 10.15$$

$$\frac{F.S._{deg}}{F.S._{deg}^{inf}} = 1 - \exp\left[-0.56 \left(\frac{H_{imp}}{B} \right)^{-1.30} \left(\frac{L_{imp}}{B} \right)^{0.38} \right] \qquad 10.16$$

To facilitate the use of the simplified relations provided earlier, Equations 10.14, 10.15 and 10.16 are solved for seven (7) different values of H_{imp}/B, i.e. 0.5, 0.75, 1.00, 1.25, 1.50, 1.75, 2.00 and a lateral width of improvement ranging from 30B down to 1B. The outcome of the above process is a set of suitable and handy design charts presented in **Figure 10.21**.

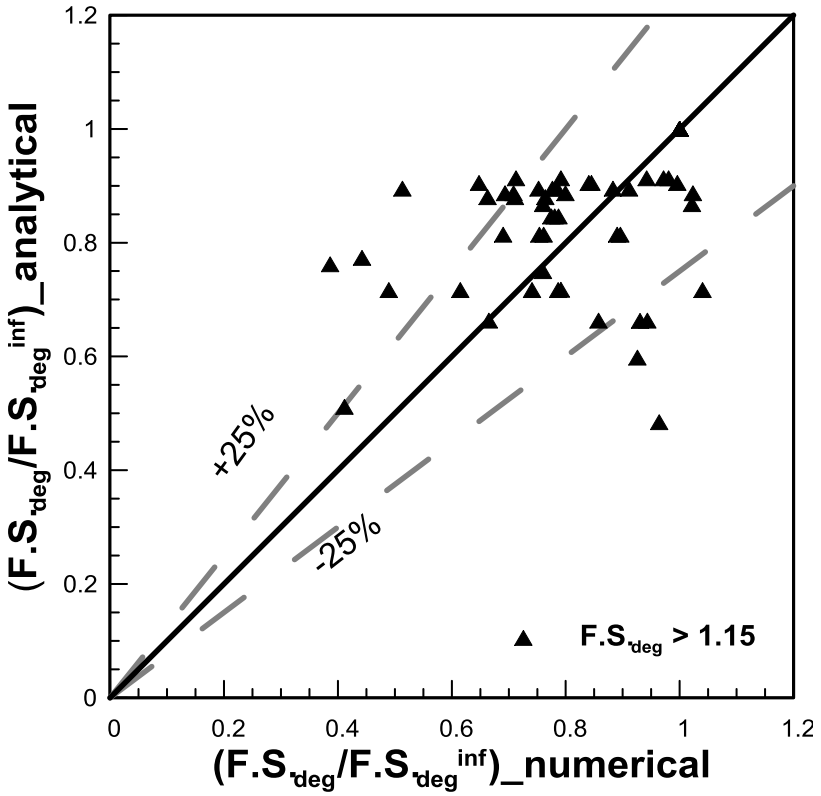

(a)

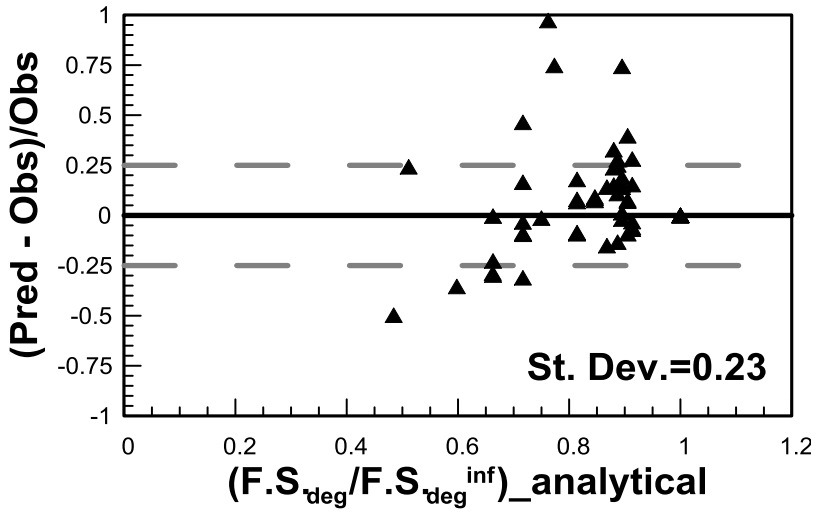

(b)

Figure 10.20: **(a)** Evaluation of the analytically obtained ratio of $F.S._{deg}/F,.S._{deg}^{inf}$ with regard to the numerically derived ratio, on a one-to-one basis **(b)** Obtained relative error plotted against the numerically derived ratio of $F.S._{deg}/F,.S._{deg}^{inf}$.

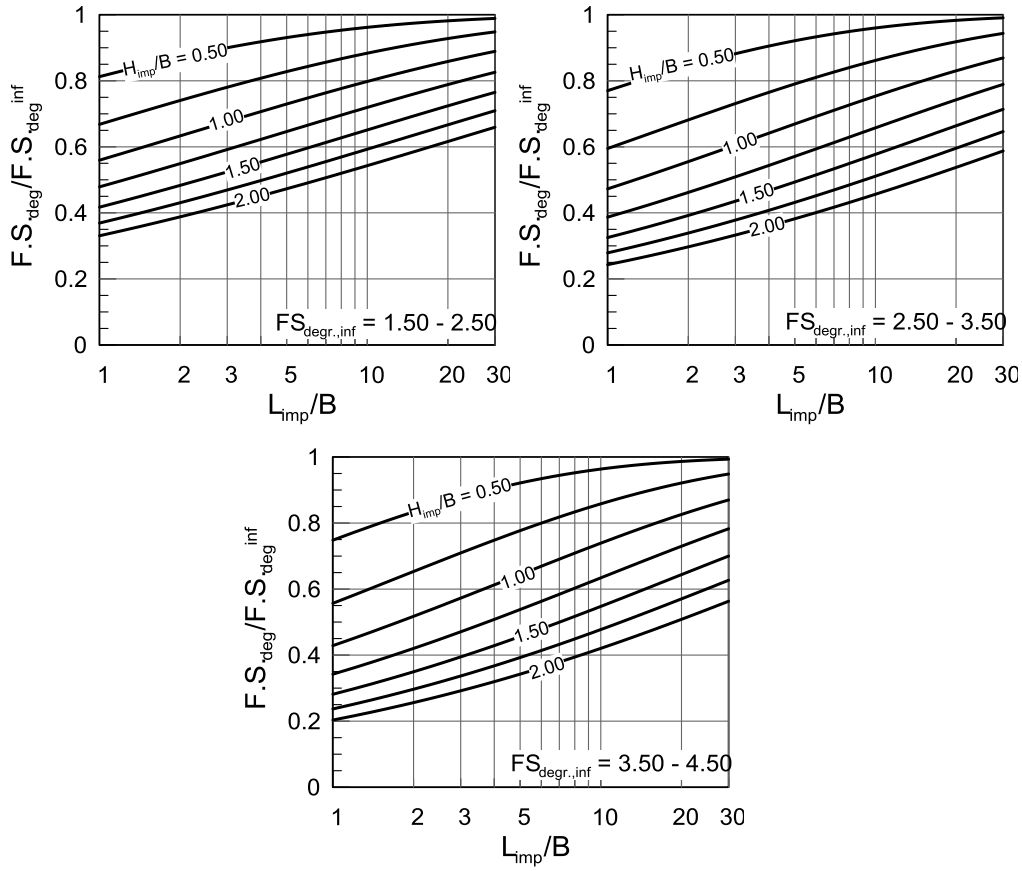

Figure 10.21: Design charts relating the $F.S._{deg}/F,.S._{deg}^{inf}$ ratio to the L_{imp}/B value, based on the simplified analytical expressions, for three initial $F.S._{deg}^{inf}$ values.

10.5 Overview of analytical methodology and design charts

Evaluation of degraded Factor of Safety $F.S._{deg}$- The first step of the proposed analytical methodology, includes the evaluation of the degraded factor of safety of the shallow foundation, immediately after the end of shaking and while the underlying soil is still under a liquefied state. This is accomplished through *Equation 10.9*, allowing the evaluation of $F.S._{deg}$ for any improved zone geometry (depth H_{imp} and width L_{imp}). The specific analytical expression is provided in a non-linear formulation, requiring an iterative solution. Moreover, it requires the prior knowledge of the degraded factor of safety for "infinite" improvement conditions, which is obtained through the application of *Equation 9.10.*

To reduce the computational effort required for the evaluation of $F.S._{deg}$, *Equation 10.9* is solved for different $F.S._{deg}^{inf}$ and H_{imp}/B values and the outcome is presented in **Figure 10.21.** The particular design charts summarize the effect of the lateral width of improvement

normalized against the footing width B (L_{imp}/B) on the degraded factor of safety, normalized against the corresponding values for conditions of "infinite" improvement.

Evaluation of dynamic settlements ρ_{dyn}.- Similarly to the analytical expressions proposed for the degraded factor of safety, the evaluation of the seismic-induced settlements ρ_{dyn} requires the prior assessment of ρ_{dyn}^{inf}. The specific parameter is evaluated using *Equation 10.6*, given the necessary input data, namely the characteristics of the seismic excitation and the degraded factor of safety for conditions of "infinite" width of improvement, $F.S._{deg}^{inf}$, as specified above. In the sequel, the ratio of $\rho_{dyn}/\rho_{dyn}^{inf}$ is computed as a function of the width and depth of improvement, normalized against the footing width B - L_{imp}/B, H_{imp}/B respectively - as illustrated in **Figure 10.12.**

Design Charts for L_{imp}/H_{imp}.- To gain additional insight regarding the practical application of the previously generated design charts, the corresponding analytical expressions are appropriately modified to incorporate the ratio of the width over the depth of the improved zone, L_{imp}/H_{imp}. Hence, *Equation 10.7* is transformed into *Equation 10.17 :*

$$\frac{\rho_{dyn}^{inf}}{\rho_{dyn}} = 1 - \exp\left[-1.05 \left(\frac{H_{imp}}{B} \right)^{-0.7} \left(\frac{L_{imp}}{H_{imp}} \right)^{0.30} \right] \qquad 10.17$$

Accordingly, the simplified analytical expressions for $F.S._{deg}$ are transformed into *Equations 10.18a, b* and *c* respectively:

$$\frac{F.S._{deg}}{F.S._{deg}^{inf}} = 1 - \exp\left[-0.82 \left(\frac{H_{imp}}{B} \right)^{-0.74} \left(\frac{L_{imp}}{H_{imp}} \right)^{0.29} \right] \quad (F.S._{deg}^{inf} = 2.00) \qquad 10.18a$$

$$\frac{F.S._{deg}}{F.S._{deg}^{inf}} = 1 - \exp\left[-0.64 \left(\frac{H_{imp}}{B} \right)^{-0.86} \left(\frac{L_{imp}}{H_{imp}} \right)^{0.34} \right] \quad (F.S._{deg}^{inf} = 3.00) \qquad 10.18b$$

$$\frac{F.S._{deg}}{F.S._{deg}^{inf}} = 1 - \exp\left[-0.56 \left(\frac{H_{imp}}{B} \right)^{-0.92} \left(\frac{L_{imp}}{H_{imp}} \right)^{0.38} \right] \quad (F.S._{deg}^{inf} = 4.00) \qquad 10.18c$$

The above equations are solved for seven (7) distinct H_{imp}/B ratios (= 0.50, 0.75, 1.00, 1.25, 1.50, 1.75, 2.00) and the outcome is summarized in an updated set of design charts, as exhibited in **Figure 10.22** and **Figure 10.23**. The thicker grey lines correspond to the points on the different curves beyond which increasing the ratio of L_{imp}/H_{imp} renders a rate of variation less than 5%, i.e. the cost-effect ratio is high.

Design Charts for V_{imp}/B^2.- The correlation between the selected dimensions of an improved zone around the shallow foundation to the generated cost becomes a lot more straightforward when incorporating the resulting volume of improvement V_{imp}, which is a more direct cost indicator. For the plane strain conditions considered in the problem, the volume of the improved area is defined as the product of the depth (H_{imp}) times the width (L_{imp}) of the improved zone. To preserve the dimensionless form of the initially proposed equations, volume is divided by B^2 and the outcome of the modification is exhibited in *Equations 10.19* and *10.20a, b* and *c*.

$$\frac{\rho_{dyn}^{\ inf}}{\rho_{dyn}} = 1 - \exp\left[-1.05\left(\frac{H_{imp}}{B}\right)^{-1.30}\left(\frac{V_{imp}}{B^2}\right)^{0.30}\right] \qquad 10.19$$

$$\frac{F.S._{deg}}{F.S._{deg}^{\ inf}} = 1 - \exp\left[-0.82\left(\frac{H_{imp}}{B}\right)^{-1.32}\left(\frac{V_{imp}}{B^2}\right)^{0.29}\right] \qquad 10.20a$$

$$\frac{F.S._{deg}}{F.S._{deg}^{\ inf}} = 1 - \exp\left[-0.64\left(\frac{H_{imp}}{B}\right)^{-1.54}\left(\frac{V_{imp}}{B^2}\right)^{0.34}\right] \qquad 11.20b$$

$$\frac{F.S._{deg}}{F.S._{deg}^{\ inf}} = 1 - \exp\left[-0.56\left(\frac{H_{imp}}{B}\right)^{-1.68}\left(\frac{V_{imp}}{B^2}\right)^{0.38}\right] \qquad 10.20c$$

The normalized dynamic settlements and the degraded factor of safety are plotted against V_{imp}/B^2 in **Figure 10.24** and **Figure 10.25** respectively. Note that the grey line connects the points on the different curves beyond which increasing the volume of the performed improvement renders a rate of variation less than 5%. The red and blue lines correspond to the empirical methodologies proposed by JDFA (1974) and Tchuchida et al. (1976) respectively. The above guidelines have been presented in the introduction of the current chapter and provide an estimate of the width of the compacted zone around shallow or slightly embedded structures. Note however, that both empirical methodologies refer to compaction as the main improvement technology and hence do not incorporate the drainage effects offered by the presence of gravel drains. Additionally, in the specific studies, it is recommended that the entire thickness of the liquefiable sand layer is mitigated. Hence, in the relevant figures, both recommendations are applied for relatively thin liquefiable layers, ranging from 0.5 – 2 times the width of the footing. The consideration of a 20m thick liquefiable layer (as it is assumed in the numerical investigation) is going to

shift the resulting curves to the right, hence severely increasing the volume of the mitigated soil and increasing the associated cost.

Based on the above sets of design charts it is concluded that the rate of variation in the ratio of dynamic settlements becomes significant, i.e. exceeds 5%, for L_{imp}/H_{imp} values greater than about 5, in the case of the maximum improvement thickness examined herein. For low values of H_{imp}/B dynamic settlements experience only a minor increase, especially for narrow widths of improvement.

Regarding the degraded factor of safety, there is a rather abrupt change in the values of the normalized ratio even for large L_{imp}/H_{imp} values, which was obvious already from the execution of the parametric investigation. Namely, even a minor reduction in the improvement width was leading to a major decline in the obtained degraded factor of safety $F.S._{deg}$. This was even more evident for greater values of improvement depth, H_{imp}.

Conditions of "infinite" width of improvement render a very un-conservative estimate both in terms of dynamic settlements and degraded factor of safety. The specific conditions are attained for at least 20 times the footing width. Such a design width is practically prohibited and can lead to excessive construction costs. Hence, the examined method of ground improvement becomes technically and financially efficient for improvement widths within 2 – 5 times the depth of the improvement, namely $L_{imp} = (2 \div 5)\ H_{imp}$.

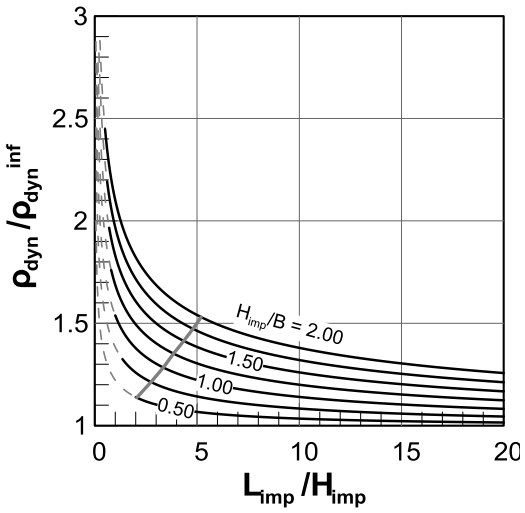

Figure 10.22: Normalized dynamic settlements plotted with respect to L_{imp}/H_{imp} for different H_{imp}/B values.

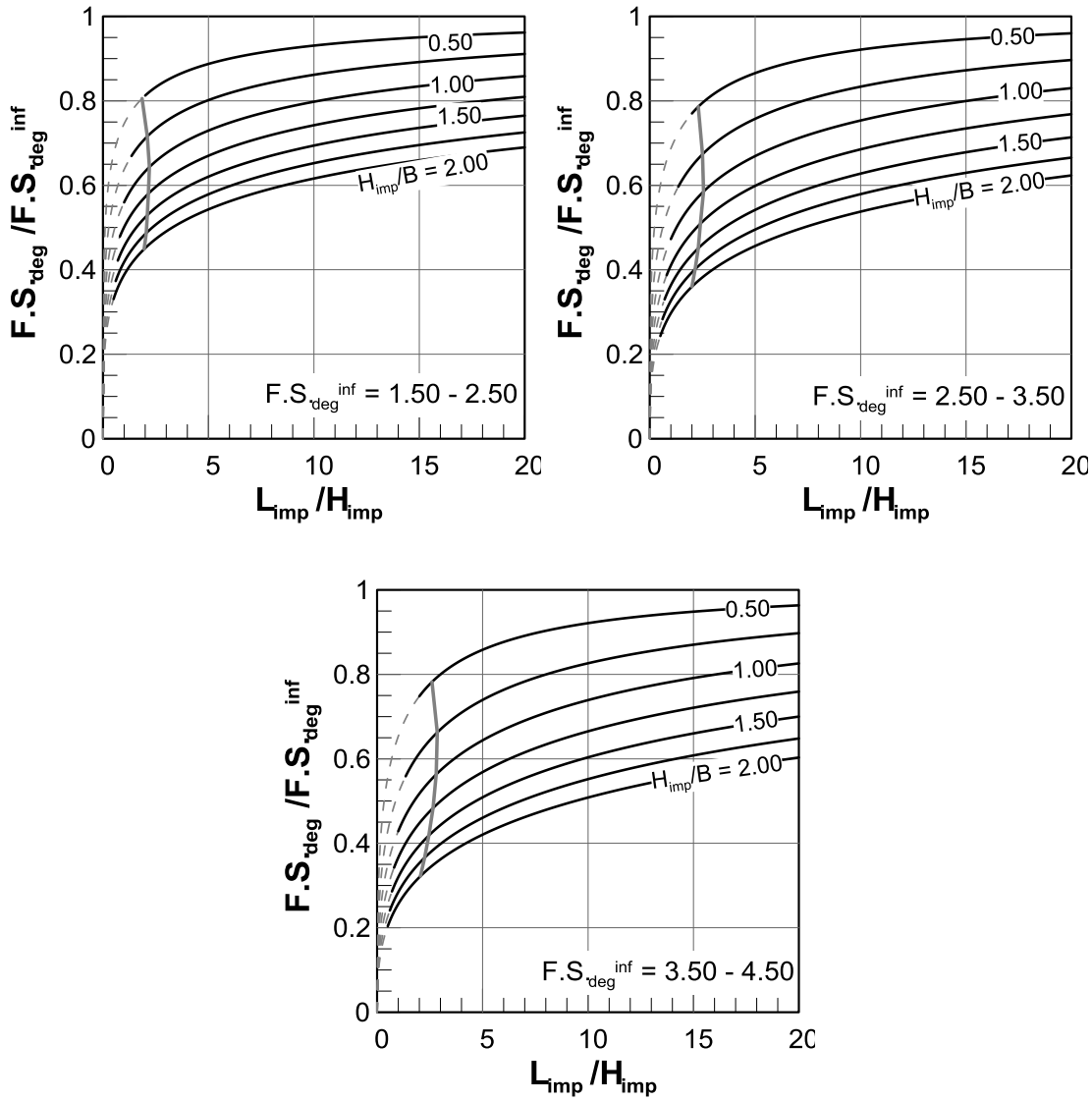

Figure 10.23: Normalized degraded factor of safety plotted with respect to L_{imp}/H_{imp} for different H_{imp}/B values and three values of $F.S._{deg}^{inf}$.

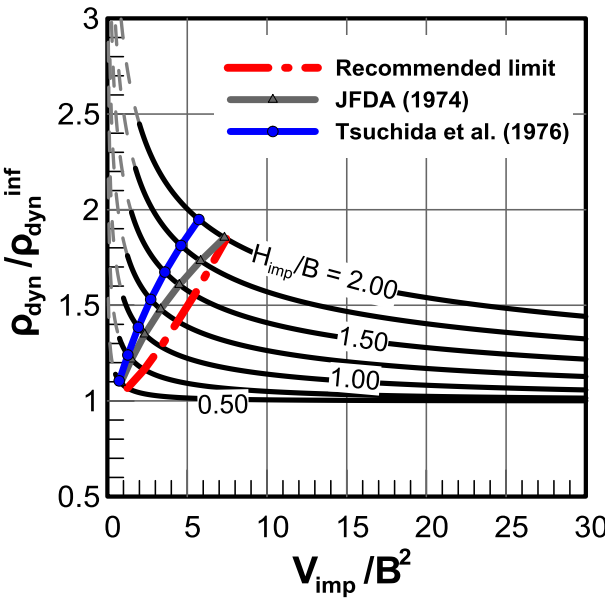

Figure 10.24: Normalized dynamic settlements plotted with respect to V_{imp}/B^2 for different H_{imp}/B values.

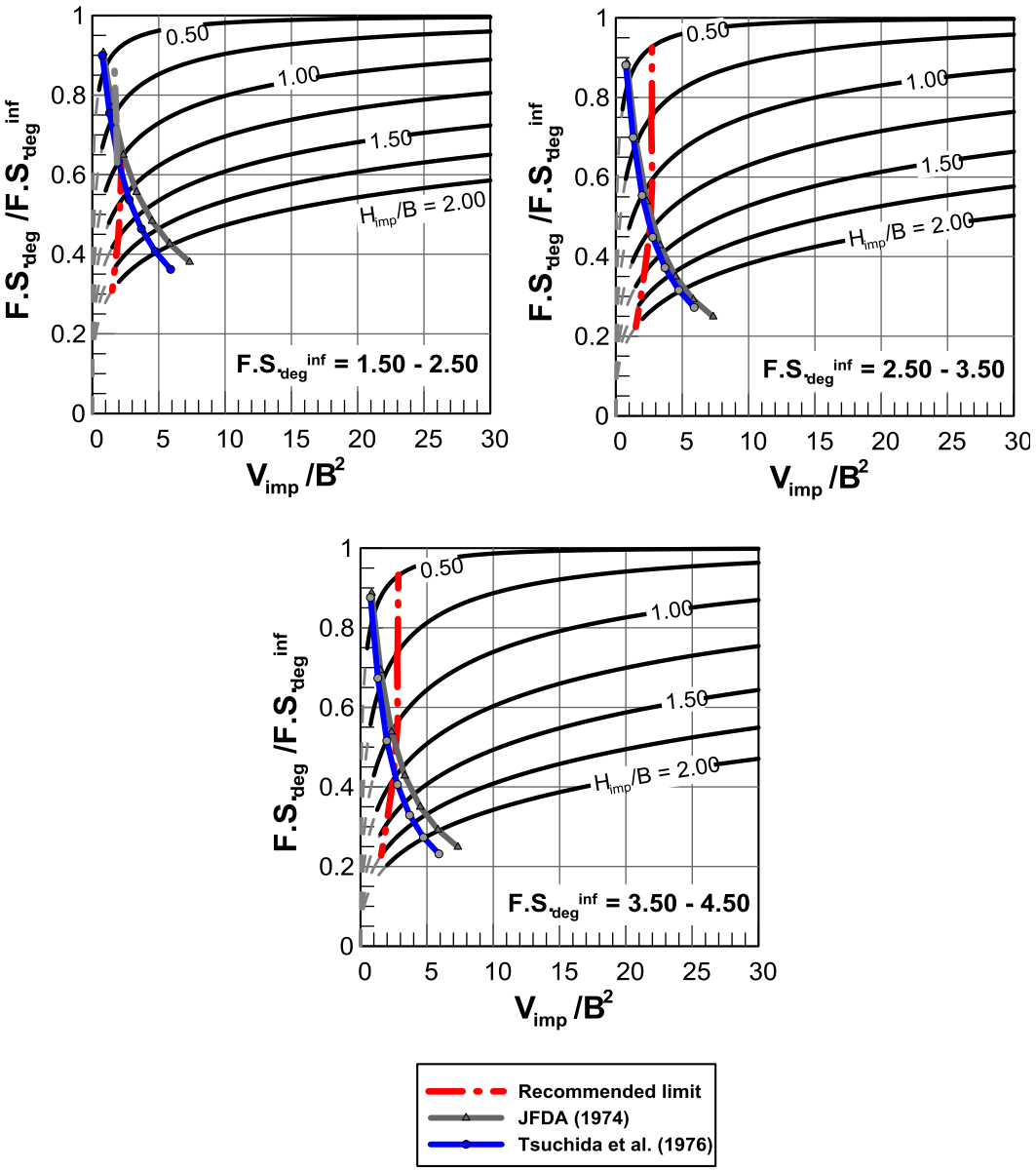

Figure 10.25: Normalized degraded factor of safety plotted with respect to V_{imp}/B^2 for different H_{imp}/B values and three values of $F.S._{deg}^{inf}$.

CHAPTER 11

Analytical Methodology & Design Charts for the Performance-Based Design of Shallow Foundations on Liquefiable Ground

11.1 Overview of proposed analytical methodology

The analytical methodology established and evaluated in the previous chapters is summarized in the current chapter. The purpose is to guide the user through the different stages of the performance – based design of shallow strip foundations starting from the selection of the appropriate spacing of gravel drains, to the evaluation of the seismic settlements and the degraded post-shaking bearing capacity of the foundation, given the dimensions of the mitigated area.

Step 1: Determination of the replacement ratio α_s.- The creation of the non-liquefiable crust involves the installation of gravel drains and the obtained soil improvement is mostly estimated through the replacement ratio α_s. The selection of the appropriate value of α_s depends on **(i)** the initial relative density of the treated soil, $D_{r,o}$ ***(%)***, (ii) the thickness of the performed improvement H_{imp}***(m)*** as well as **(iii)** the maximum excess pore pressure ratio $r_{u,max}$ allowed to develop within the improved zone, which according to current practice, is equal to $r_{u,\max} = r_{u,design} = 0.30 - 0.50$. Given the above, **Figure 11.1** allows the determination of the replacement ratio α_s, taking into account the aforementioned input parameters.

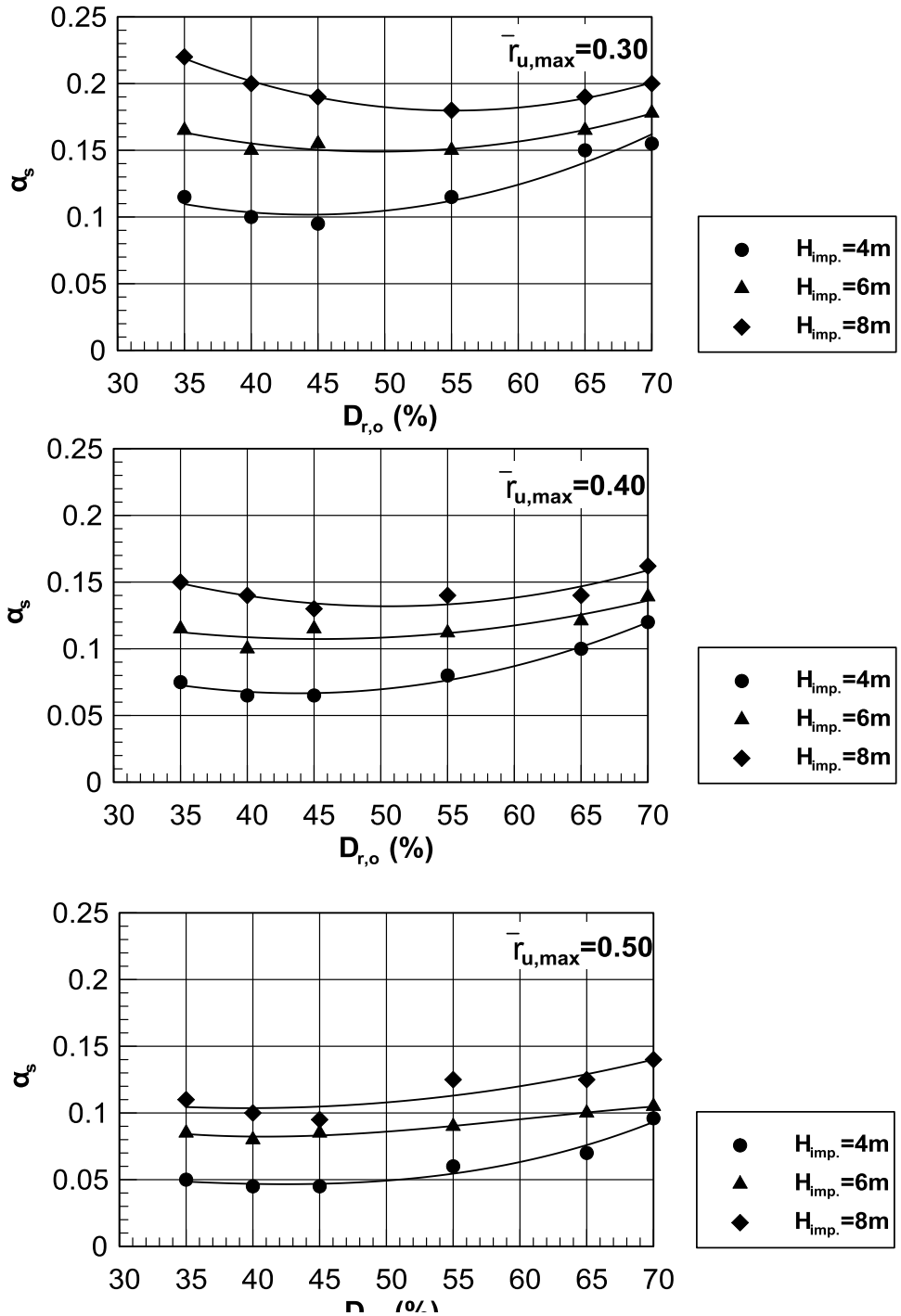

Figure 11.1: Required replacement ratio α_s with regard to initial relative density $Dr_{,o}$(%) and three allowable levels of $r_{u,max}$.

Step 2: Determination of the equivalent properties of the improved zone.- The liquefaction mitigated zone presents larger overall permeability ($k_{eq.}$, m/s) due to the presence of the gravel drains, as well as greater relative density,also denoted $D_{r,imp}$ (%) due to the vibrocompaction applied during gravel drain installation. The specific improved soil properties are determined based on **Figure 11.2** as a function of the previously selected replacement ratio α_s and the initial relative density of the liquefiable sand $D_{r,o}$ (%).

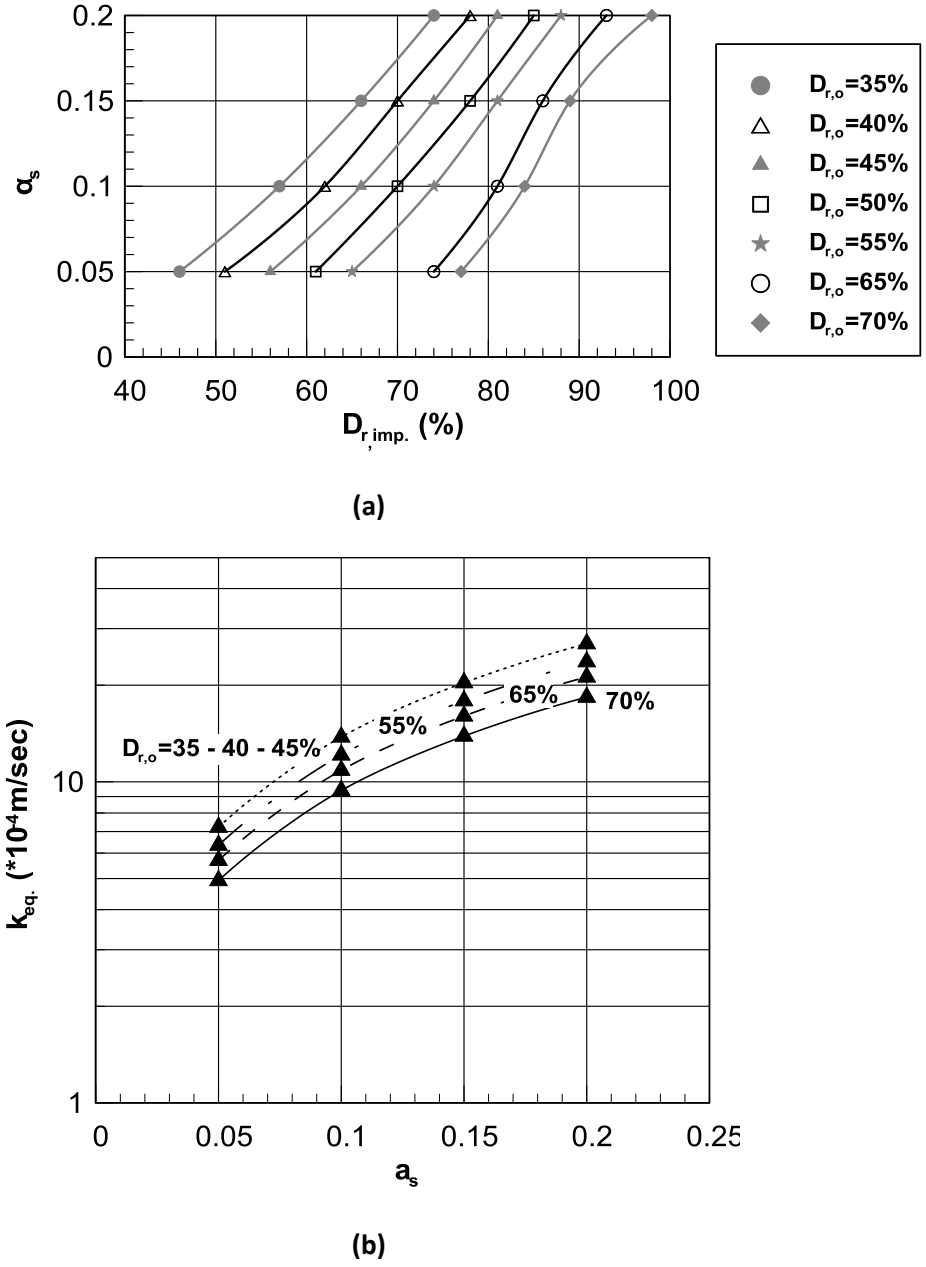

Figure 11.2: Assessment of the improved properties **(a)** relative density $Dr_{,imp}$(%) and **(b)** permeability $k_{eq.}$(m/sec), as a function of replacement ratio α_s.

<u>Step 3:</u> Evaluation of seismic performance of the shallow foundation under conditions of "Infinite" Improvement.- Having specified the equivalent properties and thickness of the improved zone, the seismic performance of the shallow foundation is evaluated initially for the two - layered soil profile. The seismic performance of the foundation includes the evaluation of **(i)** the seismically induced footing settlements ρ_{dyn} (m) and **(ii)** the degraded post-shaking bearing capacity of the footing $q_{ult.}$ (kPa)

The current step requires the prior knowledge of the basic problem parameters, namely:

- the footing characteristics, namely the average contact pressure ***q(kPa)*** and width of the footing ***B(m)***
- the excitation characteristics, including the peak bedrock acceleration ***α_{max} (g)*** the number of significant loading cycles ***N_o*** and the predominant excitation period ***T_{exc} (sec)***.
- the elastic fundamental period of the soil column ***T_{soil} (sec)***.

Evaluation of dynamic settlements ρ_{dyn}^{inf}.- Seismically-induced settlements are evaluated based on the following Newmark-based relation:

$$\rho_{dyn} = c_1 \alpha_{\max} \left(T_{exc} + aT_{soil}\right)^2 \left(N_o + 2\right) \left(\frac{1}{F.S._{deg}^{inf}}\right)^{c_2} \left[1 + c_3 \left(\frac{1}{F.S._{deg}^{inf}}\right)^{c_4}\right] \qquad 11.1$$

in which $\mathbf{c_1=0.019}$, $\mathbf{c_2=0.45}$, $\mathbf{c_3=0.25}$ $\mathbf{c_4=4.5}$ and $\mathbf{a=0.633}$.

Evaluation of degraded bearing capacity q_{ultdeg}^{inf} and associated $F.S._{deg}^{inf}$.- Degraded bearing capacity q_{ultdeg}^{inf} is calculated based on the modified analytical relation initially proposed by Meyerhoff & Hanna (1978) as follows:

$$q_{ult,deg} = \min\left\{\begin{array}{r} \frac{1}{2}\gamma' B N_{\gamma_1} \\ \gamma' H_1^2 K_s \frac{\tan\phi_{1,deg}}{B} + \gamma' \cdot [(1+\alpha)^2 - 1] \cdot H_1^2 K_s \frac{\tan\phi_{2,deg}}{B} - \gamma'(1+\alpha) H_1 + \\ + \frac{1}{2}\gamma' B N_{\gamma 3} + \gamma'(1+\alpha) H_1 N_{q3} \end{array}\right\} \qquad 11.2$$

Coefficients N_q & N_γ are provided below:

$$N_{q3} = \tan^2(45 + \phi_{3,deg}/2) e^{\pi \tan\phi_{3,deg}} \qquad 11.2a$$

$$N_{\gamma 3} = 2(N_q + 1)\tan\phi_{3,deg} \qquad 11.2b$$

The application of the above relation requires the specification of the following parameters:

Coefficient α._ is associated to the thickness of the transition partially liquefied crust, formed underneath the improved zone and is computed based in the equation below. After the statistical processing presented in Chapter 9, coefficient C_α is set equal to 3.76.

$$\alpha = C_\alpha \left[\frac{k_{eq} TN}{H_{imp}} \right]^{0.256} \qquad 11.3$$

Initial Friction angle for each layer $\varphi_{i,ini}$.- Loading and drainage conditions are not uniform across the activated failure surface, hence initial friction angle values for both layers are estimated, based on *Equation 11.4,* considering the average among TX Compresion, TX Extension and Direct Simple Shear loading under undrained and drained conditions.

$$\phi_{i,ini} = \frac{\phi_{i,TX-C} + \phi_{i,TX-E} + \phi_{i,DSS}}{3} \qquad 11.4$$

Degraded friction angle for each layer $\phi_{i,deg}$.- The friction angles appearing in the analytical expression are appropriately reduced to account for the excess pore pressure build up which is anticipated at the end of seismic shaking. To this extent, it is approximately assumed that:

$$\phi_{i,deg} = \tan^{-1}[(1-U_i)\tan\phi_{i,ini}] \qquad 11.5$$

where the subscript "ini" denotes the friction angle of the ground at the beginning of shaking, while i= 1 for the improved crust, 2 for the transition zone and 3 for the liquefied sand. The associated excess pore pressure ratios U_i are separately evaluated below.

Excess pore pressure ratio U_1 in the improved crust.- The average epp ratio ***U_1*** refers to free field conditions and at the end of shaking and is expressed as a portion of the allowable excess pore pressure ratio, ***U_{design},*** set equal to:

$$U_1 = 0.54 U_{design} \qquad 11.6$$

Excess pore pressure ratio in the transition zone *U_2*.-** Parameter ***U_2*,** corresponds to the average excess pore pressure ratio in the transitional non-liquefied zone of the natural ground and is estimated as the average between ***U_1*** and the excess pore pressure ratio in the liquefied soil, which equals unity. Thus, ***U_2*** is equal to:

$$U_2 = \frac{(1+U_1)}{2} = \frac{(1+0.54U_{design})}{2} \qquad 9.7$$

Excess pore pressure ratio in the liquefied ground U_3.- The excess pore pressure ratio U_3 refers to the liquefied ground, over a representative area underneath the footing and below the improved crust. It is evaluated through the following equation, in which coefficient C_{U3} is equal to 0.86.

$$U_3 = C_{U_3}\left(\frac{q_{ultdeg}^{inf}}{p_\alpha}\right)^{-0.18} \leq 1.00 \qquad 11.8$$

Coefficient K_s.- This parameter reflects the shear strength mobilized across the partially liquefied improved and transitional soil zones, below the edges of the footing. It is a function of the contact pressure q and the H_{imp}/B ratio as shown in *Equation 11.9*. After the statistical processing presented in Chapter 9, coefficient C_{Ks} is set equal to 1.00.

$$K_s = C_{K_s}\left(\frac{q}{p_\alpha}\right)^{-0.30}\left(\frac{H_{imp}}{B}\right)^{-0.50} \qquad 11.9$$

where p_α = 98.1kPa is the atmospheric pressure.

Due to the dependence of U_3 on q_{ult}, *Equations 11.2* and *11.8* are solved concurrently until convergence and in the sequel, the degraded factor of safety $F.S._{deg}^{inf*}$ is derived. To further improve the accuracy of the proposed methodology, a correction factor is applied on the initially obtained value as shown below:

$$F.S._{deg}^{inf} = \frac{F.S._{deg}^{inf*}}{0.05 + 0.60\left(F.S._{deg}^{inf*}\right)^{0.85}} > 0.60F.S._{deg}^{inf*} \qquad 11.10$$

<u>Step 4:</u> Evaluation of seismic performance of the shallow foundation under conditions of "Finite" Improvement.- In real applications, soil improvement is applied over a designated area of limited dimensions. The determination of the particular area should grant the optimum solution between the required performance criteria specified for the shallow foundation and the associated construction costs. Hence, the current step summarizes the proposed analytical expressions to evaluate the appropriate improvement area dimensions. Note that both aspects of the seismic performance of the foundation (i.e ρ_{dyn} & $F.S._{deg}$) appear with reference to the results for "infinite" ground improvement, implying their prior assessment.

Dynamic settlements ρ_{dyn}.- are associated to the H_{imp}/B and L_{imp}/B ratio. The ratio of $\rho_{dyn}^{inf}/\rho_{dyn}$ is evaluated based on the direct analytical expression presented below:

$$\frac{\rho_{dyn}^{inf}}{\rho_{dyn}} = 1 - \exp\left[-1.05\left(\frac{H_{imp}}{B}\right)^{-1}\left(\frac{L_{imp}}{B}\right)^{0.30}\right] \qquad 11.11$$

Degraded bearing capacity q_{ult}^{deg} and Factor of Safety $F.S._{deg}$.- Due to a number reasons thoroughly explained in Chapter 10, the ratio of $F.S._{deg}/F.S._{deg}^{inf}$, is computed through the following non-linear equation. Hence $F.S._{de}$ is the outcome of a cumbersome iterative procedure.

$$\left(\frac{F.S._{deg}}{F.S._{deg}^{inf}}\right)^{-0.45} = \left\{1 - \exp\left[-1.05\left(\frac{H_{imp}}{B}\right)^{-1}\left(\frac{L_{imp}}{B}\right)^{0.30}\right]\right\} \frac{\left(F.S._{deg}^{inf}\right)^{4.5} + 0.25\left(\frac{F.S._{deg}}{F.S._{deg}^{inf}}\right)^{4.5}}{\left(F.S._{deg}^{inf}\right)^{4.5} + 0.25} \qquad 11.12$$

Given the complexity in the use of *Equation 11.12*, a set of simplified analytical expressions is formulated, which enable the direct evaluation of the degraded factor of safety $F.S._{deg}$ for "limited" improvement conditions. The following sets of equations are expressed with regard to the required L_{imp}/H_{imp} ratio and each one of them is applicable for a different range of $F.S._{deg}^{inf}$.

$F.S._{deg}^{inf}$= 1.50 – 2.50: $$\frac{F.S._{deg}}{F.S._{deg}^{inf}} = 1 - \exp\left[-0.82\left(\frac{H_{imp}}{B}\right)^{-1.03}\left(\frac{L_{imp}}{B}\right)^{0.29}\right] \qquad 11.13$$

$F.S._{deg}^{inf}$= 2.50 – 3.50: $$\frac{F.S._{deg}}{F.S._{deg}^{inf}} = 1 - \exp\left[-0.64\left(\frac{H_{imp}}{B}\right)^{-1.30}\left(\frac{L_{imp}}{B}\right)^{0.34}\right] \qquad 11.14$$

$F.S._{deg}^{inf}$= 3.50 – 4.50: $$\frac{F.S._{deg}}{F.S._{deg}^{inf}} = 1 - \exp\left[-0.56\left(\frac{H_{imp}}{B}\right)^{-1.30}\left(\frac{L_{imp}}{B}\right)^{0.38}\right] \qquad 11.15$$

<u>Step 5:</u> Cost - Benefit Estimate.- To gain additional insight regarding the practical application of the previously generated analytical expressions, regarding ρ_{dyn} and $F.S._{deg}$, they are appropriately modified to incorporate the ratio of the width over the depth of the improved zone, L_{imp}/H_{imp}. Hence, the outcome for the ratio of dynamic settlements is summarized below:

$$\frac{\rho_{dyn}^{\ inf}}{\rho_{dyn}} = 1 - \exp\left[-1.05 \left(\frac{H_{imp}}{B} \right)^{-0.7} \left(\frac{L_{imp}}{H_{imp}} \right)^{0.30} \right] \qquad 11.16$$

Accordingly, the simplified analytical expressions for $F.S._{deg}$ are transformed into *Equations 11.17*, *11.18*, *11.19* respectively:

$F.S._{deg}^{\ inf}$= 1.50 – 2.50:
$$\frac{F.S._{deg}}{F.S._{deg}^{\ inf}} = 1 - \exp\left[-0.82 \left(\frac{H_{imp}}{B} \right)^{-0.74} \left(\frac{L_{imp}}{H_{imp}} \right)^{0.29} \right] \qquad 11.17$$

$F.S._{deg}^{\ inf}$= 2.50 – 3.50:
$$\frac{F.S._{deg}}{F.S._{deg}^{\ inf}} = 1 - \exp\left[-0.64 \left(\frac{H_{imp}}{B} \right)^{-0.86} \left(\frac{L_{imp}}{H_{imp}} \right)^{0.34} \right] \qquad 11.18$$

$F.S._{deg}^{\ inf}$= 3.50 – 4.50:
$$\frac{F.S._{deg}}{F.S._{deg}^{\ inf}} = 1 - \exp\left[-0.56 \left(\frac{H_{imp}}{B} \right)^{-0.92} \left(\frac{L_{imp}}{H_{imp}} \right)^{0.38} \right] \qquad 11.19$$

The correlation between the selected dimensions of an improved zone around the shallow foundation to the generated cost becomes a lot more straightforward when incorporating the resulting volume of improvement V_{imp}, which is a more direct cost indicator. For the plane strain conditions considered in the problem, the volume of the improved area is defined as the product of the depth (H_{imp}) times the width (L_{imp}) of the improved zone. To preserve the dimensionless form of the initially proposed equations, volume is divided by B^2 and the outcome of the modification is exhibited below both for the dynamic settlements and the degraded factor of safety.

$$\frac{\rho_{dyn}^{\ inf}}{\rho_{dyn}} = 1 - \exp\left[-1.05 \left(\frac{H_{imp}}{B} \right)^{-1.30} \left(\frac{V_{imp}}{B^2} \right)^{0.30} \right] \qquad 11.20$$

$F.S._{deg}^{\ inf}$= 1.50 – 2.50:
$$\frac{F.S._{deg}}{F.S._{deg}^{\ inf}} = 1 - \exp\left[-0.82 \left(\frac{H_{imp}}{B} \right)^{-1.32} \left(\frac{V_{imp}}{B^2} \right)^{0.29} \right] \qquad 11.21$$

$F.S._{deg}^{\ inf}$= 2.50 – 3.50:
$$\frac{F.S._{deg}}{F.S._{deg}^{\ inf}} = 1 - \exp\left[-0.64 \left(\frac{H_{imp}}{B} \right)^{-1.54} \left(\frac{V_{imp}}{B^2} \right)^{0.34} \right] \qquad 11.22$$

$F.S._{deg}^{\ inf}$= 3.50 – 4.50:
$$\frac{F.S._{deg}}{F.S._{deg}^{\ inf}} = 1 - \exp\left[-0.56 \left(\frac{H_{imp}}{B} \right)^{-1.68} \left(\frac{V_{imp}}{B^2} \right)^{0.38} \right] \qquad 11.23$$

11.2 Design charts

In the present section, the previously presented analytical expressions are used to formulated practice-oriented design charts for the direct evaluation of the two aspects of the seismic performance of shallow foundations.

The predictions of the empirical methodologies, proposed by JDFA (1974) and Tchuchida et al. (1976), are also included in the following design charts and particularly compared against the proposed methodology in terms of the required improvement volume V_{imp}. The specific guidelines have been presented in Chapter 10 and provide an estimate of the width of the compacted zone around shallow or slightly embedded structures. Nevertheless, both empirical methodologies refer to compaction as the main improvement technology and do not incorporate the drainage effects offered by the presence of gravel drains. Hence, any conclusions should be handled with caution. Moreover, the above guidelines, do not provide any quantitative means of assessing the foundation performance, as a function of the improvement area dimensions. Hence, the associated curves result from the combination of the guidelines and the proposed analytical relations.

Figure 11.3 through **Figure 11.5** allow the assessment of the **ratio of dynamic settlements** $\boldsymbol{\rho_{dyn}/\rho_{dyn}^{inf}}$ as a function of three different variables, namely the L_{imp}/B, the L_{imp}/H_{imp} and the V_{imp}/B^2 ratio. The ratio of dynamic settlements is plotted for seven (7) distinct H_{imp}/B values (= 0.50, 0.75, 1.00, 1.25, 1.50, 1.75, 2.00). The thicker dotted grey lines in **Figure 11.4** and **Figure 11.5** correspond to the points on the different curves beyond which, increasing the ratio of L_{imp}/H_{imp} renders a rate of variation less than 5%, i.e. the cost-effect ratio is high.

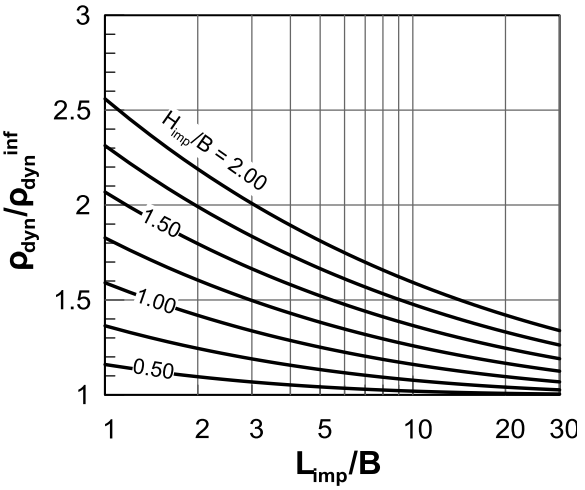

Figure 11.3: Design chart for the evaluation of the ratio of dynamic settlements $\rho_{dyn}/\rho_{dyn}^{inf}$, with regard to the L_{imp}/B ratio for different H_{imp}/B values.

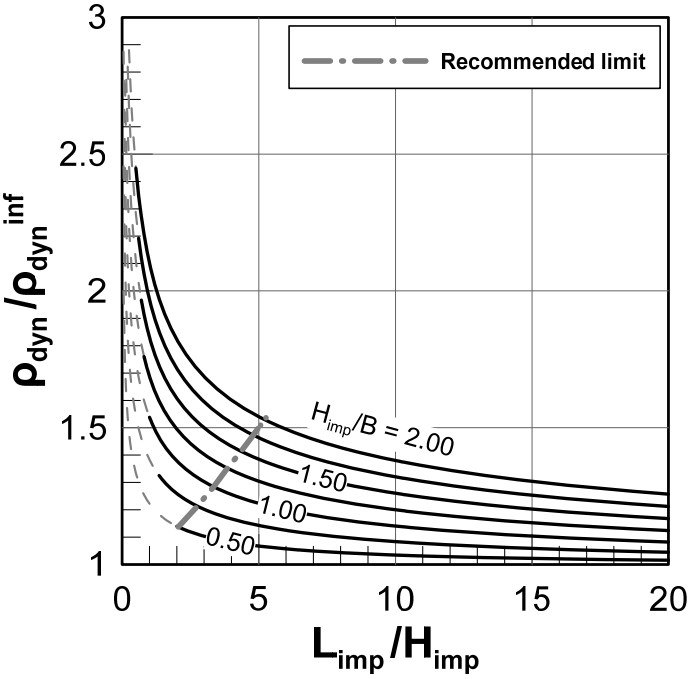

Figure 11.4: Normalized dynamic settlements plotted with respect to L_{imp}/H_{imp} for different H_{imp}/B values.

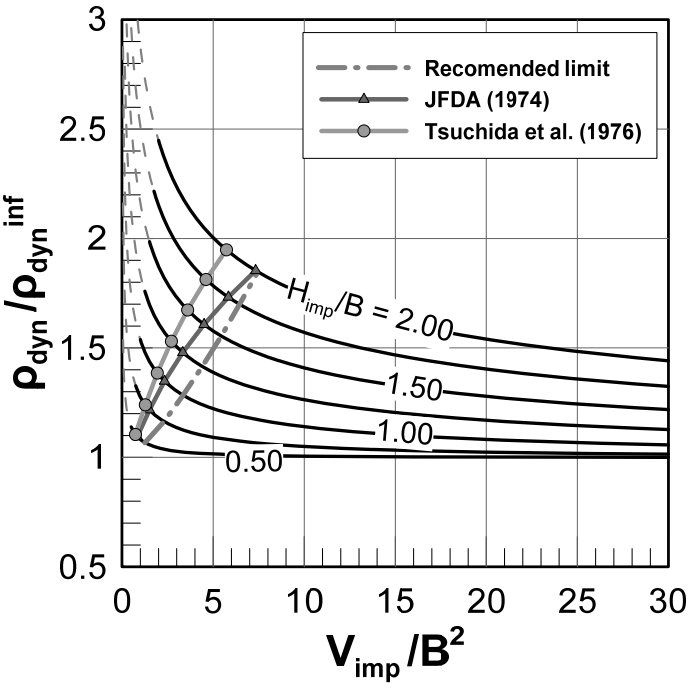

Figure 11.5: Normalized dynamic settlements plotted with respect to V_{imp}/B^2 for different H_{imp}/B values.

Regarding the normalized ratio of **the degraded factor of safety**, $F.S._{deg}/F.S._{deg}^{inf}$ the corresponding design charts are summarized in **Figure 11.6** to **Figure 11.8**. The specific charts present the $F.S._{deg}/F.S._{deg}^{inf}$ ratio also with regard to the L_{imp}/B, the L_{imp}/H_{imp} and the V_{imp}/B^2 ratio.

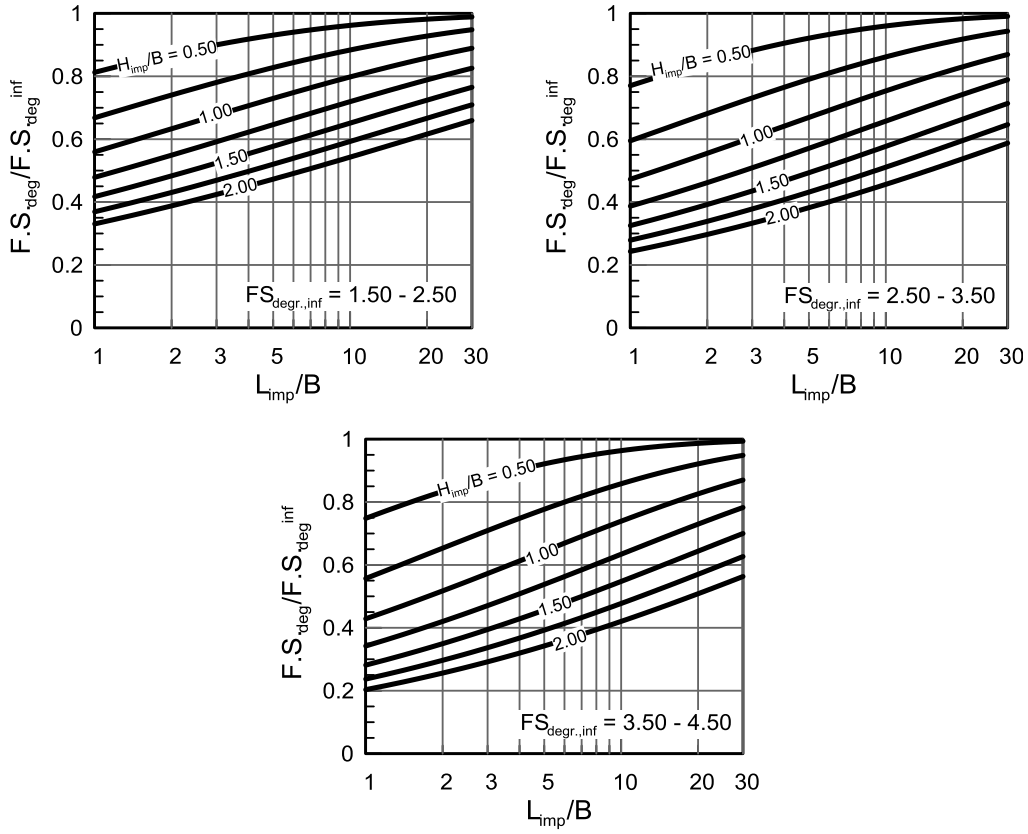

Figure 11.6: Design charts relating the $F.S._{deg}/F,.S._{deg}^{inf}$ ratio to the L_{imp}/B value, based on the simplified analytical expressions, for three initial $F.S._{deg}^{inf}$ values.

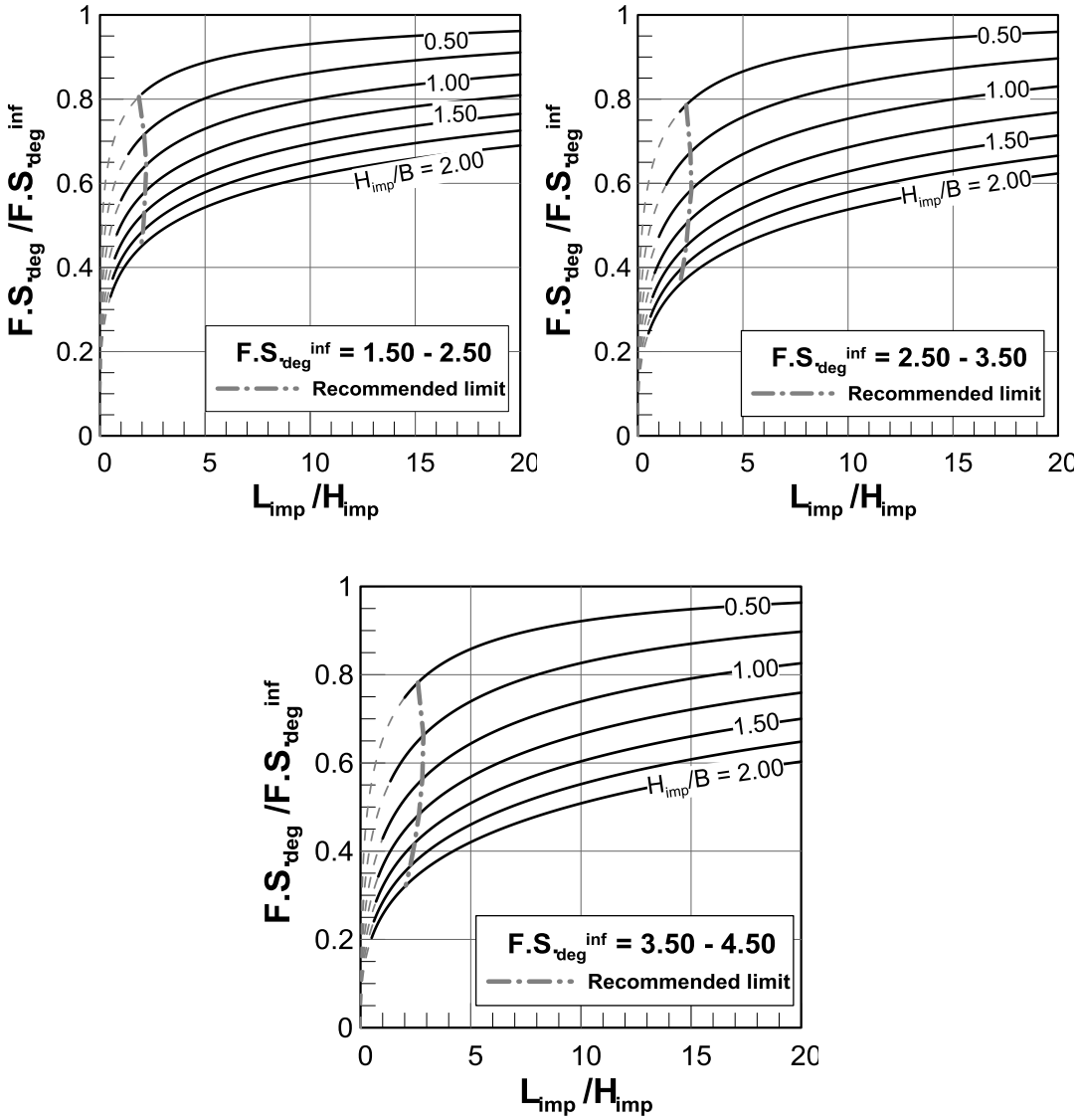

Figure 11.7: Normalized degraded factor of safety plotted with respect to L_{imp}/H_{imp} for different H_{imp}/B values and three values of $F.S._{deg}^{inf}$.

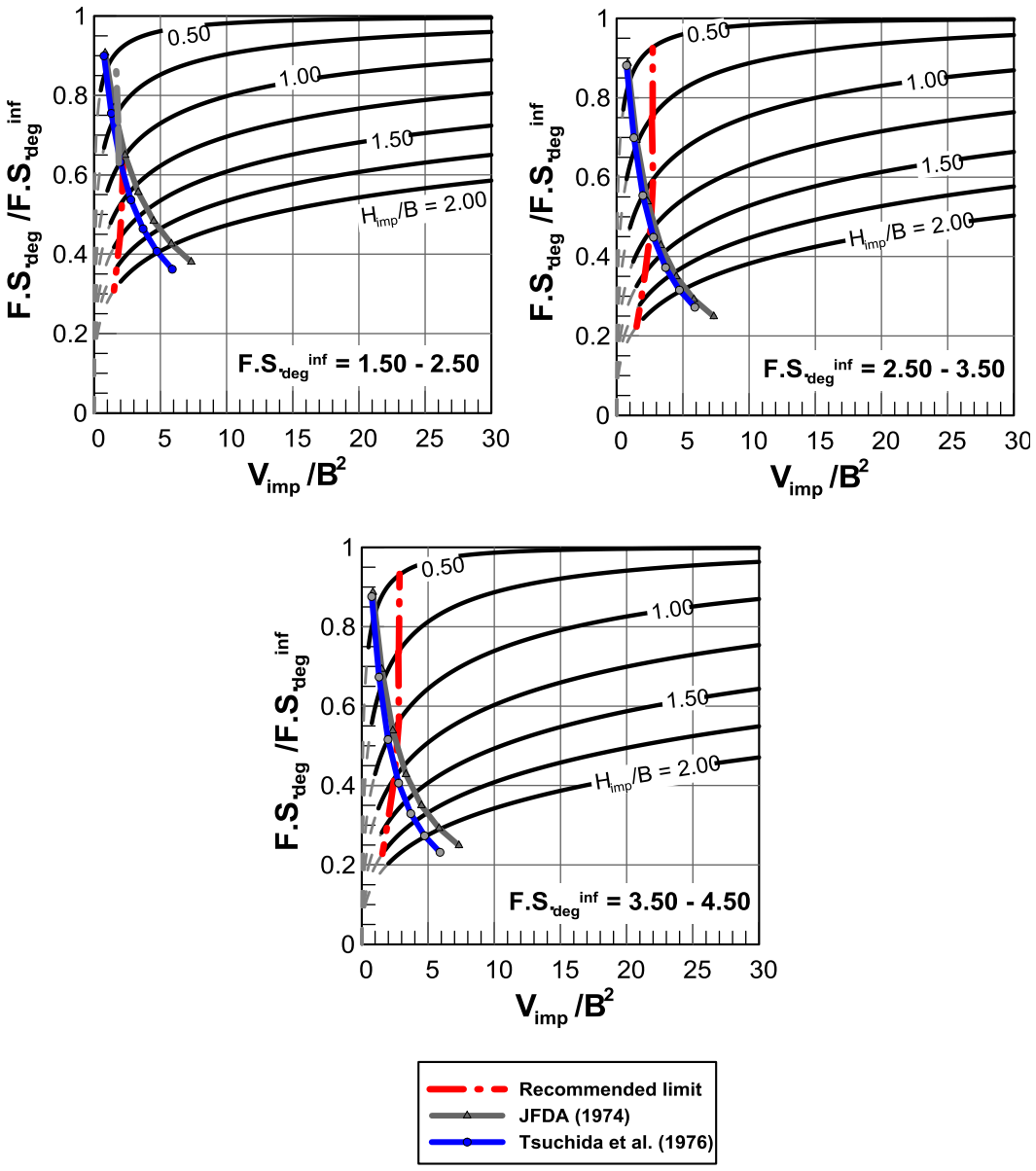

Figure 11.8: Normalized degraded factor of safety plotted with respect to V_{imp}/B^2 for different H_{imp}/B values and three values of $F.S._{deg}^{inf}$.

REFERENCES

Adalier K., Elgamal A., Meneses J., Baez J.I. (2003): “Stone columns as liquefaction countermeasure in non-plastic silty soils”, Soil Dynamics and Earthquake Engineering, Vol. 23 (7), pp. 571-584.

Anagnostopoloulos A. (2008): "Settlements of Shallow Foundations" Hellenic Society of Soil Mechanics and Geotechnical Engineering (HSSMGE), 5th Athenian Lecture in Geotechnical Engineering (in greek)

Andersen H. K., Schjetne K., (2013): “Data base of friction angles of sand and consolidation characteristics of sand, silt and clay", Journal of Geotechnical and Geoenvironmental Engineering, Vol. 139, No. 7, pp1140-1155.

Andrianopoulos K. (2006): "Numerical simulation of static and dynamic loading on elastoplastic soils" PhD Thesis, National Technical University of Athens, School of Civil Engineering, Geotechnical Department (in Greek).

Andrianopoulos K., Papadimitriou A.G. Bouckovalas G.D. (2010): "Explicit integration of bounding surface model for the analysis of earthquake soil liquefaction" International Journal for Numerical and Analytical Methods in Geomechanics, Vol. 34 pp 1586 - 1614.

Andrianopoulos, K.I., Papadimitriou, A.G., Bouckovalas, G.D. (2010): “Bounding surface plasticity model for the seismic liquefaction analysis of geostructures”, Soil Dynamics and Earthquake Engineering, Vol. 30 (10), pp. 895-911.

Arulanandan K., Sybico JJr., (1992): "Post-liquefaction settlement of sand", Proceedings of the Wroth Memorial Symposium, Oxford University, England.

Arulmoli et al. (1992): "VELACS: Verification of Liquefaction Analyses by Centrifuge Studies Laboratory Testing Program Soil Data Report" Earth Technology Project No. 90-0562.

Arulmoli, K., Muraleetharan, K.K., Hossain, M.M., Fruth, S.L., (1992): "VELACS: verification of liquefaction analyses by centrifuge studies; Laboratory Testing Program - Soil Data Report", Research Report, The Earth Technology Corporation

ATC Report 49-a (draft)/MCEER Technical Report 02-SP01 (2001): "Recommended LRFD guidelines for the seismic design of highway bridges"

Balakrishan A., (2000): "Liquefaction remediation at a bridge site", PhD Dissertation, University of California, Davis.

Barker R.M., Duncan J.M., Rojiani K.B., Ooi PSK, Tan C.K., Kim S.G. (1991): "Manuals for the design of bridge foundations: shallow foundations, driven piles, retaining walls and abutments, drilled shafts, estimating tolerable movements and load factor design specifications and commentary", Transport Research Board.

Bauer Spezialtiefbau GmbH. Web Site: www.bauer.de.

Been K., Jefferies G.M., (1985): "A state parameter for sands", Geotechnique, Vol. 35, No. 2, pp. 99-112.

Bell G.F. (1993): Engineering treatment of soils, E&FN Spon, an imprint of Chapman & Hall, 2-6 Boundary row, London SE 1 8HN, U.K.

Bjerrum (1963): Discussion to the European Conference on Soil Mechanics and Foundation Engineering Vol. II, p 135.

Bolton, D.M. (1986): “The shear strength and dilatancy of sands.” Geotechnique, Vol. 36, No. 1, pp 65-78.

Bouckovalas G. D., (2004): "Notes on Special Topics of Foundation Engineering", NTUA

Bouckovalas G.D., Papadimitriou A.G., Niarchos D., (2009): “Gravel drains for the remediation of liquefiable sites: the Seed & Booker (1977) approach revisited”, Keynote Lecture, IS-Tokyo.

Bouckovalas et al. (2011): "Dynamic Centrifuge Test: experimental verification of shallow foundation performance under earthquake-induced liquefaction” TNA project, Cambridge University Technical Services, National Technical University of Athens.

Boulanger R., Idriss I., Stewart D., Hashash Y. & Schmidt B. (1998): "Drainage capacity of stone columns or gravel drains for mitigating liquefaction", Proc., Geotechnical Earthquake Engineering and Soil Dynamics ASCE, Geotechnical Special Publication, No 75, Vol.1, pp 678-690

Braja M. Das, (1999): "Principles of foundation engineering", 4th Edition, Thomson Brooks/Cole Publications.

Burland J.B., Broms B. B., De Mello B. F. V., (1977): "Behaviour of foundations and structures" IX International Conference on Soil Mechanics and Foundation Engineering, Tokyo.

Chaloulos Y. (2012): "Numerical investigation of pile response under liquefaction and ground lateral spreading" PhD thesis.

Chang W-J, Rathje E., Stokoe II K. H., Cox B. R., (2004): " Direct evaluation of effectiveness of prefabricated vertical drains in liquefiable sand", Soil Dynamics and Earthquake Engineering, Vol. 24, pp 723-731.

Chen Y-R., Kutter B. L., (2009): “Contraction, dilation and failure of sand in triaxial, torsional and rotational shear tests”, Journal of Engineering Mechanics, Vol. 135, No.10, ASCE.

Coelho P.A.L.F., Haigh K.S., Madabhushi S.P.G. (2004): “Centrifuge modeling of the effects of earthquake-induced liquefaction on bridge foundations”, Proceedings of the 11th International Conference on Soil Dynamics and Earthquake Engineering (ICSDEE) and the 3rd International Conference on Earthquake Geotechnical Engineering, University of California, Berkeley.

Dashti S., Bray J.D., Pestana J.M., Riemer M., Wilson D., (2010): "Centrifuge testing to evaluate and mitigate liquefaction-induced buidling settlement mechanisms" Journal of Geotechnical and Geoenvironmental Engineering, Vol. 136 No. 7, pp. 918-929.

Dashti S., Bray J.D., Pestana J.M., Riemer M., Wilson D., (2010): “Mechanisms of seismically induced settlement of buildings with shallow foundations on liquefiable soil”, Journal of Geotechnical and Geoenvironmental Engineering, Vol. 136 No. 1, pp. 151-164.

De Alba P., Chan C. K., Seed H. B., (1975), "Determination of soil liquefaction characteristics by large-scale laboratory tests", Report No 75-14, Earthquake Engineering Research Center.

DeAlba P., Seed H. B., Chan K. C., (1976): "Sand liquefaction in large-scale simple shear tests", Journal of the Geotechnical Engineering Division, ASCE, Vol. 102, No. 9 pp 909-927.

Department of Defence (1997), "Handbook on soil dynamics and special design aspects"

Edrassis – Psallidas.

Ellington Cross http://www.ellingtoncross.com/.

European Committee for Standardisation (CEN, 2001), Eurocode 7: Geotechnical Design, PartI:General Rules, "Annex H: Limiting Values of structural deformation and foundation movement".

European Committee for Standardisation (2003): Eurocode 8: Design of structures for earthquake resistance Part 1: Buildings.

European Committee for Standardisation (CEN, 2003), "Eurocode 8: Design of structures for earthquake resistance Part 2: Bridges".

European Union, General Secretariat for Research and Technology (2000-2006), "X-SOILS: Foundations in seismically sensitive soils undergoing strong earthquake motions".

Frakn R. (2001) "Some recent developments on the behavior of shallow foundations", 10th European Conference on Soil Mechanics & Foundation Engineering, Florence

Friedland I., Mayes I.R., Bruneau M., (2001): "Recommended changes to the AASHTO Specifications for the Seismic Design of Highway Bridges", NCHRP - Project 12-49.

Geo-Technics America http://www.geotechnics.com/

Harada N., Towhata I., Takatsu T., Tsunoda S., Sesov V., (2004,2006): "Development of new drain method for protection of existing pile foundations from liquefaction effects" Soil Dynamics and Earthquake Engineering.

Hardin B. O., (1978): "Nature of stress-strain behavior of soils" Proc. Conference in Earthquake Engineering and Soil Dynamics, Pasadena USA, Vol. 1, pp 3-90, ASCE.

Hayward Baker Inc. Geotechnical Construction, www.HaywardBaker.com

Iai S., Koizumi K., Kurata E., (1991): "Ground compaction area as a remedial measure against liquefaction", JSSMFE, Vol. 39, No. 2, pp 35-40.

Imbsen & Associates, Inc. a TRC Company, (2006): "Updating Recommended LRFD guidelines for the seismic retrofitting of highway brigdes", NCHRP 20-07/Task 193 (Task 2 Appendix 2A).

Ishihara K., (1994): "Verification of Numerical Procedures for the Analysis of Soil Liquefaction Problems" Review of the Predictions of Model 1 in the VELACS program, Arulanandan K., Scott RF (eds.), AA Balkema, Rotterdam, pp 1353 - 1368.

Itasca (2005): “Fast Lagrangian Analysis of Continua”, Itasca Consulting Group Inc.,Minneapolis, Minnesota.

Itasca (2008): " FLAC3Dv4.0: Fast Lagrangian Analysis of Continua in 3 Dimensions" Online Manual

Jafarzadeh F., Yanajisawa E., (1995): "Settlement of Sand Models under Unidirectional Shaking", First International Conference on Earthquake Geotechnical Engineering IS-Tokyo, Ishihara K. (ed.), pp 693 - 698.

Japanese Fire Defence Agency (1974).

Japanese Geotechnical Society, (1998): "Remedial measures against soil liquefaction. From investigation and design to implementation", A.A. Balkema Publications, Rotterdam.

Japanese Road Association (2002): "Design Specifications for Highway Bridges, Part V: Seismic Design" Japanese Road Association.

Karamitros D. K., Bouckovalas G.D., Chaloulos Y.K., (2013): "Insight into the seismic liquefaction performance of shallow foundations", Journal of Geotechnical and Geoenvironmental Engineering, ASCE, Vol 139, pp. 599-607.

Karamitros D.K., Bouckovalas G.D., Chaloulos Y.K. (2013): "Seismic settlements of shallow foundations on liquefiable soil with a clay crust", Soil Dynamics and Earthquake Engineering, Vol. 46., pp. 64-76.

Karamitros D.K., Bouckovalas G.D., Chaloulos Y.K., Andrianopoulos K.I. (2013): "Numerical analysis of liquefaction-induced bearing capacity degradation of shallow foundations on a two-layered soil profile", Soil Dynamics and Earthquake Engineering, Vol. 44, pp. 90-101.

Kawasaki, K., Sakai, T., Yasuda, S., Satoh, M. (1998): “Earthquake-induced settlement of an isolated Footing forpowertransmissiotn tower”, Centrifuge Vol. 98, pp. 271-276.

Kawashima K., (2000): "Seismic design and retrofit of bridges", 12th World Conference on Earthquake Engineering, New Zealand.

Kawashima K., Unjoh S., (2004): "Seismic design of highway bridges", Journal of Japan Association for Earthquake Engineering, Vol. 4, No.3 (Special Issue)

Keller Ground Engineering Pty, Ltd.

Kutter L. B., Chen Y-R (1997): “Constant p and constant volume friction angles are different” Geotechnical Testing Journal, GTJODJ, Vol. 20, No3.

Lee K. L., Albaisa A., (1974), "Earthquake induced settlements in saturated sands", Journal of the Soil Mechanics and Foundations Division, ASCE, Vol. 100, No GT4.

Liu, L., Dobry, R. (1997): “Seismic response of shallow foundation on liquefiable sand”, Journal of Geotechnical and Geoenvironmental Engineering, Vol. 123 (6), pp. 557-566.

Loukidis D., Salgado R., (2009): "Modeling sand response using two-surface plasticity", Computers and Geotechnics, 36, pp 166-186.

Manzari M. T., Dafalias Y. F., (1997): "A critical state two-surface plasticity model for sands", Geotechnique, Vol. 47, No. 2, pp 255-272

Marinucci A., Rathje E., Kano S., Kamai R., Conlee C., Howell R., Boulanger R., Gallagher P., (2008): "Centrifuge testing of prefabricated drains for liquefaction remediation" Geotechnical Earthquake Engineering and Soil Dynamics, IV: pp. 1-10.

Martin J., Cundall P. A., (1982): "Mixed discretization procedure for accurate solution of plasticity problems", International Journal for Numerical and Analytical Methods in Geomechanics, Vol. 6, pp 129-139.

MCEER (2005): "Seismic Retrofitting Manual for Highway Structures Part 1: Bridges", U.S. Dept. of Transportation - FHWA

Meyerhof, G.G., Hanna, A.M. (1978): “Ultimate bearing capacity of foundations on layered soils under inclined load”, Canadian Geotechnical Journal, Vol. 15 (4), pp. 565-572.

Moffat B. (2007): "Soil Remediation Techniques for Reduction of Earthquake-Induced Liquefaction", Proc. Sessions of the 2007 Structures Congress.l

Moulton K. L., GangaRao V.S. H., Halvorsen T.G. (1985): "Tolerable movement criteria for highway bridges" U.S. Dept. of Transportation - Federal Highway Administration Report No. FHWA/RD-85/107.

Naesgaard Ernest, Seismic gravel drain tests: test methodology, results, conclusions, personal communication.

Nilex Corporation, www.nilex.com

Okita Yunoki, Ito, Nakajima, Shimaoka (1986): "Effect of drain permeability on nomograph of gravel drain system", Proc. 21th National Conference SMFE, Vol.1, pp 737-738.

Onoue A. (1988): Technical Note: “Diagrams considering well resistance for designing spacing ratio of gravel drains”, Soils and Foundations Vol. 28, No 3, pp 160 – 168. Japanese Society of Soil Mechanics and Foundation Engineering.

Paikovsky G. S., (2005): "Serviceability in the design of bridge foundations", Proceedings of the International Workshop on the Evaluation of Eurocode 7, Trinity College, Dublin

Papadimitriou A. G. (1999): "Elastoplastic modeling of the monotonic and dynamic behavior of soils", PhD Thesis, National Technical University of Athens.

Papadimitriou A.G., Bouckovalas G. D., (2002): "Plasticity model for sand under small and large cyclic strains: a multi-axial formulation", Soil Dynamics and Earthquake Engineering, Vol. 22, pp 191-204.

Papadimitriou A.G., Bouckovalas G., Dafalias F. Y., (2001): "Plasticity Model for Sand under Small and Large Cyclic Strains", Journal of Geotechnical and Geoenvironmental Engineering, Vol. 127, No. 11 pp 973 - 983.

Pestana J.M., Hunt E. C., Goughnour R.R., (1997): "FEQ-Drain: A finite element computer program for the analysis of the earthquake generation and dissipation of pore water pressure in layered sand deposits with vertical drains", Report No. EERC 97-15.

Pestana J.M., Hunt E. C., Goughnour R.R., (1998), " Use of prefabricated drains for the reduction of liquefaction potential", ASCE, 12th Engineering Mechanics Conference,San Diegom, California, pp. 1025-1028

Pestana J.M., Hunt C.E., Goughnour R.R., Kammerer A.M., (1998): "Effect of storage on vertical drain performance in liquefiable sand deposits", Proceedings of the 2nd International conference on Ground Improvement Techniques, Singapore.

Port and Harbour Research Institute (1997): "Handbook on liquefaction remediation of reclaimed land", A.A. Balkema Publications, Rotterdam.

Poulos H.G., (2001): "Foundations and retaining structures - Research and Practice ", Proc. 15th Conference on Soil Mechanics & Geotechnical Engineering Vol. 4 Istanbul.

Richards Jr. R., Elms, G.D., Budhu, M. (1993): "Seismic bearing capacity and settlements of foundations", Journal of Geotechnical Engineering - ASCE, Vol. 119 (4), pp. 662-674.

Richards R., Elms G.D., (1979): "Seismic behavior of gravity retaining walls", Journal of the Geotechnical Engineering Division ASCE, Vol. 105 (4) pp 449–64.

Rollins K.M. & Anderson (2008): "Cone penetration resistance variation with time after blast liquefaction testing" Geotechnical Earthuquaje Engineering and Soil Dynamics, IV: pp. 1-10.

Rollins K.M. et al. (2003): "Vertical composite drains for mitigating liquefaction hazard", Proc. 13th International Offshore and Polar Engineering Conference, Honolulu, Hawaii, U.S.A.

Rollins K.M., Anderson J., McCain A., Goughnour R., (2004): "Liquefaction Hazard mitigation by prefabricated vertical drains", Proc., 5th International Conference on Case Histories in Geotechnical Engineering, NY

Rollins, K. (2004): "Liquefaction mitigation using vertical composite drains: full scale testing" NCHRP-IDEA project 94 report.

Salgado (2007): "The Engineering of Foundations" McGraw-Hill editions, New York.

Schaefer R.V. (1997): "Ground Improvement Ground Reinforcement, Ground Treatment", Geotechnical Special Publication No 69.

Schofield A.N., (1981): "Dynamic and Earthquake Centrifuge Geotechnical Modeling", Proc. of International Conference on Recent Advances in Geotechnical Earthquake Engineering and Soil Dynamics, University of Missouri-Rolla, MO, pp 1081-1100.

Seed H.B., Martin P.P., Lysmer J., (1975): "The Generation and Dissipation of Pore Water Pressures during Soil Liquefaction", Report No. EERC 75-26.

Seed H.B. & Booker R.J. (1977): "Stabilization of potentially liquefiable sand deposits using gravel drains", Journal of the Geotechnical Engineering Division ASCE, Vol. 103, No. GT 7, PP 757-768

Shahir H., Pak A., Taiebat M., Jeremic B., (2009): "Evaluation of Variation of Permeability in Liquefiable Soil under Earthquake Loading", Computers and Geotechnics, Vol. 40, pp 74 - 88.

Sloan S. W., (1987): "Substepping schemes for the numerical integration of elastoplastic stress - strain relations", International Journal of Numerical Methods on Engineering, 24, pp 893-911.

Sloan S. W., Abbo A. J., Sheng D., (2001): "Refined explicit integration of elastoplastic models with automatic error control", Engineering Computations, Vol. 18, (1/2), pp 121-154.

South Carolina Dept. of Transportation (2002): "Seismic Design Specifications" SCDOT.

Structural Engineers' Association of California (1999): "Appendix G: Conceptual Framework for Perfomance Based Seismic Design " SEAOC.

Structural Engineers' Association of California, SEAOC (1999): "What Structural Engineers need to know about Liquefaction", Proc. of SEAOC 1999, Convention, pp. 45-63.

Taiebat M., Shahir H., Pak A., (2007): "Study of Pore-pressure Variation during Liquefaction using Two Constitutive Models for Sand", Soil Dynamics and Earthquake Engineering, Vol. 27, pp 60 - 72.

Taiebat T., Dafalias F., Y. (2008): "SANISAND: Simple anisotropic sand plasticity model", International Journal for Numerical and Analytical Methods in Geomechanics, 32, pp 915-948

Tokimatsu, K., Seed, H.B. (1987): "Evaluation of settlement in sands due to earthquake shaking", Journal of geotechnical engineering, Vol. 113 (8), pp. 861-878.

Towata Ikuo, personal communication

Towhata I., (2007),"Chapter 15: Developments of soil improvement technologies for mitigation of liquefaction risk", K.D. Pitilakis (ed.) Earthquake Geotechnical Engineering, 4th Inrernational Conference on Earthquake Geotechnical Engineering-Invited Lectures

Tsuchida, H., Iai, S., Kurata, E. (1976): "On zone of soil property improvement of soils", Proc. of 14th Meeting of Earthquake Engineering, pp. 9-12 (in Japanese).

Uniform Building Code (1997).

Vesic S.A., (1973): Analysis of ultimate loads of shallow foundations" Journal of the Soil Mechanics and Foundations Division, ASCE, Vol. 99, No. SM1, pp 45-73.

Vucetic M., Dobry R., (1991): "Effect of Soil Plasticity on Cyclic Response", Journal of Geotechnical Engineering, Vol. 117, No. 1, pp 89 - 107.

Walsh H.E., (1980): "Tolerable Settlement of Buildings", ASCE, Annual Convention and Exposition.

Yasuda S. (2005): "Recent Several Studies and Codes on Performance-based design for liquefaction in Japan", Proceedings of Geotechnical Earthquake Engineering Satellite Conference, Osaka, Japan.

Yoshimi Y., Tokimatsu K., (1977): "Settlement of buildings on saturated sand during earthquakes", Soils and Foundations, Vol. 17, No. 1 pp 23-38.

Zhao J., Sheng D., Rouainia M., Sloan S. W., (2005): "Explicit stress integration of complex soil models", International Journal for Numerical and Analytical Methods in Geomechanics, 29, pp1209-1229.

APPENDIX A

Numerical Methodology Outline

A.1 FLAC finite difference code

FLAC makes use of the Finite Difference Method, whose central idea is that every derivative in the set of governing equations is replaced by an algebraic expression written in terms of the field variables (stress, displacements) at discrete points in space, while no variation of these variables within the elements needs to be specified. A typical FLAC calculation cycle is shown in **Figure A-1**. Starting from a given displacement state at each grid point the incremental strains for each zone are first evaluated for a given displacement increment (velocity). Following, the new stresses at each zone are calculated based on the adopted constitutive law. Then, stresses are used to estimate forces at each node. If these forces are close to zero, then the system is in equilibrium or steady state flow under constant velocity. Otherwise, for non-zero nodal forces, the aforementioned unbalanced nodal forces lead to nodal accelerations. Each full circle of this loop is taken as one timestep.

The most important characteristic of the explicit finite difference method is that each box in **Figure A-1** updates all of its grid variables (stresses and displacements) from known values that remain fixed while control is within the box. For example, the new stresses computed in the lower box are based on a set of velocities already calculated, and is assumed to be "frozen" for the operation of the box. This might seem unreasonable, since a change of stresses influences the velocities of neighboring grid points. However, if the integration time step is adequately small, such that information cannot physically propagate from one

element to another, then the "frozen-velocities" assumptions can be justified. This leaves the explicit method with one major disadvantage and one major advantage:

- The disadvantage is that a large number of computation steps is required to complete an analysis, even if the latter involves linear materials.
- The advantage is that no iteration process with matrix inversion is required, since elements do not communicate with each other during each solution step. Thus, for highly non-linear problems FLAC is expected to perform better than implicit Finite Element methods.

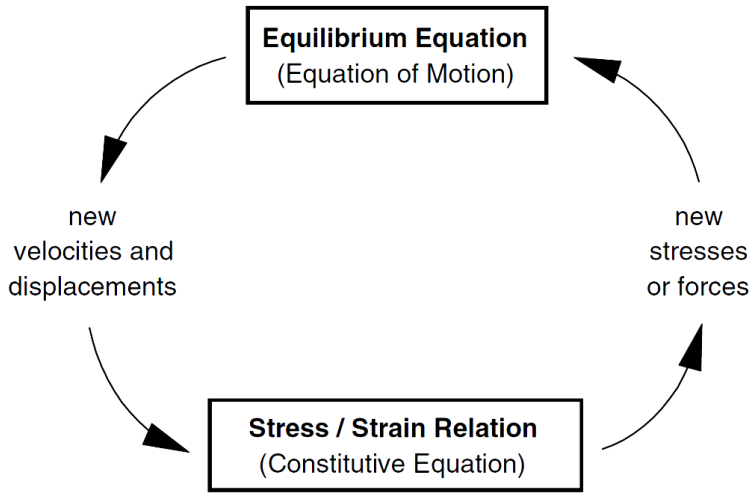

Figure A-1: Explicit calculation sequence used in FLAC.

A.1.1 The finite difference equations

The first set of equations of dynamic equilibrium is the generalized Newton's law of motion for a continuous solid body, which is expressed as:

$$\rho \frac{\partial \dot{u}_i}{\partial t} = \frac{\partial \sigma_{ij}}{\partial x_j} + \rho g_i \qquad \textit{A-1}$$

where

	t	time
	x_i	coordinate vector
	ρ	mass density
	g_i	gravitational acceleration

$\dot{u}_i$ velocity vector

σ_{ij} stress tensor

The other set of equations is the constitutive relation, or stress/strain law, which is given in following form:

$$\sigma_{ij} = M(\sigma_{ij}, \dot{\varepsilon}_{ij}, q_n) \qquad A\text{-}2$$

where M() is the functional form of the constitutive law

$\dot{\varepsilon}_{ij}$ represents strain rates

q_n are history parameters depending on the particular law

The strain rate $\dot{\varepsilon}_{ij}$ is derived from velocity gradients as:

$$\dot{\varepsilon}_{ij} = \frac{1}{2}\left(\frac{\partial \dot{u}_i}{\partial x_j} + \frac{\partial \dot{u}_j}{\partial x_i} \right) \qquad A\text{-}3$$

A.1.2 Mixed discretization

In order to solve the system of the previous equations, the continuous problem is replaced by a discrete one, where velocities and forces are assumed to be concentrated on the nodes of a grid (or mesh). Therefore, the laws of motion for the continuum are transformed into discrete forms of Newton's law at the nodes. The spatial derivatives of velocities and forces (i,e strain rates and stresses) are assumed to be constant within the zones (or elements) defined by the nodes mentioned above.

In FLAC, the finite difference mesh consists of quadrilateral elements, which are internally subdivided into two overlaid sets of constant-strain triangular elements, as shown in **Figure A-2**. The use of triangular elements eliminates problems which may occur with the deformational patterns of constant-strain finite difference quadrilaterals. More specifically, for polygons with more than three nodes, the combinations of nodal displacements may produce no strain and no opposing forces. To overcome this problem, the isotropic stress and strain components are taken to be constant and are averaged over the whole quadrilateral element, while the deviatoric components are maintained and treated independently for each triangular sub-element. Mart & Cundall (1982) describe this

procedure, using the term mixed discretization. The term arises from the different discretization for the isotropic and deviatoric parts of the stress and strain tensors.

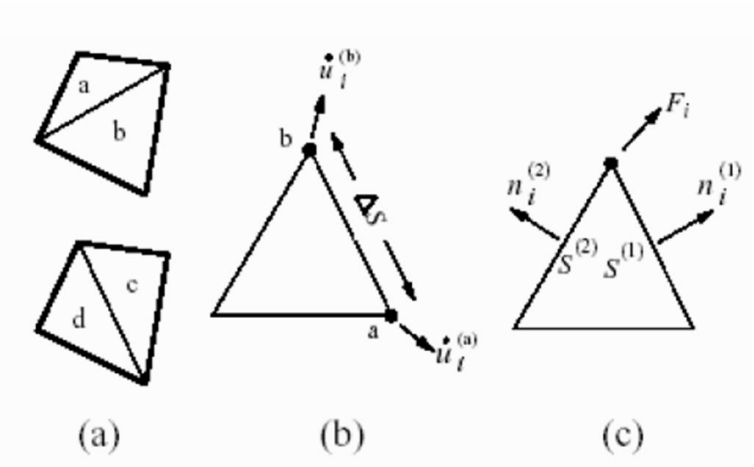

Figure A-2: **(a)** Overlaid quadrilateral elements used in FLAC, **(b)** typical triangular element with velocity vectors and **(c)** typical triangular element with force vectors and unit normal to the element's surfaces.

A.1.3 Discrete-model form of the finite different equations

The finite difference equations for the triangular sub-elements of FLAC are derived using the generalized form of Gauss' divergence theorem. According to this theorem, the average value of the gradient $\left\langle \frac{\partial f}{\partial x_i} \right\rangle$ of a scalar, vector or tensor f over the area A may be computed as follows:

$$\left\langle \frac{\partial f}{\partial x_i} \right\rangle = \frac{1}{A}\int_A \frac{\partial f}{\partial x_i} dA = \frac{1}{A}\int_S n_i f dS \Rightarrow$$

$$\left\langle \frac{\partial f}{\partial x_i} \right\rangle = \frac{1}{A}\sum_s n_i \langle f \rangle \Delta s = \frac{1}{2A}\sum_s n_i \left(f^{(a)} + f^{(b)} \right) \Delta s \qquad \text{A-4}$$

where S the boundary of a closed surface

n_i the unit normal to the surface

s the length of a side of the triangle

$\langle f \rangle$ is taken to be the average over the side

The summation occurs over the three sides of the triangular sub-zone and (a) and (b) are two consecutive nodes on a side. *Equation A-4* can be used to derive all the components of the strain rate tensor based on nodal velocities.

Given the strain-rate tensor, the constitutive law of *Equation A-2* is used to derive a new stress tensor. Once the stresses have been calculated the equivalent forces applied to each point need to be determined.

In FLAC, each quadrilateral zone contains two sets of two triangular sub-zones. Each corner of these sub-zones receives two force contributions, one from each adjoining side:

$$F_i = \frac{1}{2}\sigma_{ij}\left(n_j^{(1)}S^{(1)} + n_j^{(2)}S^{(2)}\right) \qquad A\text{-}5$$

Within each set of sub-zones, the forces from triangles meeting at each node are summed. The forces from both sets are then averaged to give the nodal force contribution of the quadrilateral. At each node, the forces from all surrounding quadrilaterals are summed to give the net nodal force vector, which includes contributions from applied loads and from body forces due to gravity. Gravity forces $F_i^{(g)}$ are computed as:

$$F_i^{(g)} = g_i m_g F \qquad A\text{-}6$$

where m_g is the gravitational mass at the node, defined as the sum of one-third of the masses of triangles connected to the node

If the body is at equilibrium, or in steady-state flow F_i on the node will be zero. Otherwise, the node will be accelerated according to the finite difference form of Newton's law of motion:

$$\dot{u}_i^{(t+\Delta t/2)} = \dot{u}_i^{(t-\Delta t/2)} + \sum F_i^{(t)}\frac{\Delta t}{m} \qquad A\text{-}7$$

Where the superscripts denote the time at which the corresponding variable is evaluated.

The above formulation is modified for the solution of static problems, by introducing into *Equation A-7* a form of damping, also referred to as local non-viscous damping, as follows:

$$\dot{u}_i^{(t+\Delta t/2)} = \dot{u}_i^{(t-\Delta t/2)} + \sum (F_i^{(t)} - F_{d,i})\frac{\Delta t}{m} \qquad A\text{-}8$$

where $F_{d,i}$ is the damping force, described by the following expression, in which by default α equals α=0.80.

$$F_{d,i} = a\left|F_i^{(t)}\right|\mathrm{sgn}\left(\dot{u}_i^{(t-\Delta t/2)}\right) \qquad A\text{-}9$$

A.1.4 Numerical stability

The explicit finite difference solution procedure is not unconditionally stable. The speed of the "calculation front" must be greater than the maximum speed at which physical information propagates. The particular numerical stability condition is expressed in terms of a critical timestep. Assuming that the pressure velocity, C_p, is the maximum speed at which information can propagate and that Δx is the smallest size of an element, then this critical time step is given as:

$$\Delta t_{\text{crit}} = \frac{\Delta x}{C_p} \qquad A\text{-}10$$

Where Δx is the minimum propagation distance, estimated as $A/\Delta x_{max}$(in FLAC)

C the p-wave velocity equal to $C_p = \sqrt{\frac{K + 4G/3}{\rho}}$

It is easily derived that the above expression is equivalent to *Equation A-11*, which refers to a general system of solid materials and networks of interconnected masses and springs:

$$\Delta t_{\text{crit}} = \frac{T_{\min}}{\pi} \qquad A\text{-}11$$

where T_{min} is the smallest eigen-period of the system. For a single mass-spring element, the above equation becomes:

$$\Delta t_{\text{crit}} = 2\sqrt{\frac{m}{k}} \qquad A\text{-}12$$

For the simple case of a rectangular zone, with area A_z, thickness t and diagonal length L_d, the grid point mass and the zone stiffness are expressed as shown in *Equations A-13* and *A-14* respectively:

$$m = \frac{1}{4}\rho A_z T \qquad A\text{-}13$$

$$k = (K + 4G/3)\frac{L_d^2}{A_z}T \qquad A\text{-}14$$

The combination of *Equations A-12*, *A-13* and *A-14* yields *Equation A-10*, implying that the latter may be regarded as an estimate of the local critical timestep, which can be easily calculated without computing the eigen-period of the entire system.

The finally selected time step must be smaller than the critical one obtained previously. For that purpose in FLAC applies a factor of 2 upon the critical time step. In dynamic problems, the specific time step refers to the simulated problem time. In static analyses, it is more efficient to assume a pseudo-static time step Δt = 1 and adjust the nodal masses. Nodal masses in FLAC are computed as follows:

$$m_n = \sum \frac{(\mathrm{K} + 4\mathrm{G}/3)\Delta \mathrm{x}_{\max}^2}{6A} \qquad A\text{-}15$$

For an affective stress analysis where groundwater is present, the bulk modulus of the fluid increases the mechanical stiffness of the saturated zone, thus reducing the selected timestep. This is done by modifying the apparent mechanical bulk modulus of the zone, according to *Equation A-16*:

$$K := K + a^2 M \qquad A\text{-}16$$

where a Biot coefficient

M Biot modulus

If the compressibility of the grains is neglected compared to that of the drained material, then a=1 and $M=K_w/n$, where K_w is the fluid bulk modulus and n is the porosity.

A.1.5 Fluid mechanical interaction

One of the fundamental features of FLAC is the capacity to model groundwater flow through permeable soils. Flow modeling may be done uncoupled, i.e. independently of the mechanical calculation, or in a coupled way so that fluid-solid interaction effects are captured. According to the latter:

- The fluid in a zone reacts to mechanically iduced volume changes by a change in the pore pressure
- Changes in pore pressures induce effective stress changes, hence affecting the response of the solid.

FLAC can calculate pore pressure effects, with or without pore pressure dissipation, while pore pressure dissipation can be modeled using built-in constitutive models. In the

constitutive model implemented herein, dynamic pore pressure is modeled indirectly, as a result of the simulated decrease of effective stress.

In the simple case of saturated flow, where grains are assumed to be incompressible compared to the soil skeleton, the equations governing the coupled fluid-deformation mechanisms are presented below.

Initially, water flow is described by Darcy's law":

$$q_i = -k_{ij} \frac{\partial}{\partial x_j}(P - \rho_w g_k x_k) \qquad A\text{-}17$$

where q_i the specific charge vector

k_{ij} mobility coefficient tensor (measure of permeability, equal to the hydraulic conductivity k_H divided by the fluid's unit weight: $k=k_H/\rho_w g$)

P fluid pressure

P_w mass density of the fluid

g_k gravitational acceleration vector

Fluid pressure follows the constitutive law of *Equation A-18*:

$$\frac{\partial P}{\partial t} = -M \frac{\partial \varepsilon_{vol}}{\partial t} \qquad A\text{-}18$$

where M Biot's fluid modulus

ε_{vol} volumetric strain

Finally, *Equations A-1* and *A-2* are expressed in terms of effective stresses $\sigma'_{ij}=\sigma_{ij}-P\delta_{ij}$, while mass density ρ is the saturated density $\rho_{sat}=\rho_d+n\rho_w$ (where ρ_d is the dry density).

The discretization and finite difference methods follow the general scheme presented in previous paragraphs:

- Pore pressures P are defined at gridpoints, and assumed to vary linearly within each sub-zone.
- The specific change vector q_i in *Equation A-17* is derived for each sub-zone through the Gauss divergence theorem
- The volumetric strain ε_{vol} is the equivalent nodal volume increase arising from mechanical deformations of the grid. It is computed as the sum of the contributions

from all sub-zones connected to the node. The resulting sum is divided by two, to account for the double overlay scheme.

- Finally, zone pressures necessary to perform an effective stress analysis are derived from the surrounding nodal values by simple averaging.

Simlar to the mechanical solution scheme, a critical timestep is defined to ensure numerical stability. The particular timestep is expressed in the following form:

$$\Delta t_{crit} = \frac{V}{M\sum K_{ij}} \qquad A\text{-}19$$

Where V equivalent nodal volume

K_{ij} permeability matrix, relating nodal pressures to nodal flow rate

The value of the used timestep is obtained by multiplication of the critical timestep with a safety factor of 0.8. Since the permeability appears at the denominator of *Equation A-19*, the flow timestep in many practical applications with low permeability values becomes larger that the corresponding mechanical timestep, and is therefore not critical. The maximum flow timestep may become critical in cases that gravel or other high permeability materials are present, such as gravel drains.

A.2 NTUA-SAND constitutive model

The *NTUA-SAND* model (Andrianopoulos et al.,2010a) is a bounding surface, critical state, plasticity model with a vanished elastic region, developed primarily for accurate simulation of the rate-independent dynamic response of non-cohesive soils under small, medium and large cyclic shear strain amplitudes. This is achieved using a single set of values for the model constants, irrespective of initial stress and density conditions, as well as loading direction. The model is equally efficient in simulating the monotonic response.

The model builds on the constitutive efforts of Manzari & Dafalias (Manzari & Dafalias, 1997) and Papadimitriou & Bouckovalas (Papadimitriou & Bouckovalas, 2002). In particular, key constitutive ingredients of the *NTUA-SAND* model are:

- the inter-dependence of the critical state, the bounding and the dilatancy (open cone) surfaces, that depict the deviatoric stress-ratios at critical state, peak strength and phase transformation, on the basis of the state parameter $\psi = e - e_{cs}$ (with e the void ratio, and e_{cs} the void ratio at critical state at the same mean effective stress p,

as per Been & Jefferies (Been & Jefferies, 1985). **Figure A-3** presents the shape of these surfaces in the π-plane (perpendicular to the hydrostatic p axis) of the deviatoric stress-ratio **r** space, where **r** = **s**/p, with **s** = **σ**-p**I** being the deviatoric stress tensor (**σ** and **I** are the effective stress and the identity second-order tensors)

- a (Ramberg-Osgood type) non-linear hysteretic formulation for the 'elastic' strain rate, that governs the response at small to medium cyclic shear strains,
- a discontinuously relocatable stress projection center $\mathbf{r}^{ref}$ related to the 'last' shear reversal point, which is used for mapping the current stress point on model surfaces (see Fig. 1) and as a reference point for introducing non-linearity in the 'elastic' strain rate, and finally,
- an empirical index of the directional effect of sand fabric evolution during shearing, which scales the plastic modulus, and governs the rate of excess pore pressure build-up and permanent strain accumulation under large cyclic shear strains potentially leading to liquefaction and cyclic mobility.

The model requires the calibration of eleven (11) dimensionless and positive constants for monotonic loading, and an additional two (2) for cyclic loading. Ten (10) out of the above thirteen (13) model constants may be directly estimated on the basis of monotonic and cyclic element tests, while the remaining three (3) constants require trial-and-error simulations of element tests. Details regarding the model formulation and the calibration procedure of the model constants can be found in Andrianopoulos et al. (2010a). What is presented here is **Table A-1**, where the model constants are outlined along with their values for Nevada sand, i.e. the uniform fine sand used in the VELACS project (Arulmoli et al, 1992) and also used for the validation of the *NTUA-SAND* model performance in element and centrifuge tests.

At element level, the performance of the model has been evaluated based on comparison with data from element laboratory tests on fine Nevada sand at relative densities of D_r = 40 & 60% and initial effective stresses between 40 and 160 kPa. In particular, data originated from tests on resonant column, direct simple shear and triaxial tests, offering a quantitative description of various aspects of non-cohesive soil response under cyclic loading, such as shear-modulus degradation and damping increase with cyclic shear strain, liquefaction resistance and cyclic mobility.

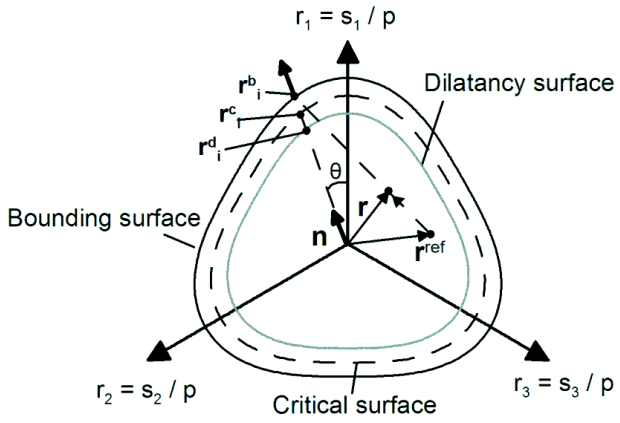

Figure A-3: Model surfaces and adopted mapping rule in the π-plane of the deviatoric stress-ratio space based on a relocatable projection center r_{ref}.

Table A-1: *NTUA-SAND* model constants: physical meaning and values for Nevada sand

#	Physical meaning	Value
M_c^c	Deviatoric stress ratio at critical state in triaxial compression (TC)	1.25
c	Ratio of deviatoric stress ratios at critical state in triaxial extension (TE) over TC	0.72
Γ_{cs}	Void ratio at critical state for p=1kPa	0.910
λ	Slope of critical state line in the [e-lnp] space	0.022
B	Elastic shear modulus constant	600*
ν	Elastic Poisson's ratio	0.33
k_c^b	Effect of ψ on peak deviatoric stress ratio in TC	1.45
k_c^d	Effect of ψ on dilatancy deviatoric stress ratio in TC	0.30
γ_1	Reference cyclic shear strain for non-linearity of "elastic" shear modulus	0.025%*
α_1	Non-linearity of "elastic" shear modulus	0.6*
A_o	Dilatancy constant	0.8
h_o	Plastic modulus constant	15,000
N_o	Fabric evolution constant	40,000

* for monotonic loading of Nevada sand: B = 180, α_1 = 1.0 (that renders the value of γ_1 irrelevant)

Focusing on the model accuracy under large cyclic shear strain amplitudes, **Figure A-4** presents a one-to-one comparison of simulations to data from a typical cyclic undrained simple shear test on Nevada sand at D_r = 40% and initial effective stress σ_{vo} = 160 kPa. In order to ascertain whether such a satisfactory accuracy is obtained for all initial conditions, **Figure A-5** compares the liquefaction resistance curves from all cyclic simple shear tests on Nevada sand (Arulmoli et al.,1992) with the respective simulations and pertinent curves from the literature (DeAlba et al.,1976). In all simulations, the values of model constants of **Table A-1** were used, showing that the model is capable of reproducing cyclic sand response with the same set of model constants irrespective of initial conditions. Similar accuracy is obtained for small and medium cyclic shear strains, i.e. in resonant column tests results of

shear-modulus degradation and damping increase with cyclic shear strain, irrespective of initial conditions with the same values of model constants presented in **Table A-1** (for details, see Andrianopoulos et al.,2010a).

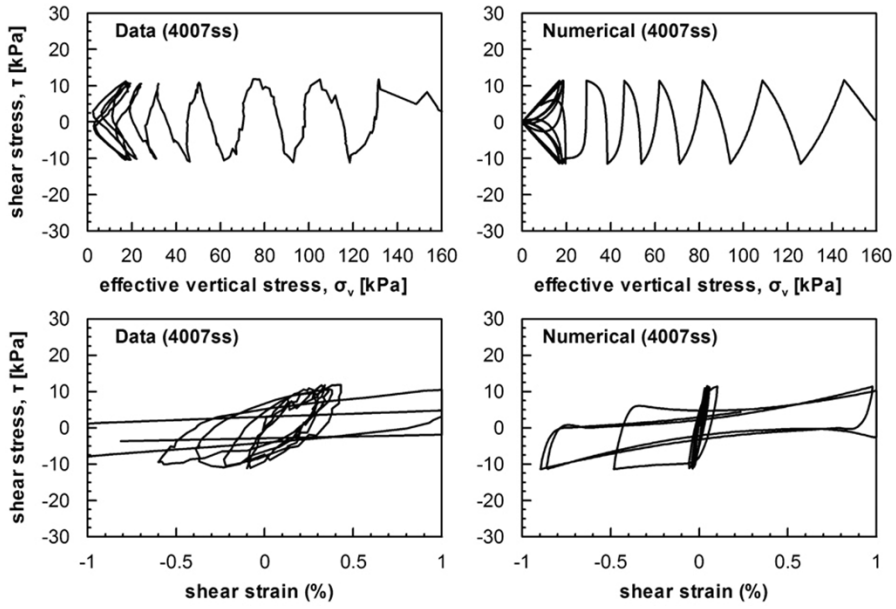

Figure A-4: Comparison of simulation (using NTUA-SAND) to data for a typical cyclic undrained simple shear test on Nevada sand with Dr = 40% (Arulmoli et al., 1992).

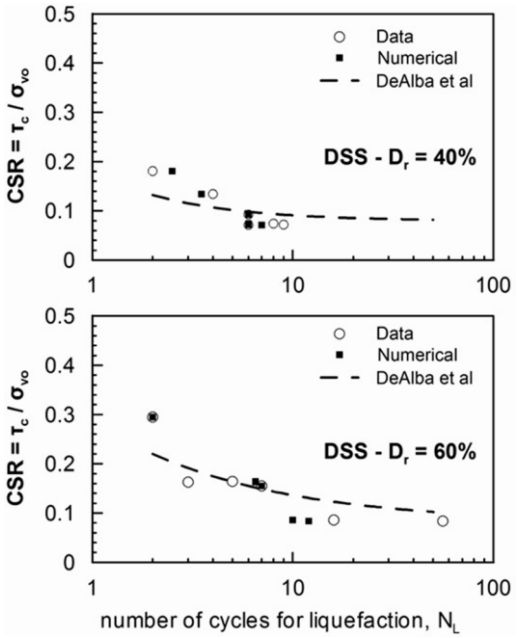

Figure A-5: Summary comparison of liquefaction curves from simulations (using *NTUA-SAND*) to data from all cyclic undrained simple shear tests on Nevada sand (Arulmoli et al.,1992), as well as established curves from the literature (DeAlba et al. 1976).

A.3 Implementation to finite difference code

The *NTUA-SAND* model was implemented to the commercially available finite-difference computer code *FLAC* (Itasca, 2005), using the User-Defined-Model (UDM) capability. Thus, the user of *FLAC* must supply an external UDM subroutine that will integrate the constitutive equations at each incremental solution step. It is then the role of this UDM to accurately estimate the effective stress increment and supply an updated set of values for the state variables and the hardening parameters, given their old set of values and the applied strain increment.

The equations of motion in *FLAC* are integrated using the explicit central difference integration rule. Therefore, small time increments are used to ensure stability. Thus, the use of an implicit stress integration scheme for the implementation of the highly non-linear new model would prove unnecessary, while it would require increased computational effort for performing iterative calculations with complex derivatives of the various constitutive ingredients. No global stiffness matrix is formulated with this computer code. Darcy's law is invoked for fluid flow in a porous solid, while the incremental formulation of coupled deformation-diffusion processes provides the numerical representations for the linear quasi-static Biot theory.

For this purpose, the sub-stepping technique with automatic error control [Sloan, (1987) Sloan et al., (2001)] was adopted. This algorithm belongs to the family of explicit stress integration schemes and divides automatically the applied strain increment into sub-increments (substeps). An appropriate size for each substep is found through the use of a modified Euler formula, which is specially constructed to provide an estimate of the local error. This scheme is particularly effective in handling multiple hardening parameters along with complicated hardening laws (Zhao et al., 2005), as required by the new constitutive model.

With the foregoing computer code, the continuum is divided into a finite difference mesh composed of quadrilateral elements (or "zones" in *FLAC* terminology). Mixed discretization, as thoroughly explained in the previous sections, (Martn & Cundall, 1982) is used to solve the problem of hourglassing, which may occur with constant-strain finite difference quadrilaterals. Namely, each element is automatically subdivided into two overlaid sets of constant-strain triangular subzones, and stress integration is performed separately for each of the four subzones of the element. However, the mean effective stress (p) and strain components (ε_p) are taken to be uniform over the whole quadrilateral element and equal to their average value over the four triangular sub-zones, while the deviatoric components (**s**

and **e**) are treated separately for each triangular sub-zone. This averaging procedure of p and ε_p is inherent in *FLAC* and is performed after the end of each applied strain increment. Similarly, the UDM subroutine of the proposed model in *FLAC* introduces averaging of the hardening parameters, to ensure that each quadrilateral element possesses uniform hardening parameters at the end of each strain increment.

Integration of the constitutive relations at each zone for a given strain increment is performed via a second order modified forward Euler method. Integration is accomplished in one or more sub-increments (or substeps), in order to maintain the local truncation error at each step below a desired tolerance level STOL. Specifically, to facilitate the integration process and especially the error control process that follows, a pseudo-time T is defined, with $0 \le T \le 1$ for each strain increment $\dot{\varepsilon}$ (with T = 0 and T = 1 marking the beginning and the end of the integration process for each strain increment). If the error control process requires it, each strain increment $\dot{\varepsilon}$ is further divided to sub-increments $\dot{\boldsymbol{\varepsilon}}^a$, with the aid of a pseudo-time sub-increment ΔT_n ($0 < \Delta T_n \le 1$) according to:

$$\dot{\boldsymbol{\varepsilon}}^a = \dot{\mathbf{e}}^a + \frac{\dot{\varepsilon}_p{}^a}{3}\mathbf{I} = \dot{\boldsymbol{\varepsilon}}\Delta T_n = \left(\dot{\mathbf{e}} + \frac{\dot{\varepsilon}_p}{3}\mathbf{I}\right)\Delta T_n \qquad \textit{A-20}$$

Thus, stress integration for each strain sub-increment is performed between pseudo-times T_{n-1} and $T_n = T_{n-1} + \Delta T_n$, with subscripts n-1 and n denoting the start and the end of the sub-increment, respectively. Note that if the error control process shows sufficient accuracy, then substepping is not performed. Initiating a sub-increment from a current stress state $\boldsymbol{\sigma}_{n-1}$, a first approximation of the effective stress increment $\dot{\boldsymbol{\sigma}}_1$ is calculated through the first order accurate Euler solution, with all state (stress and void ratio) dependent quantities and hardening parameters estimated at the current state $\boldsymbol{\sigma}_{n-1}$. In this manner, $\dot{\boldsymbol{\sigma}}_1$, its deviatoric stress ratio component and the respective increments of the hardening parameters are computed.

Then a temporary update of the stress state ($\boldsymbol{\sigma}_{n-1} + \dot{\boldsymbol{\sigma}}_1$), the void ratio e and all hardening parameters enable a second order modified Euler approximation of the stress increment $\dot{\boldsymbol{\sigma}}_2$, that is calculated with all state (stress and void ratio) dependent quantities and hardening parameters estimated at the temporary updated state. In this manner, $\dot{\boldsymbol{\sigma}}_2$, its deviatoric stress ratio component and the respective increments of the hardening parameters are computed. The new stresses ($\boldsymbol{\sigma}_n$ and $\mathbf{r}_n$) and hardening parameters at the end of the increment are computed and temporarily stored based on the average estimated

increments. This two-step averaging procedure employed by the stress integration scheme is graphically presented in **Figure A-6**.

Further on, for each sub-increment, the local error measure R is found by taking the difference between the second and first approximations of stress and hardening increments, normalized by their respective temporarily stored values. If the local error for this sub-increment exceeds the predefined tolerance level STOL, then the sub-increment is rejected and a smaller ΔT_n is introduced. This procedure uses a reduction factor ζ that takes into account how much was STOL exceeded, as well as a user-defined maximum number of sub-increments introduced (e.g. a maximum number of 1000 sub-steps may be used during a load step). Given this smaller sub-increment, all computations are repeated until R < STOL, the condition for accepting a sub-increment. In the sequel, if a sub-increment is accepted, then a growth factor ζ is enforced for the next sub-increment, with a maximum value of 10% increase relative to the previous sub-increment, and this in an effort to reduce the total computational cost. The integration process continues until T=1, a condition that marks the end of the increment and which allows for exit of the UDM routine with the final values of the stresses **σ** and all state variables. Further details about the implementation procedure adopted can be found in Andrianopoulos et al. (2010b).

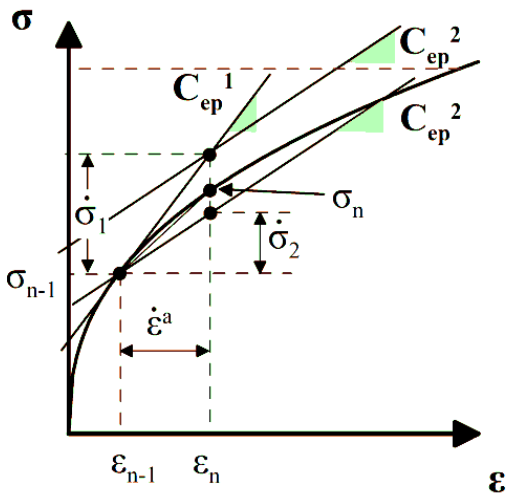

Figure A-6: Schematic illustration of the two-step modified Euler stress integration scheme

APPENDIX B

Mobilized Friction Angle in the NTUA-SAND Constitutive Model

B.1 Introduction

Friction angle ϕ is directly linked to the shear strength of a sand layer and, in the present research, it will enter the computation of the developing dynamic settlements as well as the post-shaking degraded bearing capacity (FS_{deg}) of the foundation resting on top of an improved sand layer (with gravel drains) underlain by a liquefiable sand. The constitutive model, which will be used to describe the response of the sand at the improved and the initial states does not incorporate friction angle as a distinct model parameter. Instead, it relates the particular parameter to the relative density D_r (%) through the initial void ratio e. Therefore, to define the friction angle that the NTUA-SAND model predicts, a series of element level numerical simulations was performed and is presented below.

NTUA-SAND has been originally calibrated based on laboratory tests performed on Nevada sand, and consequently the performed investigation concerns this particular material. The peak and residual shear strength were estimated through the execution of strain controlled tests in 1×1m elements in FLAC 2D, under (i) isotropic triaxial compression (ii) isotropic triaxial extension and (iii) simple shear loading conditions. All tests were performed under undrained as well as drained conditions. Additionally to the element level test simulations, friction angle is also estimated based on the equations describing the bounding surface of the NTUA-SAND constitutive model.

The above results, as well as the comparison against empirical predictions of the mobilized friction angle proposed by various researchers, have revealed that the NTUA-SAND constitutive model underpredicted the peak mobilized friction angle especially for large values of relative density and for drained loading conditions. Note though, that the initial calibration performed by Papadimitriou (1999) referred to a much narrower range of relative densities than the one examined herein, i.e. Dr = 40 & 60% and initial consolidation pressures of 40, 80 and 160kPa. Hence, it is recognized that the use of the constitutive model outside the above range of parameters is essentially an extrapolated prediction. Based on the above, the re-calibration of specific model parameters, such as the deviatoric stress ratio values $M^b_{c,e}$, within a wider range of initial conditions (D_r, σ'_{vo}) was found to be necessary.

The recalibration process focused on the enlargement of the model's bounding surface, in an attempt to achieve a stiffer shear response (directly related to the friction angle) while maintaining the originally obtained volumetric and cyclic responses. Following recalibration, peak friction angle values were re-evaluated for a range of relative densities 40 – 90% and three different initial consolidation stress levels, namely 40, 80 and 160kPa. The above procedure led to improved shear strength predictions and further increased the level of confidence of the model performance in large relative densities.

B.2 Model equations and tests layout

B.2.1 Constitutive model equations

According to Papadimitriou & Bouckovalas (2002), the mobilized friction angle in compression - $(\phi_{cs})_c$ - and extension - $(\phi_{cs})_e$ - is computed through the mobilized deviatoric stress ratios $M^b_{c,e}$, which define the shape of the bounding surface for triaxial extension and compression respectively, as illustrated in **Figure B-1**. Also, the deviatoric stress ratios are mathematically described through *Equation B-1*:

$$M^b_{c,e} = M^c_{c,e} + k^b_{c,e} < -\psi > \qquad \text{B-1}$$

where $M^c_{c,e}$ = user defined independent parameters

$k^b_{c,e}$ = positive constants and

<> are the Macauley brackets, yielding <x> = x if x>0 and <x> = 0 if x<0.

Ψ is the state parameter of Been & Jefferies, defined based on *Equation B-2*:

$$\psi = e - e_{cs} = e - (e_{cs})_a + \lambda \ln(p / p_a) \quad \text{B-2}$$

in which $(e_{cs})_\alpha$ and λ are user-defined parameters and p_a is the atmospheric pressure in the desired units. All user-defined parameters are summarized in **Table B-1**. Friction angle is linked to the deviatoric stress ratios through *Equations B-3* and *B-4* for TX compression and extension respectively.

$$M^b_c = \frac{6\sin(\phi_{cs})_c}{3 - \sin(\varphi_{cs})_c} \quad \text{B-3}$$

$$M^b_e = \frac{6\sin(\phi_{cs})_e}{3 + \sin(\varphi_{cs})_e} \quad \text{B-4}$$

Table B-1: Model parameters, calibration, and final values for the TX Compression and Extension testing of Nevada Sand.

Parameter	Physical meaning	Calibration	Nevada sand
$(e_{cs})_a$	Critical State Line location in the [e-lnp] space	Triaxial tests	0.809
λ			0.022
M^c_c	Critical state strength in triaxial compression	Triaxial compression tests	1.25
M^c_e	Critical state strength in triaxial extension	Triaxial extension tests	0.90
k^b_c	Effect of ψ on peak stress ratio for compression	Triaxial compression tests	1.45
k^b_e	Effect of ψ on peak stress ratio for extension	Triaxial extension tests	1.044

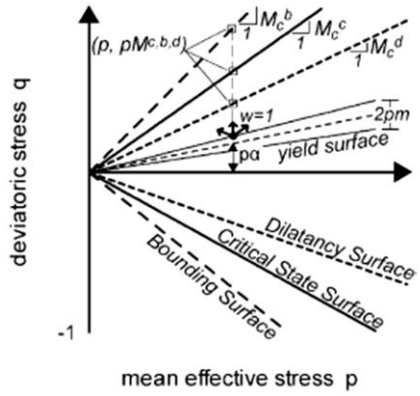

Figure B-1: Model surfaces in the p-q triaxial stress space – definition of mobilized deviatoric stress ratios $M_{d,c,b}$.

B.2.2 Isotropic TX compression tests

Isotropic Triaxial Compression laboratory test simulations were performed at two separate stages as illustrated in **Figure B-2**. Namely, consolidation of the element at the desired stress level and subsequent monotonic loading till failure were performed. The loading mode depended on whether the simulation concerns undrained or drained conditions. The following laboratory test simulations were performed under three different isotropic consolidation stresses, namely σ'_{vo} = 10, 50 and 100kPa (considering K_o=1) and a wide range of relative densities (D_r) ranging from 30 to 90%, at increments of 10%.

Undrained conditions.- They were simulated considering an axisymmetric constant volume mode of deformation, as presented again in **Figure B-2**, in which the imposed magnitude of horizontal extension is half the vertically imposed magnitude of compressive deformation. Monotonic loading is continued till failure, defined as the value of the ultimate principal stress ($p_{ult.}$), in which the void ratio meets the Critical State Line in the e-lnp space.

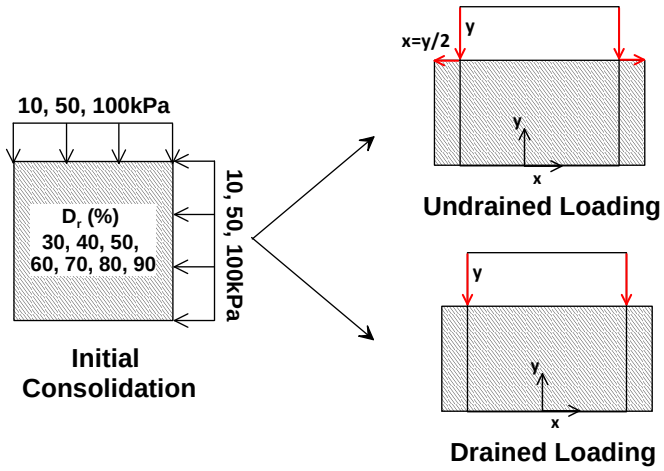

Figure B-2: Schematical representation of the Isotropic TX Compression test simulation under Undrained and Drained loading conditions.

Typical results from the above tests (stress paths, stress & excess pore pressure - strain correlations, e-p correlation) are presented in **Figure B-3, B-4** and **B-5** for isotropic consolidation stress of 100kPa and three distinct values of relative density, namely D_r = 30, 60 and 90%. In all examined cases, the peak friction angle (ϕ_{peak}) is estimated based on the developed stress state, the resulting Mohr circle and the angle of inclination of the Mohr-Coulomb failure envelope at the maximum q/p' ratio. The residual value ($\phi_{res.}$) is obtained at failure accordingly. The outcome of the above investigation is summarized in **Figure B-6**, in which the resulting values of friction angle (ϕ_{peak} and $\phi_{res.}$) are plotted as a function of relative density D_r (%). The solid black lines represent the maximum friction angle activated in each case and the dashed black lines represent the residual shear strength of the material. The application of the model *Equation B-3* is also plotted with the grey solid lines, for the same consolidation stress-levels.

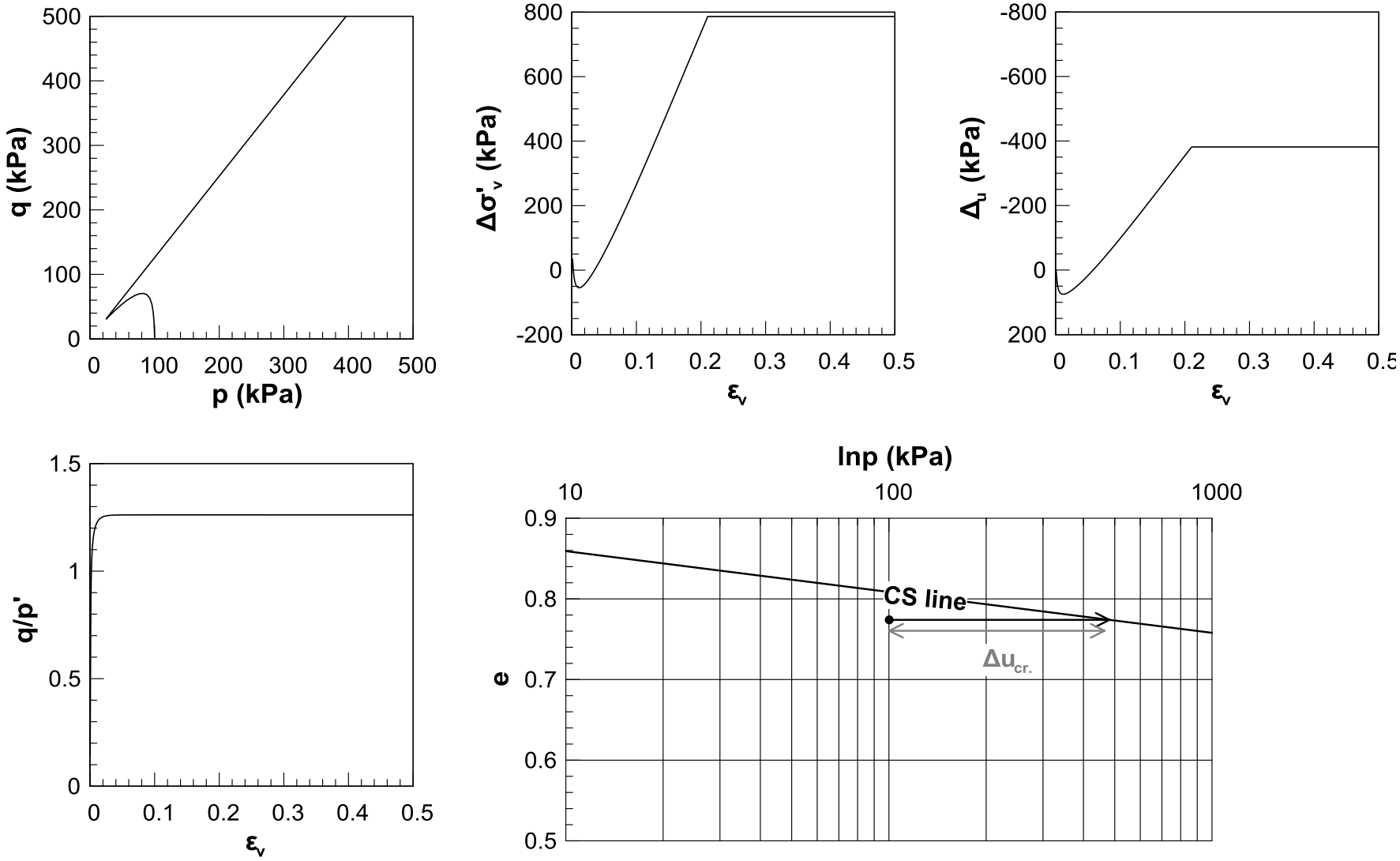

Figure B-3: Undrained TX Compression test - typical results for σ'_{vo}=100kPa, D_r = 30%.

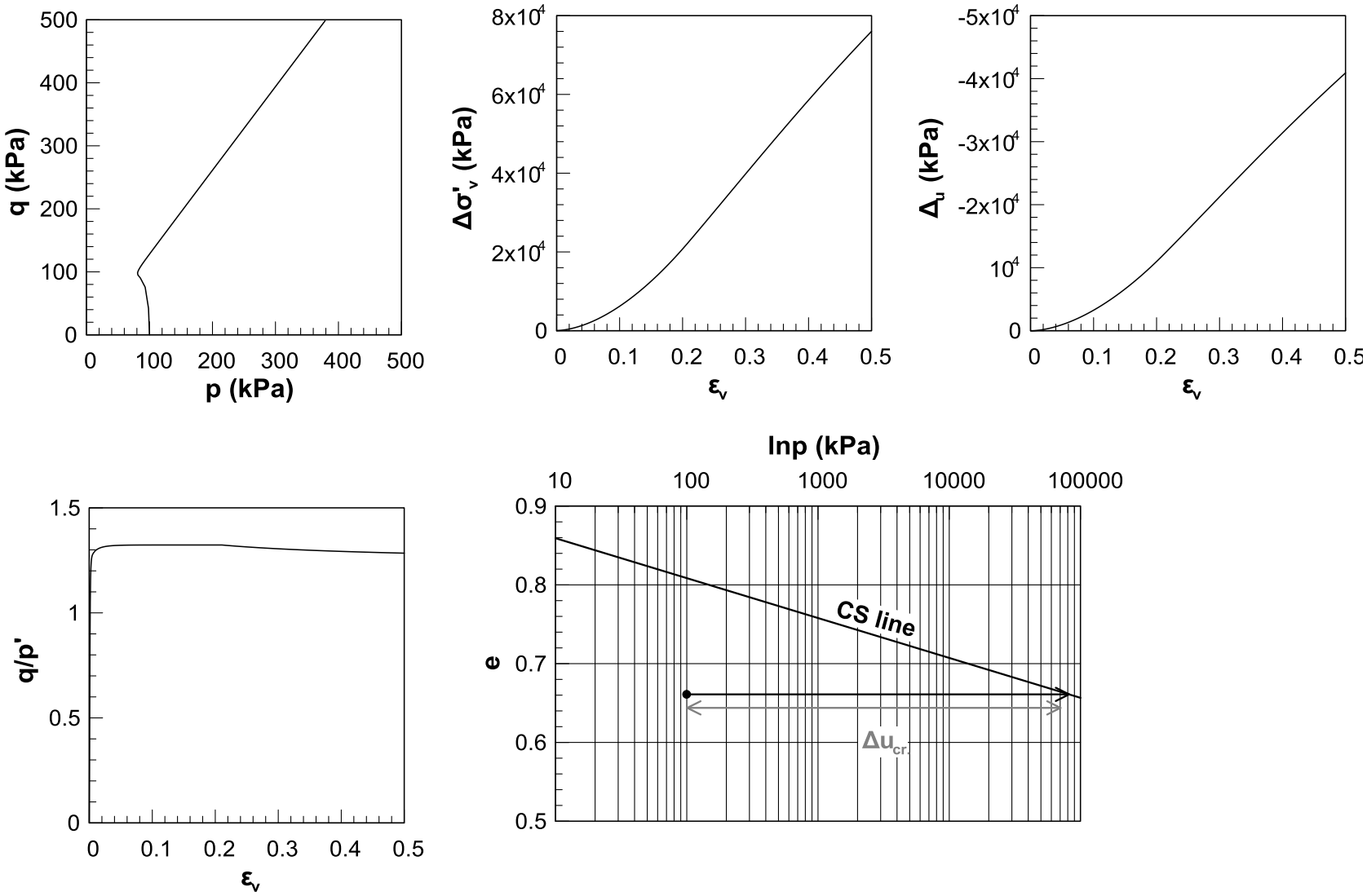

Figure B-4: Undrained TX Compression test - typical results for σ'vo=100kPa, D_r = 60%.

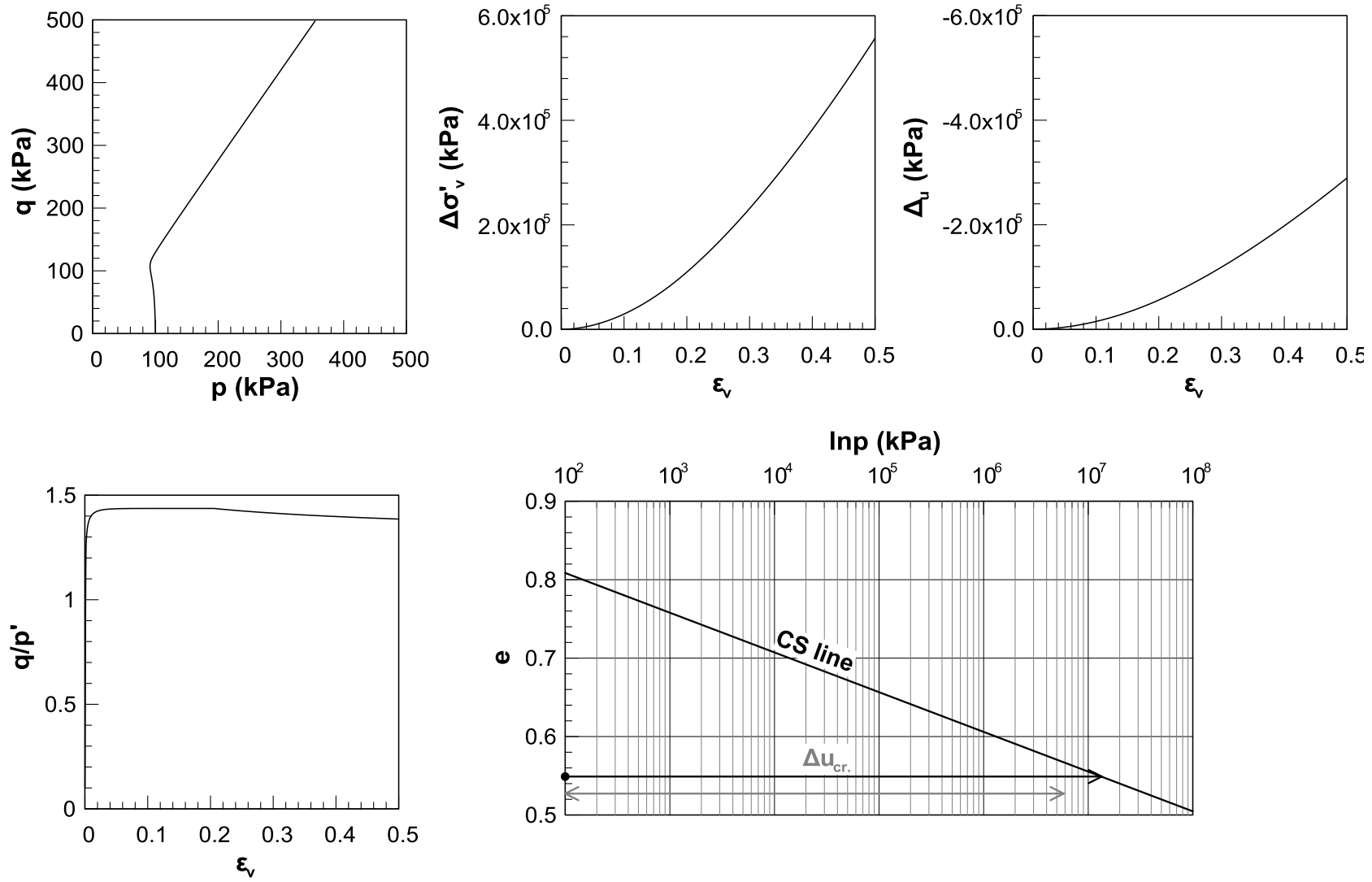

Figure B-5: Undrained TX Compression test - typical results for σ'vo=100kPa, D_r = 90%.

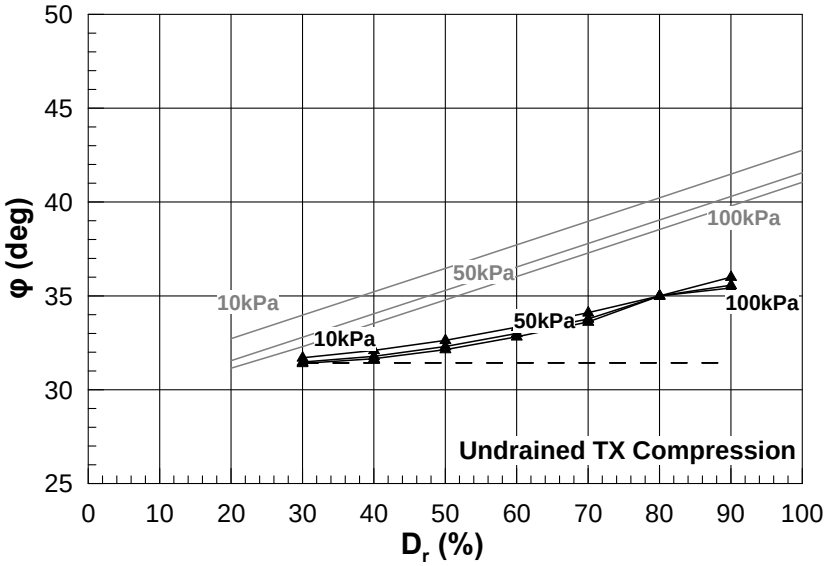

Figure B-6: Undrained TX Compression test simulations – peak (solid lines) and residual (dashed lines) values of friction angle ϕ as a function of relative density D_r.

Drained conditions.-They were simulated by applying only vertical displacement and allowing the free lateral deformation of the examined element, as presented in **Figure B-2.** Due to the drained loading conditions, volume change is now allowed. Again, peak friction angle is measured at the maximum q/p' ratio and the residual shear strength of the material is determined at the principal stress level $p_{ult.}$, in which the void ratio increase meets the CS line in the e-lnp space.

Typical results from the above tests are presented in **Figure B-7, B-8,** and **B-9**, for an isotropic consolidation stress of 100kPa and three distinct values of relative density, D_r = 30, 60 and 90%. The outcome of the above investigation is summarized in **Figure B-10**, in which the resulting values of friction angle (ϕ_{peak} and $\phi_{res.}$) are plotted as a function of relative density D_r (%). The solid black lines represent the maximum friction angle activated in each case and the dashed black lines represent the residual shear strength of the material. The application of the model equations is also plotted with the grey solid lines, for the same initial consolidation stress levels. Note that the predictions based on the constitutive equations do not differ for undrained and drained conditions, as the CS surface (and its projection – the CS line) is not associated to specific drainage conditions, the shear path direction and the initial consolidation state.

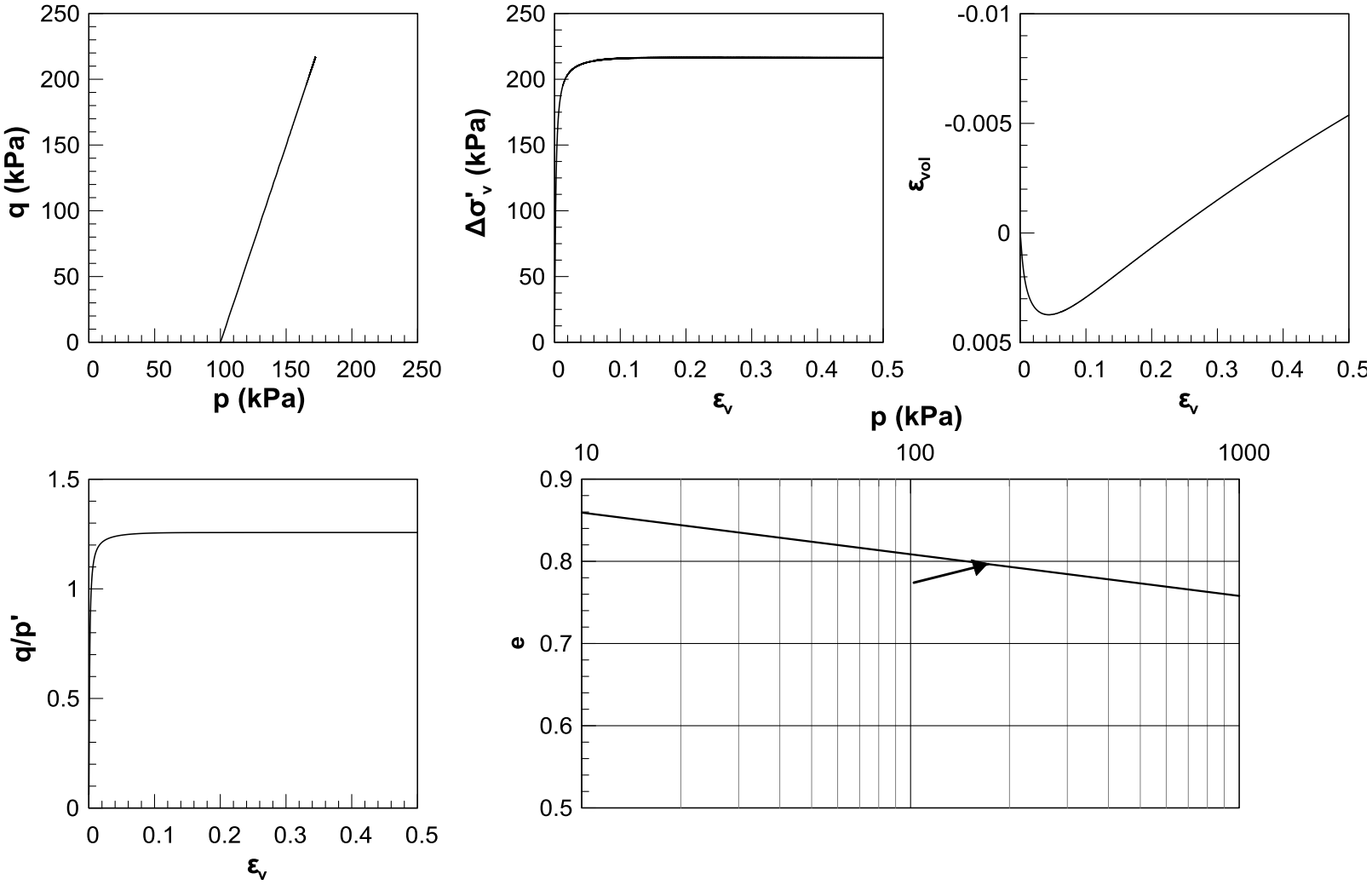

Figure B-7: Drained TX Compression test - typical results for σ'_{vo}=100kPa, D_r = 30%.

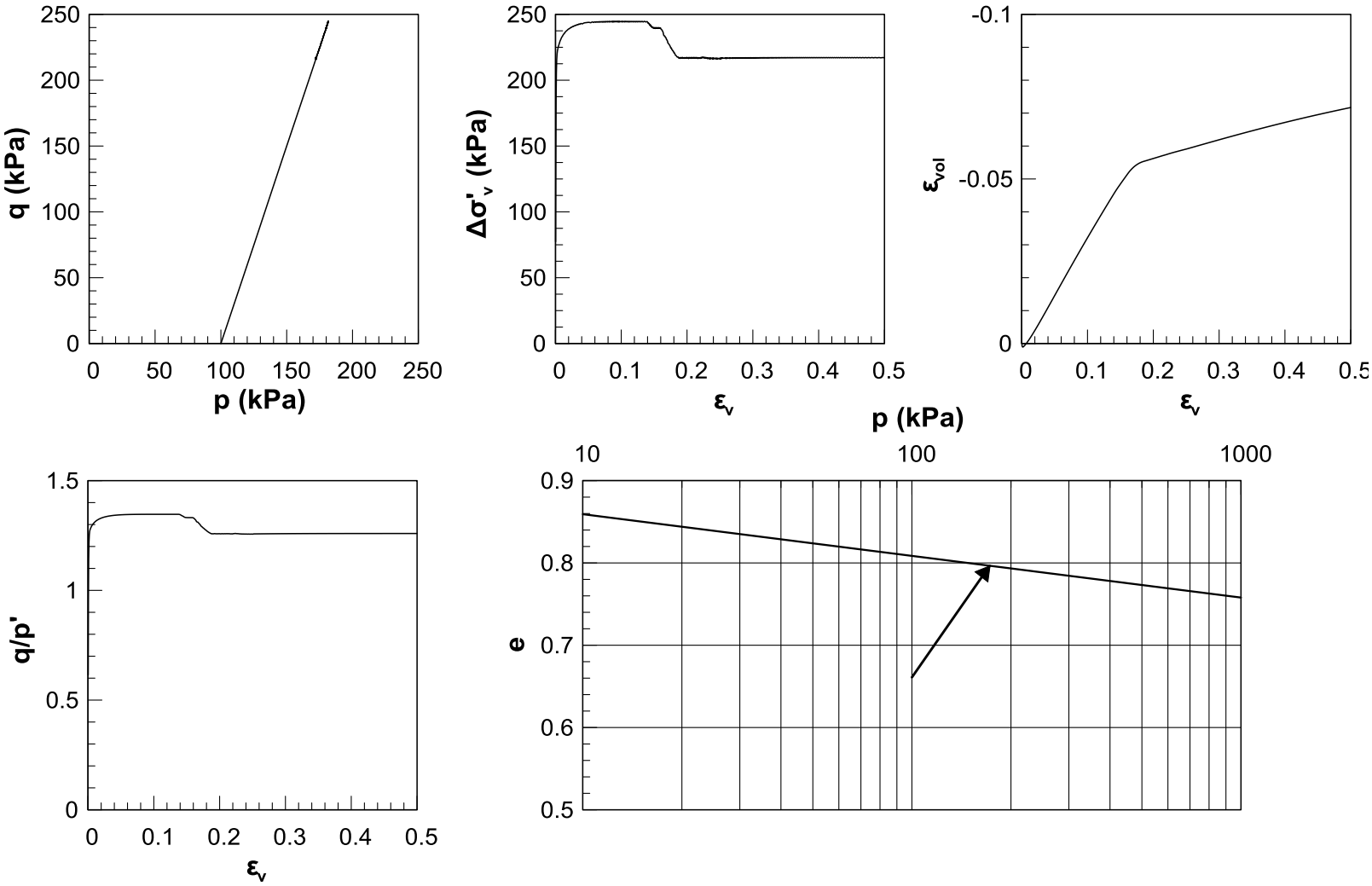

Figure B-8: Drained TX Compression test - typical results for σ'_{vo}=100kPa, D_r = 60%.

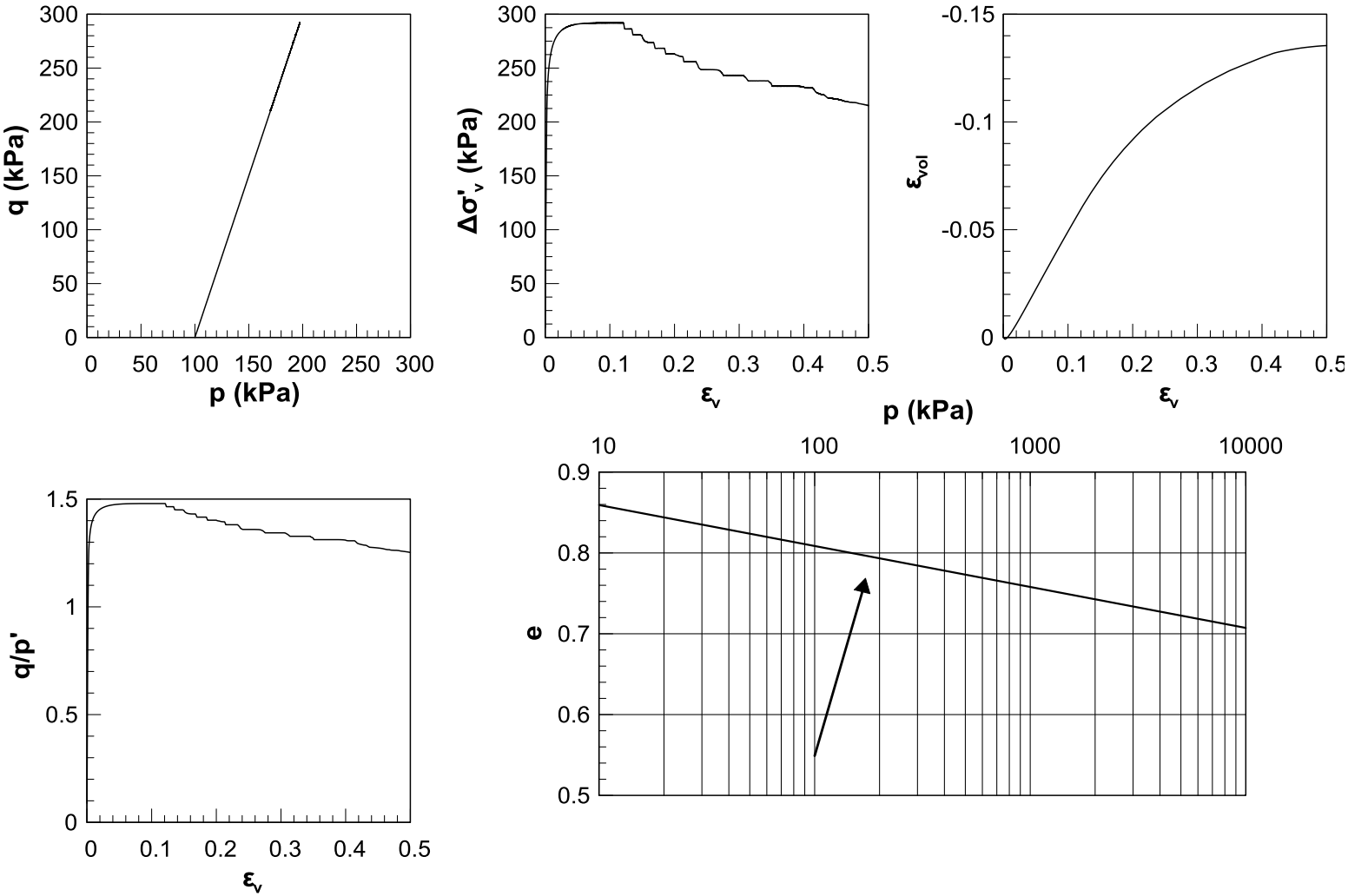

Figure B-9: Drained TX Compression test - typical results for σ'_{vo}=100kPa, D_r = 90%.

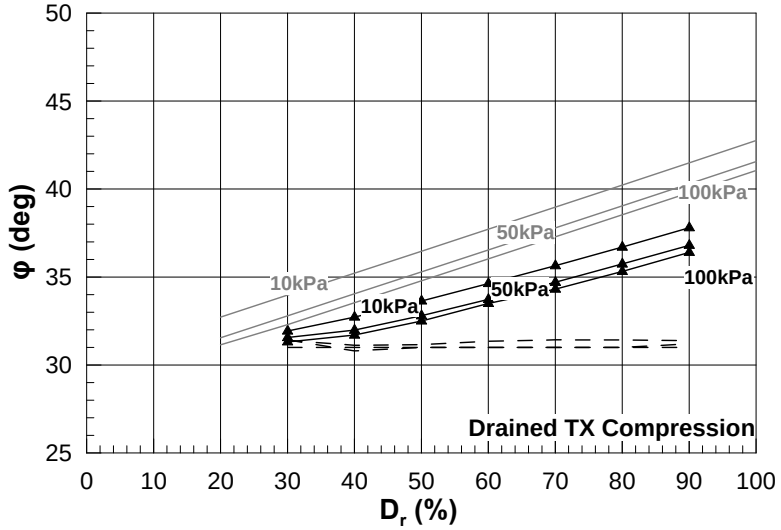

Figure B-10 : Drained TX Compression test simulations – peak (solid lines) and residual (dashed lines) values of friction angle ϕ as a function of relative density D_r (%).

B.2.3 Isotropic TX extension tests

Isotropic Triaxial Extension laboratory test simulations were performed at two separate stages as illustrated in **Figure B-11.** Namely, consolidation of the considered element at the desired stress level, and subsequent monotonic loading till failure. The loading mode depends on whether the simulation refers to undrained or drained conditions. The following laboratory test simulations were performed under three different isotropic consolidation stresses, namely σ'_{vo} = 10, 50 and 100kPa (considering K_o=1) and a wide range of relative densities (D_r) ranging from 30 to 90% at increments of 10%.

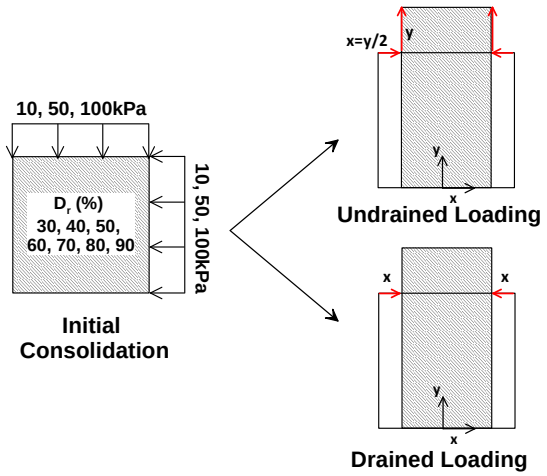

Figure B-11: Schematical representation of the Isotropic TX Extension test simulation under Undrained and Drained loading conditions.

Undrained conditions.- They were simulated considering an axisymmetric constant-volume mode of deformation, as presented in **Figure B-11**, in which the magnitude of the imposed horizontal compressive displacement is half the vertically imposed extensive displacement. The particular mode of monotonic loading is continued till failure, defined as the value of the ultimate principal stress ($p_{ult.}$), in which the void ratio meets the Critical State Line in the e-lnp space.

Typical results from the performed tests (stress paths, stress & excess pore pressure - strain correlations, e-lnp correlation) are presented in **Figures B-12, B-13 & B-14**, for an isotropic consolidation stress equal to 100kPa and three distinct values of relative density, D_r = 30, 60 and 90%. In all examined cases, peak friction angle - ϕ_{peak} - is estimated as explained earlier and the residual value of shear strength ($\phi_{res.}$), following the same procedure at failure. The outcome of the above investigation is summarized in **Figure B-16**, in which the resulting values of friction angle (ϕ_{peak} and $\phi_{res.}$) are plotted as a function of relative density D_r (%). The solid black lines represent the maximum friction angle activated in each case and the dashed black lines represent the residual shear strength of the material. The predictions of the model equations are also plotted with the grey solid lines, for the same consolidation stress levels.

Drained conditions.- They were simulated by applying only vertical extensive deformation and allowing the free lateral deformation of the examined element, as presented in **Figure B-11.** Due to the drained loading conditions, volume change is now allowed. Peak friction angle is measured at the point of maximum q/p' ratio, based again on the developed stress state and the corresponding Mohr circle. The residual shear strength of the material is determined at the principal stress level,

$p_{ult.}$, in which the void ratio change crosses the CS line in the e-lnp space. Note though, that due to the model's configuration, Critical State is reached in significantly large deformation levels, which are not obtained experimentally.

Typical results from the above tests are presented in **Figure B-16, B-17** and **B-18**, for consolidation stress of 100kPa and three distinct values of relative density, that is D_r = 30, 60 and 90%. The outcome of the above investigation is summarized in **Figure B-19**, in which the resulting values of friction angle (ϕ_{peak} and $\phi_{res.}$) are plotted as a function of relative density D_r (%). The solid black lines represent the maximum friction angle activated in each case and the dashed black lines represent the residual shear strength of the material. The predictions of the model equations are also plotted with the grey solid lines, for the same consolidation stress levels.

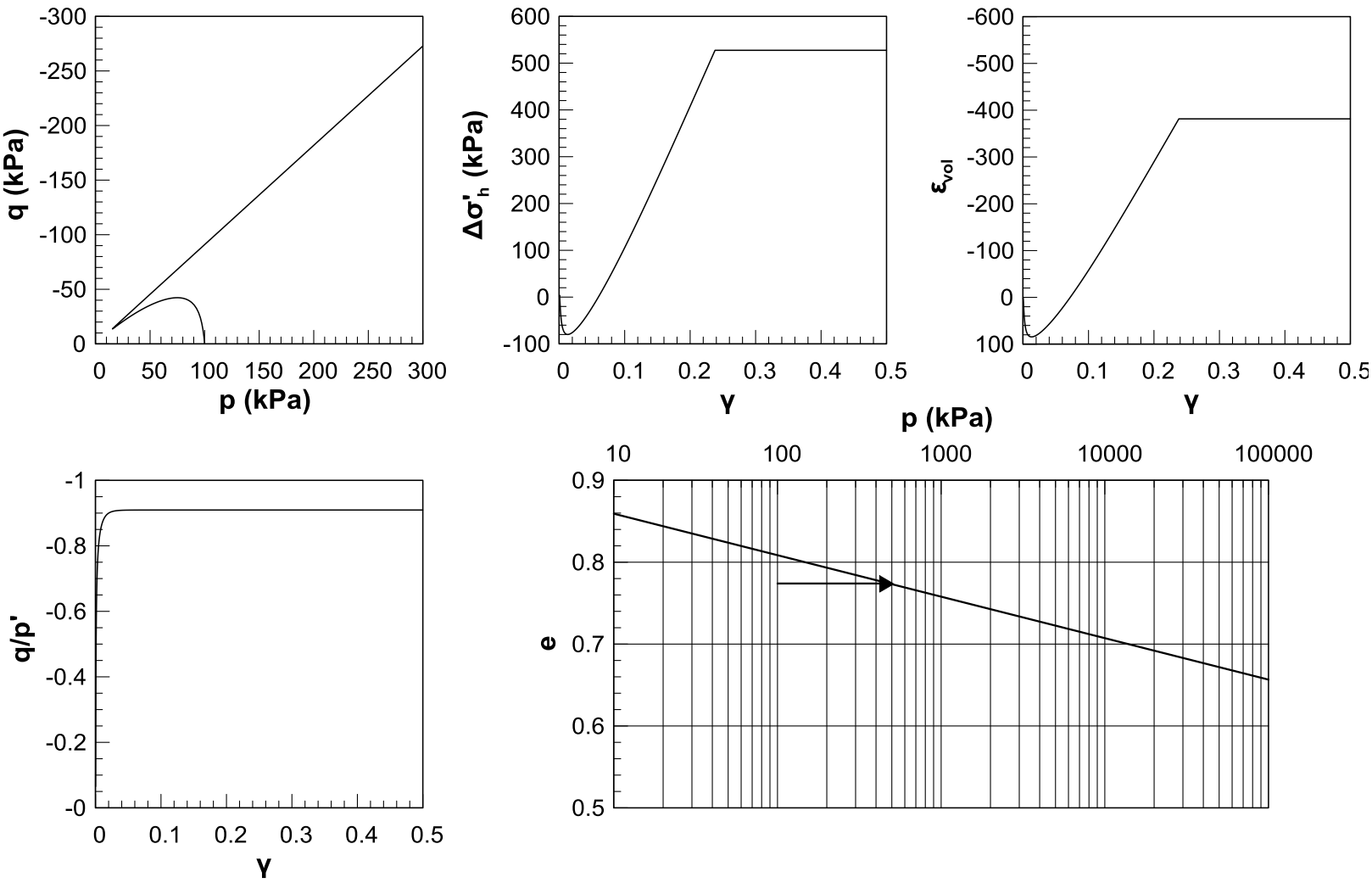

Figure B-12: Undrained TX Extension test - typical results for σ'_{vo}=100kPa, D_r = 30%.

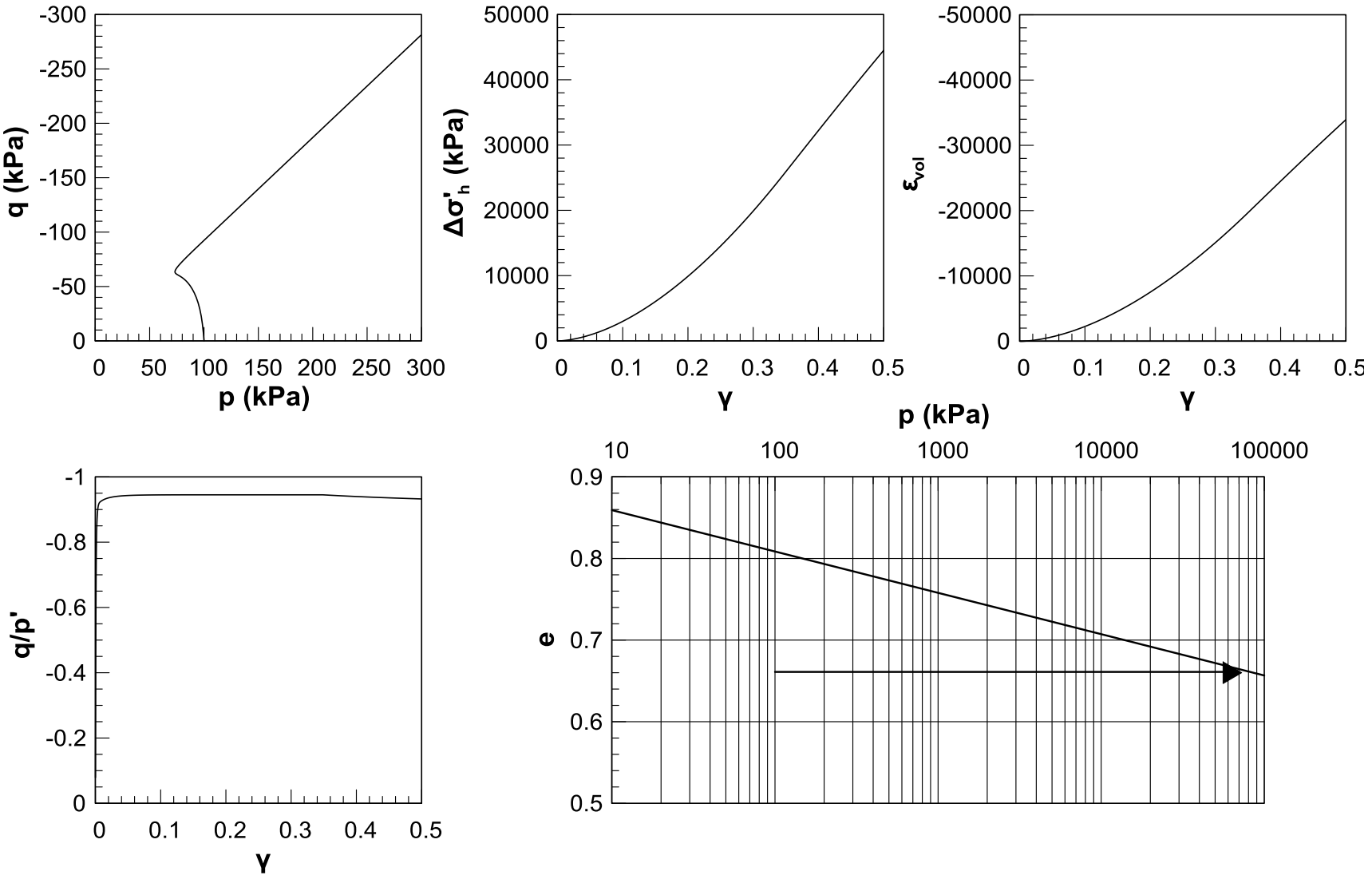

Figure B-13: Undrained TX Extension test - typical results for σ'_{vo}=100kPa, D_r = 60%.

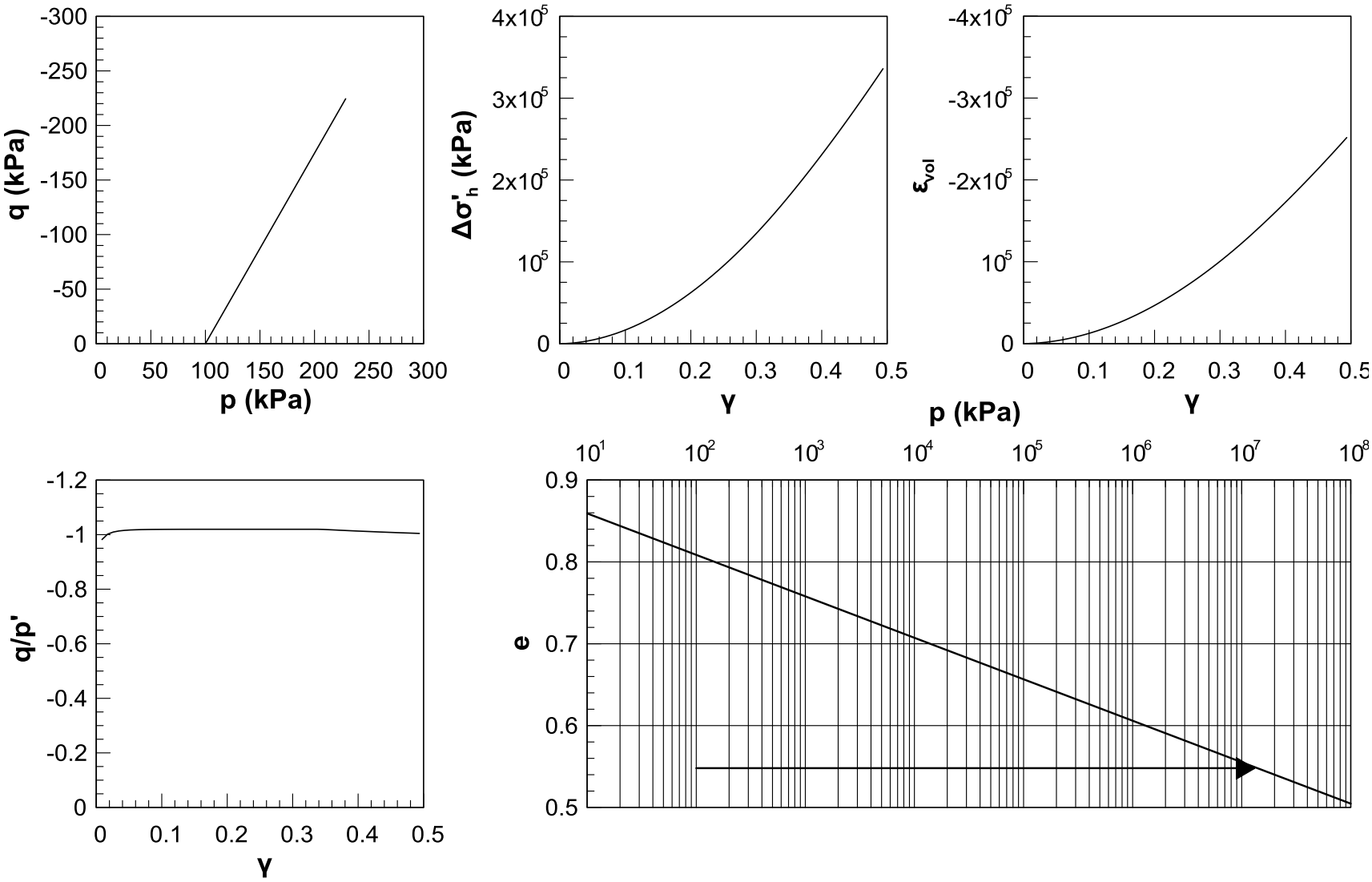

Figure B-14: Undrained TX Extension test - typical results for σ'_{vo}=100kPa, D_r = 90%.

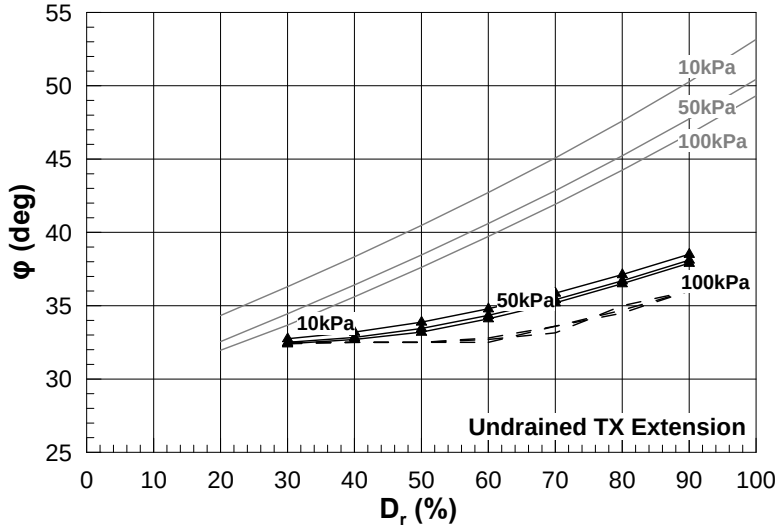

Figure B-15: Undrained TX Extension test simulations – peak (solid lines) and residual (dashed lines) values of friction angle ϕ as a function of relative density D_r (%).

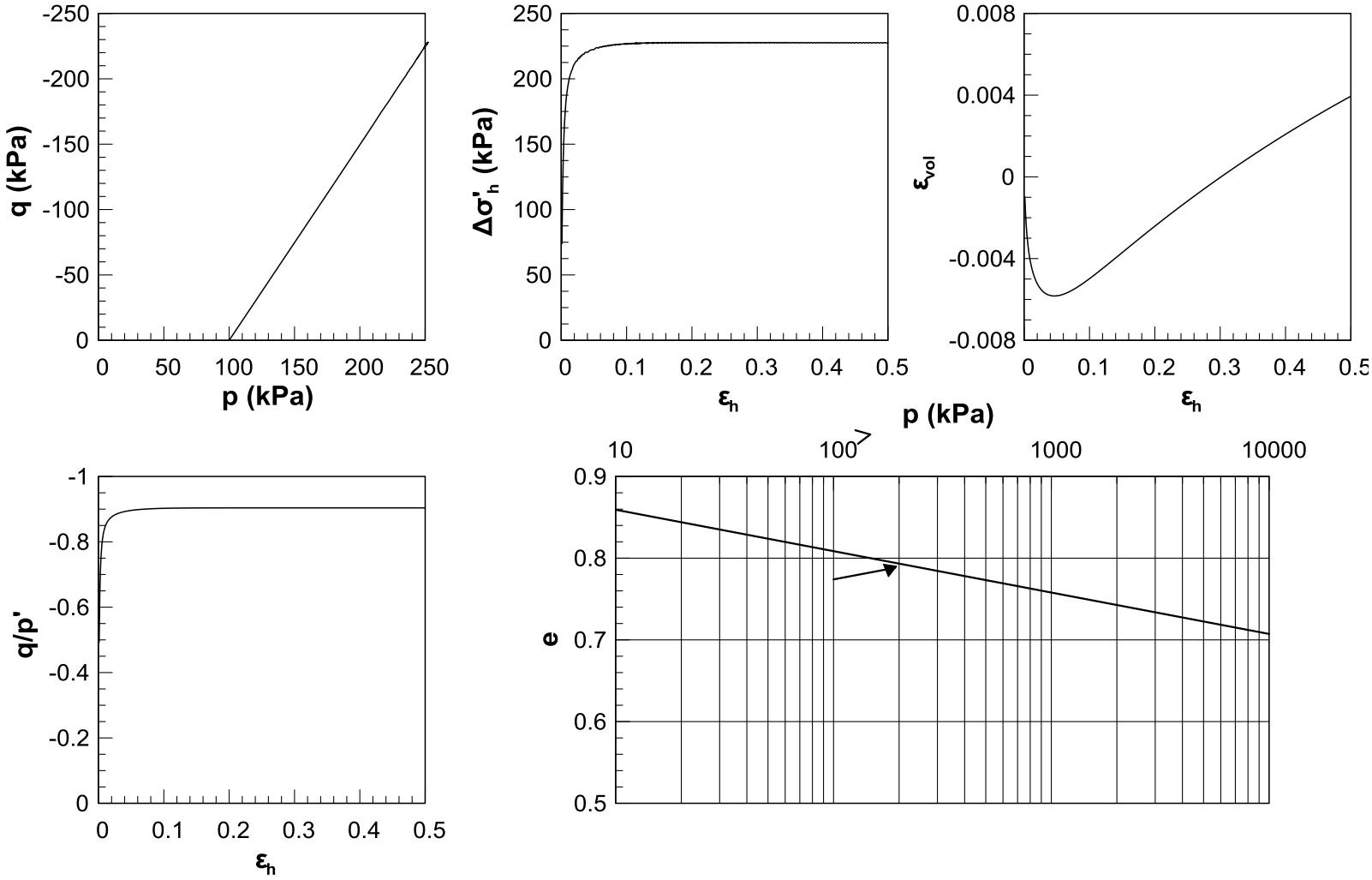

Figure B-16: Drained TX Extension test - typical results for σ'_{vo}=100kPa, D_r = 30%.

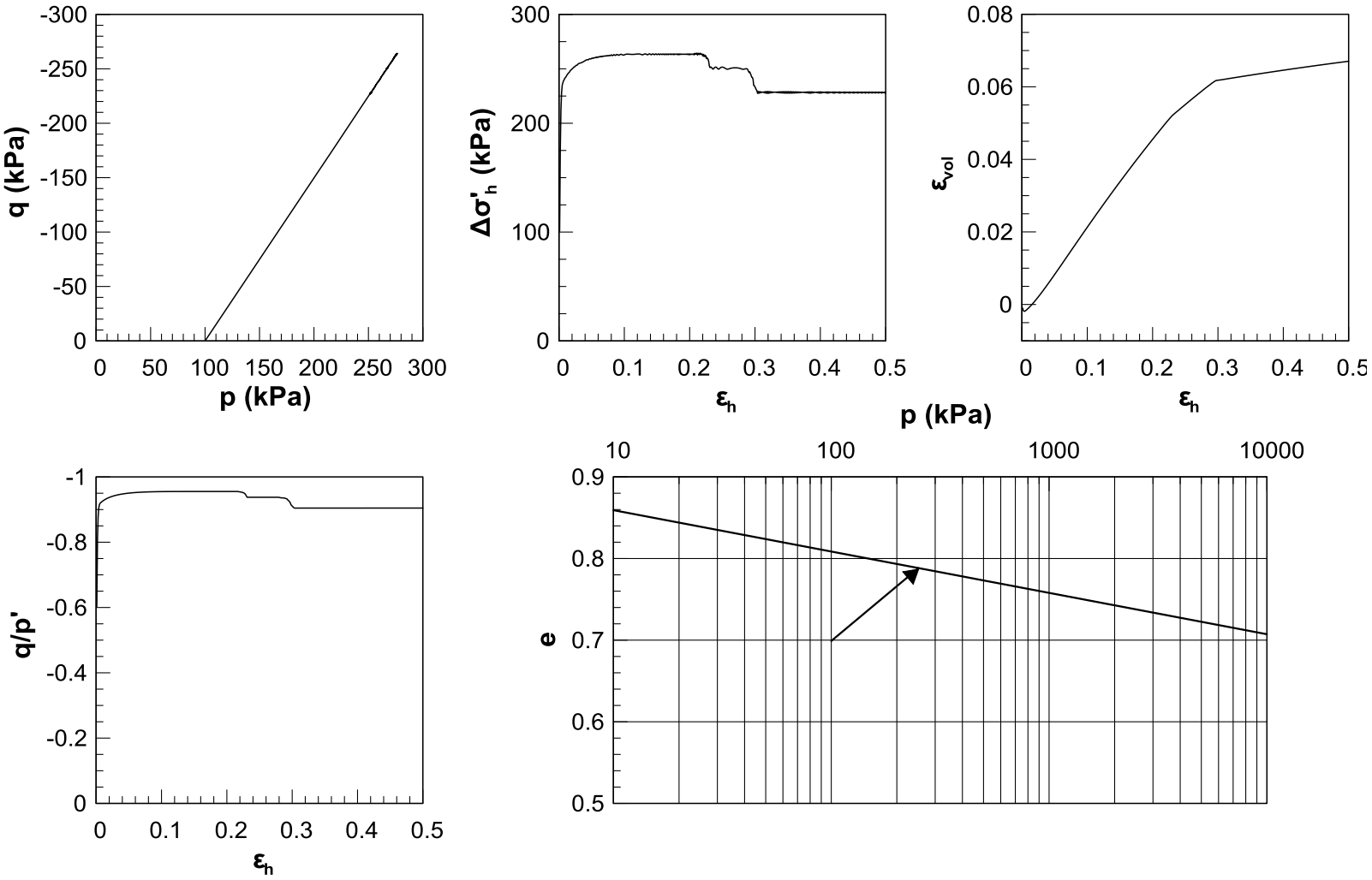

Figure B-17: Drained TX Extension test - typical results for σ'_{vo}=100kPa, D_r = 60%.

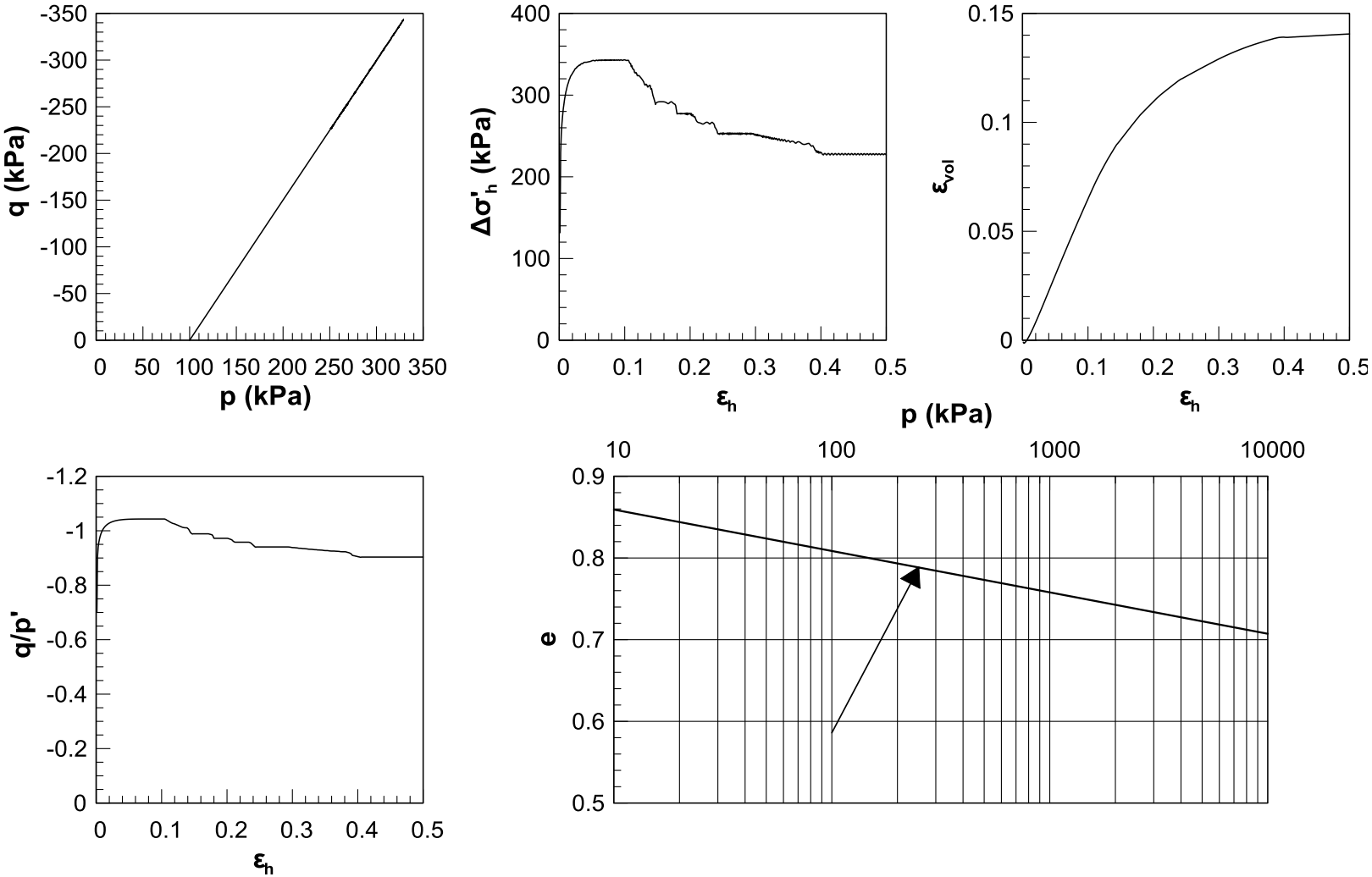

Figure B-18: Drained TX Extension test - typical results for σ'_{vo}=100kPa, D_r = 90%.

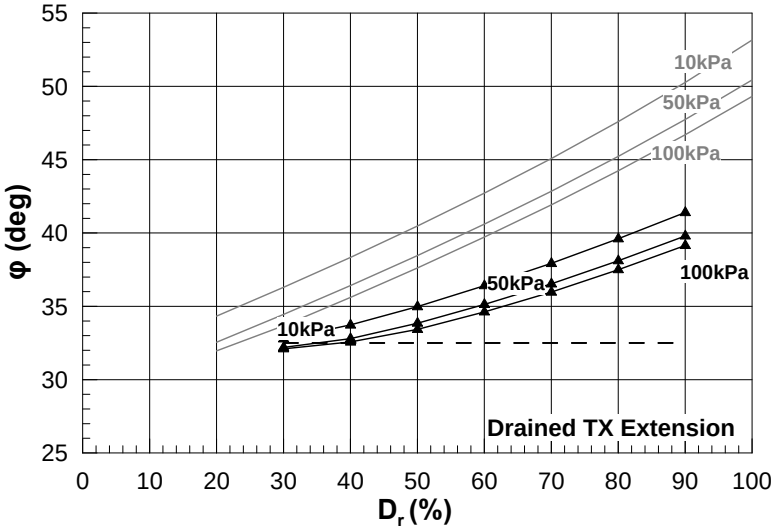

Figure B-19: Drained TX Extension test simulations – peak (solid lines) and residual (dashed lines) values of friction angle ϕ as a function of relative density D_r (%).

B.2.4 Simple shear tests

Simple Shear laboratory test simulations were performed at two separate stages as illustrated in **Figure B-20.** Namely, consolidating the considered element at the desired stress level, and subsequently monotonically loading till failure. The loading mode depends on whether the simulation concerns undrained or drained conditions. The following laboratory test simulations were performed under three different non-isotropic consolidation vertical stresses σ'_{vo}, namely 10, 50 and 100kPa, considering K_o=0.5, and a wide range of relative densities (D_r) ranging from 30 to 90%, at increments of 10%.

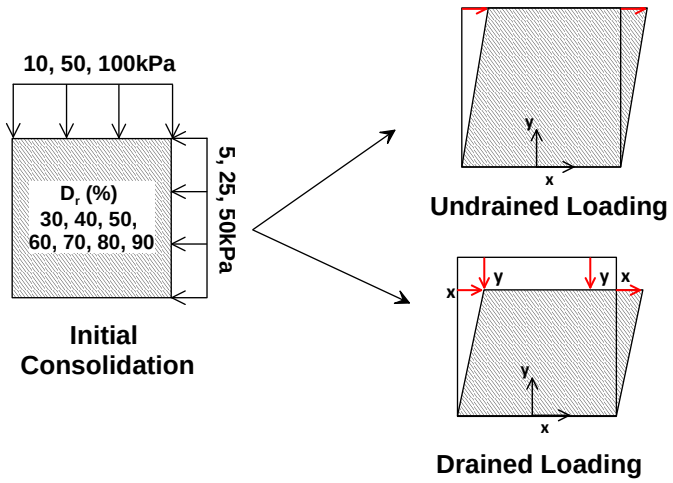

Figure B-20: Schematical representation of the Simple Shear test simulation under Undrained and Drained loading conditions.

Undrained conditions.- They were simulated considering a constant height mode of deformation, as presented in **Figure B-20**, applying only horizontal shearing displacement. The particular mode of monotonic loading is continued till failure, defined as the value of the ultimate principal stress ($p_{ult.}$), in which the void ratio meets the Critical State Line in the e-lnp space. In all examined cases, peak friction angle - ϕ_{peak} - is estimated at the occurrence of the maximum value of the q/p' ratio and the residual value of shear strength ($\phi_{res.}$) at failure. At both stages, given the stress state developing on the horizontal and vertical planes of the examined element, the friction angle is estimated through the corresponding Mohr circle and the angle of inclination of the Mohr-Coulomb failure envelope, as illustrated in **Figures B-21**, **B-22** and **B-23**. The particular figures also contain a complete set of typical results from the performed tests, for consolidation vertical stress equal to 100kPa and three distinct values of relative density, namely D_r = 30, 60 and 90%. The outcome of the above investigation is summarized in **Figure B-24**, in which the resulting values for friction angle (ϕ_{peak} and $\phi_{res.}$) are plotted as a function of relative density D_r(%). The solid black lines represent the maximum friction angle activated in each case and the dashed black lines represent the residual shear strength of the material.

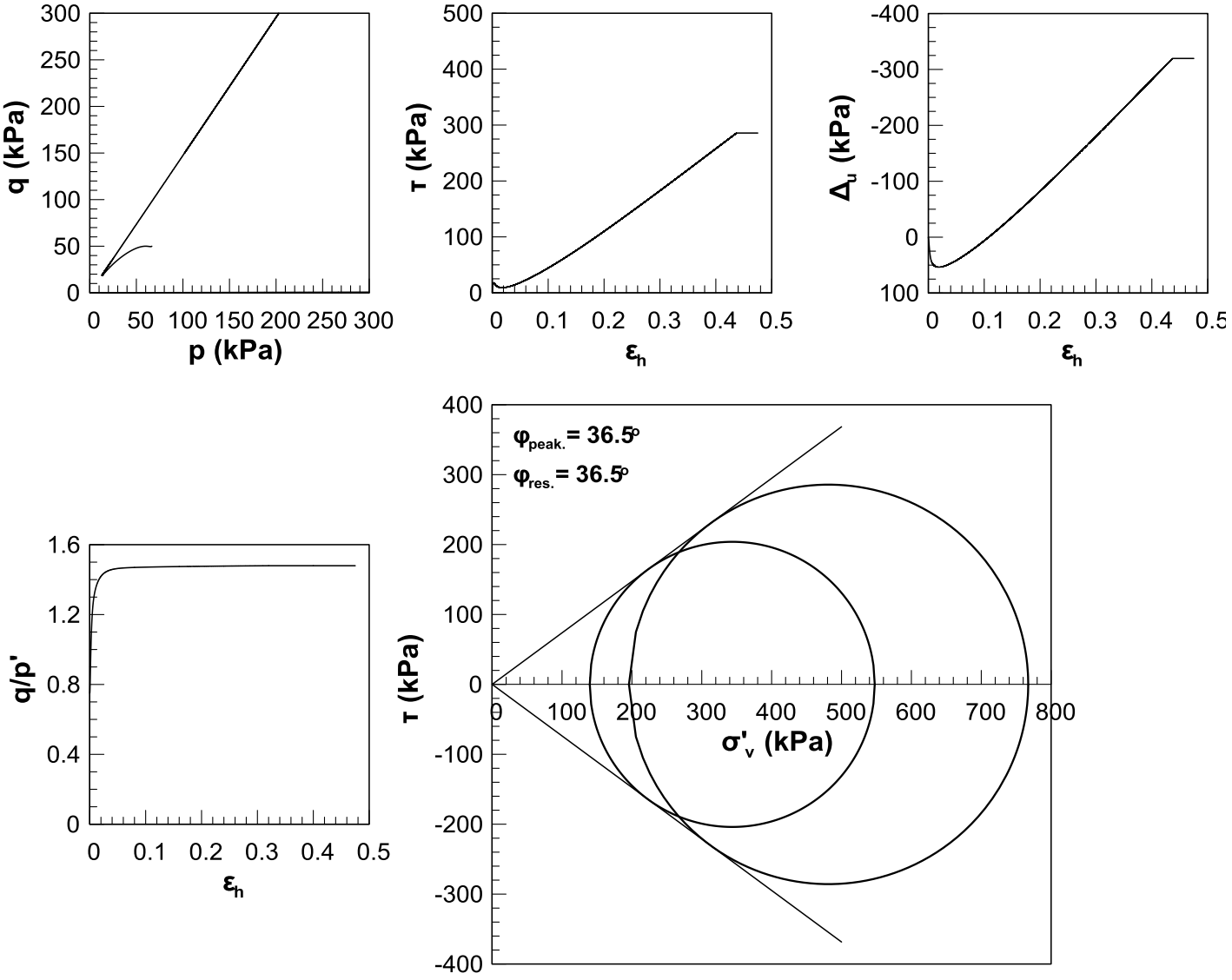

Figure B-21: Undrained Simple Shear test - typical results for σ'_{vo}=100kPa, Dr = 30%.

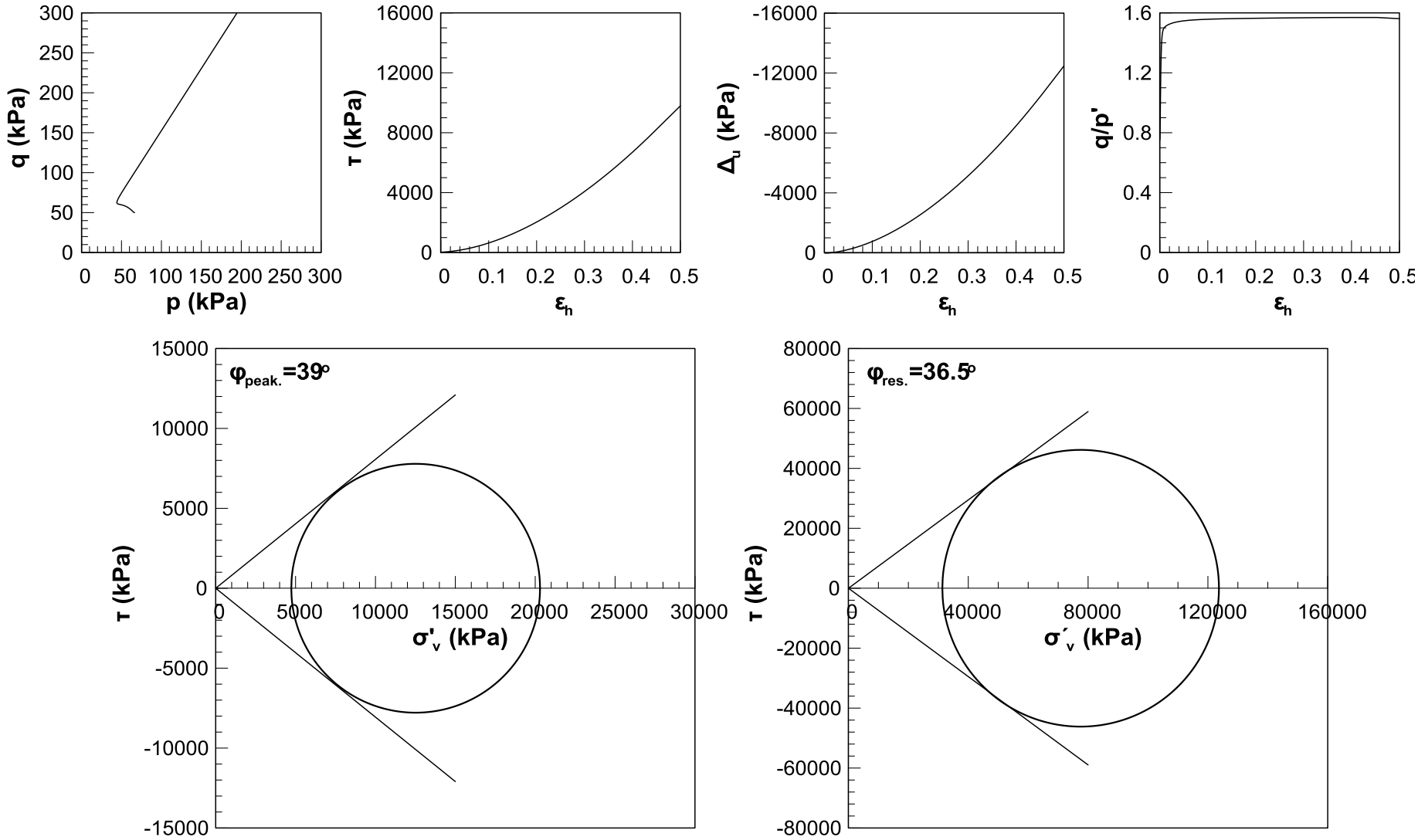

Figure B-22: Undrained Simple Shear test - typical results for σ'_{vo}=100kPa, Dr = 60%.

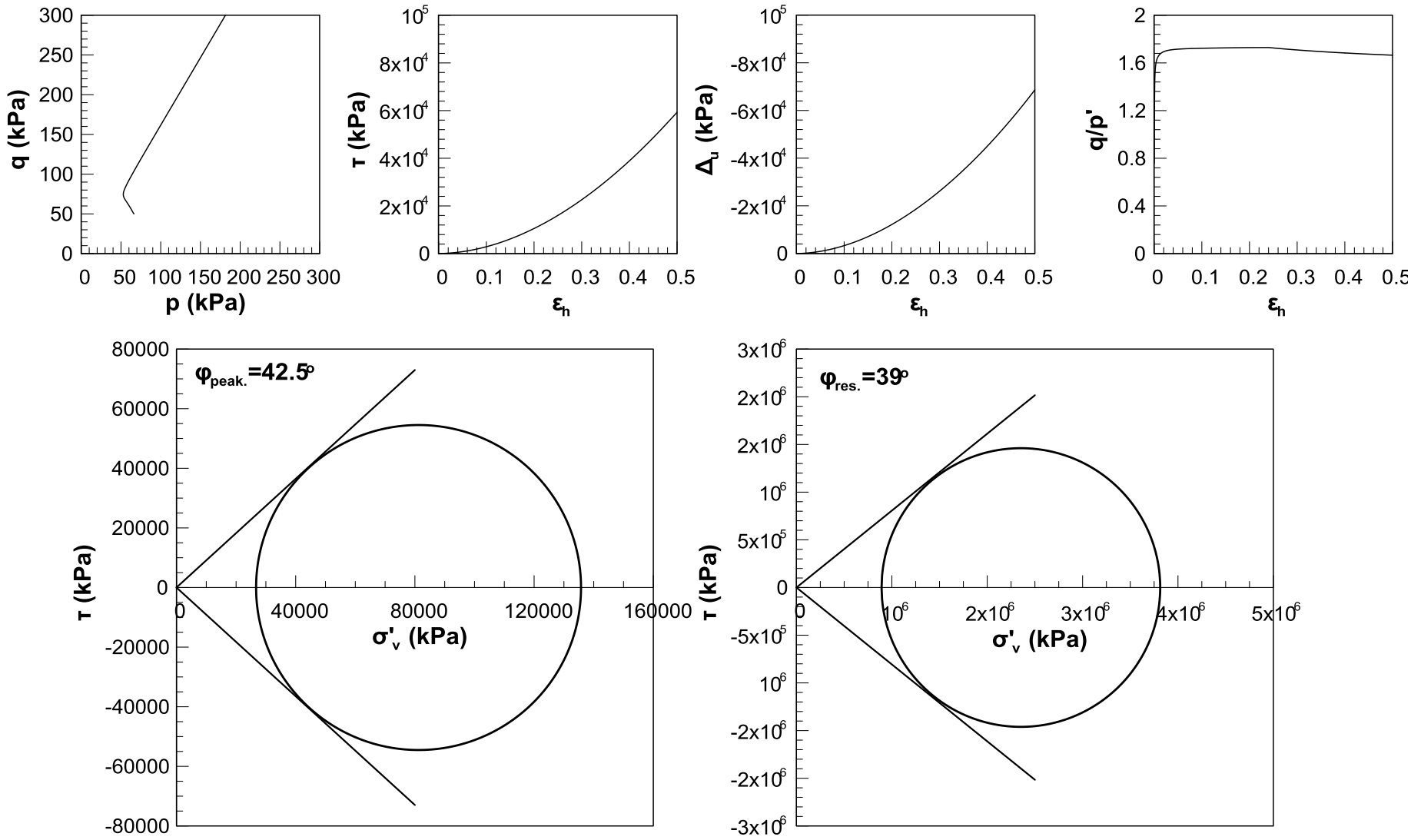

Figure B-23: Undrained Simple Shear test - typical results for σ'_{vo}=100kPa, Dr = 90%.

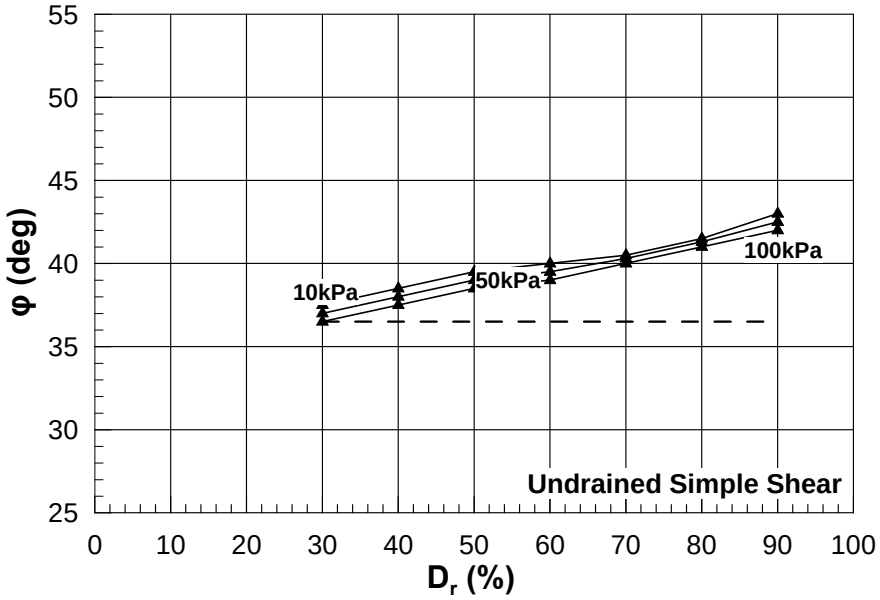

Figure B-24: Undrained Simple Shear test simulations – peak (solid lines) and residual (dashed lines) values of friction angle ϕ as a function of relative density D_r (%).

Drained conditions.- were simulated by applying a combination of shearing deformation in the form of horizontal displacement, allowing the undisturbed displacement of the upper bound of the element, under constant vertical stress, as presented in **Figure B-20**. The particular mode of loading is continued till failure. Peak friction angle - ϕ_{peak} - is computed at the maximum q/p' ratio and the residual friction angle - $\phi_{res.}$ - at failure.

Typical results from the above tests are presented in **Figures B-25, B-26** and **B-27** for consolidation vertical stress of 100kPa and three distinct values of relative density, namely D_r = 30, 60 and 90%. The outcome of the above investigation is finally summarized in **Figure B-28**, in which the resulting values of friction angle (ϕ_{peak} and $\phi_{res.}$) are plotted as a function of relative density D_r (%). The solid black lines represent the maximum friction angle activated in each case and the dashed black lines represent the residual shear strength of the material.

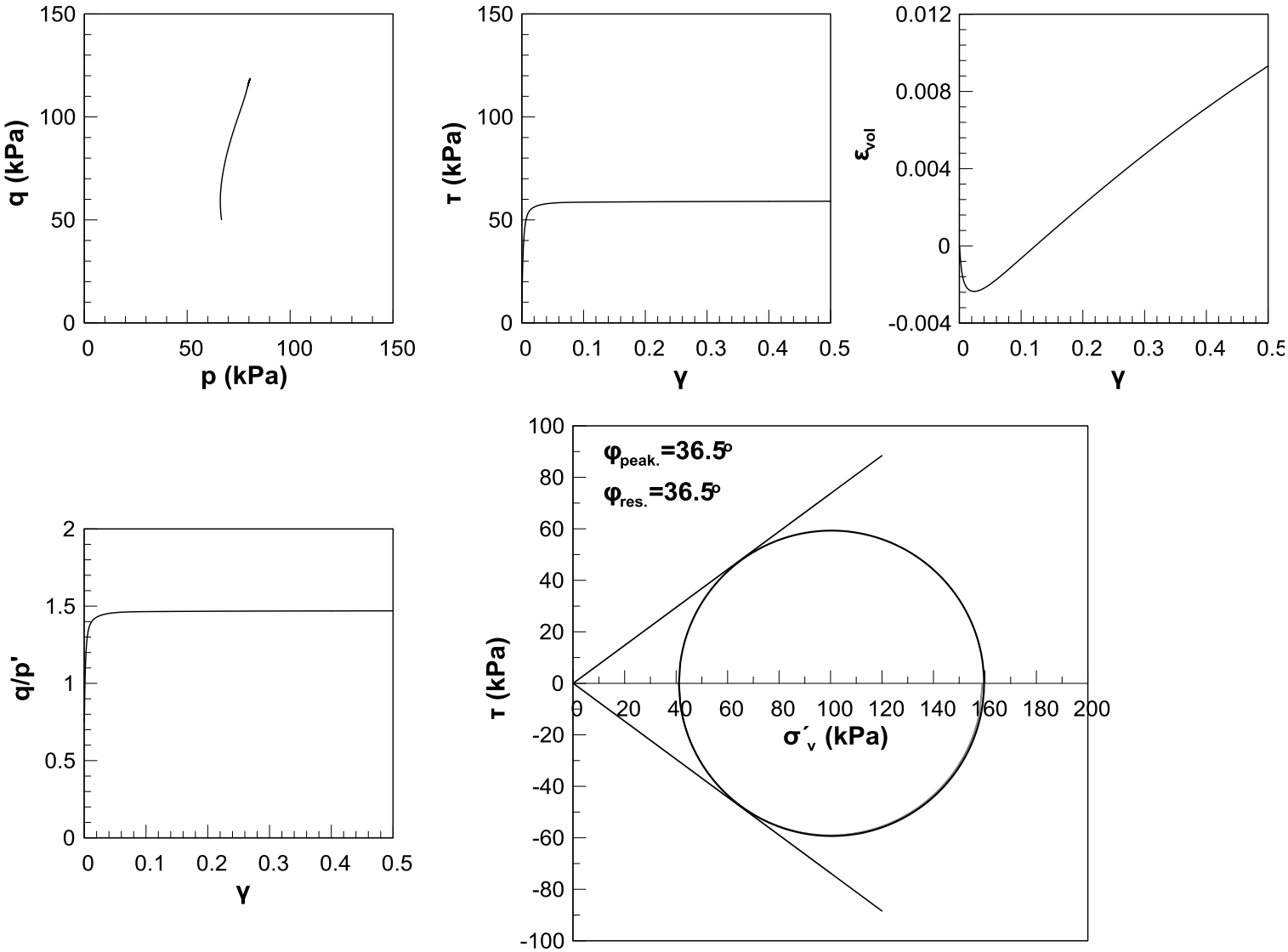

Figure B-25: Drained Simple Shear test - typical results for σ'_{vo}=100kPa, Dr = 30%.

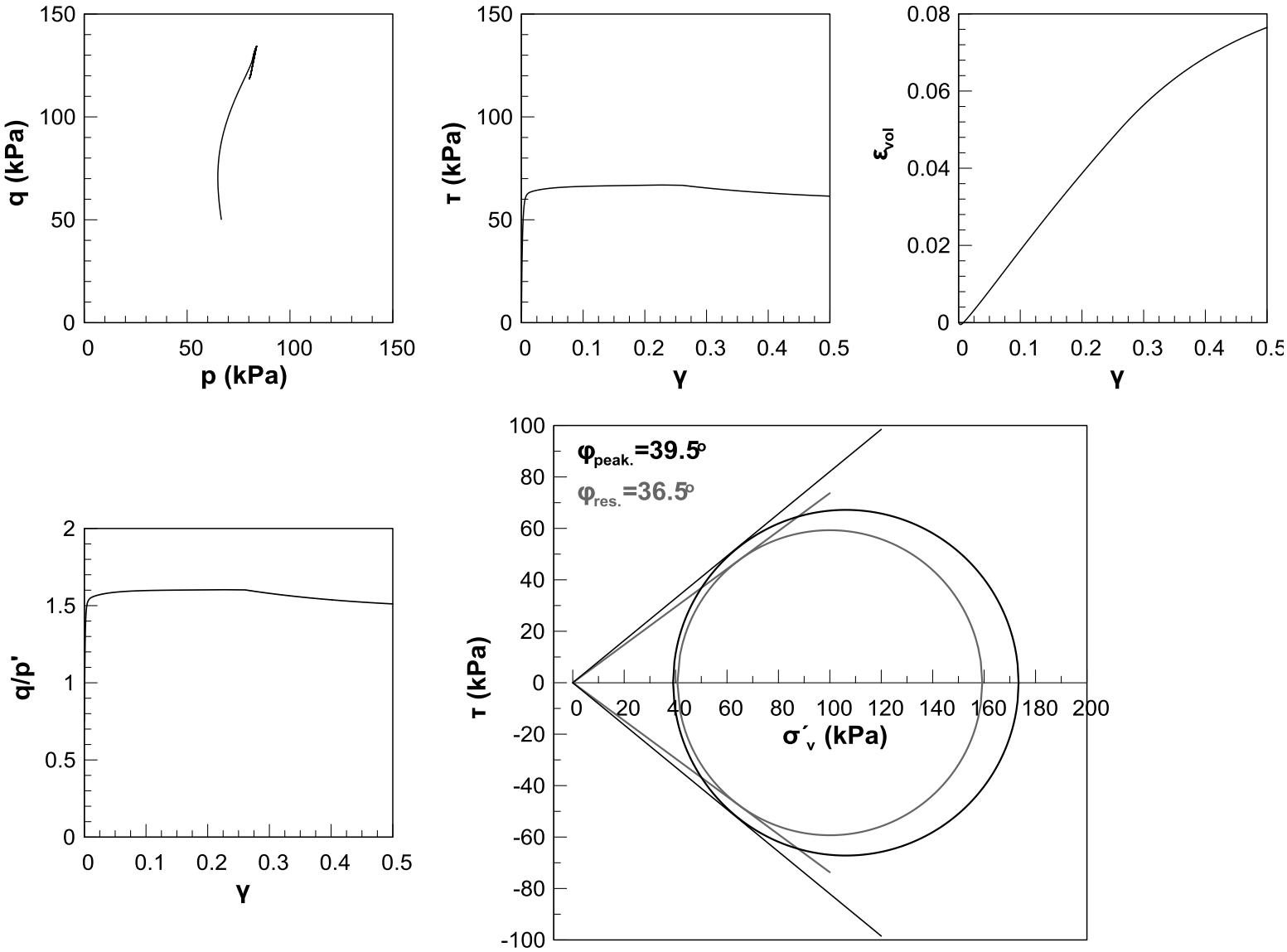

Figure B-26: Drained Simple Shear test - typical results for σ'_{vo}=100kPa, D_r = 60%.

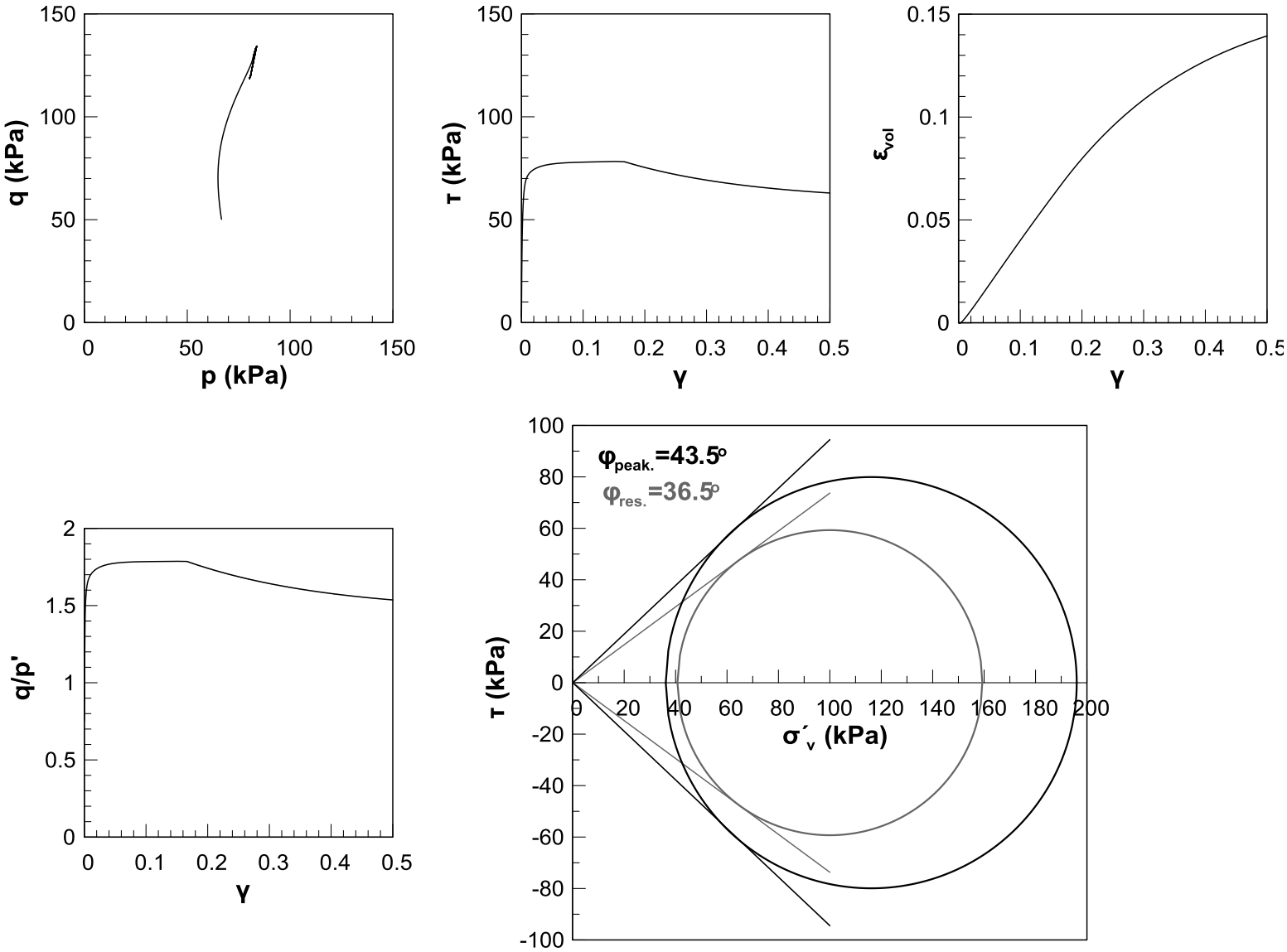

Figure B-27: Drained Simple Shear test - typical results for σ'_{vo}=100kPa, D_r = 90%.

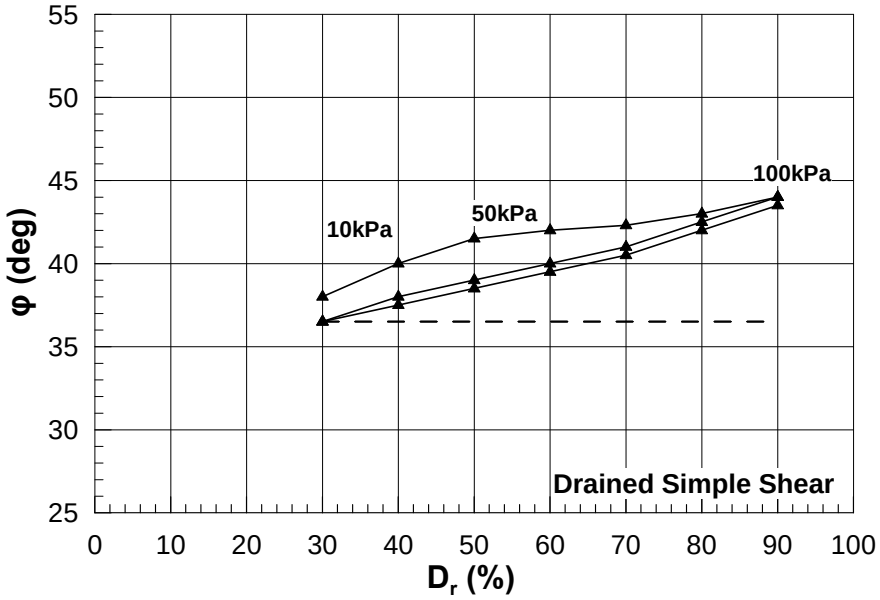

Figure B-28: Drained Simple Shear test simulations – peak (solid lines) and residual (dashed lines) values of friction angle ϕ as a function of relative density D_r (%).

B.3 Empirical data

The previously presented numerical results provide a detailed report regarding the performance of the NTUA-SAND constitutive model under different loading conditions. In the present paragraph the aforementioned results are compared against empirical relationships, which either connect relative density directly to the peak friction angle or indirectly through the N-SPT number and the effective vertical stress σ'_{vo} or mean pressure p' (kPa).

Friction angle ϕ(deg) and relative density D_r(%).- Schmertmann (1978) provides evidence that correlate peak friction angle – $\phi_{max.}$ – directly to relative density - D_r (%) - for four different sand categories, namely (i) uniform fine sand, (ii) uniform medium fine/well-graded fine sand (iii) uniform coarse sand/well graded medium fine sand and (iv) uniform gravel/well graded sand-gravel, as illustrated in **Figure B-29**.

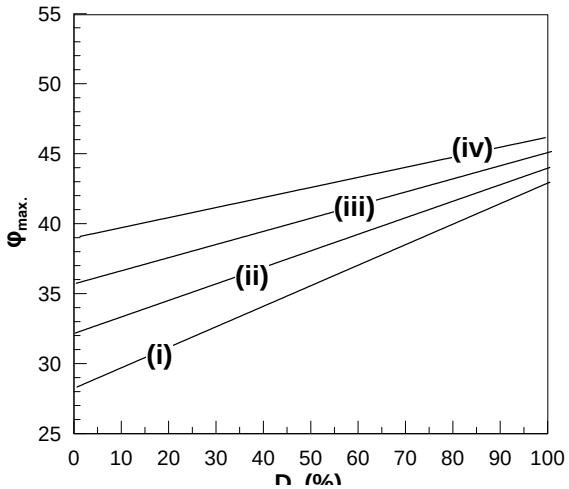

Figure B-29: Peak friction angle as a function of relative density for **(i)** uniform fine sand, **(ii)** uniform medium fine/well-graded fine sand **(iii)** uniform coarse sand/well graded medium fine sand and (iv) uniform gravel/well graded sand-gravel, Schmertmann (1978).

Andersen & Schjetne (2012) assembled a database of laboratory test results on sands under different loading and drainage conditions and provide direct correlations between peak friction angle and corresponding relative density. Namely, **Figure B-30** summarizes the outcome of 336 drained TX Compression laboratory tests performed in different sand materials under different consolidation stresses. Moreover, the results of 138 undrained TX Compression laboratory tests are summarized in

Figure B-31, for different levels of consolidation stress. Bolton (1986), proposes a correlation of the maximum friction angle to the critical value of friction angle, expressed through *Equation B-5*:

$$\phi' = \phi_{crit.} + 3I_R \qquad \text{B-5}$$

where the proposed value for $\phi_{crit.}$ equals 33^o for quartz and

$$I_R = D_r * (10 - \ln p') - 1 \qquad \text{B-6}$$

Cavallaro et al. (2001) have also proposed an empirical relationship between friction angle and relative density expressed through *Equation B-7*:

$$\phi = 0.238 \times D_r(\%) + 28.4 \qquad \text{B-7}$$

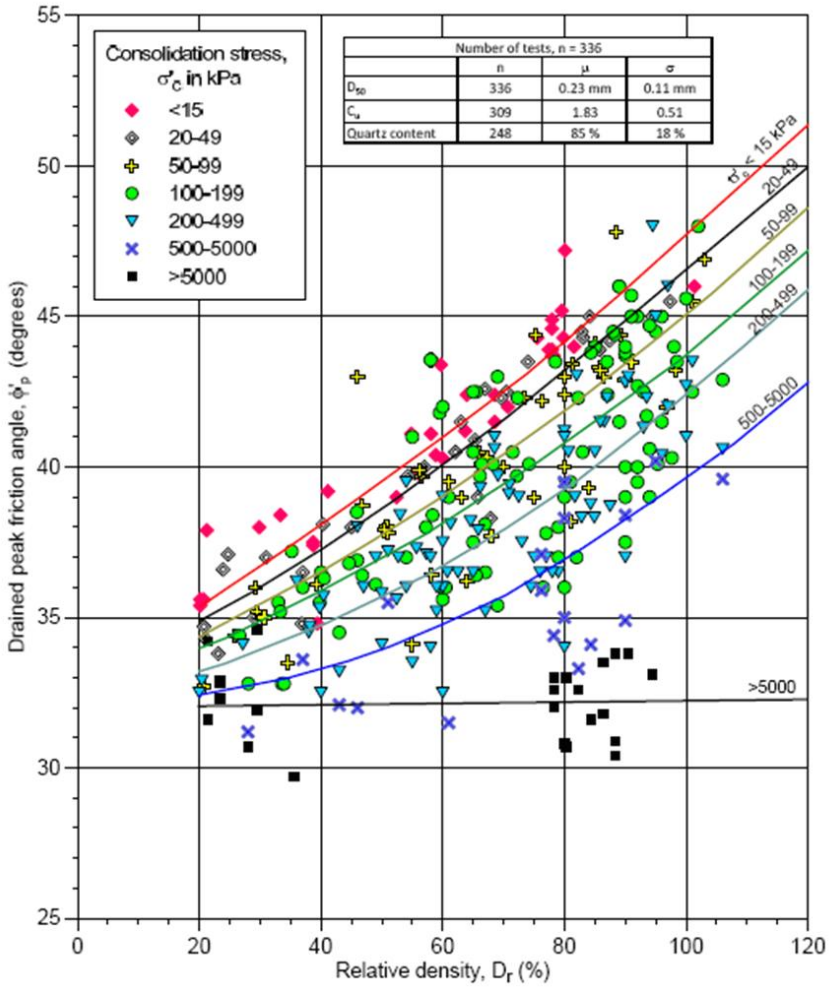

Figure B-30: Drained peak friction angle as a function of relative density Dr(%).

Friction angle and N_{SPT} number.- Peak friction angle has also been directly related to N_{SPT} number, by various researchers, such as Osaki, Dunham and Peck & Thornburn (1974). The proposed correlations are illustrated in **Figure B-32a** & **b**, while empirical mathematical expressions are provided by Osaki and Dunham below:

$$\phi = \sqrt{12N'} + 15 \qquad \text{B-8}$$

$$\phi = \sqrt{12N'} + 25 \qquad \text{B-9}$$

Also, De Mello (1971) after examining fine-grained or coarse-grained sand soils, correlated N_{SPT} test results, corrected for field conditions only, to effective vertical stress - σ'_{vo} - for distinct values of friction angle, as illustrated in

Figure B-33.

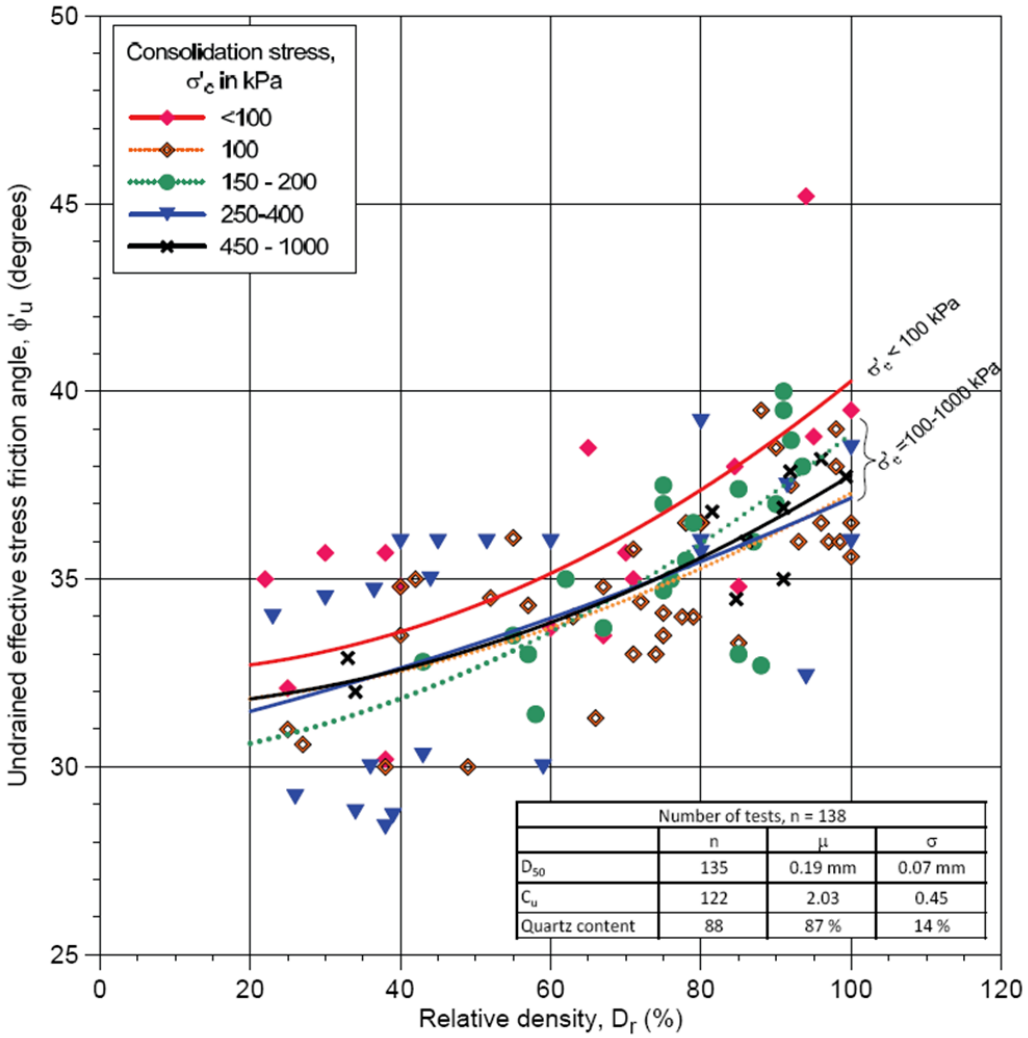

Figure B-31: Undrained effective stress friction angle as a function of relative density D_r (%).

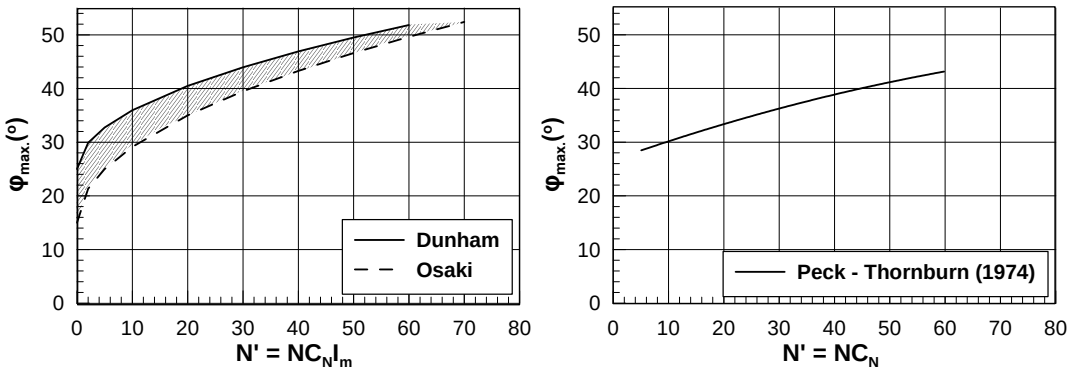

Figure B-32: Peak friction angle (ϕmax.) as a function of corrected N-SPT number N' according to **(a)** Osaki, Dunham and **(b)** Peck & Thornburn (1974).

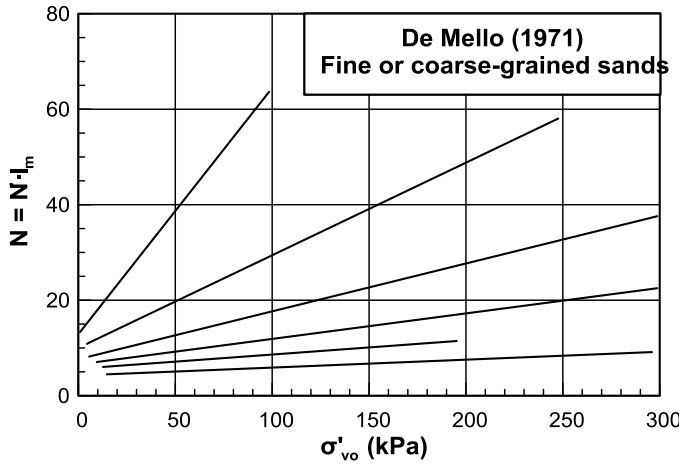

Figure B-33: Corrected N-SPT number N as a function of effective vertical stress σ'_{vo} (kPa) (De Mello, 1971).

Friction angle ϕ(deg) and initial stress conditions.- Additionally to the above empirical evidence, Kutter & Chen (1997) performed undrained and drained triaxial compression and extension tests on fine Nevada sand N_o120, within a relatively narrow range of relative densities, namely Dr = 70±7%. They also conducted undrained cyclic shear tests in a hollow cylinder with rotation of the stress directions; however, the particular results are not included in the present investigation, due to the difficulty to numerically simulate such test on element level. The Nevada sand used in the laboratory tests is a uniform fine sand with uniformity coefficient C_u = 2, mean grain size D_{50} = 0.17mm, specific gravity 2.67, maximum and minimum void ratio 0.887 and 0.511 respectively, corresponding exactly to the material parameters considered for the calibration of NTUA-SAND constitutive model. The outcome of the work by Kutter & Chen (1997) is presented in **Figure B-34**, in which peak mobilized friction angle is plotted as a function of the initial mean normal pressure p (kPa).

In a subsequent publication, Chen & Kutter (2009) comment on the prior test results and provide representative friction angle estimates. Namely, for the compression tests the q/p' ratio approaches a maximum value of about 1.45 (ϕ_{peak} = 36^o) for undrained loading and ranges from 1.7 to 2.1 for drained loading conditions, that being translated to friction angle ranging from ϕ_{peak} = 41.5 to 51^o, providing an average friction angle of about 44 degrees. For undrained extension the q/p' ratio approaches a maximum value of about -0.9 (ϕ_{peak} = 32^o), while for drained conditions the $(q/p')_{max.}$ ratio ranges from 1 to 1.1, corresponding to friction angle values from 36.8 – 42.3, with 40^o being the suggested average value. The particular results for initial consolidation pressures up to 100kPa – since the numerical

investigation referred to σ'_{vo} = 10, 50, & 100kPa - are included in the evaluation of the constitutive model's efficiency in the correct prediction of the mobilized peak friction angle.

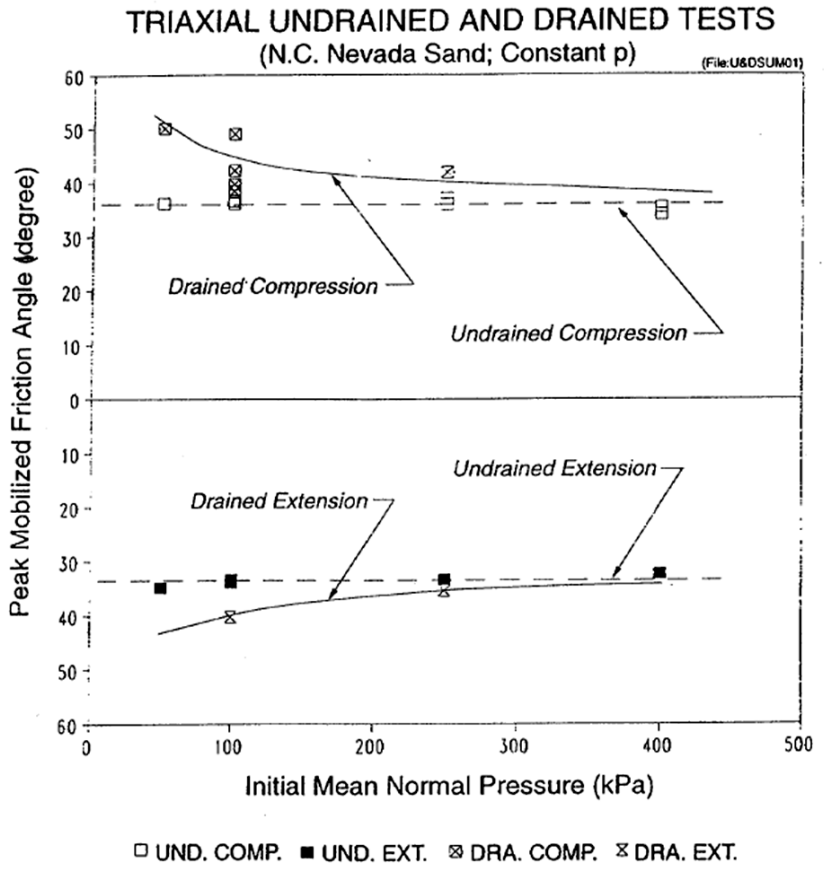

Figure B-34: Peak friction angle of Nevada sand for Dr = 70 ± 7% (Kutterand Chen, 1997).

B.4 Evaluation of the NTUA-SAND model performance

TX Compression.-

Figure B-35 summarizes the numerical and empirical predictions for the case of Isotropic TX Compression loading conditions. Apparently, the NTUA-SAND constitutive model performs satisfactorily within the range of loose to medium dense sands and predicts friction angle values, which lie at the lower boundary of the presented empirical relations. In the opposite, for values of relative density greater than D_r=60%, the peak mobilized friction angle is rather underestimated.

Namely, for loose and medium dense sands (D_r <60%) the NTUA-SAND predictions lie within the proposed range by Osaki – Dunham, while a much better agreement is noticed with the Peck-Thornburn (1974) curve. With increasing relative density, (D_r>60%) the prior acceptable agreement is not preserved and discrepancies are observed both under undrained and drained conditions. The Kutter & Chen (1997) laboratory results for Nevada sand are also included in the comparative evaluation, represented in the black dots, and refer to initial mean normal pressure p=50 – 100kPa. Note that there may be in good agreement with the numerical predictions for undrained loading conditions (with only 2 degrees difference), nevertheless, for drained loading conditions the laboratory results indicate a much higher friction angle value, which agrees with the empirical correlation by Terzaghi-Peck & DeMello. In both drainage conditions, Schmertmann's predictions lie consistently higher that the model's predictions, while there is little agreement with the Terzaghi-Peck-DeMello empirical correlation within a narrow relative density range, i.e. D_r = 30-40%.

TX-Extension.- Figure B-36 summarizes the numerical and empirical predictions for the case of Isotropic TX Extension loading conditions. The Kutter & Chen (1997) laboratory results for Nevada sand are also included in the comparative evaluation, represented in the black dots, and refer to initial mean normal pressure p=50–100kPa.

Under undrained loading conditions, the prior satisfactory performance of NTUA-SAND is repeated for relative density values of up to D_r=70%, since the numerical predictions plot between the Osaki-Dunham and Peck & Thornburn (1974) results. For higher values of relative density friction angle is underestimated and lies outside the area defined by the empirical results. Also, the Kutter & Chen (1997) laboratory results agree quite well with the NTUA-SAND predictions.

For Drained TX Extension, the constitutive model's predictions appear slightly improved and in very good agreement with most of the empirical predictions, especially Peck & Thornburn (1974), throughout the examined range of relative densities. The Kutter & Chen (1997) experimental results render ϕ values well above the numerical predictions ranging from 39 to 44 degrees for consolidation stresses from 50 -100kPa, as opposed to numerical predictions of 36 – 38 degrees, for the same relative density.

Simple Shear.- Figure B-37 summarizes the numerical and empirical predictions for the case of Simple Shear loading. Kutter & Chen (1997) conducted only TX Compression & Extension tests; hence no experimentally derived ϕ values are available. Under simple shear conditions, the NTUA-SAND model renders significantly improved ϕ values for the entire

examined range of relative densities and initial consolidation stresses. Particularly for Undrained conditions, the numerical results agree with Schmertmann's predictions (for uniform medium fine/well-graded fine sand) independently of initial consolidation stress level. Additionally, the numerical predictions agree with the Terzaghi – Peck – DeMello curves, within a narrow range of relative densities, i.e. D_r=40–50%. Accordingly, the above satisfactory performance of the constitutive model is preserved for drained conditions with minor deviations.

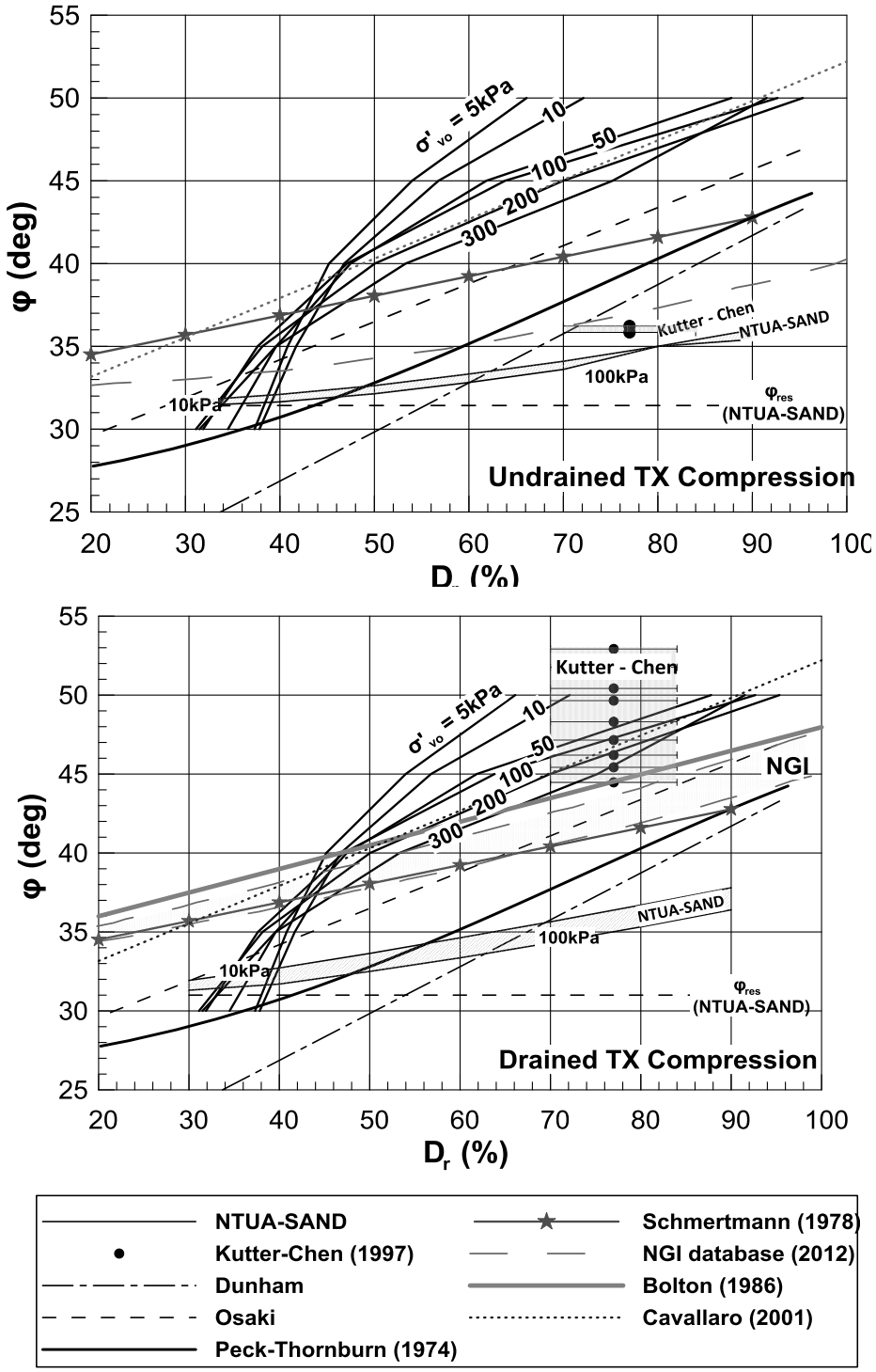

Figure B-35: Friction angle predicted from empirical relations and numerical results for TX Compression loading under Undrained and Drained conditions.

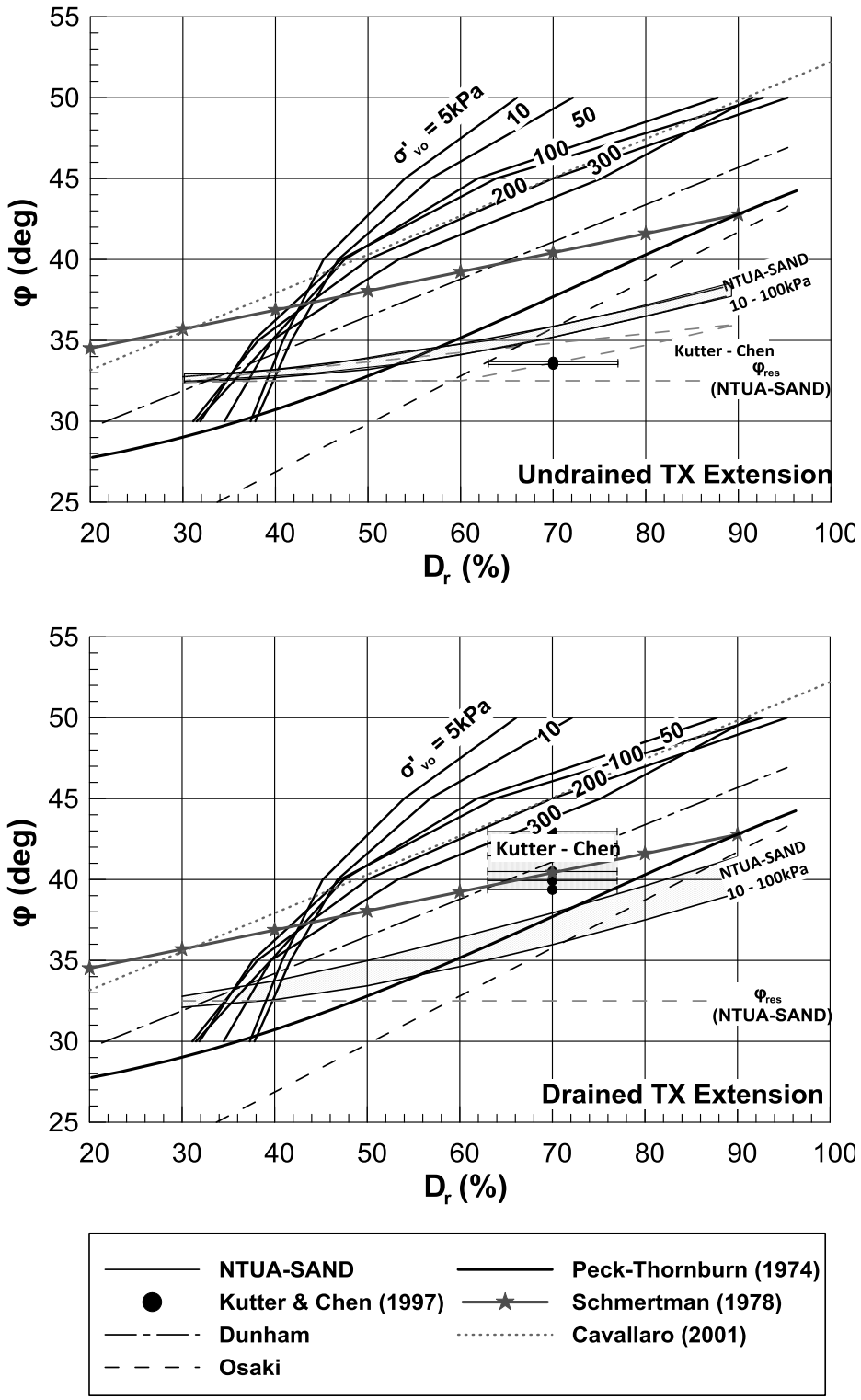

Figure B-36: Friction angle predicted from empirical relations and numerical results for TX Extension loading under Undrained and Drained conditions.

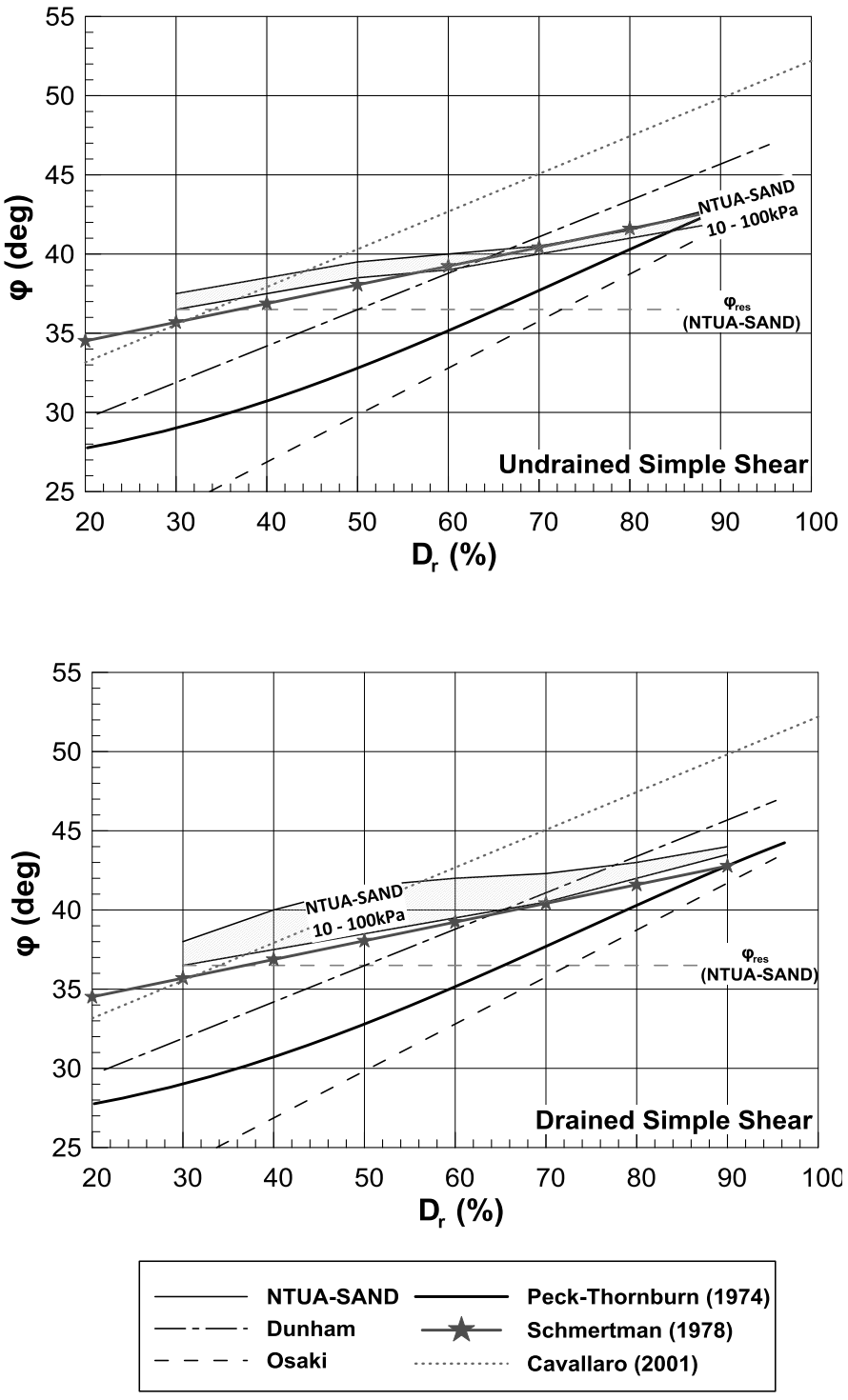

Figure B-37: Friction angle predicted from empirical relations and numerical results for Simple Shear loading under Undrained and Drained conditions.

B.5 Recalibration process of NTUA-SAND constitutive model

The low values of friction angle predicted by the NTUA-SAND constitutive model, particularly for relative density values greater than D_r=60% and isotropic loading, were attributed to the size of the bounding surface, originally controlled by the k^b_c model parameter. In the original model configuration, Papadimitriou et al. (2002) were based on triaxial compression tests on Nevada sand (Arulmoli et al., 1992), in order to quantify the k^b_c model parameter, which was finally set equal to 1.45. The particular value provided the best fit to the experimentally derived correlation between η_{max} and the initial state parameter ψ_o (for given p_o and D_r). Note that the particular parameter essentially expresses the effect of the state parameter ψ on the peak stress ratio (η_{max} = q/p') by controlling the size of the bounding surface as seen in *Equation B-1*.

In the above context, two similar constitutive models were also examined, in terms of the considered mathematical formulation of their bounding surface, namely the SANISAND model (Taiebat & Dafalias, 2008) and the model proposed by Loukidis & Salgado (2009). The particular models, which are briefly described in the following paragraph, have also been developed in the framework of critical state soil mechanics and bounding surface plasticity and therefore are directly comparable to the NTUA-SAND constitutive model.

SANISAND (Taiebat & Dafalias, 2008).- The particular constitutive model consists of a closed yield surface as well as three more surfaces, namely, the critical state, the dilatancy and the bounding surfaces, as presented in **Figure B-38**. Similarly to the NTUA-SAND model, the three surfaces appear as open wedges in the triaxial p-q space and their shape is described by the slope $a_c^{c,b,d}$ for triaxial compression. The slope of the bounding surface in compression (α^b_c) is expressed as a function of the a^c_c, related to the position of the CSL, and the ever-current value of the state parameter ψ, through an exponential relationship, as seen in *Equation B.10.* The equivalent expressions for extension conditions are described through the well-known parameter c, expressing the extension to compression ratio.

$$\alpha_c^b = \alpha_c^c \exp(-\eta^b \psi) \qquad B.10$$

SANISAND constitutive model is calibrated for Toyoura and Sacramento river sand and the necessary model parameters for the application of *Equation B.10* are provided in the following **Table B-2**.

Table B-2: Parameters for the mathematical expression of the B.S. in compression for the SANISAND model.

Parameter	Symbol	Toyoura sand	Sacramento river sand
CSL	a_c^c	1.2	1.3
Kinematic hardening	η^b	1.25	1.3

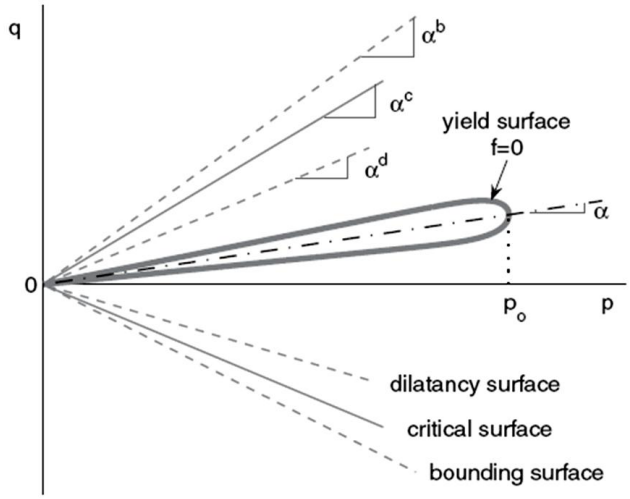

Figure B-38: Schematic representation of the SANISAND model surfaces in triaxial space.

Loukidis & Salgado (2009).- This constitutive model is also formulated considering an exponential form for the locus of the Bounding surface, which is described through *Equation B-11*:

$$M_c^b = M_c^c \exp(-k_c^b \psi) \qquad B\text{-}11$$

It has been calibrated for Toyoura and Ottawa clean sands and also for Ottawa sand with 5% and 10% silt. For the application of *Equation B-11* the required parameters are summarized in **Table B-3** for each one of the examined sand materials.

Table B-3: Parameters for the mathematical expression of the bounding surface in compression for the Loukidis & Salgado (2009) model.

	Parameter symbol	Parameter value				
		Toyoura (dry deposited)	Toyoura (moist tamped)	Ottawa CS	Ottawa 5% silt	Ottawa 10% silt
CSL	M_c^c	1.27	1.27	1.21	1.24	1.31
Bounding surface	k_c^b	1.5	1.1	1.9	1.7	1.6

Also, **Table B-4** summarizes basic characteristics for the sand materials used for the parameter calibration of the abovementioned constitutive models, thus rendering them comparable to the NTUA-SAND model.

Table B-4: Soil properties for the different sand materials used for the calibration of NTUA-SAND, SANISAND & Loukidis-Salgado constitutive models.

Material	e_{max}	e_{min}	D_{50} (mm)	Reference
Nevada	0.887	0.511	0.10	Arulmoli et al. (1992)
Toyoura	0.98	0.60	0.16-0.20	Loukidis (2009)
Sacramento river	1.03	0.61	D_{60} = 0.22	Lee & Seed (1967)
Ottawa clean sand	0.78	0.48	0.39	Murthy et al. (2007)

Recalibration of NTUA-SAND.- According to the Authors, in the previous constitutive models, η^b and k_c^b model parameters correspond to the best fit to the experimental TX Compression test results between the maximum shear stress ratio η_{max} and the state parameter ψ at failure, rather than the initial ψ_o as considered in NTUA-SAND original calibration. When performing the particular task for the VELACS experimental TX Compression results (Arulmoli et al.,1992), as presented in **Figure B-39**, it appears reasonable to adopt a k^b_c value up to 2 for the NTUA-SAND constitutive model, as opposed to the 1.45, which was initially considered. Also, when comparing *Equations B.1*, *B.10* and *B.11* in terms of η_{max} versus ψ, as illustrated in **Figure B-40** a value of 2 appears to agree satisfactorily well with the other constitutive models within the range of interest, i.e. for negative values of ψ.

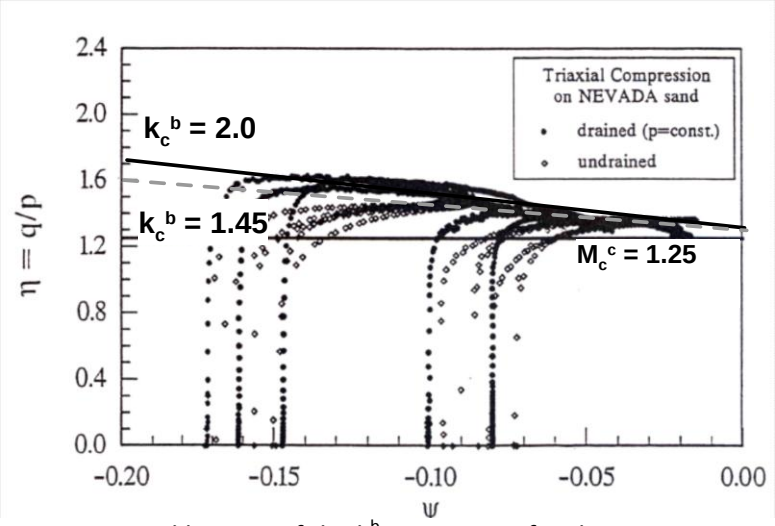

Figure B-39: Recalibration of the k^b_c parameter for the NTUA-SAND model.

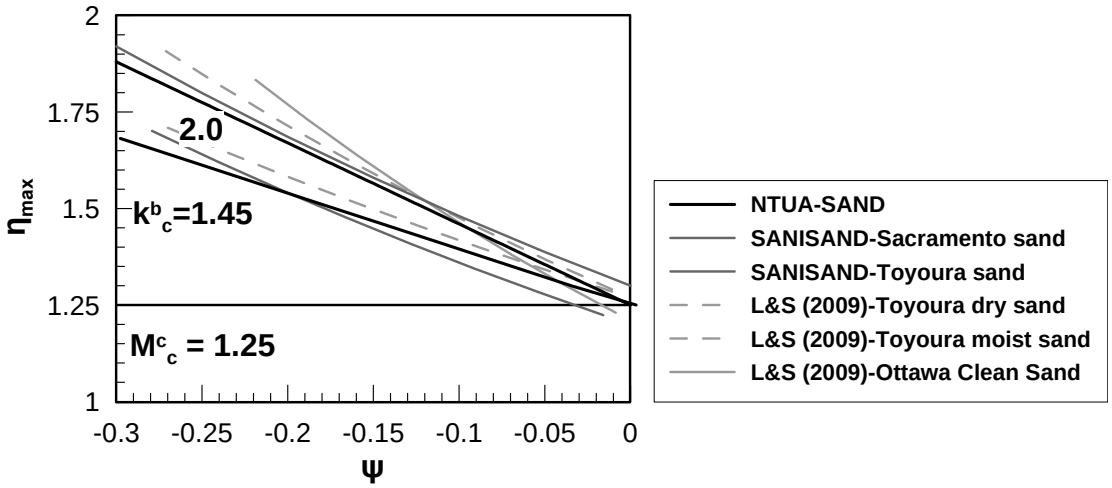

Figure B-40: η_{max} versus ψ state parameter for NTUA-SAND, SANISAND and Loukidis & Salgado constitutive models.

Setting k^b_c equal to 2, resulted in the enlargement of the bounding surface and consequently the stiffer behavior of the constitutive model under monotonic loading. Nevertheless, the ultimate purpose was to maintain the particular benefit, while leaving the remaining aspects of monotonic response intact. In parallel, another primary concern revolved around the maintenance of the original cyclic behavior of the model and the associated resistance to liquefaction, which increased after the modification of the bounding surface. The above goals were accomplished through a trial and error procedure and involved the obligatory modification of two extra model parameters, namely the dilatancy constant A_o and the plastic modulus constant h_o, as described by Andrianopoulos et al. (2010). The original and modified values of the model parameters are summarized in **Table B-5**. Subsequently, the

modified NTUA-SAND constitutive model was extensively examined under monotonic and cyclic loading conditions, in order to obtain a detailed representation of its behavior.

Table B-5: Initially proposed and modified values of NTUA-SAND model parameters.

Parameter	Physical meaning	Old value	Modified value
k_c,^{b}	Effect of ψ on peak deviatoric stress ratio in TC	1.45	2.00
A_o	Dilatancy constant	0.8	0.65
h_o	Plastic modulus constant	15,000	7,500

Monotonic element level tests were performed aiming at verifying that an increased shear strength level was obtained, along with preserving a compatible strain behavior to the initial calibration. **Figure B-41** through **B-49**, summarize typical results for the three types of element level tests, namely TX Compression, Extension and Direct Simple Shear (considering K_o=0.5 conditions) under drained and undrained loading conditions. The presented typical results concern an initial consolidation stress of 80kPa and three values of relative densities, namely 40, 60 and 90%.

Cyclic Triaxial - CTX and Cyclic Simple Shear - CSS element level, strain controlled tests were executed under three distinct initial stress conditions i.e. 40, 80 and 160kPa, and three values of relative densities, 40, 60 and 90%. The particular series of element level tests aimed at examining the response of the modified model under cyclic conditions and obtaining a compatible liquefaction resistance behavior to the original model response. **Figure B-50** and **B-51**, summarize the resistance to liquefaction with regard to the number of cycles N, for the two types of tests and the three examined values of relative densities. For comparison purposes, the original model predictions are also plotted in the particular figures, along with the VELACS experimental results (Arulmoli et al., 1992) which were used for the original calibration of the constitutive model.

Shear Strength Predictions.- Having established higher shear strength levels with a compatible cyclic response to the initial NTUA-SAND model, peak friction angle values were re-evaluated for a range of relative densities 40÷90% and three different initial consolidation stress levels, namely 40, 80 and 160kPa. **Figure B-52**, summarizes the model predictions for Triaxial Compression loading conditions under drained and undrained conditions. The black solid lines correspond to the original calibration (Papadimitriou 2002), while the dotted gray lines denote the improved predictions. **Figure B-53** & **B-54**, present the corresponding results for Triaxial Extension and Direct Simple Shear loading conditions.

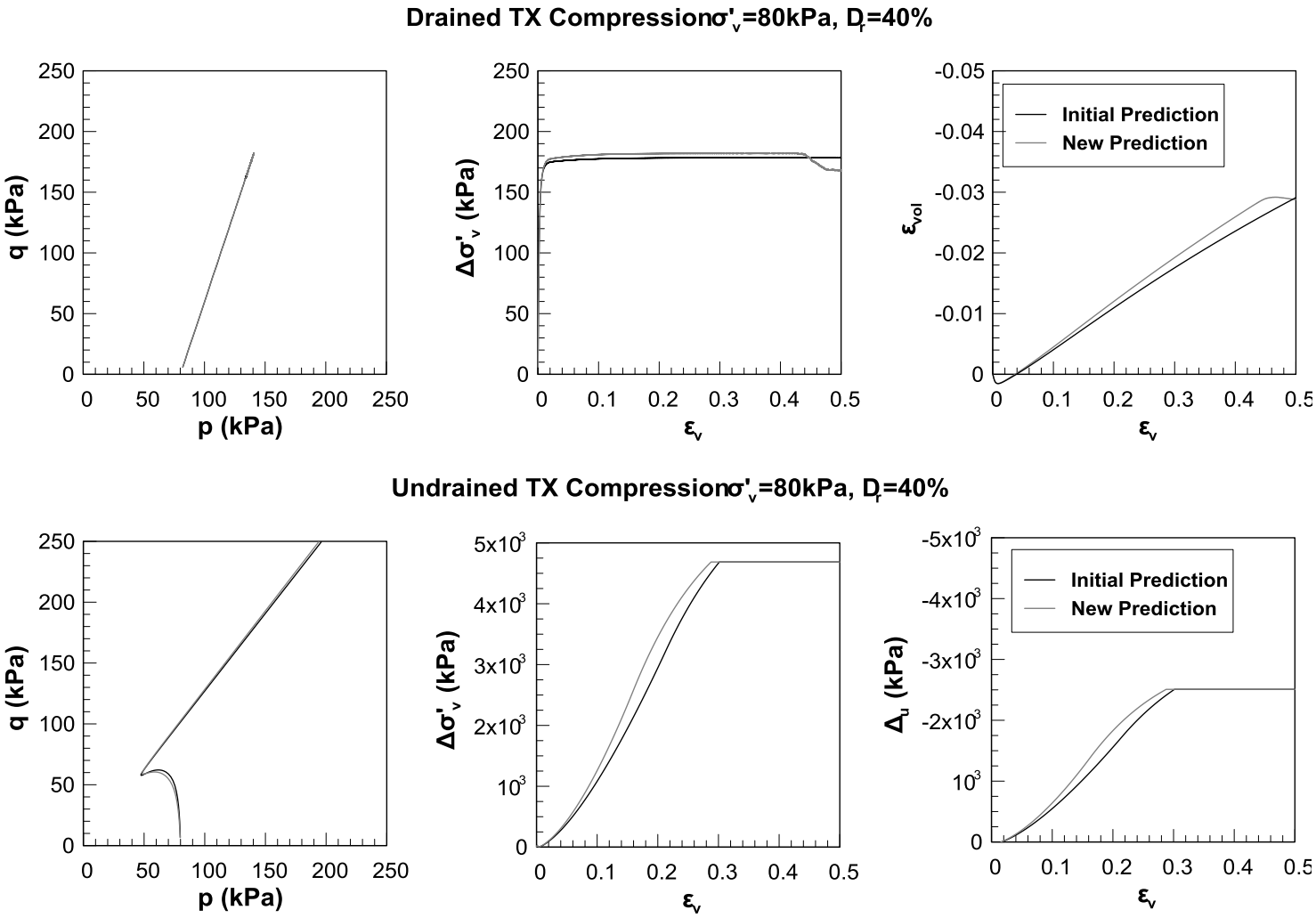

Figure B-41: Typical results for the original and recalibrated NTUA-SAND model.

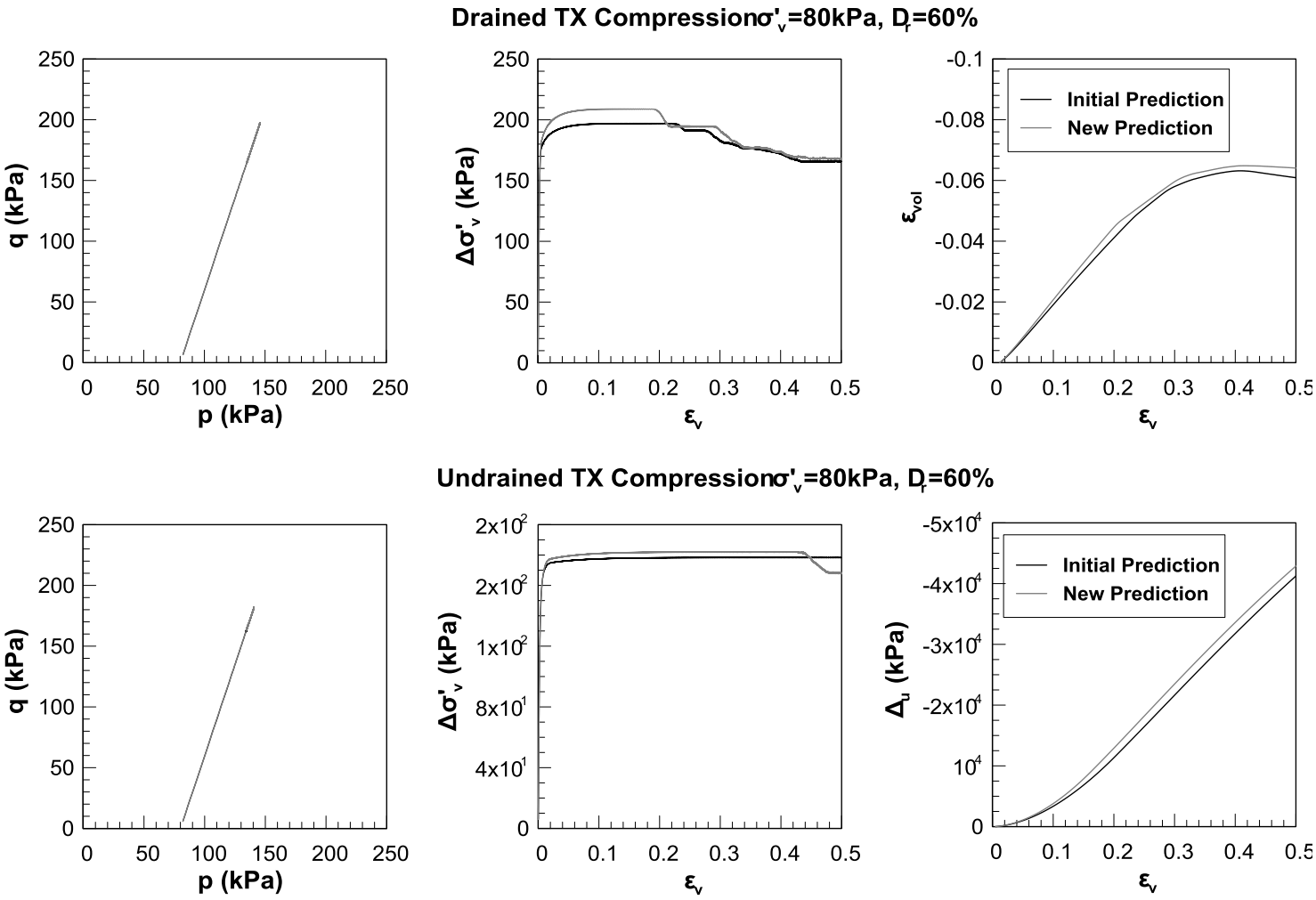

Figure B-42: Typical results for the original and recalibrated NTUA-SAND model.

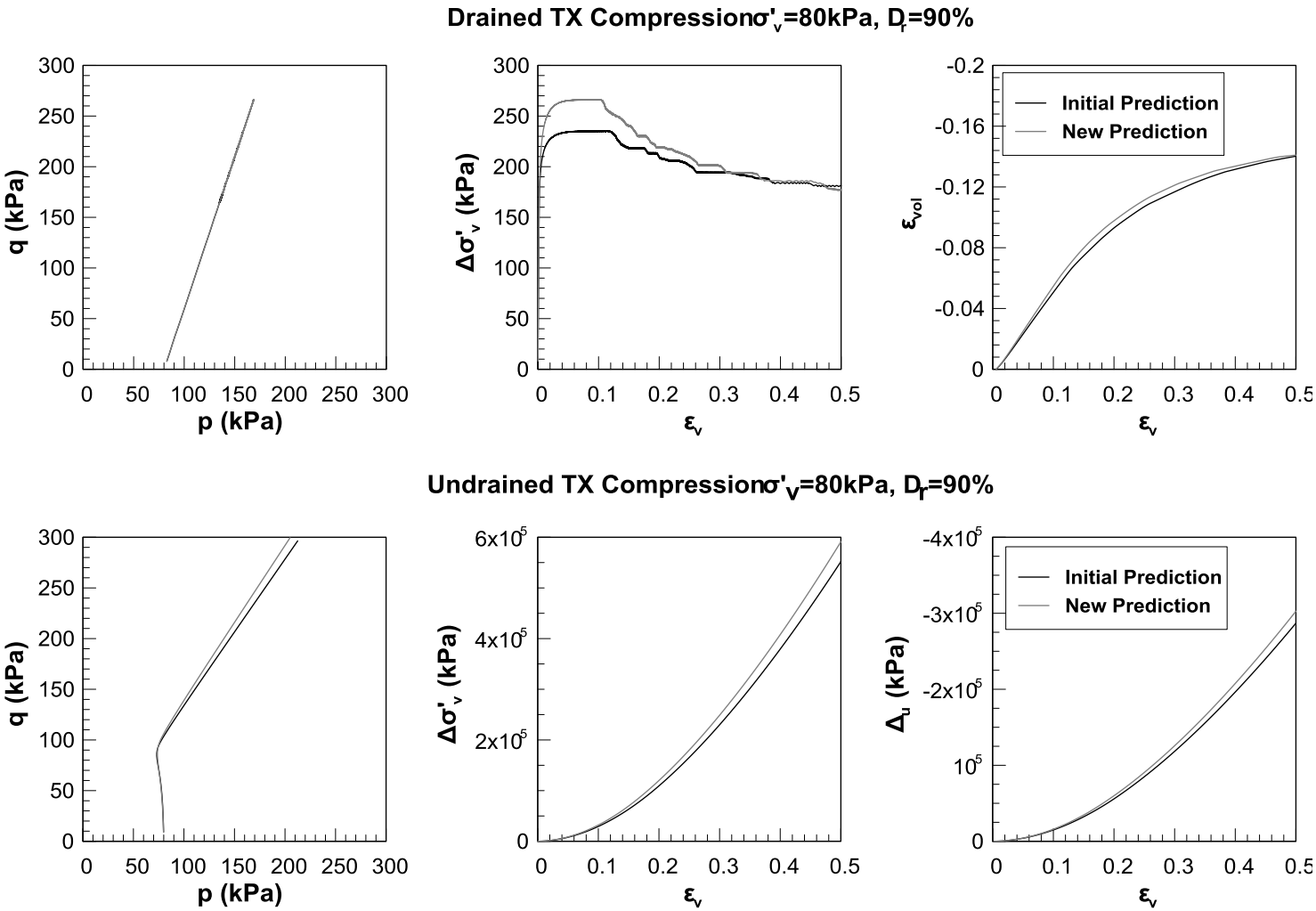

Figure B-43: Typical results for the original and recalibrated NTUA-SAND model.

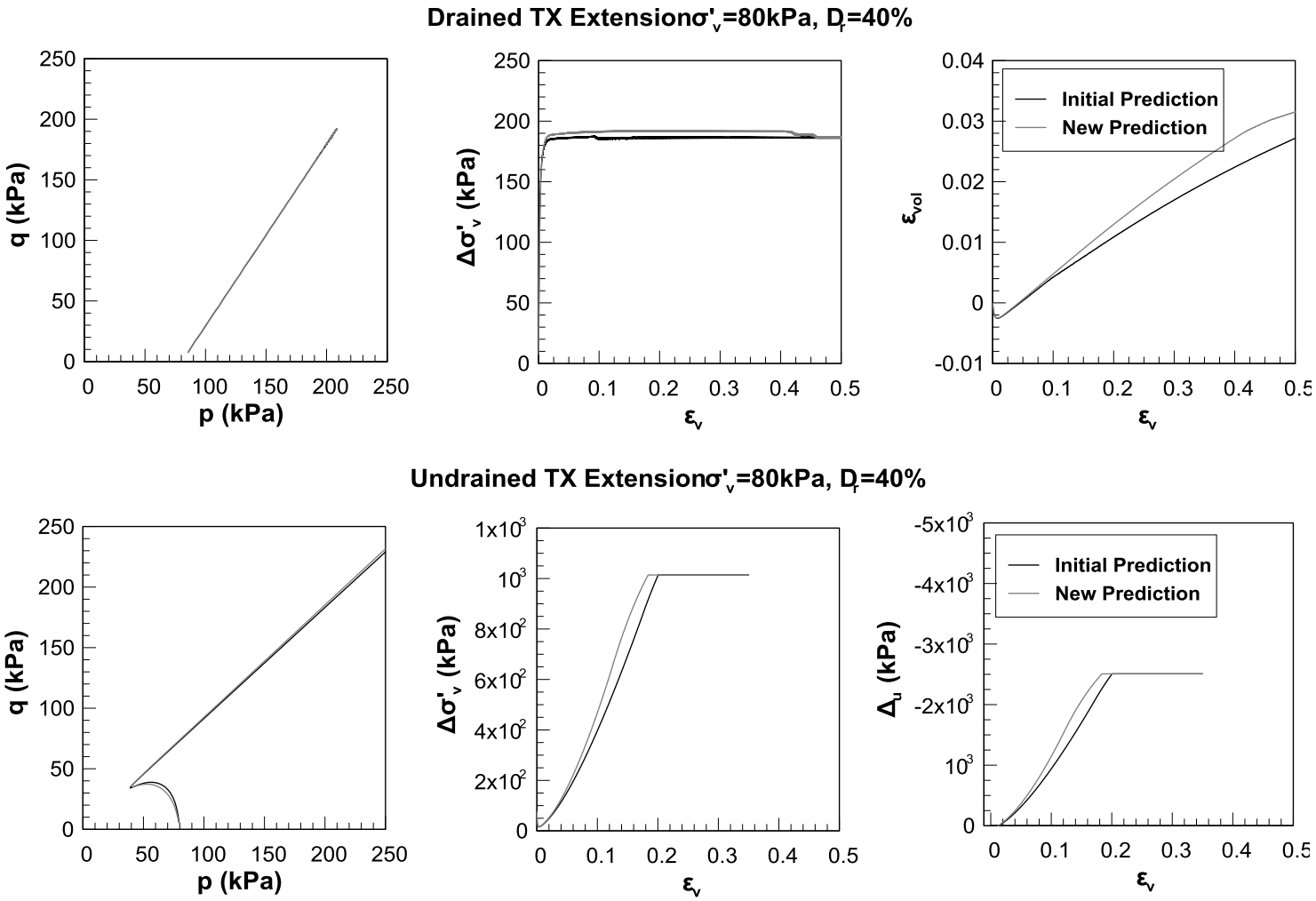

Figure B-44: Typical results for the original and recalibrated NTUA-SAND model.

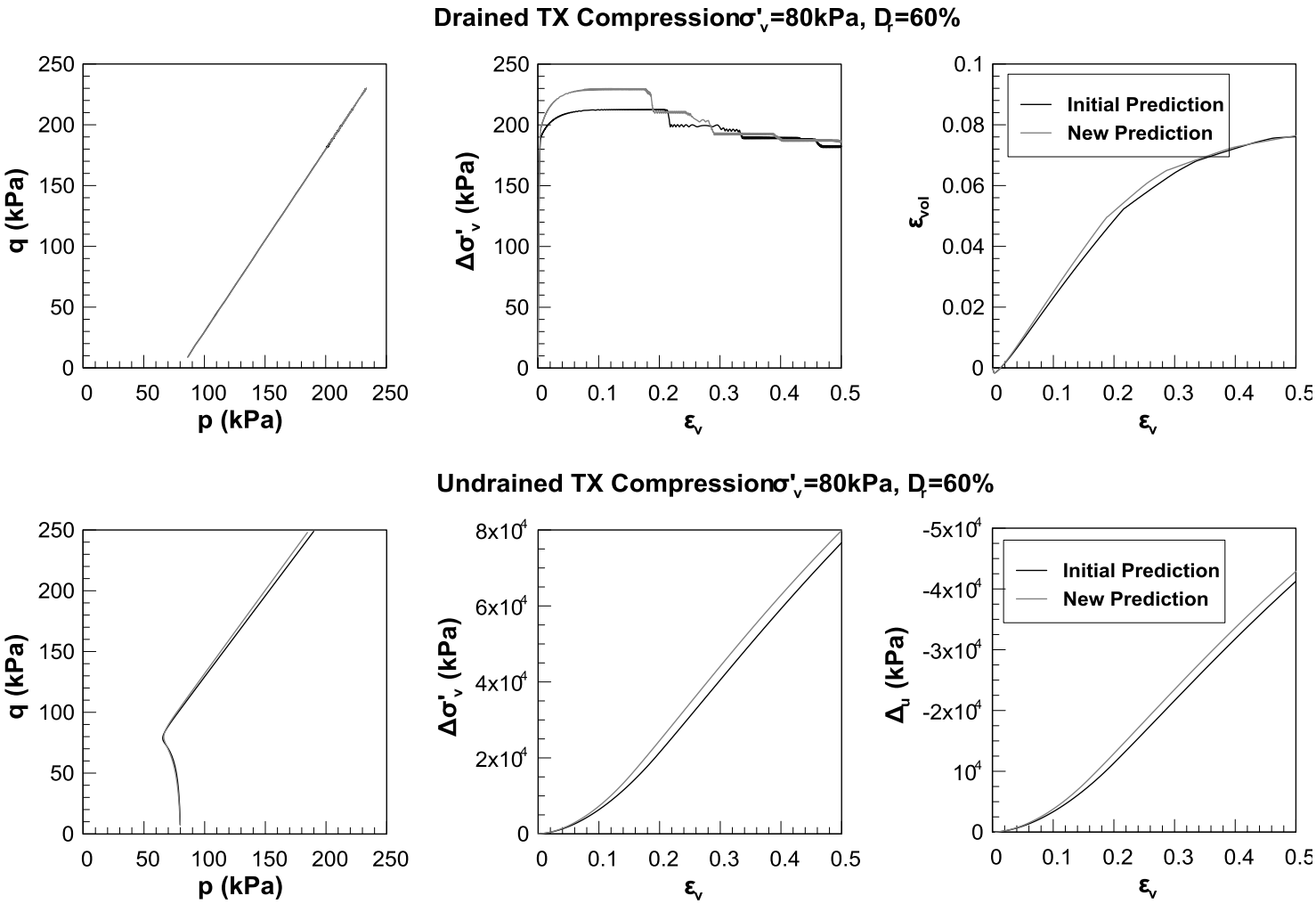

Figure B-45: Typical results for the original and recalibrated NTUA-SAND model.

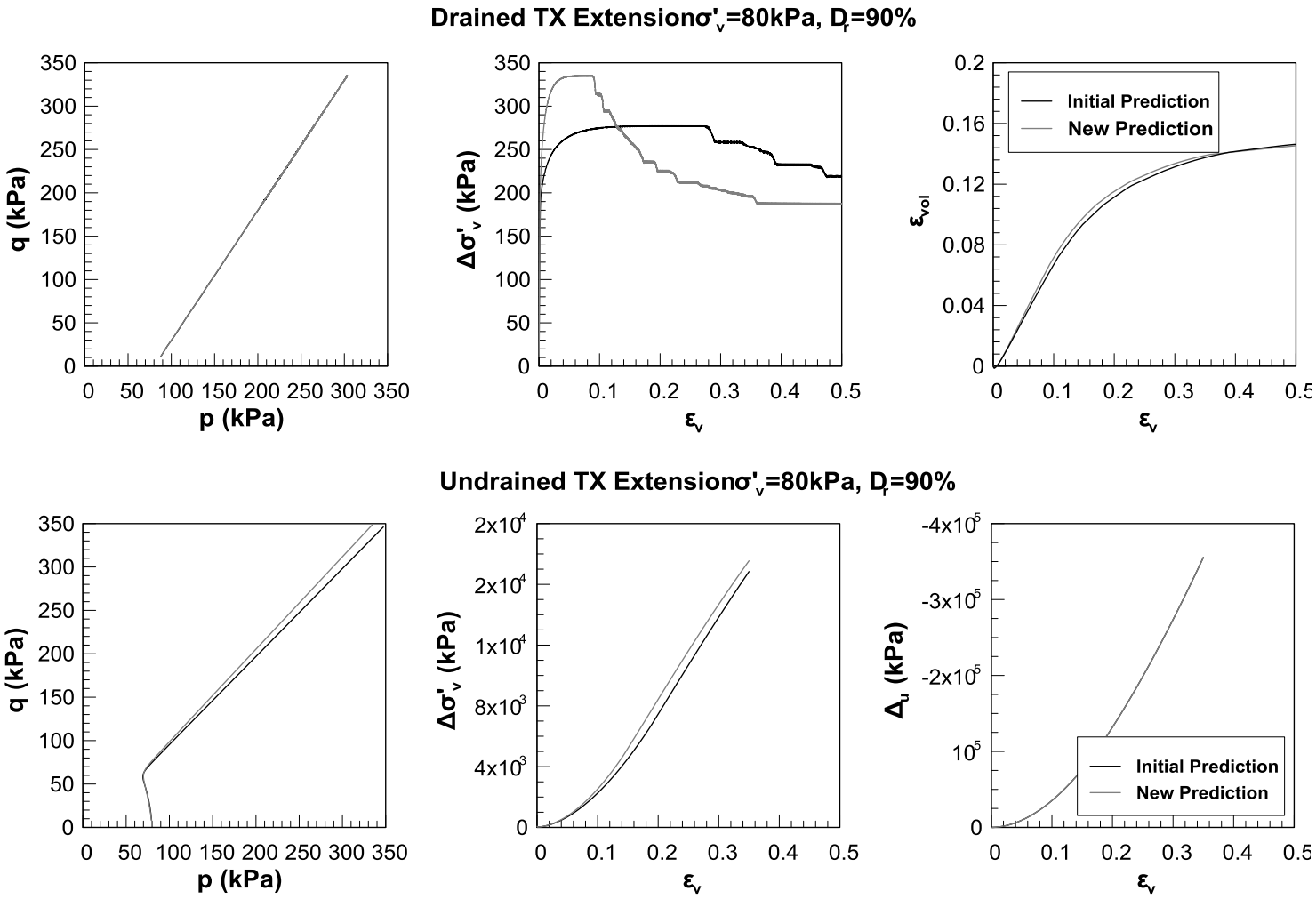

Figure B-46: Typical results for the original and recalibrated NTUA-SAND model.

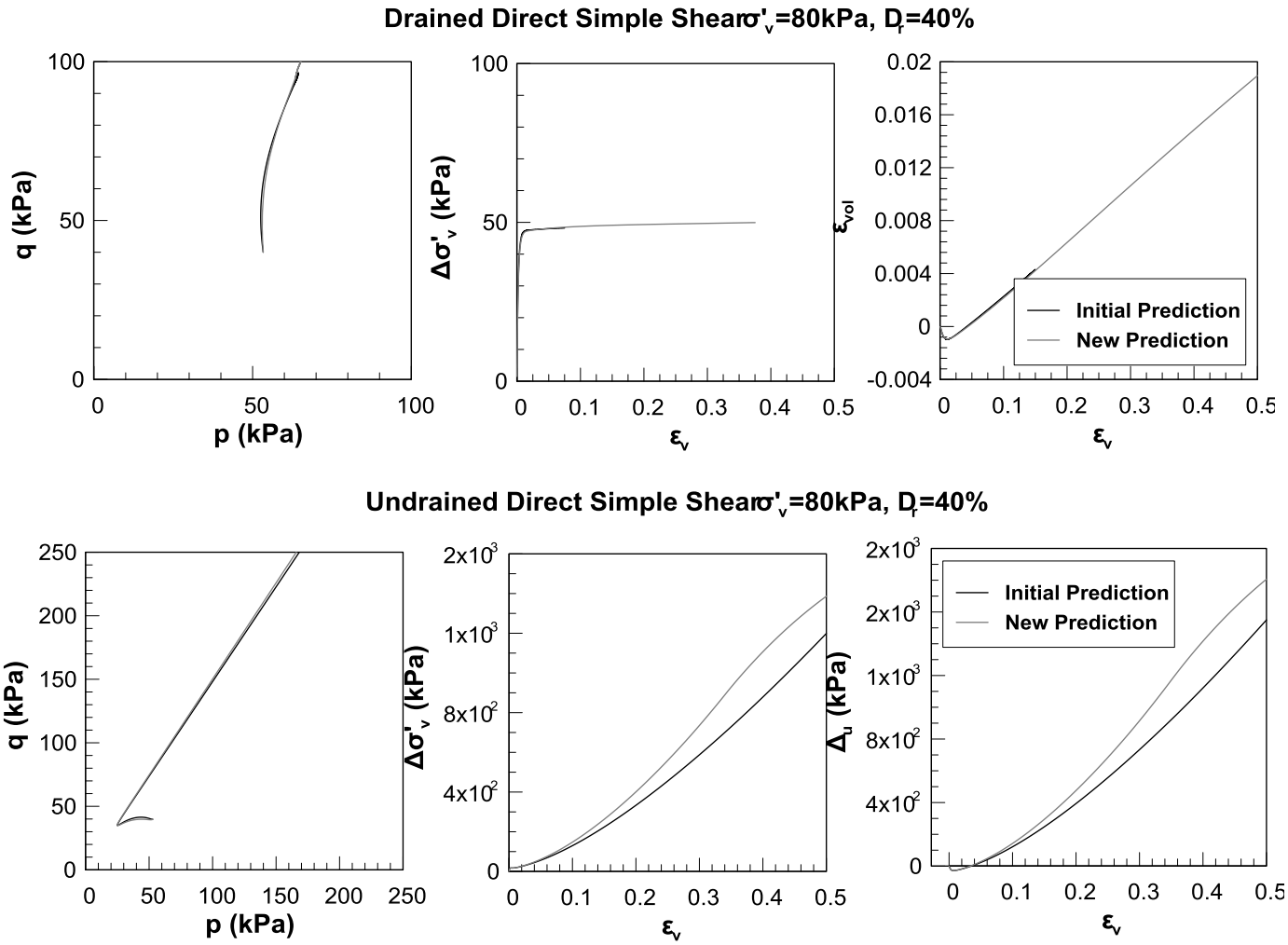

Figure B-47: Typical results for the original and recalibrated NTUA-SAND model.

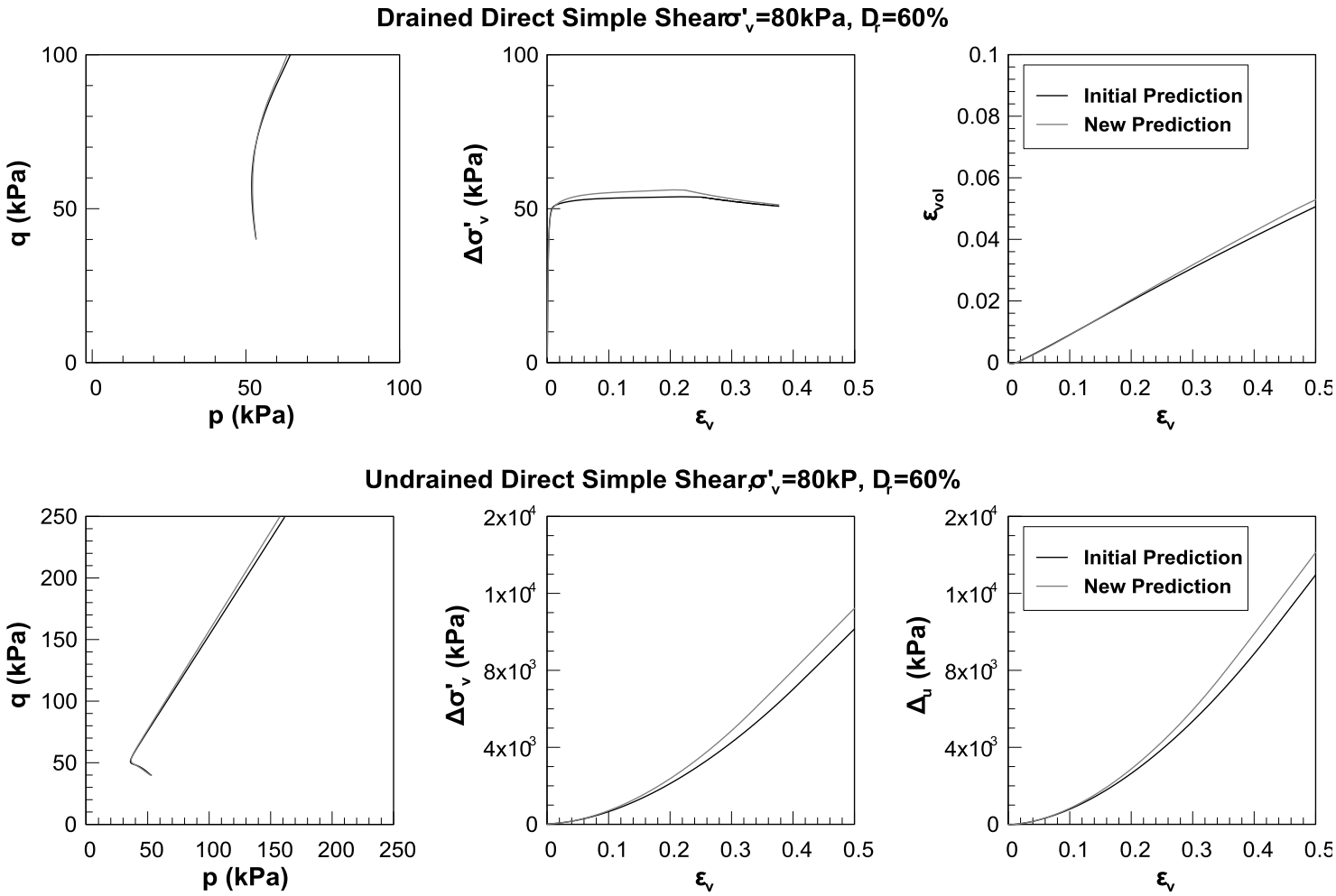

Figure B-48: Typical results for the original and recalibrated NTUA-SAND model.

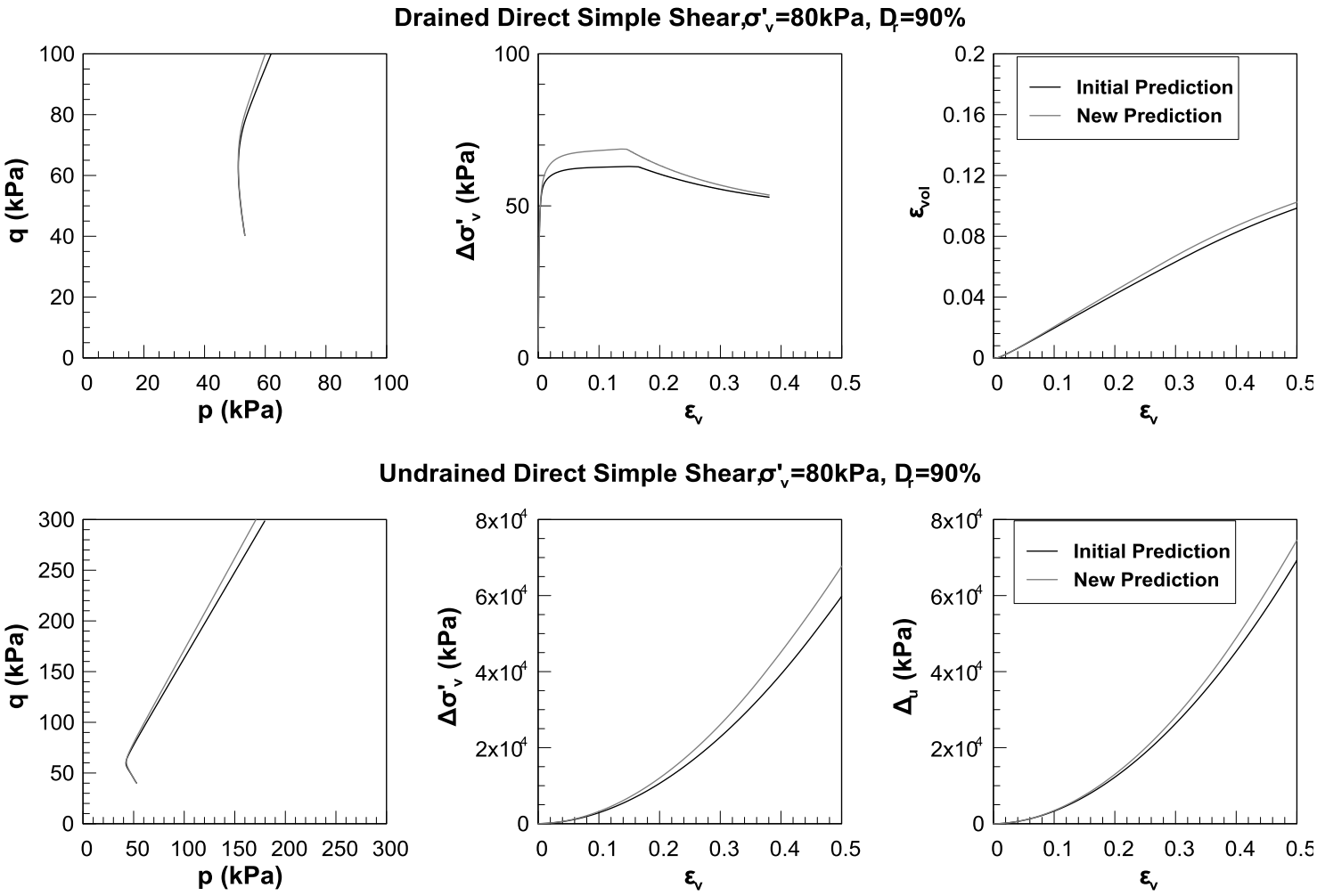

Figure B-49: Typical results for the original and recalibrated NTUA-SAND model.

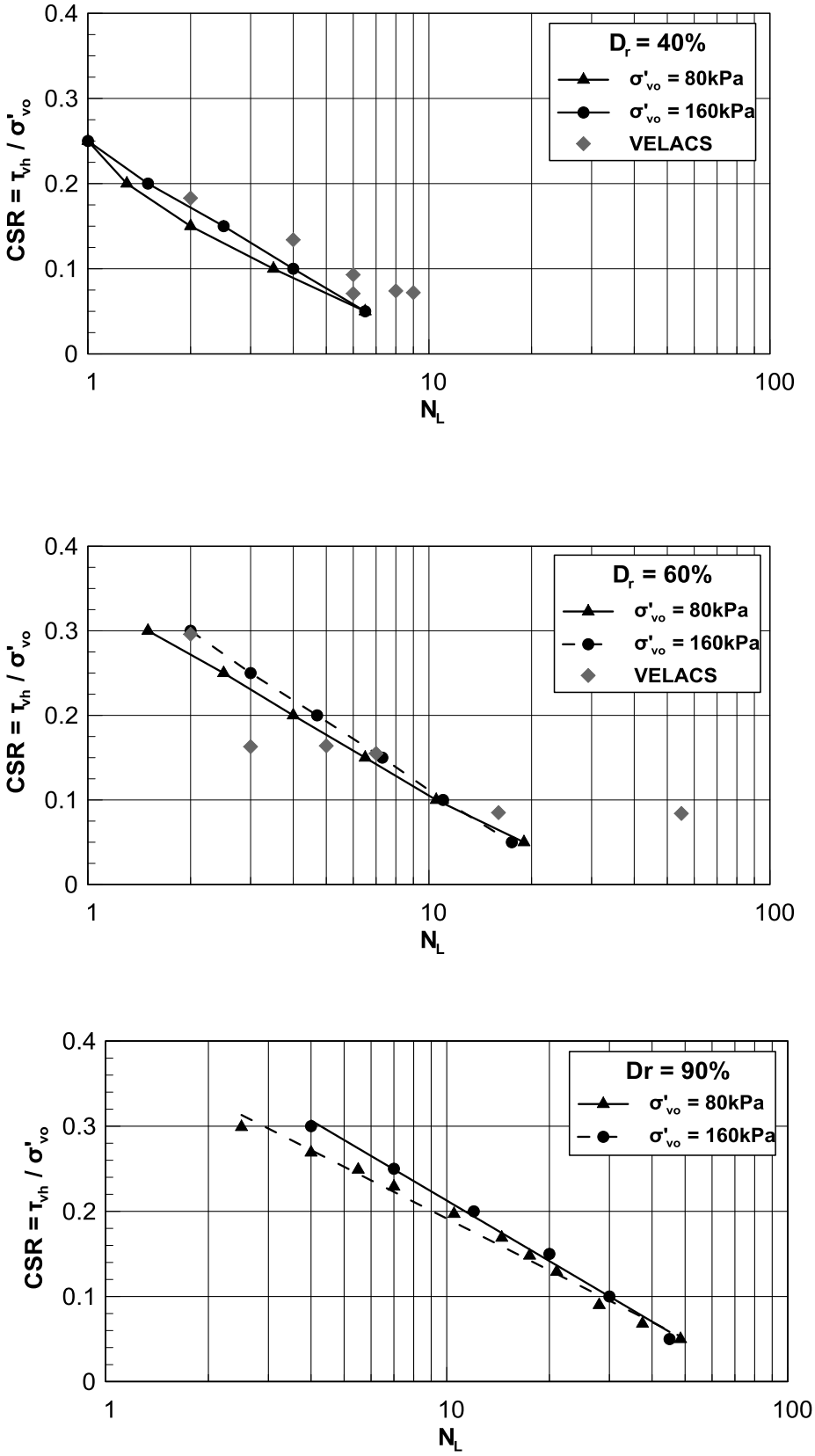

Figure B-50: Liquefaction resistance curves for the re-calibrated NTUA-SAND model for CSS test conditions.

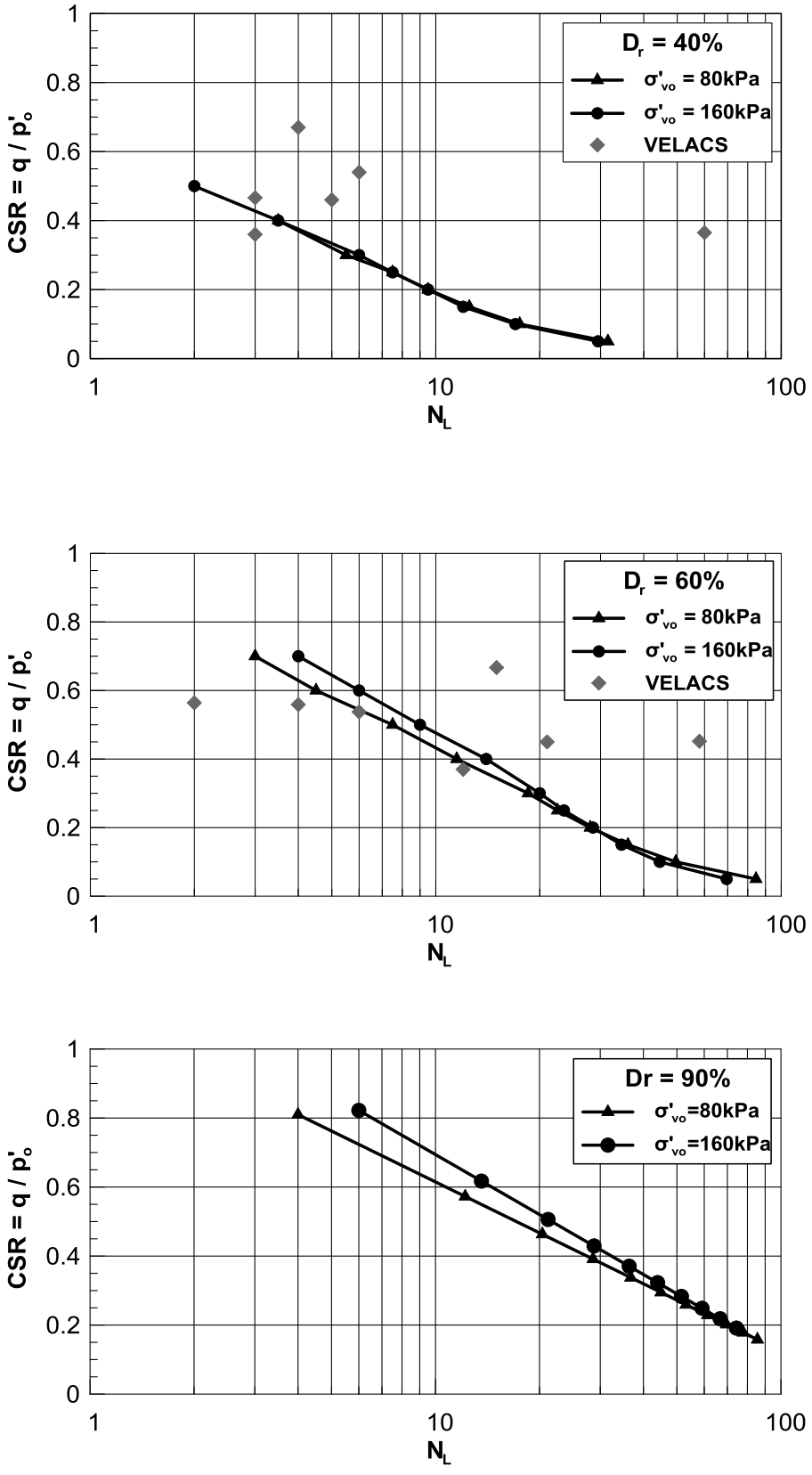

Figure B-51: Liquefaction resistance curves for the re-calibrated NTUA-SAND model for CTX test conditions.

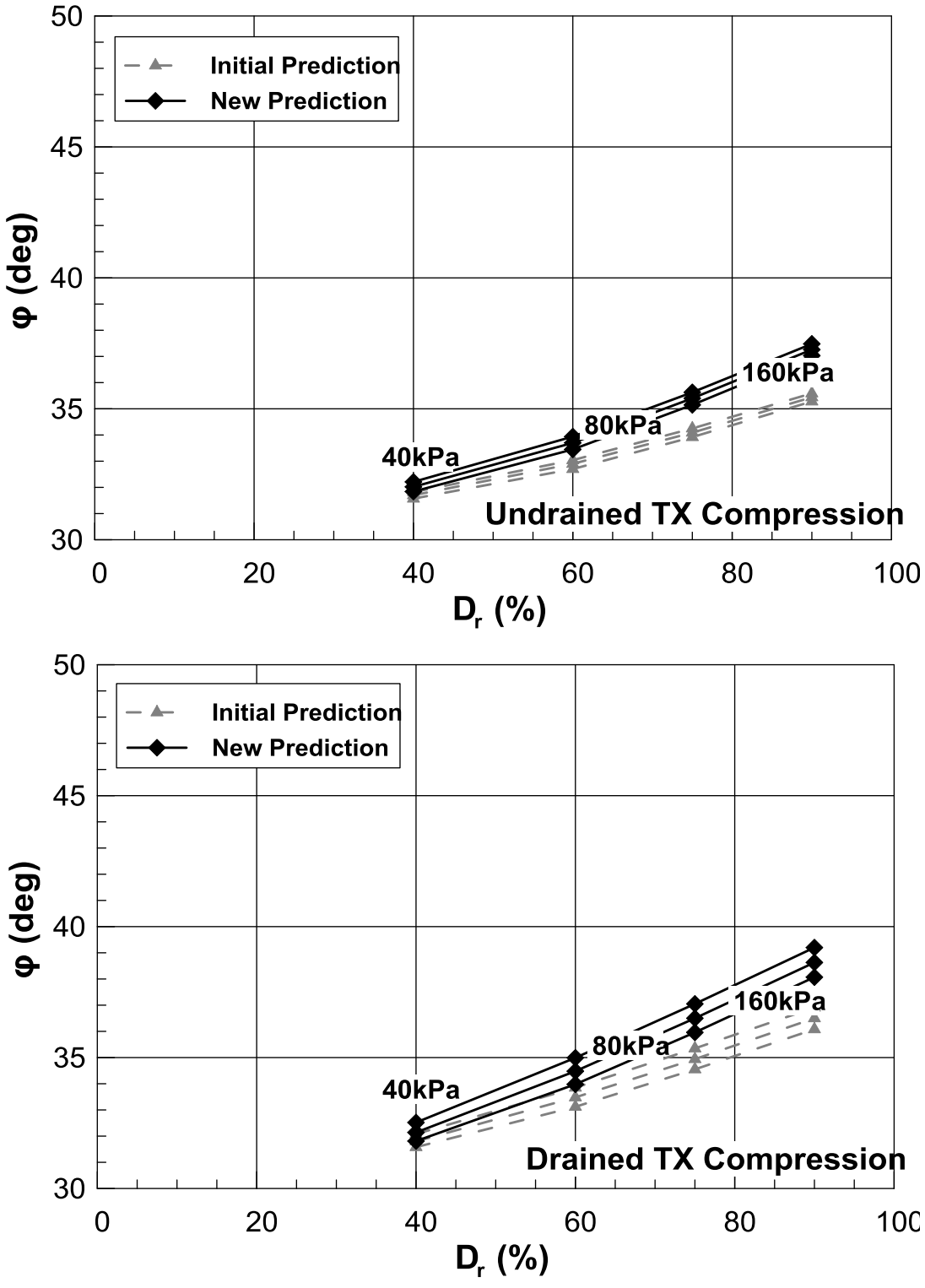

Figure B-52: Initial (dashed gray lines) and new (solid black lines) predictions of friction angle ϕ as a function of relative density D_r(%) for Triaxial Compression test simulations.

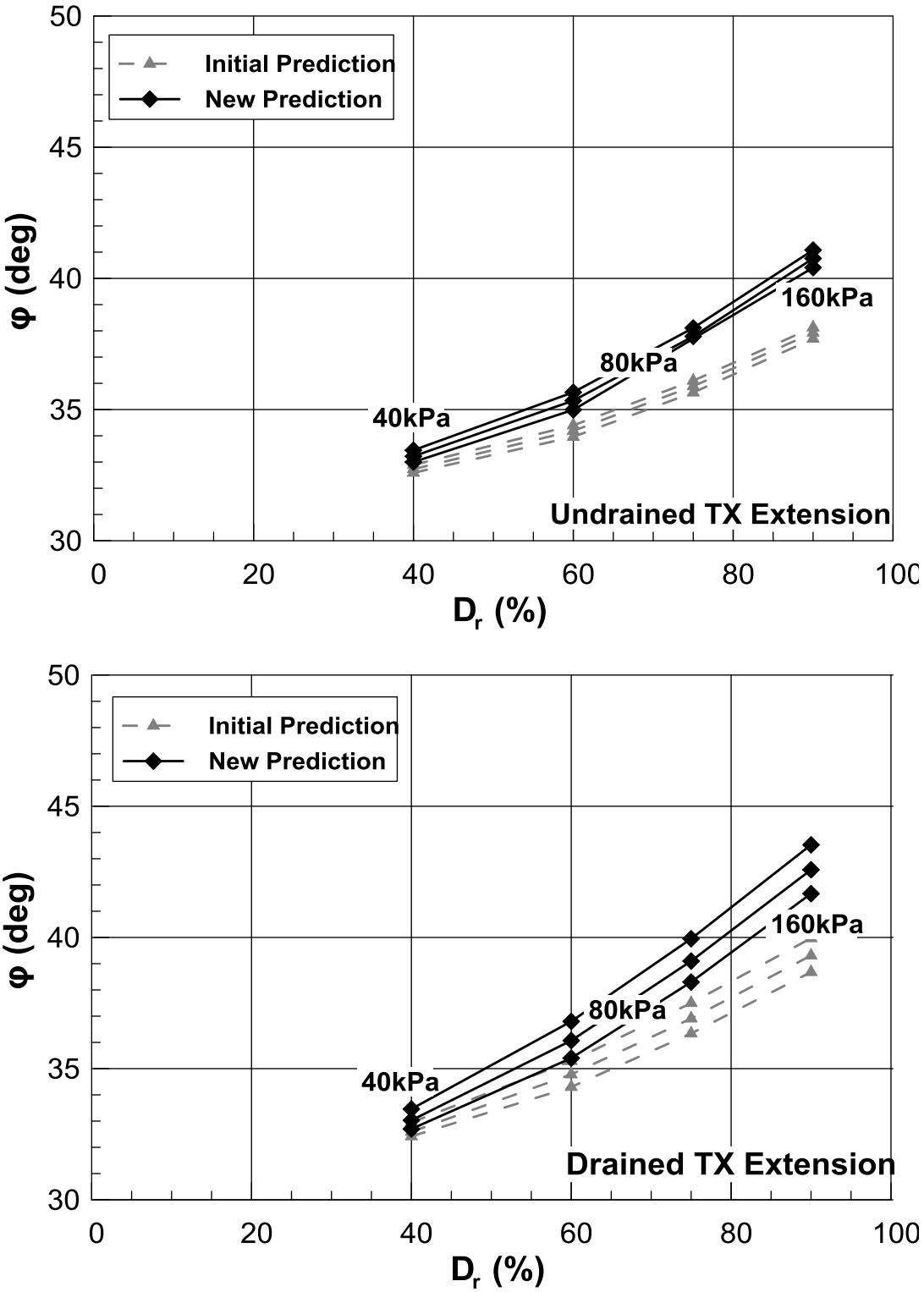

Figure B-53: Initial (dashed gray lines) and new (solid black lines) predictions of friction angle ϕ as a function of relative density D_r(%) for Triaxial Extenstion test simulations.

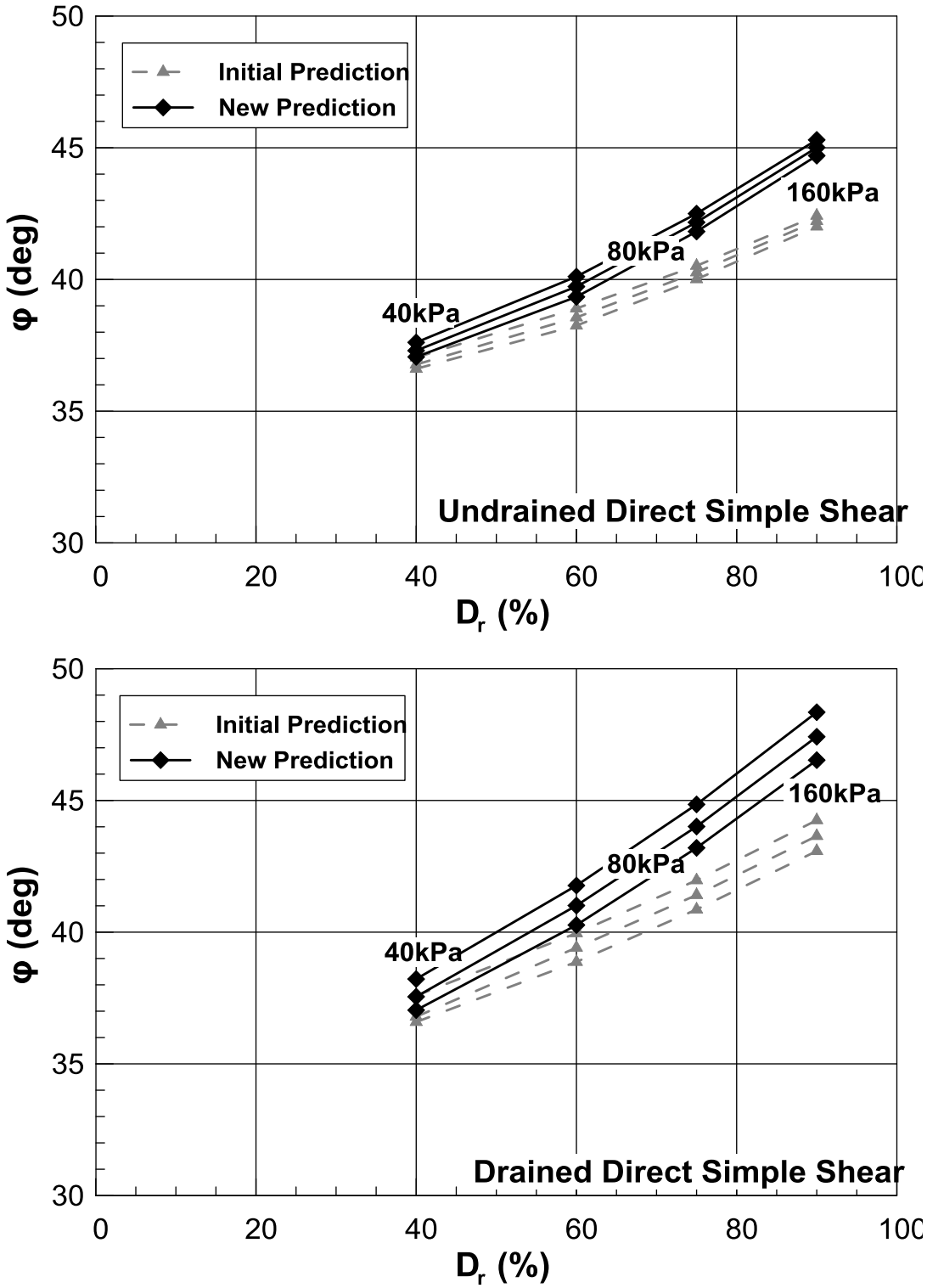

Figure B-54: Initial (dashed gray lines) and new (solid black lines) predictions of friction angle ϕ as a function of relative density D_r(%) for Simple Shear test simulations

APPENDIX C

Overview of 1-D numerical analyses - Effect of replacement ratio on excess pore pressure built-up

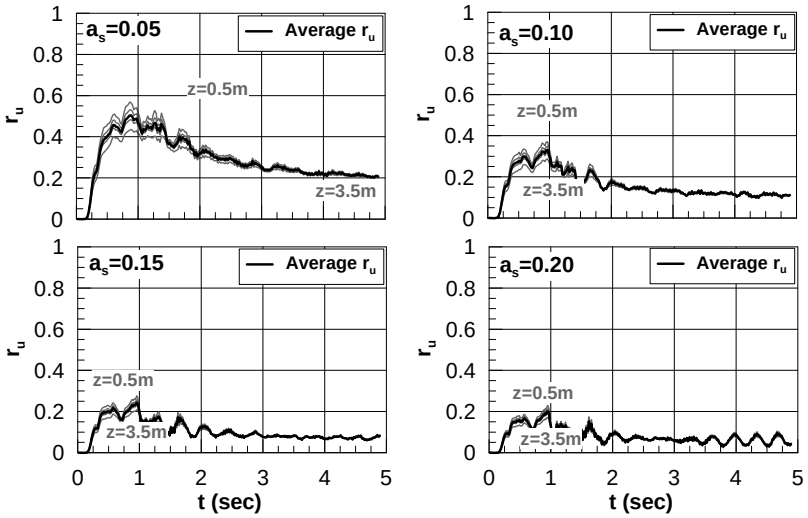

Figure C-1: r_u time histories within the improved crust for Dr_o=35%, $H_{imp.}$=4m and all α_s.

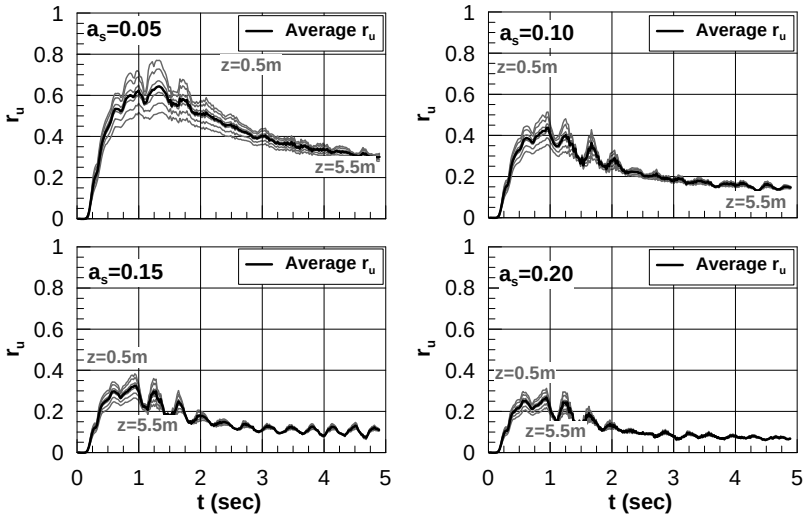

Figure C-2: r_u time histories within the improved crust for Dr_o=35%, $H_{imp.}$=6m and all α_s.

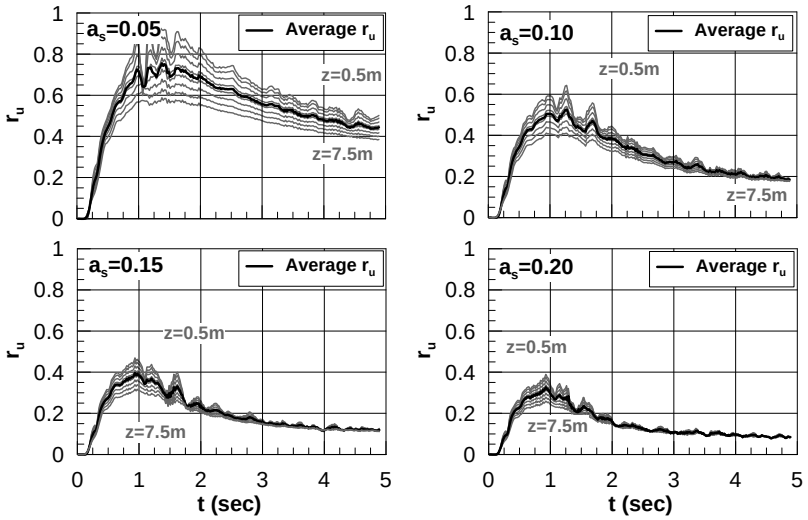

Figure C-3: r_u time histories within the improved crust for Dr_o=35%, $H_{imp.}$=8m and all α_s.

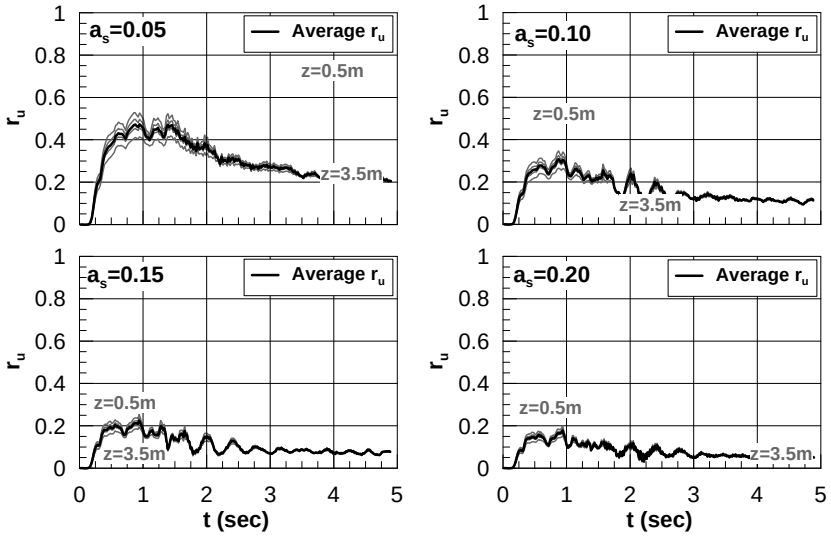

Figure C-4: r_u time histories within the improved crust for Dr_o=40%, $H_{imp.}$=4m and all α_s.

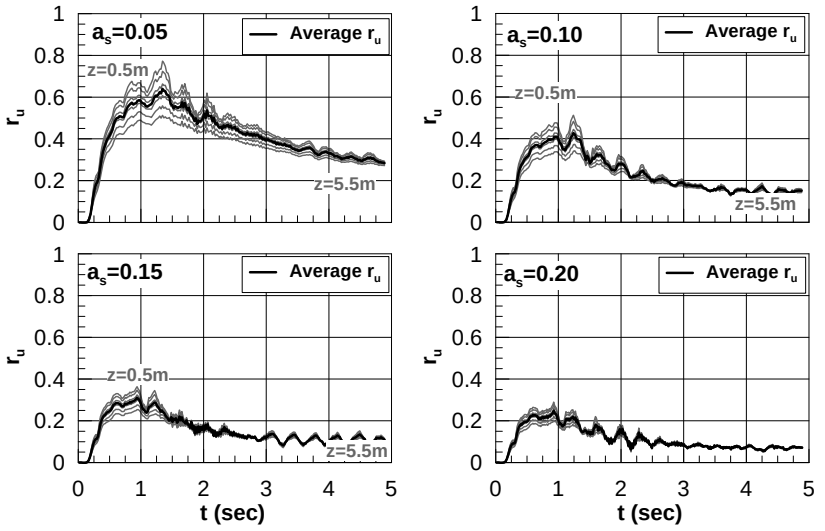

Figure C-5: r_u time histories within the improved crust for Dr_o=40%, $H_{imp.}$=6m and all α_s.

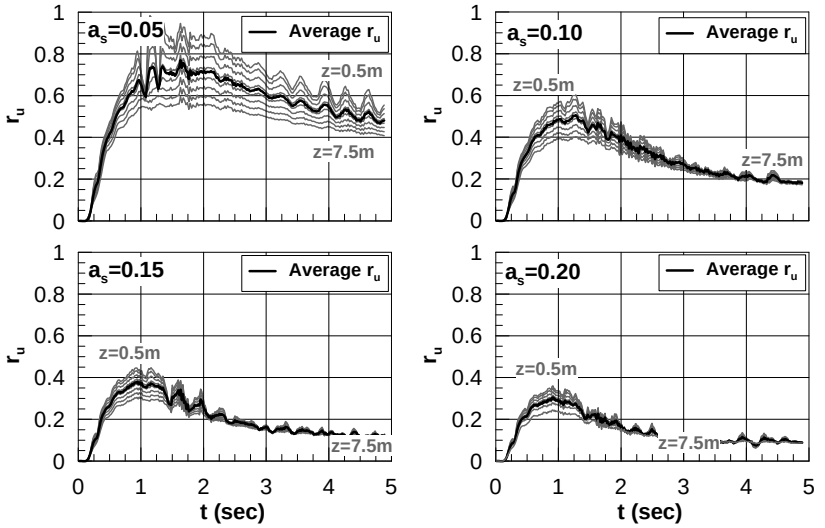

Figure C-6: $\mathbf{r_u}$ time histories within the improved crust for Dr_o=40%, $H_{imp.}$=8m and all α_s.

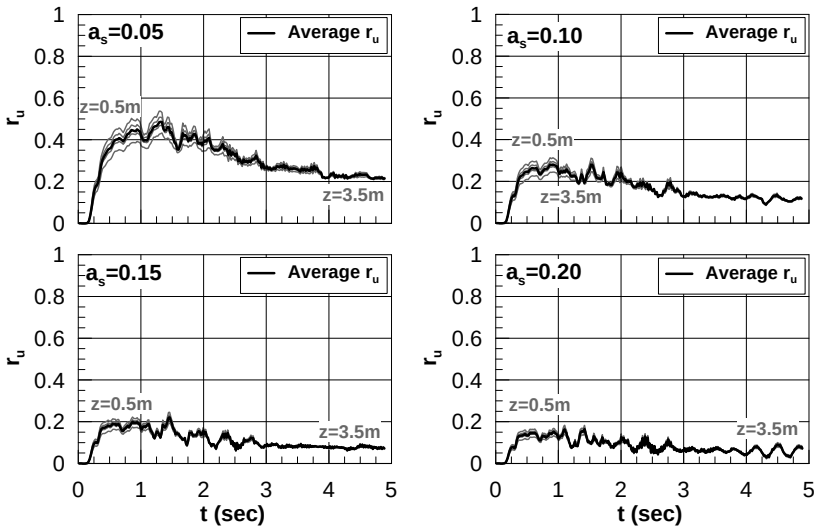

Figure C-7: r_u time histories within the improved crust for Dr_o=45%, $H_{imp.}$=4m and all α_s.

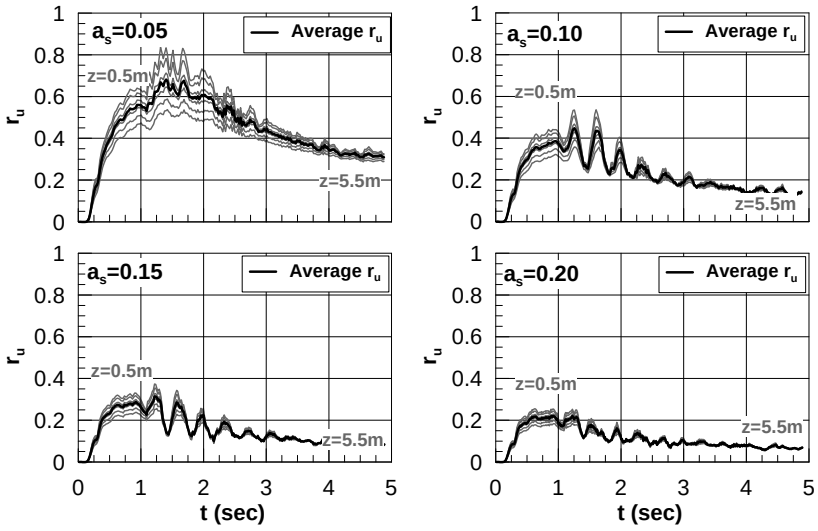

Figure C-8: r_u time histories within the improved crust for Dr_o=45%, $H_{imp.}$=6m and all α_s.

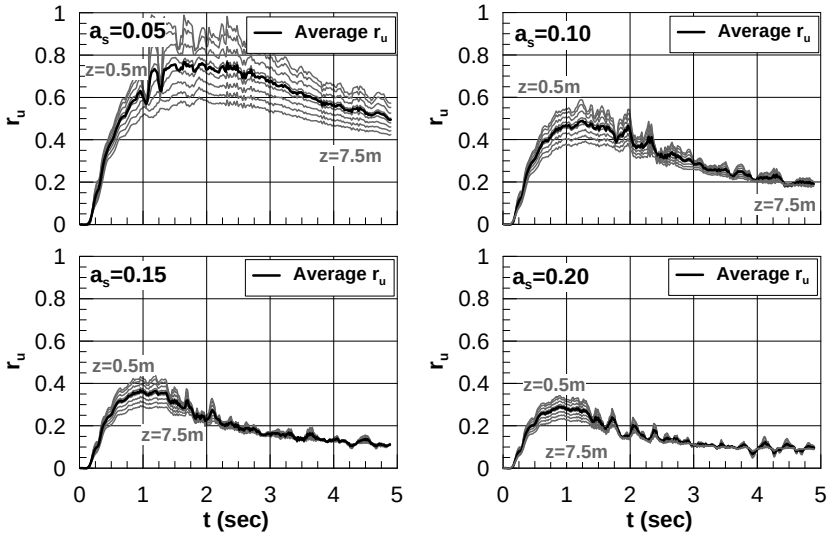

Figure C-9: r_u time histories within the improved crust for Dr_o=45%, $H_{imp.}$=8m and all α_s.

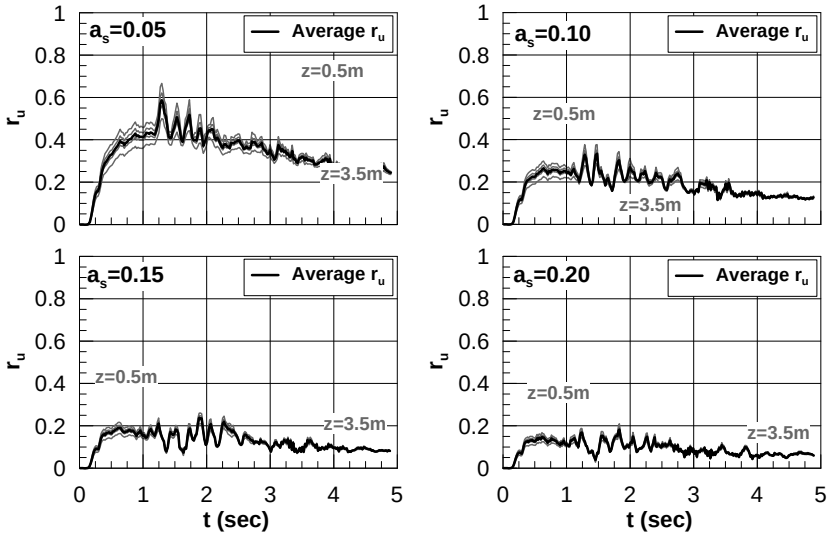

Figure C-10: r_u time histories within the improved crust for Dr_o=55%, $H_{imp.}$=4m and all α_s.

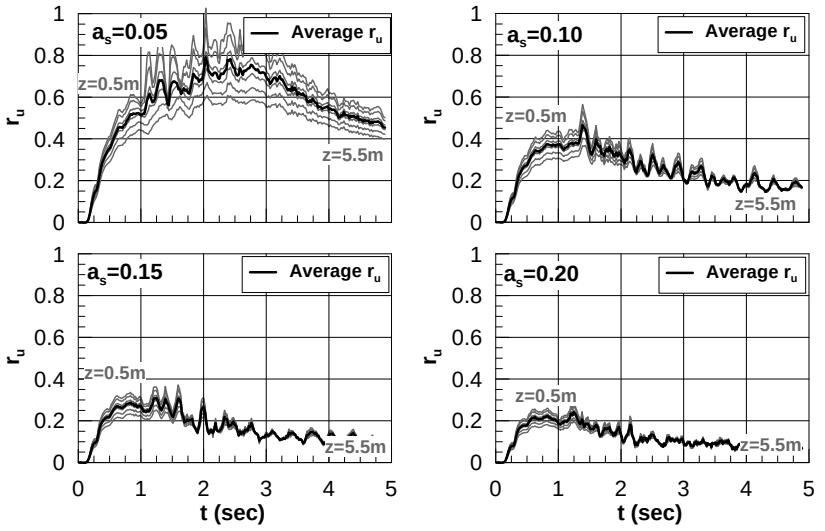

Figure C-11: r_u time histories within the improved crust for Dr_o=55%, $H_{imp.}$=6m and all α_s.

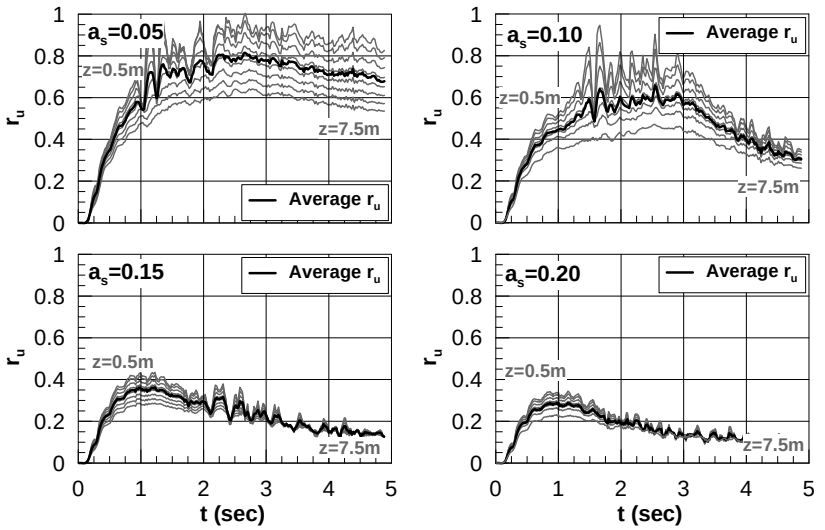

Figure C-12: r_u time histories within the improved crust for Dr_o=55%, $H_{imp.}$=8m and all α_s.

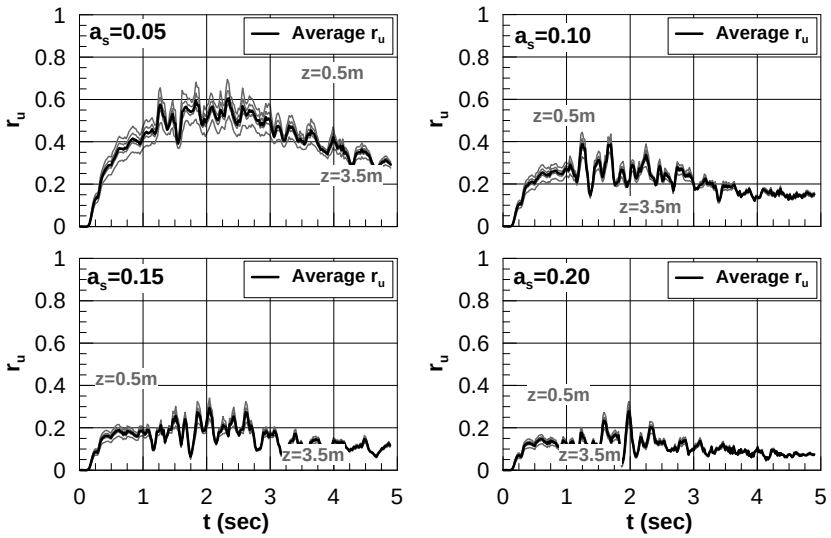

Figure C-13: r_u time histories within the improved crust for Dr_o=65%, $H_{imp.}$=4m and all α_s.

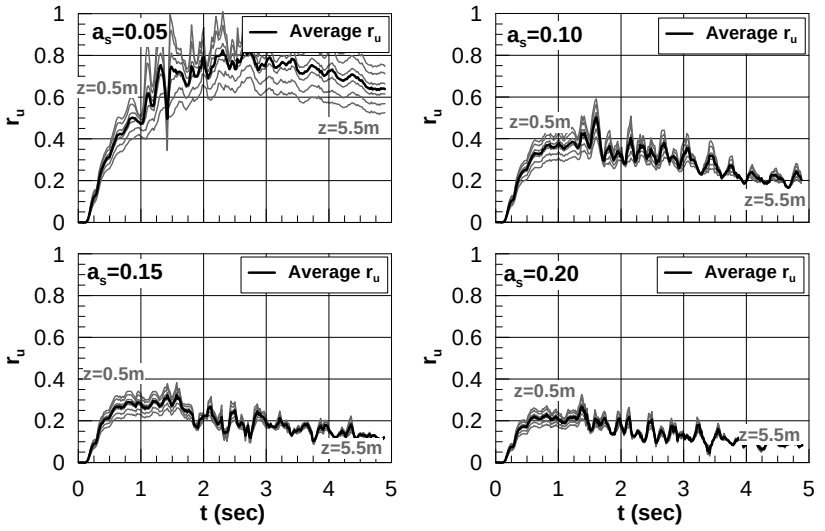

Figure C-14: r_u time histories within the improved crust for Dr_o=65%, $H_{imp.}$=6m and all α_s.

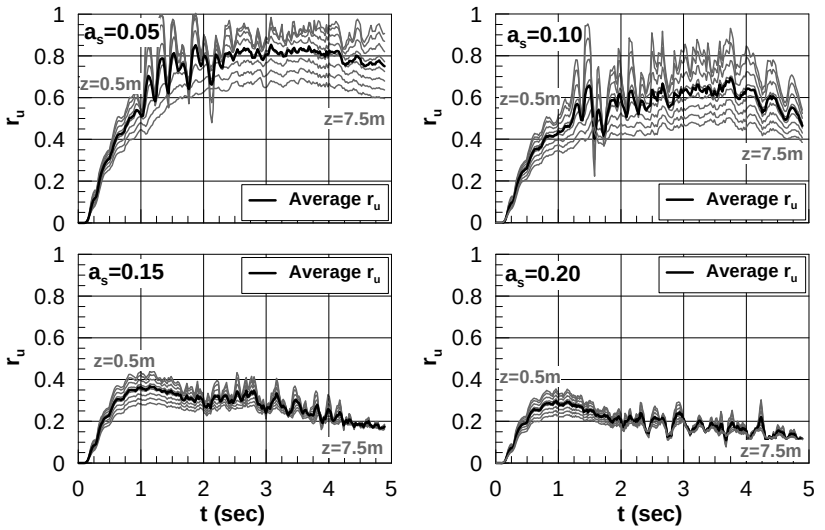

Figure C-15: r_u time histories within the improved crust Dr_o=65%, $H_{imp.}$=8m and all α_s.

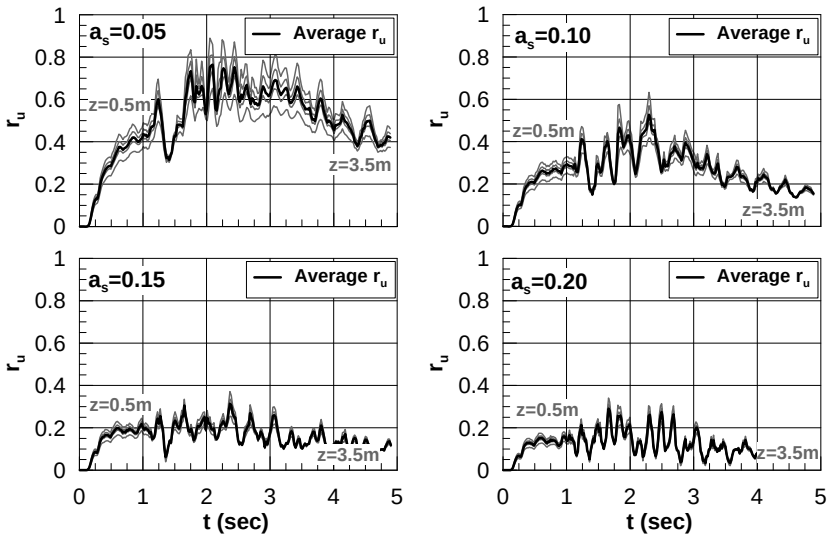

Figure C-16: r_u time histories within the improved crust for Dr_o=70%, $H_{imp.}$=4m and all α_s.

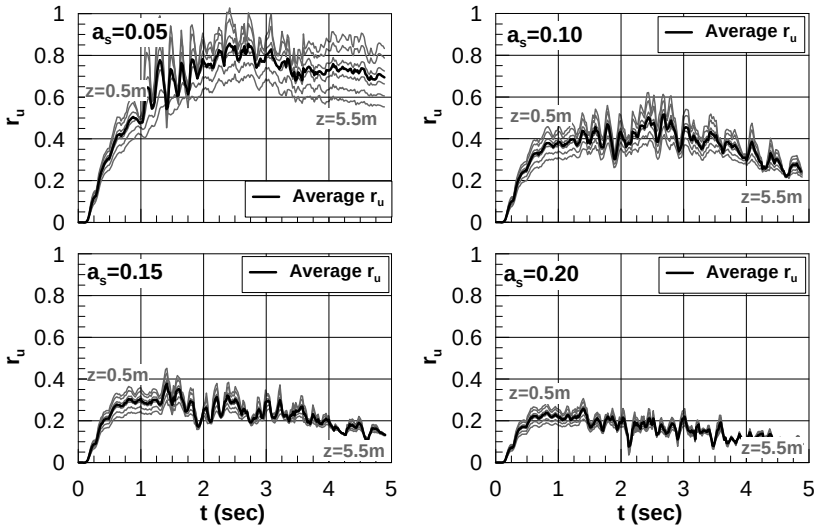

Figure C-17: r_u time histories within the improved crust for Dr_o=70%, $H_{imp.}$=6m and all α_s.

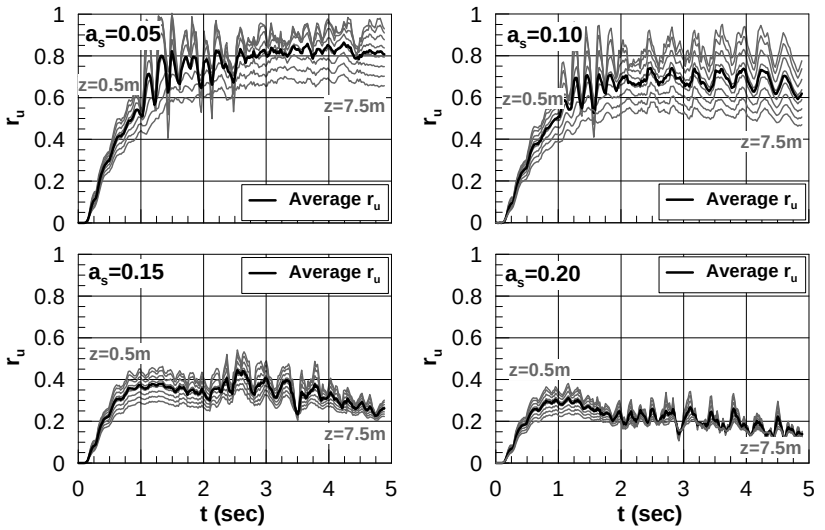

Figure C-18: r_u time histories within the improved crust for Dr_o=70%, $H_{imp.}$=8m and all α_s.